FLUID MECHANICS AND ITS APPLICATIONS

Rama Govindarajan (Ed.)

Sixth IUTAM Symposium on Laminar-Turbulent Transition

Springer

Sixth IUTAM Symposium on Laminar-Turbulent Transition

FLUID MECHANICS AND ITS APPLICATIONS
Volume 78

Series Editor: R. MOREAU
MADYLAM
Ecole Nationale Supérieure d'Hydraulique de Grenoble
Boîte Postale 95
38402 Saint Martin d'Hères Cedex, France

Aims and Scope of the Series

The purpose of this series is to focus on subjects in which fluid mechanics plays a fundamental role.

As well as the more traditional applications of aeronautics, hydraulics, heat and mass transfer etc., books will be published dealing with topics which are currently in a state of rapid development, such as turbulence, suspensions and multiphase fluids, super and hypersonic flows and numerical modelling techniques.

It is a widely held view that it is the interdisciplinary subjects that will receive intense scientific attention, bringing them to the forefront of technological advancement. Fluids have the ability to transport matter and its properties as well as transmit force, therefore fluid mechanics is a subject that is particulary open to cross fertilisation with other sciences and disciplines of engineering. The subject of fluid mechanics will be highly relevant in domains such as chemical, metallurgical, biological and ecological engineering. This series is particularly open to such new multidisciplinary domains.

The median level of presentation is the first year graduate student. Some texts are monographs defining the current state of a field; others are accessible to final year undergraduates; but essentially the emphasis is on readability and clarity.

For a list of related mechanics titles, see final pages.

Sixth IUTAM Symposium on Laminar-Turbulent Transition

Proceedings of the Sixth IUTAM Symposium
on Laminar-Turbulent Transition, Bangalore, India, 2004

Edited by

RAMA GOVINDARAJAN
Jawaharlal Nehru Centre for Advanced Scientific Research,
Engineering Mechanics Unit,
Bangalore, India

Springer

A C.I.P. Catalogue record for this book is available from the Library of Congress.

ISBN-10 1-4020-3459-8 (HB)
ISBN-13 978-1-4020-3459-6 (HB)
ISBN-10 1-4020-4159-4 (e-book)
ISBN-13 978-1-4020-4159-4 (e-book)

Published by Springer,
P.O. Box 17, 3300 AA Dordrecht, The Netherlands.

www.springer.com

Printed on acid-free paper

Printed in the Netherlands.

Contents

INVITED LECTURES

INSTABILITY I

Chairman: R. Narasimha

INSTABILITY II

Chairman: Wolfgang Rodi

INSTABILITY III

Chairman: Leonhard Kleiser

INSTABILITY IV

Chairman: Christopher Davies

INSTABILITY V

Chairman: Jonathan Healey

INSTABILITY VI

Chairman: Tom Mullin

FLOW CONTROL I

Chairman: Daniel Arnal

FLOW CONTROL II

Chairman: Vassilios Theofilis

FLOW CONTROL III

Chairman: Nobutake Itoh

TRANSITION I
Chairman: Yu Fukunishi

TRANSITION II
Chairman: PK Sen

TRANSITION III
Chairman: V Kozlov

TRANSITION IV
Chairman: Ulrich Rist

TRANSITION V

Chairman: Yasuaki Kohama

COMPRESSIBLE FLOW

Chairman: Zhou Heng

CROSS FLOW

Chairman: Ardeshir Hanifi

SEPARATED FLOW

Chairman: PR Viswanath

POSTER SESSION

Chairman: Ishikawa

Preface

The dynamics of transition from laminar to turbulent flow remains to this day a major challenge in theoretical and applied mechanics. A series of IUTAM symposia held over the last twenty five years at well-known Centres of research in the subject - Novosibirsk, Stuttgart, Toulouse, Sendai and Sedona (Arizona) - has proved to be a great catalyst which has given a boost to research and our understanding of the field. At this point of time, the field is changing significantly with several emerging directions.

The sixth IUTAM meeting in the series, which was held at the Jawaharlal Nehru Centre for Advanced Scientific Research, Bangalore, India, focused on the progress after the fifth meeting held at Sedona in 1999. The symposium, which adhered to the IUTAM format of a single session, included seven invited lectures, fifty oral presentations and eight posters.

During the course of the symposium, the following became evident. The area of laminar-turbulent transition has progressed considerably since 1999. Better theoretical tools, for handling nonlinearities as well as transient behaviour are now available. This is accompanied by an enormous increase in the level of sophistication of both experiments and direct numerical simulations. The result has been that our understanding of the early stages of the transition process is now on much firmer footing and we are now able to study many aspects of the later stages of the transition process. Consequently, considerable light was thrown during the symposium on, e.g., the role of streamwise streaks, flow separation, complex geometry, turbulent spots etc. We are also now capable of better approaches to flow control. The immediate future is likely to see important advances in this area and it is hoped that the symposium has added momentum to this effort.

I am most grateful to the scientific committee for their very active role and detailed advice at every stage. Professor R Narasimha has been involved in each single aspect of the symposium, I am indebted to him for his constant support and guidance. The constant contribution of the organising committee is highly appreciated. It was our good fortune that Anjana Krishnaswamy joined us, she has looked after every detail of both the symposium and of this proceedings in the most professional and

meticulous way. I am very touched by the selfless labour put in by the support group, and their high standards, special mention must be made of Faraz Mehdi. All the sponsors are gratefully acknowledged for making the symposium possible. Special thanks to Major Tony Mitchell of AFOSR/AOARD for his encouragement and support. Sincere thanks to the IUTAM. The Pratt and Whitney – A United Technologies Company, Dr. Jayant Sabnis, Dr. Kirit Patel and Dr. TK Vashist have been a constant and important source of support and encouragement. This conference would not have been a success without their active participation.

The facilities and logistics support provided by Jawaharlal Nehru Centre for Advanced Scientific Research is gratefully acknowledged, special thanks to Mr. Jayachandra and his team. Most important, we thank all the authors, session chairmen and all the participants, whose active involvement and contributions defined the conference. Finally, I acknowledge Kluwer-Springer for printing the proceedings.

Countries represented and number of participants

The meeting attracted 113 participants from 15 countries:

Brazil (1)	Canada (1)	China (2)
France (5)	Germany (9)	India (49)
Israel (2)	Japan (12)	Malaysia (1)
Russia (4)	Spain (1)	Sweden (6)
Switzerland (3)	The Netherlands (1)	United Kingdom (11)
USA (5)		

IUTAM Symposium on Laminar-Turbulent Transition, December 13–17, 2004, Bangalore, INDIA

Scientific Committee

Local Organizing Committee

Prof. Rama Govindarajan (Chair)
Engineering Mechanics Unit
Jawaharlal Nehru Centre for Advanced Scientific Research
Bangalore, India.

Prof. Roddam Narasimha (IUTAM Representative)
Engineering Mechanics Unit
Jawaharlal Nehru Centre for Advanced Scientific Research
Bangalore, India.

Dr. Kishore Kumar
Gas Turbine Research Establishment
Bangalore, India

Dr. Sanjay Mittal
Indian Institute of Technolgy
Kanpur, India

Dr. O. N. Ramesh
Indian Institute of Science
Bangalore, India

Prof. P. K. Sen
Indian Institute of Technolgy
Delhi, India

Dr. K. P. Singh
Aeronautical Development Agency
Bangalore, India

Dr. P. R. Viswanath
National Aerospace Laboratories
Bangalore, India

Support Personnel

Anjana (also involved in editorial help)
Faraz Mehdi
Ganesh
Kaushik Srinivasan
Kirti
Manikandan Mathur
Mukund
Om Prakash
Pinaki
Punit
Sachin Belavadi
Sameen
Saritha Azad
Shreyas
Srevatsan
Vijay Kumar
Vinod

Symposium Sponsors

We wish to thank the following for their contribution to the success of this conference:

- International Union of Theoretical and Applied Mechanics (IUTAM)
- Pratt & Whitney, A United Technologies Company, UTC Shared Business Services, Windsor, CT - USA
- Air Force Office of Scientific Research, Asian Office of Aerospace Research and Development, Tokyo, Japan

[**Disclaimer:** AFOSR/AOARD support is not intended to express or imply endorsement by the U.S. Federal Government.]

- Jawaharlal Nehru Centre for Advanced Scientific Research, Bangalore, India
- Council of Scientific and Industrial Research, Human Resource Development Group, New Delhi, India
- Kluwer-Springer Academic Publishers, Netherlands.
- Defence Research & Development Organisation, Government of India
- Indian National Science Academy, New Delhi, India
- Department of Science and Technology, Ministry of Science & Technology, Government of India
- Hitech Engineering Equipments, Bangalore, India
- Real Time Tech Solutions, Private Limited, Bangalore, India

IUTAM Symposium on Laminar-Turbulent Transition
Jawaharlal Nehru Centre for Advanced Scientific Research
Bangalore, India, December 13-17 2004

List of Participants

Name	Email	Affiliation
SK Anjana	anjana@jncasr.ac.in	Jawaharlal Nehru Centre, Bangalore, India
Jaywant Arakeri	jaywant@mecheng.iisc.ernet.in	Indian Institute of Science, Bangalore, India
Daniel Arnal	Daniel.Arnal@onecert.fr	ONERA, Toulouse, France
Masahito Asai	masai@cc.tmit.ac.jp	Tokyo Metropolitan Inst. of Tech., Japan
Sarita Azad	sarita_azad@yahoo.com	Jawaharlal Nehru Centre, Bangalore/Delhi Coll.of Eng., India
Pinaki Bhattacharya	pinakib@jncasr.ac.in	Jawaharlal Nehru Centre, Bangalore, India
Luca Brandt	luca@mech.kth.se	KTH Mechanics, Stockholm, Sweden
Michael Broadhurst	Michael.broadhurst@imperial.ac.uk	Imperial College, London, UK
Peter W Carpenter	pwcx@eng.warwick.ac.uk	Univ. of Warwick, UK
Gregoire Casalis	casalis@onecert.fr	ONERA, Toulouse, France
Mattias Chevalier	mattias.chevalier@foi.se	FOI, Sweden
Vijaykumar Chikkadi	vijay@jncasr.ac.in	Jawaharlal Nehru Centre, Bangalore, India
Paresh Chokshi	paresh_chox@yahoo.com	Indian Institute of Science, Bangalore, India
Meelan Choudhari	m.m.choudhari@larc.nasa.gov	NASA Langley Res. Centre, Hampton, USA
Jeffrey D Crouch	jeffrey.d.crouch@boeing.com	Boeing Comm. Airplane Co. Seattle, USA
Shyama Prasad Das	spdas@mecheng.iisc.ernet.in	Indian Institute of Science, Bangalore, India
Christopher Davies	daviesC9@cf.ac.uk	Cardiff Univ., Wales, UK
MD Deshpande	mdd@ctfd.cmmacs.ernet.in	National Aerospace Labs., Bangalore, India
J Dey	jd@aero.iisc.ernet.in	Indian Institute of Science, Bangalore, India
PK Dutta	pkd@ctfd.cmmacs.ernet.in	National Aerospace Labs., Bangalore, India
Lt. Col. T Erstfeld	Thomas.Erstfeld@aoard.af.mil	AOARD, AFOSR, Tokyo, Japan
Hermann Fasel	faselh@u.arizona.edu	Univ. of Arizona, Tucson, USA
Jens H Fransson	jensf@mech.kth.se	KTH Mechanics, Stockholm, Sweden
Yu Fukunishi	fushi@fluid.mech.tohoku.ac.jp	Tohoku Univ., Sendai, Japan
Jitesh Gajjar	gajjar@maths.man.ac.uk	Univ. of Manchester, UK
Mike Gaster	m.gaster@qmul.ac.uk	Queen Mary, Univ. of London, UK
J Paul Gostelow	jpg7@leicester.ac.uk	Univ. of Leicester, UK
Raghuram Goverdhan	raghu@mecheng.iisc.ernet.in	Indian Institute of Science, Bangalore, India

Rama Govindarajan	rama@jncasr.ac.in	Jawaharlal Nehru Centre, Bangalore, India
Ganesh Gurumurthy	ganesh@jncasr.ac.in	Indian Inst. of Technology, Chennai, India
Ardeshir Hanifi	ardeshir.hanifi@foi.se	Swedish Defence Res. Agency, FOI, Stockholm, Sweden
Jonathan Healey	j.j.healey@maths.keele.ac.uk	Keele Univ., Keele, UK
Sriram Hegde	hegde@am.iitd.ernet.in	Indian Inst. of Technology, Delhi, India
Stefan Hein	stefan.hein@dlr.de	DLR, Gottingen, Germany
Dan Henningson	henning@mech.kth.se	KTH Mechanics, Stockholm, Sweden
Tilmann Hetsch	hetsch@iag.uni-stuttgart.de	Univ. Stuttgart, Germany
Jerome Hoepffner	jerome@mech.kth.se	KTH Mechanics, Stockholm, Sweden
Bjorn Hof	b.hof@wbmt.tudelft.nl	TU-Delft, The Netherlands
Naoko Ishikawa	tokugawa.naoko@jaxa.jp	Japan Aero. Exploration Agency, Japan
Nobutake Itoh	itohnobu@home.email.ne.jp	Japan Aero. Exploration Agency, Japan
Seiichiro Izawa	seiizawa@yahoo.co.jp	Tohoku Univ., Sendai, Japan
Pranav R Joshi	jpranavr@mecheng.iisc.ernet.in	Indian Institute of Science, Bangalore, India
Toshiaki Kenchi	t04h410@amail.shinshu-u.ac.jp	Shinshu Univ., Nagano, Japan
Leonhard Kleiser	kleiser@ifd.mavt.ethz.ch	Inst. of Fluid Dynamics, ETH, Zurich, Switzerland
Yasuaki Kohama	kohama@ltwt.ifs.tohoku.ac.jp	Tohoku Univ., Sendai, Japan
Vladimir Kosorygin	kosor@itam.nsc.ru	Inst. of Theoretical and Applied Mech., Novosibirsk, Russia
Victor Kozlov	kozlov@itam.nsc.ru	Inst. of Theoretical and Applied Mech., Novosibirsk, Russia
LN Krishnan	krishnan@soton.ac.uk	Univ. of Southampton, UK
V Krishnan	krishnan@aimst.edu.my	Asian Inst. of Med., Sci. and Tech., Malaysia
Kishore Kumar	kishorkumars@mail.gtre.org	Gas Turbine Res. Establishment, Bangalore, India
V Kumaran	kumaran@chemeng.iisc.ernet.in	Indian Institute of Science, Bangalore, India
Patrice Le Gal	partice.legal@irphe.univ-mrs.fr	IRPHE-CNRS, Marseille, France
Jisheng Luo	jishengl@public.tpt.tj.cn	Tianjin Univ., China
Sekhar Majumdar	sekhar@ctfd.cmmacs.ernet.in	National Aerospace Labs., Bangalore, India
M Malik	malik@aero.iisc.ernet.in	Indian Institute of Science, Bangalore, India
AC Mandal	alakesh@aero.iisc.ernet.in	Indian Institute of Science, Bangalore, India
Masaharu Matsubara	mmatsu@shinshu-u.ac.jp	Shinshu Univ., Nagano, Japan
Manikandan Mathur	manikandan@jncasr.ac.in	Jawaharlal Nehru Centre, Bangalore, India
Bijoy Mazumder	bsm46@yahoo.com	Indian Statistical Institute, Kolkata, India

Marcello A Medeiros	marcello@sc.usp.br	Universidade de Sao Paulo, Brazil
Rajat Mittal	mittal@gwu.edu	The George Washington University, Washington DC, USA
Sanjay Mittal	smittal@iitk.ac.in	Indian Inst. of Technology, Kanpur, India
Albert Mosyak	mealbmo@techunix.technion.ac.il	Technion University, Haifa, Israel
VY Mudkavi	vym@ctfd.cmmacs.ernet.in	National Aerospace Labs., Bangalore, India
R Mukund	mukund@ead.cmmacs.ernet.in	National Aerospace Labs., Bangalore, India
Thomas Mullin	tom.mullin@man.ac.uk	Univ. of Manchester, UK
Srevatsan Muralidharan	srevatsan@jncasr.ac.in	Indian Institute of Technology, Chennai, India
Amador Muriel	Amador.Muriel@cern.ch	ICSC World Laboratory, Geneve, Switzerland
S.V. Ramana Murthy		Gas Turbine Res. Establishment, Bangalore, India
Roddam Narasimha	roddam@jncasr.ac.in	Jawaharlal Nehru Centre, Bangalore, India
Lian L Ng	lian.l.ng@pss.Boeing.com	Boeing Comm. Airplane Co. Seattle, USA
Manmohan Pandey	manmohan@iitg.ernet.in	Indian Inst. of Technology, Guwahati, India
Kirit Patel	Kirit.Patel@pwc.ca	Pratt & Whitney Corp. Canada
Inken Peltzer	inken.peltzer@tu-berlin.de	TU-Berlin, Germany
Ajay Pratap		Gas Turbine Res. Establishment, Bangalore, India
Baburaj Puthenveettil	apbabu@mecheng.ernet.in	Indian Institute of Science, Bangalore, India
Rajesh K	rajesh21stcentury@yahoo.com	Indian Inst. of Technology, Guwahati, India
ON Ramesh	onr@aero.iisc.ernet.in	Indian Institute of Science, Bangalore, India
Pierre Ricco	pierre.ricco@imperial.ac.uk	Imperial College, London, UK
Ulrich Rist	rist@iag.uni-stuttgart.de	Univ. Stuttgart, Germany
Jean-Christophe Robinet	robinet@paris.ensam.fr	SINUMEF Laboratory, Paris, France
Wolfgang Rodi	rodi@uka.de	University of Karlsruhe, Germany
Kirti Chandra Sahu	kirti@jncasr.ac.in	Jawaharlal Nehru Centre, Bangalore, India
A Sameen	sameen@jncasr.ac.in	Indian Institute of Science, Bangalore, India
Dieter Sartorius	dieter.sartorius@iag.uni-stuttgart.de	Universitat Stuttgart, Germany
Philipp Schlatter	schlatter@ifd.mavt.ethz.ch	Inst. of Fluid Dynamics, ETH Zurich, Switzerland
Nikolai Semionov	semion@itam.nsc.ru	Inst. of Theoretical and Applied Mech., Novosibirsk, Russia
P. K. Sen	pksen@am.iitd.ernet.in	Indian Institute of Technology, Delhi, India
Rajeswari Seshadri	oviaraji@yahoo.com	Bangalore, India

Joern Sesterhenn	jls@flm.mw.tum.de	TU Munchen, Germany
Shreyas	shreyas@jncasr.ac.in	Jawaharlal Nehru Centre, Bangalore, India
K.P. Singh	kps2121@yahoo.com	Aero. Development Agency, Bangalore, India
Om Prakash Singh	ops@mecheng.iisc.ernet.in	Indian Institute of Science, Bangalore, India
K. R. Sreenivas	krs.jncasr.ac.in	Jawaharlal Nehru Centre, Bangalore, India
Kaushik Srinivasan	kaushik@jncasr.ac.in	Jawaharlal Nehru Centre, Bangalore, India
Usha Srinivasan	usha@mecheng.iisc.ernet.in	Indian Institute of Science, Bangalore, India
Christian Stemmer	christian.stemmer@ism.mw.tu-dresden.de	TU Dresden, Germany
Gilles Studer	gilles.studer@onecert.fr	ONERA Toulouse, France
Shohei Takagi	pantaka@nal.go.jp	Japan Aero. Exploration Agency, Japan
Vassilios Theofilis	vassilis@torroja.dmt.upm.es	Universidad Politecnica de Madrid, Spain
Anurag Thripathi	anurag.tripathi@tatasteel.com	Tata Steel, Jamshedpur, India
Punit Tiwari	punit@jncasr.ac.in	Jawaharlal Nehru Centre, Bangalore, India
Maxim Ustinov	ustinov@stb.aerocenter.msk.su	Central Aero-Hydrodynamic Inst. (TsAGI), Russia
TK Vashist	tkvashist@yahoo.com	Infotech Enterprises, Bangalore, India
V Vasanta Ram	vvr@lstm.ruhr-uni-bochum.de	Ruhr Univ., Bochum, Germany
Mukund Vasudevan	mukund@jncasr.ac.in	Jawaharlal Nehru Centre, Bangalore, India
N Vinod	nvinod@jncasr.ac.in	Jawaharlal Nehru Centre, Bangalore, India
P. R. Vishwanath	vish@ead.cmmacs.ernet.in	National Aerospace Labs., Bangalore, India
Ao-Kui Xiong	xiong@fluid.mech.tohoku.ac.jp	Tohoku Univ., Sendai, Japan
Xuesong Wu	x.wu@ic.ac.uk	Imperial College, London, UK
Shuya Yoshioka	shuya@pixy.ifs.tohoku.ac.jp	Tohoku Univ., Sendai, Japan
Tal Yehoshua	taly@eng.tau.ac.il	Tel Aviv Univ. Israel
Heng Zhou	hzhoul@tju.edu.cn	Tianjin Univ., China

LAMINAR SEPARATION BUBBLES

M. Gaster
Queen Mary University of London

Abstract: The phenomenon of leading edge stall is associated with the "bursting" of leading edge separation bubbles from a short form, where the length is roughly 100 momentum thicknesses, to a long form that maybe 1000 or more momentum thicknesses long. The paper reports experiments and theoretical discussions of work carried out by the author 50 years ago during his PhD study on bubbles. Detailed measurements of the flow within bubbles are shown together with the oscillogram traces of the velocity fluctuations present. A linear model of the stability of separated shear layers was developed that suggested that the disturbances were spatially evolving waves described by modes with complex wavenumbers and not the temporal modes usually used in stability studies. It was noted that some modes appeared to have a very small group velocity. Although at the time the full implications of this were not properly understood, the conjecture was put forward that a true instability (or absolute instability as it is now called) could therefore exist. A change in the sign of the group velocity could dramatically change the transition process and thus explain the bursting phenomenon.

1. INTRODUCTION

Aerofoils designed for extensive regions of laminar flow tend to have small leading edge radii. Such aerofoils have a very abrupt stall characteristic known as "nose stall".

This behaviour is illustrated on figure 1(a) – (c). The potential flow contains a sharp suction peak on the upper surface close to the nose. At high Reynolds numbers, the flow follows the contour closely and separates close to trailing edge. However, if the pressure distributions are examined carefully with very closely spaced pressure tapping around the nose, it is apparent that there is a very small separation bubble present that is characterised by a plateau in the distribution. Oil flow can also show that there is narrow region along the upper surface close to the leading edge

R. Govindarajan (ed.), Sixth IUTAM Symposium on Laminar-Turbulent Transition, 1–13.

where something is happening to the skin friction. On a wind tunnel model this zone maybe only 2 or 3 millimetres long. The turbulent boundary layer that forms downstream of the separated region maybe slightly thicker that that of a boundary layer that has become turbulent via a normal transition process, but this has only a slight influence on the trailing edge separation on the upper surface. Progressive reduction of flow speed will make the bubble longer, but at some stage, the bubble may "Burst" and the separated layer will cover a large portion of the upper surface. The change in flow regime from a "short" bubble to a "long" bubble results in "nose stall".

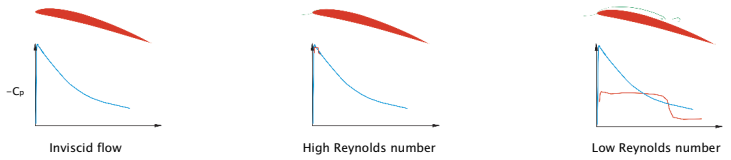

Figure 1. Nose Stall

Apart from some early reference to this behaviour it was not considered to be important until the early 1950's. Owen & Klanfer[1] noted that the short bubble occurred when the Reynolds number of the separating boundary layer was above about 400 (based on the displacement thickness), while the long bubble occurred below this value. This criterion implied that busting was controlled by the stability of the separated shear layer in some way. A number of other papers showed that this simple bursting criterion was not always applicable. Professor Piercy suggested the topic to McGregor[2] in 1951 for his PhD research and he was followed by me[3] and then by several other students. This paper focuses on my efforts during the period 1954 and 1957.

McGregor investigated leading edge bubbles on a Piercy aerofoil, successfully making some pressure distributions as well as hot-wire measurements. The bubble region was quite small and he therefore built a blunt nosed model to provide a physically larger bubble suitable for detailed probe measurements. These were certainly the first measurements of the structure of the short bubble. He did not provide any mechanism for bursting other that a suggestion that the overall energy balance within the recirculation zone could only be maintained by a large expansion of the bubble. My own efforts were directed to the study of bubbles on swept wings. Large swept models require shaped end walls to generate reasonably "infinite" swept pressure fields. An easier way of generating appropriate pressure distributions was to use a plate and auxiliary aerofoil mounted close to the surface. The aerofoil vortex together with the image will create a field

that decays like the inverse square of the distance and this reduces much of the end effects. The other advantage of this arrangement is that measurements can be made over a flat surface to a large physical scale for a range of different pressure distributions. In fact, although a swept version of this set-up was produced, I only had time to work with the two-dimensional model shown on figure 2. In order to increase the lift of the aerofoil jet blowing was incorporated.

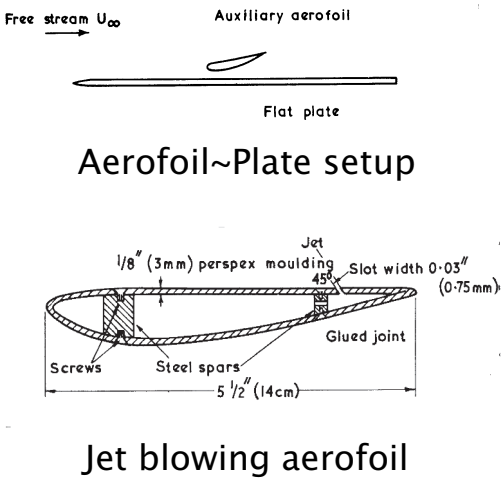

Figure 2. Windtunnel Setup

2. EXPERIMENTS

2.1 Mean Quantities

Various pressure distributions were created on the plate and the resulting separated flows explored. An example is shown on figure 3 where the pressure distributions are shown for two speeds that result in a short and a long bubble. The short bubble exhibits a flat plateau, while the lower Reynolds number long bubble shows a slight rise before transition causes the pressure to recover. This pattern is quite characteristic of a long bubble. An approximation to the inviscid pressure distribution was obtained by

measuring the pressure distribution when separation has been inhibited by tripping the boundary layer.

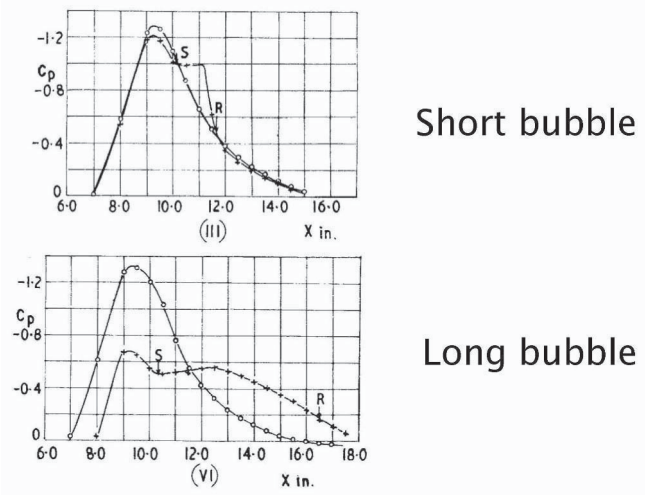

Figure 3. Pressure Distributors

A constant current hot-wire anemometer was used to explore the flow within the bubble. The wire cannot distinguish between forward or reverse flow, and it also gives incorrect mean estimates in regions of high turbulence. A set of velocity profiles for the two pressures distributions shown above are plotted on figure 4. The profiles for the long bubble are drawn with 4 times the scale thus indicating a much thicker separation bubble. This is more clearly indicted in the next figure showing contours of the mean hot-wire readings. Both pictures show an initial triangular region where the velocity, although reversed, is almost stagnant. The laminar shear layer above this region spreads very little before reaching a maximum height. At this point considerable turbulence activity occurs and the shear layer spreads out rapidly as the flow reattaches to the surface. The contour patterns in the two cases are not that dissimilar from one another for the forward part of the long and short bubbles. However, the turbulent reattachment zones are different with the long bubble zone taking a much larger portion of the bubble.

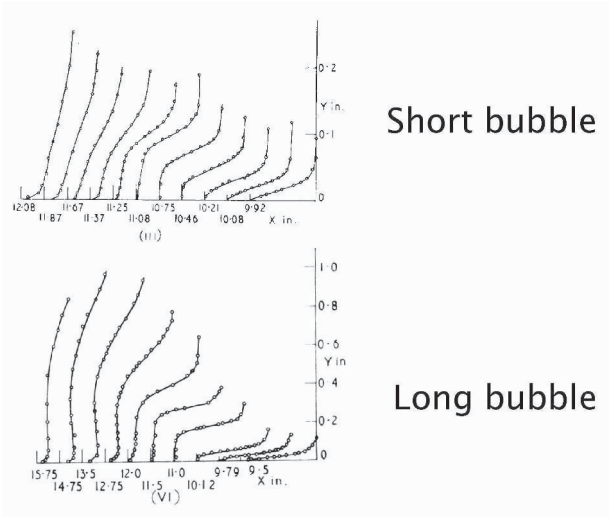

Figure 4. Velocity Profile

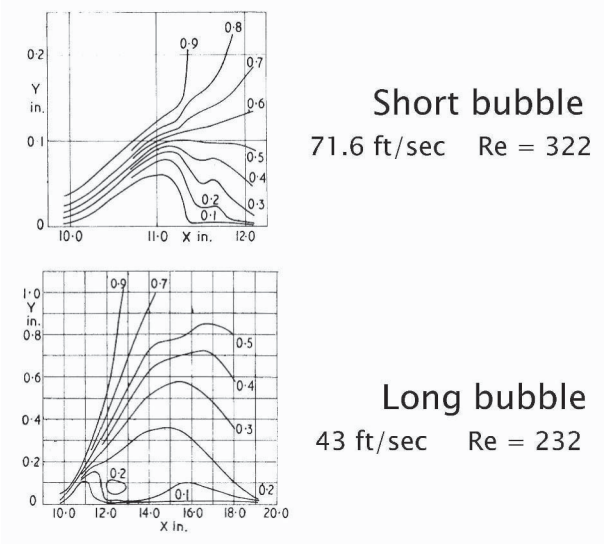

Figure 5. Contours of Hot-wire Signal

The structures of short bubbles prior to bursting as speed was reduced were studied for a range of pressure distributions. It was quite clear that the critical Reynolds number for bursting was highly dependent on the height of

the bubble amongst other parameters. Larger pressure gradients caused the bubble height to be greater and this appeared to be associated with an increase in critical Reynolds number for bursting. The height of the separated shear layer is related to the collapse in the pressure distribution arising from the displacement shape of the bubble. A suitable parameter defining this is given in terms of the pressure gradient that would have existed if there were no displacement effect. This pressure gradient scaled with the square of the momentum thickness and the viscosity is plotted against separation thickness Reynolds number at bursting on figure 6. Points from other experiments are also incorporated on the figure and show good consistency.

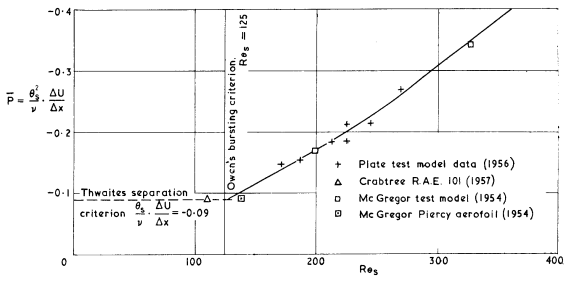

Conditions at bursting

Figure 6. Bursting Criteria

2.2 Unsteady Measurements

The signal from the hot-wire bridge, suitably amplified, provided information on the transition process taking place in the bubble. It was hoped that a careful examination of the transition processes taking place in the two types of bubble would give some clue as the reason for the phenomenon of bursting. It was noticed that short bubbles were susceptible to external excitation by sound. Even quite a weak tone of the correct frequency could excite a periodic response of the hot-wire in the separated shear layer of a short bubble. The process was so powerful that it seemed sensible to use a loud-speaker mounted on the roof of the contraction to try to excite regular waves that could then be mapped as they progressed

downstream. It was at that time known that periodic travelling waves could be generated in boundary layers. The paper of Schubauer and Skramstad[4], that had been published a few years before this work was carried out, showed that the basic instability ideas of Schlichting[5] and Tollmien[6] were substantially correct in explaining the mechanics of transition to turbulence. It seemed likely that the acoustically generated waves were of the same type and it was expected that a proper exploration of these waves in the two types of bubble would explain bursting. Initial measurements were made in a short bubble. In order to obtain the phase and amplitude of the excited wave with respect to signal feeding the speaker a rather complex sequence of operations had to be performed that involved determining the mean square of the sum and difference of the hot-wire and the loud-speaker signals. This was then repeated using a 90-degree phase shifted speaker signal. The squaring operation was carried out with a vacuum thermo-junction tube. A boundary layer traverse with the phase and amplitude is shown on figure 7. This would have taken a whole day to obtain. The phase plot is much more complex than that arising in an attached layer. Note that the outer solution shows an exponential decay for the amplitude that can be used to obtain the real part of the wavenumber, while the phase behaviour provides an estimate of the imaginary part, or spatial amplification.

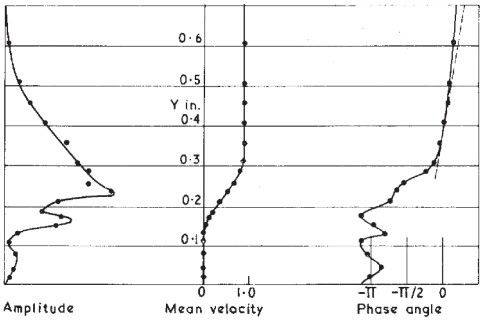

Amplitude and phase profile

Figure 7. Amplitude and Phase of Excited Wave

The whole region of a bubble was charted in this way and this is displayed on figure 8.

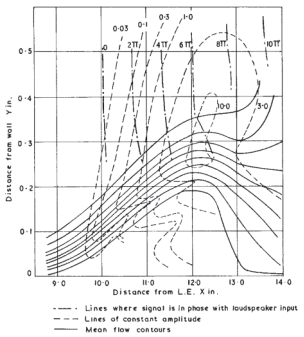

Phase and amplitude of excited waves

Figure 8. Contours of Excited Wave

Attempts to repeat these measurements on a long bubble failed because it turned out to be impossible to generate regular periodic waves in this type of flow. As this was near the end of my 3 year support it was too late to spend time in further investigation. I treated this inability to follow through my measurements to the long bubble as a failure. Hot-wire traces taken in the long bubble are shown on figure 9 without excitation and on figure 10 with periodic and pulsed excitation.

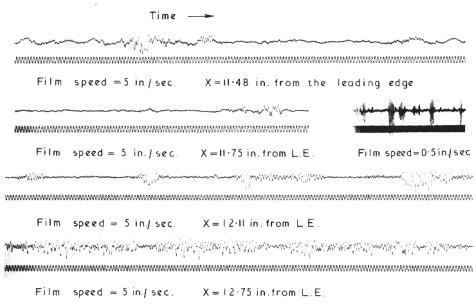

Hot-wire signals from a long bubble

Figure 9. Hot-wire Signals in a long Bubble

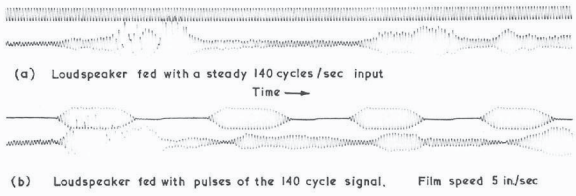

Signals from a long bubble
with continuous or pulsed excitation

Figure 10. Long Bubble Response to Periodic and Pulsed Excitation

3. STABILITY THEORY

Since experiments has shown that the separated shear layer supported unstable travelling waves it seemed sensible to address the problem of the stability of typical velocity profiles arising in a bubble. In the region of the flow where the instability waves amplified, the profiles consisted of shear layer some distance from the wall with no flow in the dead-air zone between the layer and the wall. Although Schlichting had calculated the temporal stability of Blasius flow, it was a daunting task to apply his approach to the separated profiles. A simpler approach was used on a profile modelled by three straight lines. Treating the solution in the three sectors as inviscid it was not difficult to produce a characteristic function defining the eigenmodes. In the model viscosity was included in the wall solution and curvature in the central region where there was a critical layer. Although temporal modes could easily be extracted from the characteristic function, the spatial problem was much harder to resolve. At the time it was necessary to split the equation into real and imaginary components and to find crossing points of characteristics. It was clear that the waves grew exponentially with distance travelled and not with respect to time. This was also true of the waves observed by Schubauer. In cases where the amplification factors are

weak it was shown that the two types of mode were related through the group velocity. This is of course a physically reasonably way of looking at spatial growth. However, when the imaginary components are as large it is essential to solve for real frequencies and complex wavenumbers in order to describe the appropriate solutions to the physical situation. At the time this was not an accepted procedure! The eigenvalues did not seem sensitive to Reynolds number and it was unclear how the Reynolds number could have any influence on the stability and thus be linked to bursting. Figure 11 shows the real eigenvalues for a profile close to that of figure 7 together with experimental measurements. The imaginary components also agreed roughly with the predictions.

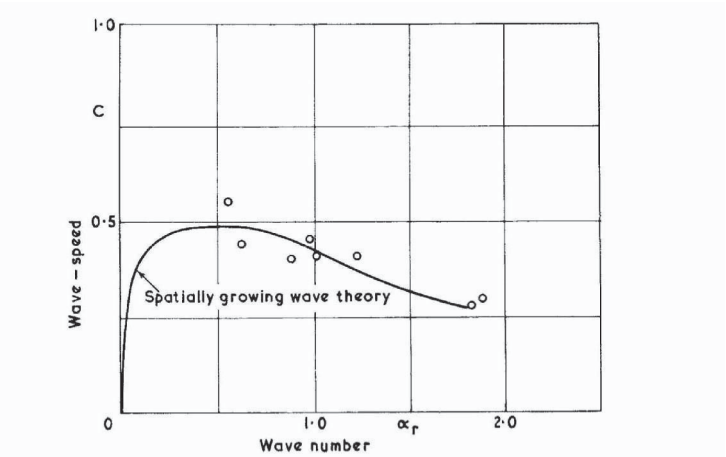

Figure 11. Comparison of Theoretical and Experimental Eigenvalues

4. DISCUSSION

Measurements of the flow patterns within bubbles provide some indication of the structure. At separation the shear layer detaches from the surface. At some distance downstream the instability of the shear layer

causes it to become turbulent, then rapid mixing creates a reverse flow vortex and the shear layer reattaches to the surface as a turbulent boundary layer. Long bubbles appear quite similar to short bubbles except that the reattachment zone appears to be greatly extended. Long bubbles form when the Reynolds number at separation is below a threshold based on the pressure rise over the bubble. It appears that virtually all short bubbles fall below the "bursting" line. It was thought that there was some overall global stability that could cause bubble to burst. A short bubble well away from the critical bursting condition would expand as the flow speed was reduced slightly. It was conjectured that there could be some type of feed back between the influence of the separated zone on the Reynolds number at separation in such a way that the process could run away as bursting was approached. No evidence was found for this idea.

Because the Reynolds number seemed to be a critical parameter controlling bursting flow stability and transition were obviously important. At the time this work was carried out there was still the idea that the critical Reynolds number for the amplification of instabilities was the vital parameter. However, it turns out that critical Reynolds number for a separated shear layer is very much smaller that the values involved in the experiment. A change in Reynolds number can influence the amplification rate, but again the change in amplification rates are negligible. Nevertheless, the stability and transition process were investigated in order to understand what was happening in the bursting process.

Detailed measurements of the acoustically excited instability waves showed that they were spatially growing modes described by complex wavenumber eigenmodes. Unfortunately, it was found that the long bubble was very unsteady and regular periodic wavetrains could not be excited. Figure 11 shows traces of the naturally occurring waves at various locations from separation in a long bubble. The wave-like ripples only arise intermittently. Figure 12 shows the signal when excited by sound. There are weak regular waves, but these were interrupted by random bursts of wavepackets. Attempts to excite such packets by feeding the loud speaker with bursts of signal showed that packets could be excited in this way, but they did not model the violent naturally occurring ones. By filtering the signal and looking at the low frequency portion at the same time as the instability waves it was clear that bursts occurred whenever the low frequency motion indicated an extreme excursion of the shear layer. This could be interpreted as large low frequency wandering of the shear layer. Whenever it was far from the plate surface a burst appeared. It was clear that without more sophisticated signal processing it was not possible to extract anything from the long bubble signals. At the time I considered this to be a disaster as the original experimental plan could not be completed and

a comparison made between the transition process in long and bubbles made. But, in fact this failure was linked to the first clear difference between the transition process in long and short bubble. At the time I did not appreciate this result.

In the forward region of a bubble the skin friction and pressure gradient are essentially zero. The momentum integral of the shear layer must therefore remain constant. But there are viscous effects that must make the shear layer spread and, if the momentum is to be conserved, there has to be some reversed flow created. Any reversed flow close to the wall will create a negative skin friction and this will enhance the degree of backflow from the diffusion of the shear layer. A scenario does therefore exist for creating increased reversed flow as the Reynolds number falls. In turn this will produce the possibility of negative group velocity instability. At the time this was an idea, but now we know that a backflow of about 20% is needed to form an absolute instability. Only half-formed ideas as to how all this could create some type of irregular relaxation oscillator were postulated. The fact that a fall in Reynolds number so far above the critical value for instability could influence the behaviour was at the time inexplicable. But the Reynolds numbers that are consistent with the necessary back flow are not that far from the critical bursting values. The last lecture of this conference given by Hermann Fasel showed that the structure of the long bubble was roughly consistent with the above scenario. His numerical simulations will, I am sure, prove to be of vital importance in understanding the problem of bursting. Certainly he showed that an absolute instability could exist for a short while and that this would cause the bubble to rapidly shorten to a state where the instability reverted back to a convective form. His numerical experiments help to explain a lot of the observations made in the experiment. But more work is needed to fully account for the observation made in the windtunnel.

5. CONCLUSIONS

Measurements made in transitional separation bubbles some 50 years ago have been presented for both long and short bubbles.

The process of bursting from a short to along bubble was shown to be linked to the separation Reynolds number as well as a parameter linked to the pressure rise over the bubble.

Instability waves excited in a short bubble by sound were measured and shown to be spatially growing complex wavenumber modes in accord with a simple model based on a segmented profile.

Disturbances in a long bubble were shown to be very irregular and to contain short duration bursts of instability waves. It appeared, therefore, that the flow could only sustain very unstable, possible absolutely unstable, modes for short periods of time.

These observations may well be explained by the computer simulations of Fasel.

REFERENCES

1. P.R. Owen and L. Klanfer, On the laminar boundary-layer separation from the leading edge of a thin aerofoil. A.R.C. C.P. 220 (1953)
2. I. McGregor, The regions of local boundary-layer separation and their role in the stalling of aerofoil. Ph.D. Queen Mary College, London (1954)--
3. M. Gaster, The stability of parallel flows and the behaviour of separation bubbles. Ph.D. Queen Mary College, London (1963)
4. G.B. Schubauer and H.K. Skramstad, Laminar boundary layer oscillations and stability of laminar flow. NACA Tech. Rep. 909 (1949)
5. H. Schlichting, Zur Enststehung der Turbulenz bei der Platenstromung Nachr. Ges. Wiss. Gottingen Math. Phys. Klasse 182 (1933)
6. W. Tollmien, Uber die Enstehung der Turbulenz Nachr. Ges. Wiss. Gottingen Math. Phys. Klasse 21 (1929)

TRANSIENT GROWTH WITH APPLICATION TO BYPASS TRANSITION

D. S. Henningson
KTH Mechancis
SE-100 44 Stockholm, Sweden
henning@mech.kth.se

Abstract: Transient growth associated with non-normal stability operators are discussed. Results for both temporal and spatial transient growth are presented. These results allow for an understanding of the type of bypass transition found when laminar boundary layers are subjected to free-stream turbulence. Direct numerical simulations of such a transition scenario show that precursors to turbulent spots are optimal streaks which undergo secondary instability. Finally aspects of the receptivity of the streaks are discussed.

Keywords: Stability, transient growth, by-pass transition

1. INTRODUCTION

In 1969 Morkovin coined the expression "bypass transition", noting that "we can bypass the TS-mechanism altogether". In fact, experiments reveal that many flows, including channel and boundary layer flows, may undergo transition for Reynolds numbers well below the critical ones from linear stability theory. A possible route was proposed by Ellingsen and Palm (1975). They considered, in the inviscid case, an initial disturbance independent of the streamwise coordinate in a shear layer and showed that the streamwise velocity component may grow linearly in time, producing alternating low- and high-velocity streaks. Hultgren and Gustavsson (1981) considered the temporal evolution of a three-dimensional disturbance in a boundary layer and found that in a viscous flow the initial growth is followed by a viscous decay (transient growth).

There is a simple physical explanation for this growth. A wall-normal displacement of a fluid element in a shear layer will cause a perturbation in the streamwise velocity, since the fluid particle will initially retain its horizontal momentum. An example is weak pairs of quasi streamwise counter rotating vortices which are able to lift up fluid with low velocity from the wall and

R. Govindarajan (ed.), Sixth IUTAM Symposium on Laminar-Turbulent Transition, 15–24.

bring high speed fluid towards the wall forcing streamwise oriented streaks of high and low streamwise velocity. This mechanism is denoted lift-up effect and it is inherently a three-dimensional phenomenon.

From a mathematical point of view, it is now clear that since the linearized Navier–Stokes operator is non-normal for many flow cases (e.g. shear flows), a significant transient growth may occur before the subsequent exponential behavior (see Schmid and Henningson, 2001). Such growth can exist for subcritical values of the Reynolds number and it is the underlying mechanism in bypass transition phenomena. In particular, for the Blasius boundary layer, Andersson et al. (1999) and Luchini (2000) used an optimization technique to determine which disturbance present at the leading edge gives the largest disturbance in the boundary layer. This optimal perturbation was found to consist of a pair of steady streamwise counter-rotating vortices, which induce strong streamwise streaks.

An interesting application of bypass transition is boundary layers in the presence of free-stream turbulence. Inside the boundary layer the turbulence is damped, but low frequency oscillations, associated with long streaky structures, appear. The first experimental study of such disturbances is due to Klebanoff (1971). Kendall (1985) denoted these disturbances as Klebanoff modes. As the streaks grow downstream, they breakdown into turbulent spots. The spots grow in size and merge with other spots until the flow is completely turbulent. Westin et al. (1994) presented detailed measurements of a laminar boundary layer subjected to free-stream turbulence. A recent review on the experimental studies of boundary-layer transition induced by free-stream turbulence can be found in Matsubara and Alfredsson (2001), while numerical simulations are presented in Jacobs and Durbin (2001) and Brandt et al. (2004).

2. TEMPORAL TRANSIENT GROWTH

To study the underlying transient growth we Fourier transform the linearized Navier-Stokes equations in the homogeneous spanwise and streamwise directions. Then we use the divergence constraint to eliminate the pressure and end up with the Orr-Sommerfeld-Squire equations governing the development of small perturbations on the parallel mean flow $U(y)$. We have

$$\frac{\partial \hat{v}}{\partial t} = \underbrace{(D^2-k^2)^{-1}\left[-i\alpha U(D^2-k^2)+i\alpha U''+\frac{1}{\mathrm{Re}}(D^2-k^2)^2\right]}_{\mathcal{L}_{OS}}\hat{v} \quad (1)$$

$$\frac{\partial \hat{\eta}}{\partial t} = \underbrace{\left[-i\alpha U+\frac{1}{\mathrm{Re}}(D^2-k^2)\right]}_{\mathcal{L}_{SQ}}\hat{\eta}+\underbrace{-i\beta U'}_{\mathcal{L}_C}\hat{v} \quad (2)$$

Table 1. Maximum transient growth for selected shear flows and the corresponding streamwise and spanwise wavenumbers. From Schmid and Henningson (2001)

Flow	$G_{\max}$ (10^{-3})	t_{max}	α	β
plane Poiseuille	0.20 Re^2	0.076 Re	0	2.04
plane Couette	1.18 Re^2	0.117 Re	35/Re	1.6
circular pipe	0.07 Re^2	0.048 Re	0	1
Blasius boundary layer	1.50 Re^2	0.778 Re	0	0.65

Here $\hat{\eta}$ and $\hat{v}$ are the Fourier transforms of the normal vorticity and the normal velocity, respectively. Further, $k^2 = \alpha^2 + \beta^2$, where α and β are the wave numbers in the streamwise and spanwise directions, respectively. We can write these equations in the following form

$$\underbrace{\frac{d}{dt}\begin{pmatrix}\hat{v}\\ \hat{\eta}\end{pmatrix}}_{d\hat{u}/dt} = \underbrace{\begin{pmatrix}\mathcal{L}_{OS} & 0\\ \mathcal{L}_C & \mathcal{L}_{SQ}\end{pmatrix}}_{\mathcal{L}}\underbrace{\begin{pmatrix}\hat{v}\\ \hat{\eta}\end{pmatrix}}_{\hat{u}} \tag{3}$$

The aspect of sub-critical growth in the linearized equations of interest here is the maximum transient growth possible. It is found by maximizing growth in solutions of the initial value problem. We calculate

$$G(t) = \max_{\hat{u}_0 \neq 0} \frac{\|\hat{u}(t)\|^2}{\|\hat{u}_0\|^2} = \|e^{\mathcal{L}t}\|^2 \leq \kappa\, e^{2\Re\{\lambda_{max}\}t} \tag{4}$$

where we use the energy norm. We have also included a bound on the maximum growth, where the constant κ can be thought of the the condition number of the "matrix of eigenfunctions", which can be generalized to infinite dimensional operators (Trefethen 1997). If $\mathcal{L}$ was a normal operator, or equivalently, if all of its eigenfunctions were orthogonal, this condition number would equal unity, i.e. $\kappa = 1$. It is streamwise independent disturbances or streaks, which experience the largest transient growth. Computations yield that $\kappa = \mathcal{O}(\mathrm{Re}^2)$, see table 1.

3. SPATIAL TRANSIENT GROWTH

The streaks that appear in boundary layers subject to free-stream turbulence develop in space and not in time. It is possible to consider the spatial equivalent of the temporal transient growth by using the linearized boundary layer equations around the mean flow $U(x, y)$. Since the frequency of the streaks is low we consider the time-independent equations, i.e.

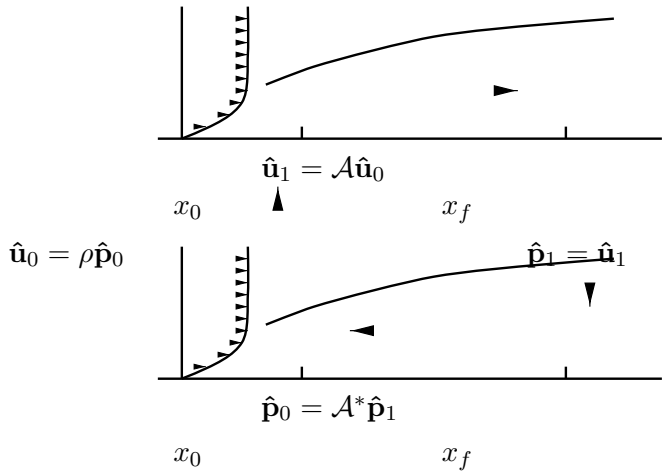

Figure 1. Sketch of optimization algorithm for computing spatial optimal disturbances. For details see Schmid and Henningson (2001)

$$\begin{aligned} u_x + v_y + \beta w &= 0 \\ (Uu)_x + Vu_y + U_y v &= u_{yy} - \beta^2 u \\ (Vu + Uv)_x + (2Vv)_y + \beta V w + p_y &= v_{yy} - \beta^2 v \\ (Uw)_x + (Vw)_y - \beta p &= w_{yy} - \beta^2 w \end{aligned}$$

We consider a disturbance at the leading edge, $\hat{\mathbf{u}}_0 = (\hat{u}_0(y), \hat{v}_0(y), \hat{w}_0(y))$, and integrate the parabolic equations forward to position x_1 and the optimal output $\hat{\mathbf{u}}_1$. We let this procedure be represented by the linear operator $\mathcal{A}$, i.e.

$$\hat{\mathbf{u}}_1 = \mathcal{A}\hat{\mathbf{u}}_0.$$

We can maximize the growth between position 1 and 2 as

$$\begin{aligned} G(x_1) &= \max_{\hat{\mathbf{u}}_0 \neq 0} \frac{\|\hat{\mathbf{u}}_1\|^2}{\|\hat{\mathbf{u}}_0\|^2} = \max_{\hat{\mathbf{u}}_0 \neq 0} \frac{\|\mathcal{A}\hat{\mathbf{u}}_0\|^2}{\|\hat{\mathbf{u}}_0\|^2} \\ &= \max_{\hat{\mathbf{u}}_0 \neq 0} \frac{(\mathcal{A}\hat{\mathbf{u}}_0, \mathcal{A}\hat{\mathbf{u}}_0)}{(\hat{\mathbf{u}}_0, \hat{\mathbf{u}}_0)} = \max_{\hat{\mathbf{u}}_0 \neq 0} \frac{(\mathcal{A}^*\mathcal{A}\hat{\mathbf{u}}_0, \hat{\mathbf{u}}_0)}{(\hat{\mathbf{u}}_0, \hat{\mathbf{u}}_0)} = \lambda_{max} \end{aligned}$$

where we have used that λ_{max} is largest eigenvalue of $\mathcal{A}^*\mathcal{A}\hat{\mathbf{u}}_0 = \lambda\hat{\mathbf{u}}_0$. The optimal disturbance is found by power iterations, $\hat{\mathbf{u}}_0^{n+1} = \rho_n \mathcal{A}^*\mathcal{A}\hat{\mathbf{u}}_0^n$, where $\mathcal{A}^*$ solves the adjoint equations backward. For a visual description of the method see figure 1.

Maximum spatial transient growth for boundary layer flow versus streamwise distance can be seen in figure 2. The growth in this figure is scaled with

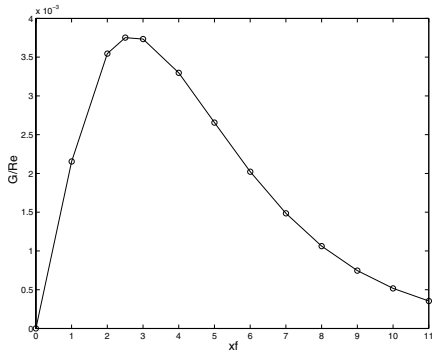

Figure 2. Maximum spatial transient growth for boundary layer flow versus streamwise distance. Adapted from Andersson et al. (1999)

$\mathrm{Re}_x \sim \mathrm{Re}^2$, since the spatial case also has a similar Reynolds number dependence as the optimal transient growth in time studied earlier. This scaling can be motivated by the following observation, we have

$$
\begin{aligned}
G(x_1) &= \max_{\hat{\mathbf{u}}_0 \neq 0} \frac{\|\hat{\mathbf{u}}_1\|^2}{\|\hat{\mathbf{u}}_0\|^2} \\
&= \max_{\hat{\mathbf{u}}_0 \neq 0} \frac{\displaystyle\int_0^\infty \left(u^2 + \frac{v^2}{\mathrm{Re}^2} + \frac{w^2}{\mathrm{Re}^2} \right) dy}{\displaystyle\int_0^\infty \left(u^2 + \frac{v^2}{\mathrm{Re}^2} + \frac{w^2}{\mathrm{Re}^2} \right) dy} \\
&\approx \max_{\hat{\mathbf{u}}_0 \neq 0} \mathrm{Re}^2 \frac{\displaystyle\int_0^\infty u^2 dy}{\displaystyle\int_0^\infty \left(v^2 + w^2 \right) dy}
\end{aligned}
$$

where we have used that the normal and spanwise velocity components in the energy norm are divided by Re^2 due to the boundary layer scaling. Thus, if growth should be maximized one must have initial disturbances with zero streamwise components and final disturbances consisting of only disturbance in the streamwise velocity. The optimal input and the resulting output is shown in figure 3.

4. BY-PASS TRANSITION

Simulations have been performed to follow the breakdown and transition to turbulence in boundary layers subjected to free-stream turbulence using the spectral DNS code of Lundbladh et al. (1999). Results are presented for three

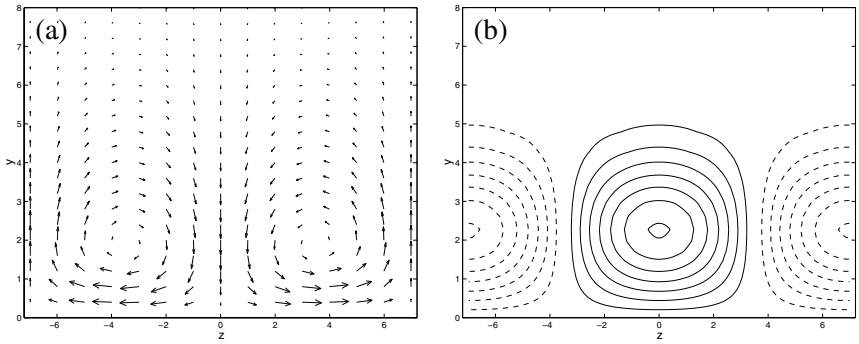

Figure 3. Spatial optimal disturbance for boundary layer flow: (a) velocity vectors in the y-z-plane at $x = x_0$; (b) contours of streamwise velocity at $x = x_1$. From Andersson et al. (1999)

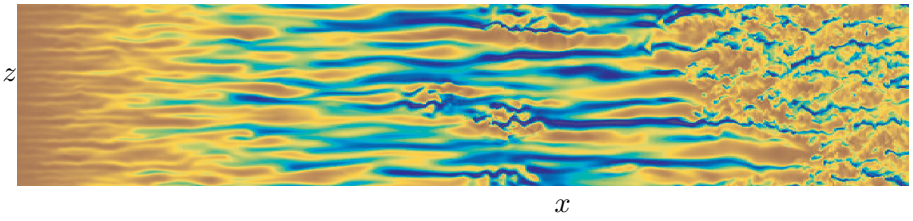

Figure 4. Instantaneous streamwise velocity in a plane parallel to the wall at $y/\delta_0^* = 2$. The plot is not to scale since the domain depicted is 900 units long and 90 units wide in terms of δ_0^*. The fringe region is not shown. From Brandt et al. (2004)

cases. In all of them the inlet of the computational box is at $\mathrm{Re} = 300$, based on the initial displacement thickness δ_0^* ($\mathrm{Re}_{x_0} = 30000$) and the free-stream turbulence intensity is 4.7%. Different integral length scales of the inflow turbulence have been used, that is $L = 2.5\,\delta_0^*$, $L = 5\,\delta_0^*$ and $L = 7.5\,\delta_0^*$. The free-stream turbulence is composed of about 800 modes of the continuous spectrum of the Orr-Sommerfeld-Squire equations, see Brandt et al. (2004) for details.

A snapshot of the flow is shown in figure 4 where the instantaneous streamwise velocitiy is plotted in a plane parallel to the wall. The overall picture of the transition scenario can be deduced from the figure. Starting from the inlet position, the perturbation in the boundary layer appears in the streamwise velocity component, in the form of elongated structures. Patches of irregular motion are seen to appear further downstream. As they travel downstream, the spots become wider and longer. The turbulent region at the end of the domain is created by the enlargement and merging of the spots.

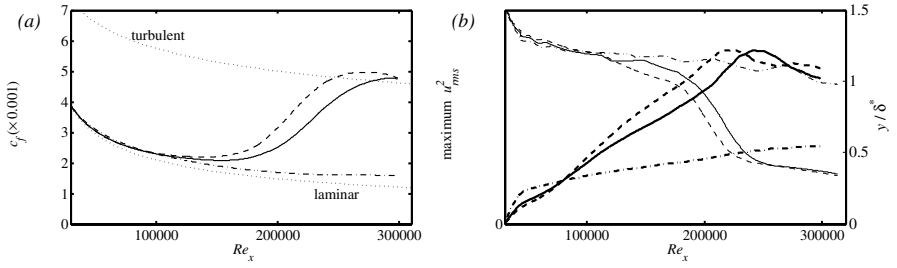

Figure 5. (a) Skin friction coefficient, (b) maximum u^2_{rms} (thick lines) and its wall-normal position (thin lines); plotted for $L = 7.5\delta^*_0$ (dashed line), $L = 5\delta^*_0$ (solid line) and $L = 2.5\delta^*_0$ (dash-dotted line). From Brandt et al. (2004)

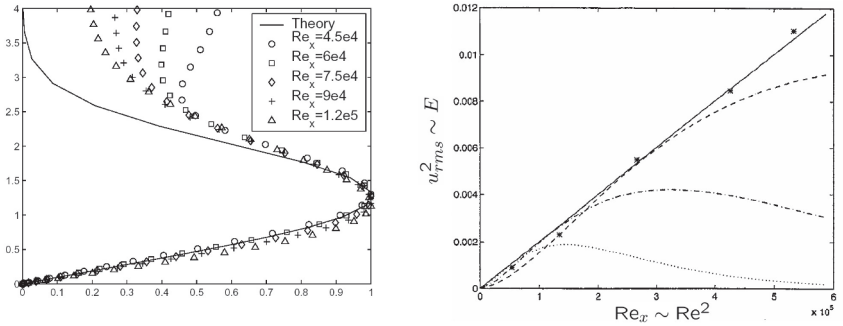

Figure 6. a) Wall-normal distribution of the u^2_{rms} of the streaks from the simulations of Brandt et al (2004) compared to the optimal output; b) the growth of individual optimal disturbances (dashed lines) together with their envelope (solid line). The slope is adjusted to fit experimental values. From Andersson et al (1999)

4.1 Charatieristics of the breakdown

Some of the data obtained by averaging in time and in the spanwise direction are displayed in figure 5. The friction coefficient is shown in figure $5(a)$; also the values for a laminar and a turbulent boundary layer are displayed for comparison. For the case with the smallest integral length scale transition does not occur within the computational domain, while the transition location is at lower Re_x for $L = 7.5\delta^*_0$, in agreement with the experimental findings in Jonas et al. (2000). In figure $5(b)$ the maximum u^2_{rms} at each downstream position is depicted to show the evolution of the streaks. In all cases the energy of the streaks is proportional to the distance from the leading edge, as observed in the experiment. In figure $5(b)$ the wall-normal position of maximum u_{rms} is also shown. The laminar streaks have a maximum at about $y = 1.3\delta^*$, while their turbulent counterparts are located much closer to the wall.

In figure 6a the wall-normal distribution of the u_{rms}^2 of the slowly meandering streaks from the simulations of Brandt et al (2004) are compared to the optimal streak calculated by the spatial procedure presented above. The streaks in the simulations can be seen to be well described by the theoretical calculations, indicating that the optimal output is a strong attractor towards which any disturbance with a non-zero projection on the optimal input will tend. In figure 6b the growth of individual optimal disturbances and their envelope are shown. The slope is a free parameter associated with the amplitude of the optimal disturbance at the leading edge, and is here adjusted to fit experimental values.

4.2 Receptivity

The optimal disturbances at the leading edge protrudes out of the boundary layer and their subsequent development into the boundary layer will thus describe a linear receptivity mechanism. This was studied by Andersson et al. (1999) and Luchini (2000) using the boundary layer approximation in the manner described above and by Wundrow and Goldstein (2001) by means of asymptotic expansions. Besides this linear receptivity, Berlin and Henningson (1999) and Brandt et al. (2002) have proposed a nonlinear mechanism. Calculations have shown that oblique waves in the free stream can interact to generate streamwise vortices, which, in turn, induce streaks inside the boundary layer.

The two mechanisms are compared by means of DNS to try to identify which of the two can be considered as the most relevant in cases with known free-stream perturbations. Different levels of free-stream turbulence intensity are considered and, moreover, the free-stream turbulence generation is manipulated to involve few or many modes with very low values of the frequency. In this way, we are able to control the amount of low-frequency content in the inflow turbulence.

The wall-normal maximum of the streamwise velocity perturbation induced inside the boundary layer is displayed in figure 7 versus the local Reynolds number for six cases considered. The results in figure $7(a)$ pertain to three different free-stream turbulence levels, $Tu = 4.7\%$, $Tu = 3\%$ and $Tu = 1.5\%$, with integral length scale $L = 7.5\delta_0^*$. For this case only a few modes characterized by low frequency are introduced as part of the inflow perturbation spectrum. It is shown in figure $7(c)$ that by dividing the u_{rms} values in figure $7(a)$ with the square of the turbulence intensity Tu, the growth of the perturbation associated with the higher turbulence intensities follow parallel lines which are rather close together. Therefore the dominating receptivity mechanism is most likely the nonlinear one (see Brandt et al. 2004 for more details). The results in figure $7(b)$ pertain to cases with the same free-stream turbulence levels and in-

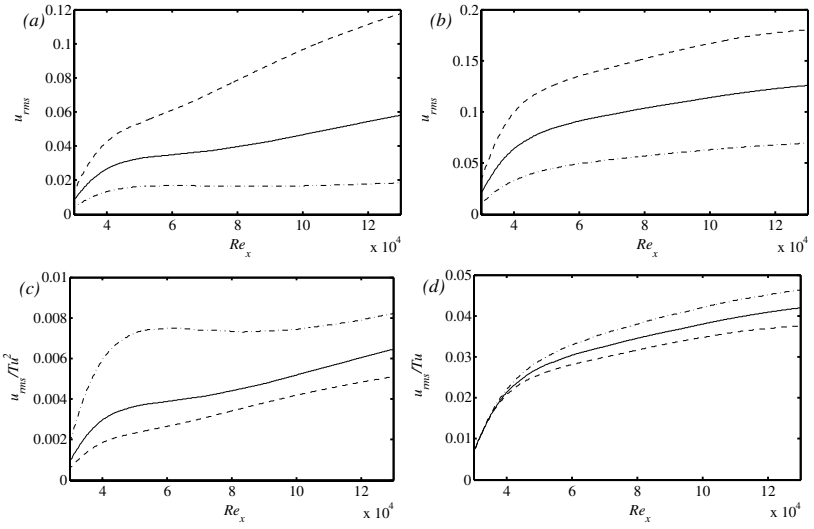

Figure 7. Streamwise evolution of the wall-normal maximum of u_{rms} for three levels of free-stream turbulence intensity: - - -, $Tu = 4.7\%$; ——, $Tu = 3\%$ and - · -, $Tu = 1.5\%$. The results in (a) pertain to the case of few low-frequency modes as part of the inflow perturbation spectrum, while the data in (b) to a free-stream turbulence spectrum rich with low-frequency modes. (c): The same rms-values as in (a) are scaled with the square of the free-stream turbulence intensity Tu. (d): The same rms-values as in (b) are scaled with the free-stream turbulence intensity Tu. From Brandt et al. (2004)

tegral length scale, but this time the perturbation spectrum is characterized by many low-frequency modes, as shown by the high u_{rms}-values already at the inlet of the computational domain. In this case the u_{rms} scales linearly with the perturbation intensity Tu (see figure $7d$) and the dominating receptivity mechanism responsible for the streak growth is therefore the linear one. From the results in the figure it is possible to conclude that the linear mechanism is the most relevant if the free-stream turbulence contains significant energy in low-frequency modes.

5. CONCLUSIONS

Transient growth associated with non-normal stability operators have been reviewed. Results for both temporal and spatial transient growth are presented and show that the energy grows proportional to the Reynolds number squared, based on the boundary layer thickness. These results allow for an understanding of the type of bypass transition found when laminar boundary layers are subjected to free-stream turbulence. Direct numerical simulations of such a transition scenario show that precursors to turbulent spots are optimal streaks which undergo transition. Finally aspects of the receptivity of the streaks are

discussed and it is indicated that in experiments with a rather large low frequency content, such as may be expected after a wind-tunnel contraction, the linear mechanism is most likely dominating.

ACKNOWLEDGEMENT

I would like to thank all my coworkers who have contributed to the investigations reviewed in this paper; Peter Schmid, Satish Reddy, Stellan Berlin, Paul Andersson, Luca Brandt, Donatella Ponziani and Philipp Schlatter.

REFERENCES

Andersson, P., Berggren, M., and Henningson, D. S. (1999). Optimal disturbances and bypass transition in boundary layers. *Phys. Fluids*, 11:134–150.

Berlin, S. and Henningson, D. S. (1999). A nonlinear mechanism for receptivity of free-stream disturbances. *Phys. Fluids*, 11(12):3749–3760.

Brandt, L., Henningson, D. S., and Ponziani, D. (2002a). Weakly non-linear analysis of boundary layer receptivity to free-stream disturbances. *Phys. Fluids*, 14(4):1426–1441.

Brandt, L., Schlatter, P., and Henningson, D. S. (2004). Transition in a boundary layers subject to free-stream turbulence. *Journal of Fluid Mech.*, 517:167–198.

Ellingsen, T. and Palm, E. (1975). Stability of linear flow. *Phys. Fluids*, 18:487–488.

Hultgren, L. S. and Gustavsson, L. H. (1981). Algebraic growth of disturbances in a laminar boundary layer. *Phys. Fluids*, 24(6):1000–1004.

Jacobs, R. J. and Durbin, P. A. (2001). Simulations of bypass transition. *J. Fluid Mech.*, 428:185–212.

Jonas, P., Mazur, O., and Uruba, V. (2000). On the receptivity of the by-pass transition to the length scale of the outer stream turbulence. *Eur. J. Mech.* B/*Fluids*, 19:707–722.

Kendall, J. M. (1985). Experimental study of disturbances produced in a pre-transitional laminar boundary layer by weak free-stream turbulence. *AIAA Paper*, 85:1695.

Klebanoff, P. S. (1971). Effect of free-stream turbulence on the laminar boundary layer. *Bull. Am. Phys. Soc.*, 10:1323.

Luchini, P. (2000). Reynolds-number independent instability of the boundary layer over a flat surface. Part 2: Optimal perturbations. *J. Fluid Mech.*, 404:289–309.

Lundbladh, A., Berlin, S., Skote, M., Hildings, C., Choi, J., Kim, J., and Henningson, D. S. (1999). An efficient spectral method for simulation of incompressible flow over a flat plate. Technical Report KTH/MEK/TR–99/11–SE, KTH, Department of Mechanics, Stockholm.

Matsubara, M. and Alfredsson, P. H. (2001). Disturbance growth in boundary layers subjected to free stream turbulence. *J. Fluid. Mech.*, 430:149–168.

Morkovin, M. V. (1969). The many faces of transition. In Wells, C. S., editor, *Viscous Drag Reduction*. Plenum Press.

Schmid, P. J. and Henningson, D. S. (2001). *Stability and Transition in Shear Flows*. Springer, New York.

Trefethen, L.N. (1997) Pseudospectra of linear operators. SIAM Review 39, 383-406.

Westin, K. J. A., Boiko, A. V., Klingmann, B. G. B., Kozlov, V. V., and Alfredsson, P. H. (1994). Experiments in a boundary layer subject to free-stream turbulence. part i: Boundary layer structure and receptivity. *J. Fluid Mech.*, 281:193–218.

Wundrow, D. W. and Goldstein, M. E. (2001). Effect on a laminar boundary layer of small-amplitude streamwise vorticity in the upstream flow. *J. Fluid Mech.*, 426:229–262.

THE ROLE OF EXTERNAL DISTURBANCES IN LAMINAR-TURBULENT TRANSITION

Xuesong Wu
Department of Mathematics, Imperial College, London SW7 2BZ
Department of Mechanics, Tianjin University, P. R. China
x.wu@imperial.ac.uk

Abstract: Transition to turbulence in parallel or nearly parallel flows is known to be critically influenced by ambient perturbations. At relatively low intensity level, external perturbations initiate transition through receptivity process, i.e. by exciting instability waves, but without affecting linear and subsequent nonlinear amplification rate. At moderate to high intensity level, however, external disturbances may directly alter the instability properties. The present paper reports some recent theoretical progresses in understanding the role of external disturbances in transition. These include (a) a self-consistent theory for the vortical receptivity, which predicts accurately the experimental measurements, (b) the demonstration that the streaks formed due to the free stream vortical fluctuations modify the viscous Tollmien-Schlichting (T-S) waves, and indeed may even induce stronger intermittent inviscid instability, and (c) a theoretical model, which links the critical Reynolds number to the external perturbations, and shows, for the case of channel flow, that the critical Reynolds number can be substantially reduced by even a minimal level of external perturbations. Several problems which require further studies are highlighted.

Keywords: External disturbance, receptivity, streak, bypass transition, subcritical instability

1. INTRODUCTION

Transition to turbulence in open flows has been investigated for more than a century as one of the fundamental problems in hydrodynamics. The first step toward understanding this exceedingly complex process is linear instability analysis, which seeks unstable eigen modes that the laminar base flow may support. Nonlinear instability theory, developed to explain numerous transition features beyond the remit of linear theory, usually follows the development of some chosen eigen mode(s) ([25], [11]). In both linear and nonlinear theo-

R. Govindarajan (ed.), Sixth IUTAM Symposium on Laminar-Turbulent Transition, 25–35.

ries, the external perturbations play an indirect role, and their effects are not explicitly accounted for.

However, ever since the earliest laboratory studies of boundary-layer transition ([8], [26]), almost all experimental evidence pointed to the fact that transition is critically influenced by ambient perturbations, such as free stream turbulence (FST) and surface roughness, which are inevitable present in many technological applications and experimental facilities. The correlation data [9] shows that the overall trend is such that with increased FST level and/or surface roughness, transition occurs considerably earlier.

From the physical point of view, the external perturbations may influence transition through at least three distinct mechanisms.

- At relatively low intensity level, external perturbations initiate transition through receptivity process, i.e. by exciting viscous T-S instability waves, which then evolve through linear and subsequent nonlinear development as if the external perturbations were absent; this is the conventional transition.
- At moderate intensity level, the instability retains its original character, but its linear and/or nonlinear growth may be substantially modified by the external disturbances.
- At high intensity level, the external disturbances may induce new inviscid instabilities, such as secondary instability of streaks. Transition then takes the so-called bypass route, i.e. without involving the usual T-S instability.

The division between these different regimes is not necessarily clear cut, because the intensity of the external disturbances is unlikely to be the only relevant parameter. The time and length scales characterizing their temporal and spatial structures may well be relevant, and so is the correlation property of highly random background perturbations, which determines whether the growth of an instability wave is dampened or enhanced.

In this lecture, I shall present some recent theoretical work that aims to quantify the role of external perturbations from the three perspectives listed above. The main thesis is that external disturbances must be explicitly taken into account in theoretical/computational models in order to address some fundamental problems in transition, including boundary-layer receptivity(§2), streaks induced by FST and their instability (§3), and subcritical transition in channel flow (§4). Investigations of such fundamental aspects on a first-principle basis should form an important part of the effort for improving the current transition prediction, because they provide physical insights and identify the key factors, which would ultimately aid the development of reliable correlation formula for transition Reynolds number.

2. BOUNDARY-LAYER RECEPTIVITY TO VORTCICAL DISTURBANCES

Receptivity refers to excitation of instability waves by ambient disturbances. Its importance owes to the fact that boundary layer is convectively unstable, which means that an impulse disturbance would generate a downstream propagating wave packet, behind which the flow remains unperturbed. Transition therefore could take place only in the presence of persistent external disturbances. But the time and length scales of the naturally present perturbations do not coincide simultaneously with those of the inherent instability. In order for them to excite instability waves, some form of scale conversion mechanisms are required. In contrast, for absolutely unstable flows, any accidental perturbation eventually spreads into the entire domain so that the receptivity requires no special attention.

The crucial breakthrough in understanding receptivity was made in 1980s; see the review [13]. Extensive researches followed, most of which were surveyed in [22]. Here we present some latest work on this particular problem.

The basic mechanism involves a vortical disturbance interacting with a localized surface roughness element, and was described in [10] using triple-deck formulation based on the assumption that the Reynolds number $R = U_\infty L/\nu \gg 1$, where L is the distance of the roughness centre to the leading edge of the plate. The frequency of the vortical disturbance and the length scale of the roughness are taken to be comparable with the characteristic frequency and wavelength of T-S waves, which are of $O(R^{-3/8}L)$ and $O(R^{1/4}U_\infty/L)$ respectively, according to the asymptotic theory ([19], [24]). More precisely, the vortical disturbance in the free stream is taken to be a convected gust, and its velocity can be represented by

$$\mathbf{u} = \epsilon_c \, \mathbf{u}_\infty(y) \, \mathrm{e}^{\mathrm{i}(\alpha_c x - \omega t)} + c.c. \quad \text{with} \quad \alpha_c = \omega \sim R^{1/4}. \tag{1}$$

The local roughness has a shape

$$y_w = R^{-5/8} h F_w(X), \quad \text{with} \quad X = R^{3/8} x, \quad h \ll 1. \tag{2}$$

The forcing resulting from the interaction between the two has both the time and length scales comparable with those of a T-S wave so that the latter is generated as a result. The leading-order approximation for the amplitude of the T-S wave excited was given in [10], but no numerical calculation was performed.

A comprehensive set of experimental data were first obtained by Dietz [7], who generated the vortical disturbances in a controlled manner. This prompted Wu [30] to develop a second-order asymptotic theory. In order to be able to make a quantitative comparison with the experiments, the analysis was performed for an arbitrary profile of the gust. The triple-deck formulation offers the advantage that the solution can be obtained in the closed form. For a single

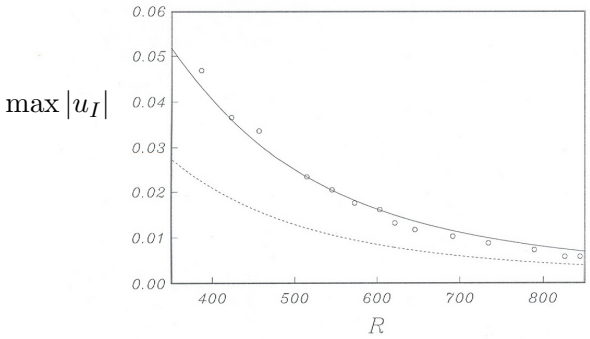

Figure 1. $\max|u_I|$ v.s. $R^{1/2}$ for a fixed excitation frequency $F = 50$. The solid line: the second-order theory; the dashed line: the 'first-order' theory; symbols: experiment

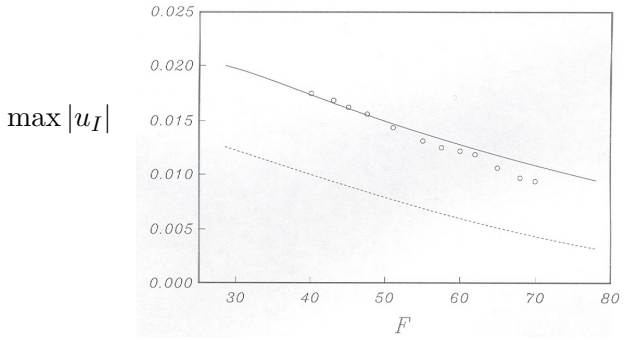

Figure 2. $\max|u_I|$ v.s. F for a fixed $R = 620^2$

roughness located at x_0, the amplitude of the T-S wave can be expressed as

$$u_I(x_0) = (\epsilon_c h R^{-1/8}) \frac{\mathcal{F}}{\partial_\alpha \Delta(\alpha; x_0)} \tilde{U}_{TS} \tag{3}$$

where α is the wavenumber, and $\Delta(\alpha; x_0)$ is the dispersion relation of the T-S wave. $\mathcal{F}$ and $\tilde{U}_{TS}$ stand for the forcing and the eigen function respectively, both of which were obtained up to $O(R^{-1/8})$ accuracy. When (3) is specialized to the case of Dietz [7], $\mathcal{F}$ is found to be proportional the slip velocity of the gust at the edge of the boundary layer, indicating that the detailed profile of the gust is unimportant. Figures 1 and 2 show the dependence of $\max|u_I|$ on the Reynolds number and frequency $F = \omega^* \nu / U_\infty^2 \times 10^6$ (ω^* being the dimensional frequency), and the comparisons with the experiments.

The result (3) was also generalized to the case of multiple elements by an appropriate superposition of the contribution from each. A theory for the distributed roughness was developed in [29]. The comprehensive comparison, presented here and in [29], [30], shows that the quantitative agreement between the second-order theory and the experiments was very satisfactory, and this puts our understanding of vortical receptivity on a firm footing.

3. STREAKS AND STREAK INSTABILITY

In the presence of high level FST, the most striking feature of the boundary layer is the emergence of streaks. These streaks oscillate at very low frequencies, and were thus called 'breathing modes' by Taylor [26] and Dryden [8], who made the first observations. In the more recent investigations ([2], [16], [28]), streaks are often referred to as 'Klebanoff modes'[17]. It is now generally understood that streaks arise because the boundary layer acts a 'filter', allowing the low-frequency (i.e. long wavelength) components to be entrained into the boundary layer while absorbing the high-frequency ones in its outer edge.

Streak instability has been suggested to be a key mechanism causing bypass transition, e.g. [27]. Supporting experimental evidence was provided in [21], where it was reported that streaks undergo rapid oscillations and quickly break down to form localized spots, even though the overall mean flow does not significantly depart from the laminar Blasius profile.

A number of investigators have analysed streak instability theoretically, e.g. [1]. The streaks in the calculations were taken to be the so-called optimal disturbances, which are completely steady. The spanwise distribution is assumed to be periodic so that Floquet theory could be used to identify the instability modes. The threshold amplitude for the inviscid instability is found to be about 26%, which is obviously too high to explain the experiments [21].

Streaks in reality, though of low frequency and exhibiting a discernible pattern, are neither steady no strictly periodic. Moreover, experiments indicate that breakdown of streaks occurs sporadically in space rather than collectively as implied by Floquet theory. For these reasons, Wu & Choudhari [31] investigated the instability of streaks that induced by free stream disturbances. These streaks are *unsteady*, and *localized* in the spanwise direction. The primary aim of [31] is to assess whether or not a relatively small-amplitude streak is able (a) to modify substantially the growth rate of T-S waves, and (b) to cause inviscid instability. These two questions are closely related to the change-over from the conventional to the bypass transition scenarios.

In the far field, the FST is taken to a convected gust

$$\mathbf{u}_\infty = \epsilon_D \Big\{ \hat{u}_\infty B'(z), \hat{v}_\infty B'(z), \hat{w}_\infty B(z) \Big\} \, \mathrm{e}^{\mathrm{i}\, k_1 (x-t) + \mathrm{i}\, k_2 y} \quad (\epsilon_D \ll 1) \quad (4)$$

where $B(z) \to 0$ as $z \to \pm\infty$. The normalization was based on Λ, the spanwise length scale of the gust, and the free stream velocity U_∞. The disturbance of relevance has a streamwise wavelength much larger than Λ so that $k_1 \ll 1$. It is assumed that Reynolds number $R_\Lambda = U_\infty \Lambda / \nu \gg 1$. The fluctuation in the major inviscid region is governed by linearized Euler equations, which can be solved to give the slip velocity in the spanwise direction $w_s(z)$. Through w_s, the FST drives the boundary layer fluctuation, the streamwise velocity of

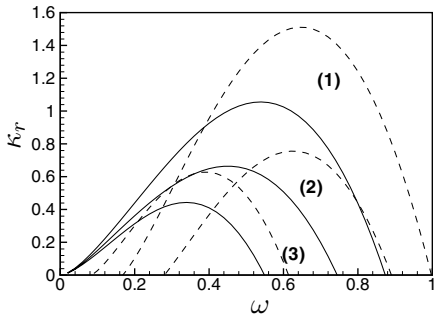

Figure 3. The growth rates of varicose (solid line) and sinuous modes (dashed line) at three instants for a fixed location $\bar{x} = 2$

which can be written as

$$u_D = \epsilon_D\Big(-w_s'(z)/k_1\Big)\bar{U}_D(y,z,\bar{x},t) \quad \text{with} \quad \bar{U}_D = O(1), \quad \bar{x} \equiv k_1 x, \quad (5)$$

which is larger than the spanwise component by a factor $k_1^{-1} \gg 1$. Note that streaks arise as a response to the forcing from the outside of the boundary layer, and their dominance is simply due to the disparity of the spanwise and streamwise length scales, rather than to the transient growth as has been frequently suggested. Because of the very long streamwise length scale, the streaks are appropriately described by linearized boundary-region equations [18]. To make analytical progress possible, it is further assumed in [31] that Λ is much larger than the local boundary layer thickness. The boundary-region equations then reduce to boundary-layer equations.

An important consequence of the unsteadiness of the streak is that close to the wall, $U_D'' \sim y$, but the curvature of the Blasius profile $U_B'' \sim y^2$ so that $\epsilon_D/k_1 U_D'' \sim U_B''$, and an inflection point may appear, even when ϵ_D/k_1 is small. It is deduced that the instability is fundamentally altered when the free stream disturbance reaches the threshold order of magnitude $\epsilon_D \sim R_\Lambda^{-1/3} k_1^{2/3}$, for which an inflection point emerges in a layer where $y \sim \sigma = O(R_\Lambda k_1)^{-1/3}$. The distorted base flow supports localized instability modes of the form

$$A(X)\Phi(z)\,\mathrm{e}^{\mathrm{i}\,\sigma^{-\frac{1}{2}}(\alpha x - \sigma\omega t)} \quad \text{with} \quad A = \mathrm{e}^{\mathrm{i}(\kappa_0+\kappa_e)X}, \quad X = \sigma^{\frac{5}{2}}x. \quad (6)$$

The streamwise wavelength of the modes is much shorter than Λ. The modal shape Φ is determined by the eigen-value problem:

$$-\Phi''(z) = [\gamma(z;\bar{x},t) - \alpha_s]\Phi(z), \quad \Phi \to 0 \quad \text{as} \quad z \to \pm\infty, \quad (7)$$

which is a Schrodinger equation with the potential $\gamma(z) \sim U_D'(0,z;\bar{x},t)$. The total growth rate $(\kappa_0 + \kappa_e)$ is a sum of the usual viscous growth rate κ_0 and the streak-induced *excess growth*

$$\kappa_e(\bar{x},t) = \int_{-\infty}^{\infty} U_D'''(0,z;\bar{x},t)\Phi^2\,\mathrm{d}\,z. \quad (8)$$

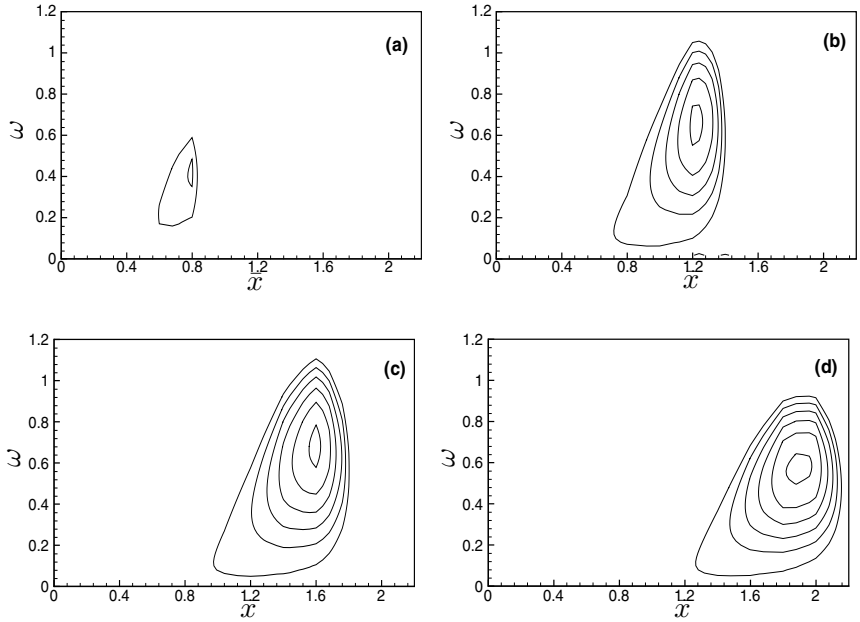

Figure 4. Contours of growth rates of the sinuous modes: (a)-(d) correspond to the instants $\bar{t} \equiv k_1 t = -1.8,\ -1.25, -0.82, -0.44$

The nature of the instability depends on ϵ_D. If $\epsilon_D \sim R_\Lambda^{-\frac{1}{20}} k_1^{\frac{21}{20}}$, the excess growth rate is comparable with the viscous growth rate, so that the instability may be viewed as modified T-S modes. If $\epsilon_D \gg R_\Lambda^{-\frac{1}{20}} k_1^{\frac{21}{20}}$, the instability is essentially inviscid with an inviscid growth rate:

$$\kappa(\omega, \bar{x}, t) = -\pi c_0^4/(4\lambda) + \kappa_e.$$

Both sinuous and varicose modes exist when the flow features a low-speed streak. Figure 3 shows typical growth rates κ. The sinuous modes have considerably larger growth rates than the varicose modes, consistent with the observation that sinuous modes were noted to occur more frequently [21].

The instability occurs only during certain phases and within a streamwise windows, and such a local and intermittent nature of the instability can be illustrated by plotting the growth-rate contours in the $\omega - \bar{x}$ plane at various instants of time (figures 4). At $\bar{t} = -1.8$, a small 'bubble' of instability is observed in the $\omega - \bar{x}$ plane, indicating the incipience of the instability. As time increases, the bubble grows in both spatial and spectral extent, reaching its maximum at $\bar{t} \approx -0.82$, after which the bubble shrinks and finally disappears, before re-emerging during the next cycle of the streak modulation. Of course, given the disparity between the temporal scales of the streak and the instability waves the latter could amplify substantially within a single period of modulation and, therefore, reach sufficiently high amplitudes to induce a local breakdown.

4. SUBCRITICAL INSTABILITY AND EXTERNAL PERTURBATIONS

Channel-flow transition probably is the most extensively studied topic in the field. Linear theory predicts that the flow loses stability at a critical Reynolds number $R_c \approx 5772$, and the onset is marked by growth of a two-dimensional disturbance, as is expected by Squire's theorem. These predictions have been verified by experiments, but only when considerable effort was made to suppress the extraneous perturbations. With increased external disturbances, transition occurs at much lower Reynolds numbers, and the onset instability is three dimensional, that is, Squire's theorem becomes invalid.

The relation between the critical Reynolds number and the external disturbances could be quantified by describing the excitation and nonlinear evolution of the T-S wave simultaneously [20]. Here nonlinearity must be included in the receptivity analysis because otherwise the waves excited decay. This is a crucial difference from the boundary layer, where the T-S waves excited in the subcritical regime will eventually amplify due to the ever increasing Reynolds number, and enter nonlinear regime subsequently, that is, receptivity and nonlinear evolution can be treated separately.

To fix the idea, the external disturbances correspond to a small oscillatory pressure gradient, $\epsilon\tilde{p}\,\mathrm{e}^{-\mathrm{i}\,\omega t}$, and distributed surface roughness, modelled by a wavy $y = \epsilon h_{\pm}\,\mathrm{e}^{\mathrm{i}\,\alpha x}\cos(\beta z)$. The mutual interaction produces a forcing $\chi\,\mathrm{e}^{\mathrm{i}(\alpha x-\omega t)}\cos(\beta z)$ to excite the T-S wave $A(t)\,\mathrm{e}^{\mathrm{i}(\alpha_c x-\omega_c t)}\cos(\beta z)$, if the near resonance condition, $(\alpha,\,\omega) \approx (\alpha_c,\,\omega_c)$, is satisfied, where $(\alpha_c,\,\omega_c)$ represents the neutral T-S wave with spanwise wavenumber β. The amplitude function A is found to be governed by the nonlinear evolution equation:

$$A' = \Big[d(\frac{1}{R}-\frac{1}{R_c})+\mathrm{i}(\omega-\omega_c)\Big]A + l_h A|A|^2 + A\int_0^t |A(t-R\xi)|^2 K(\xi)\,\mathrm{d}\,\xi + \chi \tag{9}$$

where $R_c(\beta)$ is the linear critical Reynolds number, and χ characterizes the forcing. The appropriate initial condition is: $A \to \chi t$ as $t \to 0$. The local nonlinear term is contributed by the harmonics, while the non-local nonlinear term was by the streaks, the streamwise vortices as well as the spanwise uniform mean flow distortion. It turns out that the dominant nonlinearity comes from the steaks. Very often, the dominance of streaks is attributed to the transient growth associated with non-normality of the operator governing the streaks and vortices. But presently this is not the appropriate explanation, because neither the streak, nor the vortices were seeded initially. They all arise purely due to the forcing induced by the nonlinear wave interaction. The large amplitude of the streak owes to the scale disparity, a feature that is well understood in nonlinear instability theory ([14], [12],[32]). Transient growth *per se* is irrelevant, and nonlinear effect in contrast is crucial in generating and sustaining the streaks.

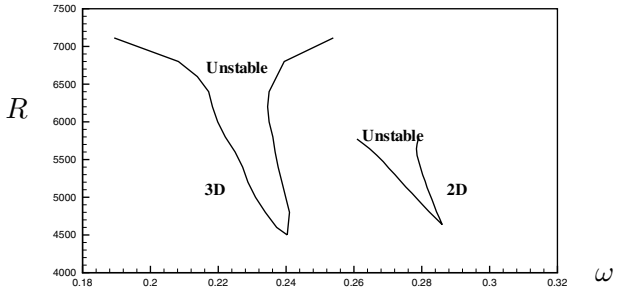

Figure 5. Tuned response leading to the 'instability tongue' in the presence of the external perturbations: pressure fluctuation is 10^{-3} and roughness height is 10^{-3} (3D) or 10^{-2} (2D)

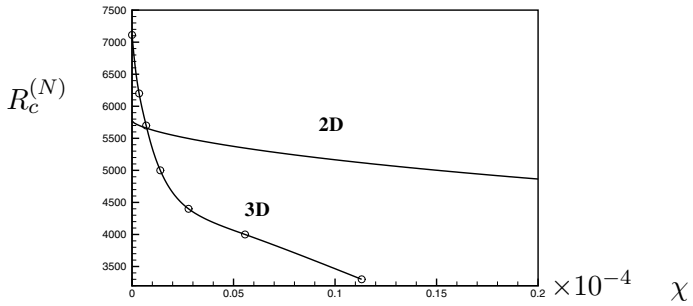

Figure 6. $R_c^{(N)}(\chi)$ v.s. χ, which measures the intensity of the external perturbations

The inhomogeneous equation (9) describes the interaction between the external disturbances and the internal dynamics. An interesting consequence of this is that the system exhibits a tuned response as shown in figure 5. For a fixed χ and $R < R_c$, there exists an interval of ω for which A blows up, i.e. there is a nonlinear subcritical instability. The width of the window shrinks as R is lowered, and eventually disappears at the tip of 'instability tongue', outside of which the amplitude remains bounded. The Reynolds number at the tip can naturally be defined as the critical Reynolds number for subcritical nonlinear instability. It depends directly on the level of the external disturbance, and so is denoted as $R_c^{(N)}(\chi)$.

Figure 6 shows that $R_c^{(N)}(\chi)$ decreases with χ. The reduction is more rapidly for 3D disturbances so much so that although in the absence of the external disturbances the critical Reynolds number is higher, it is reduced to values smaller than that for the two-dimension disturbance, when χ exceeds a critical value χ_c, marked by the cross-over of the two curves. Two-dimensional onset is expected only when $\chi < \chi_c$, beyond which 3D disturbances reign. The value of χ_c roughly corresponds to 10^{-3} roughness and 10^{-3} velocity fluctuation. This result is consistent with the experimental observation that 3D instability prevails in general.

5. CONCLUDING REMARKS AND FUTURE WORK

The boundary layer receptivity to vortical (and acoustic) disturbances is now well understood theoretically. Quantitative agreement with experimental data has been achieved, at least in the case of a flat plate.

The origin of streaks in the boundary layer is well understood. For small-amplitude disturbances, the boundary region/layer equations provide an appropriate framework for quantitative prediction. There exists experimental evidence for streak breakdown through localized & intermittent instability, and the recent theoretical work suggests this to be possible even for relatively weak streaks. It is now increasingly recognized that the external disturbances, which trigger bypass transition in the first place, must be explicitly taken into account in any relevant theoretical and computational modelling.

The 3D external disturbances (combined with the nonlinear effect) are shown to be crucial in explaining the subcritical transition in channel flow and the apparently failure of Squire's theorem.

To conclude this lecture, I now highlight a few outstanding problems for future research. A remaining mystery in receptivity concerns the generation of non-stationary cross-flow vortices, which were the dominant cause of transition in a swept wing when the FST level is high [6]. The usual receptivity mechanism of gust/roughness interaction is probably too weak. This leads one to speculate whether a stronger mechanism operates, involving the FST and the highly non-parallel nature of the base flow near the leading edge.

Recent DNS ([5], [15]) reveal some interesting aspects of bypass transition, but quantitative characteristics of streak instability, such as growth rates and frequencies, have not been computed. Further more, using the continuous modes of O-S equation to represent the disturbances at the inlet seems unsatisfactory because O-S equation neglects non-parallelism, which is particularly significant for the relevant long wavelength components. A promising way forward is to use nonlinear boundary region equations to compute the signature of streaks, and then perform a secondary instability analysis.

Stochasticity is another major obstacle. Certain ideas in the theory for waves propagating through a random medium could be borrowed to assess the impact of random FST on instability, especially on the viscous T-S waves. This may help reconcile some seemingly contradictory claims regarding the stabilizing/destabilizing role of FST ([3], [4]).

The impact of FST on transition in supersonic/hypersonic boundary layers is an important problem, where special attention should be paid to shocks and acoustic disturbances. The latter are very strong in the wind tunnel experiments, and apparently cause transition to occur much earlier than in the flight condition [23]. Their effect has to be accounted for in order to calibrate the experimental data.

REFERENCES

[1] Andersson, P., Brandt, L., Bottaro, A. & Henningson, D.S. 2001 *J. Fluid Mech.* **428**, 29-60.

[2] Arnal, D. & Juillen, J.C. 1978 *ONERA Tech.* No. 1/5018 AYD.

[3] Bakchinov, A.A., Westin, K.J.A, Kozlov, V.V. & Alfredsson, P.H. 1998 *Eur. J. Mech. B/Fluids* **17**, 847-873.

[4] Boiko, A.V, Westin, K.J.A., Klingmann, B.G.B., Kozlov, V.V. & Alfredsson, P.H. 1994 *J. Fluid Mech.* **281**, 219-245.

[5] Brandt, L., Schlatter, P. & Henningson, D.S. 2004 *J. Fluid Mech.* **517**, 167-198.

[6] Deyhle H. & Bippes, H. 1996 *J. Fluid Mech.*, 1996, **316**: 73-113.

[7] Dietz, A.J. 1999 *J. Fluid Mech.* **378**, 291-317.

[8] Dryden, H. L. 1936 *NACA Rep.* 562.

[9] Dryden, H. L. 1958 *Z. A. M. P.* , **9**b, 249-258.

[10] Duck, P.W., Ruban, A.I. & Zhikharev, C.N. 1996 *J. Fluid. Mech.* **312**, 341-371.

[11] Goldstein, M.E. 1995 *Phil. Trans. R. Lond.* **352**, 425-442.

[12] Goldstein, M.E. & Choi, S.-W. 1989 *J. Fluid Mech.* **207**, 97-120.

[13] Goldstein, M.E.& Hultgren, L.S. 1989 *Ann. Rev. Fluid Mech.* **21**, 138.

[14] Hall, P. & Smith, F.T. 1989. *Euro. J. Fluid Mech.* B**8**, 179-205.

[15] Jacobs, R.G. & Durbin, P.A. 2001 *J. Fluid Mech.* **428**, 185-212.

[16] Kendall, J.M. 1985 *AIAA Paper*, 85-1695.

[17] Klebanoff, P.S. 1971 *Bulletin. Am. Phys. Soc.* **16**.

[18] Leib, S.J., Wundrow, D.W. & Goldstein, M.E. 1999 *J. Fluid Mech.* **380**, 169-203.

[19] Lin, C.C. 1946 *Quart. Appl. Maths.* **3**(4), 277-301.

[20] Luo, J.S. & Wu, X. 2004 *Phys. Fluids* **16**(8), 2852-2863.

[21] Matsubara, M. & Alfredsson, P.H. 2001 *J. Fluid Mech.* **430**, 149-168.

[22] Saric, W.S., Reed, H.L. & Kerschen, E.J. 2002 *Ann. Rev. Fluid Mech.* **34**, 291-319.

[23] Schneider, S.P. 2001 *J. Spacecraft & Rockets* **38**, 3, 323-333.

[24] Smith, F.T. 1979 *Proc. R. Soc. Lond.* A **368**, 573-589.

[25] Stuart J. T. 1960 *J. Fluid Mech.* **9**, 353-370.

[26] Taylor, G.I. 1939 In *Proc. 5th Int. Congress for Applied Mechanics*, pp.294-310. Wiley.

[27] Waleffe, F. 1995 *Stud. Appl. Maths* **95**, 319-343.

[28] Westin, K.J., Boiko, A.V., Klingmann, B.G.B, Kozlov, V.V. & Alfredsson, P.H. *J. Fluid Mech.* **281**, 193-218.

[29] Wu, X. 2001a *J. Fluid Mech.* **431**, 91-133.

[30] Wu, X. 2001b *J. Fluid Mech.* **449**, 373-393.

[31] Wu, X. & Choudhari, M. 2003 *J. Fluid Mech.* **483**, 249-283.

[32] Wu, X., Lee, S.S. & Cowley, S.J. 1993 *J. Fluid Mech.* **253**, 681-721.

MODELING THE EFFECTS OF STEPS ON BOUNDARY-LAYER TRANSITION

J.D. Crouch, V.S. Kosorygin, L.L. Ng
The Boeing Company, PO Box 3707, Seattle, WA 98124-2207, U.S.A.; Institute of Theoretical and Applied Mechanics SB RAS, Ul. Institutskaya, 4/1, Novosibirsk 630090, Russia. E-mail: jeffrey.d.crouch@boeing.com ; kosor@itam.nsc.ru ; lian.l.ng@boeing.com

Abstract: An experimental and computational study is conducted to develop a model for the effects of surface steps on transition to turbulence in boundary layers. The step effects are captured within the framework of a variable n-factor method, where the step results in a reduction in the TS-wave transition n-factor ΔN_{TS}. Data is presented for ΔN_{TS} for favorable and adverse pressure gradients. Backward-facing steps result in significantly larger reductions in the transition n-factor when compared to forward-facing steps. The results show that step effects can be accounted for by using a ΔN_{TS} for step heights up to 1.5 times the local boundary-layer displacement thickness.

Key words: Instability, Receptivity, Steps, Transition Prediction, Variable N-Factor

1. INTRODUCTION

In many flows of practical interest, the location of the transition to turbulence is influenced by the presence of surface imperfections in the form of steps, gaps, or protuberances. In aerodynamics some of the most common surface imperfections are forward- and backward-facing steps. New methods to improve transition predictions (based on better physical modeling) need to account for these typical surface imperfections.

Currently, the most useful tools for predicting transition are based on the so-called e^n method – originally devised by Smith & Gamberoni (1956) and Van Ingen (1956). In the e^n method, transition is assumed to occur when the amplification factor n reaches a critical value N, where N is established by

R. Govindarajan (ed.), Sixth IUTAM Symposium on Laminar-Turbulent Transition, 37–44.

correlation with experiments. For controlled experimental conditions, this provides an effective prediction method. However, when applied away from the correlation conditions the method does not yield consistent results. The primary shortcoming of the basic e^n method is that the receptivity (responsible for the initial amplitude A_0) and nonlinear-breakdown physics cannot be adequately accounted for in a single value of N.

To overcome the major shortcomings of the basic e^n method, variable n-factor methods have been proposed (Mack 1977; Crouch & Ng 2000). Here the value of N is given as a function of the external conditions, which influence the receptivity or locally change the growth rate. The methods are based on experimental correlation or a combination of correlation and theory. In this paper, we consider a new form of variable N-factor to account for the effects of steps on Tollmien-Schlichting (TS) wave transition.

The investigation of the effects of steps and protuberances on transition has a long history starting from the beginning of the last century (Prandtl 1914; Goldstein 1936; Dryden 1953, etc.). These early experiments led to the concept of a "critical obstacle height" necessary for affecting transition. The data form these experiments are the foundation for current empirical approaches to transition prediction (e.g. Fage 1943).

A more clear understanding of the physical mechanisms leading to transition came with the experiments of Klebanoff & Tidstrom (1972). They have shown that surface imperfections change the boundary-layer stability characteristics, leading to an accelerated transition. Aizin & Polyakov (1979) obtained another important result showing that surface imperfections can serve as effective sources for unstable Tollmien-Schlichting (TS) waves through the enhanced receptivity to free-stream acoustic disturbances. These TS waves were later shown to superimpose on the TS waves already existing in the smooth-surface boundary layer (Kosorygin 1985, Kosorygin & Polyakov 1985/1990), resulting in movement of the transition onset location.

Analytical and numerical studies show that some of the effects of the steps can be accounted for by modeling the details of the local flow perturbations in the calculation of amplification factors (Nayfeh 1992; Perraud & Seraudie 2000). Meanwhile, Boeing has initiated transition experiments aimed at incorporating the effects of steps into the critical N value. Gaster & Wang (2004) investigated the effects of rectangular backward- and forward-facing steps in a flat-plate zero pressure-gradient boundary layer. They obtained the changes in n-factor for steps of various heights. The present investigation aims at developing a prediction scheme to account for step effects on transition in boundary layers under favorable or adverse pressure gradients, characteristic of leading-edge regions in aerodynamic flows.

2. EXPERIMENTS

The experiments are conducted in the wind tunnel T-324 at the Institute of Theoretical and Applied Mechanics, Russian Academy of Sciences (Novosibirsk). This is a low-turbulence close-circuit wind tunnel with a *1m x 1m x 4m* test section and is well suited for receptivity, stability, and transition experiments. Two flat-plate models were used in the experiments. Each of these plates is manufactured from a *6-mm* aluminum alloy sheet and they are *0.996m* wide and *2.0m* long. The leading-edge shape is a semi-cylinder machined directly on the flat plate model with radius *2.25mm*. The position of the stagnation line and the pressure distribution in the vicinity of the leading edge are controlled by a trailing-edge flap during tests.

The flat plates have movable leading edges to create backward- and forward-facing steps (as well as gaps) over a wide range of heights. The accuracy of adjustment for the step height was about $10\mu m$. The model leading edges have different lengths (*127mm* and *450mm*) to enable the placement of the step in a favorable or an adverse pressure gradient. The polished working surfaces of the flat plates have slightly different natural undulations, which have been documented. Both plates contain a row of 24 *0.35mm* static pressure orifices parallel to the centerline, but shifted in the span direction. The surface pressure variation is created by means of wall contours, as shown in figure 1.

Detailed measurements of the basic flow are used to establish the flow conditions for the stability analysis. The measured pressure distribution is shown in figure 2, along with the spline fit used for the calculations. The minimum of the pressure distribution is located at a longitudinal distance *x=250mm* and the step can be placed at either *x=127mm* or *x=450mm*, in the

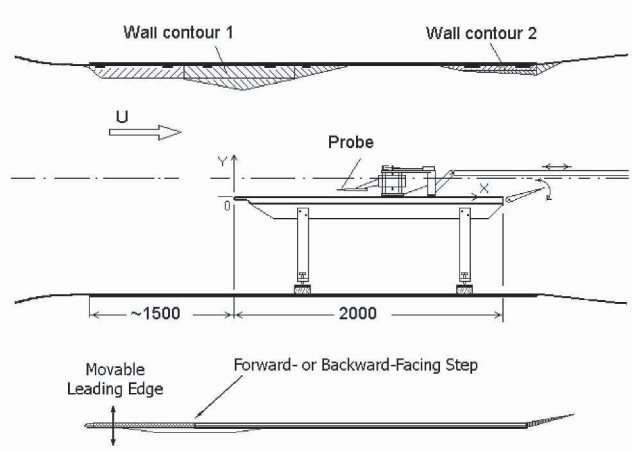

Figure 1. Experimental setup showing the flat-plate in the test section with wall contours (distances are in *mm*), and flat plate with movable leading edge

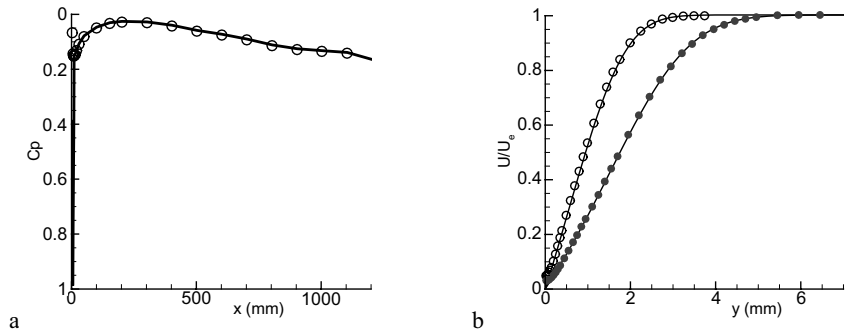

Figure 2. Basic-flow characteristics: (a) experimental pressure distribution with curve used for computations, (b) computational (line) and experimental (symbols) velocity profiles

favorable (FPG) or adverse (APG) pressure gradient, respectively. The free-stream velocity is varied from *18.3m/s* up to *27.5m/s*. All measurements are conducted under natural background disturbances, with an integral free-stream turbulence intensity of $\varepsilon = 0.028\%$ at *U=18.3m/s*, and $\varepsilon = 0.039\%$ at *U=27.5m/s* (bandwidth $2 - 4 \cdot 10^3$ Hz).

Figure 2 also shows velocity profiles measured at the streamwise locations *x=400mm* (open symbols) and *x=900mm* (closed symbols). The lines through the experimental points are boundary-layer calculations based on the measured *Cp* distribution. The experimental points were shifted in *y* using the calculated results to "find the wall." The calculated basic flow is in very good agreement with the measured flow conditions.

In addition to the mean-flow quantities, the transition location and velocity oscillations are also measured. The transition location is determined by means of a *1-mm* round Preston tube which is moved along the surface. The measured dynamic pressure can be interpreted in terms of the velocity profile slope close to wall (i.e. the skin friction). The dynamic pressure typically diminishes along the streamwise coordinate in a laminar boundary layer. At some distance downstream, the pressure (and skin friction) will rise as a result of the non-linear processes associated with transition. The transition location, x_T, is estimated based on the minimum of the dynamic pressure distribution, with an uncertainty in x_T of about *20mm*. The transition Reynolds number, $Re_T = U \cdot x_T / \nu$, is plotted in figure 3 as a function of the non-dimensional step height. An Increase in the step height results in a reduction in the extent of laminar flow. The results show a stronger reduction in Re_T for backward-facing steps.

Velocity profile measurements are made using a single-wire probe built in-house with $5\mu m \times 1mm$ Pt-plate tungsten wire. The probe is connected to a DANTEC constant-temperature anemometer. Spectra of the velocity oscillations, measured just prior to transition onset, show a band of unstable

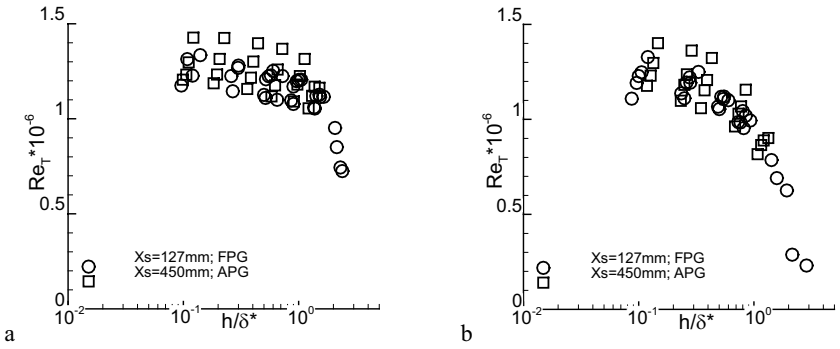

Figure 3. Transition Reynolds numbers as a function of non-dimensional step height, for: (a) forward-facing and (b) backward-facing steps, in favorable and adverse pressure gradients.

TS waves. The measurements also show the exponential growth characteristic of TS waves. Similar measurements in the presence of steps demonstrate that the same frequencies are responsible for transition, within some step-height range. However, the measured amplitudes of the leading frequencies are larger in presence of a step.

3. N-FACTOR RESULTS

Tollmien-Schlichting wave amplification n-factors are calculated based on quasi-parallel theory. The mean flow is obtained numerically by solving the compressible boundary layer equations for spanwise-uniform flow. The experimental pressure distributions are used to generate the edge velocities for the boundary layer. The instabilities are governed by the Orr-Sommerfeld equation, with imposed values for the real frequency ω and spanwise wavenumber β. The amplification n-factor is defined as:

$$n_{TS}(x) = \max_{\omega} \max_{\beta} \left(\int_{x_0}^{x} \gamma(s;\omega,\beta)\, ds \right), \qquad (1)$$

where γ is the spatial growth rate. These n-factors are calculated for the smooth-surface conditions, without accounting for any of the local effects due to the steps.

Figure 4 shows the amplification n-factors calculated for the test conditions of this study. The results show a slight destabilizing effect due to increasing the free-stream velocity from *U=18.3m/s* to *U=27.5m/s*. This corresponds to an increase in the unit Reynolds number from $1.2 \cdot 10^6\ m^{-1}$ to $1.8 \cdot 10^6\ m^{-1}$. The change in unit Reynolds number also results in a change in

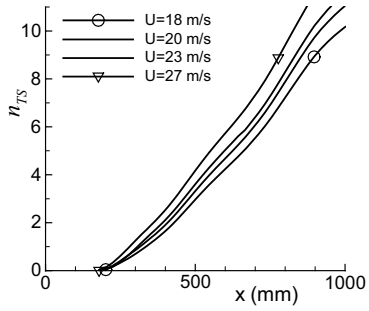

Figure 4 N-factor curves calculated for the experimental conditions, with different edge velocities: *U=18m/s, U=20m/s, U=23m/s, U=27m/s*

boundary-layer thickness at the *x=127mm* step location from $\delta^*=0.52mm$ to $\delta^*=0.42mm$. The dominant frequencies calculated from the stability theory are in agreement with the dominant frequencies measured prior to transition.

The value of $n_{TS}(x_T)$ at the transition location, x_T, is designated N_{TS}. For each step height considered, the transition location is measured and the value of N_{TS} is determined. In the absence of any step, transition occurs at $x_T=1000mm$ for $U=18m/s$, and at $x_T=760mm$ for $U=27m/s$; the corresponding transition n-factors for these two cases are $N_{TS}=10$ and $N_{TS}=8.5$, respectively. This difference in n-factor is consistent with the difference in turbulence levels given in section 2, following the relationship of Mack (1977).

In the presence of a step, the transition n-factor is reduced due to the forward movement of the transition location. The reduction in transition n-factor can be modeled with a variable n-factor relationship

$$N_{TS} = N_{TS0} - \Delta N_{TS}(h/\delta^*), \tag{2}$$

where the function ΔN_{TS} accounts for the local change in the stability characteristics at the step. The value of the smooth-surface transition n-factor N_{TS0} can account for the free-stream turbulence level as suggested by Mack (1977). Delta-n-factors are calculated for each of the step-heights considered, and are plotted against the step height in figure 5. The step heights are normalized by the local displacement thickness at the step location. Results are presented for both favorable and adverse pressure gradients. In general, the adverse-pressure-gradient ΔN_{TS} results show a better collapse, when compared to the favorable-pressure-gradient results. In both pressure gradients, the backward-facing steps have a much bigger impact on the transition n-factors. For forward-facing steps, the reduction in n-factor is generally larger for adverse pressure gradients. The ΔN_{TS} results have also been plotted against the trip-height Reynolds number, $Re_h = U \cdot h / \nu$ (not shown). This yields distinct curves for the favorable-pressure-gradient

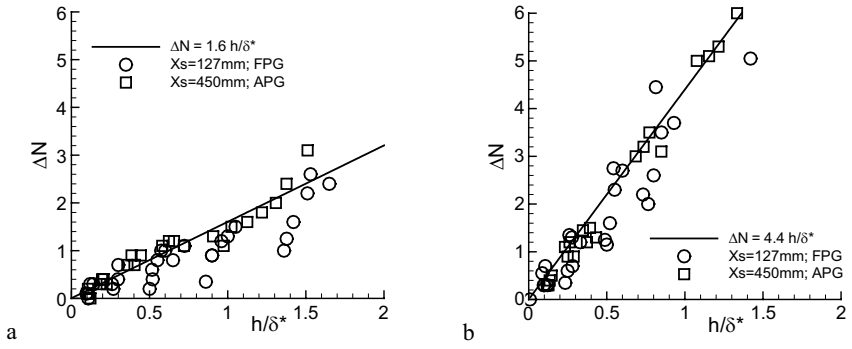

Figure 5. ΔN-factor results for: (a) forward-facing steps, and (b) backward-facing steps in favorable and adverse pressure gradients

and adverse-pressure-gradient data since it only accounts for the unit Reynolds number, and not the actual boundary-layer thickness.

The lines drawn through the calculated n-factors of figure 5 are based on a fit to the adverse-pressure-gradient data. These lines provide a rough upper bound for the favorable-pressure-gradient data. These results lead to the TS-wave n-factor expressions:

$$\text{FFS:} \quad N_{TS} = N_{TS0} - 1.6\, h/\delta^*, \tag{3}$$

$$\text{BFS:} \quad N_{TS} = N_{TS0} - 4.4\, h/\delta^*, \tag{4}$$

for forward- and backward-facing steps, respectively. For forward-facing steps, a step height equal to the displacement thickness results in a reduction in the TS-wave transition n-factor of 1.6. The delta n-factors for backward-facing steps are much larger. A backward-facing step at a height of the boundary-layer displacement thickness results in a reduction of 4.4 in the transition n-factor – almost three times the reduction of a forward-facing step of the same height. These expressions for N_{TS} capture the effects of steps on transition for step heights up to 1.5 times the boundary-layer displacement thickness.

4. CONCLUSIONS

Detailed measurements are made to quantify the effects of forward- and backward-facing steps on transition. The transition results from the amplification of TS waves, both for the smooth surface and in the presence of steps. Measurements and boundary-layer calculations are used to

establish a basic flow. The calculated boundary-layer profiles are shown to be in very good agreement with the experiments. Linear-stability theory is used to determine the amplification n-factors for the TS waves.

The effects of the steps are modeled by a variable transition n-factor. The amplification n-factors are calculated for a smooth surface, but the critical value that signifies transition is given as a function of the step height. The transition n-factor varies linearly with the step height, nondimensionalized with the boundary-layer displacement thickness at the step location. Backward-facing steps result in n-factor reductions that are almost three times as large as forward-facing steps of the same height. The variable n-factor relationships are well correlated with the experiments for steps heights up to 1.5 times the local boundary-layer displacement thickness. This provides a very useful method to account for surface steps in practical applications.

REFERENCES

Aizin L.B., Polyakov N.Ph. "Acoustic generation of Tollmien-Schlichting waves over local unevenness of surface immersed in stream," Preprint 17, Inst. Theor. Appl. Mech. USSR AS, Novosibirsk, 1979.

Crouch, J.D., Ng, L.L. "Variable n-factor method for transition prediction in three-dimensional boundary layers," *AIAA J.*, v. 38, pp.211-216, 2000.

Dryden H.L. "Review of published data on the effect of roughness on transition from laminar to turbulent flow," *JAS*, v. 20, pp. 477-482, 1953.

Fage, A. "The smallest size of a spanwise surface corrugation which affects boundary layer transition on an aerofoil," British Aeronautical Research Council Rpt. 2120, 1943.

Goldstein S. "A note on roughness," ARC RM 1763, 1936.

Klebanoff P.S., Tidstrom K.D. "Mechanism by which a two-dimensional roughness element induces boundary layer transition," *Phys. Fluids*, v.15, No.7, pp. 1173-1188, 1972.

Kosorygin V.S. "Experimental study of a laminar flat plate boundary layer under low natural and acoustic disturbances," PhD Thesis, I.T.A.M., USSR AS, Novosibirsk, 1985.

Kosorygin V.S., Polyakov N.Ph. "Auto destruction of unstable boundary layer waves," Preprint 11-90, Inst. Theor. and Appl. Mech. USSR AS, Novosibirsk, 1985/1990.

Mack, L.M. "Transition prediction and linear stability theory," *Laminar-Turbulent Transition*, CP-224, AGARD, 1977, pp.1/1-22.

Nayfeh, A. H. "Influence of two-dimensional imperfections on laminar flow," SAE Paper No. 921990, 1992.

Perraud J., Seraudie A. "Effects of steps and gaps on 2D and 3D transition," ECCOMAS 2000, Barcelona, Spain, 2000.

Prandtl L. "Der luftwiderstand von kugeln," Nachr. Ges. Wiss. Göttingen, Math. Phys. Klasse, pp. 177-190, 1914.

Smith, A.M.O., Gamberoni, A.H. "Transition, pressure gradient, and stability theory," Douglas Aircraft Co., Rept. ES26388, El Sequndo, 1956.

Van Ingen, J.L. "A suggested semi-empirical method for the calculation of the boundary layer transition region," Univ. of Technology, Rept. UTH1-74, Delft, 1956.

Wang, Y.X., Gaster, M. "Effect of surface steps on boundary layer transition," *Exp. in Fluids*, 2005, to appear.

RECENT OBSERVATIONS OF THE TRANSITION TO TURBULENCE IN A PIPE

T. Mullin & J. Peixinho
Manchester Centre for Nonlinear Dynamics,
Department of Physics and Astronomy,
The University of Manchester,
Manchester M13 9PL, UK

Abstract: We report the results of an experimental investigation of the transition to turbulence of Poiseuille flow in a long pipe. Our findings confirm that the recently established scaling law for the finite amplitude perturbation required to cause transition is $O(Re^{-1})$. New results are presented concerning the decay of disturbances injected into the flow field at values of Re where the flow is known to be globally stable. Exponential decay and critical behaviour is observed and these are consistent with observations in other shear flows. This new approach has enabled us to uncover a sharp cut off at the lower limit of the stability threshold.

The origins of turbulence in the flow along a circular pipe has intrigued scientists for more than one hundred and twenty years since Reynolds'[3] landmark experimental investigations. Mathematically, the flow is linearly stable [1] so that laminar flow ought to be observed for all flow rates. In practice, however, pipe flows are typically observed to be turbulent even at modest flow rates. Hence there is a direct conflict between theory and observation. Understanding this enigma has been one of the outstanding challenges of hydrodynamic stability for more than a century. Reynolds also showed that if disturbances at the inlet to the pipe are minimized, laminar flow can be maintained to higher flow rates than if they are not. Kelvin [2] proposed that finite amplitude perturbations are most likely to be responsible for triggering the transition to turbulence. The finite amplitude nature of the transition process was confirmed in the experiments of Pfenniger [4] who managed to obtain laminar flows up Reynolds numbers of $Re \approx 100,000$ by taking extraordinary care to control external influences. (Here $Re = \frac{Ua}{\nu}$ where U is the peak velocity, a is the pipe radius and ν the kinematic viscosity of the fluid.)

R. Govindarajan (ed.), Sixth IUTAM Symposium on Laminar-Turbulent Transition, 45–55.

The issue of transition to turbulence in pipe flow is not only of deep scientific interest, it is also of significant engineering importance. Transitional flows necessarily involve large pressure variations since the pressure gradient required to drive laminar and turbulent flows may differ by an order of magnitude. Thus flows in oil and gas pipelines are often run inefficiently turbulent to avoid the large pressure fluctuations found in the transitional regime. In addition, the control of turbulence is a dream of many practitioners, just as an understanding of turbulence is the desire of many scientists.

Linear stability of the flow means that infinitessimal disturbances added to Poiseuille flow will decay as they propagate along the pipe and laminar flow will be recovered downstream. Available experimental evidence from Reynolds and Pfenniger suggests that the influence of such disturbances is likely to become more important as Re, increases. A mathematical statement [17] of these facts is provided by: if $\epsilon = \epsilon(Re)$ denotes the minimal amplitude of all finite perturbations that can trigger transition, and if ϵ scales with Re according to

$$\epsilon = O(Re^{\gamma}) \tag{1}$$

as $Re \rightarrow \infty$, then what is the exponent γ? A negative value of γ will be consistent with the observations and one substantially less than zero would indicate that the sensitivity of the laminar flow to perturbations increases rapidly with Re. An outstanding problem is relating this theoretical concept to observation in a quantitative manner. Now, we review some recent experimental evidence which suggests that it is beneficial to consider the problem in this way. We will focus on the issues associated with the stability of fully developed Poiseuille flow. Hence we will not discuss the important practical problem of developing or entrance flow which can feature linear instability (see Da Silva and Moss [7] for a review of this problem).

In general terms, pipe flow may be considered as a nonlinear dynamical system $d\mathbf{u}/dt = f(\mathbf{u}, Re)$ which represent the Navier Stokes equations subject to appropriate forcing and boundary conditions. The single control parameter Re determines the dynamical state of the system such that there is one linearly stable fixed point, Poiseuille flow, for all Re and another attractor, turbulence, when $Re > Re_c$. Hence when $Re < Re_c$ all initial conditions are attracted to the laminar state which is the global attractor for the system. When $Re >> Re_c$ nearly all initial conditions give rise to turbulence so that the laminar state is now a local attractor. In practice, $Re_c \lesssim 1800$ so that all disturbances will decay as $t \rightarrow \infty$ for values of Re smaller than this.

Experimental evidence [9] has shown that when $Re \gtrsim 1800$, small amplitude perturbations introduced into fully developed Poiseuille flow decay as they travel downstream i.e. when $Re \lesssim 1800$ all perturbations decay and turbulent flow cannot be maintained. On the other hand, perturbations of sufficient amplitude give rise to transition to the nontrivial state of turbulence. At

these values of Re the turbulence is in the form of a turbulent 'puff' [5]. A finite amplitude threshold therefore exists, below which laminar flow is maintained and above which turbulence sets in. The boundary is not sharp but is probabilistic in nature [22]. Nevertheless, a definite demarcation can be established between perturbations which give rise to transition and those which do not.

A threshold curve was established by Darbyshire and Mullin as a function of Re using a constant mass flux experiment with impulsive perturbations. It was found that the the amplitude of perturbation required to cause transition reduced when Re was increased from 1800 and became independent of Re for $Re \gtrsim 3000$. In a more recent investigation [13] a novel type of perturbation was used to uncover a scaling relationship for the amplitude of perturbation required to cause transition to turbulence. The novel feature of the perturbation is that it allowed for a separation of amplitude and timescales by injecting a boxcar distribution of perturbation fluid into the main flow field. It was firmly established that the important criterion was the length of the flow field which was perturbed and this enabled the uncovering of a $O(Re^{-1})$ scaling law for the amplitude of perturbation required to cause transition over a wide range of Re. Some evidence for such a scaling law has been reported previously for boundary layers [23], pipe flows [6] and has also been found for plane Couette flows [20].

One surprising consequence of this finding is that the absolute amplitude of the perturbation remains relatively large with increasing Re. Therefore, theories based on local analyses of the trivial state may not provide much insight into transition since the basin of attraction of the laminar state remains finite even at modest Re. This appears to contradict many observations which show that very small amplitude disturbances are required to promote turbulence at high Re. However, most of these are concerned with the entrance or developing flow which is linearly unstable [7] whereas fully–developed flow is not. Hence, the fully developed flow always requires a finite amplitude disturbance to cause transition.

In drawing a connection between experimental observations and theory, the difficult issue of what is meant by a perturbation must be addressed. In models, the temporal and spatial form of any perturbation can be accurately specified. On the other hand, experimentalists rely on injecting and or subtracting fluid through slits or holes in an attempt to mimic the mathematical process. The perturbation can be either periodic[6, 8] or impulsive [9] but specifying a form which can be directly related to theory is difficult. Indeed, identifying the part of the physical perturbation which initiates the transition process is in itself a difficult exercise although progress is being made[8]. The robust scaling law uncovered by Hof et al [13] also shows that self consistency can be found.

Modern theoretical research may be broadly split into two approaches. In one, initially small disturbances on the laminar state grow in a transient phase [16],[21] until they reach a sufficiently large amplitude that nonlinear effect become important. These ideas have been explored for various low–dimensional models[12] and applied to plane Poiseuille flow[15, 14] and scaling laws for the amplitude of the perturbation as a function of Re have been provided. An alternative point of view[17] is that the turbulent state originates from instabilities of a finite amplitude solution which is disconnected from the base state. The basin of attraction of the turbulent state grows with Re so that any small perturbation will kick the laminar solution towards it. Such solutions of the Navier Stokes equations are known to exist other flows [19, 20, 18] and more recently they have been shown to exist in Poiseuille flows [24, 25]. Their lower limits of existence are almost a fact or two below the range of Re where turbulence can be established but recent experimental evidence [27] suggests that they may play a role in observed turbulent structures. The stability of these new solutions and their role in transition are both currently open questions.

The scaling law discussed above raises an interesting issue. The perturbation amplitude is normalized by the mass flux of the mean flow and thus is effectively scaled by Re. The dimensional perturbation amplitude is hence independent of Re which suggests that the flow can be destabilized for both high and **low** values of Re. It is known that the flow is globally stable for $Re \lesssim 1800$ and hence there is inconsistency between these new results [13] and well established facts. Here we report the results of a new experimental investigation where we study the processes whereby injected perturbations decay for $Re \lesssim 1800$.

1. EXPERIMENTAL DETAILS

The experimental system can be regarded as a large hypodermic syringe where a piston pulls water at a fixed mass flux along a 17 metre 'needle'. A schematic diagram of the apparatus is shown in figure 1. The pipe consisted of a $D = 20 \pm 0.01\ mm$ diameter Perspex tube which was constructed using 150 mm long machined sections push-fitted together and butted flush so that there was no measurable gap between each join. The sections were held on on a steel base with a total length of 15.7 m ($785D$) and were aligned using a laser.

A reservoir with a capacity of approximately 100 liters was connected to the pipe entrance via a smooth trumpet shaped inlet. This device ensures a laminar flow over the whole Re range investigated for a flow which was initially disturbance free. The maximum flow rate achievable corresponded to $Re = 23,000$ and laminar flow could be achieved with care. On the other hand a sharp cornered inlet induced transition spontaneously at a $Re \approx 2000$.

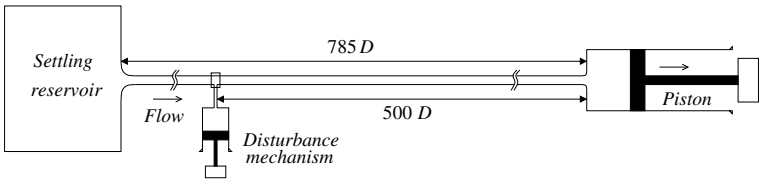

Figure 1. Schematic of the constant mass flux pipe facility

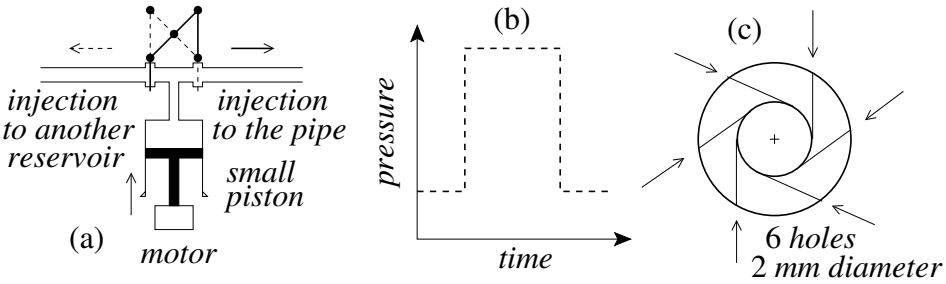

Figure 2. (*a*) Schematic of the disturbance generator. (*b*) Typical trace of the perturbation. (*c*) Inlet manifold of six jet disturbance

The fluid was pulled through the pipe by a cylindrical machined steel piston of length 1.033 m and 0.260 m diameter. The expansion aspect ratio between the piston and the pipe was 13 and a smooth trumpet joint was again used. The piston was pulled by a lead screw and nut arrangement. This was powered by d.c. motor which was computer controlled allowing the speed to be varied as a function of time to within an accuracy of 1%. Hence, even if the fluid in the pipe becomes turbulent the mass flux pulled through the pipe will be unaffected the Re constant.

The long term temperature stability of the laboratory was set at 20 ± 1 ^{o}C using several air-conditioning units which were located adjacent to the pipe. The largest temperature gradient recorded from several K thermocouple along the pipe was 0.3^{o}C which corresponds to a variation in Re of ± 30 at $Re = 2000$.

Two types of experiments were performed. In the first, fully developed laminar flow [11] was established over the Re range investigated and the stability of the flow was probed using a perturbation which was applied at 530 pipe diameters from the pipe entrance. In the second, a well defined perturbation was injected into fully developed flow and the evolution of the disturbance was observed as it progressed downstream.

Figure 3. A typical puff at $Re = 1900$

In both sets of experiments the perturbation was provided by a single box-car pulse of fluid which was injected tangentially into the flow via a ring of six equally spaced 0.5 mm holes as shown in figure 2(c). The valves which control the fluid injection had switching times of approximately 1 ms are shown schematically in figure 2(a). A typical pressure trace of the perturbation is shown figure 2(b). The injection system enabled variation of both the duration ($\triangle t0$ to 10 s) and the amplitude ($0 < \Phi_{inj} < 5\ ml/s$) of the perturbation. The displaced volume Φ_{inj} from the injector is used in our definition of the amplitude A of the perturbation. The quantities of fluid injected were in the range 0.01 to 0.1 % of the total mass flux where the larger values were required to cause transition at smaller Re. The duration of the injection set the spatial extent of the disturbed flow ($L^* = \triangle t * \overline{U}$ in pipe diameters) since it initially travel with the mean speed $\overline{U}$ of the flow in the pipe. The relative volume flux Φ_{inj}/Φ_{pipe} is used to define the amplitude of he perturbation A. In principle, the perturbation will affect the flow field globally. However, previous tests using both injection and suction [9] showed that it is localized in practice.

The flow state was monitored using flow visualization. A small amount of Mearlmaid Pearlessence were added to the water. The particles were anisotropic and had the form of $\sim 35 \times 10 \mu m$ platelets. They reflect the incident light from a $\sim 3mm$ vertical light-sheet which was formed all along the pipe. The light-sheet was switched sequentially to reduce heating effects. A photograph of a typical turbulent puff is given in figure 3.

The design of the experiment was such that it ran in single shot mode. Transients at both the beginning and the end of each run were approximately 10 s long and these were independent of Re. A typical useful experimental time was half an hour at $Re = 2000$. After each run of the experiment, the fluid was pushed back through the pipe into the reservoir and allowed to settle for a period of at least 30 minutes before the next run was started. This period was chosen empirically on the basis of observations of the fluid in the tank and it was also found to be the minimum time required to give repeatable results.

In the second set of experiments on the evolution of disturbances, it occasionally proved possible to obtain results from several sequential experimental runs. This helped improve the statistics of the measured distributions.

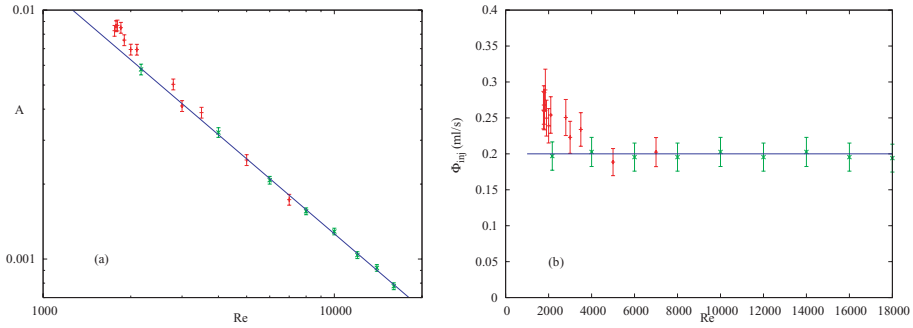

Figure 4. A versus Re

2. RESULTS

Finite Amplitude Stability Curve

As discussed in the introduction, Hof et al. [13] developed an injection system which permits the amplitude and width of the perturbation to be varied independently. This helped uncover a scaling law which indicates that the amplitude of perturbation required to cause transition scales as $O\left(Re^{-1}\right)$. One interpretation of this result is that it reflects the balance between viscous and inertia terms in the Navier Stokes equations. The smallest amplitude of perturbation required to cause transition is obtained when $L^* \gtrsim 6D$. We have added to these results and a compilation of both sets of results is presented in figure 4(a). In general, there is very good agreement between both sets of results and a $O\left(Re^{-1}\right)$ scaling law.

The amplitude A of the perturbation in figure 4(a) is made non-dimensional by dividing by the mass flux of the main flow. Hence it is effectively scaled by Re. If the data is now plotted in dimensional form as in figure 4(b) it can be seen that Φ_{inj} is almost independent of Re and only departs from a constant level for $Re \lesssim 3000$. In fact, the departure is not significant since all experimental evidence suggests that the flow is globally stable for $Re \lesssim 1800$ so that it might be expected that $\Phi_{inj} \rightarrow \infty$. Clearly, disturbances injected into the flow when $Re \lesssim 1800$ will decay as they move downstream and it is this process that we will focus on in the next section.

3. DECAY OF INJECTED DISTURBANCES

The investigation was carried out by injecting well defined perturbations into fully developed Poiseuille flow ($285D$ from the entrance) and observing their development downstream. The values of Re investigated were such that

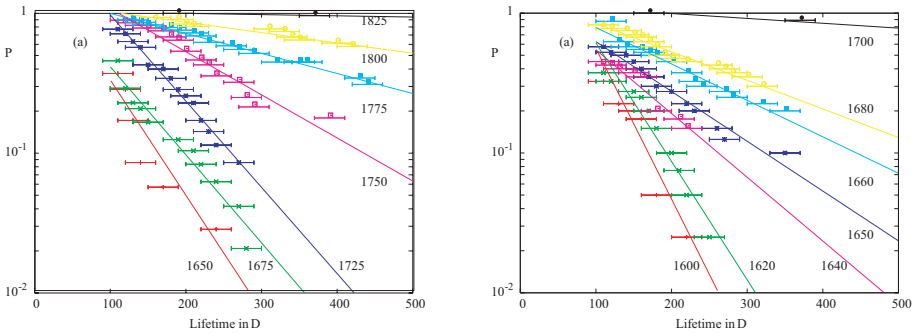

Figure 5. The probability of observing a localized region of disturbed flow plotted as a function of distance downstream from the point of injection. Data was accumulated from between 40 to 100 measurements for each of the six values of Re. The lines are least squares fits of exponentials. (a) The initial disturbance amplitude was $A = 0.01$ (b) The initial disturbance amplitude was $A = 0.1$

the final state far downstream was laminar flow. At a given Re, the disturbed flow was localized and travelled along close to the mean speed of the flow. In the first $100D$ the perturbation evolved in a complicated way as discussed by Wygnanski and Champagne [5] and Darbyshire and Mullin [9]. Several light boxes suspended above the pipe provided a light sheet along the length of the pipe and these were switched on and off sequentially to avoid heating effects. This illumination allowed the observation of the disordered fluid as it travelled along and enabled an estimate to be made of position at which the disordered spot decayed (measured in diameters D from the perturbation input).

The results presented in figure 5 are graphs of the probability of observing a localized disturbed region of flow, plotted as a function of distance downstream in D from the point of injection (zero on the abscissa). The downstream limit was set by the length of the pipe at $500D$ but this was not a severe limitation since not many disturbances survived to this station in practice. The initial conditions for the perturbation were $L^* = 10$ and the amplitudes used in figure 5 (a) and (b) were $A = 0.01$ and $A = 0.1$ respectively. Between 40 and 100 independent experimental runs were performed for each value of Re in order to obtain good statistics. The straight lines correspond to least squares fits of exponentials $P(D) \propto \exp(\epsilon D)$, where ϵ the rate of decay of the disturbed state. The quality of the fits indicate that the disturbed flow decays exponentially to

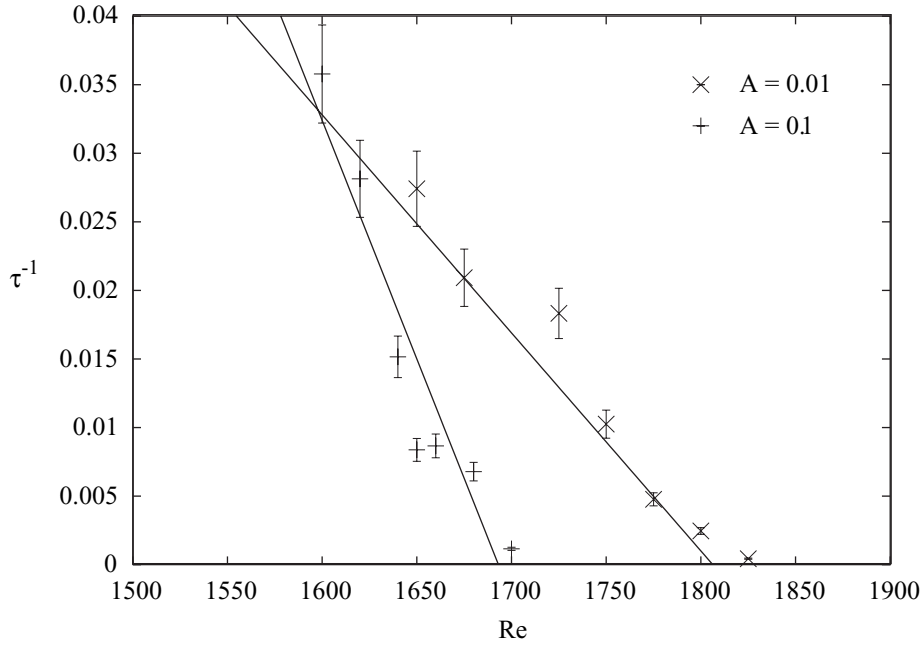

Figure 6. Half-life τ plotted as a function of Re for $A = 0.01$ and $A = 0.1$. Estimates of Re_c are 1830 ± 10 and 1710 ± 10 respectively

a reasonable approximation. In general, the slopes increase as Re decreases i.e. there is faster decay at smaller Re. Such behaviour has previously been observed by Bottin and Chate [10] in experiments on plane Couette flow.

A useful measure that can be extracted from the exponential fits is time required for half the initial states to decay which is defined as $\tau = (\ln 2)/\epsilon$ where $\epsilon = Re - Re_c$. We will refer to this as the 'half-life' of a perturbation. Plots of the inverse of half-life τ^{-1} versus Re are shown in figure 6 for the two perturbation amplitudes used in the present series of experiments viz. $A = 0.01$ and $A = 0.1$. It may be seen that τ^{-1} passes through zero at 1830 ± 10 and 1710 ± 10 respectively. At these critical values of Re the half-life τ approaches infinity and the perturbation does not decay but develops into a turbulent puff which persists. Hence this gives a method for estimating the threshold for transition to turbulence which is more accurate than the direct method of increasing the amplitude of perturbation until a threshold is crossed as in the results section labelled (Finite Amplitude Stability Curve) above. This method was used to obtain estimates of the stability threshold for $Re \lesssim 1750$ by setting the amplitude of the perturbation at a prescribed value and observing transient behaviour for a range of Re as above. The new results for the estimate

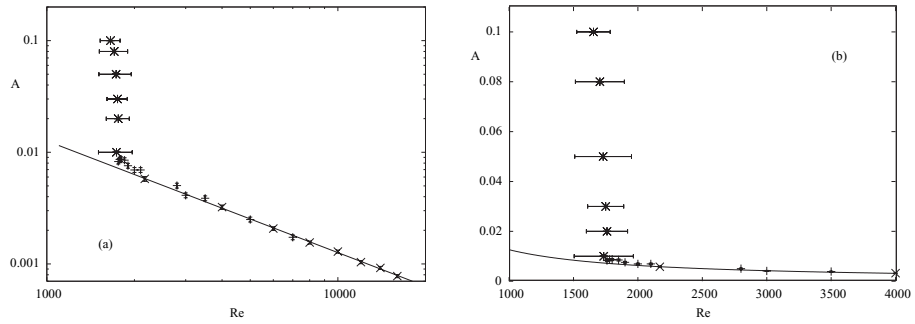

Figure 7. Finite amplitude threshold curve A vs Re with data from transient experiments included. (a) Log/linear scale (b) Linear scales.

of the threshold curve are presented together with the previous ones in Figure 7 a,b. We have again chosen to show the results on both logarithmic (Figure 7 (a)) and linear (Figure 7 (b)) scales to emphasize different aspects. There is clear consistency between the two sets of results which indicates that both methods are valid ways of estimating the stability boundary. The new estimates show clearly that the stability boundary rises almost vertically for $Re \lesssim 1750$ i.e. there is a sharp departure from the $O\left(Re^{-1}\right)$ scaling law. Hence maintaining disordered flow below $Re \lesssim 1750$ is not possible since perturbations over a wide range of amplitudes decay.

4. CONCLUSIONS

We have confirmed previous results [13] on an $O\left(Re^{-1}\right)$ scaling law for the amplitude of the perturbation required to cause transition in circular Poiseuille flow. Moreover we have extended the results using the transient decay of perturbations towards the lower values of Re. These new findings have uncovered a surprisingly sharp cut off in Re below which turbulence can not be maintained. It has been suggested [26] that such behaviour is consistent with the formation of a chaotic repellor and saddle in the solution set but much more work is required before definite conclusions in this respect can be justified.

ACKNOWLEDGEMENTS

TM is grateful to EPSRC for supporting this research through a 'Senior Fellowship' and for the research grant GR/S76137/01 .

REFERENCES

[1] P.G. Drazin & W.H. Reid An Introduction to Hydrodynamic Stability Theory (1980) Cambridge University Press.

[2] Lord Kelvin (1887) Phil. Mag. **5**,459.

[3] O. Reynolds (1883) Proc. Roy. Soc. A **35**,84.

[4] W. Pfenniger (1961) In*Boundary Layer and Flow Control,Pergamon* (ed. G.V. Lachman),970.

[5] I. J. Wygnanski and F.H. Champagne (1973) J. Fluid Mech. **59**,281.

[6] A. A. Draad, G. Kuiken and F.T.M. Nieuwstadt (1998) J. Fluid Mech. **377**,267.

[7] D. F. da Silva and E.A. Moss (1994) J. Fluids Eng. **116**, 61.

[8] G. Han, A. Tumin and I. Wygnanski (2000) J. Fluid Mech. **419**,1.

[9] A. G. Darbyshire and T. Mullin (1995) J. Fluid Mech. **289**,83.

[10] Bottin, S. & Chate, H. (1998) Eur. Phys. J. B **6**, 143.

[11] Fargie, D. & Martin, B. W. (1971) **A 321**, 461.

[12] J. S. Baggett and L. N. Trefethen (1997) Phys. Fluids **9**,1043.

[13] B. Hof, A. Juel and T. Mullin. (1999) Phys. Rev. Lett. **91**,244502.

[14] S.J. Chapman (2002) J. Fluid Mech. **451**,35.

[15] D. S. Henningson, A. Lundbladh and A. V. Johansson (1993) J. Fluid Mech. **250**,169.

[16] L.N. Trefethen, A.E. Trefethen, S.C. Reddy, and T.A. Driscoll (1993) Science **261**,578.

[17] F. Waleffe (1996) Phys. Fluids **9**,883.

[18] D. K. Anson, T. Mullin and K. A. Cliffe (1989) J. Fluid Mech. **207**,475.

[19] D. R. Barnes and R. R. Kerswell (2000) J. Fluid Mech. **417**,103.

[20] O. Dauchot and F. Daviaud (1995) Phys. Fluids **7**,335.

[21] S. Grossmann. (2000) Rev. Mod. Phys. **72**,603.

[22] B. Eckhardt and A. Mersmann. (1999) Phys. Rev. E **60**,509.

[23] R. Govindara and R. Narasihma (1991) Trans. ASME J. Fluids Eng. **113**,147.

[24] H. Wedin and R. R. Kerswell (2004) J. Fluid Mech. **508**,333.

[25] H. Faisst and B. Eckhardt (2004) Phys. Rev. Lett **91**,224502.

[26] H. Faisst and B. Eckhardt (2003) J. Fluid Mech. **504**,22.

[27] B. Hof, C.W.H. van Doorne, J. Westerweel, F.T.M. Nieuwstadt, H. Faisst, B. Eckhardt, H. Wedin, R.R. Kerswell and F. Waleffe (2004) Science **305**,1594.

LOCALISED INSTABILITY IN UNSTEADY SEPARATION BUBBLES

Jaywant H. Arakeri, S. P. Das and Usha Srinivasan
Department of Mechanical Engineering
Indian Institute of Science, Bangalore,
India
jaywant@mecheng.iisc.ernet.in

Abstract: We propose an experimental method to study the instability of thin unsteady separation bubbles, i.e. of unsteady boundary layers with reverse flow. The unsteady boundary layer is created by controlled temporal and spatial variations of the velocity external to the boundary layer. We present results of the evolution of instability in different temporally varying flows in a shallow angle diffuser. Depending on the extent of reverse flow in the boundary we observe that instability can be spatially localised.

Keywords: Laminar separation bubble, inflectional instability, unsteady boundary layer.

1. INTRODUCTION

In this paper we are concerned with the evolution of instability in thin unsteady separation bubbles. The bubble is considered thin in that the boundary layer approximation is valid, and in the boundary layer, over some length, there is flow reversal (figure 1). The external flow velocity (U_0), boundary layer thickness (δ) are in general, functions of downstream distance (x) and time (t); the extent of the reverse flow region also depends on t. We describe an experimental procedure in which it is possible to tailor the spatial and temporal dependences of the separation bubble parameters, and hence systematically study the stability characteristics of unsteady separating flows.

Laminar separation bubbles have been studied in two contexts. One type of study is of a laminar separation bubble due to an imposed steady adverse pressure gradient on a flat plate (Gaster, 1966). For the Reynolds numbers of interest, vortices are periodically shed from the bubble, and the downstream boundary layer usually is turbulent. Though recent experiments and direct numerical simulations (see for example, Rist, 2002, Alam and Sandham, 2000) have given detailed information, many questions remain with regard to the dynamics, in particular, the nature and cause of the shedding. Suggestions

R. Govindarajan (ed.), Sixth IUTAM Symposium on Laminar-Turbulent Transition, 57–70.

have been made that the shedding may be due to an instability of the reverse flow region.

The other type of study has been that of unsteady boundary layer separation. Though the term separation bubble is generally not used, a reverse flow region or separation bubble does exist in these flows, before true separation takes place. We believe unsteady separation can be classified into two types. One, as in the flow past an impulsively started cylinder, unsteady separation is characterised by local thickening of the boundary layer, perhaps with the development of a Van Dommelen - Shen (Van Dommelen and Shen, 1980) type singularity. The second type, as found in dynamic stall experiments, is in which a long reverse flow region exists which becomes unstable prior to full separation. This instability and how it relates to the final separation has not been studied. Also, there has been no effort to systematically vary the characteristics of the separation bubble.

In this paper we describe an unsteady water tunnel in which it is possible to create a variety of unsteady separation bubbles. Next we present flow visualisation results of evolution of instabilities in unsteady separation bubbles in a shallow angle diffuser. The unsteady separation bubbles are created by an adverse pressure gradient due to both a spatially decelerating ($\frac{\partial U_0}{\partial x} < 0$) and a temporally decelerating ($\frac{\partial U_0}{\partial t} < 0$) external flow. In some cases the instability is spatially localised, and preliminary stability analysis indicates it could be an absolute instability.

2. EXPERIMENTS

For an unsteady boundary layer flow shown in figure 1(a), the boundary layer momentum equation is

$$\frac{\partial u}{\partial t} + u\frac{\partial u}{\partial x} + v\frac{\partial u}{\partial y} = -\frac{1}{\rho}\frac{\partial P_0}{\partial x} + \nu\frac{\partial^2 u}{\partial y^2} \tag{1}$$

where P_0 is the pressure at the edge of the boundary layer, u is velocity component in the direction of x, coordinate along the surface, v is normal to the surface and ν is the kinematic viscosity. It is useful to split the pressure gradient into two components, temporal(Π_t) and spatial(Π_x),

$$-\frac{1}{\rho}\frac{\partial P_0}{\partial x} = \underbrace{\frac{\partial U_0}{\partial t}}_{\Pi_t} + \underbrace{U_0\frac{\partial U_0}{\partial x}}_{\Pi_x} \tag{2}$$

We have developed an unsteady water tunnel that allows control of Π_t and Π_x. It consists of two 2.4m long compartments of rectangular cross section, one over the other (figure 2). The cross sectional areas of the top and bottom

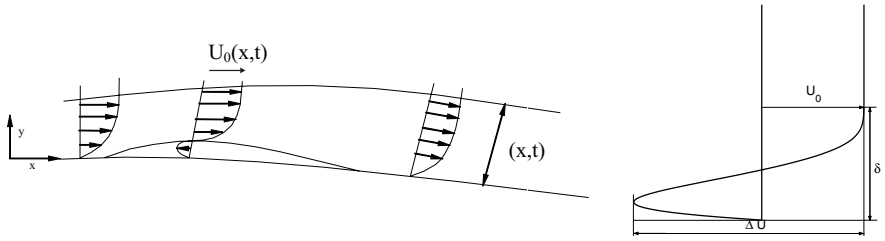

Figure 1. (a) Unsteady boundary layer, here shown with reverse flow. (b) The main parameters that characterise a velocity profile with reverse flow

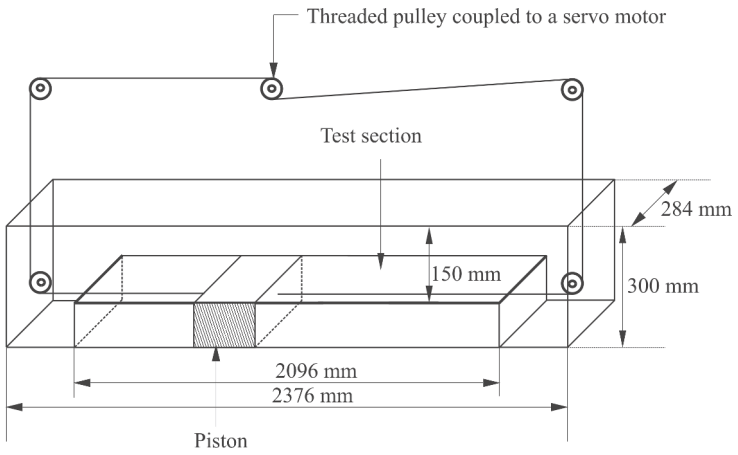

Figure 2. Piston driven unsteady water tunnel

compartments are 154 $\times$ 284 mm^2 and 134 $\times$ 276 mm^2 respectively. The top compartment contains the test section; a snugly fitted piston in the bottom compartment generates the flow. A pulley driven by an AC servomotor is connected to the piston. With this arrangement it is possible to create a specified variation with time of the free stream velocity in the test section. A test is completed before the disturbances created at the bends convect to the test section. Flow is visualised by injecting a thin layer of Fluorescein dye on the test wall before the start of the experiment. A light sheet from an Argon Ion laser beam illuminates the flow field at the mid-plane of the test section, and the the motion of the dye is captured using a CCD camera (Kodak Motion Corder Analyzer, Model - SR Ultra).

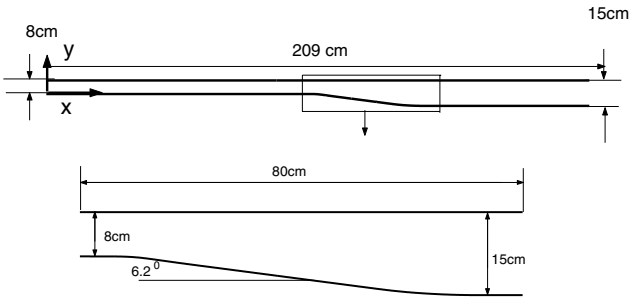

Figure 3. The geometry of the channel with the diffuser

3. RESULTS AND DISCUSSION

By a suitable combination of geometry of the model and piston motion, different types of separation bubbles may be generated. The geometry determines Π_x; for example, a bluff body will have a high Π_x. Piston acceleration and deceleration controls Π_t. To create reverse flow we need a decelerating external flow, which can be through a spatial adverse pressure gradient and / or through a decelerating piston. Here we present results of flow in a diffuser with a divergence angle of 6.2° and thus a relatively low Π_x. Upstream and downstream of the diffuser are long lengths of constant cross section (figure 3). To keep the the pressure gradient due to wall curvature small, the upstream straight portion and the inclined straight wall of the diffuser are connected by a gentle curve of 100 cm radius; a similar curvature is provided at the downstream end. The bottom and top wall pressure distributions, obtained from potential flow computation using FLUENT, are shown in figure 4.

We present results for unsteady flow in the shallow angle diffuser for different cases of piston motion variation with time. The piston velocity variation with time in all cases is trapezoidal. By varying the piston velocity profiles we are able to vary the values of the parameters characterising the unsteady boundary layer, viz, the boundary layer thickness, location of inflection point, magnitude of reverse flow velocity and the Reynolds number. How these parameters vary with x and t influences the stability behaviour of the boundary layer. Table 1 lists the important parameters for the six cases discussed in the present article; the definitions of the parameters are also given. An example of the spatial variations obtained at different times in the boundary layer thickness (δ) and in the velocity difference (ΔU) is shown in figure 5.

The flow was seen to become unstable with the formation of vortices, and usually the first vortex was seen to occur near the maximum spatial pressure

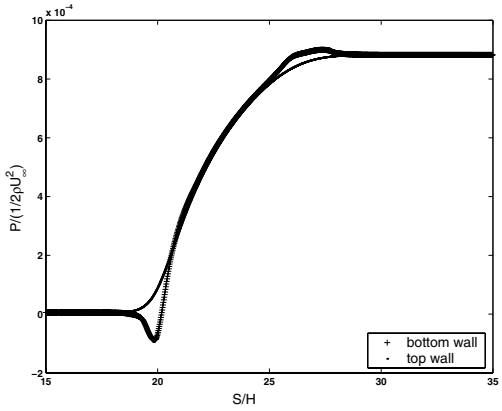

Figure 4. Pressure distributions along the lower and upper walls of the diffuser. S is distance measured along a wall, H is the upstream channel height

Table 1. Values of important parameters for different cases

Case	U_{0m} *(cm/s)*	t_0 *(s)*	t_1 *(s)*	t_2 *(s)*	t_s *(s)*	t_v *(s)*	δ_s *(mm)*	$\frac{\Delta U_s}{U_{0m}}$	$Re_{\delta s}$
I	13.72	0.6	1	2	1.2	3.83	3.66	0.79	399
II	13.72	0.6	5	5.75	4.53	6.17	7.84	1.03	1105
III	22.88	1	2	2.83	2.05	2.73	4.73	0.97	1056
IV	18.30	0.8	1	5	1.75	3.3	4.53	0.81	675
V	13.72	0.6	3.5	6.5	3.55	5.17	6.8	1.01	937
VI	13.72	0.6	3.5	5	3.55	5.07	6.8	1.0	935

U_{0m} - maximum average velocity upstream of the diffuser; piston motion times : (0-t_0) - acceleration, ($t_0 - t_1$) - constant velocity phase (U_{max}), ($t_1 - t_2$) - deceleration; t_s - time at which wall shear stress = 0 at MPGP; t_v - time at which first vortex forms; δ_s - boundary layer thickness at $t = t_s$; ΔU_s - velocity difference (see figure 1(b)) at $t = t_s$; $Re_{\delta s} = (\Delta U_s \delta_s)/\nu$

gradient point (MPGP). Figure 6 gives the piston velocity versus time variations for cases I to IV for which flow visualisation pictures have been given. Figure 7 gives the velocity profiles at the MPGP at following times : 1) t_1 - start of piston deceleration, 2) t_s - time when the wall shear stress at MPGP = 0, 3) t_v - time when the first vortex is seen to form, and 4) $t_m = (t_s + (t_v - t_s)/2)$ - time in between t_v and t_s. The software FLUENT has been used to compute the 2-D laminar flow field and the velocity profiles are from the computation. It is expected that the computed results will be valid only till the flow becomes unstable.

In the boundary layer flows with inflection points we are considering, the instability is essentially inviscid and characterised by low critical Reynolds numbers and high growth rates of disturbances. Linear stability analysis shows

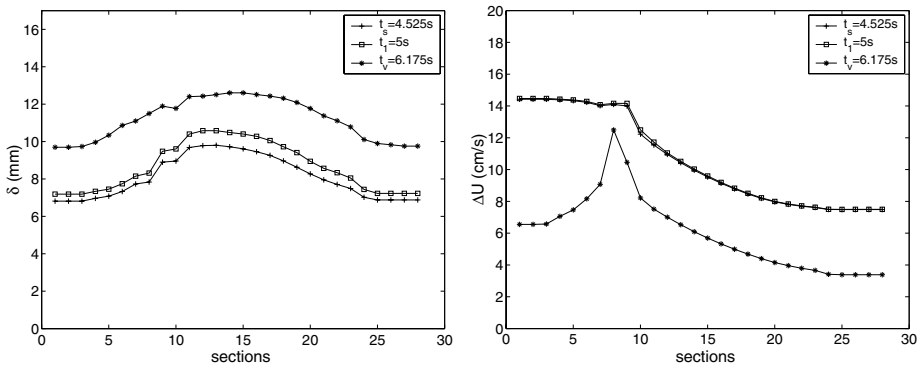

(a) Boundary layer thickness (b) ΔU

Figure 5. Spatial variations of boundary layer thickness and ΔU for Case II at $t = t_1, t_s$ and t_v. Section 8 corresponds to the maximum pressure gradient point

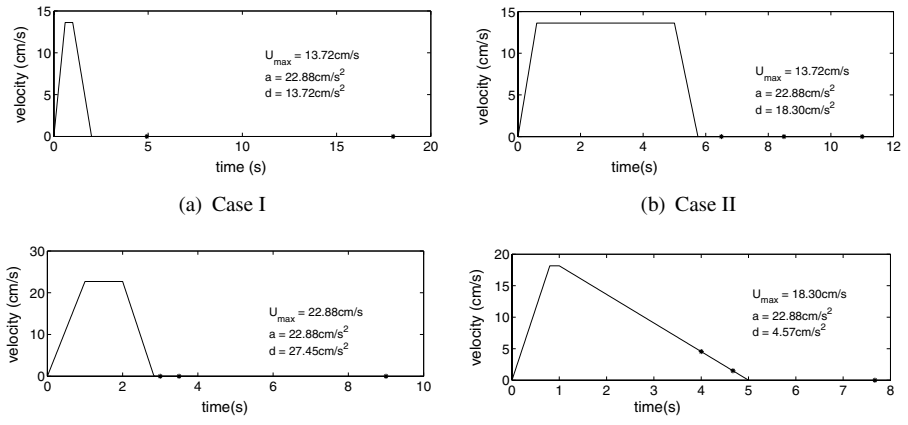

(a) Case I (b) Case II

(c) Case III (d) Case IV

Figure 6. Piston velocity variations for different cases. In Case IV piston deceleration is gradual compared to cases I - III

(Das and Arakeri, 1998) that for velocity profiles having reverse flow (figure 1(b)), the disturbance growth rate of the most unstable mode is $\simeq 0.12\Delta U$ and the most unstable wavelength $\simeq 3\delta$. Thus we may expect the instability to develop over the convective time scale, $\delta/\Delta U$.

Case I corresponds to a short piston travel, thus a small boundary layer thickness, and a small Reynolds number (see Table 1). Flow becomes unstable first near the MPGP, and a little later in the upstream straight portion of the diffuser. Multiple vortices may be seen at t=4.93s (figure 8(a)) well after the piston has stopped at t=2s. Several adjacent vortices merge with time to form bigger vortices (figure 8(b)). No vortices are observed in the downstream inclined portion of the diffuser; here ΔU is lower, the Reynolds number is smaller, and though the flow may be unstable, the growth rates of the disturbances, proportional to ΔU, are not large enough to result in vortex formation. During the development of the instability, between t_s and t_v, flow in the boundary layer is almost entirely in one (reverse) direction, much like in a wall jet (figure 7(a)).

Compared to Case I, in Case II the piston travel is longer and thus the boundary layer thickness and Reynolds numbers are larger. And, importantly, due to the longer piston travel, the effect of the spatial adverse pressure gradient is felt. During the constant piston velocity phase itself, while the velocity profiles are non-inflectional in the straight portions, in the inclined portion they become inflectional and there is flow reversal over a small length. The instability vortices are first seen near the MPGP, but rapidly form at upstream and downstream locations a little later (figure 9).

In Case III the piston velocity and Reynolds numbers are higher than in cases I and II; the flow would be expected to become unstable faster and the perturbations to grow more rapidly. Just before the piston stops, a single vortex starts to form near the MPGP at 2.73s, and is prominently visible at 3s (figure 10(a)). At this time the instability seems very localised. A little time later, vortices form on either side (figure 10(b)). The first vortex continues to grow and then becomes turbulent. Figure 10(c) shows the flow at 9s. Just as the instability, transition to turbulence is also very localised; a two dimensional strip of turbulence is formed.

In the cases considered so far the piston deceleration has occurred over a short time, and the vortex has formed at about the time or after the piston has stopped. After the piston stops, since the net mass flow across a cross section is zero, a strong reverse flow is obtained near the walls; the velocity profiles are very similar to those obtained in a wall jet, albeit with a strong spatial variation in the maximum reverse flow velocity (see figures 7(a), 7(b), 7(c)). For Case IV, however, the piston deceleration is gradual. Unlike in cases I to III, the velocity in the boundary layer is predominantly in the forward direction during the growth of the instability (figure 7(d)). Multiple vortices are observed (figure 11(a) and figure 11(b)) in the inclined portion of the diffuser,

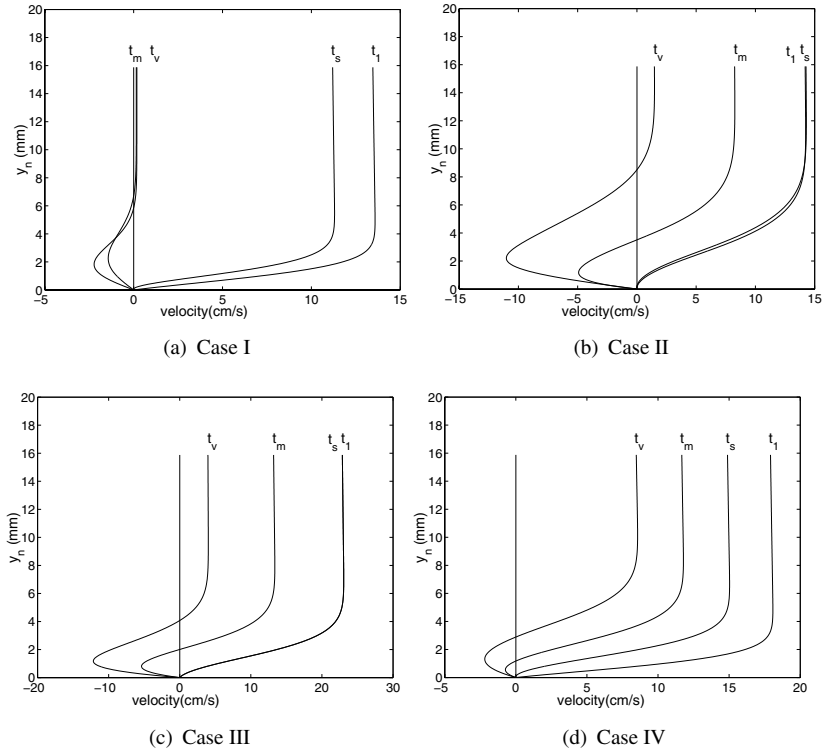

(a) Case I (b) Case II

(c) Case III (d) Case IV

Figure 7. Velocity profiles at different times at the maximum pressure gradient point (MPGP) for different cases. After the piston stops the flow in the boundary layer is predominantly in the reverse direction; e.g. Case I at $t = t_m, t_v$

where both the spatial and temporal components of the pressure gradient are present. In the straight portion where only the Π_t is present, even though the velocity profiles are inflectional, no vortices form. At later times (figure 11(c)) transition to turbulence is observed. Here, the instability appears to be of the classical convective type.

3.1 Spatio-Temporal Stability Analysis

A preliminary quasi-steady, locally parallel stability analysis is performed for the boundary layer in the neighbourhood of the MPGP using normal mode approach under the assumption that the instability arises from the inflectional nature of the flow (Akhavan et al., 1991 and Das and Arakeri, 1998), and grows at the rate of the convective scale, $\delta/\Delta U$, while, the base flow time scale is δ^2/ν. The resulting Orr-Sommerfeld equation is solved for instantaneous velocity profiles at a time interval of 0.025 seconds from t_1 up to t_v.

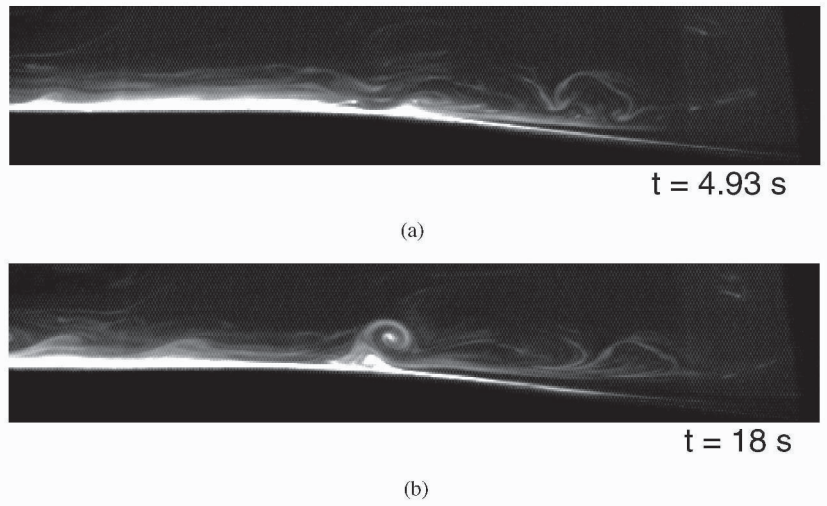

Figure 8. Flow visualisation for Case I. The prominent vortex seen at t=18s is from merger of several vortices formed earlier

Our aim is to check whether a flow is absolutely unstable at the MPGP. Because of the spatial gradients, the parallel flow assumption is not clearly valid for the present flow. But the stability analysis may indicate the nature of the instability. The least stable normal modes with zero group velocity are tracked using Hooke - Jeeves search algorithm in the 4D wave number-frequency space, $(\alpha_r + i\alpha_i,\ \omega_r + i\omega_i)$, (Rist, 2003). The contour plot of one such mode in α plane for constant ω_r, is shown in figure 12. It can be seen that the saddle point ($\alpha = 1.41 - 0.06i$), which consists of spatial branches originating from different half planes, is a pinch point as required for absolute instability (Schmid and Henningson, 2001).

The instantaneous growth rates for various locations in the neighbourhood of the MPGP are plotted as a function of time t in figure 13. The maximum growth rate and also a longer interval of time over which ω_i is positive is achieved at the MPGP. Further analysis is concentrated on the disturbance growth at the MPGP. The instantaneous growth rates ω_i at the MPGP are plotted against time in figure 14 for cases given in Table 1. The corresponding t_vs measured from the experiments are marked by circles. The instantaneous positive growth rates increase up to some time and then decrease to a negative value at a later time suggesting instantaneous decay at the convective time scale. However, the accumulated growth rate starting from the time of positive ω_i, t_+, up to t_v, $\bar{G} = \int_{t_+}^{t_v} \omega_i dt$ will characterise the true time-growing instabilities at the time t_v.

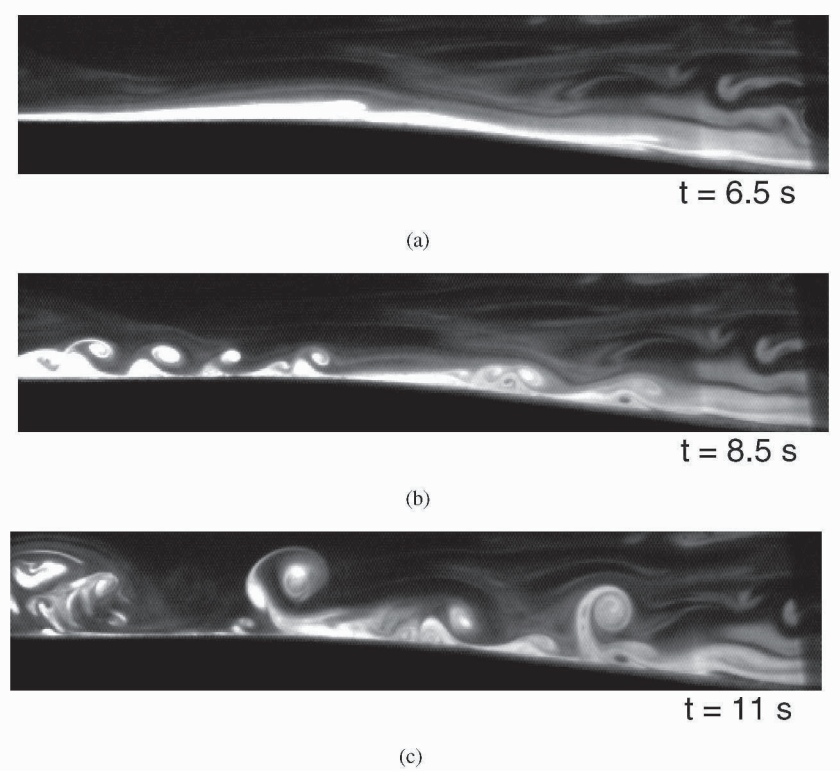

Figure 9. Flow visualisation for Case II. Initial vortex formation is near the MPGP (a), Secondary vortex formation (b) and merging of adjacent vortices (c) is observed

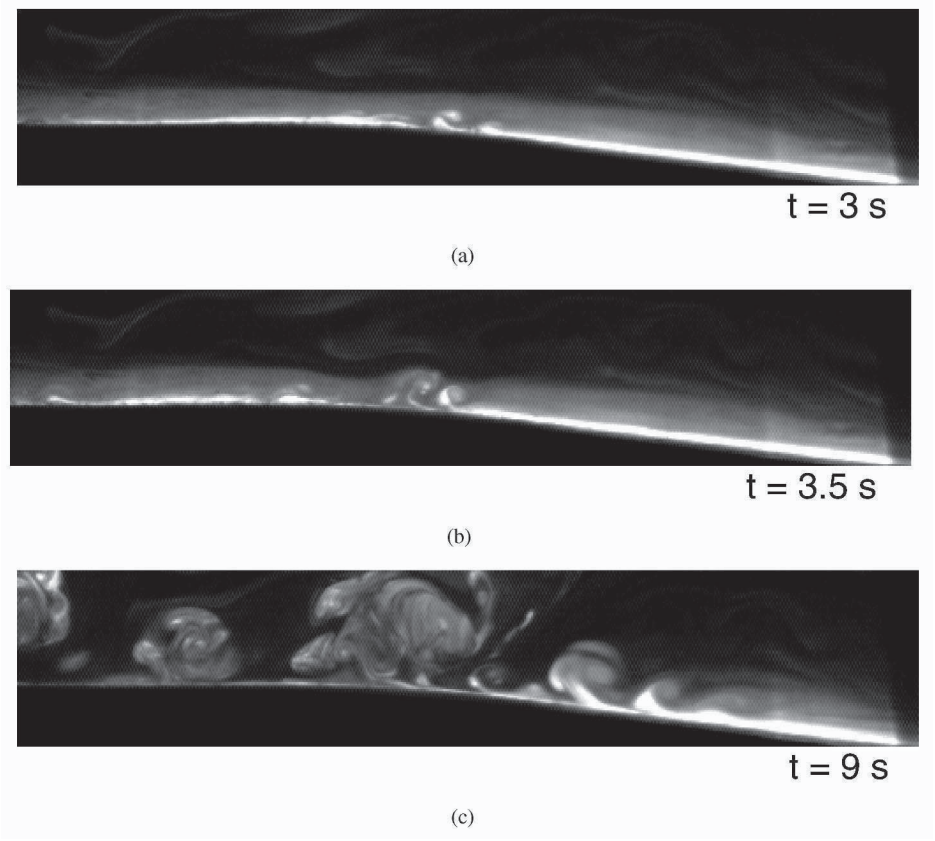

Figure 10. Flow Visualisation for Case III. Instability initiated near the MPGP develops rapidly and leads to transition to turbulence

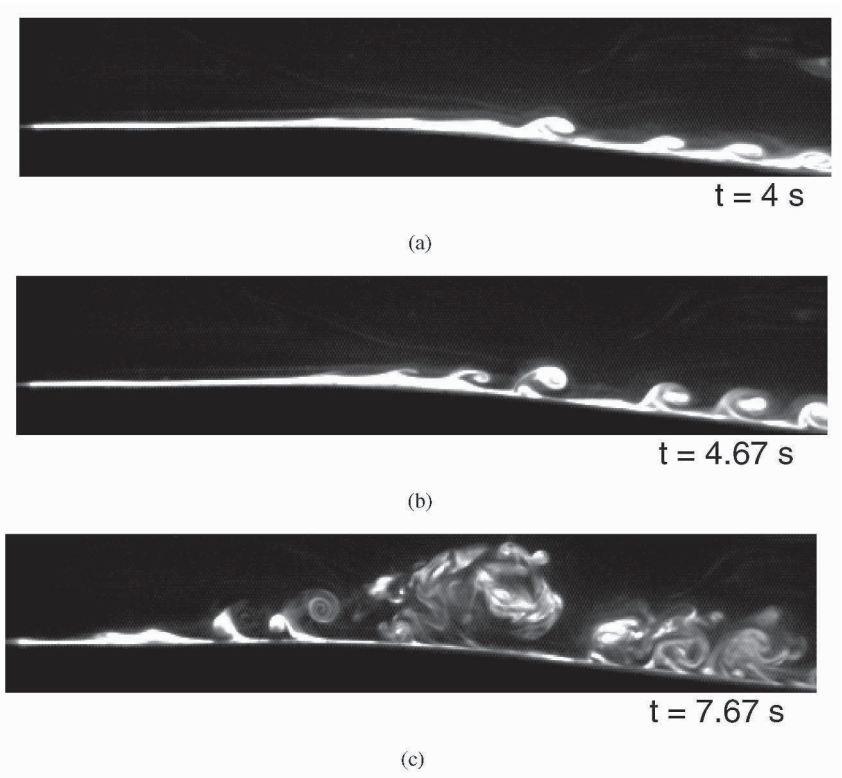

Figure 11. Flow visualisation for Case IV. Low piston deceleration results in forward flow in most of the boundary layer. Instability appears to be of convective type. t=7.67s is after the piston has stopped and the flow near the wall will be in the reverse direction

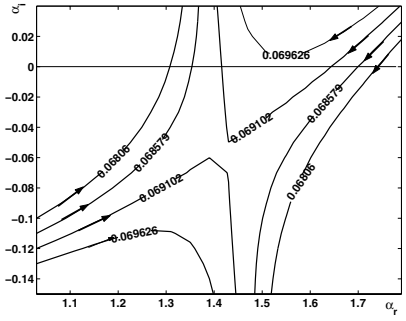

Figure 12. Constant ω_r contours in α - plane near a saddle point for Case II at t=5.5 s

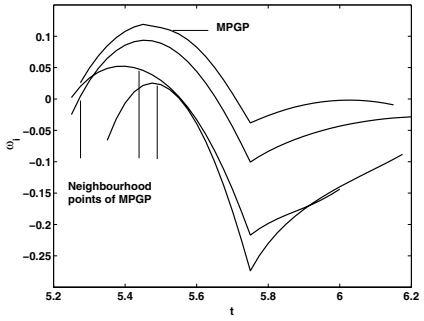

Figure 13. Variation of growth rate ω_i with time near MPGP for Case II

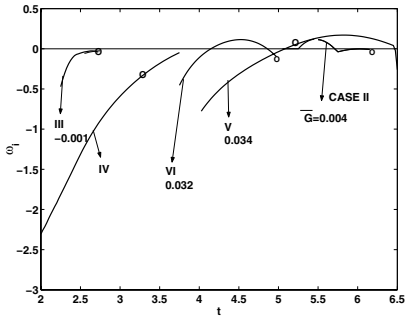

Figure 14. Variation of growth rates ω_i with time at MPGP for various piston motion

The integrated growth rates, $\bar{G}$ for the Cases V and VI (figure 14) are positive while the corresponding experiments show the growth of a single vortex at MPGP followed by the development of many vortices in the neighbourhood at a later time. When $\bar{G}$ is negative or non-existing (Case IV), simultaneous development of many vortices along the lower channel wall is observed experimentally. However, when the values of $\bar{G}$ is very close to zero (Cases II and III), predicting the nature of vortex development is difficult based on its sign. Preliminary analysis seems to suggest that in cases where localised instability is observed, the flow may be absolutely unstable.

4. CONCLUSION

We have proposed a method by which the stability characteristics of general unsteady boundary layers can be experimentally studied. For unsteady flow in the shallow angle diffuser, we have observed, depending on the piston velocity variation, two types of instabilities: classical convective type instability (Case

IV); and localised and highly spatially variable instability (Case I, II and III). In the cases where localised instability is observed, the transition to turbulence, if it occurs, is also localised. Preliminary linear stability analysis shows that in some cases the flow may be absolutely unstable. We believe the present type of study can clarify many issues related to the nature of instability in laminar separation bubbles and in unsteady boundary layer separation.

ACKNOWLEDGEMENTS

This work was supported by the Naval Research Board, India.

REFERENCES

Akhavan, R., Kamm, R. D., and Shapiro, A. H. (1991). An investigation of transition to turbulence in bounded oscillatory stokes flows. Part II. Numerical simulations. *J. Fluid. Mech.*, Vol 225:pp 423–444.

Alam, M. and Sandham, N. D. (2000). Direct numerical simulation of short laminar separation bubbles with turbulent reattachment. *J. Fluid. Mech.*, Vol 410:pp 1–28.

Das, D. and Arakeri, J. H. (1998). Transition of unsteady velocity profiles with reverse flow. *J. Fluid. Mech.*, Vol 374:pp 251–283.

Gaster, M. (1966). The structure and behaviour of laminar separation bubbles. *AGARD CP*, Vol 4:pp 813.

Rist, U. (2002). On instabilities and transition in laminar separation bubbles. *Proc. CEAS Aerospace Aerodynamics Research Conference, 10 - 12 June 2002, Cambridge, UK*.

Rist, U. (2003). Instability and transition mechanisms in laminar separation bubbles. *VKI/RTO-LS "Low Reynolds Number Aerodynamics on Aircraft Including Applications in Emerging UAV Technology", Rhode-Saint-Genese, Belgium, 24-28 November 2003*.

Schmid, P. J. and Henningson, D. S. (2001). *Stability and transition in shear flows*. Springer.

Van Dommelen, L. L. and Shen, S. F. (1980). The spontaneous generation of the singularity in a separating laminar boundary layer. *J. Comput. Phys*, Vol 38:pp 125–140.

INTERACTION OF SEPARATION AND TRANSITION IN BOUNDARY LAYERS: DIRECT NUMERICAL SIMULATIONS

Hermann F. Fasel & Dieter Postl
Department of Aerospace & Mechanical Engineering,
University of Arizona,
Tucson, AZ 85721
faselh@email.arizona.edu

Abstract: The role of hydrodynamic instability mechanisms in the presence of laminar boundary layer separation is investigated by means of Direct Numerical Simulations. In a series of simulations involving generic laminar separation bubbles we show that the "natural" onset of unsteadiness (i.e. the development of visible vortex shedding) is not necessarily caused by an absolute/global instability. Our results indicate that the entrainment of high-momentum fluid required to "close" the separation bubble is primarily provided by 2-D or "2-D coherent" structures, which are a consequence of the (inviscid) hydrodynamic instability of the separated shear layer. In a series of highly resolved simulations for a flat-plate boundary layer subjected to low-pressure turbine blade conditions, we demonstrate that this natural instability mechanism (with respect to two-dimensional disturbances) can be exploited for effective control of separation using pulsed vortex generator jets.

Keywords: laminar separation, convective/absolute instability, separation control

1. INTRODUCTION

In spite of considerable progress in recent years, both separation and laminar-turbulent transition are not well understood. Matters get highly complicated when transition and separation are present simultaneously and interact in a physically complex manner. This is the case for low Reynolds number boundary layers in the presence of strong streamwise adverse pressure gradients and for convex wall curvature. The importance of hydrodynamic instability mechanisms in understanding separation and reattachment in laminar separation bubbles was already recognized by Gaster in his Ph.D. thesis 50 years ago (see Gaster, 2004). In his seminal work involving experiments and theory, he conjectured that a "true" instability mechanism (which was later rediscovered and

R. Govindarajan (ed.), Sixth IUTAM Symposium on Laminar-Turbulent Transition, 71–88.

called absolute instability) may be at play. Practical applications where the interaction of transition and separation is relevant include unmanned aerial vehicles (UAVs), low-pressure turbines (LPTs), wind turbines, etc. In order to design efficient and robust flight vehicles or turbines, for example, it is essential that the fundamental physical mechanisms that are present in the interaction of separation and transition are understood. This understanding is particularly relevant also when passive and active flow control techniques are being considered.

For low free-stream turbulence levels, transition to turbulence in boundary layers is caused by a hydrodynamic instability, as a consequence of which disturbance waves arise that are amplified in the downstream direction. For low levels of environmental disturbances, these waves are, at first, predominantly two-dimensional. Streamwise adverse pressure gradients have a destabilizing effect such that the amplification rates increase and the critical Reynolds number decreases. If the adverse pressure gradient is strong enough, the flow separates, and the inflection point in the velocity profile moves farther and farther away from the wall. As a consequence, the flow becomes inviscidly unstable (Kelvin-Helmholtz instability), resulting in ever larger growth rates of the instability waves. Due to the high amplification rates, these waves rapidly (within the streamwise extent of the bubble) reach large (non-linear) amplitudes, visible in experiments as 2-D spanwise vortices ("rollers"). The presence of these large-amplitude waves (or vortices) facilitates an exchange of momentum between the high-momentum fluid away from the wall and the low-momentum fluid in the separated region close to the wall. This exchange of momentum limits the extent and intensity of the separation. Of course, once the two-dimensional waves have reached high enough amplitudes and the Reynolds number is large enough, secondary instabilities can take hold that will lead to a rapid breakdown to small 3-D structures and eventually to fully turbulent flow. The smaller 3-D scales (due to the added eddy-viscosity) weaken the coherence and strength of the 2-D rollers and, as a consequence of this, reduce the exchange of momentum due to these rollers. Of course, the extra eddy-viscosity caused by the small scales also has an effect of resisting separation due to the higher wall shear. Thus, both mechanisms are relevant and can be exploited for limiting the extent of separation or preventing it altogether. An example is the use of "tripping" devices for transitioning the flow so that separation is prevented or delayed. To complicate matters even further, for separated flows, the instability mechanisms may be "convective" or "absolute/global" (for a definition and detailed discussion regarding convective and absolute/global instability, see Huerre and Monkewitz, 1990). From the discussion above, it is obvious that separation and transition (and therefore also hydrodynamic instability) are intricately linked.

In our research, we are employing Direct Numerical Simulations (DNS) for investigating this intricate interplay of separation and transition, in particular also with regard to its relevance for Active Flow Control (AFC) applications. In this paper, we will attempt to shed light on some of the key physical mechanisms in the interaction of laminar separation and transition by employing simulations of simple prototypical flow geometries. The understanding gained from these simplified model simulations will then be employed for extracting the relevant mechanisms that are present in active control of separation for low-pressure turbine cascades.

2. DIRECT NUMERICAL SIMULATIONS

For the present investigations, Direct Numerical Simulations will be employed. The Navier-Stokes codes used for these simulations were developed in our Computational Fluid Dynamics Laboratory. The incompressible Navier-Stokes equations are solved in vorticity-velocity formulation,

$$\frac{\partial \vec{\omega}}{\partial t} = (\vec{\omega} \cdot \nabla)\,\vec{v} - (\vec{v} \cdot \nabla)\,\vec{\omega} + \frac{1}{Re}\nabla^2 \vec{\omega}, \tag{1}$$

where $\vec{\omega} = -\nabla \times \vec{v} = [\omega_x, \omega_y, \omega_z]^T$ is the vorticity vector and $\vec{v} = [u, v, w]^T$ is the velocity vector. The velocity equations are obtained from the definition of vorticity and from the fact that the velocity and vorticity vectors are solenoidal,

$$\nabla^2 \vec{v} = \nabla \times \vec{\omega}. \tag{2}$$

The governing equations are discretized with 4^{th}-order accurate compact differences in the streamwise and the wall-normal direction. The spanwise direction (for the 3-D simulations) is assumed to be periodic and is treated by a pseudo-spectral Fourier method. A 4^{th}-order accurate Runge-Kutta scheme is used for the time integration. The numerical method is discussed in detail in Meitz and Fasel, 2000. Parallelization using MPI is employed to allow for highly-efficient computations on vector-parallel supercomputers such as the Cray X1. Our codes have been validated in numerous simulations of transition and separation for a variety of flow geometries, flow speeds, and applications (see Wernz and Fasel, 1999; Fasel, 2002; Postl et al., 2003; Postl et al., 2004).

3. LAMINAR SEPARATION BUBBLES

In order to elucidate the complex interaction of separation and transition, we will first present and discuss results for a simple flow geometry, namely a laminar separation bubble on a flat plate. For the simulations presented here, the separation bubble is generated by a volume force field such that the boundary layer is first accelerated and then decelerated in such a way that a generic separation bubble is generated (see figure 1). In principle, the separation bub-

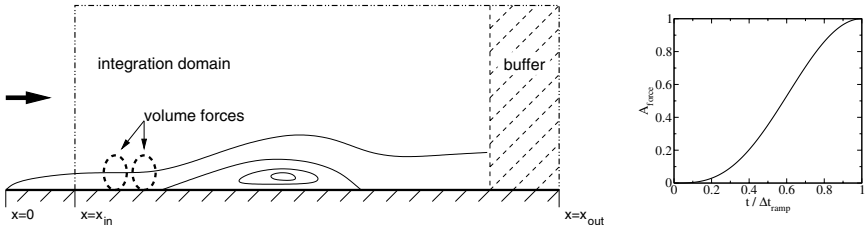

Figure 1. Computational setup for the simulations. Left: integration domain; right: "ramping" function for the volume force field to generate separation bubbles

ble could also be generated by imposing a pressure gradient at the free stream boundary. However, using volume force fields facilitates numerically the tailoring of the separation bubble such that certain properties are exposed. Depending on the strength of the volume force field, i.e. the magnitude of the acceleration or deceleration of the boundary layer, the simulations will yield separation bubbles that can be steady or unsteady, as the results presented below will demonstrate.

Case 1: Steady Separation Bubble

For this simulation, the force field is gradually imposed on an attached, zero pressure gradient boundary layer (see figure 1). The final, maximum acceleration/deceleration is chosen such that the flow reaches a steady state behavior (as shown in figure 2), albeit by a small margin. A slight increase in the maximum acceleration/deceleration would no longer yield a steady-state flow. The

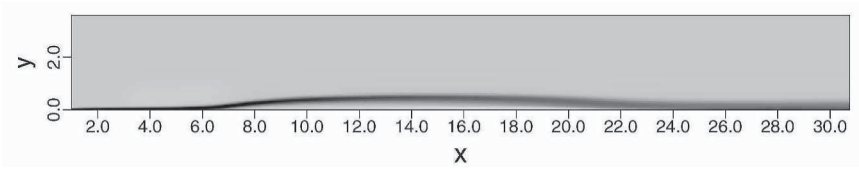

Figure 2. Case 1: Spanwise vorticity contours for the steady state

temporal development of the separated region can be observed clearly from the instantaneous wall shear, as shown in figure 3. It is obvious that the separated region increases with time until a final, steady state is reached. The velocity profile at the location of maximum negative wall shear stress is given in figure 4, indicating that a reverse flow of approximately 13% of the free stream velocity is reached. This is mentioned here since in several other research efforts, it was observed that the intensity of the reverse flow is one of the parameters that determines whether the flow is convectively or absolutely (globally) unstable.

Here, we attempt to determine if the flow is convectively or absolutely unstable by using a numerical simulation tool similar to the one proposed by Brancher and Chomaz, 1997. For this, we set up a separate simulation with a

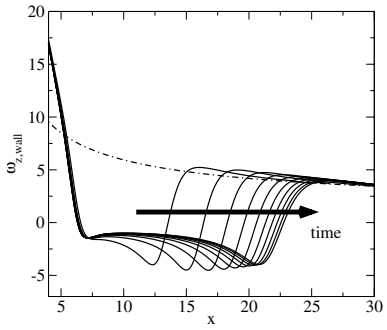

Figure 3. Case 1: Temporal development of the spanwise wall-vorticity

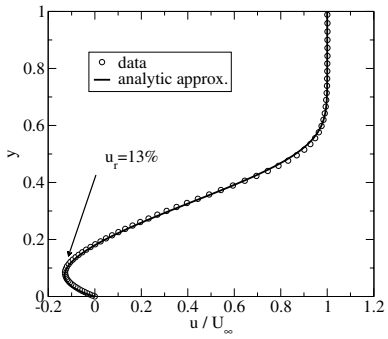

Figure 4. Case 1: Velocity profile at the location of max. negative wall shear

parallel base flow and periodic inflow/outflow boundary conditions. The base flow is constructed by using the velocity profile (from the spatial simulation) that is to be examined with respect to its convective or absolute instability (figure 5). Then, at a sufficient distance from the inflow and outflow boundaries, a very small pulse disturbance is introduced through a blowing and suction slot. The pulse generates a wave packet that grows in time and in space (if the profile is unstable), as shown schematically in figure 6. If the trailing edge of the wave packet propagates downstream (see left-hand-side of figure 6), the profile is classified as convectively unstable. If the trailing edge propagates upstream (see right-hand-side of figure 6), the profile is absolutely unstable. Of

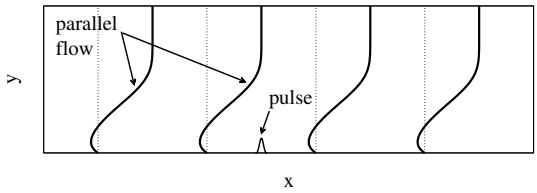

Figure 5. Computational setup for convective/absolute instability investigations

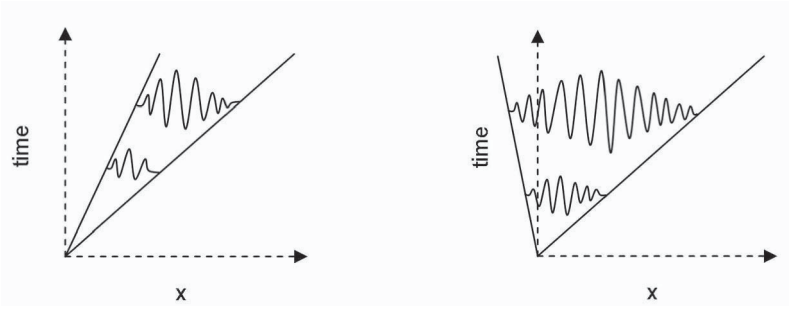

Figure 6. Schematic of convective and absolute instability. Left: convective instability; right: absolute instability (Huerre and Monkewitz, 1990)

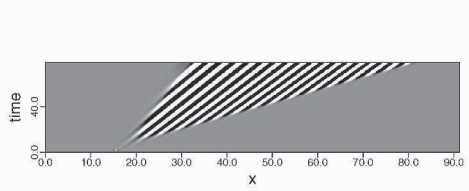

Figure 7. Case 1: t/x diagram of the disturbance wall-vorticity

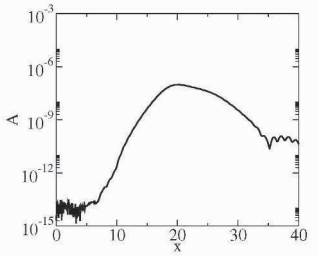

Figure 8. Case 1: Fourier amplitude of the disturbance wall-vorticity

course, the calculation becomes meaningless when the perturbations reach the inflow and/or the outflow boundaries. Therefore, it is essential that the computational domain is sufficiently large so that a clear trend is established before the perturbations reach these boundaries.

Applying this tool for the velocity profile of figure 4 yields the response given in figure 7. To construct the t/x diagram of figure 7, the spanwise vorticity perturbations at the wall are used. It is obvious that these perturbations grow, but remain contained in a wedge. The trailing edge of the wave packet propagates downstream, thus confirming that this profile is convectively unstable, but absolutely stable. This is consistent with the fact that our spatial simulation of this bubble leads to a steady behavior without unsteady perturbations. The fact that this profile is convectively unstable can be clearly observed from figure 8, where the Fourier amplitude of the spanwise disturbance vorticity at the wall is plotted versus the downstream direction. The increase in amplitude by approximately seven orders of magnitude is an indication of the very strong (convective) instability which is caused by the inviscid (inflection point) instability mechanism. However, as seen in figure 8, the amplitudes never reach levels large enough to observe a "visible" unsteadiness as "confirmed" by figure 2. Figure 8 clearly points to the difficulty and dilemma when using numerical simulations and/or experiments for determining if a flow is

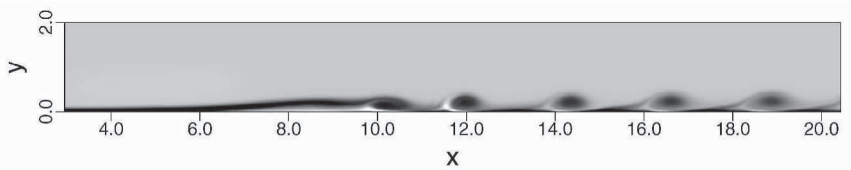

Figure 9. Case 1: Instantaneous vorticity contours for periodic forcing

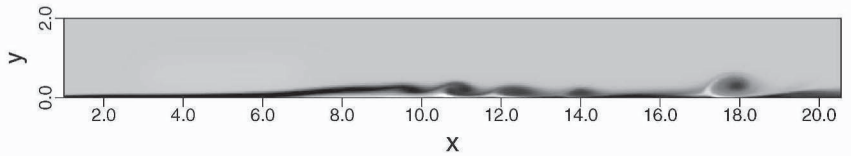

Figure 10. Case 1: Instantaneous vorticity contours for random forcing

convectively or absolutely (globally) unstable based on observations of "natural" (unforced) perturbation waves or vortex shedding. Due to the enormous amplification rates of the instability waves (see figure 8), extremely small background disturbances (for example due to round-off error in simulations or free stream turbulence in experiments) can lead to visible, large disturbance waves and vortices without additional "controlled" forcing. To demonstrate this, we used the steady flow field of the previous simulation (see figure 2) as initial condition and introduced small, controlled perturbations (with an amplitude of 0.1% of the free stream velocity) by periodic blowing and suction through a slot located upstream of the separation location (see figure 9). The perturbations quickly grow to very large amplitudes, not surprising considering the very high growth rates observed in figure 8, so that large amplitude waves develop (typically described in the literature as "vortex shedding"). The large amplitude waves or "vortices" ("rollers") enhance the exchange of momentum between the inner and outer fluid.

To answer the question of whether this phenomenon is only an artifact of the periodic forcing, we performed a simulation where random forcing was used instead of periodic forcing (everything else being the same). This is a better model of the effects of "uncontrollable" environmental disturbances that arise in experiments (free stream turbulence, vibrations, noise, etc.) or in numerical simulations (discretization and round-off errors). The response to the random forcing, as shown in figure 10, makes it obvious that the convective instability mechanism quickly leads to large perturbation waves (or vortices) as before, but, of course, not with a single frequency as the flow is unstable with regard to a band of frequencies. It is important to note that, in both simulations, the bubble returns to a steady state when the forcing is turned off.

Case 2: Marginally Unsteady Separation Bubble

In the next sequence of simulations presented here (case 2), the acceleration/deceleration in the force field was chosen such that large amplitude instability waves or "vortex shedding" occurred "naturally" (see figure 11), that is without adding "controlled" forcing, either periodic or random, as for the previous case 1. As before, the simulation starts with an attached boundary layer

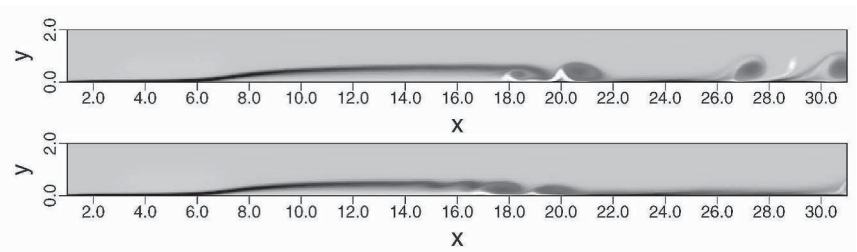

Figure 11. Case 2: Instantaneous spanwise vorticity contours

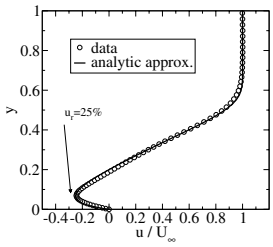

Figure 12. Case 2: Velocity profile for the stability investigation

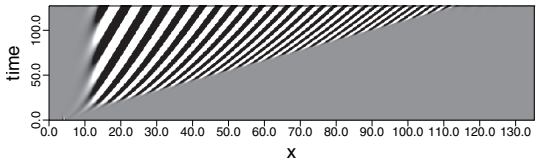

Figure 13. Case 2: t/x diagram of the disturbance wall-vorticity

flow as initial condition and then the volume force field is gradually imposed. (the time over which the force field is "ramped in" was doubled compared to case 1). It is noteworthy that the intensity of the force field is increased only by approximately 5% compared to case 1, indicating the strong sensitivity of the flow field to the increased acceleration/deceleration.

Is the observed unsteadiness due to convective or absolute instability mechanisms? As observed from the previous case, the growth rates of the convective instability are very strong (see figure 8). Now, with the stronger acceleration/deceleration and, associated with this, the stronger separation, the amplification rates of the convective instability would also be accordingly larger. Therefore, the finite amplitudes that are reached (as a result of convective growth) may be such that "visible" vortex shedding can be observed. However, the unsteadiness or vortex shedding could, of course, also result from an absolute/global instability. To answer the question of whether an absolute instability is at play, we examined the profile with the maximum reverse velocity (approximately 25%), as shown in figure 12. This profile is only reached momentarily just before the shedding sets in. In order to establish a t/x diagram, we used the same numerical tool as discussed previously. The result of this analysis is presented in figure 13. As before, the wave-packet-type disturbances grow in time and in space, and are contained in a wedge region. Contrary to the previous case, the left boundary of the wedge is now practically vertical, indicating that the trailing edge of the wave packet is stationary. Thus, disturbances never really convect entirely out of the field. Therefore, we classify this profile as "marginally" absolutely unstable. However, it is not possible to unequivocally attribute the observed vortex shedding to an absolute/global

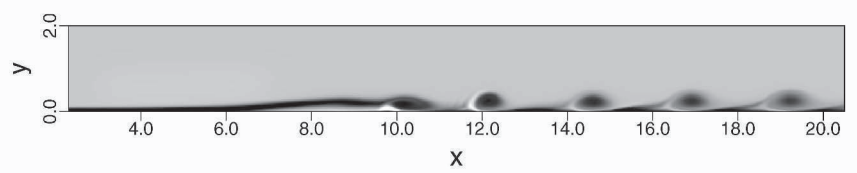

Figure 14. Case 2: Instantaneous vorticity contours for periodic forcing

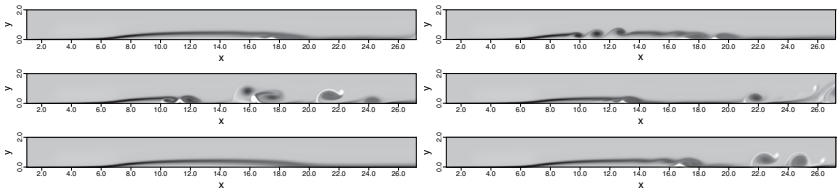

Figure 15. Case 2: Instantaneous spanwise vorticity contours for a pulse disturbance

instability mechanism, because, as discussed previously, the strong convective instability is present at the same time.

What happens now if we additionally introduce external perturbations as for the previous case? The response to upstream periodic blowing and suction with the same small amplitude as in section 1 is presented in figure 14. Comparing with figure 9 for the weaker separation (convective instability only), the responses are practically indistinguishable. This is an additional indication that judging convective versus absolute instability based on observed vortex shedding is misleading, at best. It should be noted, also, that the bubble returns to the self-sustained shedding when the additional external forcing is discontinued.

What happens if we only force with an initial pulse before the shedding has established itself (the pulse is introduced through a slot at the same location as for the periodic forcing)? A series of instantaneous plots for this simulation are presented in figure 15. After the wave packet created by the pulse has propagated through the separated region (and generating large structures in doing that), the bubble develops the same way as without the pulse forcing, that is it develops the self-sustained shedding as before, thus confirming the marginal absolute instability.

Case 3: Unsteady Separation Bubble

In a third case, the intensity of the volume force field is increased by another 5% from the previous case. The time-dependent development of the separation bubble is illustrated in figure 16. It is obvious that stronger and more energetic

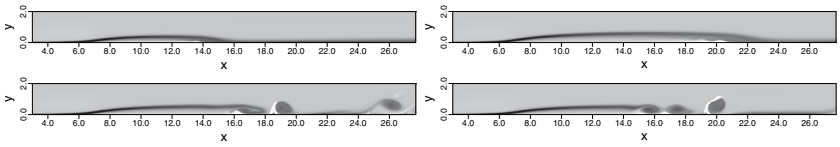

Figure 16. Case 3: Instantaneous spanwise vorticity contours

vortical structures are generated. The velocity profile for the location with the maximum reverse velocity (figure 17) now indicates a maximum reverse velocity of 38%, considerably larger than before. Thus, a "true" absolute instability should be visible in this case. This is confirmed by the t/x diagram in fig-

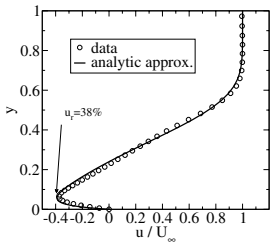

Figure 17. Case 3: Velocity profile for the stability investigation

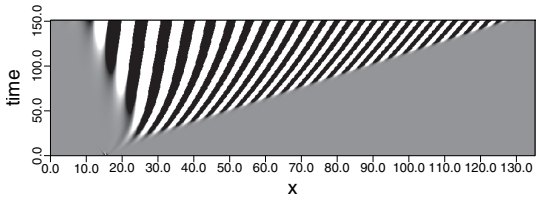

Figure 18. Case 3: t/x diagram of the disturbance wall-vorticity

ure 18, which shows, in contrast to before, that the perturbations now indeed travel upstream. For the full spatial simulation, at the location where this velocity profile arises, the disturbances grow in an absolutely unstable manner. In other words, a continuous "oscillator" is present that generates perturbations of increasing amplitude until a non-linear, finite equilibrium is attained. The streamwise extent of this absolutely unstable behavior is, of course, limited by the fact that sufficiently far away from the location where the maximum reverse flow is reached, the local profiles become absolutely *stable*. This is essentially the mechanism that leads to "global" modes (Couairon and Chomaz, 1996).

Case 4: Highly Unsteady Separation Bubble

In this final case, the force field is such that it generates velocity profiles with considerably larger reverse velocities than in all the previous simulations. The instantaneous flow field shown in figure 19 illustrates the development of highly energetic structures. The entrainment and exchange of momentum caused by these structures is so strong that the extent of the separation is drastically reduced. Shortly before vortex shedding sets in, the maximum reverse velocity for this case is approximately 55% (see figure 20). The t/x diagram of figure 21 illustrates the very strong absolute instability obtained from a local analysis as discussed before.

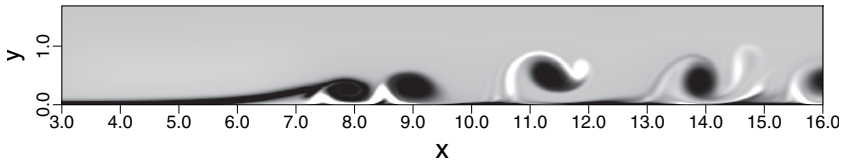

Figure 19. Case 4: Instantaneous vorticity contours

All the simulations presented so far were two-dimensional, thus all three-dimensional effects were (deliberately) neglected. As a consequence, secondary (3-D) instability mechanisms were excluded and, in particular, the breakdown to turbulence could not occur. The only mechanisms allowed so

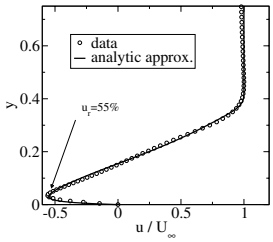

Figure 20. Case 4: Velocity profile for the stability investigation

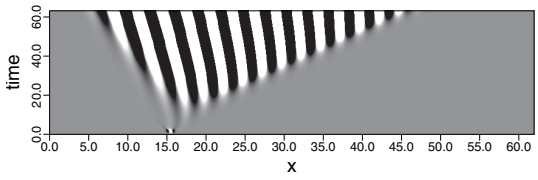

Figure 21. Case 4: t/x diagram of the disturbance wall-vorticity

far were viscous (Tollmien-Schlichting) and inviscid (Kelvin-Helmholtz) instability mechanisms. Thus, the question arises what contributions would arise from 3-D effects, and, in particular, from allowing the flow to transition? A simulation of the last case was performed for which the 2-D simulation was used as an initial condition for a 3-D simulation that now allows breakdown to turbulence. As can be observed from figure 22, compared to the 2-D simulation, the strong 2-D structures are considerably weakened, although shedding of 2-D coherent structures ("rollers") can still be observed. The weaker structures provide less exchange of momentum between outer and inner regions, and, as a consequence, the extent of the separation is greatly increased.

Finally, for the same case (pressure gradient), the simulation is started up immediately in 3-D instead of first establishing a 2-D simulation as before (for brevity, no plots are shown for this case). As in the 2-D simulation, large laminar (2-D) structures initially develop before the flow eventually transitions. In other words, the 3-D simulation looks exactly like the 2-D simulation for quite some time. This observation provides additional evidence of the fact that the flow is initially absolutely unstable with respect to two-dimensional disturbances and that the growth of 3-D perturbations is the consequence of a secondary instability mechanism. The precise nature of this secondary instability mechanism is not fully understood, as the breakdown of the flow could either be due to a *convective* secondary instability (with very large growth rates) or due to an *absolute* secondary instability (as suggested by Maucher et al., 1997 and Marxen et al., 2004).

The examples presented here demonstrate the intricate interplay of separation, hydrodynamic instability waves, and transition, where several compli-

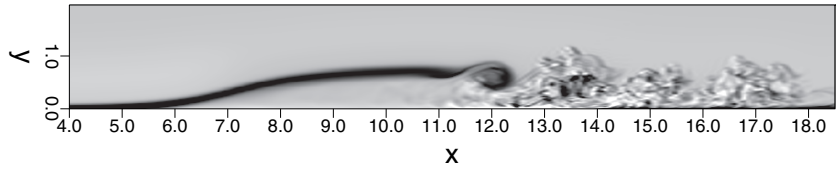

Figure 22. Case 4: Instantaneous vorticity contours (3-D simulation)

cated physical mechanisms are at play. The same (and possibly additional) mechanisms are likely to be relevant for practical applications where geometries are more complex. Therefore, the information gained from these generic investigations should serve well in interpreting the more complex situations of practical applications, and should serve particularly well for understanding and improving strategies for active control of separation. An example of this is active control of separation for low-pressure turbines using vortex generator jets, which will be discussed below.

4. ACTIVE CONTROL OF SEPARATION USING VORTEX GENERATOR JETS

In many modern gas turbines, laminar separation on the suction side of low-pressure turbine (LPT) blades can result in considerable performance losses. Boundary layer separation is especially problematic under low Reynolds number operating conditions as encountered in off-design operation, during high-altitude cruise, or in small engines such as those used in modern unmanned aerial vehicles. Experiments conducted at the Air Force Research Laboratory (AFRL) by Bons et al., 2001a; Bons et al., 2001b and Sondergaard et al., 2002 for a linear PakB LPT cascade convincingly demonstrated that losses incurred by laminar boundary layer separation could largely be reversed when pulsed vortex generator jets (VGJs) were employed upstream of the separation location. Although pulsed VGJs were shown to be much more effective than steady VGJs, the underlying physical mechanisms responsible for this observation are far from understood. As the relatively low Reynolds numbers ($Re = 25,000$ based on axial chord length, C_x) permit the use of "fully" resolved Direct Numerical Simulations (i.e. with a resolution down to the Kolmogorov scale, $(\Delta x, \Delta y, \Delta z) = \mathcal{O}(l_k)$), we have begun investigating separation for a flat-plate boundary layer which is subjected to the same streamwise pressure gradient as measured in the experiments at AFRL. In the present section, we summarize results obtained from these recent investigations (Postl et al., 2004) and attempt to interpret them in light of the understanding gained from the simu-

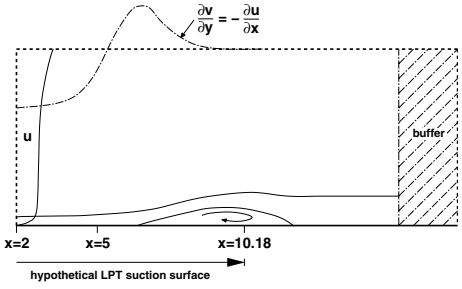

Figure 23. Computational setup for the 3-D DNS

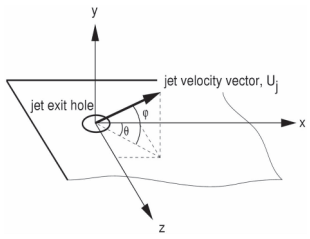

Figure 24. Schematic of the VGJ actuation

lations of section 3. For details on our simulations of the experimental LPT cascade, see Gross and Fasel, 2005.

The computational setup for the present simulations is schematically depicted in figure 23. A highly accelerated laminar boundary layer profile obtained from a pre-cursor calculation is specified at the inflow. In contrast to the simulations discussed previously, the pressure gradient is imposed at the free stream boundary by specifying a Neumann condition for the wall-normal velocity component (see figure 23). The VGJs are modeled by prescribing appropriate Dirichlet conditions for the velocity components at the wall. The setup of the VGJ actuation is schematically depicted in figure 24. The leading edge of the hypothetical LPT suction surface is located at $x = 0$, the hypothetical trailing edge is located at $x = 10.18$.

The free stream boundary condition imposed in the simulations was adjusted iteratively in a priori calculations until good agreement was obtained for the C_p distribution measured in the experiments. The wall-pressure coefficient versus suction surface length (SSL) for the uncontrolled case is shown in figure 25. The pressure plateau downstream of 62% SSL indicates the region of boundary layer separation. Velocity profiles at various streamwise locations are presented in figure 26.

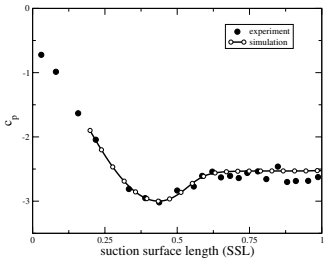

Figure 25. Wall-pressure coefficient for the uncontrolled boundary layer

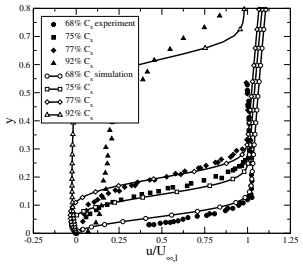

Figure 26. Velocity profiles for the uncontrolled boundary layer

The experimental profiles do not show negative velocities because the measurements were obtained from single hot-wire probes. While the profile at 92% C_x may indicate attached flow, it is in fact separated. The careful setup of the numerical simulations results in a good agreement with the experimental data for the base flow. Typical results from a simulation of the uncontrolled, separated boundary layer are presented in figure 27. In the mean, the boundary layer separates at approximately $x = 5.7$ and reattaches at approximately $x = 15.8$. Since the trailing edge of the hypothetical suction surface is located at $x = 10.18$, the flow for an actual LPT cascade would, for this case, not reattach to the blade surface.

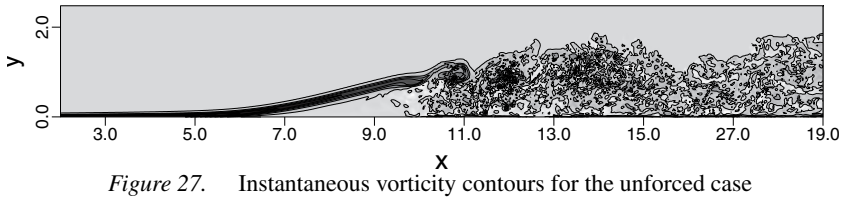

Figure 27. Instantaneous vorticity contours for the unforced case

In the simulations with pulsed VGJ control, the momentum coefficient c_μ was $1.65 \cdot 10^{-5}$ (based on maximum jet exit velocity), the hole-diameter was $D \approx 0.15$, the duty cycle τ (ratio of jet on-time to forcing period) was 10%, and the non-dimensional forcing frequency F^+ was 4.2 (based on reference velocity U_∞ and axial chord length C_x).

In figure 28 (from top to bottom), spanwise wall-vorticity contours are shown in a top view towards the wall for the unforced case, a case with pulsed, *vertical* VGJ actuation, a case with pulsed, *angled* actuation, and a 2-D simulation with periodic blowing and suction through a slot. In all three controlled cases, the forcing has a significant effect on the time-averaged extent of the separation region (bright areas represent attached flow, dark areas represent separated flow).

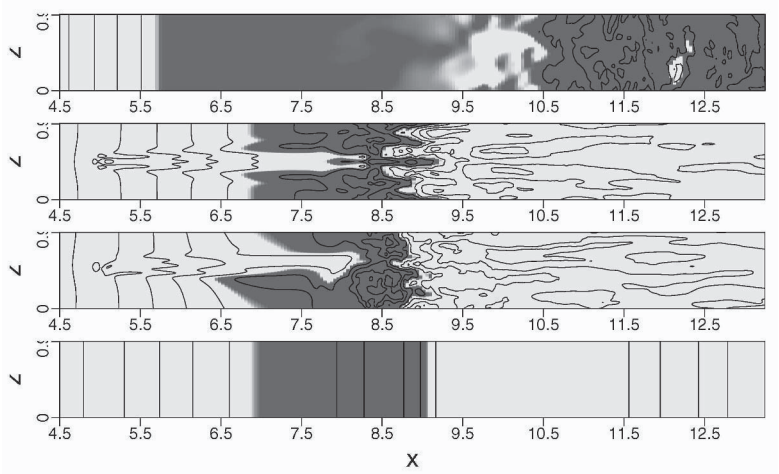

Figure 28. Time-averaged contours of spanwise wall-vorticity. Top view towards the surface

Figure 29 shows the wall-pressure coefficients obtained from these simulations in comparison to the unforced case. Also included is the curve obtained from a simulation where the boundary layer was tripped to turbulence upstream of the separation location, resulting in an attached flow along the entire surface. This curve represents the "ideal" pressure distribution for this particular pressure gradient as the trip prevents separation altogether. For each of the forced cases shown in figure 29, the location of the pressure minimum moves down-

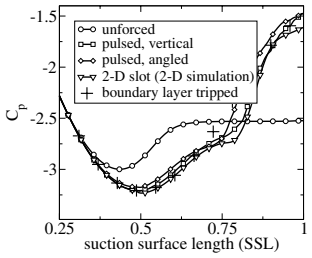

Figure 29. Wall-pressure coefficient for the controlled cases in comparison to the unforced case

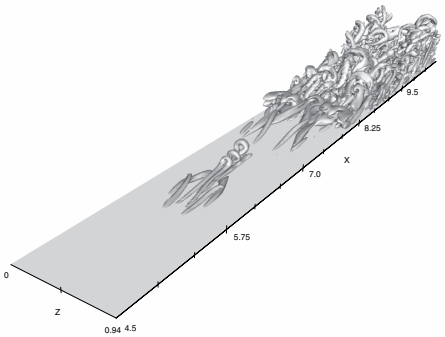

Figure 30. Vortex visualization for pulsed, vertical VGJs. Shown are iso-surfaces of negative λ_2

stream compared to the unforced case. The pressure distribution obtained from the 2-D simulation is in excellent agreement with the fully attached flow in the region between 30% and 65% SSL.

For the pulsed VGJs, the reattachment of the flow appears to be due (at least partially) to the momentum exchange as a consequence of an accelerated boundary layer transition. The transition process can be clearly observed in figure 30. Here, the λ_2 vortex identification criterion (Jeong and Hussain, 1995) is used to highlight the nature of the structures created by the pulsed jets. Λ-structures, along with the subsequent development of ring-like or hairpin vortices, appear only a short distance downstream of the forcing location. These structures closely resemble the late stages of classical Klebanoff-type transition scenarios (Rist and Fasel, 1995; Bake et al., 2002). Thus, it is obvious that the pulsed VGJs are very effective in triggering a "by-pass" mechanism leading to a relatively quick breakdown to turbulence. However, triggering breakdown to turbulence may not be the entire story because, in the 2-D simulation (where breakdown is prevented), separation can also be controlled effectively by periodic forcing. We therefore conjecture that, in addition to accelerating transition, forcing with pulsed jets also exploits an instability of the underlying base flow with respect to two-dimensional disturbances. To scrutinize this conjecture, the amplification of the two-dimensional component of the instability modes resulting from the forcing with pulsed VGJs is plotted in figure 31. Shown is the development of the Fourier amplitudes for the spanwise disturbance wall vorticity for both vertical and angled VGJs. Despite the relatively large amplitudes at the forcing holes, the disturbances grow exponentially (linear in the log-plot) downstream of an adjustment region. The exponential growth is a strong indication that linear instability mechanisms are present. Therefore, forcing with the "proper" frequencies exploits the natural

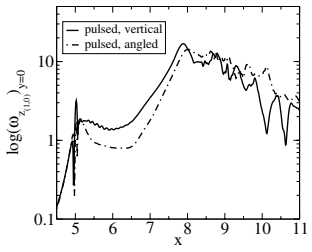

Figure 31. Fourier amplitude of the disturbance wall-vorticity for pulsed VGJ actuation

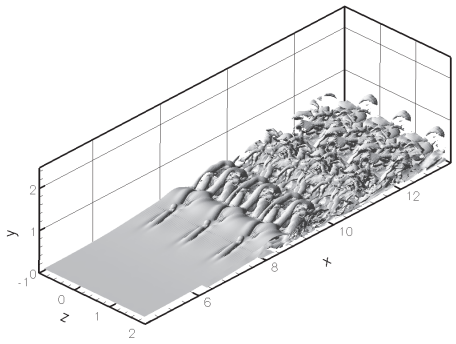

Figure 32. Instantaneous iso-surfaces of spanwise vorticity obtained from a simulation of a generic separation bubble forced with pulsed, vertical VGJs

instability of the underlying flow and the energy input required to produce large perturbations can be minimized. In other words, a relatively small disturbance input can yield strong spanwise coherent structures that aid in the entrainment of high-momentum fluid from the free stream.

The spanwise coherent structures that can develop when this two-dimensional instability mechanism is exploited are illustrated in figure 32. Shown are results obtained from simulations of a generic separating boundary layer using pulsed, vertical VGJs (Postl et al., 2003). It is obvious that, in spite of the inherent three-dimensionality of the forcing through localized holes, a two-dimensional disturbance component is introduced as part of the actuation.

In our simulations, the spanwise coherence of the large structures remains strong far into the transitional and turbulent regions for both pulsed, vertical

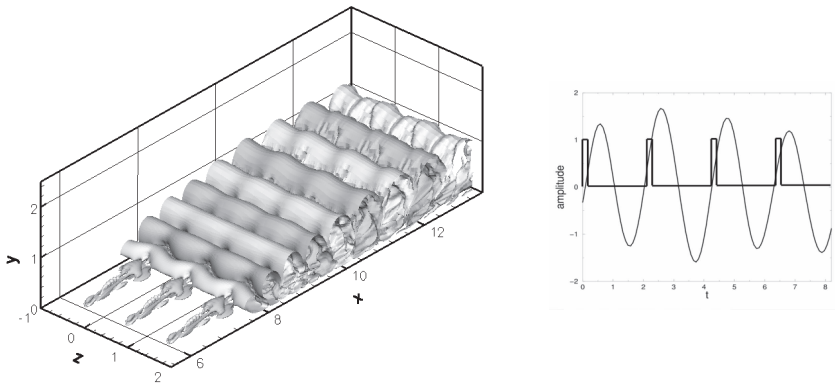

Figure 33. POD analysis of a generic separation bubble forced with pulsed, vertical VGJs. Left: iso-surfaces of wall-normal velocity for POD mode 1; right: associated POD- and forcing time signals

VGJs and pulsed, angled VGJs (not shown here). The development of the spanwise coherent structures was also confirmed by applying a Proper Orthogonal Decomposition (POD) to the time-dependent data. Shown in figure 33, for example, are wall-normal velocity contours of POD mode 1 for forcing with pulsed, vertical jets. This mode contains the most energetic unsteady structures. The coherent structures present in the flow can therefore clearly be identified as pre-dominantly two-dimensional. The time signal associated with POD mode 1 is also shown in figure 33. Comparison of this time signal to that of the VGJ input reveals that the structures are synchronized with the forcing and develop as a direct consequence of the actuation. Based on this evidence, we believe that the inviscid instability mechanism that leads to the large "coherent" two-dimensional "rollers", as demonstrated in the previously discussed model simulations (section 3), can be exploited for effective control of low-pressure turbine separation.

5. CONCLUSION

Using Direct Numerical Simulations of generic laminar separation bubbles, we demonstrated the complex interaction of separation and transition, and, in particular, also the role of hydrodynamic instability in explaining the unsteadiness observed in experiments. The understanding gained from the model geometries helped us to interpret the physical mechanisms that are at play when active flow control using pulsed VGJs is employed for controlling separation in low-pressure turbines. The presented results and discussions are "work in progress" and should therefore not be accepted as definitive. With additional simulations, we intend to scientifically substantiate the preliminary findings presented in this paper. In particular, with similar, well-tailored simulations, we plan to focus on many of the unresolved issues addressed in the paper by Gaster, 2004, such as the effect of Reynolds number, short bubbles versus long bubbles, bubble bursting, etc.

ACKNOWLEDGEMENTS

This research was funded by the Air Force Office of Scientific Research (AFOSR) under grant number F49620-02-1-0122. Computer time from the Army High Performance Computing Research Center (AHPCRC) and from the Arctic Region Supercomputing Center (ARSC) is gratefully acknowledged.

REFERENCES

Bake, S., Meyer, D., and Rist, U. (2002). Turbulence mechanism in klebanoff transition: a quantitative comparison of experiment and direct numerical simulation. *J. Fluid Mech.*, 459:217–243.

Bons, J. P., Sondergaard, R., and Rivir, R. B. (2001a). The fluid dynamics of lpt blade separation control using pulsed jets. *Proc. TURBOEXPO*, 2001-GT-0190.

Bons, J. P., Sondergaard, R., and Rivir, R. B. (2001b). Turbine separation control using pulsed vortex generator jets. *ASME J. Turbomachinery*, 123(2):198–206.

Brancher, P. and Chomaz, J. M. (1997). Absolute and convective secondary instabilities in spatially periodic shear flows. *Physical Review Letters*, 78(4):658–661.

Couairon, A. and Chomaz, J. M. (1996). Global instability in fully nonlinear systems. *Physical Review Letters*, 77(19):4015–4018.

Fasel, H. (2002). Numerical investigation of the interaction of the Klebanoff mode with Tollmien-Schlichting waves. *J. Fluid Mech.*, 450:1–33.

Gaster, M. (2004). Laminar separation bubbles. In *Laminar-Turbulent Transition, Proceedings of the IUTAM Symposium, Bangalore, India*. Springer.

Gross, A. and Fasel, H. F. (2005). Simulation of active flow control for a low pressure turbine cascade. *AIAA Paper*, 2005-0869.

Huerre, P. and Monkewitz, P. A. (1990). Local and global instabilities in spatially developing flows. *Ann. Rev. Fluid Mech.*, 22:473–537.

Jeong, J. and Hussain, F. (1995). On the identification of a vortex. *J. Fluid Mech.*, 285:69–94.

Marxen, O., Rist, U., and Wagner, S. (2004). Effect of spanwise-modulated disturbances on transition in a separated boundary layer. *AIAA J.*, 42:937–944.

Maucher, U., Rist, U., and Wagner, S. (1997). Secondary instabilities in a laminar separation bubble. In Kørner, H. and Hilbig, R., editors, *Notes on Numerical Fluid Mechanics*, pages 229–236. Vieweg Verlag.

Meitz, H. and Fasel, H. F. (2000). A compact-difference scheme for the Navier-Stokes equations in vorticity-velocity formulation. *J. Comp. Phys.*, 157:371–403.

Postl, D., Gross, A., and Fasel, H. F. (2003). Numerical investigation low-pressure turbine blade separation control. *AIAA Paper*, 2003-0614.

Postl, D., Gross, A., and Fasel, H. F. (2004). Numerical investigation of active flow control for low-pressure turbine blade separation. *AIAA Paper*, 2004-0750.

Rist, U. and Fasel, H. F. (1995). Direct numerical simulation of controlled transition in in a flat-plate boundary layer. *J. Fluid Mech.*, 298:211–248.

Sondergaard, R., Bons, J. P., and Rivir, R. B. (2002). Control of low-pressure turbine separation using vortex generator jets. *J. Prop. Power*, 18:889–895.

Wernz, S. and Fasel, H. (1999). Numerical investigation of resonance phenomena in wall jet transition. In *Laminar-Turbulent Transition, Proceedings of the IUTAM Symposium, Sedona, AZ*, pages 217–222. Springer.

ON FUNDAMENTAL INSTABILITY MECHANISMS OF NOMINALLY 2-D SEPARATION BUBBLES

M. Simens, L. González, V. Theofilis, R. Gómez-Blanco
[1]*Escuela Técnica Superior Ingeniéros Aeronáuticos, Univ. Politecnica de Madrid, Pza. Cardenal Cisneros 3, E-28040 Madrid, SPAIN;*
[2]*Escuela Técnica de Ingeniería, Univ. Pontificia Comillas de Madrid, Alberto Aguilera 25, E-28015 Madrid, SPAIN*

Abstract: The instability of nominally laminar steady two-dimensional closed separation bubbles is investigated using direct numerical simulations and BiGlobal instability analysis. The canonical flat-plate case is studied in some detail. We demonstrate that large steady two-dimensional bubbles may become unsteady and shortened in the mean upon applying periodic forcing. Using BiGlobal instability analysis we demonstrate, for the first time, the generation of Kelvin-Helmholtz instabilities as solutions of the pertinent partial-derivative eigenvalue problem, without resorting to the simplifying assumptions on the form of the underlying basic state. Finally, we employ appropriate instability analysis to study the effect of periodic forcing as means of active control of separation on a trailing-edge geometry.

Key words: Separation bubble, Wake flow, BiGlobal flow instability

1. INTRODUCTION

Our present concern is with instability of two-dimensional steady laminar separation bubbles in planar and bluff-body geometries. The numerical approaches utilized in our analyses encompass two-dimensional direct numerical simulations (DNS) and BiGlobal instability analyses via solutions of the linearized Navier-Stokes equations or the partial-derivative eigenvalue problem. Particular emphasis is placed on the identification, demarcation and classification of well-known local (Kelvin-Helmholtz) and less explored

R. Govindarajan (ed.), Sixth IUTAM Symposium on Laminar-Turbulent Transition, 89–95.

global instability mechanisms. The ultimate objective of the ongoing research is to reduce the parameter space in which either of the aforementioned instability scenarios is operative and propose criteria for efficient control of generic laminar separated flow configurations.

Two distinct applications have been chosen for the numerical work: adverse pressure-gradient flow in the boundary layer on a flat plate and the trailing edge of a bluff body. In the first application, the imposed pressure gradient is adjusted in order to control the size and shape of the separation bubble. In the second application, serving as a model for the trailing edge of airfoils or low-pressure-turbine blades, separation is induced by the geometry and the imposed boundary conditions. In the bluff-body model we are interested in exploiting global instability mechanisms to modify the structure and characteristics of the wake, while in the flat-plate model we are interested on the one hand in preventing open separation and on the other hand in shortening the length of the bubbles, without generating boundary layers with increased drag. Further motivation is provided by the recently found independence of the spatial characteristics of the amplitude functions of the leading global eigenmode of laminar separated flow on the underlying geometry [10] and the need to further explore global instability phenomena in distinct separated flow configurations.

2. THEORETICAL AND NUMERICAL METHODS

2.1 Linear instability analyses

Steady two-dimensional basic states are obtained and analyzed with respect to their three-dimensional BiGlobal linear instability. The latter problem is addressed by either solving the three-dimensional linearized Navier-Stokes and continuity equations,

$$[\partial_t + U\,\partial_x + V\,\partial_y]\,\tilde{u} + \tilde{u}\,\partial_x U + \tilde{v}\partial_y U + \partial_x \tilde{p} - 1/Re\,[\,\nabla^2 - \beta^2\,]\,\tilde{u} = 0, \quad (1)$$

$$[\partial_t + U\,\partial_x + V\,\partial_y]\,\tilde{v} + \tilde{u}\,\partial_x V + \tilde{v}\partial_y V + \partial_y \tilde{p} - 1/Re\,[\,\nabla^2 - \beta^2\,]\,\tilde{v} = 0, \quad (2)$$

$$[\partial_t + U\,\partial_x + V\,\partial_y]\,\tilde{w} - \beta\tilde{p} - 1/Re\,[\nabla^2 - \beta^2\,]\,\tilde{w} = 0, \quad (3)$$

$$\partial_x \tilde{u} + \partial_y \tilde{v} - \beta\,\tilde{w} = 0, \quad (4)$$

following a decomposition of the flow vector $\boldsymbol{q}$ according to $\boldsymbol{q}(x,y,z,t) = \boldsymbol{Q}(x,y) + \tilde{\boldsymbol{q}}\,(x,y,t)\,exp\,(-i\beta\,z\,) +$ c.c. Further, the partial-derivative eigenvalue problem is solved, as resulting from the substitution $\tilde{\boldsymbol{q}}\,(x,y,t) = \boldsymbol{q'}\,(x,y)\,\exp\,(\,-\sigma_i + i\,\sigma_r\,)\,t +$ c.c., where $\boldsymbol{Q} = (U,\ V,\ 0,\ p)^{T,}$ and

$\boldsymbol{q}'=(u',v,',w',p')^T$. The periodicity length L_z, in the spanwise direction is associated with the real wavenumber parameter through $L_z = 2\pi / \beta$.

2.2 The numerical work

A set of different codes has been developed and utilized, each being appropriate for an individual task arising in the course of the present work. Two-dimensional DNS work in the canonical flat-plate geometry is performed using a code which solves the incompressible Navier-Stokes and continuity equations in primitive variables using the fractional step method presented in [6]. The equations are discretized using fourth-order compact finite-difference schemes on a regular cartesian staggered grid [5] in the directions parallel (x) and perpendicular (y) to the wall. Third-order Runge-Kutta is used for explicit time integration of all but the viscous term in y, which is treated implicitly. The Poisson equation for the pressure is solved using multigrid. The Cartesian grid used is stretched in the y- and uniform in the x-direction. A three-dimensional extension of this code, employing Fourier collocation to resolve the homogeneous spatial direction is used for the associated 3D work.

The instability analyses of the bluff body are performed by solution of the 3D linearized Navier-Stokes and continuity equations. In the canonical flat-plate flow instability analyses are performed by solving the partial-derivative eigenvalue problem corresponding to (1 – 4) when the time-derivative is replaced by a harmonic expansion in time. Spectral collocation methods based on Chebyshev polynomials are used to discretize in a coupled manner the spatial operator in the wall-normal and the downstream direction. Boundary conditions based on extrapolation of different orders are used in the (open) downstream flow direction and Krylov subspace iteration methods are employed to identify the interesting part of the eigenspectrum, as has been successfully demonstrated, e.g. in [8, 9].

A general-purpose two-dimensional finite-element code, applicable to arbitrary geometries [4] is used for the direct numerical simulations associated with the latter part of our research. In two spatial dimensions, the code is based on the combination of the characteristics [2] and the conjugate-gradient method [3]. The latter algorithm is used to solve the Stokes problem that results after discretization of the material derivative by the semi-lagrangian scheme. A Taylor-Hood finite element type is used, the accuracy of which is quadratic for the velocity and linear for the pressure. Convective terms are treated using a semi-langrangian scheme, where the characteristic path must be sought on an unstructured mesh. The evaluation of the viscous term is performed by an implicit Crank-Nicholson

scheme. An extension of the same code solves the three-dimensional linearized Navier-Stokes equations (1 – 4) using analogous techniques.

The basic flow field around a 2D bluff-body in a rectangular domain $x \in [\ 0,\ 45\ ] \times \ y \in [\ -20,\ 20\ ]$ is resolved. The geometry is non-dimensionalized by the body width and the free-stream velocity. The immersed object, modeling the trailing edge of a low-pressure-turbine or airfoil has a length of 4 and a width of 1 unit, with circular-arc rounded corners and a curvature radius of 0.4 units. Steady and unsteady basic flows have been obtained at angles of attack $\alpha = 0^o$ and 3^o, in the Reynolds number range $Re \in [\ 60,\ 400\ ]$. Unstructured meshes with a total of $\sim 3\times 10^4$ nodes have been used to solve this geometry. Boundary conditions used are of Dirichlet type at the inflow, upper and lower sides of the domain and non-reflecting (natural) boundary conditions at the outflow boundary. At the body surface no-slip is applied for the baseline calculations, while basic states are also obtained by modifying the boundary condition at the rounded corners. The imposed velocity at the corners results in counter-rotating fluid motion and has a magnitude of $||\mathbf{u}|| = A\ [1+\cos(4\cdot\alpha-\pi)]$, where the angle α is taken along the azimuthal direction in the 1st and the 2nd quadrant. In the 3D linearized Navier-Stokes work, boundary conditions on the disturbance quantities are homogeneous Dirichlet on all surfaces, except for the outflow boundary where non- reflecting boundary conditions have been employed.

3. RESULTS

The basic states obtained on the canonical geometry are characterized by a momentum-thickness Reynolds number $Re_\theta = 28$, the numerical domain considered being defined by $x \in [0,\ 1122] \times y \in [0,\ 143]$ in inflow momentum thickness θ_0 units. Without forcing, a steady state results, as shown in the upper right part of Fig. 1. Exploiting Kelvin-Helmholtz instability to force the flow unsteady two-dimensional states result, such as that shown in the lower right part of Fig. 1. This flow, obtained at a slightly higher $Re_\theta = 30$ and using a forcing frequency $St = f\,\theta_b/U_\infty = 0.018$, where θ_b is the momentum thickness of the shear layer above the bubble at a position where the velocity inside the bubble reaches a minimum [7], is characterized by strong vortex shedding and a mean bubble length which is substantially smaller than the corresponding unforced laminar bubble.

BiGlobal instability analysis is subsequently performed, using the unforced steady basic flow with a twofold objective: first, identify frequencies in the neighborhood of that resulting in optimal modification of the separation bubble and, second, assess whether a three-dimensional instability may modify the two-dimensional steady basic state utilized (e.g. as in [8]). Results of two- $(\beta = 0)$ and three-dimensional $(\beta \neq 0)$ solutions of

the partial-derivative eigenvalue problem have been obtained. The dependence of the frequency of the three least-damped eigenmodes on β is shown in the left part of Fig. 2, while only stable BiGlobal eigenmodes have been found at $\beta = 0$. Nevertheless, the recovered eigenmodes, the least-damped of which is shown in the right part of Fig. 2, encompass structures that can be qualitatively associated with the vortex shedding shown in the lower right part of Fig. 2. Further examination of the eigenspectrum and classification of its members is currently underway.

Figure 3 shows an image of the mesh used for the bluff-body simulations. Steady basic flow results for the streamwise velocity component at $Re = 60$ in the baseline and a modified configuration, the latter obtained using A = 1% at the two angles of attack examined so far are shown in Figure 4. At the zero angle of attack at which the present simulations are performed, there is no separation bubble formed on the suction side of the object, while well-defined closed separation bubbles are present in the case of nonzero angle of attack. Instability analyses of both the baseline and the modified basic states are currently underway and results are contrasted against those in the NACA 0012 airfoil and the T106-300 low pressure turbine [10].

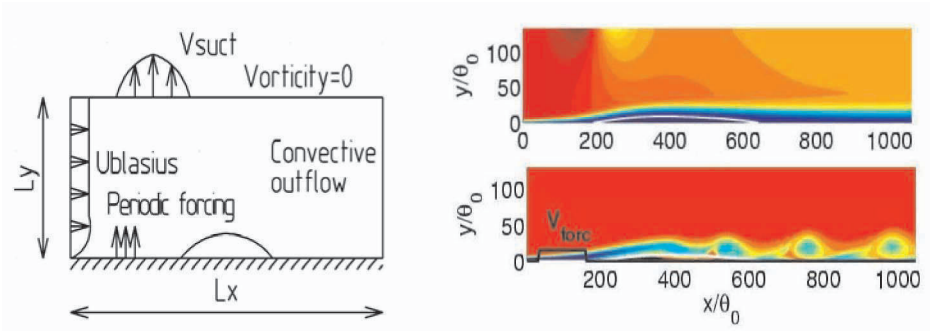

Figure 1. Left: schematic description of the canonical flow geometry, where $Vsuct = a_s \exp(-b_s (x - c_s)^2)$ [1] and $V_{forc} = a_f \sin(2\pi f t)$, with $a_s = 0.35$ and $a_f = 10^{-2}$. Right, upper: Steady basic flow; white line indicates contour of zero streamwise velocity. Right, lower: Corresponding 2D flow with forcing; black line shows the zero contour of the average streamwise velocity

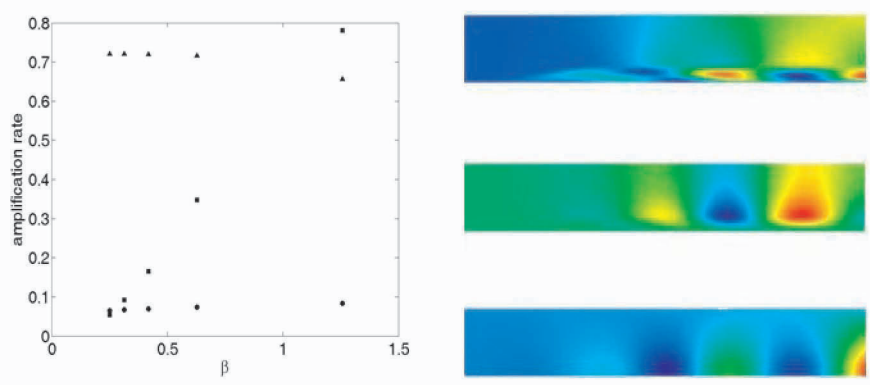

Figure 2. Left: Dependence of the amplification rate of the least damped 3D BiGlobal eigenmodes on β. Right, amplitude functions of the disturbance velocity components of the least-damped 2D damped eigenmode; u' (upper), v' (middle), p' (lower); axes scaling as in Figure 1

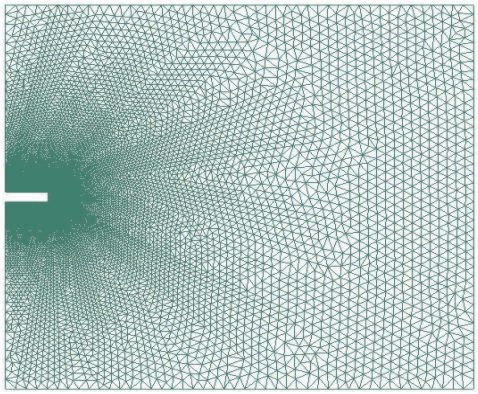

Figure 3. The unstructured mesh utilized for the bluff-body simulations

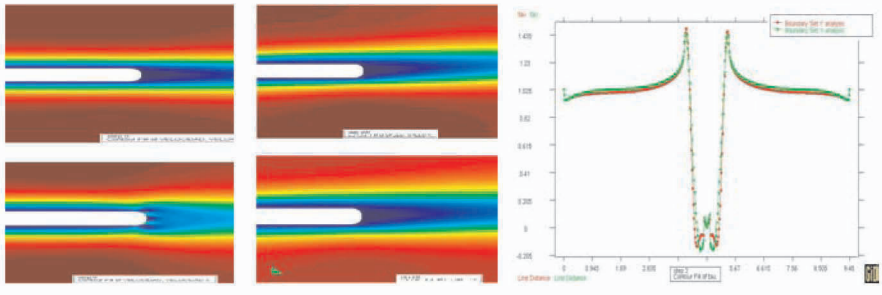

Figure 4. The steady baseline flow at Re = 60, α = 0 (upper left) and α = 3º (upper middle). The steady modified basic flow at α = 0 (lower left) and α = 3º (lower middle). Right: comparison of wall shear distribution in the α = 0 cases

ACKNOWLEDGEMENTS

MS was supported by EU Contract HPRN-CT-2002-00300, LG and RGB were partly supported by CICYT Contract No. DPI 2002-03123 and VT was partly supported by a Ramón y Cajal research fellowship of the Spanish Ministry of Education and Science.

REFERENCES

[1] Alam, M., and Sandham, N.D. 2000. Direct simulation of short laminar separation bubbles with turbulent reattachment. J. Fluid Mech. 410:223 - 250

[2] Allievi, A., and Berm ejo, R. 2000. A characteristic finite-element algorithm for the Navier-Stokes equations. Int. J. Numer. in Fluids., 32:439-464.

[3] Dean, E. J., and Glowinski, R. 1993 *On Some Finite Element Methods for the Numerical Simulation of Incompressible Viscous Flow*, Incompressible computational fluid dynamics, Eds. M. D. Gunzburger & R. A. Nicolaides, Cambridge University Press.

[4] González, L.M., 2003. Alternative treatment of the slip boundary condition for the integration of the Navier-Stokes equations in a turbulent context. XVIII CEDYA/ VIII

[5] Nagarajan, S., Lele, S.K. and Ferziger, J.H. 2003. A robust high-order compact method for large eddy simulation. J. Comput. Phys. 191:392-419.

[6] Perot, J.B. 1993 An analy sis of the fractional step method. J. Comput. Phys. 108:51-58.

[7] Simens, M. and Jiménez, J. 2004. Control of large two-dimensional laminar separation bubbles by shear-layer instabilities. Advances in Turbulence 10, ETC 10 June 29-July 2, 2004, pp. 725-728.

[8] Theofilis, V., Hein, S. & Dallmann, U.Ch. 2000. On the origins of unsteadiness and three-dimensionality in a laminar separation bubble. Phil. Trans. R. Soc. Lond. A 358:3229-3246.

[9] Theofilis, V., Fedorov, A., Obrist, D. & Dallmann, U.Ch. 2003. The extended Görtler-Hämmerlin model for linear instability of three-dimensional incompressible swept attachment-line boundary layer flow. J. Fluid Mech. 487:271-313.

[10] Theofilis, V., Sherwin, S.J. and Abdessemed, N. 2004. On global instabilities of separated bubble flows and their control in external and internal aerodynamic applications. RTO AVT-111 Specialists' meeting on *"Enhancement of NATO military flight vehicle performance by management of interacting boundary layer transition and separation*", Prague, Oct. 4 – 7, 2004, Paper 21-1 – 21-9.

A NEW STABILITY APPROACH FOR THE FLOW INDUCED BY WALL INJECTION

G. Casalis,[1] F. Chedevergne,[1] Th. Feraille,[1] and G. Avalon[2]

[1] *ONERA/DMAE, 2, avenue Ed. Belin, 31 055 Toulouse Cedex, FRANCE*
gregoire.casalis@onecert.fr, francois.chedevergne@onecert.fr

[2] *ONERA/DEFA, chemin de la Huniere, 91 761 Palaiseau Cedex, FRANCE*
gerard.avalon@onera.fr

Abstract : The present paper deals with the stability analysis of the flow induced by wall injection either in a rectangular duct or in a cylindrical pipe. As the basic flow is strongly nonparallel, the modal form gives amplitude functions which are dependent on two space variables. The linear stability problem is thus described by a PDE system whose results seem to be in good agreement with the experiments.

1. INTRODUCTION

Under some conditions, large solid rocket motors may exhibit thrust oscillations. In order to analyse this phenomenon, cold gas experiments are carried out. As suggested by numerical simulations, e.g. Lupoglazoff and Vuillot, 1996, the velocity field in the cold gas set-up is expected to reproduce faithfully the one occurring in real motors with combustion.

In the framework of the instabilities modelling, the main difficulty in the present case deals with the basic flow which is strongly non parallel. Usual stability approaches are performed within the parallel assumption. In this case, using the normal mode form, the amplitude functions depend on one space variable only and the linearized Navier-Stokes equations lead to an ordinary differential equation of Orr-Sommerfeld type. This has been successfully applied to shear flows such as the boundary layer or the jet flows. However there are some physical configurations for which the basic flow is fully non parallel, its velocity field depends on two space variables (instead of only one), like a separated boundary layer and the boundary layer around an attachment line. In these cases, the normal mode assumption leads to amplitude functions which depend

R. Govindarajan (ed.), Sixth IUTAM Symposium on Laminar-Turbulent Transition, 97–102.

on two variables and the stability equations then become an eigenvalue problem written as a system of partial differential equations.

This second approach needs obviously large computational resources mainly concerning the memory, but the major difficulty seems to be related to the boundary conditions, except for the case of the Poiseuille flow, see Tatsumi and Yoshimura, 1990. With non physical boundaries, the published results are more recent, see Lin and Malik, 1996, Theofilis, and Robinet and de la Motte, 2003 for instance. The present paper gives an outline for a flow which presents only one non physical boundary, details can be found in Féraille, 2004. The obtained results are given in comparison with measurements obtained with two cold gas set-ups, one is a planar duct, the other one a cylindrical pipe.

2. PHYSICAL MODEL

2.1 Theoretical model

Two configurations are analyzed, case 1 is a rectangular duct, case 2 a circular pipe, see figures below. In both cases, air is uniformly in-

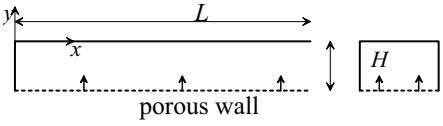

Figure 1. Scheme of VECLA set-up

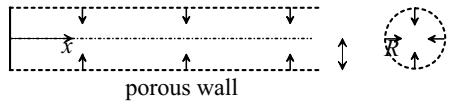

Figure 2. Scheme of VALDO set-up

jected through a porous wall. All quantities given below are made dimensionless thanks to the height H or R and the norm of the injection velocity. The characteristic Reynolds number based on these quantities is noted $\mathcal{R}_e$. In some conditions the flow is laminar at least for small values of x. A laminar analytical steady inviscid solution exists ; in both cases, corresponding streamfunctions are expressed by :

$$\Psi_1 = x \sin\left(\frac{\pi y}{2}\right) \qquad \Psi_2 = x \sin\left(\frac{\pi r^2}{2}\right) \tag{1}$$

where subscripts 1 and 2 correspond respectively to the rectangular duct and the circular pipe. For the considered large Reynolds numbers, this form is accurate enough, see Casalis et al., 1998.

The flow is strongly non parallel, particularly for small values of x, see Figure 3. A linear stability analysis of this flow is carried out. Assuming that the perturbation remains two-dimensional (case 1) or axisymmetric (case 2), a streamfunction ϕ may be associated to the fluctuation. Due to the non parallel nature of the basic flow, the normal mode writes as :

$$\phi_1(x, y, t) = \hat{\phi}_1(x, y)e^{-i\omega t} \qquad \phi_2(x, r, t) = \hat{\phi}_2(x, r)e^{-i\omega t}$$

with ω a complex number, its real part ω_r corresponds to the circular frequency of the instability mode and its imaginary part ω_i to the temporal growth rate. The amplitude function thus depends on two space variables and the linear stability problem consists in solving a partial differential equation (PDE) for ϕ_1 (resp. ϕ_2) with respect to (x, y) (resp. (x, r)) and ω is the eigenvalue to be determined.

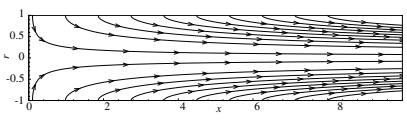

Figure 3. Steady streamlines, case 2

The PDE has to be solved in a rectangular domain. The transverse coordinate y (or r) varies between the symmetry line and the porous wall and the axial coordinate x varies from the front wall $x = 0$ up to a given exit value X_e. On the first boundary, symmetry conditions are imposed, on the second and third ones the fluctuating velocity is imposed to be zero, the fourth boundary is artificial and "ad-hoc" conditions are imposed (see section 2).

2.2 Experimental set-ups

The two configurations of figures 1 and 2 have been experimentally explored with the set-ups VECLA and VALDO using the same feeding equipment. Air coming from a pressurized tank at 250 bar is injected inside the two set-ups through elementary throats that control the mass flow rate entering the duct at several parts of the porous wall. To compensate the decrease of temperature due to its depressurization, air passes inside a gas heater before its injection. The heat quantity given to the air is controlled by a thermo-regulator whose power is adjusted to obtain a temperature of 20°C inside the ducts.

The porous walls of the two set-ups are formed of bronze poral obtained by joining together small spheres of bronze of same diameter. Low porosities, typically equal to 8 μm or 18 μm, are adopted for these porous walls in order to avoid as much as possible the transfer of acoustic energy from the duct to the backside of the porous wall. The VECLA set-up is composed of a planar chamber which is 603 mm in length and 60 mm in width whose bottom is equipped with a porous plate of 5 mm thickness and 581 mm in length. The height of the duct can be fixed to 10 mm, 20 mm, 30 mm or 40 mm by mounting metallic blocks under the top wall of the chamber which contains special ports where pressure transducers and hot wire can be introduced. A nozzle can be attached to the downstream end of the chamber. The VALDO set-up is of modular type with a conception in separate modules, each of them containing a porous cylinder of 60 mm in diameter, made in porous bronze of thick-

ness 5 mm. Air is injected into each module by three orifices which are regularly spaced around the circumference. The modules have a length of 168 mm and, since four modules are available at the present time, the maximum channel length is 672 mm. Over the four modules, one has several ports located in front of holes drilled on the surface of the porous cylinders at which the pressure, the temperature and the velocity of the air inside the central duct can be measured. The radial displacement of the hot wire is ensured by a pilotable table whose variation extent is of 100 mm. The set-up can operate in two versions depending if a nozzle attached to the end of the injecting part is used or not.

3. NUMERICAL PROCEDURE

The PDE system written for $\hat{\phi}$ (case 1 or 2) is discretized by a spectral collocation method in the two space directions. The problem becomes a generalized eigenvalue problem $\underline{\underline{A}}.\underline{X} = \omega \underline{\underline{B}}.\underline{X}$ with $\underline{\underline{A}}$ and $\underline{\underline{B}}$ two matrices and $\underline{X}$ the vector corresponding to the value of $\hat{\phi}$ on each double collocation point. Due to the size of the matrices, the spectrum (set of the eigenvalues ω) is obtained part by part using an Arnoldi algorithm, see Arnoldi, 1951. This means that a target is specified before each calculation and only the eigenvalues close to it are computed. The obtained results consist in a set of discrete complex values for ω. With 100 collocation points in x and 120 in r (case 2), table 1 gives the numerical

Table 1. Converged numerical eigenvalues for five modes, $\mathcal{R}_e = 1000$, case 2

k	1	2	3	4	5
ω_r	5.4776	10.189	14.378	18.130	21.536
ω_i	-4.9307	-6.8131	-8.5493	-10.258	-11.810

values of some modes identified by the integer k, see figure 5.

After several attempts, a simple extrapolation for $\hat{\phi}$ is imposed at the boundary X_e. The results (eigenvalue and eigenfunction) are found amazingly to be independent of the type of conditions imposed at $x = X_e$ (other conditions have been tested, see Féraille, 2004) and are also independent of the location of the exit abscissa X_e. This is clearly shown in figure 4, which gives the contours of $|Re(\hat{\phi}_2)|$ for four values of X_e. Except maybe in a region very close to X_e, each result is completely superposed to the other results obtained for larger values of X_e. This means that the general structure of the mode is determined by the upstream part of the flow : moving the non physical X_e downstream does not affect the upstream physical values associated to the eigenmode.

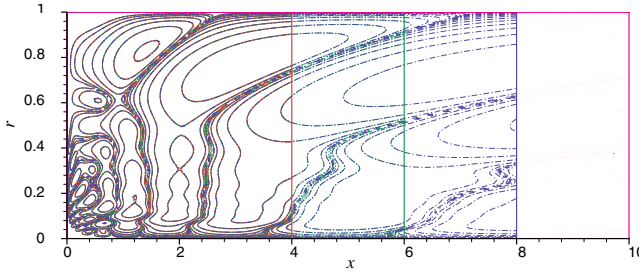

Figure 4. Norm of the real part of $\hat{\phi}_2$ associated to the mode $k = 5$. Superposed results obtained with four different exit sections : 4, 6, 8 and 10, $\mathcal{R}_e = 2100$

4. STABILITY RESULTS

The first result is the spectrum i.e. the set of the complex eigenvalues ω. For both configurations the spectrum is plotted in figure 5 in the complex plane (ω_r, ω_i). Several observations may be done, they are

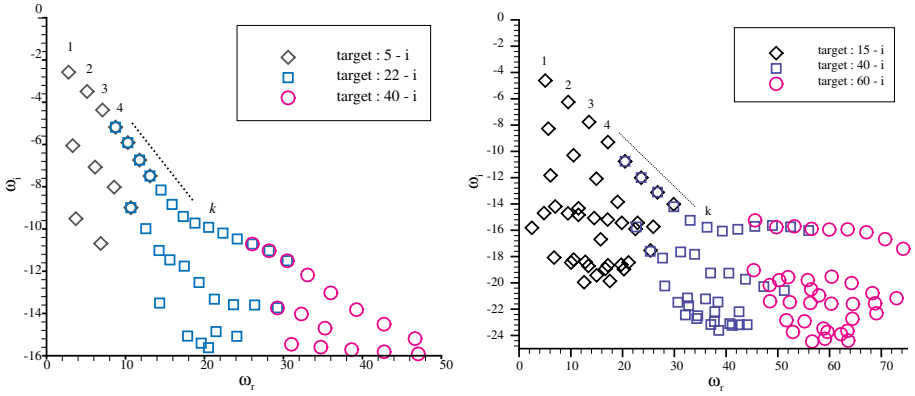

Figure 5. Spectrum in the complex (ω_r, ω_i) plane : case 1 (left) with $\mathcal{R}_e = 1000$ and case 2 (right) with $\mathcal{R}_e = 2100$

the same in both cases. Only (temporally) damped modes are obtained seeing that the temporal growth rates are all negative. The basic flow is thus stable from this point of view. The eigenfunctions especially for frequencies (dimensionless values) between 20 and 80 exhibit actually a huge growth in the x direction, in fact a growth which is nearly exponential. The modes are stable with respect to the time but exponentially growing in space (with respect to x) ! It can be also remarked that only discrete values of the frequency are obtained. This result contradicts the conclusion obtained by using the classical normal mode approach (assuming that the basic flow is parallel whereas it is clearly not, see figure 3). A continuous range of frequencies corresponding to spatially

amplified modes is predicted by this usual stability analysis, see Casalis et al., 1998. Comparison with the experiments is given in figure 6. The

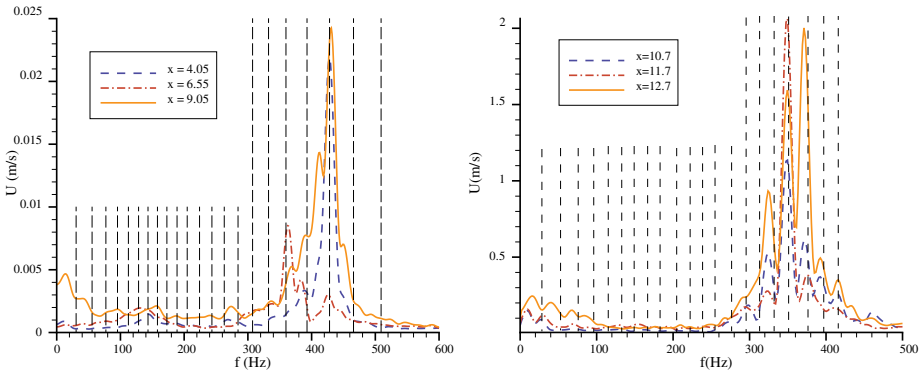

Figure 6. Comparisons between the new stability analysis and measurements of the fluctuating velocity by a hot wire : case 1 (left) and case 2 (right)

vertical dashed lines correspond to the dimensional values of the different discrete modes k shown in figure 5. A rather good agreement is obtained especially in case 2 and the experimental results seem to be closer to a discrete structure than exhibiting a continuous range of amplified frequencies. The modes are temporally damped, are exponentially growing in x and only some of them are measured. This may indicate that the environmental fluctuations are very important in terms of receptivity.

REFERENCES

Arnoldi, W. (1951). The principle of minimized iteration in the solution of the matrix eigenvalue problem. *Quart. Appl. Math.*, 9:17–29.

Casalis, G., Avalon, G., and Pineau, J. P. (1998). Spatial instability of planar channel flow with fluid injection through porous walls. *Physics of Fluid*, 10(10).

Féraille, T. (2004). *Instabilités de l'écoulement interne des moteurs à propergol solide.* PhD thesis, SUPAERO, Toulouse.

Lin, R. and Malik, M. (1996). On the stability of attachment-line boundary layers. Part 1. The incompressible swept Hiemenz flow. *J. of Fluid Mech.*, 311:239–255.

Lupoglazoff, N. and Vuillot, F. (1996). Parietal vortex shedding as a cause of instability for long solid propellant motors. Numerical simulations and comparisons with firing tests. In *34th Aerospace Sciences Meeting and Exhibit.* AIAA 96-0761.

Robinet, J. C. and de la Motte, P. (2003). Global instabilities in separated boundary layers. In *IUTAM, TSFP-3*, Sendai, Japan.

Tatsumi, T. and Yoshimura, T. (1990). Stability of the laminar flow in a rectangular duct. *J. Fluid Mech.*, 212:437–449.

Theofilis, V. Linear instability analysis in two spatial dimensions. In *Fourth ECCOMAS Computational Fluid Dynamics Conference.* ECCOMAS98.

THE PECULIARITIES OF DEVELOPMENT OF FORERUNNERS ON LONGITUDINAL STRUCTURES FRONTS IN THE BOUNDARY LAYER OF A STRAIGHT WING

Vasiliy N. Gorev, Mikhail M. Katasonov and Viktor V. Kozlov
Institute of Theoretical and Applied Mechanics SB RAS, Novosibirsk, Russia

Abstract: Wind-tunnel experiments on longitudinal structures developing in laminar boundary layers on a straight wing have been carried out. High-frequency perturbations, that is, "forerunners" occurring near the fronts of the streamwise disturbances were detected. Their characteristics and dynamics were clarified revealing similarities of the disturbances with boundary-layer instability waves.

Key words: flow; turbulence; subsonic; wind tunnel; hot-wire anemometer; boundary layer; disturbances; streaky structure; Tollmien-Schlichting wave; forerunner.

1. INTRODUCTION

In recent years the longitudinal localized vortex disturbances, so called "streaky structures", or "puffs" appearing in boundary layers under the effect of external flow turbulence are of much interest. Once these disturbances are generated, they amplify downstream, and incipient spots appear which, finally, result in laminar-turbulent transition [1, 2].

In the present paper on wave packets occurring in the regions preceding a drastic change of the velocity inside the boundary layer at the longitudinal structures fronts are in focus. Their characteristics and dynamics have been studied, thus analogy has been found between this type of the vortex disturbances and Tollmien-Schlichting waves.

R. Govindarajan (ed.), Sixth IUTAM Symposium on Laminar-Turbulent Transition, 103–108.

2. EXPERIMENTAL PROCEDURE

The investigations were carried out in the subsonic low-turbulent wind tunnel T-324, ITAM SB RAS (Fig. 1); the test section of the facility is 1000 mm x 1000 mm x 4000 mm. Free stream velocity was U_0 = 8.3 m/s at the turbulence level smaller than 0.04%. The model was a straight wing of 1000 mm span with the chord of 450 mm set vertically at the positive angle of attack of 5°. The disturbances were generated via blowing (suction) through a slot arranged in the surface perpendicularly to the free stream. The slot was located at the distance of 40 mm from the leading edge of the wing. The sizes of the slot were: width of 0.5 mm, length of 90 mm. The blowing (suction) was carried out with the aid of a compressor, their duration was controlled by a fast valve synchronized to a signal-recording system.

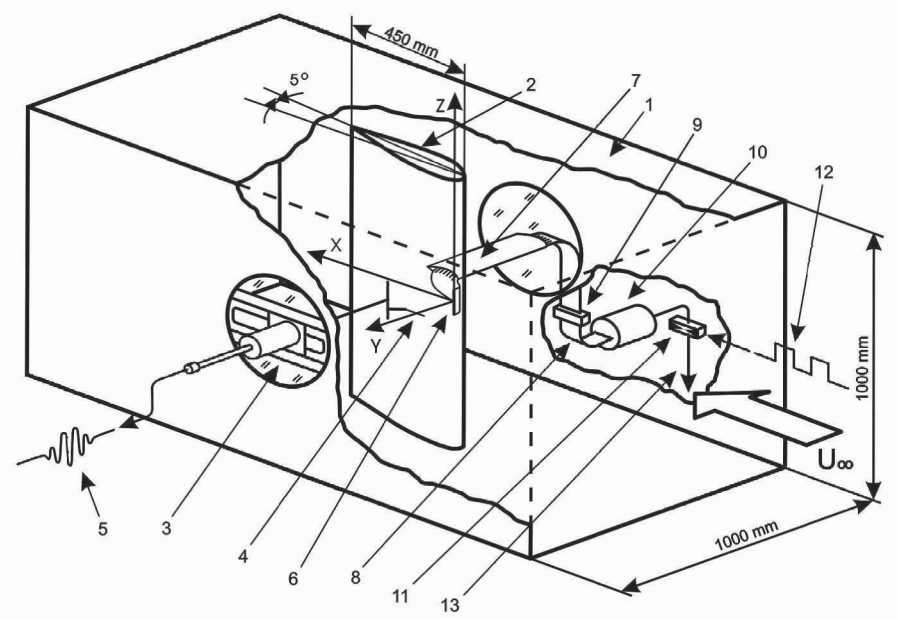

Figure 1. Layout of the experiment. 1 –test section of the wind tunnel, 2 - wing profile, 3 – traverse system, 4 - hot-wire anemometer, 5 - signal to the hot-wire meter bridge and then to the computer ADT, 6 - slot – disturbance's source, 7 - pneumatic routing cowling, 8 - pneumatic routing (45 tubes), 9 - set of controllers, 10 - damper, 11 - fast valve, 12 - valve-opening signal, 13 - pneumatic routing to the compressor

The longitudinal structures were generated with the frequency of 1 Hz. Velocity gradients (du/dt) at the leading and back fronts were controlled by a damper of 0.5 litre volume. The latter was installed between the valve and the slot. It should be noted that the local gradient du/dt can be converted into

a spatial gradient du/dx, with due regard to the constant velocity of the longitudinal disturbance propagation.

The damper and the slot were connected to each other with a pneumatic canal track consisting of 45 individual tubes with a controller of each. This system gave a possibility to assign an arbitrary profile of air blowing (suction) through the slot.

The measurements were performed with a constant temperature anemometer using single-wire probes. The mean and perturbation components of the longitudinal velocity component were measured. The wire diameter was of 6 microns, the length of about 1 mm. The coordinates origin was in the slot's center with X - measured in the streamwise direction, Z - along the span of the model, and Y - normally to X and Z with the reference point on the wing surface.

3. RESULTS AND DISCUSSION

First, the undisturbed flow characteristics including mean velocity distribution above the wing (Fig. 2a) and boundary layer profiles (Fig. 2b) were measured. Then, Y – t diagrams of the boundary layer with the excited longitudinal structures were obtained in the same streamwise sections and, further, Z – t diagrams were recorded at the disturbances maximum across the boundary layer. In this way, the structure and dynamics of the perturbations were clarified.

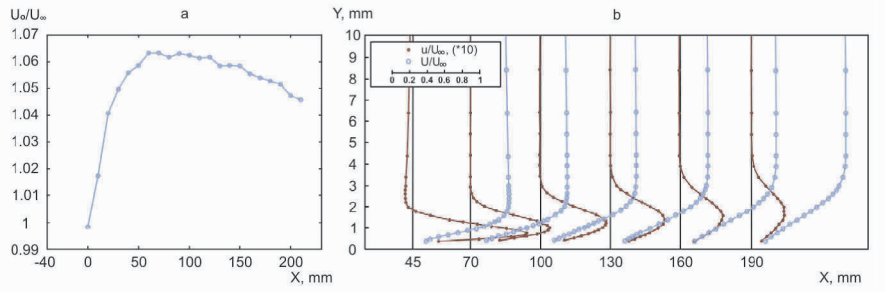

Figure 2. a Streamwise distribution of the external flow velocity, x = -40 mm corresponds to the leading edge of the wing; b mean velocity profiles of the undisturbed boundary layer U, m/s (o) and deviations of the instantaneous velocity from its mean value due to longitudinal structures u, m/s (•)

One can observe in Fig. 2b that the longitudinal structures keep inside the boundary layer while spreading normally to the wall as the boundary thickness grows. Also it was found that the mean-velocity deviation (u) from the undisturbed flow induced by the longitudinal structures is fairly smooth in the transverse direction minimizing velocity gradients du/dz. Thus, secondary instabilities one could expect at the side boundaries of the structures were excluded.

At the streamwise propagation, the longitudinal structures generate wave packets, the so-called forerunners, in the regions of strong velocity variations at the leading and the back fronts of the structures (see example in Fig. 3). Under negative pressure gradient in the upstream portion of the flow amplification of these disturbances is negligible, however, the forerunners grow rapidly in the aft part of the wing (Fig. 4a). At the same time, the streaks amplitude falls down constantly all through the x-range under examination (Fig. 4b).

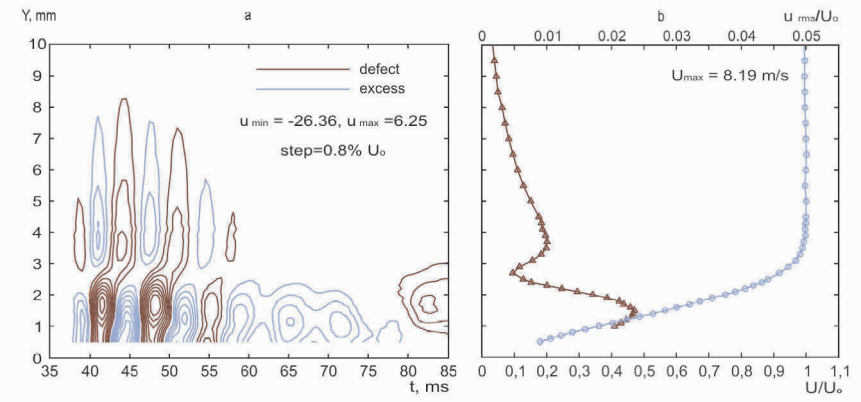

Figure 3. a Y – t diagram of the wave packet generated by blowing at the leading front of the longitudinal structure; b mean velocity profile of the undisturbed boundary layer (o) and r.m.s. distribution of the perturbations (Δ); x = 160 mm

Origination and evolution of the wave packets depend on velocity gradients dU/dx at the leading and the back fronts of the longitudinal structures. When the structure is generated by suction, high-speed motion from the outer part of the boundary layer is transferred locally towards the wall. The resultant streaky structure propagates in a slow fluid and the largest velocity gradient occurs at its leading front.

The opposite situation takes place in the case of blowing so that the velocity variation becomes higher at the back front of the perturbation. Besides this, the forerunners at the leading front of the longitudinal structures are convected in the undisturbed boundary layer whereas those at

the back front propagate through the flow distorted by the structures both at suction and blowing.

Also, we notice that the longitudinal structures have different effect upon the boundary layer depending on the way of their generation. Once they are excited by blowing, the filling of velocity profile is reduced that makes the flow receptive to external perturbations. Thus, more intensive should be development of the wave packet at the back front of the structure. In contrast, at boundary-layer suction the flow receptivity becomes lower so that the wave packet at the leading front dominates. Variations of the wave packets amplitude with the streamwise distance shown in Fig. 4a are in agreement with the above concept of the disturbances evolution. The larger velocity gradient dU/dx at the front of the longitudinal structure, the higher amplitude of the forerunner.

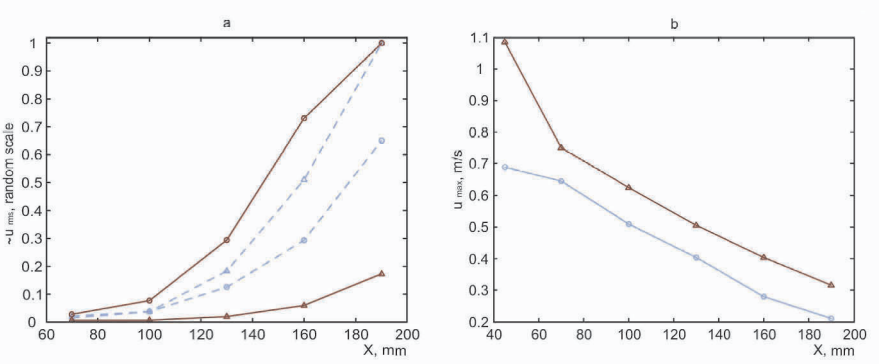

Figure 4. a Streamwise variation of the forerunners amplitude at the leading (o) and the back (Δ) fronts of the streaky structures generated by blowing (dotted line) and suction (solid line); b intensities of the streaks excited by blowing (Δ) and suction (o)

At examination of the perturbations, similarities of their characteristics in all the cases of the forerunners generation were found. Those include the group velocity determined for the wave packets center which was close to $0.34U_0$ and the specific spatial arrangement of the disturbances with 180-degrees phase difference between the oscillations in the near-wall and the outer parts of the boundary layer, see Fig.3a. Some differences were found in frequency spectra of the forerunners at the leading and back fronts of the streaky structures. For the leading-front perturbations at blowing and the back-front ones at suction a pronounced peak was observed at about 150 Hz only; otherwise, the subharmonic oscillations were amplified, as well. The above observations strongly support an idea that the forerunners are

essentially the wave packets of 3D linear and nonlinear Tollmien-Schlichting waves.

4. CONCLUSIONS

In the present experiments the high-frequency perturbations, i.e. forerunners, at the leading and back fronts of the longitudinal structures evolving in the laminar boundary layer have been found. Their characteristics affected by the external-flow pressure gradient, the way of the longitudinal structures generation, and velocity gradients induced by the latter were investigated. In particular, it was observed that the forerunners are strongly amplified in the adverse pressure gradient flow being much influenced by local velocity gradients. The results of the study make reason to consider the forerunners as wave packets of 3D instability waves.

The work was supported by the Russian Foundation for Basic Researches (grant No. 02-01-00006), President's Foundation for the support of the leading scientific schools of Russian Federation (grant No. SS-964.2003.1), and by INTAS Foundation (project No. 00-00232).

REFERENCES

1. Kozlov V.V. The role of localized vortex disturbances in the process of transition to turbulence in a boundary layer // Dynamics of localized disturbances in engineering flows: - EUROMECH Colloquim 353: Booklet of summaries. Karlsruhe, 1996. –P. 15-16.
2. Boiko A.V., Grek G.R., Dovgal A.V., Kozlov V.V. The origination of turbulence in near-wall flows. Berlin; Heidelberg; New York: Springer Verlag, 2002.

OBSERVATION OF NONLINEAR TRAVELLING WAVES IN TURBULENT PIPE FLOW

Björn Hof, Casimir W.H.van Doorne, Jerry Westerweel and Frans T.M. Nieuwstadt

Laboratory of Aero- and Hydrodynamics, Delft University of Technology, Leeghwaterstraa 21, 2628 CA Delft, The Netherlands

Abstract: Transition to turbulence in pipe flow has posed a riddle in fluid dynamics since the pioneering experiments of Reynolds[1]. Although the laminar flow is linearly stable for all flow rates, practical pipe flows become turbulent at large enough flow speeds. Turbulence arises suddenly and fully without distinct steps and without a clear critical point. The complexity of this problem has puzzled mathematicians, physicists and engineers for more than a century and no satisfactory explanation of this problem has been given. In a very recent theoretical approach it has been suggested that unstable solutions of the Navier Stokes equations may hold the key to understanding this problem. In numerical studies such unstable states have been identified as exact solutions for the idealized case of a pipe with periodic boundary conditions[2 , 3]. These solutions have the form of waves extending through the entire pipe and travelling in the streamwise direction at a phase speed close to the bulk velocity of the fluid. With the aid of a recently developed high-speed stereoscopic Particle Image Velocimetry (PIV) system, we were able to observe transients of such unstable solutions in turbulent pipe flow[4].

Key words: Hydrodynamic stability, Turbulence, Shear flow transition, Unstable states

1. INTRODUCTION

Pipe flow is governed by a single dimensionless parameter, the Reynolds number Re=UD/ν, where U is the mean (or bulk) flow speed, D the pipe diameter and ν the kinematic viscosity of the fluid. Whereas stability theory

R. Govindarajan (ed.), Sixth IUTAM Symposium on Laminar-Turbulent Transition, 109–114.

predicts that laminar pipe flow is stable for all flow rates[5], in practice pipe flows become turbulent even at moderate speeds. Turbulence sets in suddenly and fully, with no intermediate states. In experiments transition to turbulence typically occurs spontaneously at Re as low as 2000, however in carefully designed experiments the transition point can be delayed to Reynolds numbers as large as 100000[6].

Recent discoveries of disconnected unstable solutions to the governing Navier-Stokes equation[2,3,7,8], have lead to a new transition scenario for pipe and related shear flows[9]. Since these solutions are unstable they cannot persist individually in practical flows. As the Reynolds number is increased and the number of these unstable solutions grows they can form a chaotic saddle in phase space [9], which gives rise to long-lived turbulent transients. As Re is increased further the lifetimes of the turbulence transients are believed to increase exponentially and the strange saddle is believed to evolve into a turbulent attractor, which sustains disordered turbulent flow indefinitely. The relevance of such unstable travelling waves to transition in shear flows has been confirmed by the recent experimental observations of Hof et *al*.[10]. The authors observed transients of these travelling waves within turbulent flow structures in experimental pipe flow.

2. EXPERIMENTAL METHODS

The experimental set-up shown in figure 1 consists of a 26 metre long circular pipe with an inner diameter of 4 cm corresponding to a non-dimensional length of 650 diameters. Fully developed laminar pipe flow was perturbed 350 pipe diameters from the inlet by means of a jet injected through a 1mm hole perpendicularly to the pipe wall. The resulting turbulent flow was investigated 150 diameters downstream with a high-speed stereoscopic PIV system. Tests have shown that a length of 150 pipe diameters is sufficient for all transients which might be inflicted by the perturbation mechanism to subside. Careful calibration of the measurement system allowed the instantaneous measurement of all three velocity components in a cross-sectional plane. The passage of turbulent structures was recorded in this plane at a series of 1000 contiguous measurements at sampling rates up to 500 Hz. A detailed description of the experimental apparatus can be found in Hof et *al.* [4] (online material).

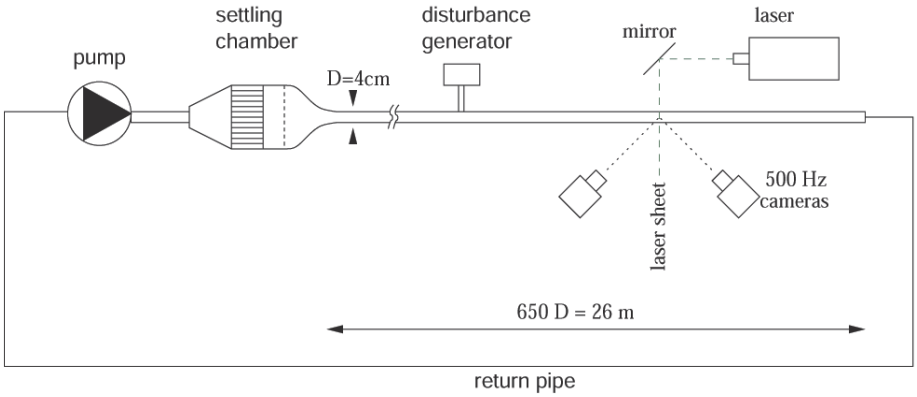

Figure 1. Experimental apparatus

3. RESULTS

In this section we report an investigation of a turbulent puff at Re=2000. Puffs are localized turbulent structures, which travel downstream at approximately the bulk velocity and are typically 10 to 50 pipe diameters long. In our measurements the characteristic quantities such as the centre line velocity during the passage of the puff were found to be in excellent agreement with those reported in earlier studies[11]. In figure 2 we show three flow profiles, measured at the leading edge, the centre and the trailing edge of the puff. At the leading edge the velocity in the central part of the pipe is clearly slower than for the laminar profile (shown on the right) whereas velocities in the near wall region are larger. In the central region of the puff the flow is turbulent and the profile is distorted by strong cross flow components and streaks. At the trailing edge the flow recovers the parabolic profile very quickly in comparison to the rather slow velocity modification observed at the leading edge. The advection speed of the turbulent puff is approximately equal to the mean velocity of the flow, which at Re=2000 is u=4.6 cm/s. Particle images were recorded at a frequency of 62.5 Hz during the passage of the turbulent puff through the measurement plane. Applying the Taylor hypothesis this corresponds to a spatial resolution of approximately 55 sampled velocity profiles per pipe diameter in the streamwise direction.

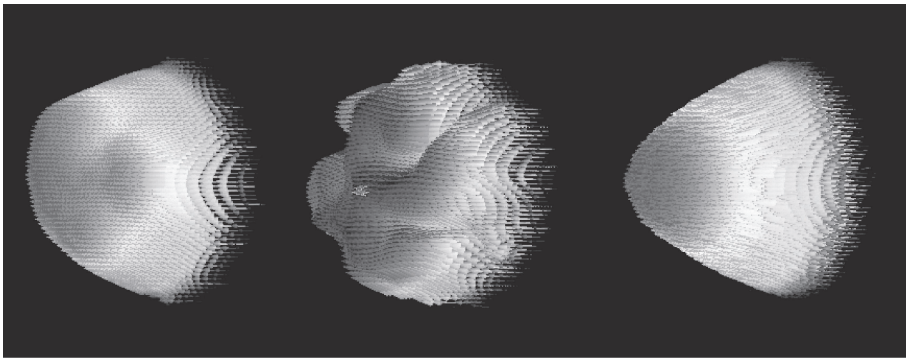

Figure 2. Three component Velocity profiles. The profile on the left was taken at the leading edge of the puff and that in the middle in the central part of the puff. The profile on the right was taken after the passage of the trailing edge where the flow is laminar again. The colour coding (red / blue corresponds to high / low velocities) shows the streamwise component

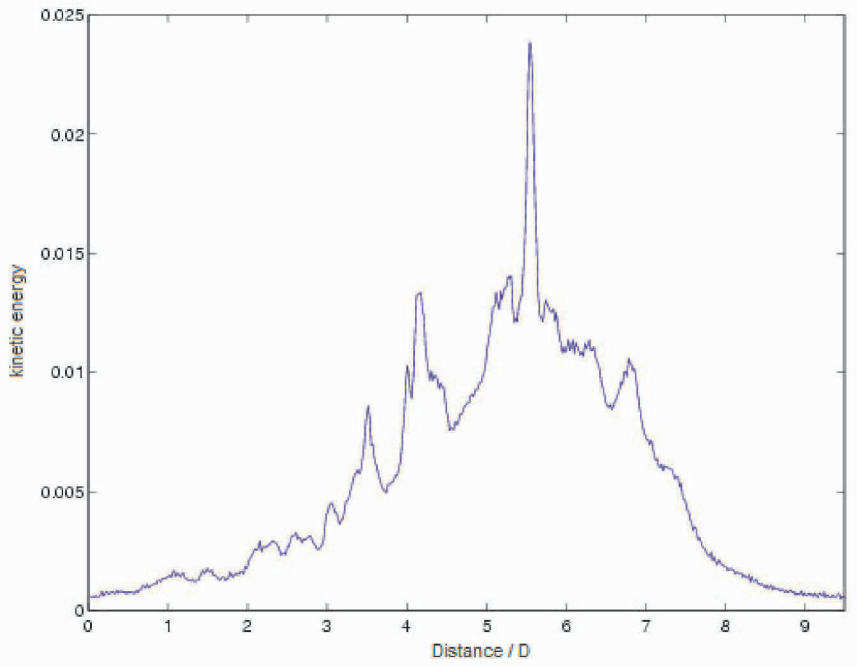

Figure 3. In plane kinetic energy during the passage of a turbulent puff

The high spatial resolution allowed us to closely monitor the in-plane kinetic energy (u^2+v^2) during the passage of the turbulent puff (figure 3). At the leading edge the in-plane kinetic energy increases relatively slowly in

comparison to the rather fast decline at the trailing edge. The most surprising features of the curve are the sudden changes in the kinetic energy. The largest spike occurs approximately 2 D from the trailing edge and here the energy almost doubles over a distance of a tenth of a pipe diameter. In the vicinity of this energy spike we were able to identify streak-vortex configurations which closely resemble those of the numerically calculated travelling wave solutions. Here a 3-fold symmetric travelling wave transient was observed and it is shown in figure 4 together with its numerical counterpart.

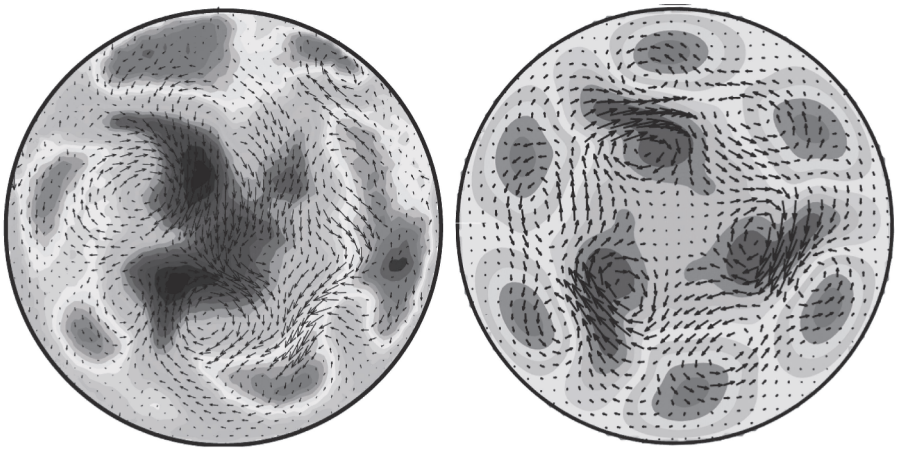

Figure 4. 3-fold nonlinear travelling wave. Left: Experimental observation at Re=2000. Right: Exact travelling wave solution

4. CONCLUSION

We present observations of vortex streak configurations which are in striking agreement with those found in nonlinear travelling waves calculated numerically for pipe flow[2,3]. The high sampling speed and spatial resolution of the measurement technique enables us to identify large spikes in the in-plane kinetic energy during the passage of turbulent puffs.

REFERENCES

[1] Reynolds, O. 1883 'An experimental investigation of the circumstances which determine whether the motion of water shall be direct or sinuous and of the law of resistance in parallel channels.' *Philos. Trans. Roy.. Soc. London* **174**, 935

[2] Faisst, H. & Eckhardt, B. 2003 'Travelling waves in pipe flow' *Phys. Rev. Lett.***91**, 224502

[3] Wedin, H. & Kerswell, R.R. 2003 'Exact coherent solutions in pipe flow: travelling wave solutions' *J. Fluid Mech.* **508**, 333

[4] Hof, B., van Doorne, C.W.H., Westerweel, J., Nieuwstadt, F.T.M., Faisst, H., Eckhardt, B., Wedin, H., Kerswell, R.R., & Waleffe, F. 2004 'Experimental observation of nonlinear traveling Waves in Turbulent Pipe Flow', *Science*, **305**, 1594-1598.

[5] Drazin, P.G., Reid, W.H. 'Hydrodynamic Stability.' *Cambridge University Press* (1981).

[6] Pfenniger, W. 1961 'Transition in the inlet length of tubes at high Reynolds numbers.' *In Boundary layer and flow control, Pergamon* (ed G.V. Lachman), 970.

[7] Nagata, M. 1990 'Three-dimensional finite-amplitude solutions in plane Couette flow: bifurcation from infinity.' *J. Fluid Mech.* **217**, 519-527.

[8] Clever, R.M., Busse, F.H. 1997 'Tertiary and quarternary solutions for plane Couette flow.' *J. Fluid Mech.* **344**, 137-153 .

[9] Faisst, H., Eckhardt, B. 2004 'Sensitive dependence on initial conditions in transition to turbulence in pipe flow.' *J. Fluid Mech.* **504**, 343-352.

[10] Hof, B., van Doorne, C.W.H., Westerweel, J., Nieuwstadt, F.T.M., Faisst, H., Eckhardt, B., Wedin, H., Kerswell, R.R., & Waleffe, F. (2004) Experimental Observation of Nonlinear Traveling Waves in Turbulent Pipe Flow, *Science*, **305**, 1594-1598.

[11] Wygnanski, I.J., Champagne, F.H. 1973 'On transition in a pipe. Part 1. The origin of puffs and slugs and the flow in a turbulent slug.' *J. Fluid Mech.* **59**, 281 (1973)

A STRANGE INSTABILITY WITH GROWTH NORMAL TO A BOUNDARY LAYER

J. J. Healey
Department of Mathematics, Keele University, Keele, Staffordshire, ST5 5BG, UK[*]
j.j.healey@maths.keele.ac.uk

Abstract: We present recent results concerning the linearized inviscid stability and propagation characteristics of disturbances to the boundary-layer flow due to an infinite rotating disk in otherwise still fluid. Such disturbances are expected to decay exponentially outside the boundary layer, but we have found a situation where exponential growth can occur in the wall-normal direction. It is shown, by considering the solution to the initial-value problem, that this behaviour can be predicted by using modes with exponentially divergent eigenfunctions.

Keywords: Absolute instability, convective instability, rotating disk boundary layer, initial value problems

1. INTRODUCTION

Early theories of the stability of boundary layers considered spatially harmonic disturbances that might grow or decay exponentially in time, and yet early experiments used vibrating ribbons to excite disturbances that were harmonic in time and which might grow or decay exponentially with downstream distance from the ribbon. In principle, the evolution of any disturbance to the flow can be decomposed into a superposition of spatially harmonic waves, but, as shown by Gaster, [2], [3], a much simpler and more direct comparison between theory and these experiments can be realized by solving for roots of the dispersion relation with real frequency (to give time-harmonic behaviour) and complex wavenumber (to give growth or decay in the downstream coordinate).

Although these spatial theories are now completely accepted, one objection to complex wavenumbers is that they are modes whose amplitudes tend to infinity in the streamwise direction. Is such a mode really suitable for a linear stability theory? This objection is overcome by pointing out that in practice we

[*]The author is grateful to the Royal Society of London for partially funding his attendance at this conference.

R. Govindarajan (ed.), Sixth IUTAM Symposium on Laminar-Turbulent Transition, 115–120.

are interested in studying initial-value problems, in which a localized disturbance has only propagated a finite distance downstream from the source after a finite time, and therefore only shows spatial growth over a finite distance from the source. (In practice, this distance is also limited by the size of the experimental apparatus).

In this paper we extend the idea of spatial instability in the downstream direction to spatial instability in the wall-normal direction. A scenario is presented in which a propagation takes place that is efficiently described by modes with 'eigenfunctions' that grow exponentially in the wall-normal direction. These modes fail to satisfy homogeneous boundary conditions and so the objection might be raised that they are not allowable roots of the dispersion relation. (In fact, they are analytic continuations of the dispersion relation). Nonetheless, consideration of the initial value problem for the generation of these waves shows that they do describe actual disturbance evolutions. After a finite time, growth only extends over a finite distance *above* the source, though this distance increases with time. These divergent modes therefore describe a new type of convective instability in the wall-normal direction.

The results presented in this conference paper are a brief summary of work recently submitted for journal publication [8], and the reader should consult that paper for full details and discussion.

The physical problem giving rise to this behaviour is introduced in § 2, together with equations describing the disturbances. A saddle point theory extended to include the case of wall-normal propagation is presented in § 3. Comparisons between the results of saddle-point theories based on modes with divergent eigenfunctions and numerical evaluations of impulsive disturbances are made in § 4, and conclusions drawn in § 5.

2. PHYSICAL PROBLEM

The basic flow is the boundary layer that forms adjacent to a disk rotating at constant angular velocity under a body of fluid at rest far from the disk. This flow is described by the classic von Karman similarity solution in which the radial component has a wall-jet character (fluid near the disk is thrown outwards by centrifugal forces) and there is a typical boundary layer structure in the azimuthal direction. This cross-flow structure generates inviscid waves with zero phase velocity relative to the disk (the stationary vortices) that produce a striped pattern in flow visualizations, [5]. Furthermore, Lingwood has shown that this inviscid problem has unstable waves with zero group velocity, generating absolute instability, [10], the onset of which seems intimately related to the transition to turbulence.

Absolute instability characteristics are determined by the dominant saddle-point contribution in certain inverse Fourier transforms, [4] ('pinch-points' in

the Briggs-Bers formulation, [1]). Lingwood assumed that the dominant saddle in the viscous version of the problem asymptotes at large Reynolds number towards the dominant saddle in the inviscid problem. However, there are several saddles in the viscous problem and it is now known that different saddles are dominant in different parts of parameter space, [6]. Lingwood's saddle seems to remain dominant along the lower-branch of the neutral curve for absolute instability, but becomes subdominant at a point along the upper-branch. An analytic description of Lingwood's saddle point at large Reynolds numbers will therefore require a long-wave lower-branch theory. As a first step towards such a theory, an inviscid long-wave theory has now been developed, [7].

However, the long-wave inviscid theory predicts that the dominant saddle becomes asymptotically close to the imaginary axis of the complex wavenumber plane as wavelengths increase. We can quickly show why this might have significance for the character of absolutely unstable waves outside the boundary layer. Linearized inviscid waves far from the axis of rotation of the disk can be described by the Rayleigh equation, see [5],

$$(Q-c)(w''-\gamma^2 w)-Q''w=0 \tag{1}$$

where primes denote differentiation with respect to z (the axial, wall-normal, coordinate), $Q=U+(\beta/\alpha)V$, U and V are scaled radial and azimuthal components of the basic flow, α and β are scaled radial and azimuthal wavenumbers, $\gamma^2=\alpha^2+\beta^2$, $c=\omega/\alpha$, ω is the scaled angular frequency of the disturbance and w is the eigenfunction for the normal mode, i.e. $\hat{w}(r,\theta,z,t)=w(z)\exp[\mathrm{i}Re(\alpha r+\beta\theta-\omega t)]$, where $\hat{w}$ is the axial component of the disturbance velocity, symbols have their usual meanings in cylindrical coordinates and Re is a Reynolds number (distance to axis of rotation in terms of boundary layer thickness, assumed large, $Re\,\beta$ is an integer). Outside the boundary layer the basic flow is uniform, $Q''\to 0$, and (1) reduces to $w''-\gamma^2 w=0$ with general solution

$$w=C_1\exp\left(-\sqrt{\gamma^2}z\right)+C_2\exp\left(\sqrt{\gamma^2}z\right). \tag{2}$$

It is usually convenient to define $\sqrt{\ }$ to denote the root with positive real part, so that homogeneous boundary conditions are satisfied by taking $C_2=0$, producing exponential decay as $z\to\infty$. This has the effect of introducing branch-cuts along the imaginary α-axis with branch-points at $\alpha=\pm\mathrm{i}\beta$. If the dominant saddle approaches the imaginary axis then the decay outside the boundary layer becomes very weak.

3. SADDLE-POINT THEORY

The physical solution to an impulsive disturbance of particular azimuthal wavenumber, β, can be found by integrating normal modes over α using an

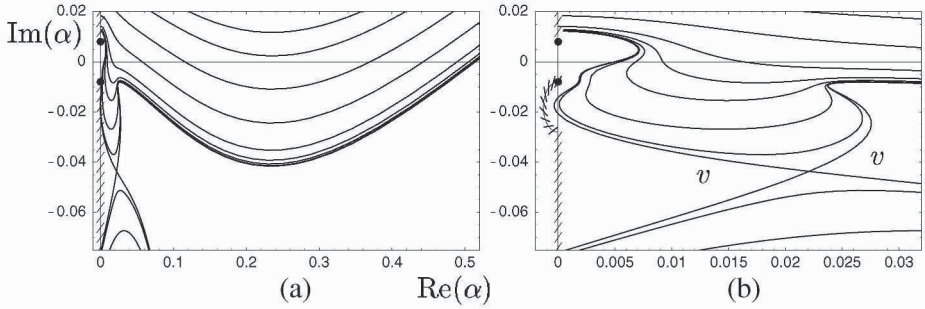

Figure 1. Contours of constant $\mathrm{Re}(\phi) = \mathrm{Im}(\omega)$ for $\beta = 0.008$, hatched lines are branch-cuts, (b) is a detail of (a). Valleys of the saddles (pinch-points) are indicated by a v.

expression of the form

$$\hat{w}(r,\theta,z,t) = \mathrm{e}^{\mathrm{i}Re\,\beta\theta} \int_A \frac{w(z)}{\Delta_\omega} \exp \mathrm{i}Re(\alpha r - \omega t)\, \mathrm{d}\alpha \tag{3}$$

where $\omega = \omega(\alpha)$ is a root of the dispersion relation $\Delta(\alpha,\omega) = 0$, see [8]. The dominant contribution to the integral in (3) as $t \to \infty$ comes from certain saddle points of the phase function

$$\phi = \mathrm{i}Re\left(\alpha\frac{r}{t} - \omega\right) \tag{4}$$

satisfying $\mathrm{d}\phi/\mathrm{d}\alpha = 0$, i.e.

$$\frac{\mathrm{d}\omega}{\mathrm{d}\alpha} = \frac{r}{t} \tag{5}$$

where $r/t = O(1)$. For a saddle point to make a contribution its valleys must include the real α-axis as $|\mathrm{Re}(\alpha)| \to \infty$. The saddles, and their valleys, can be found by plotting contours of $\mathrm{Re}(\phi)$ in the complex α-plane. For the particular case $r/t = 0$, these contours correspond to the spatial branches used in Briggs' method, and the branches at the pinch-point are the contours at the saddle point.

Figure 1 shows the contours of $\mathrm{Re}(\phi)$ for $\beta = 0.008$. It can be seen that the dominant saddle is sufficiently close to the imaginary α-axis that the integration path A can only remain within the valleys of the saddle if the branch-cut is moved away from the imaginary α-axis. The part of the complex α-plane revealed in this way corresponds to exponentially growing eigenfunctions, i.e. taking $C_1 = 0$, $C_2 \neq 0$ in (2). Although such solutions appear unphysical, the physical solution does not depend on the position of branch-cuts, so we need to find a physical interpretation for solutions with diverging eigenfunctions. This is achieved by considering propagation in the wall-normal direction.

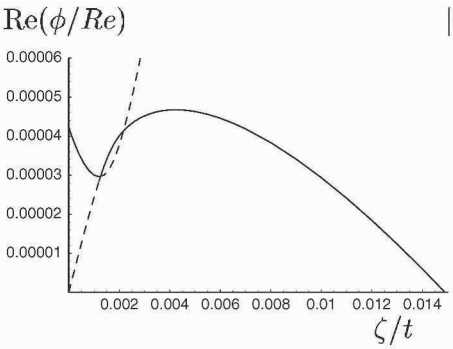

Figure 2. Growth rates predicted by saddles of (6) when $\beta = 0.007$ and $r/t = 0$. Solid lines indicate the dominant saddle, dashed lines indicate saddles that are either subdominant, or irrelevant

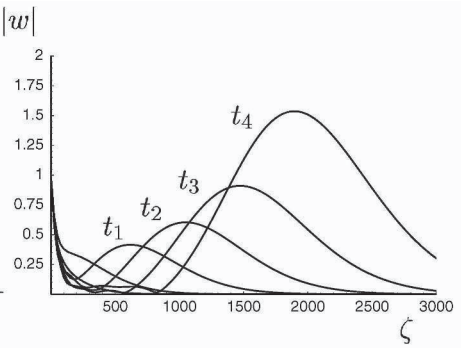

Figure 3. Normalized wall-normal disturbance profiles at a succession of times and $\beta = 0.007$. The latest times shown are $t_1 = 2 \times 10^5$, $t_2 = 3 \times 10^5$, $t_3 = 4 \times 10^5$ and $t_4 = 5 \times 10^5$

Outside the boundary layer we can substitute (2), with $C_2 = 0$, into (3) and thereby modify the phase function to give

$$\phi = Re\left[\mathrm{i}\left(\alpha\frac{r}{t} - \omega\right) - \sqrt{\gamma^2}\frac{\zeta}{t}\right] \tag{6}$$

where $z = Re\,\zeta$, with saddles occuring when

$$\frac{\mathrm{d}\omega}{\mathrm{d}\alpha} = \frac{r}{t} + \frac{\mathrm{i}\alpha}{\sqrt{\gamma^2}}\frac{\zeta}{t}. \tag{7}$$

Taking $\zeta/t > 0$ corresponds to moving into a frame of reference moving away from the surface of the disk. Figure 2 shows the growth rate of saddles as a function of ζ/t. When ζ/t is increased from zero the dominant saddle shown in figure 1 moves to the left, and crosses the imaginary axis, and acquires a diverging eigenfunction in the process. However, there is a second saddle that originates in the left half-plane with diverging eigenfunction, that moves to the right as ζ/t increases. This saddle is subdominant for $\zeta/t < 0.00127$, and is shown by the dashed line at the left of figure 2, but it becomes dominant for $\zeta/t > 0.00127$. For yet larger ζ/t it crosses onto the right half-plane, and eventually stabilizes at the right of figure 2. The original saddle giving the absolute instability at the left of figure 2 becomes irrelevant to the integral for $\zeta/t > 0.00216$ because the orientation of its valleys rotates and they no longer include the real α-axis at large $|\mathrm{Re}(\alpha)|$ (it becomes a non-pinching branch-point in the Briggs-Bers terminology).

Figure 2 predicts that the maximum growth rate occurs at a propagation velocity of $\zeta/t = 0.0042$, and the saddle making this prediction originates from the left half-plane with diverging eigenfunction.

4. NUMERICAL SOLUTION TO IMPULSIVE DISTURBANCES

We can test this surprising prediction by carrying out a numerical evaluation of (3) while maintaining the branch-cuts along the imaginary α-axes, and choosing an integration path A that is restricted to conventional modes with decaying eigenfunctions. The details are given in [8], and the results are shown in figure 3 (the results are normalized so that the disturbance profiles at different times can be compared on the same graph — the underlying absolute instability causes significant growth in time). The maximum growth does indeed propagate out of the boundary layer at a group velocity close to $\zeta/t = 0.0042$.

5. CONCLUSIONS

The collective behaviour of a superposition of modes with decaying eigenfunctions can, nonetheless, produce sustained growth in the wall-normal direction. Such behaviour can be captured by saddles with divergent eigenfunctions. The source of energy supplying this growth is described in [8]. Long-wave asymptotic theories have been developed in [9] showing that this behaviour is generic in the long-wave limit for this problem. This behaviour can be considered to be the result of an instablity of the continuous spectrum, which is present for flows unbounded in the direction perpendicular to the stream, and which represents the contribution to the integral (3) due to the branch-cuts arising from the square-root terms in (2).

REFERENCES

[1] Briggs, R. J. 1964 *Electron-Stream Interaction with Plasmas.* MIT Press.

[2] Gaster, M. 1962 A note on the relation between temporally-increasing and spatially-increasing disturbances in hydrodynamic stability. *J. Fluid Mech.* **14**, 222–224.

[3] Gaster, M. 1965 On the generation of spatially growing waves in a boundary layer. *J. Fluid Mech.* **22**, 433–441.

[4] Gaster, M. 1968 Growth of disturbances in both space and time. *Phys. Fluids* **11**, 723–727.

[5] Gregory, N., Stuart, J. T. & Walker, W. S. 1955 On the stability of three-dimensional boundary layers with application to the flow due to a rotating disk. *Phil. Trans. R. Soc. Lond.* A **248**, 155–199.

[6] Healey, J. J. 2004 On the relation between the viscous and inviscid absolute instabilities of the rotating-disk boundary-layer. *J. Fluid Mech.* **511**, 179–199.

[7] Healey, J. J. 2005a Inviscid long-wave theory for the absolute instability of the rotating-disk boundary-layer. *J. Fluid Mech.* Submitted for publication.

[8] Healey, J. J. 2005b A new convective instability of the rotating-disk boundary-layer with growth normal to the disk. *J. Fluid Mech.* Submitted for publication.

[9] Healey, J. J. 2005c Long-wave theory for a new convective instability with exponential growth normal to the wall. *Phil. Trans. R. Soc. Lond.* A. Accepted for publication.

[10] Lingwood, R. J. 1995 Absolute instability of the boundary layer on a rotating disk. *J. Fluid Mech.* **299**, 17–33.

NUMERICAL STUDIES OF STREAK INSTABILITY IN BOUNDARY LAYERS

Luca Brandt,[1] Carlo Cossu,[2] Dan S. Henningson,[1] Jean-Marc Chomaz,[2] Patrick Huerre[2]

[1] *KTH Mechanics, SE-100 44 Stockholm, Sweden*

[2] *LadHyX, CNRS-Ecole Polytechnique, F-91128 Palaiseau, France*

Abstract: Numerical results on the stability of boundary layers in the presence of streaks, assumed steady and spanwise periodic, are presented. The instability features are retrieved both from stability analysis and from the numerical simulation of the flow impulse response. It is found that the presence of streaks of moderate amplitudes is able to quench the viscous Tollmien-Schlichting waves. However, a threshold exists beyond which secondary inflectional instabilities occur. Streaky basic flows unstable to both sinuous and varicose perturbations are considered. To gain physical understanding of the instability mechanisms the equation for the perturbation kinetic energy is analysed. To investigate the sinuous instability modes an analytical model streak is also proposed.

Keywords: Instability, Boundary layer, Streamwise streaks

1. INTRODUCTION

Due to non-modal growth mechanisms, small amounts of streamwise vorticity in a laminar boundary layer are very effective in moving low-momentum particles away from the wall and high-momentum particles toward the wall, thus forming elongated spanwise modulations of the streamwise velocity, called streaks. Since the latter perturbations are expected to arise whenever a boundary layer is exposed to free-stream vortical disturbances, the stability of boundary layers in the presence of streaks, assumed steady and spanwise periodic, is investigated. The instability features are retrieved both from classical stability analysis (Schmid and Henningson, 2001) and from the numerical simulation of the flow impulse response (Delbende et al., 1998, Brandt et al., 2003).

In order to examine the instability mechanisms, the distribution of the kinetic energy production terms in the cross-stream (y, z) plane is

R. Govindarajan (ed.), Sixth IUTAM Symposium on Laminar-Turbulent Transition, 121–126.

evaluated. Assuming waves periodic in the streamwise direction, the perturbation kinetic energy equation averaged over the streamwise length of the perturbation reads

$$\frac{d}{dt}\left[\int_0^{y_{max}}\int_0^{\lambda_z}\frac{1}{2}(\overline{u^2}+\overline{v^2}+\overline{w^2})\,dy\,dz\right] = -\int_0^{y_{max}}\int_0^{\lambda_z}\frac{\partial U}{\partial y}\overline{uv}\,dy\,dz + \\ -\int_0^{y_{max}}\int_0^{\lambda_z}\frac{\partial U}{\partial z}\overline{uw}\,dy\,dz - \frac{1}{Re}\int_0^{y_{max}}\int_0^{\lambda_z}\overline{\boldsymbol{\omega}\cdot\boldsymbol{\omega}}\,dy\,dz, \quad (1)$$

where a bar denotes the streamwise average, λ_z is the spanwise wavelength of the streak and $\boldsymbol{\omega}$ the perturbation vorticity vector. This balance equation is derived by linearising the Navier–Stokes equations around the streak profile $U(y,z)$. The first production term of density $-\frac{\partial U}{\partial y}\overline{uv}$ represents the work of the Reynolds stress $\tau_{xy}=-\overline{uv}$ on the wall-normal basic shear $\frac{\partial U}{\partial y}$, while the second production term of density $-\frac{\partial U}{\partial z}\overline{uw}$ is associated with the work of the Reynolds stress $\tau_{xz}=-\overline{uw}$ on the spanwise basic shear $\frac{\partial U}{\partial z}$. The last term represents viscous dissipation.

Considering only temporal modes and further integrating in the wall-normal and spanwise direction, one equation relating the various production terms to the temporal growth rate ω_i of the wave can be obtained,

$$\omega_i = \frac{\tilde{T_y}}{2\tilde{E}} + \frac{\tilde{T_z}}{2\tilde{E}} - \frac{\tilde{D}}{2\tilde{E}}. \quad (2)$$

In the equation above, the quantity $\tilde{E}$ is the total perturbation kinetic energy and $\tilde{D}$ is the viscous dissipation term . $\tilde{T_y}$ and $\tilde{T_z}$ are the perturbation kinetic energy production terms associated with the work of the Reynolds stresses against, respectively, the wall-normal shear $\partial U/\partial y$ and spanwise shear $\partial U/\partial z$ of the basic flow.

2. OPTIMAL STREAKS

Streaks obtained from the nonlinear evolution of optimally growing streamwise vortices are first considered. It is shown that low-amplitude streaks have a stabilising effect on the viscous Tollmien-Schlichting instability (Cossu and Brandt, 2002). These results are confirmed by the experiments by Fransson et al., 2004, also presented at the this symposium, and can be explained by considering the energy balance introduced above. It is found that the production of perturbation kinetic energy associated with the spanwise shear of the streaks is found to play an essential role in the observed stabilisation. Increasing the streak amplitude, in fact, the negative production associated to spanwise shear and the viscous dissipation are able to more than balance the positive production due to the wall-normal shear.

However, above a certain threshold streak amplitude, secondary inflectional instabilities occur (Andersson et al., 2001, Brandt and Henningson, 2002). These unstable waves can be either symmetric or antisymmetric in the spanwise direction, the latter type of instability being, by far, the dominating one for this type of streaks. Analysis of the kinetic energy balance reveals that the spanwise shear is responsible for the antisymmetric sinuous instability, whereas the wall-normal shear weakly counteracts it. In particular, for a streak of amplitude $A = 0.36U_\infty$, where A is defined as half the maximum distortion with respect to the Blasius profile, and for sinuous perturbations with the most amplified streamwise wavenumber $\alpha = 0.6$, the terms in eqn. (2) take the following values. $\omega_i = 0.0338, \quad \tilde{T}_y/2\tilde{E} = -0.0095, \quad \tilde{T}_z/2\tilde{E} = 0.0505, \quad \tilde{D}/2\tilde{E} = 0.0071.$

3. MODEL STREAK FOR SINUOUS INSTABILITY

To study the instability characteristics of the antisymmetric/sinuous modes, an analytical model streak is proposed. The basic flow considered is given by the sum of the Blasius profile U_B and a wake-like low-speed streak obtained as product of a function of the wall-normal coordinate y and a function of the spanwise variable z

$$U(y, z) = U_B(y) - \Delta U F(y) W(z). \tag{3}$$

ΔU represents the strength of the streak while $F(y)$ is an ad hoc function similar to that used in Schoppa and Hussain, 1997 and Kawahara et al., 1998 and defined by

$$F(y) \equiv C_y \, y \exp[-\rho(y - y^*)^2], \tag{4}$$

where ρ defines the distance over which $F(y)$ vanishes, y^* determines the distance y_M at which $F(y)$ is maximum, and C_y normalises this

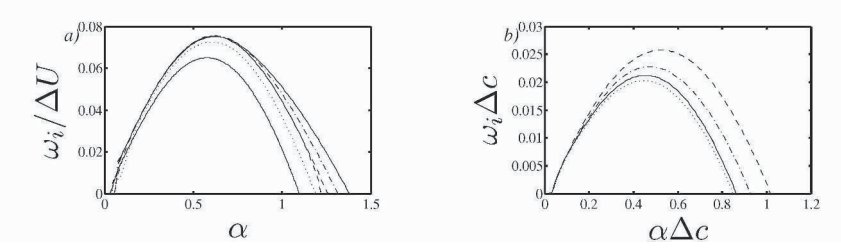

Figure 1. *a*) Temporal growth rates $\omega_i/\Delta U$ versus streamwise wavenumber k_x and for increasing values of the wake depth $\Delta U = 0.45, 0.7, 0.95, 1.15, 1.35$. *b*) Temporal growth rates $\omega_i \, \Delta c$ versus streamwise wavenumber $k_x \, \Delta c$ for streaks with $\Delta c = 1$ (dotted line), $\Delta c = 0.8$ (solid line), $\Delta c = 0.6$ (dashed-dotted line), $\Delta c = 0.4$ (dashed line). The variables are made non dimensional with respect to the free-stream velocity U_∞ and the local boundary layer displacement thickness δ^*

maximum value to unity. The wake profile $W(z)$ is similar to the one used by Monkewitz, 1988 to study two-dimensional wake profiles

$$W(z) \equiv \frac{1}{1+\sinh^{2N}[z/\Delta c\,\sinh^{-1}(1)]}, \tag{5}$$

where $2\,\Delta c$ defines the width of the wake by the spanwise distance between the two inflectional points on the side of the wake and N (equal to 1 in the present case) determines the steepness of the profile.

This basic flow can be shown to reproduce satisfactorily well the spatio-temporal instability of the saturated optimal streak computed in Brandt et al., 2003. Results obtained using the model are displayed in figure 1. In 1*a*) the temporal growth rates for a set basic flows obtained by increasing the wake depth ΔU while keeping all the other parameters constant are presented. The basic flows considered in 1*b*), instead, differ only in the spanwise scale Δc. It can be seen that in both cases the growth rates of the sinuous modes scales more than linearly with the streak spanwise shear, proportional in our model to both ΔU and Δc. Further, the cut-off wavenumber is increasing when Δc decreases since shorter length scales are now introduced in the problem. Analysis of the group velocities of the unstable wave-packet reveals that the most amplified waves travel at the same velocity attained by the underlying streak at the location of maximum spanwise shear. The spreading rate of the wave packet is proportional to the wake depth ΔU, whereas it is unaffected by Δc. The effect of the spanwise extension of the computational domain enclosing the streak is also investigated. It is found that imposing periodic boundary conditions at different distances from the low-speed streak has a small effect on the instability characteristics.

4. VARICOSE INSTABILITY

The symmetric/varicose instability is studied by reproducing numerically the experimental set-up in Asai et al., 2002. The latter authors generated a region of defect velocity by using a small piece of screen set normal to the wall. In agreement with the experimental results it is found that both types of instability are present. The varicose modes are characterised by higher frequencies and are the most amplified, while the sinuous instability is active in a longer streamwise region. The growth rate of the varicose modes is found to increase with the screen width.

By analysing the kinetic energy balance it is found that the varicose instability is driven by the work of the Reynolds stress $\tilde{\tau}_{uv}$ against the wall-normal shear $\partial U/\partial y$. The cross-stream distribution of the term appearing in eqn. (1) is displayed in figure 2 for the streak profile induced 50 mm downstream of the wider screen.

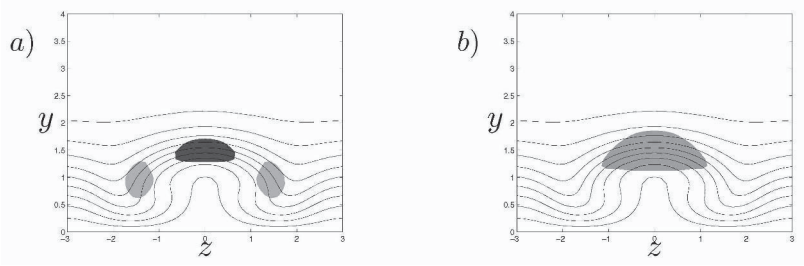

Figure 2. Density of perturbation kinetic energy production for the streak extracted 50 mm downstream of the wider screen. The shaded areas represent the region of the cross-stream plane where the terms exceed 30% of their maxima. *a*) $\tilde{T}_y$: dark grey, $\tilde{T}_z$: light gray. *b*) Viscous dissipation. Varicose mode with $\alpha = 1$. $\omega_i = 0.0696$, $\tilde{T}_y/2\tilde{E} = 0.0970$, $\tilde{T}_z/2\tilde{E} = 0.0070$, $\tilde{D}/2\tilde{E} = 0.0345$

Unexpected results are obtained in the case of the sinuous instability: the wall-normal shear is responsible also for this type of instability modes, despite $\tilde{\tau}_{uv}$ and $\partial U/\partial y$ now having opposite spanwise symmetry (see figure 3). Following the streak evolution further downstream, where the wall-normal shear has decreased more than its spanwise counterpart, it is still observed that the term $\tilde{T}_y$ is larger than $\tilde{T}_z$, even if of comparable amplitude. The production associated to the spanwise shear is seen to be the strongest term for a sinuous instability for the streak induced by the narrower screen and 120 mm downstream of it.

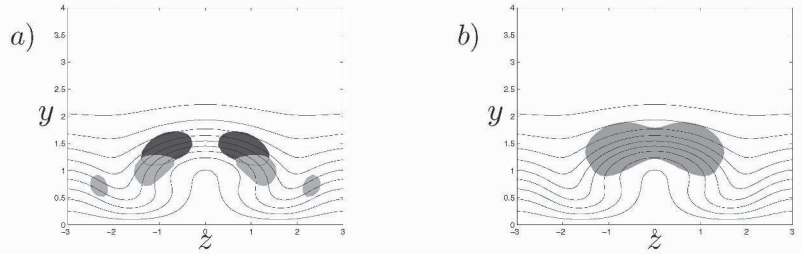

Figure 3. Same as figure 2 for the sinuous mode with $\alpha = 0.4$. $\omega_i = 0.0385$, $\tilde{T}_y/2\tilde{E} = 0.0543$, $\tilde{T}_z/2\tilde{E} = 0.0021$, $\tilde{D}/2\tilde{E} = 0.0171$

5. CONCLUSIONS

The occurrence of the streak instability has been recently related to the breakdown into turbulent spots observed in boundary layers subject to high levels of free-stream turbulence (see invited lecture by D. Henningson and Brandt et al., 2004). Here we have investigated the in-

stability of boundary layers in the presence of steaks assumed steady and spanwise periodic. Two type of streaks are considered: those induced by optimally growing streamwise vortices and the streak induced by placing an obstacle normal to the plate (Asai et al., 2002). The former type is mostly unstable to sinuous modes, whereas in the latter case the varicose is the dominant instability.

It is found that when the basic flow is characterised by strong spanwise shear the sinuous instability is dominant. Conversely, when strong wall-normal shear is induced, as in the case of an obstacle normal to the flow, the varicose mode is the strongest. However, in the latter case, unstable sinuous modes are found which are driven by the wall-normal shear of the streak. Therefore, there is no obvious relation between the sinuous/varicose instability and the streak spanwise/wall-normal shear.

REFERENCES

Andersson, P., Brandt, L., Bottaro, A., and Henningson, D. S. (2001). On the breakdown of boundary layers streaks. *J. Fluid Mech.*, 428:29–60.

Asai, M., Minagawa, M., and Nishioka, M. (2002). The instability and breakdown of a near-wall low-speed streak. *J. Fluid Mech.*, 455:289–314.

Brandt, L., Cossu, C., Chomaz, J.-M., Huerre, P., and Henningson, D. S. (2003). On the convectively unstable nature of optimal streaks in boundary layers. *J. Fluid Mech.*, 485:221–242.

Brandt, L. and Henningson, D. S. (2002). Transition of streamwise streaks in zero-pressure-gradient boundary layers. *J. Fluid Mech.*, 472:229–262.

Brandt, L., Schlatter, P., and Henningson, D. S. (2004). Transition in boundary layers subject to free-stream turbulence. *J. Fluid Mech.*, 517:167–198.

Cossu, C. and Brandt, L. (2002). Stabilization of Tollmien-Schlichting waves by finite amplitude optimal streaks in the Blasius boundary layer. *Phys. Fluids*, 14:L57–L60.

Delbende, I., Chomaz, J.-M., and Huerre, P. (1998). Absolute and convective instabilities in the Batchelor vortex: a numerical study of the linear impulse response. *Journal of Fluid Mech.*, 355:229–254.

Fransson, J. H. M., Brandt, L., Talamelli, A., and Cossu, C. (2004). Experimental study of the stabilization of Tollmien–Schlichting waves by finite amplitude streaks. *Proceeding IUTAM Symposium, Bangalore.*

Kawahara, G., Jiménez, J., Uhlmann, M., and Pinelli, A. (1998). The instability of streaks in near-wall turbulence. Technical report, NASA-Stanford University Center for Turbulence Research, Annual Research Briefs, pp. 155-170.

Monkewitz, P. (1988). The absolute and convective nature of instability in two-dimensional wakes at low Reynolds numbers. *Phys. Fluids*, 31(5):999–1006.

Schmid, P. J. and Henningson, D. S. (2001). *Stability and Transition in Shear Flows.* Springer, New York.

Schoppa, W. and Hussain, F. (1997). Genesis and dynamics of coherent structures in near-wall turbulence: a new look. In Panton, R. L., editor, *Self-Sustaining Mechanisms of Wall Turbulence*, chapter 7, pages 385–422. Computational Mechanics Publications, Southampton.

A POSSIBLE LINEAR INSTABILITY MECHANISM IN SMALL-SCALE PIPE FLOWS

Kirti Chandra Sahu
Engineering Mechanics Unit
Jawaharlal Nehru Centre for Advanced Scientific Research Bangalore, 560 064, INDIA.
kirti@jncasr.ac.in

Abstract: The laminar flow through a pipe of constant *average* radius is shown to display linear instability at low Reynolds number. This is offered as a possible mechanism that could be operating in small-scale flows. The effect of changing geometry, which could be a significant factor, is studied. A multigrid algorithm is used for computing the meanflow and a full non-parallel stability analysis is conducted.

Keywords: pipe, small-scale, stability.

1. INTRODUCTION

It is well known that the fully-developed flow in a circular pipe is linearly stable for any Reynolds number. The transition to turbulence is therefore driven by nonlinear mechanisms. The route observed often [see e.g. Schmid and Henningson, 2001] is transient growth of a combination of linear (stable) nonorthogonal eigenmodes, leading to streamwise vortices, and secondary instabilities of the resulting azimuthally-modulated flow. It has also been demonstrated both theoretically and experimentally that nonlinearities appearing in the form of travelling waves provide a self-sustaining mechanism for transition to turbulence [Waleffe, 2001; Waleffe, 1998; Faisst and Eckhardt, 2003; Faisst and Eckhardt, 2004; Hof et al., 2004]. We study here the effect of changing geometry, which could be a significant factor, especially in small-scale flows, and show that a linear mechanism of instability is operational even at surprisingly low Reynolds numbers.

In the literature, much work has been done on spatially developing boundary layers [e.g. Gaster, 1974, Bertolotti et al., 1992, Govindarajan and Narasimha, 1995], but to our knowledge, no work has been done on the nonparallel stability of flow through spatially developing pipes. In the present work, we consider a variety of diverging-converging pipes whose average radius is constant. The

R. Govindarajan (ed.), Sixth IUTAM Symposium on Laminar-Turbulent Transition, 127–132.

pipes have serrated walls as shown in figure (1). The main results are that (i) linear instability occurs at surprisingly low Reynolds number and (ii) the instability behaviour can be changed dramatically by reversing the direction of flow. The following two sections describe the basic flow computations and the stability analysis respectively and results are discussed in the last section.

2. THE MEAN FLOW

For the mean flow calculation alone, the centerline velocity U_i and the radius R_i of the pipe, at the smallest cross-section, are used as velocity and length scales respectively. The axisymmetric Navier-Stokes equations for steady, incompressible Newtonian flow in the streamfunction vorticity formulation, in non-dimensional form, are given by

$$\frac{\partial \Omega}{\partial t} + (\vec{U}.\nabla)\Omega = \frac{1}{Re_i}\nabla^2\Omega, \tag{1}$$

$$\Omega = -\nabla^2\Psi, \tag{2}$$

where $Re_i \equiv U_i R_i/\nu$, $\Omega(x,r)$ is the azimuthal vorticity, $\vec{U}$ is the velocity vector, ν is the kinematic viscosity, ψ is the streamfunction, and t is time. To accelerate the rate of convergence of the Possion solver, a full-multigrid algorithm has been used. The vorticity is obtained by time-marching, details are available in Sahu, 2003. A transformation of coordinates, given by

$$\zeta = x, \quad \eta = \frac{r}{f(x)},$$

where $f(x)$ is a function describing the boundary, is adopted. The boundary conditions at the centerline are $\Psi = \Omega = V = \partial U/\partial r = 0$. No-slip and impermeable boundary conditions are imposed at the wall. The functional forms of the streamfunction at the centerline, and the vorticity at the wall, are described by employing fictitious points outside the domain. Because of the periodicity in the boundary, a periodic boundary condition is implemented in the streamwise direction. Sample streamwise and radial velocity profiles are shown in the figures (2a) and (2b) respectively, for the geometry shown in figure (1b). The length of the domain considered for the computation is 53.8.

3. NON-PARALLEL STABILITY ANALYSIS

We now use the local radius $R(x)$ and the local centerline velocity $U_c(x)$ at a given x as scales. Each flow quantity is expressed as the sum of a steady mean and a time-dependent perturbation, such as

$$u = U(x,r) + \hat{u}(x,r,\theta,t). \tag{3}$$

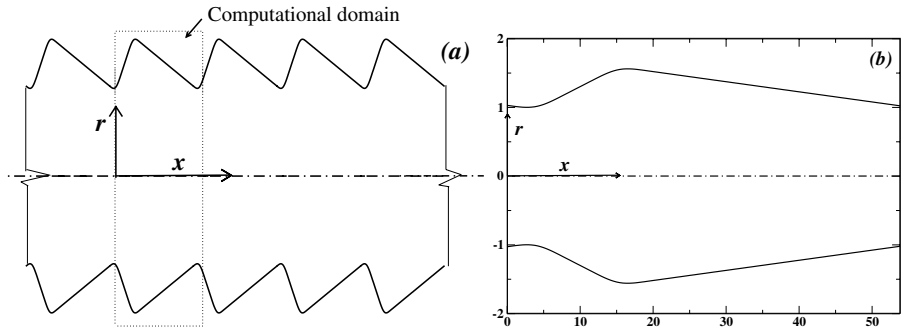

Figure 1. (a) Schematic diagram of the geometry. (b) The computational domain

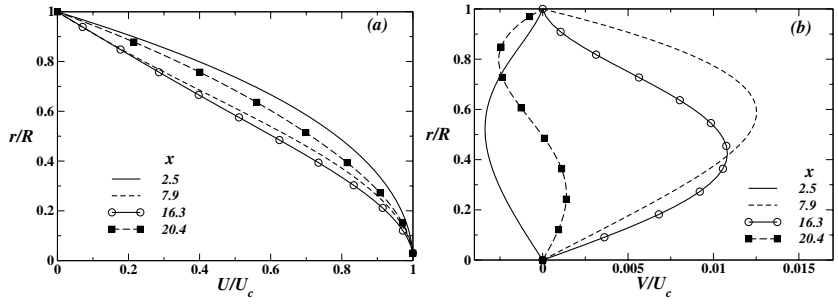

Figure 2. Velocity profiles for the flow from left to right in the pipe shown in figure (1b), $Re_i = 50$. (a) Streamwise, and (b) radial velocity profiles at different streamwise locations

Since the flow under consideration varies significantly in the axial direction, a normal mode form may be used only in time and in the azimuthal coordinate θ. In the axial coordinate, the perturbation may be expressed as a rapidly varying wave-like part [of local axial wavenumber $\alpha(x)$] scaled by a relatively slowly varying function [see e.g. Bertolotti et al., 1992; Govindarajan and Narasimha, 1995], such as

$$[\hat{u}, \hat{v}, \hat{w}, \hat{p}] = \mathrm{Real}\left\{[u, v, w, p] \exp\left[\mathrm{i}\left(\int \alpha(x)\mathrm{d}x + n\theta - \beta_d t_d\right)\right]\right\}, \quad (4)$$

where $u(x,r)$, $v(x,r)$ and $w(x,r)$ are the amplitudes of the velocity perturbations in the axial, radial and the azimuthal directions respectively, $p(x,r)$ is the amplitude of the pressure perturbation, n is the number of waves in the azimuthal direction, and $\beta(= \beta_d R/U_c)$ is the disturbance frequency. It is to be noted that the apportionment in (4) between the x-dependences of α and the eigenfunction is arbitrary, and there are many ways of performing it. However, as long as the rapid (wavelike) change is included in α_r, there is no difference

in the prediction of the growth of any physical quantity [Bertolotti et al., 1992]. We have checked that this is the case for the present flow as well.

The equations are linearised in the standard manner, and terms of higher order $[O(a^2), O(Re^{-2}), O(Re^{-1}a)]$ are neglected, where a is the local slope of the pipe. The result is a set of partial differential equations for the perturbation velocities and pressure, each of first order in x and up to second order in r, which amounts to a seventh order system in r. These may be expressed in the form

$$\mathcal{H}\phi(x,r) + \mathcal{G}\frac{\partial\phi(x,r)}{\partial x} = \beta\mathcal{B}\phi(x,r). \tag{5}$$

Here $\phi = [u, v, w, p]$, and the nonzero elements of the 4×4 matrix operators $\mathcal{H}$, $\mathcal{G}$ and $\mathcal{B}$ are given by [Sahu & Govindarajan (preprint, 2004)]

$$h_{11} = U\Big[2\frac{U_c'}{U_c} + \mathrm{i}\alpha - ar\frac{\partial}{\partial r}\Big] + \frac{\partial U}{\partial x} - ar\frac{\partial U}{\partial r} + V\frac{\partial}{\partial r} + \frac{1}{Re}\Big[\alpha^2 + \frac{n^2}{r^2} - \frac{1}{r}\frac{\partial}{\partial r} - \frac{\partial^2}{\partial r^2}\Big],$$

$$h_{22} = V\frac{\partial}{\partial r} + \frac{\partial V}{\partial r} + U\Big[\frac{U_c'}{U_c} + \mathrm{i}\alpha - ar\frac{\partial}{\partial r}\Big] - \frac{1}{Re}\Big[\frac{\partial^2}{\partial r^2} + \frac{1}{r}\frac{\partial}{\partial r} - \frac{(1+n^2)}{r^2} - \alpha^2\Big],$$

$$h_{33} = V\frac{\partial}{\partial r} - \frac{V}{r} + U\Big[\frac{U_c'}{U_c} + \mathrm{i}\alpha - ar\frac{\partial}{\partial r}\Big] - \frac{1}{Re}\Big[\frac{\partial^2}{\partial r^2} + \frac{1}{r}\frac{\partial}{\partial r} - \frac{(1+n^2)}{r^2} - \alpha^2\Big],$$

$$h_{12} = \frac{\partial U}{\partial r},\quad h_{14} = \Big(2\frac{U_c'}{U_c} + \mathrm{i}\alpha - ar\frac{\partial}{\partial r}\Big),\quad h_{23} = \frac{2}{Re}\frac{\mathrm{i}n}{r^2},$$

$$h_{24} = \frac{\partial}{\partial r},\quad h_{32} = -\frac{2}{Re}\frac{\mathrm{i}n}{r^2},\quad h_{34} = \frac{in}{r},\quad h_{41} = \frac{\mathrm{i}\alpha}{Re}\frac{\partial}{\partial r},$$

$$h_{42} = V\frac{\partial}{\partial r} + \frac{\partial V}{\partial r} + U\Big(\frac{U_c'}{U_c} + \mathrm{i}\alpha - ar\frac{\partial}{\partial r}\Big) + \frac{1}{Re}\Big(\frac{n^2}{r^2} + \alpha^2\Big),$$

$$h_{43} = \frac{\mathrm{i}n}{Re}\Big(\frac{1}{r^2} + \frac{1}{r}\frac{\partial}{\partial r}\Big),\quad h_{44} = \frac{\partial}{\partial r},\quad g_{11} = g_{22} = g_{33} = g_{42} = U,$$

$$g_{14} = 1,\ \text{ and }\ b_{11} = b_{22} = b_{33} = b_{42} = \mathrm{i}.\quad \text{Here}\quad U_c' = \mathrm{d}U_c/\mathrm{d}x.$$

In equation (5), we confirm that if we set a, U_c' and $\partial\phi/\partial x$ to zero, we get the parallel stability equations of Gill, 1973 and Lessen et al., 1968. The boundary conditions emerge from requiring that all quantities vary continuously with r at the centerline [Batchelor and Gill, 1962], and obey no-slip at the wall:

$$u = v = w = p = 0, \qquad \text{at } r = 0, \text{ for } n \neq 1, \tag{6}$$

$$u = p = 0, \quad v + \mathrm{i}w = 0, \qquad \text{at } r = 0, \text{ for } n = 1, \tag{7}$$

$$u = v = w = 0, \qquad \text{at } r = 1. \tag{8}$$

For $n = 1$, we generate an extra boundary condition by differentiating the continuity equation with respect to r. Equation (5) is solved as an eigenvalue

problem of larger size as described in detail in Sahu & Govindarajan [preprint, 2004].

We consider downstream growth of disturbances followed at a constant value of the non-dimensional radius r. The amplitude of a given disturbance at a particular streamwise location is given by

$$\frac{A}{A_{cr}} = \exp\left[\int_{x_{cr}}^{x} g(x)\mathrm{d}x\right] \tag{9}$$

where g is the growth rate of a disturbance, as defined below, and the subscript cr stands for the critical (neutral) location, at which $g = 0$. The growth rate of the nondimensional disturbance kinetic energy, $\hat{E}$, for example, is given by

$$g = \frac{1}{\hat{E}}\frac{\partial \hat{E}}{\partial x} = -2\alpha_i + \frac{1}{E}\frac{\partial E}{\partial x}\Big|_r, \quad \text{where} \quad E = \frac{1}{2}\left(uu^* + vv^* + ww^*\right), \tag{10}$$

the star denotes a complex conjugate. We see that a disturbance may amplify at one r and decay at another. Secondly, one disturbance quantity could be amplifying while others decay.

4. RESULTS AND DISCUSSION

In the present case as in straight pipes, we find that the swirl $(n = 1)$ mode is always the most unstable. A typical amplitude of the disturbance kinetic

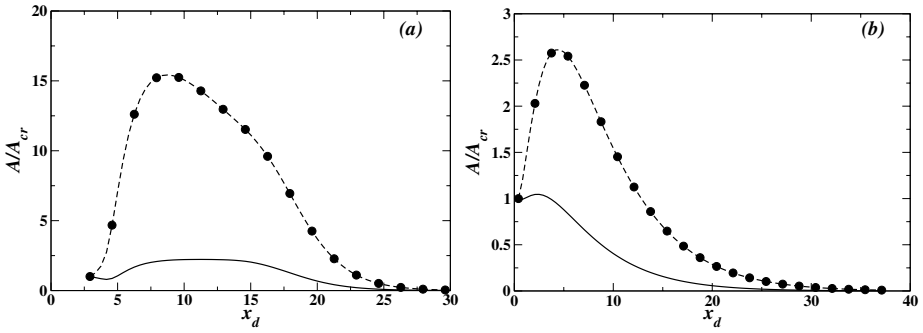

Figure 3. Amplification of disturbance kinetic energy for $Re = 50$, $n = 1$ (solid line: average across the pipe, dashed line: at a particular radial location) (a) Flow from left to right (case I) for $\beta_d = 0.287$ and $r = 0.58$. (b) Flow from right to left (case II) in figure (1b) for $\beta_d = 0.262$ and $r = 0.50$. The dimensional frequency in each case is maintained constant downstream

energy of the $(n = 1)$ mode is shown in figure 3. When the flow is from left to right (case I), the maximum growth occurs at $r = 0.58$, but when the flow is from right to left (case II), $r = 0.50$ is the location for highest growth. It

is found (not shown here) that there is no amplification near the centerline or in the wall region. The disturbance kinetic energy integrated across the pipe is decaying in case II and amplifying in case I (figure 3). It is seen that the flow is much more unstable when the flow is from left to right. For the small divergence and shown here the flow is already linearly unstable at $Re = 50$. For a larger divergence the instability Reynolds number is much lower. The linear mechanism may thus be important in small scale flows (e.g. with pipe diameters in mm and velocities in cm/s.)

ACKNOWLEDGEMENTS

Author acknowledges Prof. Rama Govindarajan, Jawaharlal Nehru Centre for Advanced Scientific Research, India with deep gratitude for her involvement in the present work. The author also thanks the Defence Research and Development Organisation, India for financial support.

REFERENCES

Batchelor, G. K. and Gill, A. E. (1962). Analysis of the stability of axisymmetric jets. *J. Fluid Mech.*, 14:529–551.

Bertolotti, F. P., Herbert, T., and Spalart, P. R. (1992). Linear and nonlinear stability of the Blasius boundary layer. *J. Fluid Mech.*, 242:441–474.

Faisst, H. and Eckhardt, B. (2003). Travelling waves in pipes. *Phys. Rev. Lett.*, 91(22):224502.

Faisst, H. and Eckhardt, B. (2004). Sensitive dependence on initial conditions in transition to turbulence in pipe flow. *J. Fluid Mech.*, 504:343–352.

Gaster, M. (1974). On the effects of boundary layer growth on flow stability. *J. Fluid Mech.*, 221:311–347.

Gill, A. E. (1973). The least-damped disturbance to Poiseuille flow in a circular pipe. *J. Fluid Mech.*, 61:97–107.

Govindarajan, R. and Narasimha, R. (1995). Stability of spatially developng boundary layers in pressure gradients. *J. Fluid Mech.*, 300:117–147.

Hof, B., van Doorne, C. W. H., Westerweel, J., Nieuwstadt, F. T. M., Faisst, H., Eckhardt, B., Wedin, H., Kerswell, R. R., and Waleffe, F. (2004). Experimental observation of nonlinear traveling waves in turbulent pipe flow. *Science*, 305:1594.

Lessen, M., Sadler, S. G., and Liu, T. Y. (1968). Stability of pipe poiseuille flow. *Phys. Fluids*, 11:1404–1409.

Sahu, K. C. (2003). Numerical computation of spatially developing flows by full-multigrid technique. Master's thesis, Jawaharlal Nehru Centre for Advanced Scientific Research, Bangalore, India.

Schmid, P. J. and Henningson, D. S. (2001). *Stability and Transition in Shear Flows*. Springer-Verlag, New York.

Waleffe, F. (1998). Three-dimensional coherent states in plane shear flows. *Phys. Rev. Lett.*, 81(19):4140–4143.

Waleffe, F. (2001). Exact coherent structures in channel flow. *J. Fluid Mech.*, 435:93–102.

EFFECTS OF STRONG ADVERSE PRESSURE GRADIENTS AND INCIDENT WAKES ON TRANSITION AND CALMING

J.P. GOSTELOW and R.L. THOMAS

University of Leicester

Abstract: At a previous meeting results based on wavelet analysis demonstrated similarities between triggered turbulent spots and the turbulent patches caused by wake interactions on compressor and turbine blading[1]. Hughes and Walker[2] went further and used wavelet conditioning to identify the prevalence of Tollmien-Schlichting instability phenomena in the flow over axial flow compressor blades. In the current investigation transition phenomena occurring in axial flow compressors are simulated on a larger scale to provide further evidence on the similarities between turbomachinery and wind tunnel flows. The applicability of the intermittency-based approaches to the closure of laminar separation bubbles is demonstrated. The spacing between impinging wakes is systematically varied and it is found that the calmed region acts to suppress turbulence, even for closely spaced wakes.

Key words: Transition; calming; wakes; turbomachinery.

1. INTRODUCTION

It is often assumed that turbomachinery flows have a high freestream turbulence level and that transition is not an important consideration for blading. For many important applications this is not correct. Altitude cruise conditions for aircraft engines result in a blade Reynolds number more like 10^5 than 10^6; the same applies to late stages in steam turbines. Investigations of wake interactions, and especially the calmed region effect, have resulted in massive reductions in blade count, hence cost and weight.

Following research demonstrating that flows in rotating machines could be replicated on a wind tunnel flat plate, work was undertaken to elucidate flow features such as natural and by-pass transition, laminar separation, the calmed region and wake interaction effects on a large scale.

The experiments were conducted in a low speed wind tunnel having a working section of 1.00 m x 1.15 m and containing a flat plate 2.4 m long. The Reynolds number based on plate length was maintained at 1.4×10^6 and

R. Govindarajan (ed.), Sixth IUTAM Symposium on Laminar-Turbulent Transition, 133–138.

the freestream turbulence level was less than 0.2%. The top wall was contoured to produce a self-similar adverse pressure gradient sufficiently strong to produce a long, thin laminar separation bubble. The flat plate, under this adverse pressure gradient, was subjected to wakes generated by a rod moving transversely upstream of the leading edge.

In the undisturbed flow the long and thin laminar separation bubble exhibited linear growth of Tollmien-Schlichting waves. The bubble was terminated by a short, but conventional, transition region. In 1957 Narasimha had produced his seminal paper on intermittency[3] and, 40 years later, speculated that intermittency might be of value in predicting laminar separation bubble closure. Intermittency had provided a robust basis for predicting attached flow transition lengths. The method of Solomon *et al.*[4] predicted transition length under varying pressure gradients, based on spot formation rates and spreading angles. New data have extended this prediction capability into the laminar separation region. The intermittency approach can be extended to separated-flow transition and bubble closure, which can be characterized by the universal intermittency distribution.

Wake interaction experiments have involved the systematic variation of spacing between incident upstream wakes. This series of experiments was prompted by the work of Gutmark and Blackwelder[5] who performed similar investigations on triggered turbulent spots.

2. THE RESULTS

The results highlighted the interaction between incoming wakes and the undisturbed boundary layer[6]. Each wake provoked a vigorous turbulent patch, resulting in the instantaneous collapse of the separation bubble. Throughout the investigation the wake interactions closely resembled a spanwise assemblage of turbulent spots or patches. The principal features of classical turbulent spots were evident reinforcing confidence in the use of on turbulent spot data and approaches to modeling based on such information.

The turbulent patch triggered by the wake interaction was followed by a very strong and stable calmed region. The calming effect accompanying the turbulent patch induced by a wake interaction is stronger than that of an isolated turbulent spot and has beneficial effects both in suppressing the harmonic development leading to transition and in stabilizing the velocity profile against laminar separation. Further work on the extent of the calmed region is aimed at optimizing the interval between wake disturbances, corresponding to the spacing between upstream blades.

3. INSTABILITY, WAVELETS AND INTERMITTENCY

At previous meetings results were shown, based on wavelet analysis, that demonstrated similarities between the behaviour of triggered turbulent spots and the turbulent patches caused by wake interactions on compressor and turbine blades. Hughes and Walker[2] subsequently used wavelet conditioning to identify instability phenomena on blading in an operating axial flow compressor. Estimated values of most likely T-S frequency closely matched the measured frequencies indicating that T-S instability was prevalent.

The Narasimha universal intermittency distribution has provided a robust basis for predicting attached flow transition. The intermittency-based method of Solomon *et al.*[4] has predicted transition length reliably under varying pressure gradients. Can this approach be extended to separated flow transition and bubble closure?

Figure 1 shows the time-averaged intermittency distribution for the undisturbed flow over the flat plate in the region of separation bubble closure. The data were recorded at a constant height of 2 mm above the surface and showed good agreement with the universal intermittency distribution. This demonstrated that intermittency-based methods would be suitable for predicting the closure of this bubble.

This finding confirms the earlier findings of Malkiel and Mayle[7] and of Volino and Hultgren[8] who also observed agreement with the universal intermittency distribution in the reattachment region of a laminar separation bubble. It also justifies the extension of intermittency-based procedures to flows having laminar separation bubbles. Good examples of such a practice are given in the work of Sanz and Platzer[9] and Hobson and Weber[10].

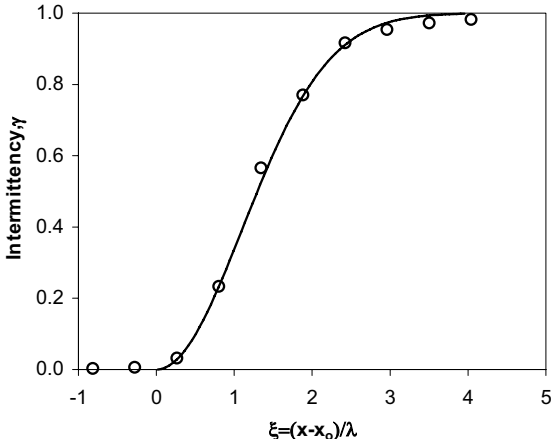

Figure 1. Measurements of intermittency - compared with Narasimha distribution

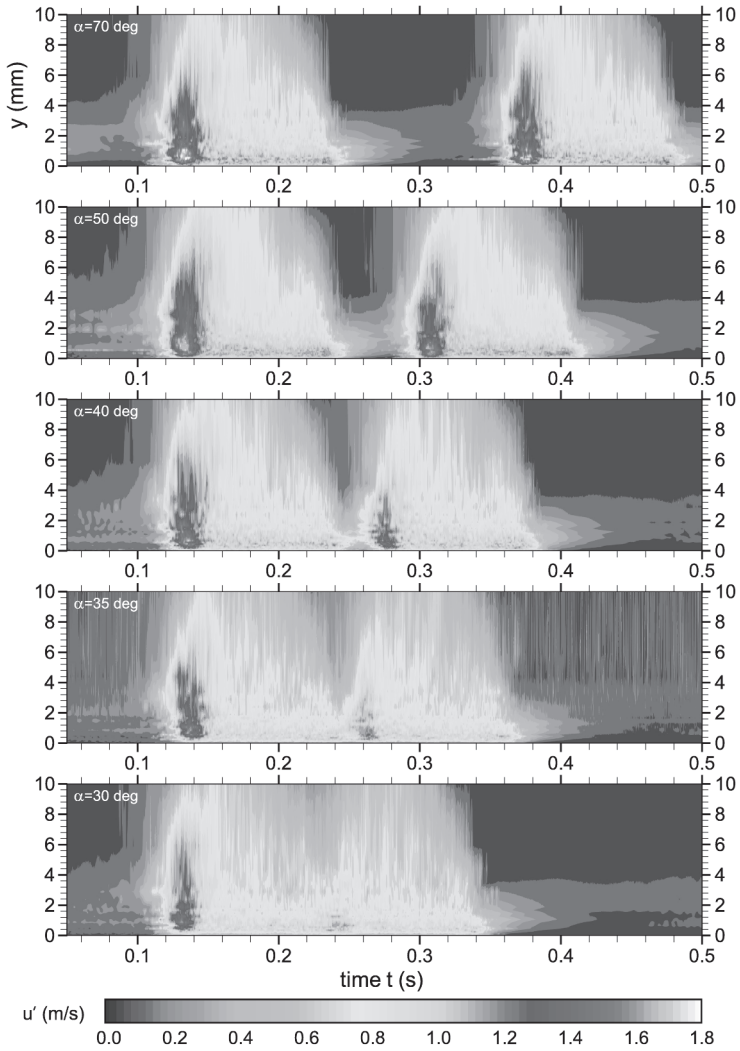

Figure 2. Effect of increasing wake proximity on RMS velocity

4. WAKE PROXIMITY

In the current investigation these transition phenomena were simulated on a large scale to provide further evidence on the similarities turbomachinery and wind tunnel flows. In these tests the relationship between classical transition, wake-induced transition and the calmed region to transition inception and development were investigated.

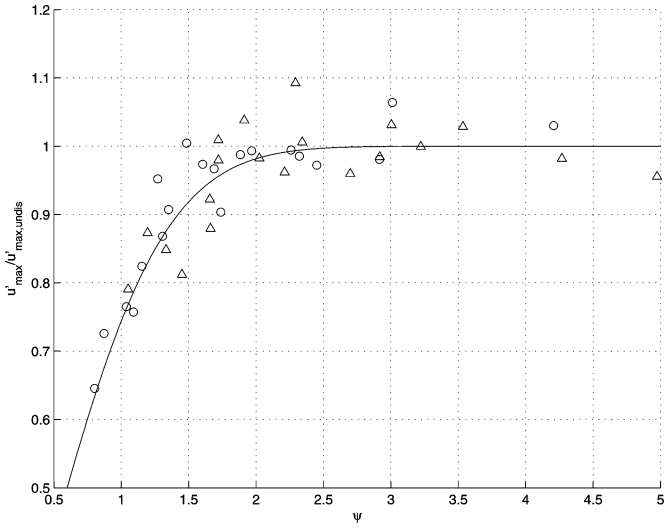

Figure 3. Variation of peak RMS with wake proximity parameter

Gutmark and Blackwelder[5] had performed an interesting experiment in which the time interval between one triggered turbulent spot and a following spot was systematically varied. Close proximity saw the celerity and disturbance level of the following spot diminished. If a wake-induced turbulent patch is really an ensemble of spots does a wake-induced patch exhibit similar behaviour?

No such trends were observed for celerity but Figures 2 and 3 demonstrate that the RMS disturbance level of the following wake-induced turbulent patch was clearly diminished when the two wakes were in close proximity. Figure 2 gives contours of RMS plotted on a $y \sim t$ basis for varying degrees of spacing between wakes. The plot for $\alpha = 30^{o}$ has the wakes closest together and shows a clear diminution of RMS. In Figure 3 the peak value of RMS has been plotted for all the data against a wake proximity parameter ψ, which normalises the wake temporal spacing by the duration of the turbulent patch, and shows that this trend is a consistent one.

5. CONCLUSIONS

Behavioral similarities were found between wind tunnel results on triggered turbulent spots and wake-disturbed flat plate boundary layers under strong adverse pressure gradients, and wake-disturbed boundary layers on axial flow compressor blading.

Wavelet analysis and conditioning supported the findings of natural transition from the axial-flow compressor testing, a viscous instability

predominating. The universal intermittency distribution was found to be valid for the closure of laminar separation bubbles. The results from wakes generated by a rod moving transversely upstream of the plate highlight interaction between incident wakes and an undisturbed boundary layer, featuring a long, thin laminar separation bubble. The wakes resulted in turbulent patches, and a resulting strong calmed region; this stabilised the boundary layer, delayed laminar separation and suppressed disturbances, even within the turbulent region of a following wake-induced patch. The implications for turbomachinery are that the controlled manipulation of wakes inherent in multi-stage design may allow for the continual prevention of separation between the calming wake interactions, and also reduced time-mean surface flow turbulence intensities, thus reducing losses and local heat transfer rates on turbine blade suction surfaces.

REFERENCES

1. J. P. Gostelow, H. P. Hodson, and G. J. Walker, Comparisons between triggered turbulent spots and unsteady transition phenomena on compressor and turbine blading, in "Laminar-Turbulent Transition" eds. H. F. Fasel and W. S. Saric, Proc. IUTAM Symp., Sedona, AZ. pp. 365-370 (1999).
2. J. D. Hughes, and G. J. Walker, Natural transition phenomena on an axial compressor blade, ASME Journal of Turbomachinery, 123, pp. 392-401 (2001).
3. R. Narasimha, On the distribution of intermittency in the transition region of the boundary layer, J. Aero. Sci., Vol. 24, pp. 711-712 (1957).
4. W. J. Solomon, G. J. Walker, and J. P. Gostelow, Transition length prediction for flows with rapidly changing pressure gradients, ASME Journal of Turbomachinery, Vol. 118, pp. 744-751 (1996).
5. E. Gutmark, and R. F. Blackwelder, On the structure of a turbulent spot in a heated laminar boundary layer, Experiments in Fluids, Vol. 5, pp. 27-229 (1987).
6. R. L. Thomas, Closure of a laminar separation bubble by natural and wake-induced transition, PhD thesis, University of Leicester (2004).
7. E. Malkiel, and R. E. Mayle, Transition in a separation bubble, ASME Journal of Turbomachinery, Vol. 118, pp. 752-759 (1996).
8. R. J. Volino, and L. S. Hultgren, Measurements in separated and transitional boundary layers under low-pressure turbine airfoil conditions, ASME Paper 2000-GT-260 (2000).
9. W. Sanz, and M. F. Platzer, On the Navier-Stokes calculation of separation bubbles, ASME Paper 96-GT-487 (1996).
10. G. V. Hobson and S. Weber, Prediction of a laminar separation bubble over a controlled-diffusion compressor blade, ASME Paper 2000-GT-277 (2000).

EFFECT OF FREE-STREAM TURBULENCE ON A COMPRESSIBLE LAMINAR BOUNDARY LAYER

Pierre Ricco & Xuesong Wu
Department of Mathematics, Imperial College, London
180 Queen's Gate - London SW7 2BZ - United Kingdom
pierre.ricco@imperial.ac.uk, x.wu@imperial.ac.uk
http://www.ma.ic.ac.uk/~par, http://www.ma.ic.ac.uk/~xwu

Abstract: We investigate the influence of free-stream turbulent vortical disturbances on a compressible laminar boundary layer by solving the unsteady linear boundary-*region* equations for the velocity and temperature fluctuations. These equations describe the evolution of the perturbations when the boundary layer thickness becomes of the order of the transverse free-stream integral length scale of turbulence. Similar to the incompressible case, low-frequency disturbances penetrate into the boundary layer to form streamwise-elongated streaks, often referred to as "Klebanoff" modes. High-frequency fluctuations are instead absorbed in the outer edge layer. We find that increasing the Mach number and the free-stream turbulent length scale both have a stabilizing effect on the growth of r.m.s. of mass flux fluctuations in the core of the boundary layer.

Keywords: Klebanoff modes, compressible boundary layer, bypass transition.

1. INTRODUCTION

This paper investigates how a compressible laminar boundary layer responds to small free-stream turbulent vortical disturbances. The work can be viewed as the extension of the seminal work by Leib *et al.* (1999) (LWG) to the compressible case. The interest is in the mechanism by which the free-stream vortical motions are entrained into the viscous region and evolve downstream. The growth of these disturbances is likely to be one of the relevant precursors of bypass transition to turbulence, which refers to a laminar flow breaking down to turbulence without experiencing the classical exponential growth as predicted by linear stability theory.

We focus on compressible flows because of the importance of bypass transition for the design of engineering high-speed fluid systems. The most relevant features during transition are undoubtedly the increase of wall-friction drag and heat transfer, and the aerodynamic heating at high Mach numbers, which

R. Govindarajan (ed.), Sixth IUTAM Symposium on Laminar-Turbulent Transition, 139–144.

are both of concern in a wide range of technology applications, encompassing high-speed vehicle aerodynamics, turbomachinery design and the problem of space capsule re-entry into the atmosphere.

The first experiments of laminar boundary layers disturbed by free-stream turbulence were conducted at low velocity (Dryden 1936; Taylor 1939). The low-frequency disturbances significantly amplified during the first stage of evolution. The idea that the boundary layer acts like a filter, allowing low-frequency perturbations to penetrate into the boundary layer and convect downstream, has been the topic of further research (Morkovin 1984; Goldstein *et al.* 1992; Goldstein & Leib 1993), which showed that these fluctuations develop in the form of streak-like structures elongated in the streamwise direction ("Klebanoff" modes - Klebanoff 1971; Kendall 1991). Their behaviour is initially linear, while further downstream nonlinearity generates smaller scales of motion which then form turbulent spots and eventually the turbulent boundary layer. The conventional TS instability mechanism does not seem to play a relevant role so that the exponential growth of disturbances triggered by receptivity is bypassed.

The compressible version of these phenomena is however largely unexplored. Dryden (1955) briefly reviewed the data at that time, but no account was provided on the effects of the different kinds of external perturbations. Further experimental studies have followed (Laufer & Vrebalovich 1960; Kendall 1975; Lebiga *et al.* 1979; Demetriades 1989), in which the free-stream flow was always disturbed by high-intesity fluctuations of acoustic nature. A more recent study was carried out by Graziosi & Brown (2002) (GB), who reported mass flow fluctuation measurements in a supersonic boundary layer. The properties of the acoustic free-stream disturbances were analyzed in detail and the focus was directed at the linear growth of disturbances and on the initial departure of the mean profile from the similarity solution. A tentative theoretical approach was put forward by Mack (1975), who studied the boundary layer forcing by free-stream Mach waves of pressure fluctuations. The noise from the wind tunnel walls seemed unavoidable in the above experiments, which often resulted in the transition Reynolds number measured in flight conditions being higher than in ground experiments (Schneider 2001). All these findings are thus not comparable with the present ones since they pertain to boundary layers perturbed by acoustic disturbances, whilst ours are limited to freestream forcing by gust-like perturbations. Our analysis is however likely to more closely resemble a flight situation, where vortical disturbances are always present and the noise level may be low.

We first present the influence of Mach number on the evolution of boundary layer fluctuations produced by a single Fourier component in the free-stream. We then investigate the effect of Mach number and of the transverse integral

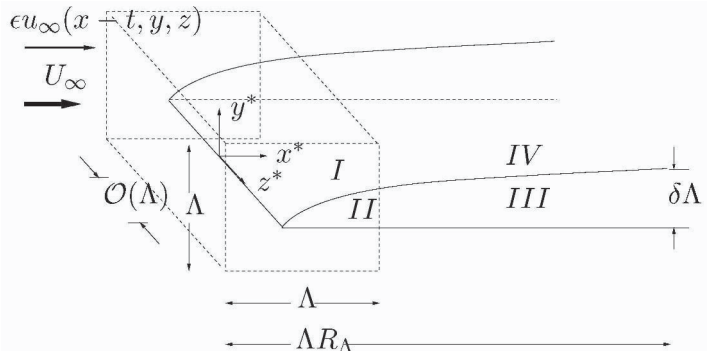

Figure 1. Sketch of the problem of the asymptotic regions

turbulent length scale on the full-spectrum mass flux fluctuations, calculated by rapid distortion theory.

2. PROBLEM FORMULATION: SCALING AND EQUATIONS OF MOTION

We study the flow of air of uniform velocity U_∞ and temperature T_∞ past an infinitely thin flat plate. Vortical fluctuations of the convecting gust type are superposed. The Mach number $M \equiv U_\infty/c_\infty$ is taken to be $\mathcal{O}(1)$, where c_∞ is the free-stream speed of sound. The Cartesian coordinate system is represented by $\mathbf{x} = x\hat{\mathbf{i}} + y\hat{\mathbf{j}} + z\hat{\mathbf{k}} = x_1\hat{\mathbf{i}} + x_2\hat{\mathbf{j}} + x_3\hat{\mathbf{k}}$. The lengths are non-dimensionalized by the free-stream transverse integral scale of turbulence Λ. The velocities and the temperature are scaled by their free-stream values, and the pressure and the time by $\rho_\infty U_\infty^2$ and Λ/U_∞, respectively. The intensity of turbulent velocity fluctuations is assumed to be low so that the problem can be treated as a linear perturbation about the laminar solution. The free-stream fluctuations are represented as a superposition of sinusoidal disturbances:

$$\mathbf{u} - \hat{\mathbf{i}} = \epsilon \mathbf{u}_\infty(x - t, y, z) = \epsilon \hat{\mathbf{u}}^\infty e^{i(\mathbf{k}\cdot\mathbf{x} - k_1 t)}, \tag{1}$$

where $\mathbf{k} = \{k_1, k_2, k_3\}$. The linear nature of the problem allows us to calculate the signature of the individual Fourier components within the boundary layer; the overall effect of the continuous free-stream spectrum is accounted for by a proper summation to compute the r.m.s.. We define $R_\Lambda \equiv U_\infty \Lambda/\nu_\infty$ and, like LWG, as $\epsilon \to 0$ while $\epsilon R_\Lambda = \mathcal{O}(1)$, the domain can be divided into four asymptotic regions (I, II, III, IV), shown in figure 1 (see LWG for a detailed description). The results describe the flow when the boundary layer thickness is of the order of the transverse length scale (region III).

The equations of motion for the mean flow $\{U, V, 0, T\}$ are cast into the similarity solution by introducing $\eta \equiv (R_\Lambda/(2x))^{1/2} \int_0^y \rho \, \mathrm{d}\hat{y}$ and $U = F'(\eta)$, where the prime indicates differentiation w. r. t. η. The equations are thus:

$$(CF'')' + FF'' = 0, \;\; \left(\frac{C}{\mathrm{Pr}}T'\right)' + FT' + (\gamma - 1)M^2 CF''^2 = 0, \;\; C = \rho\mu, \;\; (2)$$

with $F(0) = F'(0) = T'(0) = 0, F'(\infty) = 1$. The Prandtl number Pr and the ratio of the specific heats γ are constant (Pr $= 0.7$ and $\gamma = 1.4$), and $\mu = T^\omega$, with $\omega = 0.76$. For a single Fourier component of the disturbance, the solution in the boundary layer can be expressed as:

$$\{u, v, w, \tau, p\} = \left\{U, V, 0, T, -\frac{1}{2}\right\} \; + \;$$

$$+ \; \epsilon \left\{\overline{u}_0(\overline{x}, \eta), \left(\frac{2\overline{x}k_1}{R_\Lambda}\right)^{\frac{1}{2}} \overline{v}_0(\overline{x}, \eta), \overline{w}_0(\overline{x}, \eta), \overline{\tau}_0(\overline{x}, \eta), \overline{p}_0(\overline{x}, \eta)\right\} e^{i(k_3 z - k_1 t)}, \quad (3)$$

where $\overline{x} = k_1 x$. The condition $k_1 << k_2, k_3$ is assumed. Only the three-dimensional components of the perturbation $\{\overline{u}, \overline{v}, \overline{w}, \overline{\tau}, \overline{p}\}$ are retained (LWG). They are governed by the unsteady compressible linear boundary-region equations, which are obtained from the Navier-Stokes equations by discarding the streamwise diffusion and streamwise pressure gradient terms. The formulation for the initial condition and the free-stream boundary condition is analogous to LWG. A composite solution is sought for the initial condition while the displacement effect produced by the thickening of the boundary layer gives the outer boundary conditions.

3. RESULTS AND OUTLOOK

The influence of Mach number on the downstream development of the peak streamwise three-dimensional vortical fluctuations induced by a single free-stream mode is first investigated. Figure 2 shows that compressibility has a different effect depending on the values of $\kappa \equiv k_3/(k_1 R_\Lambda)^{1/2}$ and $\kappa_2 \equiv k_2/(k_1 R_\Lambda)^{1/2}$. When $\kappa = -\kappa_2 \approx 0$, increasing the Mach number produces more intense fluctuations, whereas the opposite occurs when $\kappa = \mathcal{O}(1)$. However, the core of the boundary layer is likely to be dominated by fluctuations of the second kind since high-k_1 fluctuations quickly move towards the edge of the boundary layer, while low-k_1 motions persist at $\eta = \mathcal{O}(1)$ for a longer distance. Furthermore, temperature fluctuations always increase with Mach number for all the values of $\kappa = -\kappa_2$. Figure 3 shows the profiles of velocity $\overline{u}$ and temperature $\overline{\tau}$ at different downstream locations for $M = 3$ and $\kappa = \kappa_2 = 0$. Both the velocity and temperature fluctuations increase substantially and move upwards towards the free-stream.

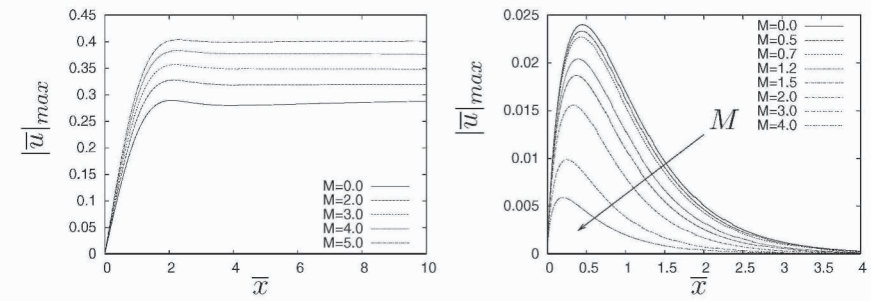

Figure 2. Evolution of peak streamwise three-dimensional velocity perturbation for different Mach numbers; $\kappa = \kappa_2 = 0$ (left) and $\kappa = -\kappa_2 = 1$ (right)

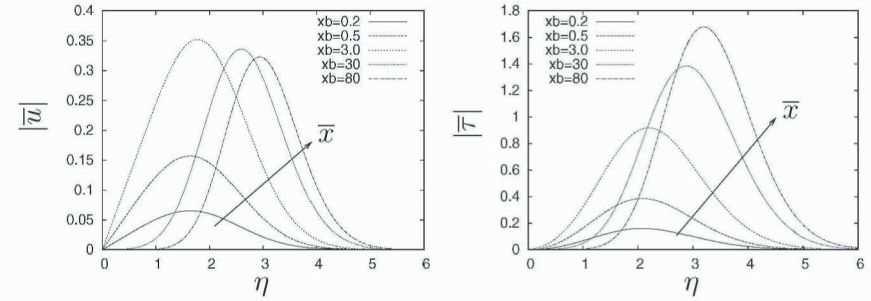

Figure 3. Profiles of three-dimensional component of streamwise velocity and temperature at $M = 3$ at different $\overline{x}$ locations (xb in the graph) - $\kappa = \kappa_2 = 0$

The development of full-spectrum fluctuations in the boundary layer can be computed by adding the contribution from the individual components using the rapid distortion theory of turbulence (LWG, pp. 186–195). We calculate the r.m.s. of mass flux for the frequency range $\{0 - 0.02\}$ (scaled by U_∞ and Λ). This interval gives the main contribution to the broadband r.m.s. signal. We further assume that the free-stream fluctuations are anisotropic and described by the same turbulence spectrum adopted by LWG (p. 191, eq. (7.3)), which characterizes the flow studied by Kendall (1998) . The integral turbulence scale Λ presents a marked influence on the streamwise evolution of the r.m.s. of the mass flux fluctuations: larger Λ values generate less intense fluctuations for the same free-stream turbulence intensity (figure 4). An analogous effect is observed with increasing Mach number. This is expected since the dominant low-frequency vortical motions are attenuated at higher mean flow velocities. Future research topics include the study of free-stream entropy and acoustic modes, for which the theoretical results may be compared with the experimental data by GB. We are further interested in elucidating the effect of nonlinearity and the possible secondary instability of streaks.

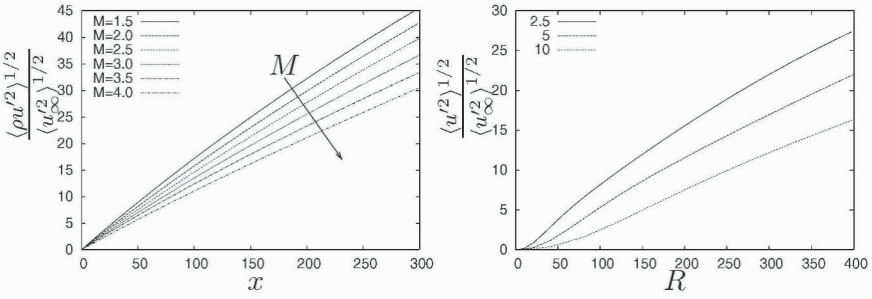

Figure 4. Downstream evolution of r.m.s of mass flux fluctuations at $\eta = 1.64$; Effect of Mach number with $\Lambda = 2.5$ mm (left) - Effect of Λ (mm - L in the graph) at $M = 0$ (right). $R = \sqrt{U_\infty x^* \nu_\infty^{-1}}$

ACKNOWLEDGEMENTS

Pierre Ricco would like to kindly thank the Department of Mathematics, Imperial College, London, the Jawaharlal Nehru Centre for Advanced Scientific Research, Bangalore, India and the Institute of Physics for the financial support.

REFERENCES

Demetriades, A. 1989. Physics of Fluids A, Vol. 1, pp. 312–317.

Dryden, H. L. 1936. NACA Rep. 562.

Dryden, H. L. 1955. In Proc. Conf. on High-Speed Aeronautics, 41, Polytechnic of Brooklyn, NY.

Goldstein, M.E. & Leib, S.J. and Cowley, S.J. 1992. Journ. Fluid Mech., Vol. 237, 231–260.

Goldstein, M.E. and Leib, S.J. 1993. Jour. Fluid Mech., Vol. 246, 21–41.

Graziosi, P. and Brown, G. L. 2002. Jour. Fluid Mech., Vol. 472, 83–124.

Kendall, J.M. 1975. AIAA Journal, Vol. 13, pp. 290–299.

Kendall, J.M. 1991. In Boundary Layer Stability and Transition to Turbulence (ed. D.C. Reda, H.L. Reed & Kobayashi). ASME FED, Vol. 114, 23–30.

Kendall, J.M. 1998. AIAA Paper 98-0530.

Klebanoff, P.S. 1971. Bull. Am. Phys. Soc., Vol. 16.

Laufer, J. and Vrebalovich, T. 1960. Jour. Fluid Mech., Vol. 9, 257–299.

Lebiga, V.A. and Maslov, A.A. and Pridanov, V.G. 1979. Arch. Mech., Vol. 31, pp. 397–405.

Leib, S.J. and Wundrow, D.W. and Goldstein, M.E. 1999. Jour. Fluid Mech., Vol. 380, 169–203.

Mack, L. M. 1975. AIAA Journal, Vol. 3, 278–289.

Morkovin, M.V. 1984. NASA CP-2386 Transition in Turbines, 161-204.

Schneider, S. P. 2001. Journal of Spacecraft and Rockets, Vol. 38-3, 323–333.

Taylor, G.I. 1939. In Proc. Fifth Intl. Congr. for Appl. Mech. (ed. J.P. Den Hartog & Peters), 294–310.

EFFECT OF VISCOSITY STRATIFICATION ON SECONDARY AND NONMODAL INSTABILITIES

A. Sameen
Department of Aerospace Engineering,
Indian Institute of Science,
Bangalore, INDIA[*]
sameen@aero.iisc.ernet.in

Abstract: The effect of viscosity stratification on the different mechanism of transition to turbulence is not well understood. In this paper, a viscosity variation normal to the flow in a channel is investigated. The primary and secondary instability are computed, and the transient growth is analysed. It is found that viscosity stratification can have different effects in each case.

Keywords: Transient growth, secondary instability, viscosity stratification

1. INTRODUCTION

It has been shown by numerous authors that a viscosity stratification brings a large change in the stability characteristics [Wall and Wilson, 1996, Yih, 1967, Govindarajan et al., 2001, Ranganathan and Govindarajan, 2001]. A stratification of viscosity in the direction normal to a laminar shear flow often has a large effect on the instability behaviour. If the viscosity decreases as one approaches the wall, the linear mode of disturbance growth is usually stabilized. Consequently, transition to turbulence is presumed to take place at a significantly higher Reynolds number than in an unstratified flow. The reverse is expected when the viscosity increases towards the wall. The process of transition, however, is markedly different in different shear flows. Our focus here is the flow through a channel, in which the effect of viscosity stratification on the transient growth and secondary instability has not been understood. An unstratified channel flow often reaches turbulence at a Reynolds number ($Re \equiv Uh/\nu$, where U is the centerline velocity, h the half channel width and ν the kinematic viscosity) of about 1500, well below the value

[*]Also: Engineering Mechanics Unit, Jawaharlal Nehru Center for Advanced Scientific Research, Bangalore, INDIA

R. Govindarajan (ed.), Sixth IUTAM Symposium on Laminar-Turbulent Transition, 145–151.

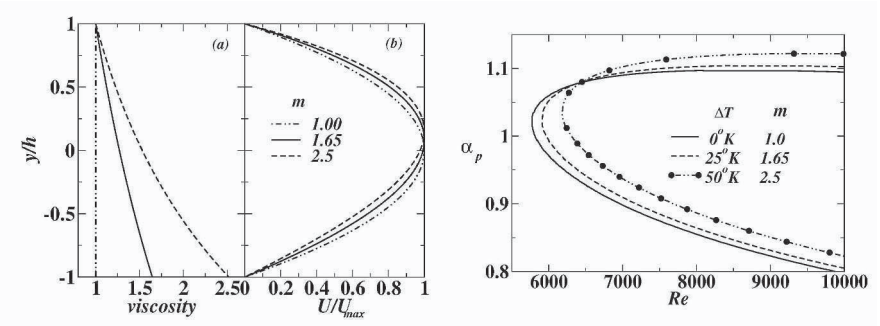

Figure 1. Variation of non-dimensional (a) viscosity and (b) velocity with y. The velocity is scaled by maximum and the viscosity is scaled by its value at the hot wall

Figure 2. The neutral curve for various viscosity ratio. At $T_{cold} = 295^oK$, for the unstratified case, i.e., at $m = 1.0$, Re_{cr} is 5772.2

($Re = 5772$) at which the laminar flow first becomes unstable to linear disturbances. One mechanism which makes this possible is the interaction of different linear modes to give a transient algebraic growth for some finite amount of time. Such an interaction takes place because the eigen-modes of the stability equation are non-orthogonal (i.e., the stability operator is not self-adjoint). For an unstratified flow the transient growth is highest [Schmid and Henningson, 2001, Reddy and Henningson, 1993] when the disturbance waves are invariant in the streamwise direction. In this paper we study the case of asymmetric heating of channel walls. The secondary instability and transient growth analyses are done and it is shown that the viscosity stratification can have different effects on these distinct mechanisms.

2. MEAN PROFILES

The temperature is assumed to vary linearly across the channel. The viscosity dependence on temperature is assumed to be of Arrhenius type: $\mu(T) = C_1 \exp(C_2/T)$. This model works fairly well for most liquids, e.g. water, alcohol. The viscosity is non-dimensionalised with that at the higher temperature wall. The mean flow equation for the viscosity stratified channel flow will then be, $(\nu U')' = dP/dxRe$. The above equation is solved numerically and the velocity and viscosity profiles are presented in figure 1.

3. TRANSIENT GROWTH

The growth of small perturbations introduced into the mean flow is studied. The perturbed quantities in normal mode form are given as

$$\Big[\hat{u}_p, \hat{v}_p, \hat{w}_p\Big] = \Big[u_p(y), v_p(y), w_p(y)\Big] \exp[i(\alpha_p x + \beta_p z - \omega_p t)], \qquad (1)$$

where α_p and β_p are the wave numbers in streamwise and spanwise directions respectively, and ω_p is the complex frequency of the wave. The full stability equations are derived in the traditional way [White, 1991]:

$$\begin{aligned} & i\alpha_p[(v_p'' - (\alpha_p^2 + \beta_p^2))(U - \omega_p/\alpha_p) - U''v_p] \\ & = \frac{1}{Re}[\mu v_p^{iv} + 2\mu' v_p''' + (\mu'' - 2(\alpha_p^2 + \beta_p^2)\mu)v_p'' - 2(\alpha_p^2 + \beta_p^2)\mu' v_p' \\ & +((\alpha_p^2 + \beta_p^2)\mu'' + (\alpha_p^2 + \beta_p^2)^2\mu)v_p], \end{aligned} \tag{2}$$

$$i(\omega_p - \alpha_p U)\eta + i\beta_p U' v_p = \frac{1}{Re}\Big[\mu[\eta'' - (\alpha_p^2 + \beta_p^2)\eta] + \mu'\eta'\Big], \tag{3}$$

with the perturbation vorticity η in the normal direction given by

$$\eta = i\beta_p u_p - i\alpha_p w_p. \tag{4}$$

Equations 2 and 3 form an eigenvalue problem with the boundary conditions

$$v_p(\pm 1) = v_p'(\pm 1) = \eta(\pm 1) = 0. \tag{5}$$

Equations 2 & 3 (with appropriate boundary conditions from equation 5) constitute the modified Orr-Sommerfeld equation and the Squires equation for viscosity-stratified flow. The neutral curves are shown in figure 2. As the viscosity ratio increases the flow stabilises for asymmetric heating. We focus next on the transient algebraic growth of linear perturbations. The methodology is the same as used in Schmid and Henningson, 2001, Reddy and Henningson, 1993 or Meseguer, 2002. If v_{pj} is the j^{th} eigenvector, a linear combination of v_{pj} will produce a perturbation $\hat{v}_p$, such as

$$\hat{v}_p(y,t) = \sum_{j=1}^{N} \kappa_j(0) e^{-i\Lambda t} v_{pj}(y) = \sum_{j=1}^{N} \kappa_j(t) v_{pj}(y), \tag{6}$$

where κ_j is the j^{th} expansion coefficient of eigenfunction, $\kappa = (\kappa_1, \kappa_2, ..., \kappa_N)^T$ and $\Lambda = diag\{\omega_1, \omega_2, ...\omega_N\}$. We may define the energy growth, $g(t)$ [Schmid and Henningson, 2001], for a given initial condition $\kappa(0)$ as,

$$g(t) = \frac{\|\kappa(t)\|_E^2}{\|\kappa(0)\|_E^2} = \frac{\|e^{-i\Lambda t}\kappa(0)\|_E^2}{\|\kappa(0)\|_E^2}. \tag{7}$$

Maximising $g(t)$ in equation (7) for all possible initial conditions $\kappa(0)$, we define

$$G(t) \equiv \max_{\kappa \neq 0} g(t) \tag{8}$$

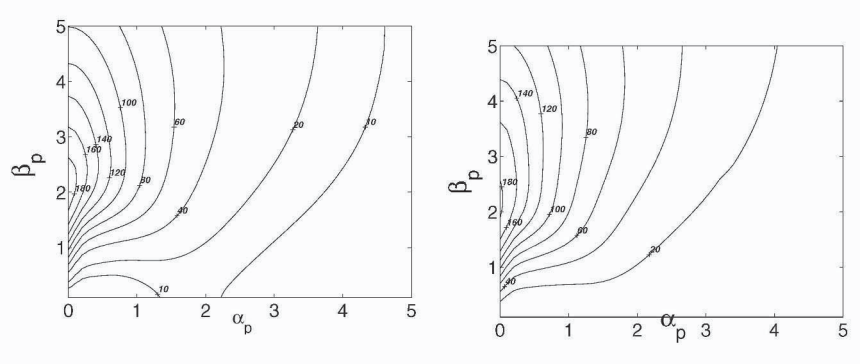

Figure 3. The contour of G_{max} for $Re = 1000$ for asymmetric heating. $\Delta T = 50^o K$

Figure 4. Same as figure 3 but with $\Delta T = 100^o K$

We next define G_{max} as the maximum of $G(t)$ over time, for one particular Re, α_p and m. The main interest here is the effect of m on G_{max}. From figure 3 & 4, we see that transient growth is affected only marginally by asymmetric viscosity stratification. We conclude that viscosity stratification has only minimal effect on transient growth in channel flow.

4. SECONDARY INSTABILITY ANALYSIS

The method here is as in Herbert, 1983 and Bayly et al., 1988. All flow variables are decomposed in the form

$$u = \bar{u} + A_p(\hat{u}_p) + A_s\hat{u}_s, \tag{9}$$

where $\bar{u}$ comes from the basic flow, $\hat{u}_p$ is the solution from linear stability analysis and $\hat{u}_s$ is the secondary instability solution that we seek. The direct interactions between primary instabilities are negligible, which means A_p^2 terms are neglected (also means $A_p^2 << A_pU, A_p\partial u/\partial y$). Assuming $1 >> A_p > A_s$, we get a linear system of partial differential equations.

The secondary and primary waves have a phase difference with a corresponding frequency shift. The phase shift, P_S is defined as $P_S = \omega_p\alpha_+/\alpha_p - \omega_s$. Herbert, 1983 showed that for a subharmonic mode the frequency shift vanishes for high value of β suggesting a *phase lock*.

The secondary perturbation quantities are three dimensional and are assumed to be of a form such as

$$\hat{u}_s = \frac{1}{2}\Big[u_+(y,t)e^{i(\alpha_+ x+\beta z)} + u_-(y,t)e^{i(\alpha_- x-\beta z)} + \text{c.c.}\Big], \tag{10}$$

where α_+ and α_- are the wave numbers of the secondary waves in the streamwise direction, β is the wave number in the spanwise direction.

For the flow under consideration, the growth/ decay rates of the primary mode are so small that dA_p/dt can be neglected during one period of time, the primary flow may be taken to be periodic. The most unstable primary mode (which is two dimensional in accordance with Squire's theorem) alone is considered for the secondary instability analysis. We substitute these in the three momentum equations, eliminating pressure and neglecting non-linear terms in the secondary disturbance. On averaging over x, z and t, all terms become zero except the resonant modes, given by, $\alpha_+ + \alpha_- = \alpha_p$. Using the continuity equation the streamwise component of secondary velocity is eliminated and we get the secondary perturbation equations:

$$\begin{aligned} &-D\frac{\partial v_+}{\partial t} + s\frac{\partial f_+}{\partial t} = -sAf_+ + (AD - i\alpha_+(DU))v_+ \\ &-A_p\Big[\frac{i\alpha_+^2}{2\alpha_-}u_pD + \frac{v_p\alpha_+D^2}{2\alpha_-} + \frac{i(Du_p)\alpha_+}{2}\Big]v_-^* \\ &+\frac{A_p\alpha_+^2}{2}\Big[-v_pD + i\alpha_-u_p + \frac{i\beta^2}{\alpha_-}u_p + \frac{\beta^2}{\alpha_+\alpha_-}v_pD\Big]f_-^*, \end{aligned} \tag{11}$$

$$\begin{aligned} &\frac{\partial v_+}{\partial t} - D\frac{\partial f_+}{\partial t} = -Av_+ + (AD + (DA))f_+ - \frac{A_p(\alpha_p+\alpha_-)}{2}\Big[\frac{v_p}{\alpha_-}D \\ &-iu_p\Big]v_-^* + \frac{A_p}{2}\Big[-i(\alpha_p+\alpha_-)u_pD - i\alpha_-(Du_p) + v_p\Big(\frac{\alpha_+\beta^2}{\alpha_-} + D^2\Big)\Big]f_-^*. \end{aligned} \tag{12}$$

where $A = [i\alpha_+U + \nu s - \nu d^2 - \nu' D]$, $f_+ = -\frac{i}{\beta}w_+$, $D = d/dy$ Equations (11) & (12) and complementary equations for v_-^* and f_-^* are solved using Chebyshev collocation spectral methods, with the boundary conditions $\hat{u}_s, \hat{v}_s, \hat{w}_s = 0$ at $y = \pm 1$. The dispersion relation is $F(A_p, \beta, m, Re, \alpha_p, c,) = 0$ (see Herbert, 1983).

The variation of secondary growth rate with the spanwise wave number for various viscosity ratios is plotted in figures 5. For a non-zero temperature difference, a second mode appears, which does not exist in unstratified flow. This second mode is highly unstable, compared to the usual unstratified mode. Another interesting feature to note is the stabilizing effect of temperature difference for low wave numbers. At the point from where the new mode dominates, the secondary wave has no phase shift from the primary wave, as demonstrated in figure 6. Phase locking is achieved at an earlier β than for the unstratified case.

5. CONCLUSIONS

The primary instability mode was stabilised with increase in temperature difference, while the secondary stability analysis showed a high level of desta-

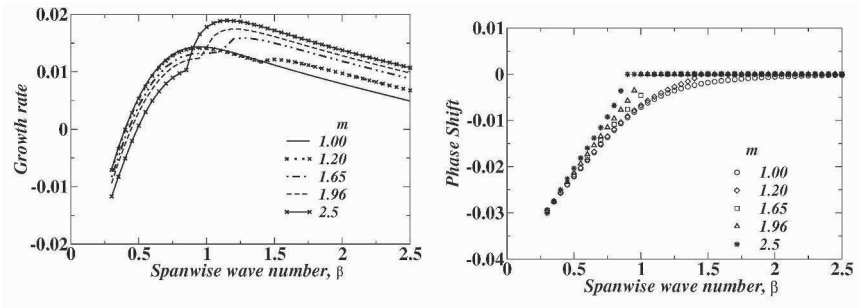

Figure 5. The dependence of growth rate on spanwise wave number of the secondary disturbance for various viscosity ratios, subharmonic case. $\alpha_p = 1.0$, $A_p = 0.01$, $Re = 5000$

Figure 6. The variation of P_S with spanwise wave number for various viscosity ratios, subharmonic case. $\alpha_p = 1.0$, $A_p = 0.01$, $Re = 5000$

bilisation. The transient growth, however, was only marginally affected by viscosity stratification. Since the level of background noise can determine which route to turbulence will be followed, viscosity stratification can have effects completely at variance.

ACKNOWLEDGEMENTS

The discussions with and involvements of Prof. Rama Govindarajan, Jawaharlal Nehru Centre for Advanced Scientific Research, India is deeply acknowledged. The financial support of Defence R & D Organisation, India, is greatly thanked.

REFERENCES

Bayly, B. J., Orszag, S. A., and Herbert, T. (1988). Instability mechanisms in shear-flow transition. *Ann. Rev. Fluid Mech.*, 20:359–391.

Govindarajan, R., L'vov, S. V., and Procaccia, I. (2001). Retardation of the onset of turbulence by minor viscosity contrasts. *Phys. Rev. Lett.*, 87:174501.

Herbert, T. (1983). Secondary instability of plane channel flow to subharmonic three-dimensional disturbances. *Phys. Fluids*, 26(4):871–874.

Meseguer, A. (2002). Energy transient growth in the Taylor-Couette problem. *Phys. Fluids*, 14(5).

Ranganathan, B. T. and Govindarajan, R. (2001). Stabilisation and destabilisation of channel flow by location of viscosity-stratified fluid layer. *Phys. Fluids.*, 13(1):1–3.

Reddy, S. C. and Henningson, D. S. (1993). Energy growth in viscous channel flows. *J. Fluid Mech*, 252:209–238.

Schmid, P. J. and Henningson, D. S. (2001). *Stability and Transition in Shear Flows*. Springer-Verlag, New York.

Wall, D. P. and Wilson, S. K. (1996). The linear stability of channel flow of fluid with temperature-dependent viscosity. *J. Fluid Mech*, 323:107–132.

White, F. W. (1991). *Viscous Fluid Flow*. McGraw-Hill, Inc., 2nd ed. edition.

Yih, C. S. (1967). Instability due to viscosity stratification. *J. Fluid Mech.*, 27:337.

SPECTRAL ELEMENT STABILITY ANALYSIS OF VORTICAL FLOWS

Michael S. Broadhurst[1], Vassilios Theofilis[2] and Spencer J. Sherwin[1]
[1]*Department of Aeronautics, Imperial College London, UK;* [2]*School of Aeronautics, Universidad Politecnica de Madrid, Spain*

Abstract: The scope of the present study is to demonstrate the use of spectral/*hp*-element methods in understanding the global instability mechanisms of vortex dominated flows. Using a BiGlobal stability analysis, analytically constructed and numerically evaluated base flows have been investigated, with the leading eigenvalues obtained by the Arnoldi algorithm. Subsequently, Direct Numerical Simulation (DNS) was used to investigate the non-linear development of an unstable Batchelor vortex. It was found that a spiral-type instability, if allowed to develop in an axially unconstrained manner, leads to an axial loss of energy and the formation of a stagnation point.

Keywords: BiGlobal; stability; vortex breakdown; DNS; PSE

1. INTRODUCTION

Although vortex breakdown has been researched for some time, there remains no accepted explanation of the phenomenon. Following Leibovich, 1978, breakdown is defined as, 'a disturbance characterised by the formation of an internal stagnation point on the vortex axis, followed by reversed flow in a region of limited extent'. The main theories associated with breakdown are those of vortex stability; and the wave-motion theories, primarily attributed to Squire (1960) and Benjamin (1962).

The concept of hydrodynamic stability, and its advancement to global linear instability theory (summarised by Theofilis, 2003), has resulted in considerable investigation into the unstable modes of the Batchelor (1964) vortex model. Initially investigated by Lessen et al. (1974) and more recently by Ash and Khorrami (1995), several spiral-type modes of instability exist. It is not immediately evident, however, how an instability can lead to an abrupt change in flow structure; although the DNS of Abid and Brachet (1998) does relate the non-linear development with a lateral expansion. The aim of the current research is to unify linear stability analysis with three-dimensional DNS to show how a slowly developing spiral instability can lead to an axial stagnation.

R. Govindarajan (ed.), Sixth IUTAM Symposium on Laminar-Turbulent Transition, 153–158.

2. NUMERICAL METHOD

The numerical method applied consists of solving the eigenvalues of a matrix system corresponding to the linearised incompressible Navier-Stokes equations. Following the methods of Barkley and Tuckerman (2000), an exponential power method – coupled with an Arnoldi algorithm – is used to evaluate the leading eigenvalues of the system; which is reduced to a Krylov subspace spanning the number of eigenvalues sought. Validation of the method was achieved by comparing the results for an isolated Batchelor Trailing Vortex (BTV) with the classical one-dimensional stability analysis of Mayer and Powell (1992), which assumes both a streamwise and an azimuthal Fourier decomposition.

Linearised stability analysis is based upon the decomposition of all flow variables into a steady mean component upon which small-amplitude three-dimensional disturbances are permitted to develop (i.e. $\mathbf{q} = \bar{\mathbf{q}} + \mathbf{q}'$). By allowing a mild dependence of the base flow on the streamwise spatial coordinate z, an eigenmode Ansatz is introduced, according to which

$$\mathbf{q}'(x,y,z) = \hat{\mathbf{q}}(x,y,z^*)\exp i\Theta + c.c. \quad (1)$$

$$\Theta = \Theta_{3D} = \int_{z_0}^{z} \beta(\xi)d\xi - \Omega t \quad (2)$$

Applied to the linearised Navier-Stokes equations this leads to the following system of equations that define the Parabolised Stability Equation (PSE) concept (originally developed by Herbert, 1997) for three-dimensional flows

$$\hat{u}_x + \hat{v}_y + i\beta\hat{w} = -\hat{w}_z \quad (3)$$

$$\{\mathcal{L} - \bar{u}_x\}\hat{u} - \bar{u}_y\hat{v} - \hat{p}_x + i\Omega\hat{u} = \bar{w}\hat{u}_z + \bar{u}_z\hat{w} - \frac{2i\beta}{Re}\hat{u}_z \quad (4)$$

$$-\bar{v}_x\hat{u} + \{\mathcal{L} - \bar{v}_y\}\hat{v} - \hat{p}_y + i\Omega\hat{v} = \bar{w}\hat{v}_z + \bar{v}_z\hat{w} - \frac{2i\beta}{Re}\hat{v}_z \quad (5)$$

$$-\bar{w}_x\hat{u} - \bar{w}_y\hat{v} + \mathcal{L}\hat{w} - i\beta\hat{p} + i\Omega\hat{w} = \bar{w}\hat{w}_z + \bar{w}_z\hat{w} - \frac{2i\beta}{Re}\hat{w}_z + \hat{p}_z \quad (6)$$

Where $\mathcal{L} = (1/Re)\{\partial_{xx} + \partial_{yy} - \beta^2\} - \bar{u}\partial_x - \bar{v}\partial_y - i\beta\bar{w}$. Implicit in this derivation is that the disturbance takes the form of a rapidly varying phase function and a slowly varying shape function, for which second derivatives with respect to z (along with products of first derivatives) can be neglected.

3. STABILITY OF A BATCHELOR VORTEX

A single Batchelor vortex (defined by Batchelor, 1964) with a swirl value of $q = 0.8$ and a co-flow parameter of $a = 0$ has been investigated. A typical linearly unstable perturbation mode is illustrated in Figure 1 for a Reynolds

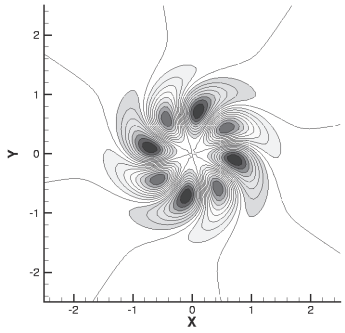

Figure 1. Two-dimensional view of the linear perturbation mode for an isolated Batchelor vortex with $\beta = 2.0$. Visualised using contours of axial velocity

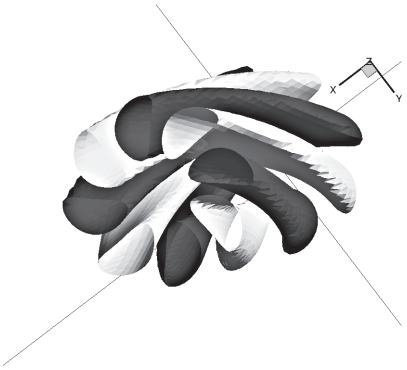

Figure 2. Three-dimensional view of the linear perturbation mode for an isolated Batchelor vortex with $\beta = 2.0$. Visualised using iso-surfaces of axial velocity

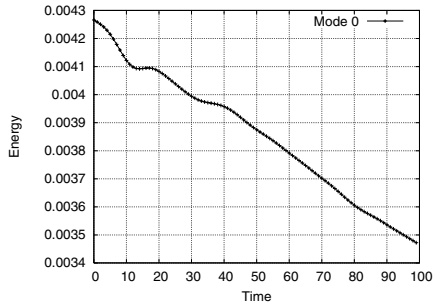

Figure 3. Temporal development of the kinetic energy within the zeroth axial Fourier mode

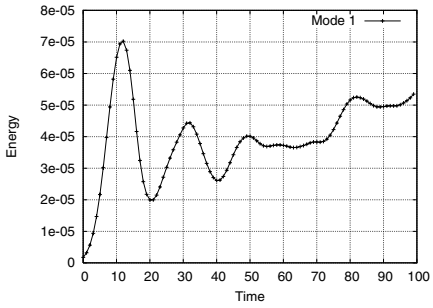

Figure 4. Temporal development of the kinetic energy within the first axial Fourier mode

number based on the vortex core radius of $Re = 667$; the corresponding eigenvalue is $0.296 \pm 1.189i$. This was evaluated using a BiGlobal stability analysis; equivalent to Eqs. (3)–(6) with the RHS terms – which are related with derivatives of the basic flow and the disturbance terms in the z-direction – neglected.

4. NON-LINEAR DEVELOPMENT

The non-linear development of an isolated vortex has been analysed by DNS using $\mathcal{N}\epsilon\kappa\tau\alpha r$ [1], for $Re = 1000$. Initially, a periodic representation was applied in the axial direction, with the non-linear temporal development analysed from initial conditions constituting the isolated BTV with the first mode of instability superimposed as a small perturbation. As illustrated in Figures 3 and

[1] A spectral/*hp*-element solver developed by Sherwin and Karniadakis (1995)

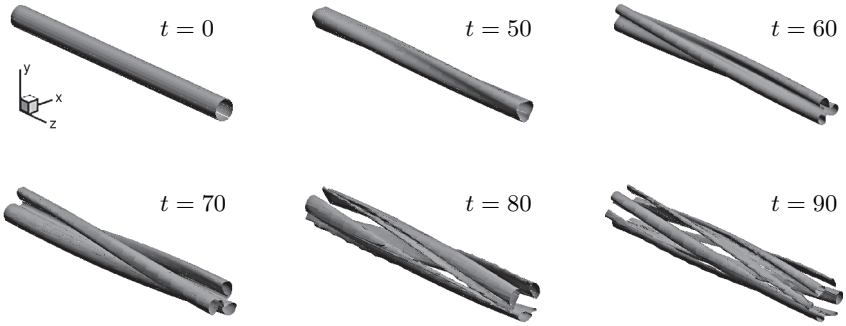

Figure 5. Non-linear development of an isolated Batchelor vortex assuming a periodic representation in the axial z-direction and a Fourier approximation consisting of the first 16 modes. Visualised using iso-surfaces of $\lambda_2 = -0.2$

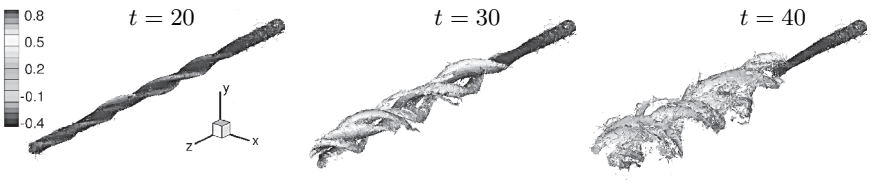

Figure 6. Three-dimensional temporal development of an isolated Batchelor vortex illustrating axial deceleration and formation of a stagnation point. Visualised using iso-surfaces of $\lambda_2 = -0.4$, shaded by axial velocity

4, an energy transfer between the zeroth axial Fourier mode and the linear perturbation mode is identified. This is significant, since it implies that the growth of the linear instability leads to a loss of axial energy in the mean flow, which must be accompanied by a cross-section expansion to satisfy continuity, visualised in Figure 5. Consequently, the associated drop in axial velocity suggests a causal relationship between instability and breakdown.

Enforcing an axial periodicity in the solution restricts how the streamwise w-component of the velocity can change, limiting the extent of axial deceleration. To resolve this problem, 3D-DNS on the same BTV has been conducted (Figure 6). Although the initial development correlates well with the periodic representation, the axial deceleration now develops into a stagnation point – confirming the link between a spiral-type of instability and vortex breakdown.

5. POTENTIAL APPLICATIONS

Whereas classical stability analysis places restrictions on the complexity of the instability modes that can be studied, BiGlobal analysis allows more gen-

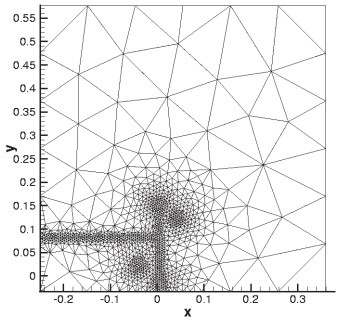

Figure 7. Computational grid in the wake of a low aspect ratio wing

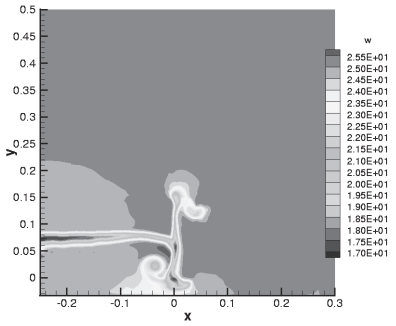

Figure 8. RANS-evaluated base flow computed about a low aspect ratio wing

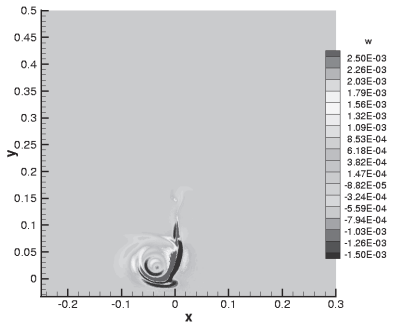

Figure 9. Short wavelength unstable perturbation mode of the trailing vortex

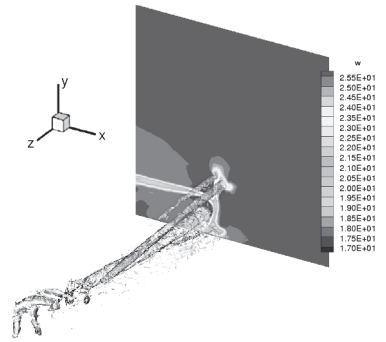

Figure 10. DNS of wake vortex system illustrating development of breakdown

eral flows, with arbitrarily complicated vorticity distributions in the plane normal to the axial flow direction. The use of unstructured grids, coupled with the high spatial accuracy of spectral methods, also offers a significant flexibility to the method. For example, the complicated vortex system originating from a low aspect ratio wing close to the ground, along with a corresponding short-wavelength mode of instability, is illustrated in Figures 8 and 9 respectively; where the base flow was evaluated from a RANS-simulation.

Although there is a question on the appropriateness of taking such a solution from an analytic perspective, DNS of the RANS-evaluated wake system (visualised using λ_2 iso-surfaces in Figure 10) confirmed the development of an instability with a wavelength ($\beta = 100$) comparable with the most unstable perturbation mode. Analogous to an isolated Batchelor vortex, the development of the instability also leads to an axial loss of velocity in the vortex core. In a similar analysis, Crouch et al. (2004) used RANS-obtained basic states, coupled with a compressible BiGlobal stability analysis to obtain realistic eigenmodes related to the buffeting of an 18% thick bi-convex airfoil. This illustrates the scope of the method and suggests that it is valid.

6. CONCLUSIONS AND FUTURE RESEARCH

A unified approach to analysing vortex stability has been discussed, and a causal relationship between stability and breakdown implied. Spiral modes of instability were found to cause a lateral expansion of the cross-section, and a corresponding drop in axial velocity (a prerequisite of vortex breakdown). This confirms the proposals of Ash and Khorrami (1995), who describe breakdown as, 'a final outcome of vortex instability, with the caveat that vortex breakdown can also be produced by external means'.

External influences might include an adverse pressure gradient, which cannot be investigated through BiGlobal stability analysis. A suitable technique is the Parabolised Stability Equation concept derived in Section 2. This formulation permits flows with a mild variation in the axial direction and is currently being implemented to address the influence of axial pressure gradients, and their role in vortex instability and development to breakdown.

REFERENCES

Abid, M. and Brachet, M.E. (1998). Direct numerical simulations of the Batchelor trailing vortex by a spectral element method. *Physics of Fluids*, 10(2).

Ash, R.L. and Khorrami, M.R. (1995). Vortex stability. In Green, S.I., editor, *Fluid Vortices*, pages 317–372. Kluwer Academic Publishers.

Barkley, D. and Tuckerman, L.S. (2000). Bifurcation analysis for timesteppers. In Doedel, E. and Tuckerman, L.S., editors, *Numerical Methods for Bifurcation Problems and Large-Scale Dynamical Systems*, pages 466–543. Springer, New York.

Batchelor, G.K. (1964). Axial flow in trailing line vortices. *Journal of Fluid Mechanics*, 20:645–658.

Benjamin, T.B. (1962). Theory of the vortex breakdown phenomenon. *Journal of Fluid Mechanics*, 14(4):593–629.

Crouch, J.D., Garbaruk, A., Shur, M., and Strelets, M. (2004). Predicting unsteady buffet onset using RANS solutions. TM 2004-212913, NASA.

Herbert, T. (1997). Parabolized stability equations. *Annual Review of Fluid Mechanics*, 29:245–283.

Leibovich, S. (1978). The structure of vortex breakdown. *Annual Reiew of Fluid Mechanics*, 10:221–246.

Lessen, M., Singh, P.J., and Paillet, F. (1974). The stability of a trailing line vortex: Part 1 - inviscid theory. *Journal of Fluid Mechanics*, 63:753–763.

Mayer, E.W. and Powell, K.G. (1992). Viscous and inviscid instabilities of a trailing vortex. *Journal of Fluid Mechanics*, 245:91–114.

Sherwin, S.J. and Karniadakis, G.E. (1995). A triangular spectral element method: Applications to the incompressible Navier-Stokes equations. *Computer Methods in Applied Mechanics and Engineering*, 123:189–229.

Squire, H.B. (1960). Analysis of the vortex breakdown phenomenon, part I. Report No. 102, Aeronautics Department, Imperial College, London.

Theofilis, V. (2003). Advances in global linear instability analysis of nonparallel and three-dimensional flows. *Progress in Aerospace Sciences*, 39:249–315.

EXPERIMENTAL STUDY OF RESONANT INTERACTIONS OF INSTABILITY WAVES IN AN AIRFOIL BOUNDARY LAYER

D. Sartorius[1], W. Würz[1], T. Ries[1], M. Kloker[1], S. Wagner[1], V.I. Borodulin[2] and Y.S. Kachanov[2]

[1]*Institut für Aerodynamik und Gasdynamik (IAG), Universität Stuttgart, Pfaffenwaldring 21, 70550 Stuttgart, Germany*

[2]*Institute of Theoretical and Applied Mechanics (ITAM), Russian Academy of Science, 630090 Novosibirsk, Russia*

Abstract: The present paper is devoted to the detailed experimental study of weakly nonlinear resonant interactions of Tollmien-Schlichting waves in a specially designed 2D non self-similar boundary layer on an airfoil. The influence of the fundamental frequency on the efficiency of the tuned subharmonic resonance is investigated as well as the influence of frequency and spanwise wavenumber detunings. The results are compared with Direct Numerical Simulations based on a vorticity-velocity formulation of the complete Navier-Stokes equations. Good overall agreement is achieved.

1. INTRODUCTION

For the design of subsonic, natural laminar flow (NLF) airfoils usually half-empirical transition prediction codes based on linear stability theory (LST) are applied. This approach gives reliable results as long as the streamwise extend of the nonlinear disturbance growth is short in comparison to the linear part. Detailed optimizations of boundary layer parameters with respect to a long laminar run now take advantage of the successive (linear) amplification and damping of Tollmien-Schlichting (TS) waves in a way that the resulting amplitudes just remain below a certain critical threshold. In this case the onset of nonlinear interactions is of significant importance for the extent of the laminar run.

At this stage the disturbances in the boundary layer can still be described as different modes of the frequency-wavenumber spectrum. The basic properties, like amplitude and phase in the y-profiles, remain the same as predicted by linear theory. The interaction of those modes is dominated by so called reso-

R. Govindarajan (ed.), Sixth IUTAM Symposium on Laminar-Turbulent Transition, 159–165.

nant interactions (see review by Herbert [1] and Kachanov [2]). The classical resonance is the Craik Triad [3], consisting of a 2D fundamental wave with a pair of 3D subharmonic waves with half of the fundamental wave frequency. Subsequent theoretical and experimental studies [4, 5] have shown that this resonance is not only possible for the classical tuned case, where frequency, streamwise and spanwise wavenumber and phase fit. In experiments [5] on a self-similar adverse pressure gradient (APG) flow the highest amplification rates were observed for detuned (mainly with respect to frequency) modes. The double-exponential growth of these modes leads very fast to flow randomization and transition. In previous investigations [6, 7] those systematic studies were extended to the case of a non self-similar boundary layer, which exhibits a rather strong change of the resonance conditions in streamwise direction in comparison to the self-similar one. The present paper is devoted to the comparison of the results obtained in these experiments with DNS.

2. EXPERIMENTAL SETUP

The experiments were conducted in the Laminar Wind Tunnel (LWT) of the IAG. The LWT is an open return tunnel with a turbulence level less than $\mathrm{Tu} = 2{\cdot}10^{-4}$. The boundary layer measurements were performed on the lower surface of the WW03BL106 airfoil section, which was specially designed to give a constant threshold of a n-factor of $n = \ln(A(f)/A_0(f)) = 6$ (downstream of $s/s_{\max} = 0.3$, $s_{\max} = 604$ mm, arc length measured from the leading edge) at an angle of attack of 2 degree and a Reynolds number of approx. $0.7 \cdot 10^6$. The experiments were carried out at controlled disturbance conditions. The TS-waves were excited by a slit source which was mounted flush to the surface at $s/s_{\max} = 0.13$. The slit is 0.2 mm wide and extends 290 mm in spanwise direction. Below the slit, 116 equally spaced pneumatic tubes are connected to 32 micro loudspeakers which are driven by power amplifiers and a 16 channel signal generator. Independent memory of 4096 points (12 bit resolution) for each channel and external triggering by a quartz based clock enables the generation of disturbances with different frequencies and spanwise wavenumbers. Hot-wire measurements were performed downstream of the slit with a phase locked (with respect to the disturbance generator) data acquisition. Due to the quadratic influence of the velocity on the stability characteristics the velocity ($U_\infty = 18$ m/s) was fixed rather than the Reynolds number (the kinematic viscosity varied between $14.5 \cdot 10^{-6}$ and $16.4 \cdot 10^{-6}\mathrm{m}^2$/s due to temperature effects). The AC-signal of the Dantec 55M10 bridge was band pass filtered and optimal adjusted to the input range of the 12 bit AD-converter by a programmable amplifier. A total of 2^{15} points were sampled at approximately 10 kHz at every measurement station. The time traces are corrected for the influence of the filters by a forward-backward Fourier transform before applying King's

Law to the total signal. The complex TS-wave amplitudes were determined by a final Fourier transform. Spanwise scans and sets of wall normal profiles were performed at several downstream positions. All necessary base flow parameters were obtained, including stability characteristics for 2D and 3D TS-waves in a range of frequencies from 255 to 610 Hz (see figures 1 and 2).

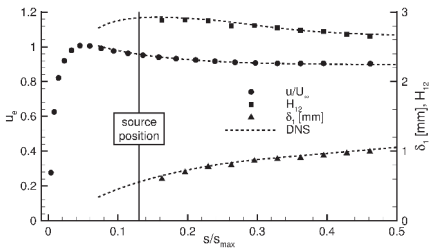

Figure 1. Distribution of velocity, shape factor and displacement thickness

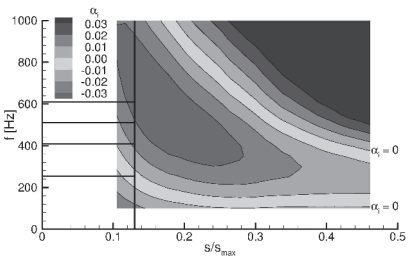

Figure 2. 2D stability diagram with position of source and investigated fundamental frequencies

3. EXPERIMENTAL RESULTS

In a first step resonant triplets were excited consisting of a 2D fundamental wave with an amplitude of approximately 0.06% of u_e at 20 mm downstream of the disturbance source and a pair of 3D subharmonic waves with an amplitude of about one order below the fundamental one [6]. The resonance condition was always satisfied at the position of the disturbance source. Despite the rather strong downstream variation of the resonant subharmonic spanwise wavenumber, resonant growth is present in a wide range of tuned and detuned frequencies and spanwise wavenumbers in general consistence with experiments [5, 8] in a self-similar APG boundary layer.

It was found, as shown in figure 3, that the resonant amplification is the strongest at high fundamental wave frequencies (which are most unstable at the initial section of the airfoil) and subsides quickly with decreasing frequency. This phenomenon seems to be explained by the frequency variation of the dispersion characteristics of the base flow due to its essential non self-similarity. The dependence of the resonant amplification on the initial phase shift led to an anti-resonance regime where suppression of the subharmonic mode is observed as shown in figure 4.

Measurements with frequency detuning [7] showed that for high fundamental frequencies the strongest amplification occurs at small positive frequency detunings, while at low frequencies at very large detunings (about 80% of the subharmonic frequency). For fundamental frequencies $f_1 \geq 400$ Hz the maximum amplification of the subharmonic mode occurred in a rather narrow

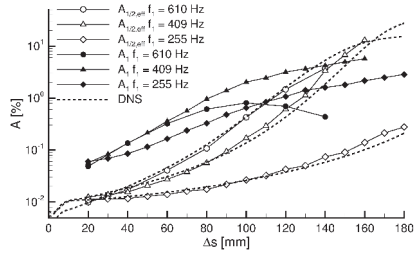

Figure 3. Amplification curves for investigated fundamental frequencies in tuned regimes

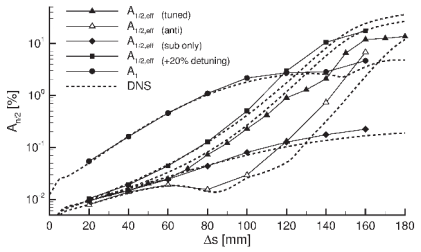

Figure 4. Amplification curves for tuned, anti-resonance, subharmonic only and maximum resonance detuned regimes

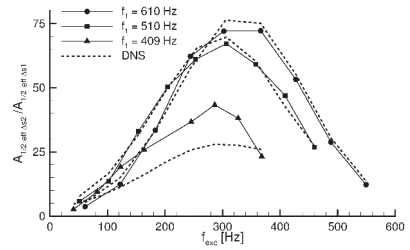

Figure 5. Effective mode amplification factors vs. frequency of excitation

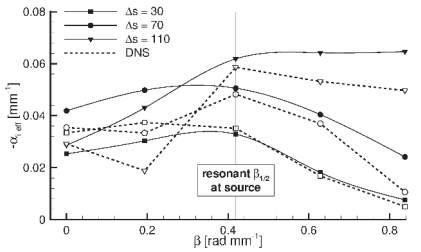

Figure 6. Influence of wavenumber detuning on subharmonic growth rates

frequency range close to 300 Hz for the excited subharmonic mode, shown in figure 5. This finding let to a joint interaction regime of a quasi-subharmonic 3D wave pair with two 2D fundamental waves. It was shown that a superposition principle is satisfied which is leading to a very rapid growth of quasi-subharmonic waves with increments, which are as large as (or even somewhat greater than) those observed in the same two resonances when they occur separately.

The subharmonic spanwise wavenumber detuning was shown to influence significantly the resonant amplification of subharmonics, while the tuned regimes still dominate over the corresponding detuned ones (figure 6). The character of this influence correlates with the streamwise variation of the base flow properties.

4. COMPARISON WITH DIRECT NUMERICAL SIMULATIONS

The DNS are based on the vorticity-velocity formulation of the complete Navier-Stokes equations for incompressible flat-plate flow with streamwise pressure gradient. 6^{th}-order compact FDs are employed for the streamwise and wall-normal direction, and a Fourier spectral representation for the spanwise

direction, with RK4-O4 time stepping. The disturbances are introduced at the same position as in the experiment at $\Delta s = 0$ mm by time wise periodic blowing and suction within a spanwise disturbance strip at the wall. For details of the method see [9, 10]. Simulations were made with the average Reynolds number and kinematic viscosity obtained from all measurements. The DNS disturbances are determined by matching the amplitudes at $\Delta s = 20$ mm to the ones measured at this position.

Experimental and DNS amplification curves for tuned resonance regimes are shown in figure 3. The comparison shows good quantitative agreement up to the end of the parametric stage at $\Delta s \approx 130$ mm for a wide rage of fundamental frequencies.

Figure 4 shows the subharmonic growth rates for different experimental and DNS regimes with the same fundamental frequency $f_1 = 510$ Hz (sub only: no excitation of fundamental wave). Except for the anti-resonance regime all other subharmonic amplitudes coincide within each regime. The difference in the anti-resonance regime is attributed to the inaccuracy of the experimental determination of the exact phase shift within a adequate time frame. The experimentally found phase shifts varied from 146° for $f_1 = 610$ Hz to 153° for $f_1 = 409$ Hz whereas the DNS phase shifts were found to be approx. 4° higher. Therefor the streamwise length of suppression of the measured subharmonic is shorter than the one found in DNS. Upstream of the suppression both growth rates are again identical.

The dependence of the effective subharmonic mode amplification on frequency detuning is shown in figure 5. The amplitudes were measured close to the disturbance source $\Delta s_1 = 40$ mm and farther downstream at $\Delta s_2 = 120$ mm (160 mm for $f_1 = 255$ Hz). The same positions were used for the determination of the amplification found in DNS. For the highest fundamental frequencies ($f_1 = 510$ and 610 Hz) very good quantitative agreement was found over the entire range of investigated detunings ($\pm 80\%$). The different amplifications for lower fundamental frequencies are showing good qualitative agreement by matching the excited subharmonic frequency where the maximum resonant interaction is observed in the experiment. The quantitative deviation can be explained by a slight difference in the growth rate of the subharmonic modes leading to lower intergral amplitudes in DNS.

The influence of spanwise wavenumber detunings on the resonant amplification of subharmonic waves was investigated in detail for the strongest resonant interaction ($f_1 = 610$ Hz) in a range of $\pm 100\%$ of the resonant spanwise wavenumber (-100% is equivalent to 2D excitation). The estimated values of the subharmonic growth rates are presented in figure 6 versus the spanwise wavenumber for three streamwise positions. In general the behavior is similar with good agreement for positions closer to the disturbance source and for the

resonant or higher spanwise wavenumbers. The cause for the differences and especially for $\beta = 0.2$ rad/mm have yet to be determined.

5. CONCLUSION

Weakly nonlinear interactions of TS-waves have been studied under controlled disturbance conditions in an essentially non self-similar APG boundary layer on an airfoil. Despite rather strong downstream variation of the resonant subharmonic spanwise wavenumber the resonant growth is found in a wide range of tuned and detuned frequencies and spanwise wavenumbers in general consistence with previous experiments [5, 8]. The obtained DNS results showed in a wide range of experimental regimes an excellent agreement. Minor differences were found only in the anti-resonance regimes cause by uncertainties in the determination of the experimental phase shift for maximum suppression of the subharmonic mode and in the comparison of the estimated values of the subharmonic growth rates for different spanwise wavenumbers.

ACKNOWLEDGEMENTS

This work was performed under grant of the Deutsche Forschungsgemeinschaft (N 436 RUS 113/749/0-1) and the Russian Foundation for Basic Research (N 03-01-04003). The contribution of Y.S. Kachanov was supported by Alexander von Humboldt-Foundation.

REFERENCES

[1] Herbert T.: *Secondary instability of boundary layers.* Annu. Rev. Fluid Mech. 20, pp. 487-526, 1988

[2] Kachanov Y.S.: *Physical mechanisms of laminar-boundary-layer transition.* Annu. Rev. Fluid Mech. 26, pp. 411-482, 1994

[3] Craik A.D.D.: *Nonlinear resonant instability in boundary layers.* J. Fluid Mech. 50, pp. 393-413, 1971

[4] Zelman M.B., Maslennikova I.I.: *Tollmien-Schlichting-wave resonant mechanism for subharmonic-type transition.* J. Fluid Mech. 252, pp. 449-478, 1993

[5] Borodulin V.I., Kachanov Y.S., Koptsev D.B., Roschektayev A.P.: *Experimental study of resonant interactions of instability waves in self-similar boundary layer with an adverse pressure gradient: II. Detuned resonances.* J. Turbulence 3, No. 063, 2002

[6] Würz W., Sartorius D., Wagner S., Borodulin V.I., Kachanov Y.S.: *Experimental study of weakly nonlinear interactions of instability waves in a non self-similar boundary layer on an airfoil. Part I: Base flow and initially tuned resonances*. ICMAR proc. part II: pp. 201-206, Novosibirsk, ITAM, 2004

[7] Sartorius D., Würz W., Wagner S., Borodulin V.I., Kachanov Y.S.: *Experimental study of weakly nonlinear interactions of instability waves in a non self-similar boundary layer on an airfoil. Part II: Influence of frequency and spanwise-wavenumber detunings*. ICMAR proc. part II: pp. 207-212, Novosibirsk, ITAM, 2004

[8] Borodulin V.I., Kachanov Y.S., Koptsev D.B.: *Experimental study of resonant interactions of instability waves in self-similar boundary layer with an adverse pressure gradient: I. Tuned resonances.* J. Turbulence 3, No. 062, 2002

[9] Stemmer C., Kloker M., Wagner S.: *Navier-Stokes Simulation of Harmonic Point Disturbances in an Airfoil Boundary Layer.* AIAA-J. 38, No. 8, pp. 1369-1376, 2000

[10] Wassermann P., Kloker M.: *Mechanisms and passive control of crossflow-vortex-induced transition in a three-dimensional boundary layer.* J. Fluid Mech. 456, pp. 49-84, 2002

KLEBANOFF MODES IN SWEPT BOUNDARY LAYERS

Karen Kudar[1], Peter W. Carpenter[1] and Christopher Davies[2]
[1]School of Engineering, University of Warwick, Coventry, CV4 7AL, England; [2]School of Mathematics, Cardiff University, Senghennyd Road, Cardiff, CF24 4AG, Wales, U.K.

Abstract: A simplified DNS study is presented of the evolution of Klebanoff-type modes in swept 3D boundary layers (Falkner-Skan-Cooke flows) with adverse and favourable streamwise pressure gradients.

Key words: Boundary-layer stability; Falkner-Skan-Cooke; laminar-turbulent transition; freestream turbulence; Klebanoff modes; transient growth.

1. INTRODUCTION

Klebanoff (K) modes are flow structures in the form of streamwise streaks that appear to be caused by freestream turbulence. They were first observed by Klebanoff [1]. His basic findings have been confirmed by many subsequent authors. The K modes are fundamentally different from Tollmien-Schlichting (TS) waves in that they grow algebraically and reach a steady state rather than growing exponentially. Moreover they are not wave-like in form. Recently Fasel[2] has carried out a direct numerical simulation (DNS) study that elucidates the role of K modes in transition for the Blasius boundary layer, showing that their interaction with TS waves can explain many of the features of the transition process including intermittency and turbulent spots. Here we present a simplified DNS study of the behaviour of K-type modes in swept 3D laminar boundary layers using the Falkner-Skan-Cooke family of velocity profiles as a base flow. The present study extends our recent methods[3] for simulating the evolution of K-modes to 2D and 3D boundary layers with streamwise pressure gradients.

R. Govindarajan (ed.), Sixth IUTAM Symposium on Laminar-Turbulent Transition, 167–172.

2. METHOD

The numerical simulations are based on our velocity-vorticity formulation of the Navier-Stokes equations[4]. For 3D swept boundary layers there is a natural co-ordinate system at any given station whereby the cross-flow velocity is zero at the boundary-layer edge (see Figure 1). It should be noted that the external streamline is deflected by an angle (θ) that is approximately equal to the angle of the swept leading edge. The formulation is based on three primary variables (ω_x, ω_y, w), namely the perturbation vorticity components in the x and y directions and the wall-normal velocity perturbation. These primary variables satisfy three governing equations: two vorticity transport equations for ω_x and ω_y and a Poisson equation for w. For the present study the perturbations are assumed to be small and the governing equations have been linearized. Furthermore, for simplicity we have made a quasi-parallel-flow approximation which implies that the undisturbed velocity and vorticity fields correspond to the Falkner-Skan-Cooke profiles with the wall-normal velocity $W = 0$. High levels of freestream turbulence generate the K modes; to approximate the effects of freestream turbulence a body force $(0, F_y, 0)$ is used. This leads to a vorticity source on the right-hand side of the governing equation for ω_x that takes the form of a delta-function (δ):

$$\frac{\partial F_y}{\partial z} = G e^{i\beta y} \delta\left(x - x_f\right)\delta\left(z - z_f\right)H(t) \qquad (1)$$

Thus the steady vorticity source has magnitude G, varies sinusoidally in the spanwise direction with wavenumber β and is located at (x_f, z_f) where z_f is located at the boundary-layer edge. All variables are non-dimensionalised with respect to the length parameter $L^* = \sqrt{(\nu x/U_e)}$, where ν is the kinematic viscosity, and the velocity parameter U_e.

3. RESULTS

The K modes produced by a constant-strength body force suddenly applied at time t=0 are shown in Figure 2; the structures produced are long in the streamwise direction, narrow in the spanwise direction and appear as alternating high- and low-speed streaks. The optimal spacing of the K modes within a Blasius boundary layer also coincides with that found by Klebanoff himself (reported in Bertolotti[5]).

The transient nature of the K modes is shown by the fact that, for the Blasius boundary layer, their strength initially rises as time increases, ultimately reaching an asymptotic (steady-state) value.

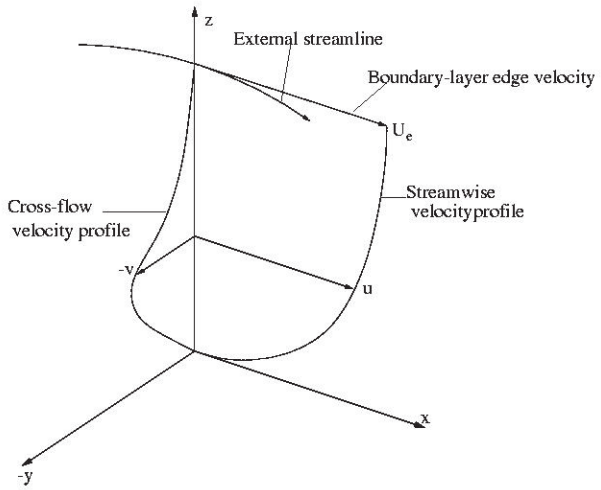

Figure 1. The natural co-ordinate system

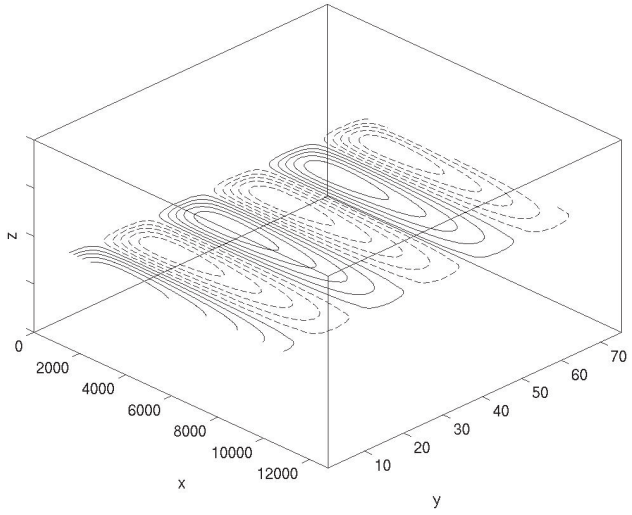

Figure 2. Contour plots of the streamwise velocity component showing the numerically generated K modes produced in an unswept Blasius boundary layer at $z = 2.0$. Dashed lines indicate a negative contour plots. Parameters are as follows: $R_{L^*} = 1000$, $\beta L^* = 0.225$

In two-dimensional flows, the pressure gradient is shown to have a strong effect on the maximum strength (in this case the maximum value of the streamwise velocity component) and the optimal spacing of the K modes (see Figure 3); the more adverse the pressure gradient the stronger the streaks produced and the smaller the optimum spanwise wavenumber.

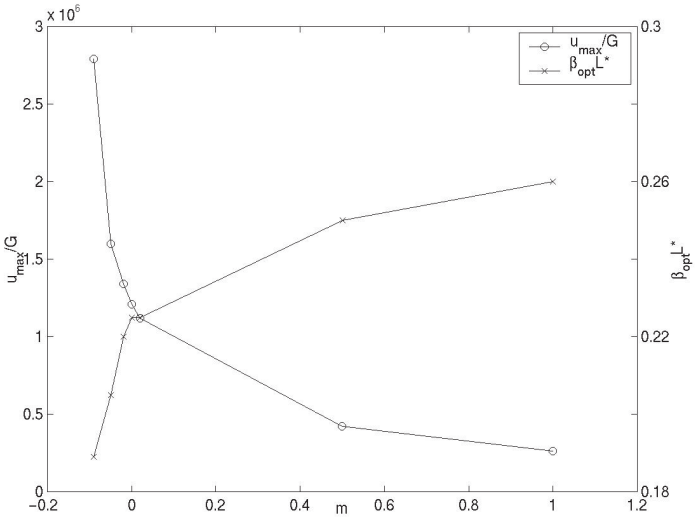

Figure 3. The variation of the optimum spanwise wavenumber ($\beta_{opt}L^*$) with streamwise pressure gradient (m) and also the maximum strength of the K mode achieved at this optimum spacing. Parameters are as follows: R_{L^*} =1000

Figure 4 shows the temporal evolution of the K mode within a swept boundary layer with a favourable streamwise pressure gradient viewed from above. The K mode grows in the negative-y direction, beneath the adjacent streak, with the maximum strength remaining toward the upstream end. Eventually, the growth of the streaks causes the relatively weaker downstream-end of the adjacent streak to become detached and this subsequently gets swept downstream.

Figure 5 shows the temporal evolution of the K mode in a swept boundary layer with an adverse streamwise pressure gradient when viewed from above. This time, the K mode grows in the positive-y direction and the maximum strength of the streak moves towards the downstream-end. A wave-like instability is then shown to occur that grows bigger with time.

Further investigation reveals that the wave-like instability is not a numerical artefact nor impulsively driven. It resembles a secondary instability and a secondary instability is a nonlinear phenomena. It is possible that the disturbance is the superposition of two forms of stationary disturbance with disparate wavenumbers and receptivity.

With both a favourable and adverse streamwise pressure gradient, the evolution of K modes in a swept boundary layer is much more complex and the larger the angle-of-sweep, the more rapidly they develop (see Figure 6).

Further details of our study are given in Kudar[6]. However, further investigation is required in order to fully elucidate the flow physics involved in the phenomena described above.

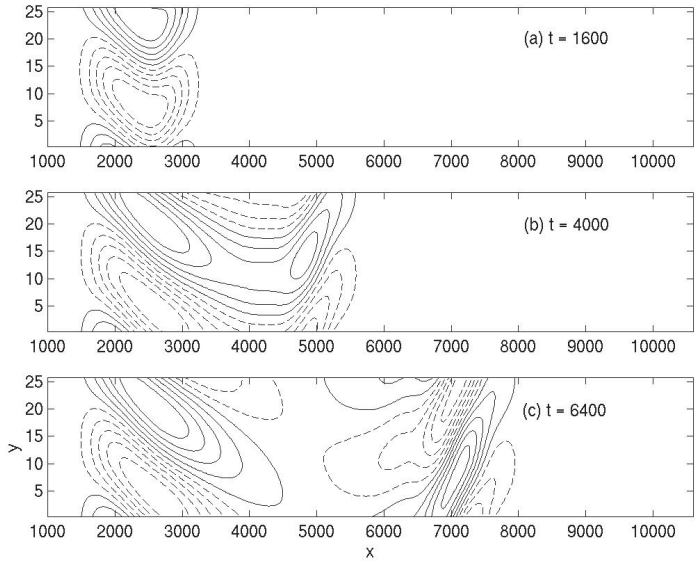

Figure 4. Streamwise velocity contour plots showing the evolution of the K mode, with time, from above in a swept boundary layer (45°) with a favourable (m = 0.0204) streamwise pressure gradient applied. Dashed lines indicate a negative contour plot. Parameters are as follows: $\beta L^* = 0.2$, $R_{L^*} = 1000$, $x_f = 1600$, $z_f = 4.5$

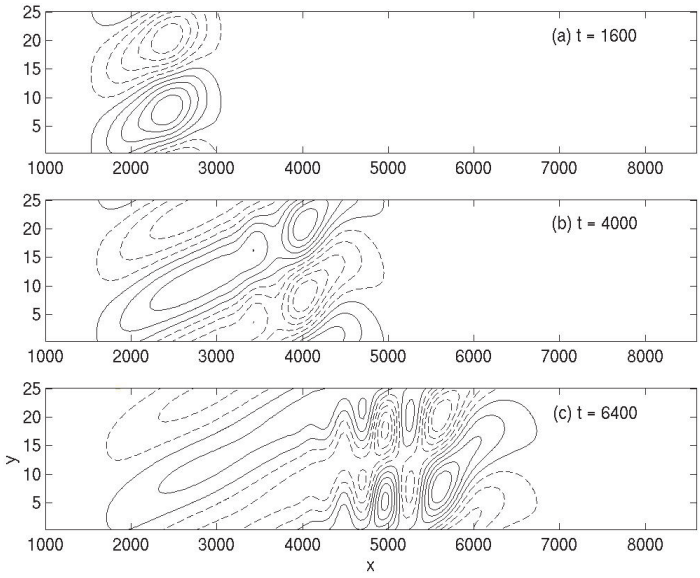

Figure 5. Streamwise velocity contour plots showing the evolution of the K mode, with time, from above in a swept boundary layer (45°) with an adverse (m = -0.0196) streamwise pressure gradient applied. Dashed lines indicate a negative contour plot. Parameters are as Figure 4

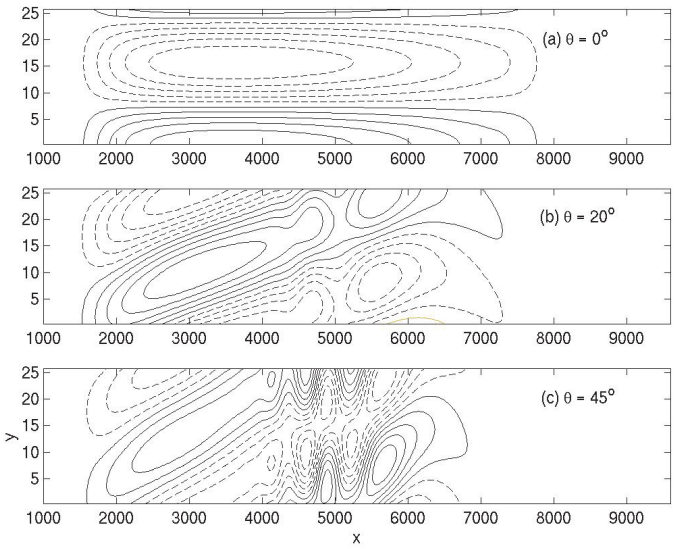

Figure 6. Streamwise velocity contour plots showing the evolution of the K mode, at t = 6400, from above in a boundary layer, with an adverse (m = -0.0196) streamwise pressure gradient, swept at different angles. Dashed lines indicate a negative contour plot. Parameters are as Figure 4

ACKNOWLEDGEMENTS

The research reported herein was supported partly by the U.K. Engineering and Physical Sciences Research Council and partly by the AEROMEMS II project. The AEROMEMS II project is a collaboration between BAE Systems, Dassault, Airbus Deutschland GmbH, EADS-Military, Snecma, ONERA, DLR, LPMO, Manchester University, LML, Warwick University, TUB, Cranfield University, NTUA, and Auxitrol. The project is funded by the European Union and the project partners.

REFERENCES

1. P. Klebanoff, Effect of freestream turbulence on the laminar boundary layer, *Bull. Amer. Phys. Soc.* **10**(11), 103 (1971)
2. H.F. Fasel, Numerical investigation of the interaction of the Klebanoff-mode with a Tollmien-Schlichting wave, *J. Fluid Mech.* **450**, 1-33 (2002).
3. R. Ali and P.W. Carpenter, Klebanoff (K-) modes in boundary layers over compliant surfaces, *Bull. Amer. Phys. Soc.* **47**(11), 52 (2002).
4. C. Davies & P.W. Carpenter, A novel velocity-vorticity formulation of the Navier-Stokes equations with applications to boundary layer disturbance evolution, *J. Comp. Phys*. **172**, 119-165 (2001).
5. F.P. Bertolotti, Response of the Blasius boundary layer to freestream vorticity, *Phys. Fluids*, **9**(8), 2286-2299 (1997).
6. K.L. Kudar, Flow control using pulsed jets, *PhD Thesis*, University of Warwick (2004).

EFFECTS OF COMPRESSIBILITY AND NOSE RADIUS ON INSTABILITIES NEAR THE ATTACHMENT LINE OF SWEPT WINGS

J. Sesterhenn and R. Friedrich
Fachgebiet Stroemungsmechanik
Technische Universitaet Muenchen
joern.sesterhenn@lrz.tum.de, r.friedrich@lrz.tum.de

Abstract: The flow in the vicinity of the attachment line of a swept airfoil is investigated numerically. The typical Goertler–Haemmerlin modes are recovered at the attachment line and found to be stabilised with an increase of the Mach number and reduction of the nose radius. Away from the leading edge, another instability, most probably a streamline–curvature instability as described by Itoh, 1994, was found which dominates the attachment line instability.

Keywords: attachment line –, centrifugal –, crossflow instability

1. INTRODUCTION

Empirically, the attachment–line instability was found to be important for laminar/turbulent transition on swept wings since the early fifties. A review of the early theoretical and experimental work is due to Poll, 1979. The linear stability analysis by Hall et al., 1984 for the incompressible flat plate yields a critical Reynolds number $Re = 583$. This Reynolds number is based on the spanwise velocity and the viscous length scale defined below. This finding is consistent with DNS studies as for example the first one performed by Spalart, 1988. Flat plate experiments do not exist and curved surface experiments supposedly confirm this results. But recently a finite nose radius was found to increase the critical Reynolds number. Based on linear stability analysis, Lin and Malik, 1997 predict an increase up to $Re = 637$ for $R/\delta = 143$. The flat plate case is recovered for $R/\delta > 1430$. Little is known for compressible flow. For the weak compressible regime on a flat plate, Le Duc et al., 2002 confirmed the existence of the instability for $Re = 644$.

R. Govindarajan (ed.), Sixth IUTAM Symposium on Laminar-Turbulent Transition, 173–179.

In this contribution we study the flow about a parabolic leading edge in supersonic flow and the nature of the instabilities appearing on and away from the stagnation line.

2. BASE FLOW

2.1 Parameters

The base flow on a curved leading edge in compressible flow is described by several parameters.

The proper length scale is the viscous length, which is about a third of the boundary layer thickness. It is formed by the velocity gradient and the viscosity and reads $\delta = \sqrt{\nu / \frac{\partial u_\infty}{\partial x}}$. x denotes the chord direction, z the spanwise direction and y is perpendicular to both. Below, we will also refer to n as the normal direction to the body surface and s as the coordinate along the body surface starting at the leading edge. In the flat plate case the velocity gradient is an arbitrary parameter and in the curved case approximated by the velocity gradient of a potential flow at the wall of a circular cylinder $\frac{\partial u_\infty}{\partial x} = 2u_\infty / R$. The nose radius may be expressed in terms of this length scale, being a first dimensionless parameter of the problem. If we omit blowing and suction or the use of trip-wires, we are left with three more dimensionless parameters. The Reynolds number is $Re = \frac{w_\infty \delta}{\nu}$. It is constructed with the sweep velocity w_∞ parallel to the leading edge, the viscous length scale and a reference viscosity. The reference viscosity is taken to be the viscosity on the stagnation line for an adiabatic wall. The adiabatic wall temperature T_r is available from Reshotko and Beckwith, 1958. In our investigation, the wall temperature T_w was always adiabatic thus, the dimensionless parameter $\tau = \frac{T_w - T_r}{T_o - T_\infty}$ was kept zero. Additionally a sweep Mach number $M = w_\infty / c_\infty$ can be defined.

Please note that the sweepback angle is hidden in the Reynolds number by the ratio of the two velocity components. It is thus no longer a formal parameter of the problem.

It is known from the literature Hall et al., 1984, Obrist and Schmid, 2003 that below a critical Reynolds number of $Re = 583$ the flow is linearly stable. This value is raised by a finite nose radius Lin and Malik, 1997 and compressibility Le Duc et al., 2004.

Practical situations, e.g. for an airplane or fighter, typically involve Reynolds numbers of $Re = 400 - 1000$, nose radii of $R/\delta = 300 - 1000$ and sweep Mach numbers of $M = 0.3 - 1.5$.

2.2 Model assumptions and numerical method

We have introduced the assumption of periodicity in spanwise direction for our computations. Thus we neglect spanwise boundary layer growth. By this

assumption we are able to compute the base flow in two dimensions only. This makes the investigation of the relevant parameter space more affordable. In future, we want to perform three—dimensional computations in representative regions of the parameter space and quantify the validity of the periodicity assumption.

At the outflow, non-reflecting boundary conditions are employed. At the inlet we consider in this paper supersonic conditions with a moving bow shock which is prescribed by use of the Rankine–Hugoniot conditions. The body surface is taken to be a parabolic leading edge.

We use a characteristic-type numerical scheme which was developed for DNS of compressible transitional and turbulent flow by Sesterhenn, 2001. Its features are low numerical dissipation and dispersion and 5th, respectively 4th order accuracy in space and time. The bow shock, if present, is treated explicitly with a shock-fitting procedure as demonstrated in Fabre et al. Fabre et al., 2001.

In the present simulations we use grids with $350 \times 128 \times (16...64)$ points in wall-normal, tangential and spanwise direction. Only few points in spanwise direction are needed to resolve the principal mode.

2.3 Description of the base flow

In the sequel, we consider a flow of $M_\infty = 8$ over a swept wing of $\Lambda = 30^\circ$, leading to a sweep Mach number $M = 1.25$. The spanwise velocity component at the attachment–line has the typical Blasius–like profile, whereas the wall normal velocity increases almost linearly with wall distance.

The velocity away from the attachment–line is depicted in fig.1. We show the velocity components in a coordinate system which uses the wall normal n/δ, the potential streamline and the cross–product of these two directions for its base. The u profile looks like a Blasius boundary layer but there is a crossflow component which leads to an inflection point of the overall profile.
The local streamline curvature is depicted in figure 2. In that diagram a cut normal to the stagnation line is presented. We show contour lines of the local streamline curvature. The flow is from top to bottom. The upper border is the location of a detached bow shock and the lower border is the body surface.

The local curvature is maximal away from the leading edge and the locus of maximal streamline curvature is at $(x/\delta, y/\delta) \approx (100, \pm 200)$. Additionally the primary instability vortices are shown. They are visible as the two thin stripes along the body surface. They will be discussed later. The streamlines are concave and exhibit no inflection point.

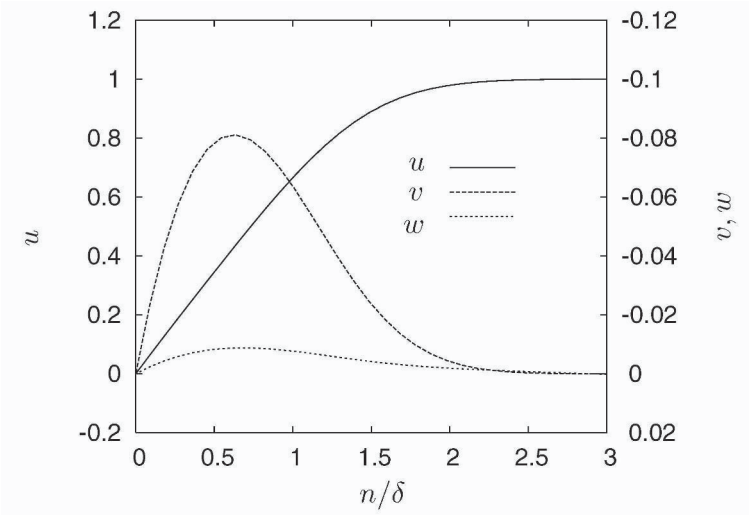

Figure 1. Velocity profile in streamline coordinates. u is the velocity in direction of the streamline, v the crossflow velocity and w the wall–normal one

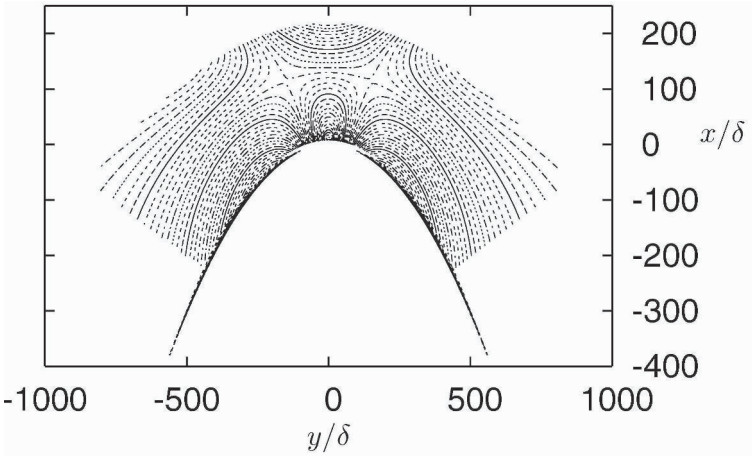

Figure 2. Local streamline curvature depicted in a plane perpendicular to the attachment line

3. PERTURBED FLOW

The steady base flow was perturbed in two ways: randomly in the vicinity of the leading edge and coherently by an entropy perturbation upstream of the shock. Both perturbations were introduced with an amplitude such that the response was linear. This was checked afterwards.

The first method instantaneously triggered the crossflow or centrifugal instability. Very close to the attachment line the growth of an instability was observed, but it could not easily be identified as the attachment-line instability

due to the fact that it was rapidly superseded by the other growth mechanism. For identification, tailored perturbations were introduced which generate a vortex pair travelling along the boundary layer edge. Thus it was hoped to favour the attachment line instability.

Computations were performed for the parameters indicated in the following table 1. The extension of the computational domain in z-direction fixes

Table 1. Overview of Reynolds numbers and nose radii

Re	600	642	700	750	800
R/δ	377	409	446	472	504

the wavelength of the possible growing modes. Therefore different depths in this direction had to be investigated. For time being the computational domain is only large enough to host one principal wavelength and its higher harmonics. The most unstable mode for the incompressible case has a wavelength of $\lambda \approx 23\delta$. Thus we have chosen to vary the dimensionless wavenumber $\alpha = 2\pi\delta/\lambda = 2\pi/30 - 2\pi/20$.

Random perturbations lead to an unconditional growth of kinetic energy of the principal mode when measured globally in the full computational domain or in the full boundary layer. The growth rate was measured between 2 and 6, based on the dimensionless time $(\frac{\partial u_\infty}{\partial x})^{-1}$, given above. Flow visualisations revealed that this was due to vortices roughly inclined as the potential streamlines. They did not extend along the full body surface but were locally confined to the region of the strongest streamline curvature of the flow. A cut in a plane parallel to the leading edge and normal to the body surface is presented in figure 3. The plane is located near the locus of maximal streamline curvature at a distance of $s = 189\delta$ from the stagnation line. Contour lines of the v velocity component are shown. They resemble very closely the known pattern of the crossflow instability. Figure 4 shows the phase of the Fourier component of this mode. It shows a strong phase shift which is typical for crossflow modes. Atypical, and rather indicating a centrifugal instability is the local confinement of the the vortices.

In order to identify the attachment line instability, separate measurements of the kinetic energy of the perturbation were performed at the locus of maximal streamline curvature and in the vicinity of the leading edge. They revealed that the main kinetic energy is found in the strong vortices described above. At the leading edge a conditionally unstable mode was found. Its growth rates were measured to be a factor of ten less. The critical Reynolds number is shifted towards $Re = 635$ and the wave number is lowered as compared to the flat incompressible case.

In a second test series, the flow was perturbed by an entropy spot ahead of the detached bow shock. Upon interaction with the shock, entropy, vorticity

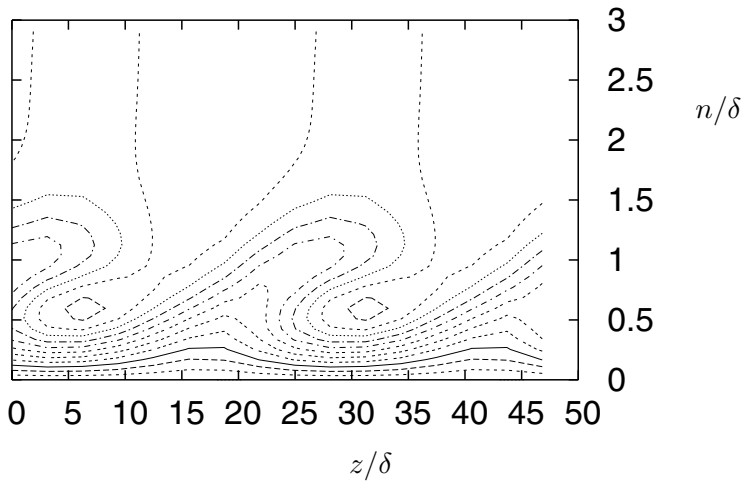

Figure 3. Contour lines of the v–velocity at $s = 189\delta$. The distance of the contourlines is ten percent of the reference velocity behind the shock

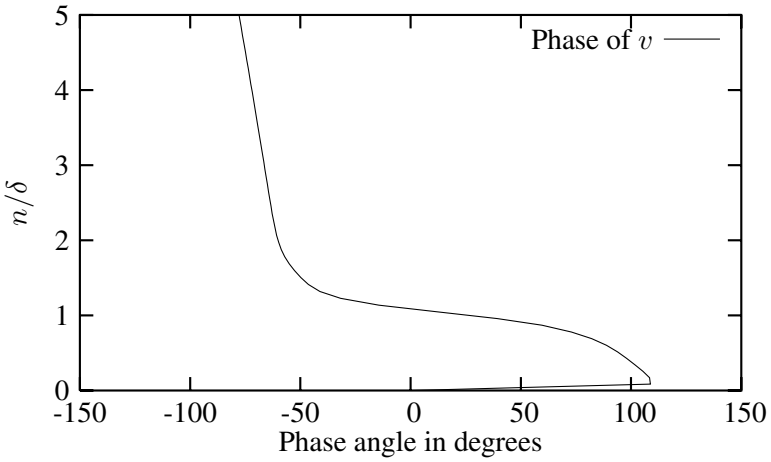

Figure 4. Phase relation of the observed instabilities

and acoustic disturbances are generated behind the shock. The vorticity perturbations have the form of two counterrotating vortices Fabre et al., 2001, and it was hoped that they strongly favour the weaker attachment–line instability. These attempts proved unsuccessful and it was not possible to excite the attachment–line instability strong enough to temporarily exceed the other instabilities.

4. CONCLUSIONS

For the compressible swept leading edge flow at a sweep Mach number of $M = 1.25$ with adiabatic wall conditions at a parabolic leading edge with a nose radius of $300 - 500$, the attachment–line instability was observed. It is substantially weaker than a crossflow or centrifugal instability which is locally confined to the locus of maximal streamline curvature. The critical Reynolds number is increased whereas the corresponding wavenumber decreases. The dominating instability is unconditionally unstable in the investigated parameter range. The exact nature of this instability is uncertain. The phase relationship indicates a crossflow instability whereas the local confinement of the instability to the place of maximal streamline curvature indicates a centrifugal instability.

For further investigations a global stability solver based on the current DNS-code is being developed since the DNS data is difficult to analyse and expensive to obtain.

REFERENCES

Fabre, D., Jacquin, L., and Sesterhenn, J. (2001). Linear interaction of a cylindrical entropy spot with a shock. *Physics of Fluids*, 13(8):2403–2422.

Hall, P., Malik, M., and Poll, D. (1984). On the stability of an infinite swept attachment–line boundary layer. *Proc. R. Soc. Lond.*, A(395):229–245.

Itoh, N. (1994). Instability of three-dimensional boundary layers due to streamline curvature. *Fluid Dyn. Res.*, 14:353–66.

Le Duc, A., Sesterhenn, J., and Friedrich, R. (2002). Direct numerical simulation of instabilities of the compressible swept Hiemenz flow. In Dussauge, J. and Chikhaoui, A., editors, *Aerodynamics and Termochemistry of High Speed Flow*, EUROMECH 440.

Le Duc, A., Sesterhenn, J., and Friedrich, R. (2004). On instabilities in compressible attachment–line boundary layers. *Physics of Fluids*. submitted.

Lin, R.-S. and Malik, M. R. (1997). On the stability of attachment–line boundary layers. part 2. the effect of leading edge curvature. *J. Fluid Mech.*, 333:125–137.

Obrist, D. and Schmid, P. (2003). On the linear stability of swept attachment-line boundary layer flow. Part 1. Spectrum and asymptotic behaviour. *Journal of Fluid Mechanics*, 493:1–29.

Poll, D. (1979). Transition in the infinite swept attachment–line boundary layer. *Aeronautical Quarterly*, 30:607–628.

Reshotko, E. and Beckwith, I. E. (1958). Compressible laminar boundary layer over a yawed infinite cylinder with heat transfer and arbitrary Prandtl number. Technical Report 1379, National Advisory Committee for Aeronautics.

Sesterhenn, J. (2001). A characteristic–type formulation of the Navier–Stokes equations for high order upwind schemes. *CAF*, 30(1):37–67.

Spalart, P. (1988). Direct numerical study of leading edge contamination. Technical Report CP-438, Fluid Dyn. of 3D Turb. Shear Flows and Transition, AGARD.

TWO-DIMENSIONAL LOCAL INSTABILITY: COMPLETE EIGENVALUE SPECTRUM

Jean-Christophe Robinet and Chloé Pfauwadel
SINUMEF Laboratory ENSAM-PARIS
151, Boulevard de l'Hôpital 75013 PARIS, FRANCE
robinet@paris.ensam.fr

Abstract: The study of "simple" flows such as Poiseuille flow have been for a long time studied and their simplicity has permitted us to highlight different instability mechanisms. More recently, several authors have shown, through transient growth studies and by the identification of the nonnormal character of the operator of Orr-Sommerfeld, that these two flows could have subcritical dynamics. However, the assumption of one-dimensionality of the basic flow limits the comparison with the experiment where the basic flow is not exactly one-dimensional. Although different studies have been realized on the stability of a two-dimensional basic flow, all were interested only in the most unstable mode. In this present paper, the stability of the laminar flow in a rectangular duct of an arbitrary aspect ratio is investigated numerically with for objective the computation of the complete spectrum. This study will highlight strong similarities between the 1D and 2D spectra but, in spite of a powerful numerical method, will show the numerical limitations observed to obtain a spectrum converged in a sufficiently large field in ω.

Keywords: Two-dimensional instability, collocation spectral, eigenvalue problem, Poiseuille flow.

1. INTRODUCTION

Since many years it is well-known that for some flows the prediction of linear eigenvalue analysis fail to match most experiments. Poiseuille flow is this kind of flows. Recently it has emerged that the failure of eigenvalue analysis may more justly be attributable to the non-normality of the linearized system. It is a fact of linear algebra that even if all eigenvalues of a linear system are distinct and stable, inputs to that system may be amplifed by arbitrarily large factors if the eigenfunctions are not orthogonal.

S. C. Reddy and Henningson, 1993, have discovered that the operator that arises in Poiseuille flow is in some sense exponentially far from normal and Butler and Farrell, 1992, have shown that small perturbations to these flows may be amplified by factors of many thousands, even if all the eigenvalues are stable.

R. Govindarajan (ed.), Sixth IUTAM Symposium on Laminar-Turbulent Transition, 181–188.

However, although these new approaches have considerably evolved the comprehension of the mechanisms of transition to the turbulence in open flows such as Poiseuille flow, the modeling of these flows remains rather simple. Indeed, for all of these flows only one spatial direction is supposed to be homogeneous, at least in an approximate sense. This restriction may be relaxed by considering an extension of the classic linear theory in which the condition of spatial homogeneity in the laminar basic state is required of one spatial direction only, while the other two spatial direction are resolved. This extension was already used by some authors like Tatsumi and Yoshimura, 1990, and Theofilis, 1998, Theofilis, 2000, for the calculation of instabilities in a rectangular duct flow and Theofilis et al., 2000, Theofilis, 2003, for many academic flows. However, all these studies related to the calculation of the most unstable modes and not of the complete spectrum of the discrete eigenvalues necessary for the computation of transient growth.

The objective of this paper is to study the structure of the discretized operator spectrum, to compare it with the spectrum when $A \rightarrow \infty$ and to evaluate the capacity of the computational techniques usually used to calculate the "whole" of the discrete eigenvalues spectrum in simple flow in a duct of rectangular cross-section: two-dimensional Poiseuille flow.

2. DECOMPOSITION OF THE INSTANTANEOUS FLOW FIELD

The main idea of the linear stability theory is to split the flow field in two parts. The first part is of order O(1) and is called the basic flow (noted $\overline{\bullet}$). It is supposed to be steady and solution of the Navier Stokes equations. The second part is the disturbance term and is assumed to be of small amplitude. Considering that the basic flow is two-dimensional in (x, y) and the third direction is assumed to be homogeneous. In cartesian coordinates, each physical quantity $\boldsymbol{Z}$ of the flow field (velocity components, pressure, temperature, density) is thus written :

$$\boldsymbol{Z}(x, y, z, t) = \overline{\boldsymbol{Z}}(x, y) + \varepsilon \tilde{\boldsymbol{Z}}(x, y) e^{i(\beta z - \omega t)} + cc., \ \varepsilon \ll 1. \tag{1}$$

The aim is to determine the disturbance field. Filling the Navier Stokes equations with this ansatz, a new system is obtained, from which the basic flow terms can be dropped, as they already solve the equations. By linearising, the quadratic flow terms also disappear.

In the temporal framework, as considered here, β is a real wavenumber parameter and ω is the complex eigenvalue being seeked; whose real part indicates frequency and whose positive imaginary part is the growth rate in time t. The imaginary unit is $i = \sqrt{-1}$ and $c.c.$ denotes complex conjugate. The solutions of the problem are thus seeked under the form of temporal waves behaving periodically in the z-direction, and of amplitude the unknown eigenfunction vector $\tilde{\boldsymbol{Z}}(x, y)$.

3. BASIC FLOWS

We considers a duct with rectangular section $[-A, A] \times [-1, 1]$ following x and y directions respectively and of infinite extension in z direction. According to the geometry of the problem, one can suppose that the velocity field does not depend on z, the velocity is thus: $\overline{\mathbf{V}} = [0, 0, \overline{W}(x, y)]^t$ and pressure can be written as $\overline{P}(x, y, z)$. Under these assumptions, the Navier Stokes equations can be written as Poisson equation $\partial^2\overline{W}/\partial x^2 + \partial^2\overline{W}/\partial y^2 = \lambda R_e$, and the pressure $\overline{P}$ is linear in the z-direction. where $\lambda = \partial\overline{P}/\partial z$ is a constant. This equation is discretized by spectral collocation méthod and solved by classical numerical method. The boundary conditions are for the two-dimensional Poiseuille flow: $\bar{W}(\pm A, y) = \bar{W}(x, \pm 1) = 0, \ \forall (x, y) \in [-A, A] \times [-1, 1]$.

4. LINEARIZED NAVIER-STOKES (LNS) FORMULATION

The decomposition (1) is substituted into the incompressible equations of motion. Linearisation about $\overline{\boldsymbol{Z}}$ follows, based on the argument of smallness of ε and the basic flow terms, themselves satisfying the equations of motion, are subtracted out. The linearised Navier-Stokes equations become a partial differential system and can be written in matrix form:

$$\left[\boldsymbol{M}_1\frac{\partial^2}{\partial x^2} + \boldsymbol{M}_2\frac{\partial^2}{\partial y^2} + \boldsymbol{M}_3\frac{\partial^2}{\partial x\partial y} + \boldsymbol{M}_4\frac{\partial}{\partial x} + \boldsymbol{M}_5\frac{\partial}{\partial y} + \boldsymbol{M}_6\right]\tilde{\boldsymbol{Z}} = 0, \quad (2)$$

with $\tilde{\boldsymbol{Z}}(x, y) = [\tilde{u}, \tilde{v}, \tilde{w}, \tilde{p}]^t\,(x, y)$ and where $\boldsymbol{M}_j$, $j = 1, \ldots, 6$ are real or complex (4×4) matrices. For more details, see Theofilis, 2003. In this formulation the boundary conditions are :

$$\begin{aligned} &\tilde{u}(x, \pm 1) = \tilde{v}(x, \pm 1) = \tilde{w}(x, \pm 1) = 0 \ \text{ and } \ \frac{\partial\tilde{p}}{\partial y}(x, \pm 1) = 0, \ \forall x, \\ &\tilde{u}(\pm A, y) = \tilde{v}(\pm A, y) = \tilde{w}(\pm A, y) = 0 \ \text{ and } \ \frac{\partial\tilde{p}}{\partial x}(\pm A, y) = 0, \ \forall y. \end{aligned} \quad (3)$$

5. TWO-DIMENSIONAL ORR-SOMMERFELD (2DOS) FORMULATION

Here we have a system of four variables. In order to spare computer memory, it is possible to combine the equations and obtain two two-variable systems: the two-dimensionnal extension of the Orr-Sommerfeld equation. Finally the EDP system can be written in the following matrix form:

$$\begin{aligned} &\left[\boldsymbol{M_1}\frac{\partial^4}{\partial x^4} + \boldsymbol{M_2}\frac{\partial^4}{\partial y^4} + \boldsymbol{M_3}\frac{\partial^4}{\partial x^3\partial y} + \boldsymbol{M_4}\frac{\partial^4}{\partial x^2\partial y^2} + \boldsymbol{M_5}\frac{\partial^4}{\partial x\partial y^3} + \right. \\ &\left.\boldsymbol{M_6}\frac{\partial^2}{\partial x^2} + \boldsymbol{M_7}\frac{\partial^2}{\partial y^2} + \boldsymbol{M_8}\frac{\partial^2}{\partial x\partial y} + \boldsymbol{M_9}\frac{\partial}{\partial x} + \boldsymbol{M_{10}}\frac{\partial}{\partial y} + \boldsymbol{M_{11}}\right]\tilde{\boldsymbol{Z}} = 0, \end{aligned} \quad (4)$$

with $\tilde{\boldsymbol{Z}}(x,y) = [\tilde{u}(x,y), \tilde{v}(x,y)]^t$. For more details, see Tatsumi and Yoshimura, 1990. In this formulation the boundary conditions are :

$$\begin{cases} \forall x,\ \tilde{u}(x,\pm 1) = \tilde{v}(x,\pm 1) = \dfrac{\partial \tilde{v}}{\partial y}(x,\pm 1) = 0, \\ \forall y,\ \tilde{u}(\pm A, y) = \tilde{v}(\pm A, y) = \dfrac{\partial \tilde{u}}{\partial x}(\pm A, y) = 0. \end{cases} \tag{5}$$

The problem so formulated is an eigenvalue problem. In other words, there exists an implicit dispersion relation where the different parameters are connected between them. The resolution of the eigenvalue problem brings the family of eigenvalues ω_j and the corresponding eigenfunctions $\tilde{\boldsymbol{Z}}$. The real part $\Re(\omega_j)$ is the disturbance wave frequency and its imaginary part $\Im(\omega_j)$ is its growth or damping rate.

6. NUMERICAL METHODS

Spectral Chebychev collocation method is used in both directions. The grid is built with Gauss-Lobatto nodes. The principal numerical difficulties lie in the resolution of 2DOS formulation because it is 4 order system of two equations. In two formulations, it is possible to separate symmetric and antisymmetric solutions in order to divise by four the size of the computational domain. Finally, the discretized system is represented by a general eigenvalue problem $\boldsymbol{AX} = \omega \boldsymbol{X}$. The eigenvalues ω and its associated eigenvectors are determined by using the Arnoldi algorithm. In order to improve the precision of the computations and the convergence, different numerical techniques are used in particular in the numerical processing of the boundary conditions of 2DOS formulation.

7. NUMERICAL RESULTS

If we want to compute the transient growth of a two-dimensional Poiseuille flow, it is necessary to know whole eigenvalue spectrum and not only the most unstable mode. In the two following sections, the spectrum of two-dimensional Poiseuille flow is computed by the numerical method descrived above.

7.1 Discretized Spectrum Computation

A complete spectrum (superposition of the four modes) of the Poiseuille flow is shown in figure 1. The parameters are chosen according to Tatsumi and Yoshimura, 1990, so that the flow field is at its neutral point. The neutral mode is found to have a value of $\omega = (0.2112(2), 2.9(75).10^{-5})$, which is close to the result given by Theofilis, 1998, $\omega = (0.21167, 1.10^{-5})$ for a grid (60×40).

The spectrum in figure 2 is found to have a similar structure to that obtained with a one-dimensional approach. However important differences between the 1D and 2D spectrum are nevertheless observed. In the 1D spectrum, the eigenvalues

are located on three main branches which have been labeled A, P and S by Mack (1976). In the 2D spectrum these branches seem always exist but in a different way. The global Y shape characteristic to a 1D Poiseuille flow is roughly found in the 2D configuration. Although the P, S and A branches seem to be located at the same place as those in 1D, important differences between the 1D and 2D spectrum are nevertheless observed. The P branch seems to be composed of two series of aligned modes, the S branch seems as complicated as the P branch with an additional difficulty because $\mid \omega \mid$ is not small and the convergence is weak. More number of points are necessary to reach convergence. The structure of the A branch is more difficult to identify, this branch is strongly modified in comparison with that obtained in 1D approach. In the 1D configuration, the A branch is composed of several isolated modes. In the 2D configuration, the A branch seems to be made up of aligned modes on segments of curve where one extremity of these segments corresponds to the locus of the 1D modes. These "segments of modes" are well converged. It is obvious in this figure that some part of the spectrum is not totally converged in spite of a significant number of points. In fact the P and S branches are not well converged. There are still plenty of disorganized modes lying between the left of the P branches and the right of the A branch and on the left of the S branch. These unconverged modes move if the grid is refined. Indeed, above the P branch, the spectrum seems to be composed of two series of line of modes. With a low discretisation, these lines of modes are in segments like form whose one of these ends is not converged instead of forming a line of modes like in the 1D case, these diverge in two different directions like a fork. The length of the portion of lines increases when the number of points increase but the convergence is slow when the number of point increase. This phenomenon explains why there are many modes between the P and A branches organized more or less in lines. The same arguments apply to the S branch. In order to study the possible existence of two series of branches in the spectrum (for the P branch), a computation with a (65×51) points has been realized for $R_e = 10400$, $\beta = 0.91$ and $A = 2$. We note on figure 3 that P branch is in fact composed of two distinct P branches as we have supposed for $A = 5$ and these branches get closer when the A ratio increase and when $A \rightarrow \infty$ these branches collapse in unique branch. Moreover, in accordance with Tatsumi and Yoshimura, 1990 results, the basic flow is linearly stable when $A = 2$. Figure 3 shows this spectrum.

However, when $A = 5$ and for a grid (65×51) the spectrum is not sufficiently converged to be usable for the transient growth calculation in future. This figure establishes a very close relation with 1D and 2D instabilities. It seems like the transversal walls of the 2D duct only play a minor role on the spectrum structure at $A = 5$. Moreover, at this aspect ratio, the flow can not be considered to one-dimensional. Indeed, if we consider the critical Reynolds number it is equal to 10400 when $A = 5$ and it is only equal to 5772.22 when $A \rightarrow \infty$. The walls affect the flow by stabilizing it.

7.2 Comparison Between 2DLNS and 2DOS

A comparison between the codes written with the Orr-Sommerfeld formulation (4) and the linearized Navier-Stokes equations (2) was performed. The spectra can be observed in figure 4. They are in very good correspondence. That validates the approaches and their equivalence. In 1D approach, the LNS spectrum is equal to the sum of OS spectrum and Squire spectrum, in 2D approach, the 2DOS spectrum and 2DLNS spectrum are totally equivalent.

From a numerical point of view, the Orr-Sommerfeld formulation is much cheaper than the 2DLNS formulation, the memory space is divided by 3 and time by nearly 10. Convergence at a given number of points is equivalent in both cases. However, the Orr-Sommerfeld formulation is more sensitive to numerical characteristics, as discussed earlier. Moreover, the spectra shown here are obtained with derivative matrices containing information about parity. When the comparison is established for "natural" symmetric boundary conditions, it appears that the NSL spectrum is much converged than the Orr-Sommerfeld. The former looks very much like the one shown here whereas the latter is very polluted and the modes so scattered that the structure is barely recognizable. This is an other argument to say that the Orr-Sommerfeld formulation is very interesting in terms of costs, but also very sensitive to numerical conditions.

8. SUMMARY AND CONCLUSIONS

In this present paper, the complete spectrum of a two-dimensional Poiseuille flow has been shown. It was highlighted, as soon as $A \geq 5$, that the spectrum resulting from a one-dimensional approach and those resulting from a two-dimensional approach present strong similarities in their structures. Although the existence of a finished aspect ratio A rather tends to stabilize the flow with respect to the monodimensional result ($A \rightarrow \infty$). The spectrum of Poiseuille flow seems to have three branches like its 1D counterpart. However, when $A < \infty$, the P branch seems to be double and tends towards a single branch when $A \rightarrow \infty$. This characteristic must undoubtedly play an important role in the mechanisms of transient growth of such flows because the modes resulting from the P and S branch in the one-dimensional case play a considerable part in the transient growth of the disturbances. However this study has shown, in spite of a powerful numerical method, that the convergence of the complete spectrum (in a rather broad field in ω) is not easily realizable, in particular in the vicinity of the P and S branches to make it usable in a transient growth study. An improvement of the numerical methods must be carried out.

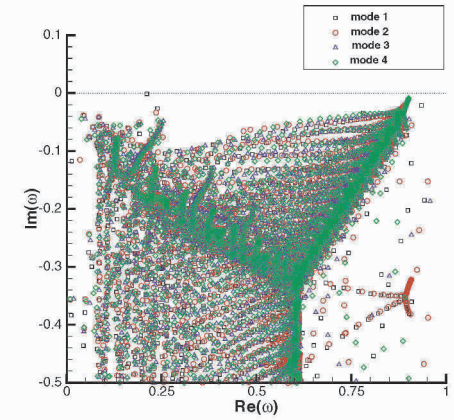

Figure 1. Complete spectrum of linear stability for a Poiseuille flow in a rectangular duct of aspect ratio $A = 5$. Grid (65×51), $R_e = 10400$ and $\beta = 0.91$

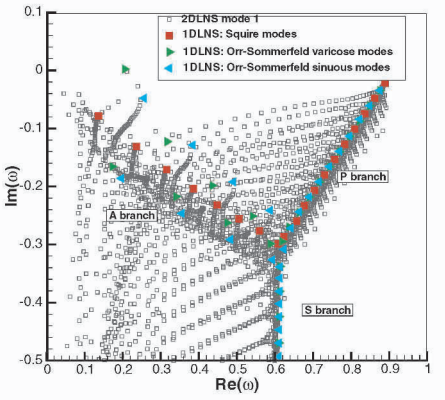

Figure 2. Poiseuille flow. Superposition of the linear stability spectra : ○ 1D and □ 2D (mode 1). Aspect ratio $A = 5$. Grid (65×51) for 2D spectrum. $R_e = 10400$ and $\beta = 0.91$

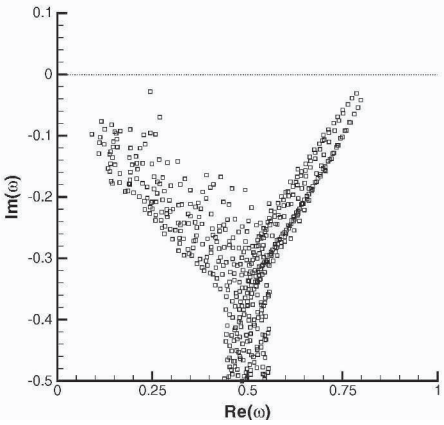

Figure 3. Discretized linear stability spectrum for aspect ratio $A = 2$, grid (65×51), $R_e = 10400$ and $\beta = 0.91$

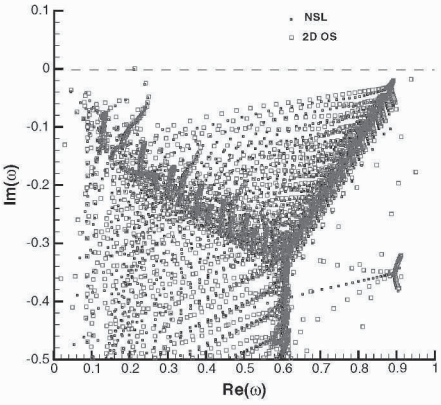

Figure 4. Poiseuille spectra (mode 1) obtained with different formulation of the equations of motion. □ : 2DOS; ○ : 2DLNS. Grids (65×51). $A = 5$, $R_e = 10400$ and $\beta = 0.91$

REFERENCES

Butler, K. M. and Farrell, B. F. (1992). Three-dimensional optimal perturbations in viscous shear flow. *Phys. Fluids*, A(4):1637–1650.

S. C. Reddy, P. J. S. and Henningson, D. S. (1993). Pseudospectra of the orr-sommerfeld operator. *SIAM J. Appl. Math.*, 53:15–47.

Tatsumi, T. and Yoshimura, T. (1990). Stability of the laminar flow in a rectangular duct. *Journal of Fluid Mechanics*, 212:437–449.

Theofilis, V. (1998). Linear instability analysis in two spatial dimensions. ECCOMAS98, John Wiley & Sons, Ltd.

Theofilis, V. (2000). On the spatial structure of global linear instabilities and their experimental identification. *Aerosp. Sci. Technol.*, 4:249–262.

Theofilis, V. (2003). Advances in global linear instability analysis of nonparallel and three-dimensional flows. *Progress in Aerospace Sciences*, 39:249–315.

Theofilis, V., Hein, S., and Dallmann, U. (2000). On the origin of unsteadiness and three-dimensionality in a laminar separation bubble. *Phil. Trans. R. Lond. A*, 358:3229–3246.

INSTABILITY OF FLOW PAST A CASCADE OF CIRCULAR CYLINDERS

J.S.B. Gajjar
School of Mathematics,
University of Manchester, Oxford Road, Manchester M13 9PL, U.K.
gajjar@manchester.ac.uk

Keywords: Stability, Cylinder, Navier-Stokes.

1. INTRODUCTION

The unsteady dynamics of laminar separation bubbles such as those arising in bluff body flows, or behind obstacles, is of considerable practical interest. Bubble formation near the leading edge of an aerofoil can dramatically alter the characteristics of the flow over the wing and induce stall. Similarly, laminar separation near the trailing edge of an aerofoil and instability of the separation bubble can influence the dynamics of the wake flow. The flow past a row bluff bodies placed in a uniform stream, is often used to model engine inlet flows, and thus an understanding of the unsteady dynamics of the eddies which form behind the bluff bodies and the unsteady development of the wake flow is useful in predicting the flow impinging on subsequent rotor blades.

There have been a number of recent studies aimed at investigating the instability of bubbles and wakes by using an idealised model for the mean flow. For example, in [1] a family of modified Falkner-Skan profiles is used to generate velocity profiles containing regions of reverse flow and the linear stability of these model profiles is then examined using the Orr-Sommerfeld equation. Based on their findings, Hammond and Redekopp [1] suggest that the flow in a separation bubble will be absolutely unstable and likely to trigger a global mode instability if the the extent of the reverse flow within the bubble approaches about 30% of the free stream value. Whilst such conclusions are interesting, as the authors point out, their analysis is based on the parallel flow assumption. The mean flow in a separation bubble is highly non-uniform and cannot be taken as being non-parallel. Work by Davies & Carpenter[2] have

R. Govindarajan (ed.), Sixth IUTAM Symposium on Laminar-Turbulent Transition, 189–194.

shown that in rotating disk flow, the inclusion of non-parallel terms can give rise to different conclusions as to whether a flow is absolutely or convectively uunstable.

Numerical simulations of separation bubbles in a boundary layer by Alam & Sandham [3] also conclude that a considerable region of reverse flow is required for the flow in the bubble region to be absolutely unstable. In this work, the linear stability analysis is based on the Orr-Sommerfeld equation with a model velocity profile fitted to the numerically generated data. Again, the highly non-parallel nature of the mean flow raises serious questions about the validity of the stability analysis employed.

In the experimental work of [4, 5] the flow past a flat plate placed normal to an oncoming uniform flow, and with a splitter plate aligned with the flow direction, is studied. Hudy & Naguib [4] suggest that under certain conditions, an absolute instability associated with the flow in the middle of the separation region may be responsible for the low frequency 'flapping' of the shear layer.

Recently Castro [6] has looked at the stability of the wake flow generated by a row of flat plates placed normal to the oncoming stream. Computations of the unsteady Navier-Stokes equations indicate a global instability, and the conclusions are further supported by linear Orr-Sommerfeld stability calculations of model velocity profiles fitted to the numerical data. Whilst the latter stability analysis is questionable, the numerical evidence from the time integrated Navier-Stokes equations is more convincing.

In the present study we consider an infinite row of circular cylinders placed in a uniform stream. The techniques that we have adopted to study the instability involve solving the two-dimensional eigenvalue problem, as in Cliffe & Tavener [7]. Once the mean flow is computed, the stability analysis is conducted by looking for perturbations proportional to $e^{-\beta t}$, where β is a complex frequency, and t is non-dimensional time. This leads to the solution of a generalised eigenvalue problem.

In what follows, we describe the problem formulation and give brief details of the numerical method. Some sample mean flow results are discussed. The results of the stabilty problem were felt to be too preliminary to include and will be published later when fully tested and validated.

2. PROBLEM FORMULATION AND NUMERICAL TECHNIQUES EMPLOYED

Consider an infinite row of cylinders placed in a uniform stream with U_∞ in the $x-$direction. The centre of the cylinders lie on the $y-$axis at $x = 0$, see figure 1.

We consider the unsteady Navier-Stokes equations, with lengthscales nondimensionalised with respect to the cylinder radius, and velocities with U_∞. The

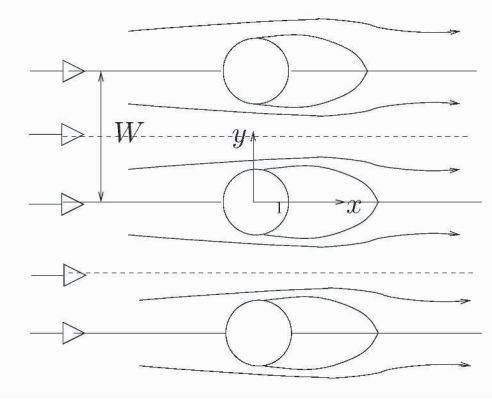

Figure 1. Sketch of flow past a cascade of circular cylinder

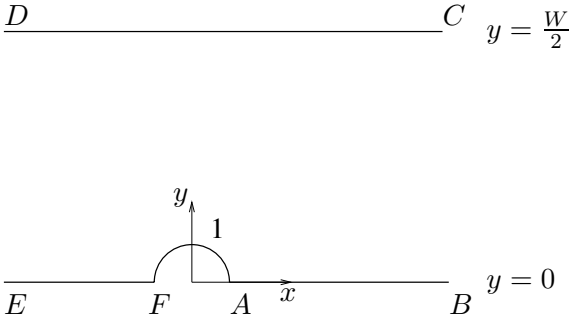

Figure 2. Sketch of the physical domain

equations written in streamfunction-vorticty formulation are:

$$\omega_t + \psi_y \omega_x - \psi_x \omega_y = \frac{2}{R}\nabla^2 \omega, \tag{1}$$

$$\nabla^2 \psi + \omega = 0. \tag{2}$$

Here ψ is the streamfunction, ω the vorticity, and $R = Ud/v$, where U is the uniform speed relative to the cylinder at large distances from the cylinder, d the diameter of the cylinder and v is the kinematic viscosity of the fluid, and t is non-dimensional time. With refernce to figure 1, the non-dimensional gap width between the cylinders is W.

Let $\psi_B(x, y)$, $\omega_B(x, y)$ denote the steady mean flow. In computing the mean flow, we exploit the symmetry in the problem by computing only in the region as shown in figure 2.

Perturbations to the mean flow are introduced as follows with

$$\psi(x,y,t) = \psi_B(x,y) + e^{-\beta t}\tilde{\psi}(x,y), \quad \omega(x,y,t) = \omega_B(x,y) + e^{-\beta t}\tilde{\omega}(x,y) \tag{3}$$

and after substituting into (1,2) we linearise for small pertubations $\tilde{\psi}, \tilde{\omega}$. The perturbation equations are linearised using the same techniques as used for computing the mean flow with high-order finite differences in the $x-$direction and chebychev collocation in the other direction. For further details of the computation of the mean flow, see [8]. Finally the resulting eigenvalue problem for determining β is of the form

$$\mathbf{Az} = \beta\mathbf{Bz}. \tag{4}$$

This is the generalised eigenvalue problem. The eigenvalue problem here is not dissimilar to that arising in other contexts such as in the finite Taylor problem for the flow in the annular region between two concentric cylinders. Methods for the solution of (4) are discussed in Cliffe *et al.* [9], and we have adopted similar procedures. The main objective is to determine the eigenvalue spectrum for β with the two parameters, the Reynolds number R and gap-width W. Standard results demonstrate that the basic flow is stable if $Re(\beta) > 0$ for all eigenvalues of (4). We are particularly interested in determining what happens to the eigenvalues when the parameters change leading to loss of stability when a real eigenvalue crosses the imaginary axis, or when a complex conjugate pair crosses the imaginary axis leading to a Hopf bifurcation.

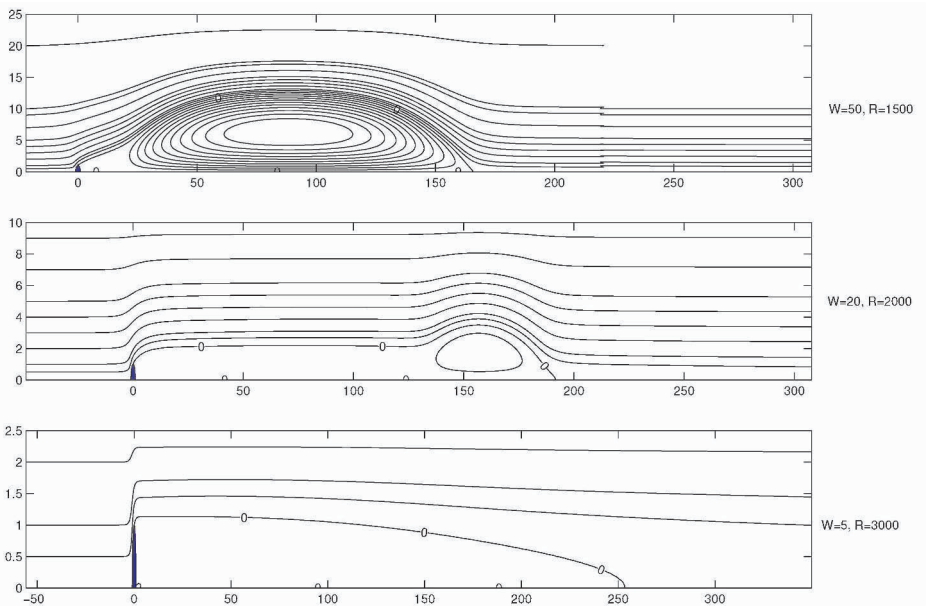

Figure 3. Contours of the stream function for gap widths $W = 5, 20$ and 50 at selected values of the Reynolds number

3. RESULTS

The results for the steady flow have been extensively discussed in Gajjar & Nazzam [8]. The solution properties can be categorised into three distinct types, depending mainly on value of the gap width W between the cylinders. For small values of the gap width the flow which develops in the wake is of boundary layer type with a long eddy forming behind the cylinder, see figure 3, with the vorticity being non-uniform in the eddy region. For moderate gap widths the solution properties change dramatically particularly near the reattachment region. The solution, see figures 3,4, comprise a long thin eddy followed by a much shorter fatter eddy near reattachment. The vorticity in the eddy near reattachment is uniform suggesting that the eddy is dominated by inviscid dynamics. Finally for large gap widths the flow in the wake is dominated by a very large eddy which initially grows linearly in size with increasing Reynolds numbers. For very large Reynolds numbers the eddy width eventually reaches some limiting value, although the length of the eddy is still linearly proportional to the Reynolds number, see figure 5.

Further comments and comparisons of the results with previous numerical and theoretical work for the steady flow is extensively documented in [8].

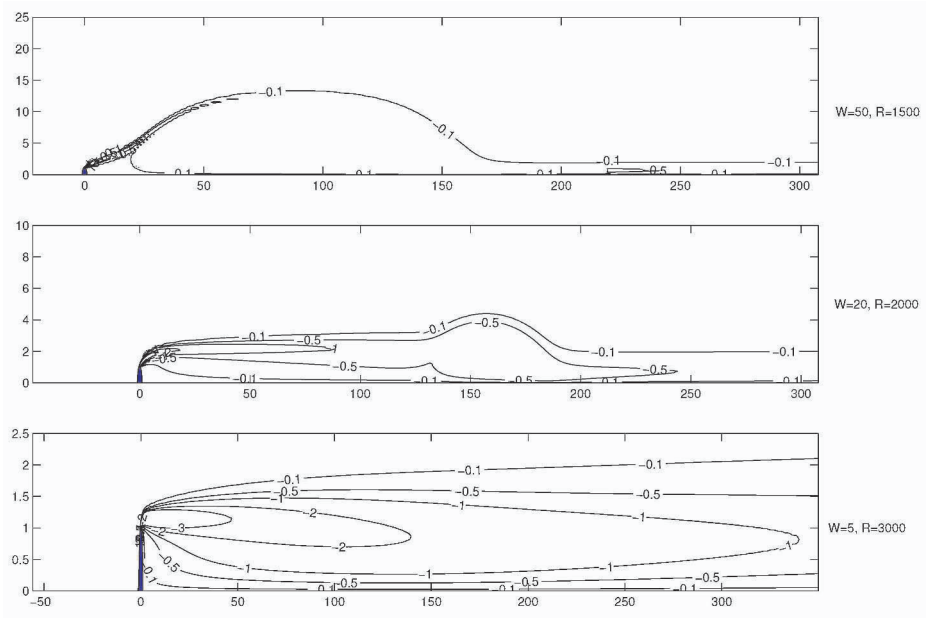

Figure 4. Contours of the vorticity function for gap widths $W = 5, 20$ and 50 at selected values of the Reynolds number

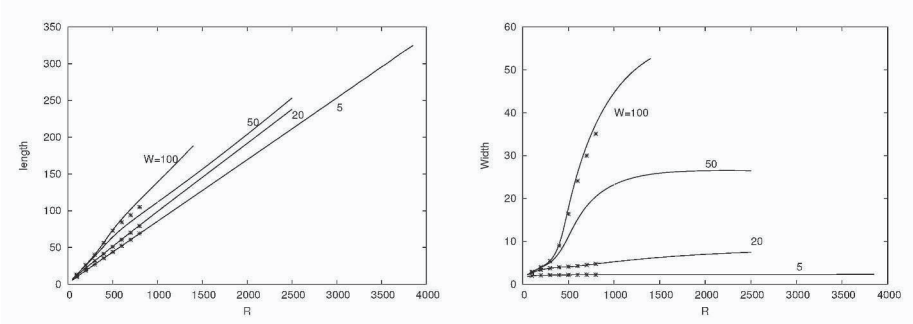

Figure 5. A plot of the eddy length and eddy width versus Reynolds number R for gap widths of $W = 5, 20, 50, 100$. The symbols represent the data points of Fornberg [10]

[8] Gajjar, J.S.B. and Azzam, N., (2004). *"Numerical solution of the Navier-Stokes equations for the flow in a cylinder cascade,"* J.Fluid Mech., **520**, 51-82.

[9] Cliffe, K.A., Garratt, T.J. and Spence, A., (1993). *"Eigenvalues of the discretised Navier-Stokes equations with application to the detection of Hopf bifurcations,"* Adv. Comp. Maths, **1**, 337-356.

[10] Fornberg, B., (1991). *"Steady Incompressible Flow Past a Row of Circular Cylinders",* J. Fluid Mech., **225**, 655-671.

Finally concering the stability of the flow, our results are still at a preliminary stage and therefore not discussed here.

The author is grateful to the Royal Society of London for a travel grant to enable him to attend the meeting.

REFERENCES

[1] Hammond, D.A. and Redekopp, L.G. (1998). *"Local and global instability properties of separation bubbles,"* Eur. J. Mech. B/Fluids, **17**. 145-164.

[2] Davies, C. and Carpenter, P.W., (2003). *"Global behaviour corresponding to the absolute instability of the rotating disc boundary layer",* J. Fluid Mech., **486**, 287-329.

[3] Alam, M. and Sandham, N.D., (2000). *"Direct numerical simulation of 'short' laminar separation bubbles with turbulent reattachment,"* J. Fluid Mech., **410**, 1-28.

[4] Hudy, L.M. and Naguib, A.M., (2003). *"Wall-pressure measurements beneath a separating/reattaching flow region,"* Phy. Fluids, **15(3)**, 706-717.

[5] Cherry, N.J., Hillier, R. and Latour, M.P., (1984). *"Unsteady measurements in a separated and reattaching flow,"* J. Fluid Mech., **144**, 13.

[6] Castro, I.P, (2004). *"Stability of separated wakes,"* submitted to J. Fluid Mech.

[7] Cliffe, K.A., and Tavener S.J., (2004). *"The effect of cylinder rotation and blockage ratios on the onset of periodic flows,"*, J. Fluid Mech., **501**, 125-133.

A WAVE DRIVER THEORY FOR VORTICAL WAVES PROPAGATING ACROSS JUNCTIONS BETWEEN RIGID AND COMPLIANT WALLS

P.K. Sen, P.W. Carpenter[1], S. Hegde and C. Davies[2]
Department of Applied Mechanics, IIT Delhi, New Delhi-110016

[1] *School of Engineering,University of Warwick, Coventry CV4 7AL, UK*

[2] *School of Mathematics, Cardiff University, Cardiff CF24 4YH, UK*

Abstract: A novel theoretical method is presented based on the theory of adjoints for analyzing the behaviour of Tollimein - Schlichting waves and other wall-based waves incident on junctions between rigid and compliant walls.

Keywords: Wave driver, jump conditions, compliant wall, vortical wave, cutoff frequency

1. INTRODUCTION

We present a novel method for analyzing and understanding a class of receptivity problems. The method is believed to have general applicability, but it is applied to a specific problem investigated by Davies and Carpenter [1] using direct numerical simulation, namely, the behavior of Tollimien - Schlichting waves propagating in plane Poiseuille flow and incident on a junction between rigid and compliant walls. This is illustrated in figure 1. Previous unsuccessful attempts at solving this receptivity problem are reviewed in [2]. The practical motivation for Davies and Carpenter was the proposal that transition could be postponed to indefinitely high Reynolds number by designing a wall consisting of a series of alternate rigid and compliant panels, each tailored to local flow conditions. According to conventional stability theory, the growth of Tollimien - Schlichting waves could be suppressed along the entire length of the compliant wall. The question of the effect of the junctions at the leading and trailing edges of the panels on the Tollimien - Schlichting waves was both an obvious and a practical one. The present paper adresses this question.

R. Govindarajan (ed.), Sixth IUTAM Symposium on Laminar-Turbulent Transition, 195–200.

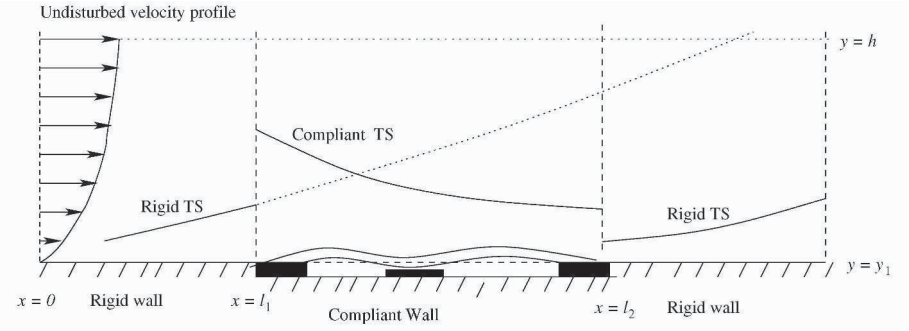

Figure 1. Schematic of case below cut-off

2. FORMULATION OF THE WAVE DRIVER

A two dimensional parallel flow is being considered here. A disturbance stream function $\psi(x, y, t)$ can be defined. The governing equation is obtained from the linearized Navier-Stokes equation in vorticity ($\nabla^2\psi$) form, in terms of ψ, expressed as $\psi(x, y, t) = f(x, y)e^{-i\omega t}$. Here, $f(x, y)$ is the amplitude function of normal modes. For the sake of distinguishing the rigid and compliant sides, the function $f(x, y)$ is defined in two halves: $f(x', y) = H(-x')f_u(x', y) + H(x')f_d(x', y)$, where, $H(x)$ is the Heaviside step function. Also, the suffixes u and d denote the rigid-side (upstream) and the compliant-side (downstream) amplitude functions respectively. The junction region is very narrow compared with the wave-length of the incident TS wave. Thus these pair of functions can be written in the following form:

$$f_u(x', y) = \mathcal{R}[\underbrace{\phi_u(y)\mathrm{e}^{-i\alpha_u x'}}_{\text{far field}} + \underbrace{f_{nu}(\xi, y)}_{\text{near field}}] \quad : \quad x' < 0; \qquad (1a)$$

$$f_d(x', y) = \mathcal{R}[\underbrace{\lambda\phi_d(y)\mathrm{e}^{-i\alpha_d x'}}_{\text{far field}} + \underbrace{f_{nd}(\xi, y)}_{\text{near field}}] \quad : \quad x' > 0, \qquad (1b)$$

where in (1a,b), ϕ_u and ϕ_d are suitably normaslised, and λ in (1b) is the jump in amplitude. Substituting the stream function as defined above in the linearsied Navier-Stokes equation yields the operative differential equation for the problem:

$$-i\omega(\nabla^2 f) + \bar{u}\frac{\partial}{\partial x}(\nabla^2 f) - \bar{u}''\frac{\partial f}{\partial x} - \frac{1}{R}\nabla^4 f = 0 \; . \qquad (2)$$

Half-range Fourier transforms in the wave number α, are now defined for $f(x,y)$, again in two halves, on either side of the junction.

$$F_u(y,\alpha) = \int_{-\infty}^{0} f_u(x',y)e^{-i\alpha x'}dx' \; ; \tag{3a}$$

$$F_d(y,\alpha) = \int_{0}^{+\infty} f_d(x',y)e^{-i\alpha x'}dx' \; . \tag{3b}$$

Taking the half-range Fourier transforms of the operative differential equation (2), and making an order of magnitude analysis on each term, we obtain the following pair of equations

$$L(\alpha)F_{u,d} = \pm\bar{u}\Big\{\cdots + + \underbrace{\Big(\frac{\partial^2 f_{u,d}}{\partial x^2}\Big)}_{O(1/\epsilon^2)}\Big\} \mp h.o.t \tag{4a,b}$$

where $h.o.t$ means higher order terms, and $L(\alpha)$ is the linear Orr-Sommerfeld operator, namely

$$L(\alpha)F \;=\; i(\alpha\bar{u}-\omega)(F''-\alpha^2F) - i\alpha\bar{u}''F - \frac{1}{R}(F^{iv}-2\alpha^2F''+\alpha^4F) \; . \tag{5}$$

We assume that the pair of functins $f_{u,d}$ to be the same in the near field of $x'=0$. Further it can be shown that the width of the near field at the junction is $O(\epsilon^{-2})$ leading to $\frac{\partial^2 f_{u,d}}{\partial x^2} \sim O(\epsilon^{-2})$. Moreover, it can also be shown that $(\frac{\partial^2 f_{u,d}}{\partial x^2})_{x'=0}$ is independent of y and can be expressed as $(\frac{\partial^2 f_{u,d}}{\partial x^2})_{x'=0} = C$, where C is a constant. C is thus a measure of the vorticity of the virtual wave driver created at the junction. Hence the upstream and the downstream equations are given respectively as,

$$L(\alpha_r)F_u = \bar{u}C; \tag{6a}$$

$$L(\alpha_c)F_d = -\bar{u}C. \tag{6b}$$

Subscripts r and c refer respectively to rigid and compliant sides. Next we rewrite (6a) as follows,

$$L(\alpha_r)F_u + (\alpha-\alpha_r)L_2(\alpha_r)F_u \;=\; (\overline{u}C - \lambda_r L_2(\alpha_r)\overline{\phi}_r) + \lambda_r L_2(\alpha_r)\overline{\phi}_r \; . \tag{7}$$

We note that λ_r is the amplitude of the wave on the rigid side, $\overline{\phi}_r$ is the normalised rigid wall eigenfunction and α_r is the rigid wall eigenvalue. By choosing $\lambda_r = 1$ for the rigid side, as reference normalization, one actually obtains the value of the strength of the local wave driver. Using the solvability condition of (7) one obtains,

$$C \;=\; \frac{\int_0^1 [L_2(\alpha_r)\overline{\phi}_r]\theta_r dy}{\int_0^1 \theta_r \overline{u} dy} \, , \tag{8}$$

where θ_r is the rigid-side adjoint eigenfunction. A similar consideration for F_d, gives the amplitude for the compliant side as

$$\lambda_c = \frac{C \int_0^1 \theta_c \overline{u} dy}{\int_0^1 [L_2(\alpha_c)\overline{\phi}_c]\theta_c dy} . \tag{9}$$

Straightaway therefore

$$F_u = \frac{\lambda_r}{(\alpha - \alpha_r)} \overline{\phi}_r. \tag{10}$$

Inversion of the half-Fourier transform yields f_u as

$$f_u = \lambda_r \overline{\phi}_r e^{i\alpha_r x}. \tag{11}$$

Identical considerations similarly determine f_d as

$$f_d = \lambda_c \overline{\phi}_c e^{i\alpha_c x} . \tag{12}$$

Now let $\lambda_r = 1$, then λ_c gives the jump.

3. RESULTS AND DISCUSSIONS

We present two cases of results, one corresponding to the below-cutoff frequency of the panel and the other to the above-cutoff frequency when the TS wave propagates across the rigid-compliant junction. Wall vorticity is plotted for the below cutoff case in figure 2. We notice the jumps at both the leading edge and the trailing edge of the compliant panel. The results are in good agreement with Davies and Carpenter (1997)

Next, the wall vorticity of a long panel is shown for the above-cutoff case in figure 3. The case above cutoff has, on the compliant side, a non-vortical long wave, the compliant side TS wave, and an upstream travelling vortical mode. The complete wave system on the compliant side is obtained by matching the boundary conditions at the leading and trailing edge junctions. The bottom plot is from the Davies and Carpenter (1997) numerical simulations. There are actually two set of waves corresponding to two different lengths of the panel. Figure 4 shows the TS component for figure 3. We notice that the TS wave has decayed totally at the trailing edge. But there is a downstream TS wave. This is possible because the vortical wave combined with the (residual) TS wave is able to excite the trailing edge junction to create a wave driver there. This wave driver is formed even if the compliant TS wave has decayed to zero at the trailing edge. This wave driver generates the downstream TS wave. The virtual wave drivers at the leading and trailing edge are thus vortical wave drivers.

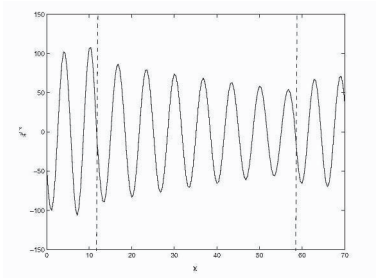

Figure 2. Wall vorticity ω_w for the case below cutoff. Junctions are at: $x = x_1 = 12$ and $x = x_2 = 48$

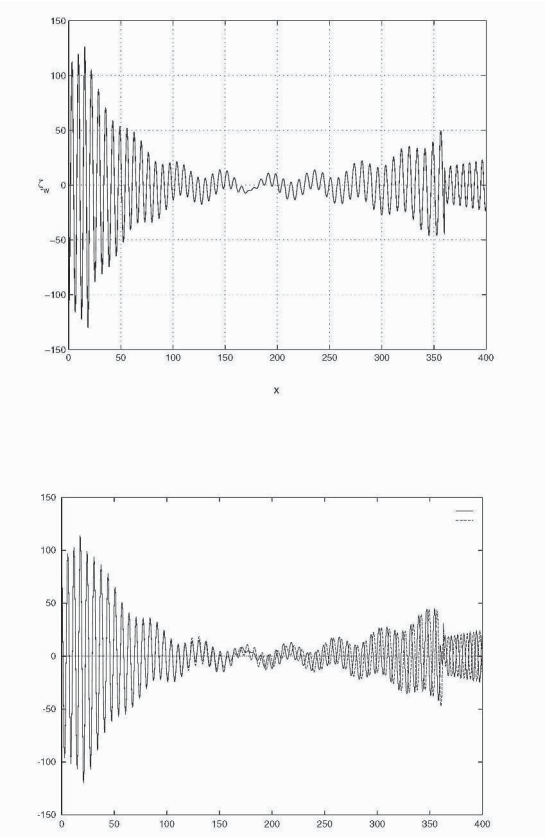

Figure 3. Comparison of wall vorticity plots for the case of a long panel. The length, $L = 340$. Junctions are at: $x = x_1 = 20$ and $x = x_2 = 360$ (a) Top: Present results (b)Bottom: Corresponding results from Davis and Carpenter simulation program

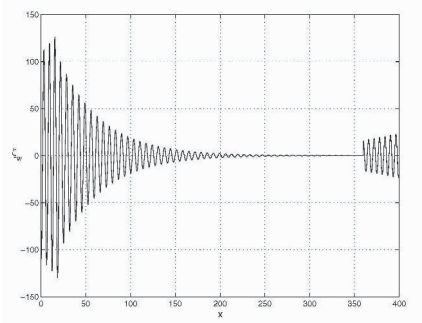

Figure 4. Tollmien-Schlichting component in figure 3; junctions are at: $x = x_1 = 20$ and $x = x_2 = 360$

REFERENCES

1. Carpenter, P.W., Davies, C. & Lucey, A.D. 2000, Hydrodynamics and compliant walls: Does the dolphin have a secret? *Current Science* **79**, 758-765.
2. Carpenter, P.W. & Garrad, A.D. 1985, The hydrodynamic stability of flow over Kramer-type compliant surfaces. Part 1. Tollmien-Schlichting instabilities. *J. Fluid Mech.* **155**, 465-510.
3. Davies, C. & Carpenter, P.W. 1997, Numerical simulation of the evolution of Tollmien-Schlichting waves over finite compliant panels. *J. Fluid Mech.* **335**, 361-392.
4. Carpenter, P. W., Davies, C. and Lucey, A. D., 2000, Hydrodynamics and compliant walls: Does the dolphin have a secret?, Current Science., vol. 79 No. 6, pp. 758-765.
5. Hegde, S.,2002,Study of Small Disturbance Waves Across Alternate Rigid and Compliant Panels, with Analytical Jump Conditions at the Junction, PhD Thesis, Dept. of App. Mech, IIT Delhi, India.
6. Carpenter, P. W., Sen, P. K. Hegde, S., and Davies, C., 2002, Wave propagation in flows across junctions between rigid and flexible walls, Proc. of 5th Int. Symposium of FSI, AE & FIV+N: 2002 ASME Int. Mech. Engg. Congress & Exposition, New Orleans.
7. Sen, P. K., Arora, D. S., 1988 On the stability of laminar Boundary layer flow over a flat plate, J. Fluid Mech., **197**, pp. 201-240.

OPTIMAL SUCTION DESIGN FOR HYBRID LAMINAR FLOW CONTROL

Jan O. Pralits,[1] Ardeshir Hanifi [2]

[1]*DIMEC, Universita di Salerno,*
84084 Fisciano (SA), Italy
jan.pralits@foi.se

[2]*Swedish Defence Research Agency, FOI, Aeronautics Division, FFA,*
SE-172 90 Stockholm, Sweden
ardeshir.hanifi@foi.se

Abstract: We present a theory for computing the optimal steady suction distribution in order to minimize the growth of convectively unstable disturbances, and thus delay laminar-turbulent transition on swept wings. Here, we use the optimal control theory and minimize an objective function based on a sum of the kinetic energy of an arbitrary number of disturbances. The optimization procedure is gradient-based where the gradients are obtained using the adjoint of the parabolized stability equations and the adjoint of the boundary layer equations. Results are presented for an air foil designed for medium range commercial air crafts.

Keywords: HLFC, flow control, optimal suction, Tollmien-Schlichting, PSE, adjoint

1. INTRODUCTION

The stabilization effect of steady boundary layer suction on disturbance growth has been known for a long time, see Schlichting, 1943, and has been utilized for laminar flow control, for an extensive review see Joslin, 1998. However, in most cases the design of suction distributions rely on the experiences of the engineers which may not always give the optimal solution, i.e. giving the largest delay of laminar-turbulence transition for a given suction power. In the recent decade, the development of optimal control theory applied in ßuid mechanics problems has been rapid and a number of attempts have been made to optimize the steady suction distribution in order to control growth of disturbances Airiau et al., 2003, Balakumar and Hall, 1999, Cathalifaud and

R. Govindarajan (ed.), Sixth IUTAM Symposium on Laminar-Turbulent Transition, 201–206.

Luchini, 2000, Pralits et al., 2002 . In all of these investigations the optimization methods are gradient based and they utilize the potential of adjoint methods to obtain the gradients of interest. A common approach is to minimize some measure of the disturbance growth, either the disturbance kinetic energy or the so called N-factor. In real applications the steady boundary-layer suction is usually done through a number of discrete pressure chambers, see e.g. Atkin, 2000, Bieler and Preist, 1992, Joslin, 1998. The suction velocity is then a function of the surface porosity, hole geometry and the pressure difference between the pressure distribution on the wing and static pressure in the chambers. In this case, the size and position of the boxes, and the internal static pressure of each box are the design variables, and the suction distribution is given by the specific choice of these parameters.

2. PROBLEM FORMULATION

We assume the laminar-turbulence transition is caused by breakdown of convectively unstable disturbances inside the boundary layer. Our aim is to Þnd the distribution of wall-suction such that the growth of these disturbances is minimized. We formulate the problem using the optimal control theory, where a suitable objective function is to be minimized. Here, we choose the objective function to be an integral of the disturbance kinetic energy defined as

$$E = \sum_{k=1}^{M} \frac{1}{2} \int_{X_0}^{X_1} \int_{Z_0}^{Z_1} \int_{0}^{+\infty} |\mathbf{u}|_k^2 h_1 dx^3 dx^2 dx^1,$$

where, x^1, x^2 and x^3 are streamwise, spanwise and normal coordinates, respectively, and h_1 the scale factor. Notice that E is given as the sum over M different disturbances. The reason for considering more than one disturbance is to ensure that all types of disturbances present in the boundary layer are controlled, see Pralits et al., 2002. The optimization procedure used here is a gradient-based method. An efÞcient way of calculating the gradient of the objective function, when the number of control parameters is large, is to solve the adjoint of the governing equations. Here, the mean flow is given as the solution of the boundary-layer equations for an infinite long swept wing. The evolution of convective disturbances inside the boundary-layer is modeled by the parabolized stability equations (PSE), see e.g. Bertolotti et al., 1992.

We consider two different control scenarios. In the first, the mass ßux on the wall $\dot{m}_{\mathrm{w}} = W_{\mathrm{w}} \rho_{\mathrm{w}}$ is optimized in a continuous control domain $\Gamma_c = [X_{cs}, X_{ce}]$. Here, W is the normal velocity, ρ the density and subscript $_{\mathrm{w}}$ refers to values at the wall. In the second, we consider the available control domain divided into K pressure chambers such that $\Gamma_c = [X_{cs_j}, X_{ce_j}]$, $j = 1 \cdots, K$. Each chamber has a fixed length and position and a variable static pressure. The corresponding suction profile in each domain $[X_{cs_j}, X_{ce_j}]$ is then obtained

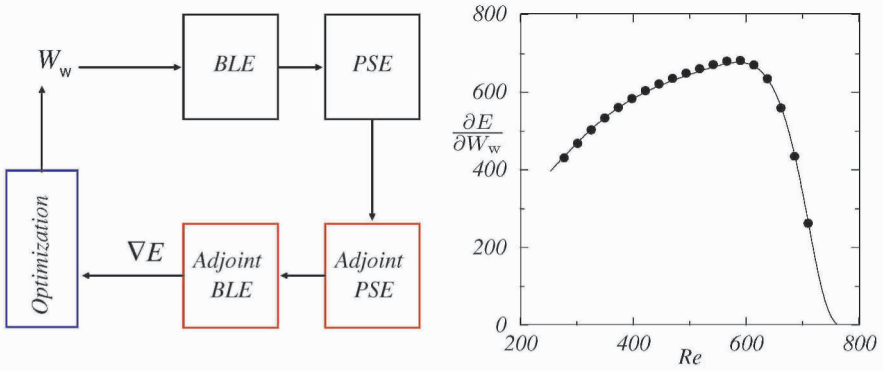

Figure 1. Left: Schematic of the optimization procedure for suction distribution. Right: Comparison of calculated derivatives of disturbance energy using Þnite differences and adjoint method. Blasius boundary layer, $F = 10^{-4}$, $\beta = 0$, from Pralits et al., 2002

from the following relation

$$\Delta P_j = P_e - P_{c_j} = \frac{C_1}{\rho_w}\dot{m}_w^2 + C_2\frac{\mu_w}{\rho_w}\dot{m}_w,$$

as given in Bieler and Preist, 1992. Here, P_e is the pressure distribution on the wing and P_{c_j} the static pressure in chamber number j and μ_w the dynamic viscosity at the wall. The coefficients C_1 and C_2 depend on porosity of surface and hole geometry, see Pralits and Hanifi, 2003. In this case the static pressure of each box is optimized. The control effort, which is directly related to the power of the suction system, is quantified by the control energy

$$E_C = \int_{X_{cs}}^{X_{ce}} \dot{m}_w^2 h_1 dx^1.$$

As mentioned before, the solution of the adjoint boundary layer equations, when appropriate initial and boundary conditions are used, gives the desired gradient of the objective function with respect to the mean flow quantities. Instead, its gradient w.r.t. mean mass flow at the wall is given as, see Pralits and Hanifi, 2003,

$$\frac{\partial E}{\partial \dot{m}_w} = W_w^*, \qquad \frac{\partial E}{\partial P_{c_j}} = -\int_{\Gamma_j} W_w^* \frac{\partial \dot{m}_w}{\partial P_{c_j}}\, h_1\, dx^1.$$

where W^* is the Lagrangian multiplier of the mean continuity equation. For derivation of the adjoint equations see Pralits and Hanifi, 2003. In Figure 1 (left) a schematic of design procedure for optimal suction distribution is given. In Figure 1 (right) the derivative of the objective function, as a function of the streamwise position, calculated using the adjoint technique and finite differences, are compared. As can be seen there the agreement is excellent.

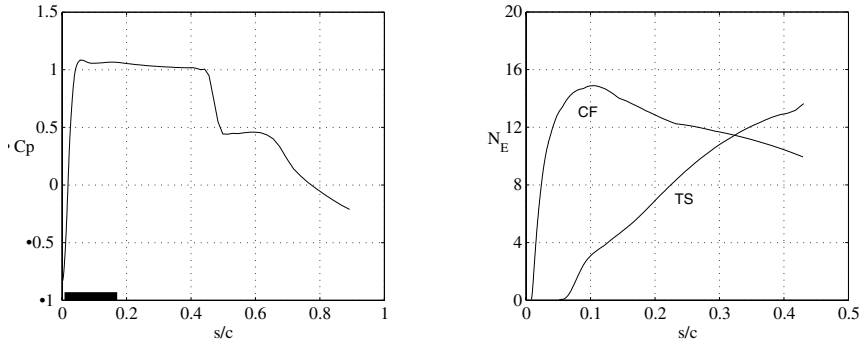

Figure 2. Left: Pressure distribution, C_p, as a function of the arc-length normal to the leading edge, s/c. The black box shows the domain available for suction systems, Γ_c. Right: EoE of N_E-factor curves for Tollmien-Schlichting (TS) and cross-ßow (CF) waves for zero suction

3. RESULTS

The flow studied here is the boundary layer on the upper side of a wing designed for commercial air crafts, see Figure 2. The flow conditions are characterized by a free-stream Mach number $M_\infty = 0.8$, temperature $T_\infty = 230$ K, Reynolds number $Re_\infty = 3.04 \times 10^7$ and the leading edge sweep angle $\phi_{le} = 30.2°$. The pressure distribution of an air foil designed for commercial air crafts can be seen in Figure 2 (left) together with a domain, Γ_C, available for mounting the suction system. The envelope of envelopes (EoE) of N-factor curves, based on the disturbance kinetic energy, for cross flow (CF) and Tollmien-Schlichting (TS) waves can be seen in Figure 2 (right).

In the results shown here, the total disturbance kinetic energy is calculated as the sum of the CF and TS wave with the largest disturbance kinetic energy over a large number of other disturbances. The dimensional frequency and spanwise wave number for these CF and TS waves are ($f_1^* = 5500\ s^{-1}$, $\beta_1^* = 2500\ m^{-1}$) and ($f_2^* = 5750\ s^{-1}$, $\beta_2^* = 225\ m^{-1}$) respectively. In these calculations, the magnitude of the control effort is $E_C = 0.35 Re_\infty^{-1}$. In Figure 3 (left), the optimal static pressures of the chambers (thick lines) are plotted for the cases of 5, 6 and 7 pressure chambers together with the pressure distribution P_e of the wing (thin lines). To show the details, the region s/c=[0.05,0.175] has been magnified. As it is shown there, the pressure drop $\Delta P_j = P_e - P_{c_j}$ is larger close to the leading edge and decreases downstream.

The suction distributions corresponding to the optimal static pressure in Figure 3 (left) are plotted in Figure 3 (right). Note that the uppermost streamwise suction distribution in each case is due to a stagnation line control and is taken to be fixed. For each case in Figure 3 (right), a comparison is done with a

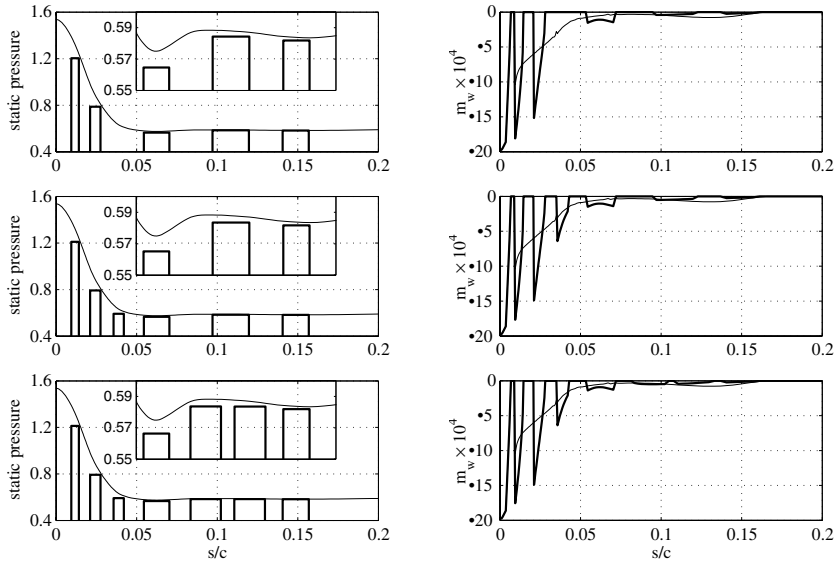

Figure 3. Left: Pressure distribution on the wing (thin lines) and optimal static pressure in the chambers (thick lines) for the cases of 5, 6 and 7 pressure chambers minimizing the disturbance kinetic energy for dominating CF and TS wave with $E_C = 0.35 Re_\infty^{-1}$. Right: Corresponding suction distributions (thick lines). A comparison is done with a suction distribution (thin lines) obtained by optimizing $\dot{m}_\mathrm{w}$ in a continuous control domain

suction distribution obtained by optimizing $\dot{m}_\mathrm{w}$ (thin lines) in a continuous domain. As the same control effort is used in these calculations, a direct comparison of the optimal suction distributions for these cases is possible. It is seen that the distribution using pressure chambers approaches the continuous one when the number of chambers is increased. This is most evident downstream of $s/c = 0.05$.

The effect on the disturbance growth using the optimal chamber pressures for the cases of 5, 6 and 7 pressure chambers is shown in Figure 4 (left). Here the EoE of the N_E-factor curves for CF and TS waves are plotted for zero and optimal chamber pressures of all cases (solid lines). The arrows mark increasing number of pressure chambers. A decrease in both the growth of CF and TS waves is obtained in all cases using the optimal chamber pressures calculated here compared to zero control. A comparison is done with EoE of the N_E-factor curves which are calculated using the suction distribution obtained by optimizing $\dot{m}_\mathrm{w}$ in Figure 3 (right) (dashed lines). It is seen that as the number of pressure chambers are increased, the results within the control domain using pressure chambers approach those using a suction distribution in a continuous control domain. The relatively small effect on the mean flow for the cases in

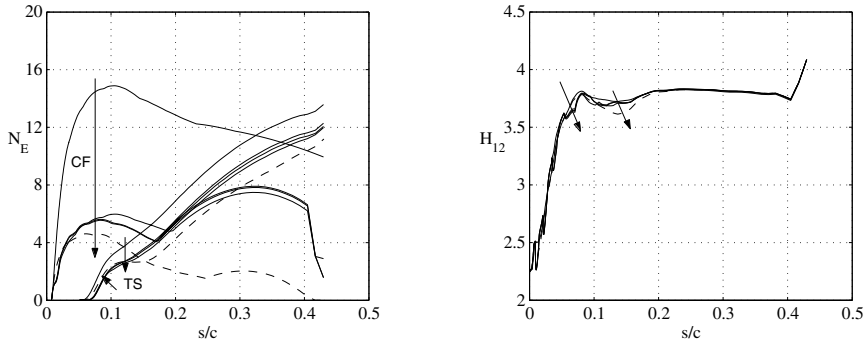

Figure 4. Left: EoE of N_E-factor curves (solid lines) for CF and TS waves for zero control and the pressure chambers in Þgure 3. Arrows mark increasing number of chambers. Comparison with the EoE of N_E-factor curves (dashed lines) given the continuous optimal suction distribution in Figure 3. Right: Corresponding shape factors H_{12}

Figure 4 (left) are shown by the shape factor H_{12} in Figure 4 (right).

The Þnancial support of the EU project (ALTTA contract G4RD-CT-2000-00143) is gratefully acknowledged.

REFERENCES

Airiau, C., Bottaro, A., Walther, S. and Legendre, D., 2003. A methodology for optimal laminar flow control: Application to the damping of Tollmien-Schlichting waves in a boundary layer. *Phys. Fluids*, **15**, pp. 1131 Ð1145.

Atkin, C. (2000). New aerodynamic approach to suction system design. In Thiede, P., editor, *CEAS/DragNet European Drag Reduction Conference*, Potsdam, Germany. Springer.

Balakumar, P. and Hall, P., 1999. Optimum suction distribution for transition prediction. *Theor. Comput. Fluid Dyn.*, **13**, pp. 1Ð19.

Bertolotti, F.P., Herbert, Th. and Spalart, S.P. (1992). Linear and Nonlinear Stability of the Blasius Boundary Layer. *J. Fluid Mech.*, **242**, pp. 441Ð474.

Bieler, H. and Preist, J. (1992). HLFC for commercial aircraft. In *First european forum on laminar flow technology*, pages 193Ð199, Hamburg.

Cathalifaud, P. and Luchini, P., 2000. Algebraic growth in a boundary layer: optimal control by blowing and suction at the wall. *Eur. J. Mech. B/Fluids*, **19**(4), pp. 469Ð490.

Joslin, R. (1998). Overview of laminar ßow control. Technical Report 1998-208705, NASA, Langley Research Center, Hampton, Virginia.

Pralits, J. O. and HaniÞ, A. (2003). Optimization of Steady Suction for Disturbance Control on InÞnite Swept Wings. *Phys. Fluids*, **15**, pp. 2756Ð2772.

Pralits, J. O., HaniÞ, A. and Henningson, D. S. (2002). Adjoint-based optimization of steady suction for disturbance control in incompressible ßows. *J. Fluid Mech.*, 467:129Ð161.

Schlichting, H. (1943). Die beeinßussung der grenzschicht durch absaugung und ausblasen. *Jb. dt. Adad. d. Luftfahrtforschung*, 90-108.

TRANSITION CONTROL IN A FLAT-PLATE BOUNDARY LAYER

Seiichiro Izawa*, Takeshi Sakai*, Ayumu Inasawa*,
Ao-Kui Xiong*, Yu Fukunishi*
*Tohoku University, Sendai, Japan

Abstract: A semi-automatic and active control of T-S waves and oblique waves is performed using an array of piezo-ceramic actuators attached on a flat-plate surface. The actuators generate counter waves to cancel the incoming instability waves. The actuator's operating amplitudes and phases are successively updated using the velocity fluctuations monitored downstream by a rake of hotwires. It is shown that the system could weaken these waves when their sweep angles are less than 15 degrees. However, it has difficulty in controlling the waves of large sweep angles. Through the results from the experiment activating only one actuator, it is shown that the difficulty arises because the wave front of the waves generated by each actuator deforms into an arch.

Keywords: Transition, Boundary Layer, Active Control, Feedback, Piezo Actuator

1. INTRODUCTION

The primary objective of this study is to develop a system that can automatically control T-S waves or oblique waves in a flat-plate boundary layer. These instability waves are cancelled in their linear stages of transition by superimposing the counter waves. Many attempts to generate a wave in a boundary layer have been proposed for the last several decades. A vibrating ribbon attached on a surface [1], periodic heating of thin nichrome films [2], and suction/blowing system [3] are examples of activators for generating the waves in the boundary layer. In the flow controlling attempts, Sturzebecher & Nitsche [4] used the slot system which is all-in-one device including a speaker and a sensor. An open-loop control using an array of PZT actuators was attempted by Fukunishi et al. [5, 6].

On the other hand, in this experiment small and thin piezo-ceramic (PZT) actuators are used as the control device to generate the counter waves against the incoming waves. The actuators aligned in the spanwise direction attached on a flat-plate surface were designed so that they could be operated independently with different amplitudes and phases, allowing the device to generate

R. Govindarajan (ed.), Sixth IUTAM Symposium on Laminar-Turbulent Transition, 207–212.

two dimensional or oblique waves of various angles. The actuator's operating signals are successively updated using the velocity fluctuations monitored downstream by a rake of hotwires. A simple feedback system is applied to the semi-automatic and active control of T-S waves and oblique waves.

2. EXPERIMENTAL SETUP

2.1 Flat Plate and Actuators

The experiments are conducted in the low turbulence wind tunnel at the Institute of Fluid Science of Tohoku University. The wind tunnel is a Göttingen type with an octagonal test section, which is 3,200mm long and 1,010mm from wall-to-wall. The contraction ratio between a settling chamber and a test section is 12:1.

The schematic view of the experimental setup is shown in Fig. 1. A smooth flat plate made of Aluminum alloy, which is 3,200mm long, 1,000mm wide and 10mm thick, is mounted vertically in the middle of the test section. From the leading edge of the plate, Scotch tapes, actuators, and error sensors are attached to its surface. Target waves, either T-S waves or oblique waves, are excited upstream by a combination of Scotch tapes on the surface and an acoustic forcing using a loudspeaker set upstream of the settling chamber. The operating frequency of loudspeaker is 77.8Hz. The sweep angle of generated waves is changed by inclining the tapes. The axes x, y, and z are in the streamwise, wall-normal, and spanwise directions, respectively.

Fig. 2 shows the details of the piezo-ceramic actuators. Each actuator is wired separately so that they can be manipulated independently using a computer. If the tip of an actuator is shifted slightly up or down because it was tilted when attached, it was found that a slight difference in the tilt angle of the actuator, resulting in the minute up or down shift of their tips could lead to large differences in the amplitude of the introduced velocity fluctuations. Thus, additional insulator is inserted between the actuators and the bottom insulator on the surface to make the upper surfaces of all actuators leveled. Both the upstream and downstream ends of the actuators are sloped to prevent separations and high-receptivity at the edges. In the current experiment, six middle pieces (channel 1 though 6) among the twelve pieces of the actuator array is used. A hotwire sensor is installed straight downstream of the center of each activated actuator, about 2mm away from the wall. Reynolds number Re_x at the actuators' position, x = 1,000mm, is 9.9×10^5. The total thickness of each actuator is approximately 0.6mm, which is 13% of the boundary layer thickness at the location. The freestream velocity U_∞ is 14.0m/s and the velocity fluctuation within the freestream is 0.07%.

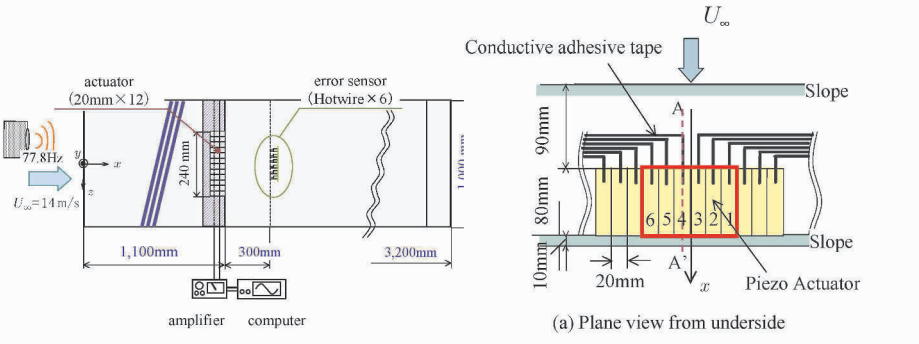

Figure 1. Experimental setup (above)

Figure 2. Piezo-ceramic actuators (right)

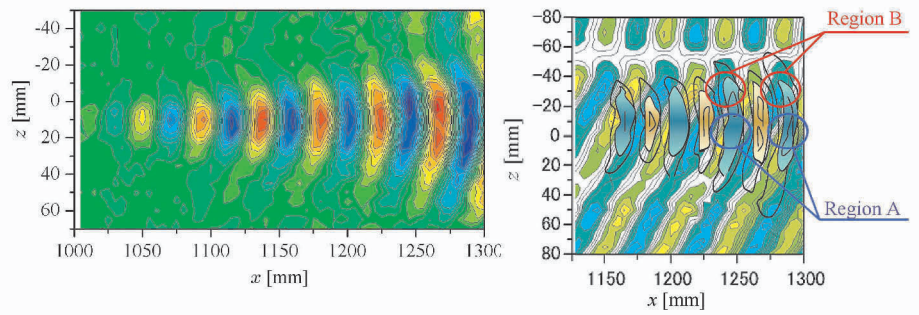

Figure 3. (a) Contour map of velocity fluctuation $<u'>/U_\infty$ in xz plane. at U_∞ = 14m/s and contour interval = $0.01U_\infty$. (b) Overlapping of the original waves and the wave from a single actuator

2.2 Control System

The details of the controlling system are described in this section. A feedback loop system for an active flow control using actuators and error sensors is constructed. First, the sensors capture the velocity fluctuations of the waves generated upstream. Each signal is filtered and stored for three cycles and then, based on the ensemble averaged property of the signal, the operating amplitude and the phase of each actuator is determined and successively updated. The adjustment is performed for only one actuator piece at a time, and the actuators are adjusted in turn. This adjustment process is repeated until the waves are damped to a level lower than a certain criterion.

As a result of the previous experiment, shown in Fig. 3, it was found that the waves' pattern generated by a single actuator located between $z = 0 \sim 20$mm spreads in the spanwise direction as the waves travel downstream, and each wave becomes curved forming an arch. When the amplitude of one actuator is increased in order to cancel the locally concentrated velocity fluctuation spot in downstream, the middle parts of the arches will work to neutralize that concentration (see Region A in Fig. 3(b)). However, because the wave front is curved, one end of the arch will work to enhance the original fluctuation (see Region B in Fig. 3(b)). Due to this phenomenon, the system will end up creating another concentrated velocity fluctuation region next to the region it tried to erase. By taking this effect into account, each adjustment is limited to below 5% of the previous value. Because the influence of one actuator spreads in the spanwise downstream, it is difficult to satisfy the control criteria at the sensors of the spanwise ends. So, six actuators (channel 1 through 6) are adjusted to satisfy the criteria at four inner sensors (channel 2 though 5).

3. RESULTS AND DISCUSSION

Velocity fluctuation waves captured by the downstream sensors for the controlled and non-controlled cases against the T-S wave are shown in Fig. 4. When the velocity fluctuations measured at the two sensors (channel 3 and 4) are reduced for more than 10dB, the control is judged to be a success, and further adjustment is stopped. In this case 97 adjustments are performed. In Fig. 4, it can be found that the velocity fluctuation became much weaker for all sensors. It should be mentioned here that the amplitudes of the waves does not monotonously decrease as the adjustment progresses.

In Fig. 5, the RMS profiles of fluctuating velocity components, measured 250mm downstream from the actuator array is presented. The weakening effect reaches approximately 66% after the 97th adjustment. In the figure, a very high value of RMS can be found near the wall. This comes from a minute and local unevenness of the downstream slope behind the actuator, x = 1,000mm and $z \simeq 0$mm. It is found that this particular slope very slightly moves up and down accompanied by the generated waves, amplifying the waves..

Fig. 6 shows the effect of the active control when the target waves are inclining 15 degrees. The target for this weakening control is set at 6dB, instead of 10dB, because the flow control is more difficult. As well as the T-S wave case, the amplitude of each velocity fluctuation is well suppressed as the result of the control. The weakening effect reached 6dB after the 44th adjustment. The RMS value of the velocity fluctuation at the peak around $\eta = 1.5$, decreased to nearly half as the result of the control, which is shown in Fig. 7.

The control becomes more difficult with the increase in the sweep angle. Fig. 8 shows the control attempt against the oblique waves with a 30 degree

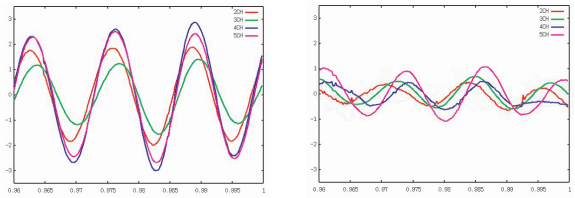

Figure 4. Control effect on velocity fluctuation waves (T-S waves), (a) before and (b) after the 97th adjustment

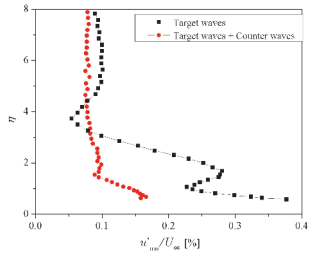

Figure 5. RMS profile of the velocity fluctuation at x = 1,350mm, z = 0mm (T-S waves)

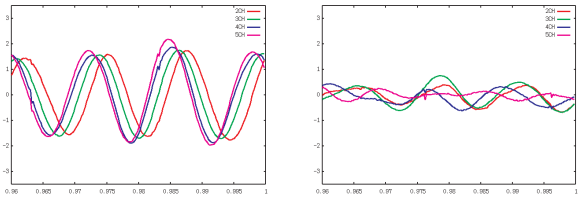

Figure 6. Control effect on velocity fluctuation waves (15 degree oblique waves.), (a) before and (b) after the 44th adjustment

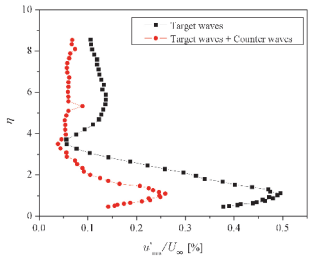

Figure 7. RMS profile of the velocity fluctuation at x = 1,350mm, z = 0mm (15 degree oblique waves)

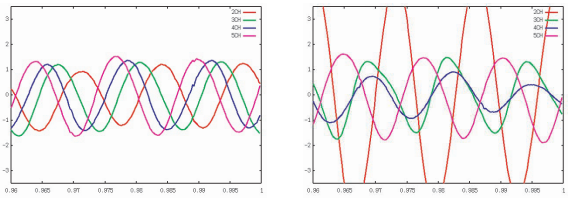

Figure 8. Control effect on velocity fluctuation waves (30 degree oblique waves.), (a) before and (b) after the 67th adjustment

sweep angle. The target for weakening is set at 6dB as in the 15 degrees case. Unfortunately, the amplitude of the velocity fluctuation does not show any sign of decreasing even after more than 70 adjustments. The reason for the difficulty, besides the effect of wave front forming an arch described before, is not clear yet. It may require more actuators along the spanwise direction for the more accurate generation of the waves with large sweep angles. More improvement in the control algorithm may be also needed.

4. CONCLUDING REMARKS

A semi-automatic active control of the T-S waves and the oblique waves was attempted using an array of piezo-ceramic actuators attached on a flat-plate surface. It was shown that the system could reduce the two-dimensional T-S waves and the oblique waves whose sweep angles were not large. However, it was found that the system was not effective against oblique waves of a large sweep angle.

REFERENCES

[1] A.S.W. Thomas. The control of boundary-layer transition using a wave-superposition principle. *J. Fluid Mech.*, 137:233-250, 1983.

[2] H. W. Liepmann, G. L. Brown and D. M. Nosenchuck. Control of laminar-instability waves using a new technique. *J. Fluid Mech.*, 118:187-200, 1982.

[3] J. Kim. Control of turbulent boundary layer. *Phys. Fluids*, 15:1093-1105, 2003.

[4] D. Sturzebecher and W. Nitsche. Active cancellation of Tollmien-Schlichting instabilities on an unswept wing using multi-channel sensor actuator systems. *Int. J. Heat and Fluid Flow*, 24:575-583, 2003.

[5] T. Sakai, K. Shibamoto, S. Izawa, A.K. Xiong and Y. Fukunishi. Active control of flow field structure in a transitional flat plate boundary layer. *Proc. 4rd ASME.JSME Joint Fluid Eng.*, CD-ROM, 2003.

[6] Y. Fukunishi, S. Izawa, and K. Morita. Development of a new device to control oblique waves in transitional boundary layers. *Fluid Dyn. Res.*, paper accepted, 2004.

LINEAR FEEDBACK CONTROL OF TRANSITION IN SHEAR FLOWS

Jérôme Hœpffner[1], Mattias Chevalier[1,2], Thomas Bewley[3], and Dan Henningson[1,2]
[1] *Department of Mechanics, Royal Institute of Technology (KTH) SE-100 44 Stockholm, Sweden,* [2] *The Swedish Defense Research Agency (FOI), SE-172 90, Stockholm Sweden*
[3] *Flow Control Lab, Dept of MAE, UC San Diego, La Jolla, CA 92093-0411, USA.*

Abstract: This work focuses on the application of linear feedback control to transition to turbulence in shear flows. The controller uses wall-mounted sensor information to estimate the flow disturbances and uses wall actuators to prevent transition to turbulence. The flow disturbances are induced by external sources of perturbations described by means of a stochastic volume forcing. We show that improved performance can be achieved if the proper destabilisation mechanisms are targeted.

Keywords: Feedback control, LQG, state estimation, Kalman filter, stochastic disturbance model.

1. INTRODUCTION

In many applications like aeroplane wings, pipes, turbine blades, growth of small disturbances due to external sources of excitation can lead to transition to turbulence and thus increase the friction drag. Control is being increasingly applied to fluid flow as the theories and devices are being developed (see Bewley, 2001, Kim, 2003). A powerful theory for linear feedback control is available and can be applied to flow control, assuming a linear dynamics for the flow (small amplitude disturbances), with a quadratic objective function, and a Gaussian distribution for the external sources of excitation and measurement noise. This method known as LQG (Linear, Quadratic, Gaussian) or L_2 control (see Green and Limebeer, 1995) is used in this work.

2. SYSTEM AND CONTROL SETUP

In this work, the dynamics of small perturbations to a laminar base flow is modelled by the linearized Navier–Stokes equation. Measure-

R. Govindarajan (ed.), Sixth IUTAM Symposium on Laminar-Turbulent Transition, 213–218.

ments are extracted as the instantaneous value of the two components of the wall skin friction and pressure. Control is applied by means of blowing and suction at the wall. In the LQG control formulation, the systems can be written in state space

$$\begin{cases} \dot{q} = Aq + B_1 f + B_2 u \\ y = Cq + g, \end{cases}, \quad \begin{cases} \dot{\hat{q}} = A\hat{q} + B_2 u - v \\ \hat{y} = C\hat{q} \end{cases}, \quad \begin{array}{l} u = K\hat{q}, \\ v = L(y - \hat{y}). \end{array} \tag{1}$$

The equations above show the four elements of a LQG formulation. The flow system to be controlled, the estimator providing an estimate of the instantaneous flow state, and the estimator and control feedback gains L and K.

The flow state $q = (v, \eta)^T$ is constructed with the wall normal velocity v and wall normal vorticity η. It is affected by external disturbances in the form of a stochastic forcing f. The measurement vector y contains all the available information about the flow state. It is corrupted by the sensor noise g with covariance G.

The estimator is built with analogous form. The estimator state $\hat{q}$ is forced to approach the flow state by a 3D volume forcing v, feedback of the measurements. The flow and estimator states q and $\hat{q}$ are controlled by means of the blowing and suction u. The control actuation is a feedback of the estimated flow state.

For the dynamic operator A, we use the linearised Navier–Stokes equations transformed to Fourier space, i.e. the Orr-Sommerfeld/Squire equations (see e.g. Schmid and Henningson, 2001)

$$A = \begin{pmatrix} \mathcal{L}_{OS} & 0 \\ \mathcal{L}_C & \mathcal{L}_{SQ} \end{pmatrix}, \begin{cases} \mathcal{L}_{OS} = \Delta^{-1}(-ik_x U\Delta + ik_x U'' + \Delta^2/Re), \\ \mathcal{L}_{SQ} = -ik_x U\Delta/Re, \quad \mathcal{L}_C = -ik_z U', \end{cases} \tag{2}$$

where U, U', U'' are the base flow and its wall normal derivatives, Δ denotes the Laplacian operator, k_x and k_z are the streamwise and spanwise wavenumbers, and Re is the Reynolds number.

The main issues in designing such a controller, is the description of the external disturbances f by their covariance R_{ff} (Hœpffner et al., 2003), and the control objective $\mathcal{J}$ by the quadratic norm Q,

$$R_{ff} = E[ff^*], \quad \mathcal{J} = \frac{1}{2}\int_0^\infty (q^* Q q + \ell^2 u^* u)\,\mathrm{d}t, \tag{3}$$

where $E[\cdot]$ denotes the expectation operator, and ℓ plays the role of a penalty on the control effort. The optimal feedback gains L and K can be computed independently for each wave number pair by solving two

Riccati equations (see e.g. Glover et al., 1989)

$$\begin{cases} A^*X + XA - \frac{1}{l^2} XB_2B_2^*X + Q = 0, & K = -\frac{1}{l^2}B^*X, \\ AP + PA^* + B_1R_{ff}B_1^* - PC^*G^{-1}CP = 0, & L = -PC^*G^{-1}. \end{cases} \tag{4}$$

The performance of the estimator is monitored by the estimation error energy, i.e. the kinetic energy of $(q - \hat{q})$. The flow state is well estimated when this energy is low compared to the flow energy. The performance of the controller is seen by the controlled flow energy. The flow is well controlled when its energy is low compared to the uncontrolled flow. We will see in the following sections how these performance can be fine-tuned.

3. RESULTS

3.1 Control and estimation

The evolution of a localized initial condition in channel flow, and its evolution when controlled are depicted in figure 1 . The objective function is designed to minimize the kinetic energy of the disturbance to the laminar flow profile. The model for the disturbances assumes finite length correlation for the external disturbances (see Hœpffner et al., 2003). The covariance model for the disturbances assumes the form

$$\begin{cases} R_{f_jf_k}(y, y', k_x, k_z) = d_1\, \delta_{jk} \mathcal{M}(y, y'), \\ \mathcal{M}(y, y') = e^{-(y-y')^2/2d_y}, \\ d_1(k_x, k_z) = d_a\, k_d^2\, \mathrm{e}^{-k_d^2+1} \quad \text{with} \quad k_d^2 = (k_x/d_x)^2 + (k_z/d_z)^2, \end{cases} \tag{5}$$

where $\mathcal{M}$ describes the covariance of f in the wall normal direction for a single wavenumber pair, and d_1 accounts for the variation in wavenumber pair space of the strength of this forcing. The model parameters d_y, d_a, d_x, and d_z can be freely chosen to fit the flow type at hand.

The initial condition presented is the localized perturbation that may originate from a jet normal from the bottom channel wall. This perturbation initially grows in energy and is finally damped by viscous effects. We show two cases of controller. The first one is turned on at time 0 and the second one at time 20. In both cases the feedback uses estimated flow state information. The performance for both cases for full information controller and estimation error is depicted with dashed dotted and dotted thin lines. When the controller is started at time 0, there is an initial growth of the controlled flow energy and estimation error energy due to a strong component of growing disturbance. But when controller and estimator are started up later, monotonous decay is observed.

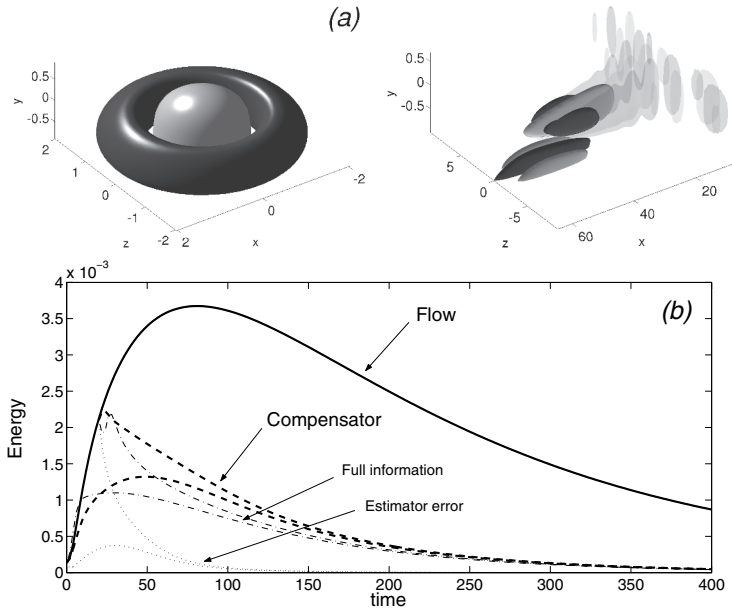

Figure 1. *(a)* Isosurfaces of the wall normal velocity, for time 0 and 90 of the evolution of the localised initial condition in a channel. Flow without control is transparent and with control is opaque. *(b)* Energy evolution in time for the flow (bold solid) and the compensated flow (bold dashed). Two cases are represented: when the compensator is turned on at initial time and turned on at time 20. The flow energy evolution with full information control is represented with a dash-dotted line and the estimation error energy with dotted lines

See on figure 1(b) an isosurface plot of the wall normal velocity for the initial disturbance and its evolved state at time 90 for no control (transparent) and estimation-based control (opaque). When controlled, the wave packet is prevented from spreading in the channel. The actuation is visible in this figure as the non-zero value of the wall normal velocity at the lower wall. It can be seen that the wall blowing and suction is of the same order of magnitude as the wall normal velocity of the flow disturbance to be controlled. The control effort is though of relatively low amplitude since most of the energy of the disturbance is carried by the streamwise velocity component.

3.2 Flexibility in the objective function

If one seeks to minimize the disturbance kinetic energy everywhere and all the time, the objective function (3) is well suited. We will now

demonstrate that different goals can be reached by simple modifications of the quadratic norm defined by Q.

Two examples of the flexibility of the quadratic objective function for the case of a single wavenumber pair $(k_x, k_z) = (0, 0.5)$ of a Blasius boundary layer are depicted in figure 2 .

On figure 2(a) the control is turned off at time 100 in the time evolution of the initial condition that lead to the greatest reachable energy growth. If a strong (though not energetic) component of the potentially growing initial condition is still present at time 100, the growth resumes when the actuation is stopped as can be seen for case 1. To avoid this the controller in case 2 targets the growth mechanism by an extra penalty Re on the wall normal velocity responsible for the lift up effect (see e.g. Schmid and Henningson, 2001). This way, the growth is reduced after the actuation interval. Note that the control performance is only marginally affected by the extra penalization if the control is not stopped (dashed lines).

In figure 2(b) the same flow system is constantly excited by stochastic disturbances and has reached statistical steady state. For the three cases presented, the controller targets respectively the total kinetic energy, the kinetic energy integrated in the wall normal direction up to 2 and up to 1 (in displacement thickness units). Such a controller seeks to eject the disturbances away from the wall instead of killing disturbance energy everywhere. When only targeting the disturbance energy up to 1, the goal is met, and very little disturbances are in contact with the wall surface.

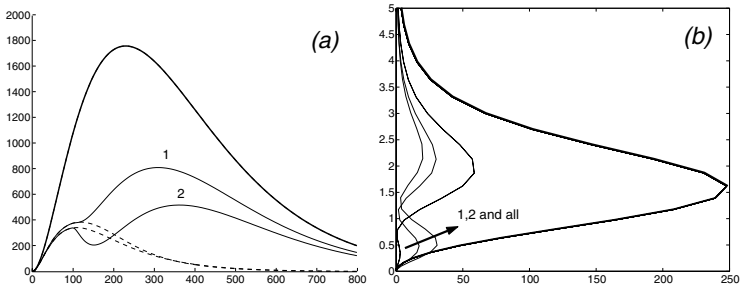

Figure 2. Illustration of the flexibility in the choice of the objective function. *(a)* time evolution of the flow energy with full information control all the time (thin dashed) and when the controller is turned off at time 100 (thin solid). In case 1, the controller minimizes the kinetic energy, and in case 2 there is an additional Reynolds number penalisation on the wall normal velocity component. *(b)* Steady state distribution of perturbation kinetic energy in the wall normal direction for a boundary layer constantly excited by external forcing. The bold line is the flow kinetic energy and the thin lines are the full information controlled flow when only the kinetic energy up to 1, 2, y_{max} is minimised in the objective function, as shown by the arrow

4. CONCLUSION

We show in this work that improved control performance can be achieved for control of transition to turbulence in shear flows, if the proper destabilisation mechanisms are targeted. This means that a thorough physical understanding of the phenomenon to be controlled is necessary. We use a stochastic model for external disturbances, that may account for a wide range of flow disturbances. We design the quadratic objective function to target the main destabilisation mechanism, as for example streamwise elongated vortices in bypass transition.

REFERENCES

Bewley, T. R. (2001). Flow control: new challenges for a new renaissance. *Progress in Aerospace Sciences*, 37:21–58.

Glover, J. C. D. K., Khargonegar, P. P., and Francis, B. A. (1989). State space solutions to standard $\mathcal{H}_2$ and $\mathcal{H}_\infty$ control problems. *IEEE transactions on automatic control*, 34(8).

Green, M. and Limebeer, D. J. N. (1995). *Linear robust control*. Prentice Hall.

Hœpffner, J., Chevalier, M., Bewley, T. R., and Henningson, D. S. (2003). State estimation in wall-bounded flow systems. part I : laminar flow. *J. Fluid Mech.* Submitted.

Kim, J. (2003). Control of turbulent boundary layers. *Physics of fluids*, 15(5).

Schmid, P. J. and Henningson, D. S. (2001). *Stability and transition in shear flows*. Springer.

EFFECTS OF AMBIENT VISCOSITY ON THE ENTRAINMENT AND DYNAMICS OF A BUOYANT JET

Manikandan Mathur and K.R. Sreenivas
Engineering Mechanics Unit, Jawaharlal Nehru Centre for Advanced Scientific Research, Bangalore - 560064, India.

Abstract: In this paper we present results on the behavior of a turbulent, negatively buoyant jet in an ambient fluid having a higher viscosity than the jet fluid. Our experimental results indicate that the turbulent jet undergoes a reverse transition. Large scale eddies at the interface are suppressed, and the observed entrainment rate also reduces dramatically for the jet in a higher-viscosity medium. We also present results from numerical simulations, using vortex methods with a viscous diffusion scheme, to corroborate the results from our experiments.

Key words: Entrainment; Ambient-viscosity; Jet; Plume.

1. INTRODUCTION

Modeling the dynamics of turbulent jets and plumes is of importance in many applications like dispersion of pollutants and predicting the behavior of a cloud in the atmosphere. Entrainment is the process by which irrotational ambient fluid is incorporated into the turbulent jet-flow. Entrainment process and hence the dynamical behavior of the jet depend on several parameters such as ambient density stratification[1], axial-pressure gradient[2,3], cross-flow and off-source buoyancy addition[4,5,6], temperature and viscosity contrasts[7] between the free-shear flow and the ambient medium. There are other applications in which free-shear flows can encounter an ambient fluid with a higher viscosity. For example, the flow of

R. Govindarajan (ed.), Sixth IUTAM Symposium on Laminar-Turbulent Transition, 219–224.

lava into a magma chamber, where viscosity variation arises due to a change in temperature and/or constituents, and in the process industry where polymers have to be blended with additives or with other polymers having different physical properties. Except for the work reported by Campbell and Turner[7], there is no other study, to our knowledge, that explores the interaction of a free-shear flow in an ambient fluid of a different viscosity. Campbell and Turner's work [7] is of exploratory nature. In their study, the flow configuration does not correspond to a standard jet/plume. In the present study we report results for a negatively buoyant jet discharged into an ambient fluid of a different viscosity. We also use vortex method based numerical simulations to study the effects of ambient viscosity on the dynamics of a jet.

2. EXPERIMENTS

All the experiments were conducted in a glass tank of dimensions 30x30x45 cm (see figure 1). A pipette with an internal diameter of 1.4 mm at the exit was used to discharge the jet vertically down in the tank. By adding salt, the density of the jet fluid was increased in comparison to that of the ambient fluid, making it negatively buoyant. The jet fluid was dyed with either potassium permanganate or fluorescein dye for visualization. CMC was used to change the viscosity of the ambient fluid. The discharge velocity was maintained constant by using a constant pressure-head arrangement discharging across a constant resistance, as suggested by Arakeri et. al[8].

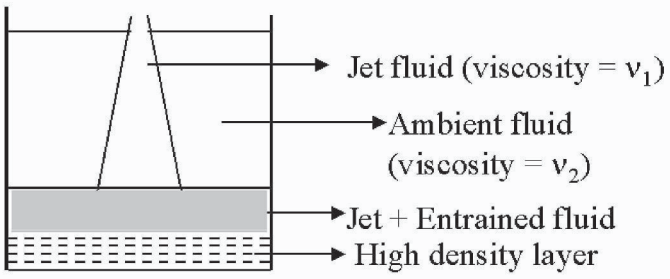

Figure 1: Schematic of the main glass tank

2.1 Results

For a given inlet Reynolds number (1700), when the viscosity of the ambient fluid is 680 times of that of the jet fluid (Figure 2b), the entrainment was observed to reduce dramatically in comparison to the case shown in figure 2a. We also observe that the large-scale eddies (coherent structures) at the

interface between the two fluids have been completely suppressed in the latter case. This suppression plays a crucial role in reducing entrainment and

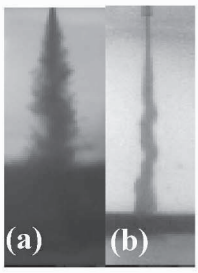

Figure 2: Flow visualization images for two viscosity ratios and inlet Reynolds number (**a**: 1, 1700; **b**: 680, 1700)

Figure 3: Coherent structures for Re_{inlet} = 700 and $\nu_2 = \nu_1$

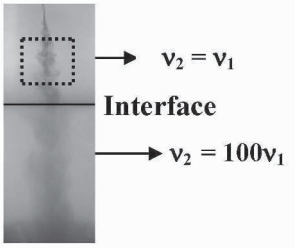

Figure 4: Entrainment through two different layers. Re_{inlet} = 450

will be discussed later. For the values of the inlet Reynolds number and the ambient viscosity specified in figure 2b, we observe that the jet is almost laminar and hence the entrainment is also very low. It can be concluded that the inlet Reynolds number, at which the instabilities and hence appreciable entrainment set in, is higher for a higher ambient to jet viscosity ratio. Also, the flow tends towards the laminar regime as the viscosity of the ambient fluid is increased without changing the inlet Reynolds number. Figure 3 represents a closer look into the large-scale eddies (coherent structures) for an inlet Reynolds number and ambient viscosity specified in the figure.

In Figure 4, we present a result indicating the behavior of the jet when it enters a high viscosity fluid after passing through a fluid of its own viscosity. The transition takes place at the interface indicated by the dark line in the figure. In the dotted box shown in the figure, small-scale fluctuations in the turbulent jet are evident. When it passes into the high viscosity region, all small-scale fluctuations are suppressed, however, small wave-number fluctuations still persist. In the higher-viscosity medium, the flow seems to have undergone a reverse transition (tending towards the laminar regime) resulting in lower entrainment. In this case, suppression of large scale eddies has reduced entrainment. In contrast, for the off-source buoyancy added flows[4,5] and for axial accelerated flows[3,9], the small wave-number fluctuations are disrupted resulting in lower entrainment. The two results put together will support the model proposed by Narasimha and Roshko[10]. They argue that the entrainment process involves three steps: (a) Induction -- purely a kinematic process, bringing in ambient fluid into the turbulent region; large scale eddies are responsible, (b) Diastrophy -- stretching and folding which increases the area of interaction between the ambient fluid and the jet fluid; dominated by small scale processes and (c) Molecular diffusion -- molecular mixing. Factors inhibiting any of the above steps will reduce

entrainment. Off-source buoyancy addition and axial acceleration inhibit the *induction phase* whereas high viscosity ambient suppresses both the *induction* and the *diastrophy phases*.

3. 2-D SIMULATIONS

We simulate the entrainment process in a jet using 2-D discrete-vortex method (DVM). In free-shear flows, the vorticity is confined to certain areas and this is exploited by DVM, which restricts its computations to regions of non-zero vorticity. The details of the simulations are given in [9].

3.1 Results

First set of results presented here is for an inlet Reynolds number of 2500 and viscosity ratio equal to unity. The instantaneous velocity at the edge of the jet and the corresponding fluctuating vorticity are shown in figure 5. The mean entrainment coefficient (ratio of the velocity with which the ambient fluid moves into the main jet and the local mean axial centreline velocity) and an instantaneous vorticity field are shown in Figures 6a and 6b respectively. For a Y/D ratio up to 30, coherent structures do not form. At all times, the net circulation across a horizontal section in this region is close to zero. Mean entrainment coefficient in this initial phase is also low (Figure 6a). However, for Y/D ratio greater than 30, the jet undergoes a transition and the positive and negative circulations in the shear layers occur in clusters (Figure 6b). Clustering of circulation, which indicates formation of coherent structures, is accompanied by an increase in entrainment (Figure 6a). The inlet laminar portion, represented by two parallel vortex sheets (resulting in no net vorticity at the axial location) will induce no velocity in the ambient fluid and hence the induction phase is ineffective.

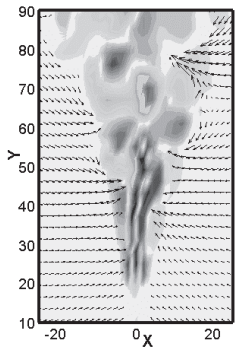

Figure 5 Fluctuating vorticity and velocity at the edge of the jet. Purple line indicates horizontal sum of circulation at each height

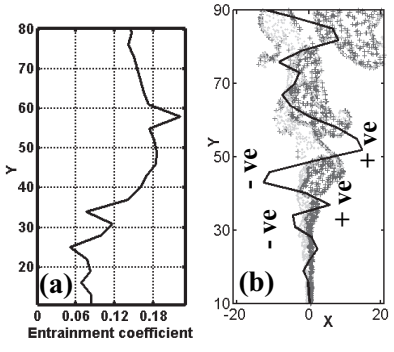

Figure 6 (a) Entrainment coefficient; (**b**) instantaneous net circulation at the axial location and eddy-structures

Axial motion of large-scale structures as a function of time and the corresponding entrainment episodes are presented in Figures 7a and 7b respectively.

The two plots are highly correlated. The calculated correlation coefficient is greater than 0.9 at all times. Results in Figure 7 clearly demonstrate the close relation between the coherent structures and the entrainment process.

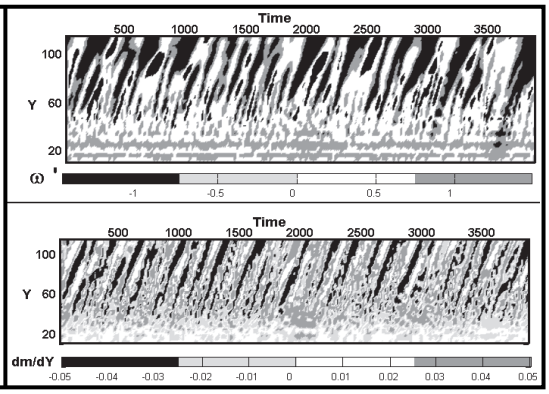

Figure **7 (a)** Instantaneous, horizontal sum of fluctuating vorticity, indicating motion of coherent structures with time; and (**b)** corresponding entrainment episodes. Note the high correlation between the two plots

We also present some of the preliminary results obtained for a jet in an ambient fluid of higher viscosity using the same program. For the inlet Reynolds number and ambient viscosity specified in Figure 8, we observe that the (1/e) velocity width is much greater than the (1/e) concentration width after the initial region. This result is verified experimentally as shown in figure 9. We observe that, even though the inlet fluid is restricted to a very small width, the momentum has diffused over a much wider region. It is hence important to look at the concentration widths rather than the velocity widths in entrainment studies, as the former determines important dynamics like the combustion efficiency in a flame.

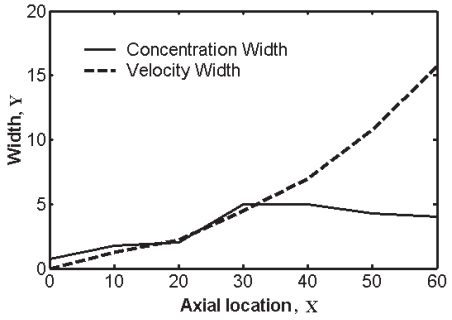

Figure 8: Simulations: $Re_{inlet} = 100$, $\nu_2 = 50\nu_1$; Concentration and velocity widths. The velocity width is much greater than the concentration width

Figure 9: Experiments: $Re_{inlet} = 1500$, $\nu_2 = 680\nu_1$; right dye streak indicates the spread of momentum into the ambient, whereas the jet fluid is confined to a smaller region

4. CONCLUSIONS

Results from experiments and numerical simulations clearly indicate that the higher viscosity of the ambient fluid suppresses the formation of large-scale coherent structures. A strong correlation between the coherent structures and the rate of entrainment has been established. Absence of coherent structures for a jet in high viscosity ambient fluid is due to the increased stability of the shear layers. Large velocity width of the jet in comparison to its small concentration width indicates moving away of the inflection point in the velocity profile from the region of high shear and this may contribute to the increased stability of the shear layers. Thus, relating shear layer instability to the entrainment process in free-shear flows will be helpful in modeling their behavior and can address the observed variation of entrainment coefficient in free-shear flows subjected to different body forces as suggested by [3].

The financial support received from the Defence R&D Organization, India (Project no. ERIP/ER/0202094/M/01) is thankfully acknowledged.

REFERENCES

[1] List, E. J., Turbulent jets and plumes, Ann. Rev. Fluid Mech. 14: 189-212, 1982.

[2] Choi, D. W., Gessner, F. B. and Oates, C. G., Measurements of confined, coaxial jet mixing with pressure gradient, J. Fluid Eng. 108: 39-46, 1986.

[3] Sreenivas, K. R. and Prasad A. K, Vortex dynamics model for entrainment in jets and plumes, Phys. Fluids, 12(8): 2101-2107, 2000.

[4] Bhat, G. S. and Narasimha R., Volumetrically heated jet: large eddy structure and entrainment characteristics, J. Fluid Mech. 329: 303-330, 1996.

[5] Venkatakrishnan L, Bhat G.S., Prabhu A., and Narasimha R., Visualization studies of cloud-like flows, Current Science 74: 597-606, 1998.

[6] Basu, A. J., and Narasimha, R., Direct numerical simulation of turbulent flows with cloud-like off-source heating,
J. Fluid Mech. 385: 199-228, 1999.

[7] Campbell, I.H., Turner, J.S., Turbulent mixing between fluids with different viscosities. Nature, 313: 39-42, 1985.

[8] Arakeri, J.H., Das, D., & Srinivasan, J., Bifurcation in a buoyant horizontal laminar jet, JFM, 412, 61-73, 2000.

[9] Sreenivas K. R., Study of entrainment process in a planar jet using diffusion-vortex method, Proceedings of The Tenth Asian Congress of Fluid Mechanics, B33, Peradeniya, Sri Lanka, 17-21 May 2004.

[10] Dimotakis, P. E, Two-dimensional shear-layer entrainment, AIAA J. 24: 1791-1796, 1986.

[11] Yoshifumi Ogami and Teruaki Akamatsu, Viscous Flow Simulation using the Discrete Vortex Model – The Diffusion Velocity Method, Computers and Fluids, v.19 n.3-4, p.433- 441, 1991

DISTURBANCE DEVELOPMENT IN BOUNDARY LAYERS OVER COMPLIANT SURFACES

Christopher Davies,[1] Peter W. Carpenter,[2] Reza Ali[2] and Duncan A. Lockerby[3]
[1]*School of Mathematics, Cardiff University, Senghennydd Road, Cardiff CF24 4AG, U.K.*
[2]*School of Engineering, University of Warwick, Coventry CV4 7AL, U.K.*
[3]*Department of Mechanical Engineering, Brunel University, Uxbridge UB8 3PHS, U.K.*

Abstract: Numerical simulation results for the behaviour of disturbances in flows over compliant surfaces are described. Most attention is given to the propagation of Tollmien-Schlichting waves over compliant panels and the self-excited generation of such waves by very short panels. The use of compliant walls to suppress transiently growing forms of boundary-layer disturbance and the effects of surface compliance on the rotating disc boundary layer are also briefly discussed.

Keywords: Boundary-layer stability; transition delay; compliant surfaces; numerical simulation.

1. INTRODUCTION

The influence of surface compliance on the development of disturbances in transitional boundary layers has been the subject of many theoretical studies over the last forty years. (A number of review articles can be found in the recent book edited by Carpenter & Pedley [1].) Much of this work has been concerned with the use of compliant surfaces to stabilize Tollmien-Schlichting waves for relatively simple two-dimensional flows, in particular Blasius flow over a flat plate and plane-channel flow. For these model flows a standard linear stability eigenvalue analysis, conducted for compliant surfaces with an assumed infinite streamwise extent, can be used to demonstrate that it is feasible to select surface compliance properties that will completely eliminate the Tollmien-Schlichting mode of instability [2–5]. Though such results are very promising they do not establish, unequivocally, that compliant surfaces provide a practical means for delaying transition in technological applications. They only demonstrate that the specific transition route that begins with the spatial amplification of Tollmien-Schlichting waves may, in principle, be closed off

R. Govindarajan (ed.), Sixth IUTAM Symposium on Laminar-Turbulent Transition, 225–230.

for model two-dimensional boundary-layer flows over uniform compliant surfaces that can be treated as if they were arbitrarily long.

There remain many other features of boundary-layer disturbance development in transitional boundary layers over compliant surfaces that merit a careful study. For example, all of the following are pertinent to the practical deployment of compliant surfaces for transition delay: (i) the influence of compliant surfaces on transiently growing forms of disturbance; (ii) the effects of three-dimensionality in the basic boundary-layer flow, which can introduce other modes of instability such as crossflow vortices; (iii) the effects of using finite length compliant surfaces in order to tailor local surface compliancy properties so that they match the local flow conditions. We will briefly review work that we have undertaken in order to investigate the nature of each of the effects that have just been mentioned. Due to space limitations, most attention will be given to some interesting, and rather puzzling, behaviour that has recently been found for very short compliant panels.

The work that we shall report has involved the direct numerical simulation of linearized boundary-layer disturbance evolution for a number of different flow and compliant surface configurations. These simulations were all undertaken using a new velocity-vorticity formulation of the Navier-Stokes equations that has proved to be particularly well-suited for studying flow-structure interactions for boundary layers [6–10].

2. NUMERICAL SIMULATION RESULTS

Klebanoff modes. We have used numerical simulations for three-dimensional disturbances to study the effects of surface compliance on the development of transiently growing streaks that are associated with Klebanoff modes of disturbance [11–13]. Transient streaks can occur, for example, in flow environments where the level of free-stream turbulence is relatively high. In our simulations we employed body-forcing localized in the free stream at the boundary-layer edge in order to generate streaks. For the Blasius boundary layer, the simulations demonstrated that the growth of streaks could be very significantly diminished by a compliant surface, but also that these more weakly growing streaks may persist over a wider range of spanwise wavenumbers than in the case when the wall is rigid. The simulation results thus suggest that compliant surfaces can be designed so that they are still effective in delaying transition in circumstances where transient streak-like structures play a more important role in the transition process than conventional eigenmode forms of disturbance, such as Tollmien-Schlichting waves.

Rotating disc flow. Numerical simulations have also been used to investigate the spatial and temporal development of three-dimensional forms of linearized disturbance in the three-dimensional von Karman boundary-layer flow

formed over a rotating disc with a compliant surface [7, 14]. The rotating disc boundary layer can be viewed as a canonical model for more complicated and realistic three-dimensional flows that are susceptible to crossflow instability. In addition to confirming that a compliant disc surface can be strongly stabilizing for both travelling and stationary crossflow vortices [15, 16], the simulation results served to highlight the strongly non-parabolic nature of the rotating disc boundary layer. It was found that a compliant annulus inserted into an otherwise rigid disc was capable of stabilizing disturbances even at locations that were radially inboard from the compliant part of the disc surface.

Flow-stabilization using finite compliant panels. A variety of numerical simulations have been conducted to investigate the behaviour that can occur for two-dimensional disturbance waves in boundary-layer flows over finite-length compliant panels [3–6, 17]. Initially we studied the spatial development of Tollmien-Schlichting waves as they propagated over the ends of relatively long compliant panels that were embedded in otherwise rigid walls. Simulations were carried out both for plane channel flow and for parallelized Blasius flow, with qualitatively similar results found in each case. To ensure the pertinence of the simulations to transition delay applications, the stiffness and mass parameters of the compliant part of the wall were selected so that if the compliant panel was, instead of being finite, taken to be of indefinite extent both upstream and downstream, then it would be flexible enough to stabilize Tollmien-Schlichting waves without being so soft as to allow surface-based waves to become destabilized. Typically, the simulations for such configurations showed that the Tollmien-Schlichting wave could become very rapidly stabilized as it propagated over the rigid-compliant wall join at the upstream end of the compliant panel. But it could also trigger a complex response involving stable surface-based waves that propagated up and down along the remainder of the compliant panel. The wall motion associated with these surface-based waves could then, in the near vicinity of the compliant-rigid join at the far end of the compliant panel, act as a generator to create a new Tollmien-Schlichting wave that propagated downstream, away from the compliant-walled section. Despite the somewhat complex dynamics that could occur over the full length of the compliant panel, it was still found to be possible to obtain a strong reduction in the overall growth of the Tollmien-Schlichting wave. Such results offer encouraging prospects for the construction of technologically feasible transition delaying surfaces using compliant panels.

Self-excited Tollmien-Schlichting wave generation. For both plane-channel flow and Blasius flow, numerical simulations also showed that, in some circumstances, sufficiently short compliant panels could become subject to a self-excited form of instability. Rather surprisingly, this was found even in cases

where there was known to be no corresponding instability for an infinitely long compliant surface with the same material properties. Clearly, a detailed understanding of the mechanism behind this new form of instability is needed so that it can be accounted for, and hence avoided, in any practical applications of compliant surfaces to transition delay. For the present, we will just illustrate some preliminary simulation results to indicate the kind of behaviour that can be found.

In order to keep things as simple as possible, we will consider results from a plane channel flow simulation where the Reynolds number has been chosen to be low enough to ensure that Tollmien-Schlichting waves of all frequencies would be stable if the wall was entirely rigid. Similar results were obtained for higher, post-critical, Reynolds numbers where the rigid-walled Tollmien-Schlichting mode was unstable and also for corresponding cases for Blasius flow. Figure 1 shows a snapshot of the wall-normal velocity while Figure 2 displays time histories of the wall vorticity at successive rigid-walled locations that are downstream from the short compliant panel that extends from $x = 25$ to $x = 28.5$. The disturbances were triggered by the passage of a disturbance wavepacket that was generated upstream of the panel, but the exact form of the initial excitation is unimportant for the eventual self-excited response. From Figure 2 it can be seen that there is temporal disturbance growth, with a distinct resonant frequency, at all of the depicted streamwise locations. There is also spatial decay of the disturbance along the downstream direction. There are two factors that can be used to explain this decay. Firstly, the disturbance in the flow downstream of the panel takes the form of a Tollmien-Schlichting wave that is 'forced' by the compliant panel motion and this wave must be spatially decaying because the Reynolds number has been chosen to be subcritical for the rigid-walled Tollmien-Schlichting mode. But secondly, and in many cases more importantly, the effective level of forcing due to the compliant panel motion is increasing with time, so that the waves found further downstream were generated at a time when the forcing level was lower. This latter effect explains why the disturbance was still found to be spatially decaying even when the Reynolds number was chosen to be above critical and the Tollmien-Schlichting waves downstream of the panel were characterized by a frequency that would have led to strong spatial growth if the effective forcing amplitude had been kept constant.

Simulations conducted at a given Reynolds number for compliant panels with fixed material properties but varying panel lengths L showed that it was possible to identify a definite range $L_{\text{min}} < L < L_{\text{max}}$ over which there was self-excited compliant wall motion yielding Tollmien-Schlichting waves downstream of the compliant section. It was also found that the wavelength of these waves was approximately proportional to the panel length, but that the constant of proportionality was not given by any obvious geometrical con-

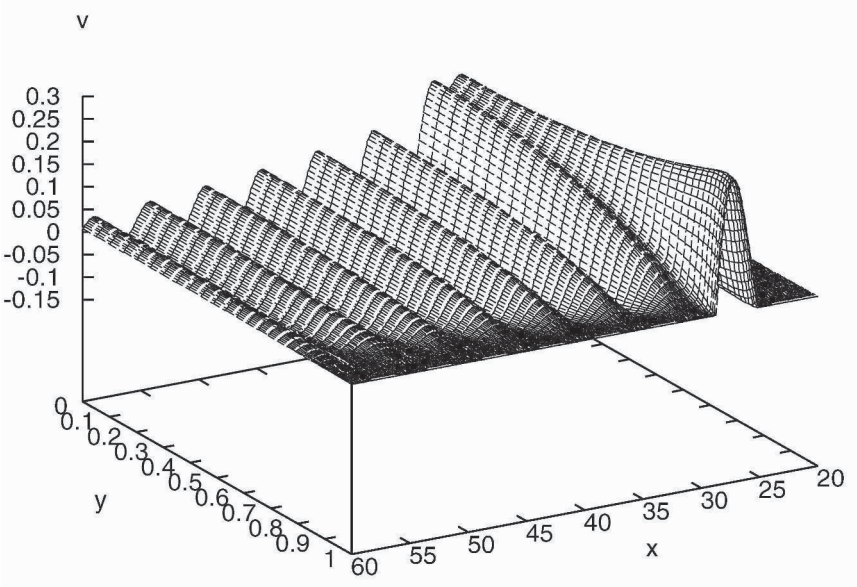

Figure 1. Normal wall velocity for a selected time instant from a numerical simulation of a self-excited disturbance in plane-channel flow with a compliant panel insert. The panel is positioned along the streamwise direction between $x = 25$ and $x = 28.75$. The Reynolds number based on the channel half-width and the centre-line velocity is $R = 3000$. The material properties of the compliant panel are chosen such that the same flow over a corresponding but infinitely long compliant surface would be stable

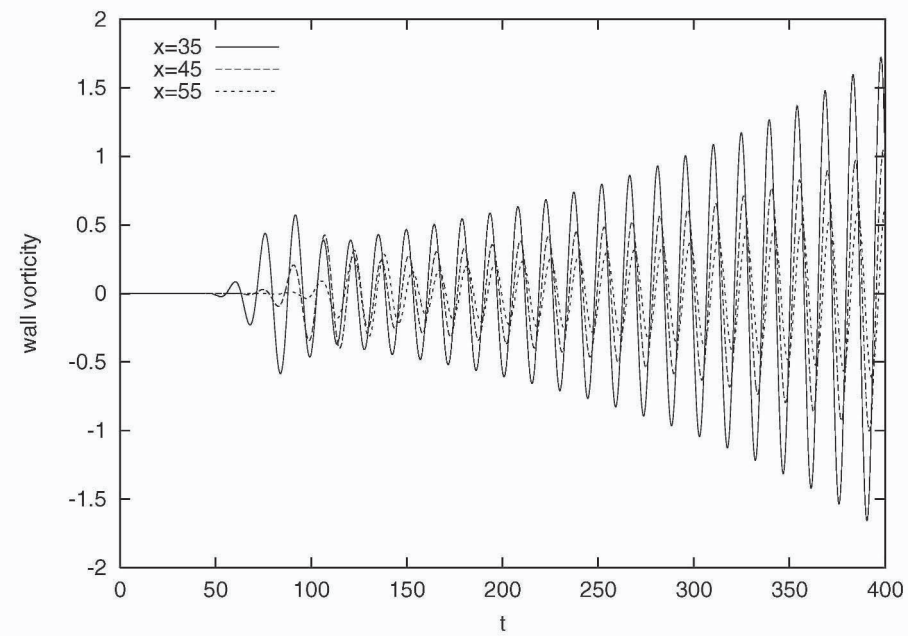

Figure 2. Time histories for the wall vorticity at various streamwise positions for the same simulation as in the previous figure

straint. (Such as would be dictated by the formation of half-sine waves, or any other sinusoidal standing waves, over the length of compliant panel). This unexplained behaviour is currently the subject of further investigation.

REFERENCES

[1] Carpenter, P.W. & Pedley, T.J. (eds) 2003 *Flow past highly compliant boundaries and in collapsible tubes*. Kluwer Academic Publishers.

[2] Davies, C.& Carpenter, P.W. 1997 Instabilities in a plane channel flow between compliant walls. *J. Fluid Mech.* **352** 205-243.

[3] Carpenter, P.W., Davies, C. & Lucey, A.D. 2000 Hydrodynamics and compliant walls: Does the dolphin have a secret? *Current Sci.* **79** 758-765.

[4] Carpenter, P.W., Lucey, A.D. & Davies, C. 2001 Progress on the use of compliant walls for laminar-flow control. *J. Aircraft* **38** 504-512.

[5] Davies, C. 2003 Convective and absolute instabilities of flow over compliant walls. In *Flow past highly compliant boundaries and in collapsible tubes* (eds. Carpenter, P.W. & Pedley, T.J.), ch. 4, pp. 69-93. Kluwer Academic Publishers.

[6] Davies, C. & Carpenter, P.W. 1997 Numerical simulation of the evolution of Tollmien-Schlichting waves over finite compliant panels. *J. Fluid Mech.* **335** 361-392.

[7] Davies, C & Carpenter P.W. 2001 A novel velocity-vorticity formulation of the Navier-Stokes equations with applications to boundary layer disturbance evolution. *J. Comp. Phys.* **172** 119-165.

[8] Lockerby, D.A., Carpenter, P.W., & Davies, C. 2002 Numerical simulation of the interaction of microactuators and boundary layers. *AIAA J.* **40** 67-73.

[9] Davies, C., 2004 Numerical simulation of boundary-layer disturbance evolution. *Phil. Trans. R. Soc. London A*, (in press).

[10] Davies, C., 2004 Computational studies of boundary-layer disturbance development. In *One Hundred Years of Boundary Layer Research*, IUTAM Symposium, Gottingen, Germany. Kluwer Academic Publishers (in press).

[11] Ali, R. & Carpenter, P.W. 2001 Klenbanoff modes in boundary layers over compliant surfaces. *Bull. Amer. Phys. Soc.* **46** 29-30.

[12] Ali, R. 2003 Receptivity and transition in boundary layers over rigid and compliant surfaces. PhD thesis, University of Warwick.

[13] Lockerby, D.A., Carpenter, P.W., & Davies, C. 2004 Control of sub-layer streaks using microjet actuators. *AIAA J.* (submitted).

[14] Davies, C. & Carpenter, P.W. 2003 Global behaviour corresponding to the absolute instability of the rotating-disc boundary layer. *J. Fluid Mech.* **486** 287-329.

[15] Cooper, A.J. & Carpenter, P.W. 1997 The stability of rotating disc boundary-layer flow over a compliant wall. Part 1. Types I and II instabilities. *J. Fluid Mech.* **350** 231-259.

[16] Cooper, A.J. & Carpenter, P.W. 1997 The stability of rotating disc boundary-layer flow over a compliant wall. Part 2. Absolute instability. *J. Fluid Mech.* **350** 261-270.

[17] Carpenter, P.W., Sen, P.K., Hegde, S. & Davies, C. 2004 A wave-driver theory for vortical wavess propagating across junctions with application to those between rigid and compliant walls. *J. Fluid Mech.* (submitted).

SUPPRESSION OF WALL TURBULENCE BASED ON STABILITY AND TURBULENCE ANALYSIS USING A COMPLIANT SURFACE

P. K. Sen, P. S. Josan and S. V. Veeravalli
Department of Applied Mechanics Indian Institute of Technology, New Delhi 10016, India

Abstract: This paper discusses the role of hydrodynamic stability theory in understanding wall turbulence and its possible suppression by using compliant surfaces. Our work reveals that, in wall turbulent flows, there are three important 'mode classes'; namely, the Tollmien-Schlichting (TS) mode class, the Static Divergence (SD) mode class, and the High-speed highly damped (HSHD) mode class. All these modes scale with inner wall variables and so do the material properties of the compliant surface. The general thrust should be to replace TS modes by the HSHD stable modes. Outer modes were also investigated and found to be damped.

Key words: Wall turbulence, Compliant surface, Stability

1. INTRODUCTION

The recent work of Sen and Veeravalli (1998, 1999 & 2000) has established a connection between instability and fully developed wall turbulence. The extended OS equation developed therein mimics some of the key features of fully developed wall flows extremely well, e.g. the location of the production peak, the range of unstable wave numbers etc. Thus Sen & Veeravalli (1998 – 2000) suggest that stability theory yields the '*root cause mechanism*' responsible for the sustenance of turbulence in fully developed turbulent wall flows. The question that naturally arises is whether one can interfere with this root cause mechanism and thereby suppress turbulence? The present work addresses this question using a compliant wall as a possible means of turbulence suppression.

R. Govindarajan (ed.), Sixth IUTAM Symposium on Laminar-Turbulent Transition, 231–236.

The use of Compliant surfaces has been widely proposed in the past to delay laminar-to-turbulent transition. We have used two types of wall models, on the lines of those used by Carpenter and Garrad (1985) and Sen & Arora (1988). The inverse methods as discussed in Sen & Arora (1988) were used both for selecting the parameters for stabilisation of the flow, and also, investigating physical realisability of the predicted modes. The results obtained in the rigid wall case with our new simplified numerical scheme are similar to the ones reported in Sen and Veeravalli (1998, 2000). Numerical computation was also done for outer modes. However, they do not scale with inner variables and are not relevant here.

2. FORMULATION

In the present study the formulation is based on a combined fluid-solid problem. This requires the separate specification of the dynamics of the fluid side and that of the solid side, and matching the two at the interface.

We now discuss briefly the Sen and Veeravalli theory (details may be seen in Sen and Veeravalli, 1998, 2000). In the discussion to follow the instantaneous velocity vector u_i and pressure p obey the well known Navier-Stokes and continuity equations. Typically, in turbulent flows the velocity and pressure fields are decomposed by the well-known Reynolds decomposition, however, here we prefer a triple decomposition as follows:

$$u_i = \overline{u}_i + \tilde{u}_i + u_i'; \quad p = \overline{p} + \tilde{p} + p'. \tag{1}$$

Here $\overline{u}_i$, $\overline{p}$ are respectively the mean velocity and pressure, u_i', p' are the (random) turbulent fluctuations and $\tilde{u}_i$, $\tilde{p}$ correspond to an organised (solenoidal) disturbance (with zero mean). The organized disturbance is assumed to be small compared to the turbulent fluctuations.

After some algebra, one is in a position to obtain the dynamic equation for the organised disturbance. Using normal mode analysis, like the disturbance stream function ψ being expressed as $\psi = \phi(y)e^{i\alpha(x-ct)}$, one obtains the extended forms of the Orr-Sommerfeld equation, given below: [for details see Sen and Veeravalli (1998, 2000)].

$$\begin{aligned} &i\alpha[(\overline{u}-c)(\phi''-\alpha^2\phi)-\overline{u}''\phi]-1/R[\phi''''-2\alpha^2\phi''+\alpha^4\phi] \\ &-1/R[E\{\phi''''-2\alpha^2\phi''+\alpha^4\phi\}+2E'\{\phi'''-\alpha^2\phi'\}+E''\{\phi''+\alpha^2\phi\}] \\ &-\lambda E/R[-2i\alpha\phi''''+2i\alpha^3\phi']-2i\alpha\phi'/R[\lambda E''+2\lambda' E'+\lambda'' E]=0 \end{aligned} \tag{2}$$

Here α is the spatial wavenmumber, $c = c_r + ic_i$ is the complex wave speed, E is the eddy viscosity non-dimensionalised by molecular viscosity ν and λ is anisotropy function. All quantities in eq. (2) have been non-dimensionalised by outer variables. Equation (2) may also be written in terms of inner variables using

the friction velocity u_* as the velocity scale and ν / u_* as the length scale. It then becomes nearly universal for wall modes. Quantities non-dimensionalised by inner scales are denoted with superscript '+'.

2.1 Boundary Conditions

The boundary conditions for the rigid wall are presented in Sen & Veeravalli (2000). Here we will discuss the compliant wall only. The boundary conditions at y = 0, after linearisation, are $\phi(0) = ac$ and $\phi'(0) = -aU'_w$, where subscript w refers to the wall, and, a is a non-dimensional form of the amplitude of the wall displacement. Substituting $a = \phi_w / c$ we get:

$$c\phi'_w + U'_w\phi_w = 0 \quad \text{at} \quad y = 0. \tag{3}$$

The second boundary condition is obtained by equating the wall pressures, or a pressure-derived response coefficient, like admittance Y, calculated from the fluid side and from the solid side. In the inverse method of Sen-Arora (1988) ϕ_w is parametrised as $\phi_w = |\phi_w| e^{i\theta}$ and $|\phi_w|$ & θ become the two kinematic parameters. Physical realisability entails that the two back-calculated generic properties, viz. the surface wave speed, C_o and the damping $\overline{d}$, satisfy $C_o^2 > 0$ and $\overline{d} > 0$. Thereafter the flexural rigidity, K, and the material damping d can be back-calculated for different given values of the mass m.

3. RESULTS, DISCUSSION AND CONCLUSIONS

i) Figure 1A shows the growth rate $\alpha^+ c_i^+$ plotted against α^+. The result is universal in wall-bounded flows and independent of Reynolds number.

ii) Figure 1B shows experimental confirmation of the eigen function computed for the rigid wall. Experiments were performed in a fully developed turbulent channel. An organised disturbance was introduced by means of a loud speaker system, the velocity field was measured using a hot-wire and the organised part was educed by phase-averaging.

iii) Figure 2 shows variation of c_i^+ as a function of the kinematic wall phase θ, for the TS mode class. The data collapse over a range of Reynolds numbers and it is seen that wall compliance does not affect c_i^+ much.

iv) Figure 3 similarly, shows the variation of c_i^+ and c_r^+ with θ, for the SD mode class. Again the data for different R collapse well.

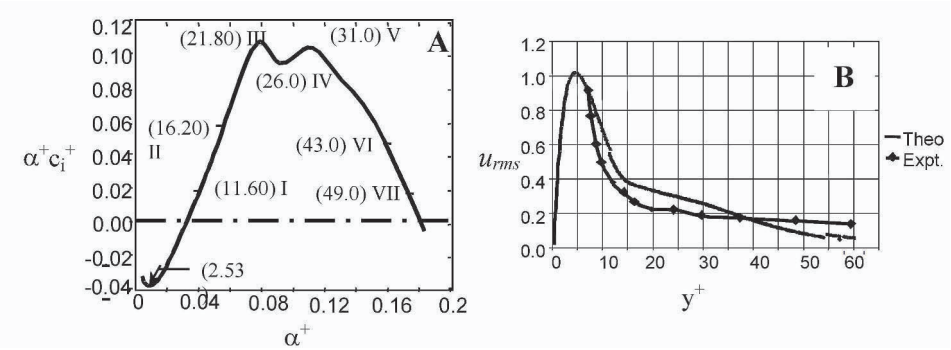

Figure 1A. Growth rate $\alpha^+ c_i^+$ versus α^+ (inner variable scaling). Figures in brackets correspond to unstable wave numbers α for R = 5000

Figure 1B. Graph of comparison of experimental and theoretical graphs of u_{rms} versus y+ in the channel flow. α^+ = 0.17 (experimental) and 0.078 (theoretical)

v) Figure 4 shows the variation of c_i^+ with θ for the HSHD mode class. We note that over most of the parameter space the HSHD mode is strongly damped.

vi) Figure 5 shows a plot of the flexural rigidity K^+ versus θ for various values of m^+ for the TS, SD and HSHD modes. It can be seen that K^+ (and simultaneously d^+) may be chosen so as to eliminate most of the TS and SD modes while allowing HSHD modes. This would be the thrust for stabilizing the flow.

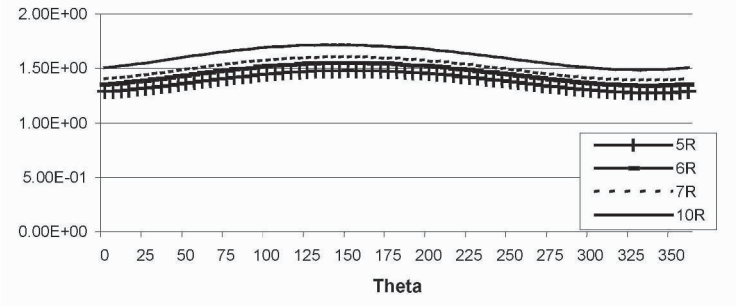

Figure 2. . c_i^+ versus θ (Theta), in TS mode, for α^+= 0.10878 and m^+ (corresponding to m =0.3, at R=5000). Key to the legend: e.g. R =5000 is specified as 5R

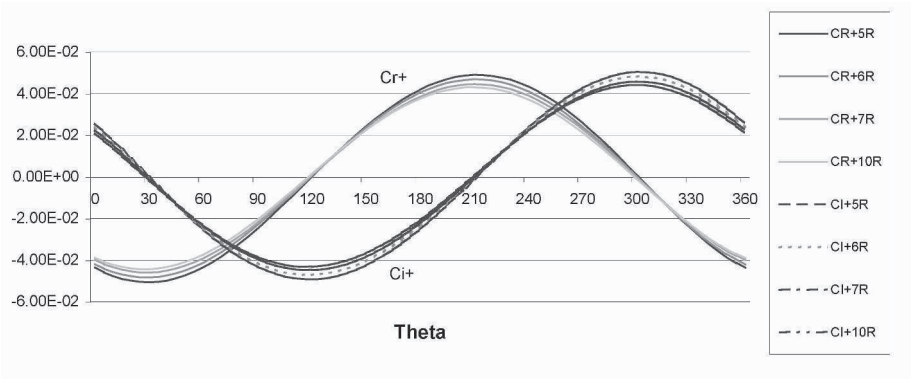

Figure 3. c_i^+ and c_r^+ versus θ (Theta), in SD mode, for $\alpha^+ = 0.10878$ and m^+ (corresponding to m =0.3, at R=5000). Key to the legend: e.g. R =5000 is indicated as 5R CR-Real and CI-Imaginary parts of c^+

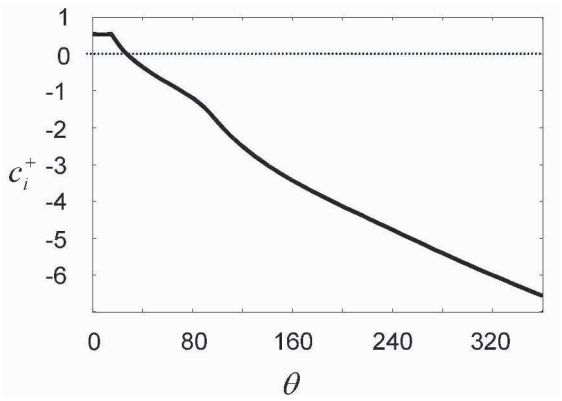

Figure 4. Graph for c_i^+ versus θ for channel-flow for HSHD stable mode class, corresponding to mode class III (Fig. 1A), for R = 5000 and with $|\overline{\phi}_w| = 60\%$

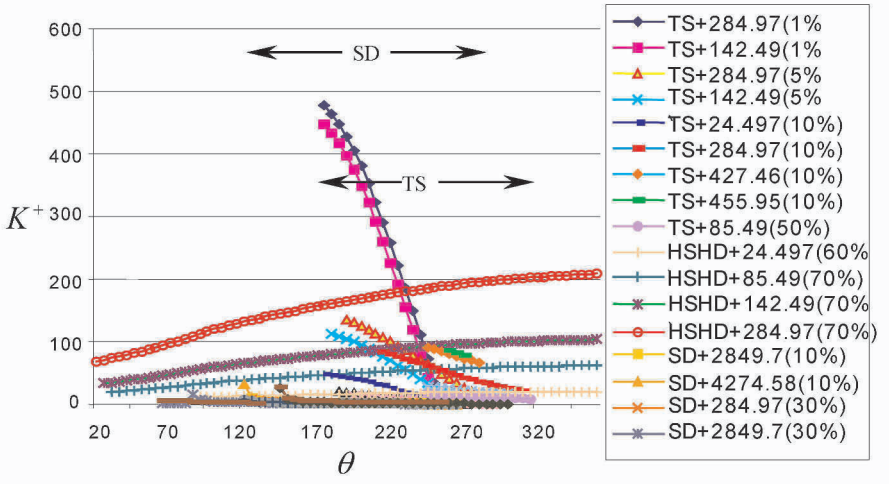

Figure 5. Graph of K^+ and versus θ for the TS and SD modes, corresponding to mode class III with $|\phi_w|$ ranging from 1% to 70% and with m^+ ranging from 28.497 to 4274.58 (corresponding to m = 0.1 to 15.0 at R = 5000)

Key to legend: TS+105.44(50%) means values of K^+ in TS mode, $m^+ = 105.44$ and $|\phi_w| =$ 50% or HSHD+284.97(70%) means values of K^+ in HSHD mode, $m^+ = 284.97$ and $|\phi_w| =$ 70%.

REFERENCES

1. Carpenter, P.W., & Garrad, A.D., 1985, J. Fluid Mech. Vol. 150, p 465.
2. Gad-el-Hak, M., Blackwelder, R.F. & Riley, J.J. 1984, J. Fluid Mech. 140.
3. Josan P.S. 2004, Ph.D. Thesis, Indian Inst. of Technology, Delhi
4. Pope, S.B., 1975, J. Fluid Mech., 72, part 2, p 331.
5. Reynolds, W.C. & Hussain, A.K.M.F., 1972, J. Fluid Mech, 54, part 2, p 263.
6. Roshko, A., 1992, '*Theoretical and Applied Mechanics'*, Eds. S.R. Bodner, J. Singer, A. Solan & Z. Hussain, Publ, Elsevier Science.
7. Sen, P.K. & Arora, D.S., 1988, J. Fluid Mech. Vol. 197, p 201.
8. Sen, P.K. & Veeravalli, S.V., 1998, Sadhana, Vol. 23. part 2. p 167.
9. Sen, P.K. & Veeravalli, S.V., 1999, *J. Mech. Engg. Res. and Development*, Vol. **21–22**, p. 81.
10. Sen, P.K. & Veeravalli, S.V., 2000, Sadhana, Vol. 25. part 5. p 423.

ROUGHNESS INDUCED TRANSIENT GROWTH: NONLINEAR EFFECTS

Meelan Choudhari* and Paul Fischer**
* *NASA Langley Research Center, Hampton, VA 23681*
** *Argonne National Laboratory, Argonne, IL 60439*

Abstræt: Numerical simulations are used to model the disturbance field associated with a spanwise periodic array of circular disks in a laminar boundary layer. Besides capturing the major trends from the recent wind tunnel measurements by White and Ergin (2003), the simulations reveal the intricate effects of disturbance nonlinearity and roughness geometry on the transient growth characteristics in the wake of the roughness array and provide a numerical database for validating detailed features of optimal growth theory in the context of roughness induced stationary disturbances.

Key words: Transient growth, bypass transition, roughness

1. BACKGROUND

The transient growth phenomenon refers to an algebraic amplification of small-amplitude disturbances prior to an exponential decay farther downstream (Landahl, 1980). For suitable inflow conditions, the transient amplification ratios can be comparable to the growth factors that correlate with the onset of transition due to exponential growth of linearly unstable eigenmodes. Consequently, the transient growth paradigm has emerged as an alternate scenario for laminar-turbulent transition, especially under subcritical (i.e., linearly stable) flow conditions (Reshotko, 2001). An upper bound on the transient growth ratios is provided by the optimal growth theory (Andersson et al. 1999, Luchini 2000, Tumin and Reshotko 2001). According to this theory, the optimal initial conditions are associated with purely wall normal and spanwise velocity perturbations resembling a spanwise array of streamwise vortices; the transient growth occurs as these

R. Govindarajan (ed.), Sixth IUTAM Symposium on Laminar-Turbulent Transition, 237–242.

initial conditions evolve into streak-like motions that are dominated by perturbations in the streamwise velocity.

The physical relevance of optimal growth theory to boundary-layer transition depends on receptivity characteristics of the laminar boundary layer, in particular, whether and how such optimal (or near-optimal) initial conditions can be realized in a natural disturbance environment. Transient growth of low-frequency boundary-layer disturbances due to free-stream turbulence of weak through moderate intensity has been documented in experiments (Kendall 1985) and also predicted using theoretical models (Leib et al. 1999). The recent correlation between subcritical transition on rough axisymmetric nosetips and a linear amplitude criterion based on optimal disturbance growth (Reshotko and Tumin, 2002) provides the motivation to study the role of surface roughness in promoting the transient growth of purely stationary disturbances.

Wind tunnel measurements by Gaster et al. (1994), White (2002), White and Ergin (2003), and Fransson et al. (2004) have established the typically suboptimal roughness-induced transient growth for a variety of roughness distributions. Theoretical analysis by Tumin and Reshotko (2004) has shown that transient growth also occurs in the limit of small roughness heights, a challenging case for accurate disturbance measurements in a wind tunnel. Here, we present numerical simulations of roughness-induced transient growth to help bridge the gap between theory and experiment. Specific issues of interest include: a comparison with the measurements by White and Ergin (2003) for a spanwise periodic array of roughness elements, the range of validity of the measured empirical scaling for perturbation energy as function of Re_k, and unsteady vortex shedding at large values of Re_k. An earlier account of these simulations was presented by Fischer and Choudhari (2003), henceforth referred to as FC.

2. NUMERICAL RESULTS

The primary flow configuration used for the numerical simulations corresponds to a flat-plate boundary layer with a spanwise periodic array of circular-disk roughness elements, located at a distance of x_0 = 230 mm from the sharp leading edge. The diameter of the roughness elements is equal to 6.35 mm, with the spacing between each pair of adjacent elements being λ_0 = 19 mm, i.e., approximately 3 times the roughness diameter. The free-stream speed is 10 m/s. All numerical simulations have been performed using the spectral element code Nek5000 (Fischer et al. 2002). Details of the computational procedure and grid convergence studies are described in FC.

Simulation results for the baseline roughness height of h = 0.57 mm ($Re_k \approx 119$) are presented in Fig. 1, which shows the streamwise evolution of integrated modal energy for the first four spanwise modes. Similar to the experiment, the modes $\lambda = \lambda_0$, $\lambda = \lambda_0/3$, and $\lambda = \lambda_0/4$ exhibit transient growth before decaying farther downstream. The fundamental mode undergoes a rapid and substantial decay before the beginning of its algebraic growth. In contrast, the shorter wavelength modes begin to amplify almost immediately in the wake of the array. The $\lambda = \lambda_0/4$ mode reaches its peak amplitude before the other modes, and is closely followed by the $\lambda = \lambda_0/3$ mode which dominates the disturbance amplitudes in the intermediate wake region, up to approximately 200 mm downstream of the roughness array.

As discussed by FC, the streamwise velocity perturbations at $\lambda = \lambda_0$ undergo a sign reversal near $x - x_0 = 35$ mm (i.e., $x_{exp} = 335$ mm, where the subscript $_{exp}$ denotes distances from the physical leading edge in the experiment by White and Ergin (2003)), which results in optimal-like initial conditions for transient growth downstream of this location. Because the integrated modal energies $E_i(x)$ (i=1−4) are defined using a streamwise varying (similarity) length scale, the energy metric for the fundamental mode appears to reach a plateau near $x_{exp} = 600$ mm (i.e., $x - x_0 = 300$ mm), even though the actual disturbance energy continues to grow up to $x_{exp} \approx 1025$ mm. The latter location is somewhat upstream of $x_{exp} = 1245$ mm, where the local spanwise wave number reaches the theoretical optimum of 0.45 for transient growth beginning at the leading edge. After accounting for the thickening of the mean boundary layer over the transient growth interval, one finds the transient growth ratio for the $\lambda = \lambda_0$ mode to be approximately 320. However, because this growth is preceded by an even larger disturbance decay upstream of the minimum energy location, the exact significance of transient growth via a spanwise periodic roughness array cannot be determined at this stage.

White and Ergin were able to correlate their data for the transient growth of $\lambda = \lambda_0/3$ and $\lambda = \lambda_0/4$ modes with a quadratic fit of the form $E_3, E_4 \propto Re_k^2$ at a fixed x. To assess this scaling behavior within the computational framework, additional simulations were carried out for h = 0.665 mm (i.e., $Re_k \approx 162$). Modal analysis of the wake disturbances (Fig. 2(a)) suggests that the Re_k^2 scaling applies uniformly to modal energies of all four modes under consideration (i.e., $\lambda = \lambda_0$, $\lambda_0/2$, $\lambda_0/3$, and $\lambda_0/4$), at least within the narrow range of Re_k included in the figure.

Fig. 2(b) indicates that the empirical scaling for $E_3(x)$ is approximately valid over the range of $75 < Re_k < 250$. For Re_k values below this range, the

qualitative behavior of the modal energy evolution for $\lambda = \lambda_0/3$ was found to deviate from that seen earlier in Fig. 1. Specifically, there is noticeable decay in $E_3(x)$ behind the roughness element before its transient growth ensues. The decay becomes stronger at smaller roughness heights, such that little or no transient growth is observed for the $\lambda = \lambda_0/3$ mode prior to its original peak near x_{exp} = 360 mm for the baseline roughness configuration. The modes $\lambda = \lambda_0$ and $\lambda = \lambda_0/4$ exhibit transient growth as before, but the onset of transient growth and/or peak modal amplitudes occur at significantly different locations than those in Fig. 1. Therefore, the amplitude scaling for the different Fourier harmonics becomes nonuniform at these lower values of Re_k.

At a roughness height of h = 1.14mm (i.e. twice the height in the baseline case), the separated flow behind the roughness element is found to be unsteady. The unsteady vortex structures in the plane of symmetry (Fig. 3) resemble the flow structures observed during natural transition in a flat plate boundary layer. Follow-up computations will reveal the critical Re_k value at which vortex shedding begins and whether or not these vortex structures decay eventually or lead to an earlier onset of transition.

3. CONCLUDING REMARKS

In summary, we have presented numerical simulations of transient growth due to a spanwise periodic array of cylindrical roughness elements. The agreement between simulation results and the measured data confirms the accuracy of the spanwise-global wall-finding algorithm used by White and Ergin (2003) over the local wall-finding procedure used previously by White (2002). Results for smaller roughness heights support the linear theory predictions of Tumin and Reshotko (2004) concerning a decay of the $\lambda = \lambda_0/3$ mode across a considerable distance downstream of the roughness array. At intermediate roughness heights (i.e. approximately $75 < Re_k < 250$), simulation results are nearly consistent with the Re_k^2 fit for disturbance energy as derived from the measured data. Self-sustained, unsteady vortex shedding occurs at sufficiently large roughness heights, and unsteady flow structures in the form of high shear layers are observed along the symmetry plane.

By underscoring the experimentally observed variation of transient growth characteristics with roughness geometry, the present computational findings indicate the challenges in physical understanding of subcritical transition due to distributed surface roughness. Our future work will focus on transient growth due to other relevant roughness configurations, including

the interactions among multiple roughness arrays, as well as on the onset of transition due to vortex shedding at large roughness heights.

ACKNOWLEDGMENTS

The authors acknowledge technical communications with Prof. Edward White of Case Western Reserve University and Prof. Anatoli Tumin from the University of Arizona.

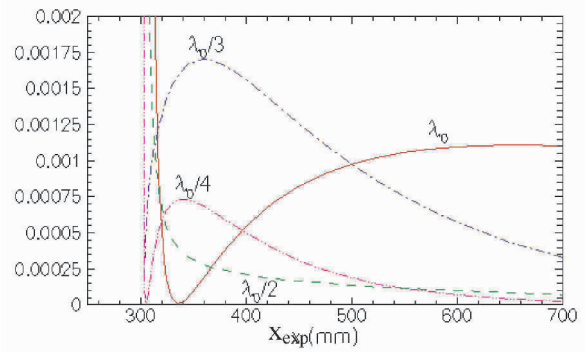

Figure 1. Downstream evolution of modal energy E_i (x_{exp}) in selected disturbance harmonics (i=1–4) for h = 0.57 mm

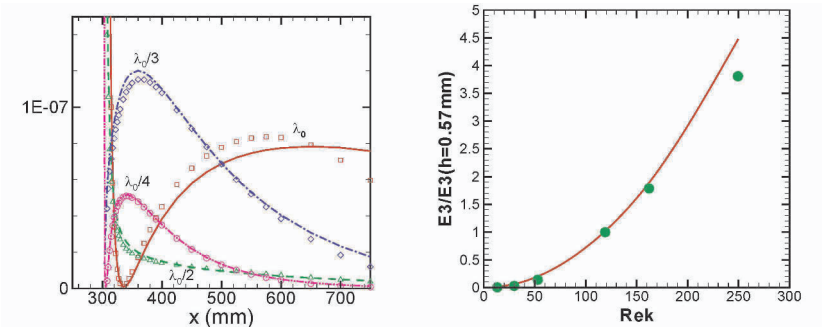

Figure 2. Nonlinear effects on roughness induced transient growth

(a) Effect of roughness height on transient growth: normalized modal energies E_i/Re_k^2 (i=1–4), plotted as functions of x_{exp}. Lines denote modal evolution for baseline array (Re_k = 119); symbols represents the case of larger-height array with Re_k = 162.

(b) Energy of $\lambda = \lambda_0/3$ mode at a fixed streamwise location, x_{exp} = 370mm, as function of Re_k. Symbols denote simulation data, whereas the line indicates the empirical, Re_k^2 scaling based on the baseline results.

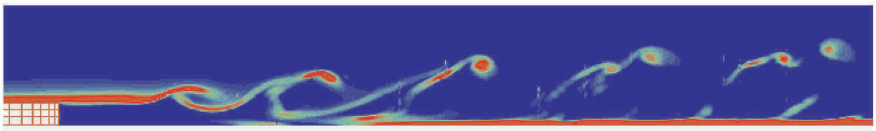

Figure 3. Unsteady vortex shedding in z = 0 plane behind roughness array with h = 1.14 mm

REFERENCES

Andersson, P., Berggren, M., and Henningson, D.S., "Optimal Disturbances and Bypass Transition in Boundary Layers," *Phys. Fluids*, Vol. 11(1), pp. 134-150, 1999.

Fischer, P.F., and Choudhari, M., "Numerical Simulations of Roughness-Induced Transient Growth in a Laminar Boundary Layer," AIAA Paper 2004-2539, 2004.

Fischer, P.F., Kruse, G.W., and Loth, F., "Spectral element methods for transitional flows in complex geometries," *J. of Sci. Comput.* Vol. 17, 1, pp. 81-98, 2002.

Fransson, J.H.M., Brandt, L., Talamelli, A., and Cossu, C., "Experimental and Theoretical Investigation of the Nonmodal Growth of Steady Streaks in a Flat Plate Boundary Layer," *Phys. Fluids*, Vol. 16(10), pp. 3627-3638, 2004.

Gaster, M., Grosch, C.E., and Jackson, T.L., "The Velocity Field Created by a Shallow Bump in a Boundary Layer," *Phys. Fluids*, Vol. 6(9), pp. 3079-3085, 1994.

Kendall, J.M., "Experimental Study of Disturbances Produced in a Pre-Transitional Laminar Boundary Layer by Weak Free-Stream Turbulence," AIAA Paper 85-1695, 1985.

Landahl, M.T., "A Note on an Algebraic Instability of Inviscid Parallel Shear Flows," *J. Fluid Mech.*, Vol. 98, pp. 243-251, 1980.

Leib, S.J., Wundrow, D.W., and Goldstein, M.E., "Effect of Free-Stream Turbulence and Other Vortical Disturbances on a Laminar Boundary Layer," *J. Fluid Mech.*, Vol. 380, pp. 169-203, 1999.

Luchini, P., "Reynolds-Number-Independent Instability of the Boundary Layer over a Flat Surface: Optimal Perturbations," *J. Fluid Mech.*, Vol. 404, pp. 289-309, 2000.

Reshotko, E., "Transient Growth – A Factor in Bypass Transition," *Phys. Fluids*, Vol. 13(5), pp. 1067-1075, 2001.

Reshotko, E. and Tumin, A., "Investigation of the Role of Transient Growth in Roughness-Induced Transition," AIAA Paper 2002-2850, 2002.

Tumin, A., and Reshotko, E., "Spatial Theory of Optimal Disturbances in Boundary Layers," *Phys. Fluids*, Vol. 13(7), pp. 2097-2104, 2001.

Tumin, A., and Reshotko, E., "The Problem of Boundary-Layer Flow Encountering a Three-Dimensional Hump Revisited," AIAA Paper 2004-0101, 2004.

White, E.B., "Transient Growth of Stationary Disturbances in a Flat Plate Boundary Layer," *Phys. Fluids*, Vol. 14(2), pp. 4429-4439, 2002.

White, E.B., and Ergin, F.G., "Receptivity and Transient Growth of Roughness-Induced Disturbances," AIAA Paper 2003-4243, 2003 (submitted for publication to *Phys. Fluids*).

FEEDBACK CONTROL IN SPATIALLY GROWING BOUNDARY LAYERS

Mattias Chevalier,[1,2] Jérôme Hœpffner,[2] Espen Åkervik,[2] and Dan S. Henningson[1,2]

[1] *Department of Computational Physics*
The Swedish Defence Research Agency (FOI), Stockholm, Sweden
mattias.chevalier@foi.se

[2] *Department of Mechanics*
Royal Institute of Technology (KTH), Stockholm, Sweden
henning@mech.kth.se

Abstract: Linear feedback control has been applied to transitional boundary layer flows. Information from wall-mounted sensors is used to estimate the flow state. The estimated state is then used to compute the optimal feedback control which is applied as blowing and suction with zero net mass-flux through the wall. The performance of the controller is tested in direct numerical simulations of a spatially growing Falkner–Skan–Cooke boundary layer where an inflectional instability is triggered. The extension to spatial boundary layer flows is an important step towards real applications.

Keywords: Flow control, LQG, control, estimation, Navier–Stokes equations, Falkner–Skan–Cooke, Orr–Sommerfeld/Squire

1. INTRODUCTION

By applying control to flows with strong inherent instabilities, through sensors and devices acting only on small parts of the flow, one may achieve dramatic effects by only minute amounts of control energy expenditure. Such control devices can be used in a wide variety of applications, for example, maintaining laminar flow on aircraft wings, relaminarizing/decreasing drag in turbulent flows and enhancing mixing in turbulent flows. Here we use linear optimal control theory where it is possible to formulate a control problem in which the control is computed from limited measurements from the flow. Recent overviews of similar flow control attempts are found in Bewley, 2001 and Kim, 2003.

R. Govindarajan (ed.), Sixth IUTAM Symposium on Laminar-Turbulent Transition, 243–248.

2. FEEDBACK CONTROL

A standard state-space formulation (e.g. Lewis and Syrmos, 1995) of the control problem can be written

$$\begin{aligned} \dot{q} &= Aq + B_1 f + Bu, \quad q(0) = q_0, \\ y &= Cq + g, \end{aligned} \tag{1}$$

where q is the state, A is the linear operator representing the dynamics of the system, the stochastic forcing f acts on the system through operator B_1, and the control u acts on the system through operator B. Furthermore q_0 is the initial condition and operator C extracts the measurements from the state and g adds stochastic measurement noise with given statistical properties which leaves the actual measured quantity in y. The measurements used in this study are the streamwise and spanwise shear stresses and wall pressure fluctuations.

An estimator, similar to system (1), can be formulated where an additional volume force v is added,

$$\begin{aligned} \dot{\hat{q}} &= A\hat{q} + Bu - v, \quad \hat{q}(0) = \hat{q}_0, \\ \hat{y} &= C\hat{q}, \end{aligned} \tag{2}$$

and where $\hat{q}$ is the estimated state and $\hat{y}$ is the measurement of the estimated flow. The purpose of the volume force is to make the estimator flow converge toward the "real" flow q.

The control u and the estimator volume force v are defined as $u = K\hat{q}$ and $v = L\tilde{y} = L(y - \hat{y})$ respectively where K and L are the control and estimation gains respectively which are computed as optimal feedback gains. This can be done independently for each wavenumber pair by solving two Riccati equations, see for example Green and Limebeer, 1995 for details on the theory.

In order to fit the incompressible Navier–Stokes equations into the state-space formulation we linearize the equations and transform them to Fourier space which give us the Orr–Sommerfeld / Squire equations (Schmid and Henningson, 2001). Note that the gains can be precomputed and then applied online in the simulations.

When designing the controller and estimator the objective function that determines what we want to minimize and the description of the external disturbances f, modeled through the covariance R_{ff}, are crucial quantities as they appear in the respective Riccati equations. In Hœpffner et al., 2004 and Chevalier et al., 2004 different covariance models have been studied for the case of channel flow and the estimator performance has been improved markedly by making physically relevant

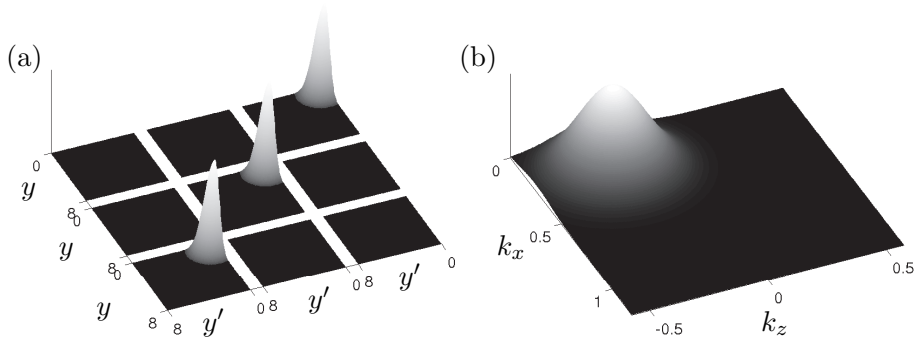

Figure 1. The covariance $R_{f_i f_j}$ of the external disturbances is depicted in (a). From top to bottom and right to left each square represent to covariance for f_1, f_2, and f_3. The wavenumber space amplitude function is shown in (b). The peak is moved to $\{0.25, -0.25\}$ which is the mode that is triggered in the FSC simulations

choices. Here we take the significant step of extending the work to spatially developing boundary layers. A first attempt in that direction was performed in Högberg et al., 2003.

In this work we model the covariance of the external disturbances as

$$R_{f_j f_k}(y, y', k_x, k_z) = \exp[-((k_x - k_x^0)/d_x)^2 - ((k_z - k_z^0)/d_z)^2]\delta_{jk}\mathcal{M}^y(y, y').$$

The model parameters k_x^0 and k_z^0 can be used to locate the peak energy of the disturbances in Fourier space, and d_x and d_z to tune the width of this peak. These parameters are specific for each flow case and are here chosen as $k_x^0 = 0.25$ and $k_z^0 = -0.25$. The y-variation of $R_{f_j f_k}$, depicted in figure 1(a), is given by the function

$$\mathcal{M}^y(y, y') = w\left((y + y')/2\right) \exp(-(y - y')^2/2d_y),$$

where the design parameter d_y governs the width of the two-point correlation of the disturbance in the wall-normal direction. The function $w(\xi) = U'(\xi)/U'(0)$ describes the variances at different distances from the wall. Here, the estimator is applied to disturbances inside the boundary layer, we thus use the wall-normal derivative of the mean flow.

Each of the three measurements is assumed to be corrupted by random sensor noise processes, the amplitude of which is determined by the assumed quality of the sensors. The covariance of the sensor noise vector g can thus be described in Fourier space by a 3×3 matrix G whose diagonal elements α_ι^2 are the variances of the sensor noise assumed to be associated with each individual sensor $R_{g_\iota(t) g_\kappa(t')} = \delta_{\iota\kappa}\delta(t - t')\alpha_\iota^2$.

The combination of full-state control and state-estimation is sometimes referred to as a compensator. The compensator consists of a "real"

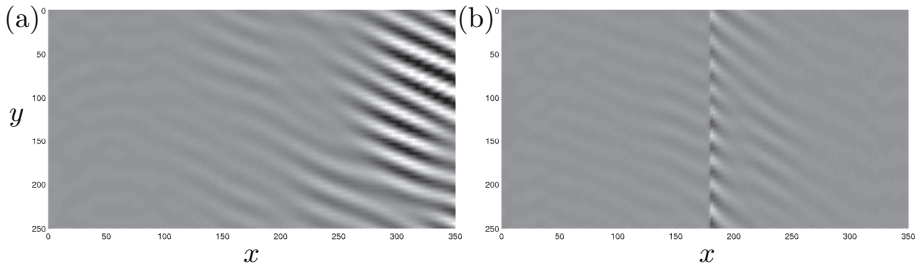

Figure 2. Snapshots of the wall-normal velocity component at $y = 0.5$. The flow state is depicted in part (a). In (b) the effect of the compensator control is shown. In both controlled flows the actuation was applied for 2000 time units, and reached its steady state. The black to white scales lies within $v \in [-0.00045, 0.00045]$

and an estimated flow. The "real" flow could be an experimental setup where only wall information is extracted. In our studies the "real" flow is represented by a direct numerical simulation (DNS). The estimator is another DNS, which is used to recover the state from sensor information. The compensation algorithm can be summarized in the following steps. First compute the difference between the measurements from the estimator flow and the "real" flow. Secondly compute the estimator forcing and apply it to the estimator. The new estimated state is then used to update the control signal. Finally the control is applied to both the "real" flow and the estimator.

3. DIRECT NUMERICAL SIMULATIONS

The DNS has been performed with the code reported in Lundbladh et al., 1999, which solves the incompressible Navier–Stokes equations by a pseudo-spectral approach. In order to allow spatially developing flows, a fringe region technique as described in e.g. Nordström et al., 1999 has been applied. This adds a forcing in the fringe region located in the downstream end of the computational box where the outflow and inflow conditions are blended together. The control is applied as a zero mass-flux blowing and suction boundary condition on the wall.

The computational domain is discretized in space by Fourier series in both horizontal directions and with Chebyshev polynomials in the wall-normal direction. The time integration is done using a four-step third-order Runge–Kutta method for the advective and forcing terms whereas the viscous terms are treated with a Crank-Nicolson method. The computational box has the dimensions $[0, 500] \times [0, 8] \times [0, 251.4]$ based on the displacement thickness δ_0^* at the beginning of the box where $Re_{\delta_0^*} = 337.9$. The corresponding resolution is $192 \times 49 \times 48$ modes.

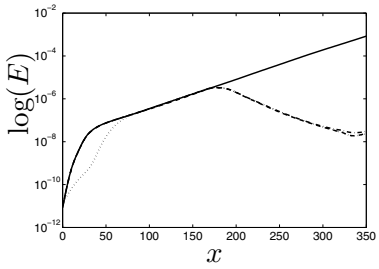

Figure 3. Time averaged perturbation energy for cross-flow vortices in a FSC boundary layer. Solid: uncontrolled. Dashed: full information control. Dash-dotted: compensator control. The dotted line shows the energy is the estimator

An inflectional instability is studied in a Falkner–Skan–Cooke (FSC) boundary layer where the Reynolds number is $Re_{\delta_0^*}$ and the Hartree parameter $\beta_h = 0.5098$ with a cross-flow component $W_\infty = 1.442$. The same FSC boundary layer flow studied in this paper is subject to several other studies, for example Högberg and Henningson, 1998 and Högberg and Henningson, 2002. The measurement region is located in $x \in [40, 150]$ and the control region in $x \in [175, 325]$. A random perturbation in space and time, upstream in the box, generates cross-flow vortices downstream.

The uncontrolled flow develops downstream and forms the cross-flow vortices depicted in figure 2(a). The figure shows the wall-normal perturbation velocity plotted at $y = 0.5$. The corresponding plot when compensator control has been applied is shown in figure 2(b). The simulations are run until a statistically stationary state is reached where we sample and time average the disturbance energy in the streamwise direction as shown in figure 3. The solid line shows the uncontrolled flow whereas the dashed and dash-dotted lines show full-information and compensator control respectively.

The control removes the exponential growth. However, adjacent to the downstream end of the control region the disturbance starts to grow exponentially again since the wave is unstable over the whole box.

4. CONCLUSION

Based on findings on how to improve the performance of the state estimator, reported in Hœpffner et al., 2004, combined with the state-feedback control used in, for example, Bewley and Liu, 1998 and Högberg and Henningson, 2002 inflectional instabilities in spatially developing boundary layer flows are controlled based on wall measurement.

The key to the improved performance of the estimator is the design of a physically relevant stochastic model for the external sources of disturbances which should account for as much as possible of the flow system that cannot be taken into account in the linear dynamic model that is used to formulate the control and estimator problem.

Note that so far we have given the estimator ample time to converge before turning on the compensator control. In future work one could reduce the time frame for the estimator to converge as well as experiment with smaller measurement regions.

ACKNOWLEDGEMENTS

This work has been financed by the Swedish Defence Research Agency (FOI) which is greatfully acknowledged.

REFERENCES

Bewley, T. R. (2001). Flow control: New Challenges for a New Renaissance. *Prog. Aero. Sci.*, 37:21–58.

Bewley, T. R. and Liu, S. (1998). Optimal and robust control and estimation of linear paths to transition. *J. Fluid Mech.*, 365:305–349.

Chevalier, M., Hœpffner, J., Bewley, T. R., and Henningson, D. S. (2004). State estimation of wall bounded flow systems. Part 2. Turbulent flows. *J. Fluid Mech.* Submitted.

Green, M. and Limebeer, D. J. N. (1995). *Linear robust control*. Prentice Hall.

Hœpffner, J., Chevalier, M., Bewley, T. R., and Henningson, D. S. (2004). State estimation in wall-bounded flow systems, Part 1. Laminar flows. *J. Fluid Mech.* Submitted.

Högberg, M., Chevalier, M., and Henningson, D. S. (2003). Linear compensator control of a pointsource induced perturbation in a Falkner–Skan–Cooke boundary layer. *Phys. Fluids*, 15(8):2449–2452.

Högberg, M. and Henningson, D. S. (1998). Secondary instability of cross-flow vortices in Falkner–Skan–Cooke boundary layers. *J. Fluid Mech.*, 368:339–357.

Högberg, M. and Henningson, D. S. (2002). Linear optimal control applied to instabilities in spatially developing boundary layers. *J. Fluid Mech.*, 470:151–179.

Kim, J. (2003). Control of turbulent boundary layers. *Phys. Fluids*, 15(5):1093–1105.

Lewis, F. L. and Syrmos, V. L. (1995). *Optimal control*. Wiley-Interscience.

Lundbladh, A., Berlin, S., Skote, M., Hildings, C., Choi, J., Kim, J., and Henningson, D. S. (1999). An Efficient Spectral Method for Simulations of Incompressible Flow over a Flat Plate. Technical Report TRITA-MEK 1999:11, Department of Mechanics, Royal Institute of Technology, KTH.

Nordström, J., Nordin, N., and Henningson, D. S. (1999). The fringe region technique and the Fourier method used in the direct numerical simulation of spatially evolving viscous flows. *SIAM J. Sci. Comp.*, 20(4):1365–1393.

Schmid, P. J. and Henningson, D. S. (2001). *Stability and transition in shear flows*, volume 142 of *Applied Mathematical Sciences*. Springer-Verlag.

EFFECT OF ELASTIC SUPPORTS ON THE CRITICAL VALUE OF REYNOLDS NUMBER PAST A CYLINDER

Sanjay Mittal and Saurav Singh
Department of Aerospace Engineering, Indian Institute of Technology Kanpur, UP 208 016, India
smittal@iitk.ac.in

Abstract: Flow past a cylinder becomes unstable at $Re \sim 47$ and vortex shedding ensues. A cylinder mounted on lightly damped springs can undergo vibrations as result of the unsteady forces experienced by it due to the vortex shedding. In this paper we examine the effect of elastic supports on the critical Reynolds number at which the vortex shedding sets in. It is found that for a cylinder with elastic supports, vortex shedding can be observed for Reynolds number as low as 22.

1. INTRODUCTION

Flow past a circular cylinder is associated with a variety of instabilities. The first instability is that of the wake. At $Re \sim 47$ the steady flow past a cylinder becomes unstable resulting in the von Karman vortex street (Williamson, 1996). Beyond $Re > 47$, Vortex Induced Vibrations (VIV) are observed for a cylinder that is mounted on elastic/non-rigid supports. It is well known that the motion of the cylinder can alter the flow-field significantly. Under certain conditions, the motion can cause the vortex-shedding frequency to match the vibration frequency. This is referred to as *lock-in* or *synchronization*. In addition, near the low- and high-end of the *lock-in* regime, the flow and cylinder response may exhibit *hysteresis*. Significant research has gone into the understanding of various phenomena associated with VIV. For a comprehensive review of the research, on various aspects of VIV, the reader is referred to a recent article Govardhan and Williamson, 2004.

The objective of the present work is to investigate the possibility of observing vortex shedding at $Re < 47$ for an elastically mounted cylinder. To this extent, 2D numerical simulations for VIV of a cylinder are presented. A stabilized space-time finite element formulation is utilized to solve the incompressible flow equations in primitive variables. The results of the simulations

R. Govindarajan (ed.), Sixth IUTAM Symposium on Laminar-Turbulent Transition, 249–254.

are confirmed via a global linear stability analysis of the combined equation systems for fluid flow and the motion of the oscillator.

2. GOVERNING EQUATIONS

Let $\Omega_t \subset I\!R^{n_{sd}}$ and $(0,T)$ be the spatial and temporal domains respectively, where n_{sd} is the number of space dimensions, and let Γ_t denote the boundary of Ω_t. The spatial and temporal coordinates are denoted by $\mathbf{x}$ and t. The Navier-Stokes equations governing incompressible fluid flow are

$$\rho(\frac{\partial \mathbf{u}}{\partial t} + \mathbf{u}\cdot\nabla\mathbf{u} - \mathbf{f}) - \nabla\cdot\boldsymbol{\sigma} = 0 \qquad \text{on } \Omega_t \; for \; (0,T), \tag{1}$$

$$\nabla\cdot\mathbf{u} = 0 \qquad \text{on } \Omega_t \; for \; (0,T). \tag{2}$$

Here ρ, $\mathbf{u}$, $\mathbf{f}$ and $\boldsymbol{\sigma}$ are the density, velocity, body force and the stress tensor, respectively. The stress tensor is written as the sum of its isotropic and deviatoric parts:

$$\boldsymbol{\sigma} = -p\mathbf{I} + \mathbf{T}, \quad \mathbf{T} = 2\mu\boldsymbol{\varepsilon}(\mathbf{u}), \quad \boldsymbol{\varepsilon}(\mathbf{u}) = \frac{1}{2}((\nabla\mathbf{u}) + (\nabla\mathbf{u})^T), \tag{3}$$

where p and μ are the pressure and dynamic viscosity, respectively. These equations are supplemented with appropriate boundary and initial conditions.

The motion of the cylinder is represented by a spring-mass system that is allowed two degrees of freedom: cross-flow and in-line vibrations. The non-dimensional equation for the cross-flow motion of the cylinder is given as:

$$\ddot{Y} + 2\pi F_n \zeta \dot{Y} + (\pi F_n)^2 Y = \frac{C_L}{\pi m^*}, \tag{4}$$

A similar equation describes the in-line motion. The reduced natural frequency of the system, F_n is defined as $\frac{f_n D}{U_\infty}$ where f_n is the actual frequency of the oscillator. Another related parameter is the reduced speed, U^*. It is defined as $U^* = \frac{U_\infty}{f_n D} = 1/F_n$, where, D is the diameter of the cylinder and is also used to non-dimensionalize the cylinder displacement. C_L is the lift coefficient. To encourage high amplitude oscillations, the structural damping is assumed to be zero. The non-dimensional mass of the cylinder (normalized with the mass of surrounding fluid of same volume as the cylinder) is $m^* = 4.73$.

3. FINITE ELEMENT FORMULATION

To accommodate the motion of the cylinder and the deformation of the mesh, the Deforming Spatial Domain/Stabilized Space-Time (DSD/SST) method (Tezduyar et al., 1992a, Tezduyar et al., 1992b) is utilized. In order to construct the finite element function spaces for the space-time method, we partition the time interval $(0,T)$ into subintervals $I_n = (t_n, t_{n+1})$, where t_n and t_{n+1} belong to an ordered series of time levels: $0 = t_0 < t_1 < \cdots < t_N = T$. Let

$\Omega_n = \Omega_{t_n}$ and $\Gamma_n = \Gamma_{t_n}$. We define the space-time slab Q_n as the domain enclosed by the surfaces Ω_n, Ω_{n+1}, and P_n, where P_n is the surface described by the boundary Γ_t as t traverses I_n. As is the case with Γ_t, the surface P_n is decomposed into $(P_n)_g$ and $(P_n)_h$ with respect to the type of boundary condition (Dirichlet or Neumann) being imposed. For each space-time slab we define the corresponding finite element function spaces: $(\mathcal{S}^h_{\mathbf{u}})_n$, $(\mathcal{V}^h_{\mathbf{u}})_n$, $(\mathcal{S}^h_p)_n$, and $(\mathcal{V}^h_p)_n$. Over the element domain, this space is formed by using first-order polynomials in space and time. Globally, the interpolation functions are continuous in space but discontinuous in time.

The stabilized space-time formulation for deforming domains is then written as follows: given $(\mathbf{u}^h)_{n^-}$, given $(\mathbf{u}^h)_{n^-}$, find $\mathbf{u}^h \in (\mathcal{S}^h_{\mathbf{u}})_n$ and $p^h \in (\mathcal{S}^h_p)_n$ such that $\forall \mathbf{w}^h \in (\mathcal{V}^h_{\mathbf{u}})_n$, $q^h \in (\mathcal{V}^h_p)_n$,

$$\begin{aligned}
&\int_{Q_n} \mathbf{w}^h \cdot \rho \left(\frac{\partial \mathbf{u}^h}{\partial t} + \mathbf{u}^h \cdot \boldsymbol{\nabla} \mathbf{u}^h - \mathbf{f} \right) d\Omega + \int_{Q_n} \boldsymbol{\varepsilon}(\mathbf{w}^h) : \boldsymbol{\sigma}(p^h, \mathbf{u}^h) dQ \\
&\qquad + \int_{Q_n} q^h \boldsymbol{\nabla} \cdot \mathbf{u}^h dQ + \sum_{e=1}^{n_{el}} \int_{Q_n^e} \delta \boldsymbol{\nabla} \cdot \mathbf{w}^h \rho \boldsymbol{\nabla} \cdot \mathbf{u}^h dQ \\
&+ \sum_{e=1}^{n_{el}} \int_{Q_n^e} \frac{1}{\rho} \tau \left[\rho \left(\frac{\partial \mathbf{w}^h}{\partial t} + \mathbf{u}^h \cdot \boldsymbol{\nabla} \mathbf{w}^h \right) - \boldsymbol{\nabla} \cdot \boldsymbol{\sigma}(q^h, \mathbf{w}^h) \right] \cdot \\
&\qquad \left[\rho \left(\frac{\partial \mathbf{u}^h}{\partial t} + \mathbf{u}^h \cdot \boldsymbol{\nabla} \mathbf{u}^h - \mathbf{f} \right) - \boldsymbol{\nabla} \cdot \boldsymbol{\sigma}(p^h, \mathbf{u}^h) \right] dQ \\
&+ \int_{\Omega_n} (\mathbf{w}^h)_n^+ . \rho \left((\mathbf{u}^h)_n^+ - (\mathbf{u}^h)_n^- \right) d\Omega = \int_{(P_n)_h} \mathbf{w}^h \cdot \mathbf{h}^h dP \qquad (5)
\end{aligned}$$

This process is applied sequentially to all the space-time slabs $Q_0, Q_1, \ldots, Q_{N-1}$. In the variational formulation given by Eq. (5), the notation being used is: $(\mathbf{u}^h)_n^{\pm} = \lim_{\varepsilon \to 0} \mathbf{u}(t_n \pm \varepsilon)$, $\int_{Q_n}(\ldots)dQ = \int_{I_n} \int_{\Omega_n}(\ldots)d\Omega dt$, $\int_{P_n}(\ldots)dP = \int_{I_n} \int_{\Gamma_n}(\ldots)d\Gamma dt$. The computations start with $(\mathbf{u}^h)_0^- = \mathbf{u}_0$, where $\mathbf{u}_0$ is divergence free.

The variational formulation given by Eq.(5), includes certain stabilization terms added to the basic Galerkin formulation to enhance its numerical stability. Details on the formulation, including the definitions of the coefficients τ and δ, can be found in the papers by Tezduyar et al., 1992c and Mittal, 2003. Equal-in-order basis functions for velocity and pressure, that are bilinear in space and linear in time, are used. The non-linear equation systems resulting from the finite-element discretization of the flow equations are solved using the Generalized Minimal RESidual *(GMRES)* technique in conjunction with diagonal preconditioners. The equations of motion for the oscillator, as given by Eq. (4), are also cast in the space-time formulation.

4. NUMERICAL RESULTS

The *rms* values of the aerodynamic coefficients and the non-dimensional shedding frequency, for a stationary cylinder at $Re = 50$ and 100, is compared with already published data. Good match is observed. The $Re = 25$ flow with a freely vibrating cylinder, is computed with three different finite element meshes. While the coarsest mesh has $24,604$ nodes, the finest one consists of $46,410$ nodes. The difference between the results from these meshes is less than 1%. This establishes the confidence in the present computations and the method being used.

Figure 1 shows the response of the cylinder and the associated flow at various Re. Vortex shedding can be observed for $22 \leq Re \leq 34$. The cylinder oscillations begin at $Re \sim 21.7$, reach maximum intensity at $Re \sim 26$ and then die beyond $Re \sim 34$. Also, the maximum oscillations occur at a reduced velocity of $U^* \sim 8$. The initial condition for all the computations corresponds to the steady flow at that Re for a stationary cylinder. This implies that the observed instability is intrinsic to the aeroelastic system. Further, it implies that the critical Re (Re_c) for a cylinder on elastic supports is significantly lower than that for a rigid cylinder. This has also been confirmed by carrying out a global linear stability analysis of the combined equations for the flow as well as the cylinder motion. The linear stability analysis has been carried out in a frame of reference attached to the cylinder. The finite element formulation results in a generalized eigenvalue problem that is solved via subspace iteration for tracking the rightmost (most unstable) eigenvalue. Figure 2 shows the real and imaginary part of the eigenvectors of the vorticity field close to the onset of the instability. The vortex shedding frequency at the onset, predicted by the linear stability analysis and the direct numerical simulations, are virtually identical.

The non-dimensional vortex shedding frequency for the freely vibrating cylinder at various Re are shown in Figure 3. It is found that the vortex shedding frequency and the vibration frequency of the cylinder match. This is the classical phenomenon of "lock-in". However, the vortex shedding frequency of the vibrating cylinder is significantly different than the structural frequency. Our computations for a cylinder of higher non-dimensional mass ($m = 50$) show that for heavier cylinders the vibration and vortex shedding frequency are much closer to the natural frequency of the spring mass oscillator. This observation was also made in our earlier work Mittal and Kumar, 1999 for higher Re flows. Also shown in Figure 3 are the results from Buffoni 2003 from laboratory experiments for forced oscillations of a cylinder. Clearly, there are differences in the vortex shedding frequency from the two studies. This might be related to the difference between the forced and free vibrations. More work is presently being carried out to address some of these observations.

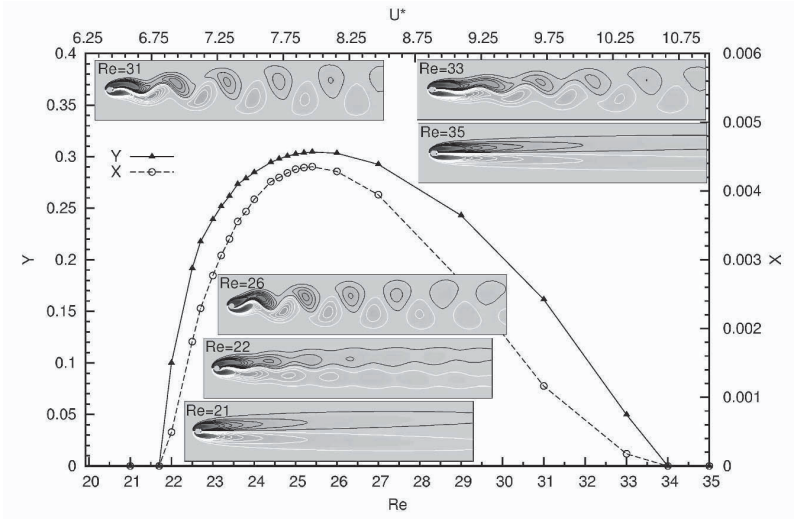

Figure 1. Flow past a freely vibrating cylinder: amplitude of the cylinder response (normalized with its diameter) and the vorticity field at various Re. White color contour lines correspond to positive vorticity while the black color lines show the negative vorticity

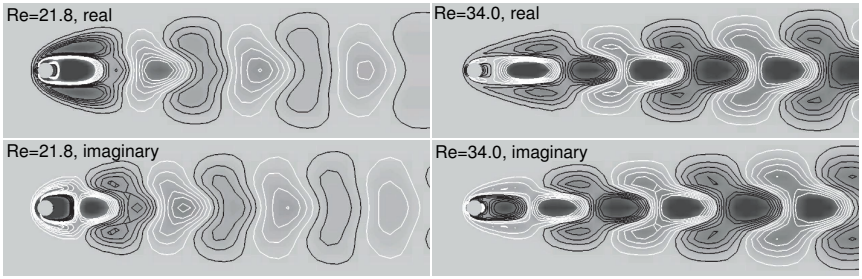

Figure 2. Flow past a freely vibrating cylinder: real and imaginary part of the eigenmodes, computed via linear stability analysis, at the onset of vortex shedding

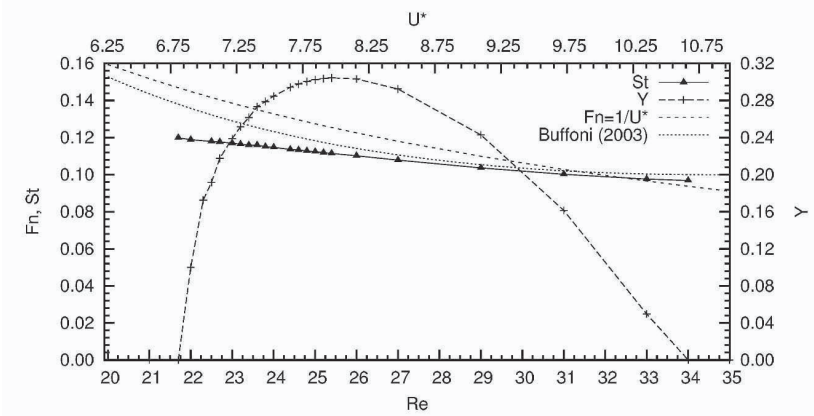

Figure 3. Flow past a freely vibrating cylinder: the non-dimensional vortex shedding frequency and natural frequency at various Re

5. CONCLUSIONS

These computations show that the aeroelastic instability can result in the lowering of critical Reynolds number for vortex shedding. These oscillations are self excited in nature. This might, to some extent, also explain some of the scatter of data in the literature for the critical parameters for the onset of shedding. The results for vortex induced oscillations at subcritical Reynolds numbers, from the direct numerical simulations and linear stability analysis agree quite well.

REFERENCES

Buffoni, E. (2003). Vortex shedding in subcritical conditions. *Physics of Fluids*, 15:814–816.

Govardhan, C.H.K. Williamson & R. (2004). Vortex-induced vibration. *Annual Review of Fluid Mechanics*, 36:413–455.

Mittal, S. (2003). Effect of a "slip" splitter plate on vortex shedding from a cylinder. *Physics of Fluids*, 15:817–820.

Mittal, S. and Kumar, V. (1999). Finite element study of vortex-induced cross-flow and in-line oscillations of a circular cylinder at low Reynolds numbers. *International Journal for Numerical Methods in Fluids*, 31:1087–1120.

Tezduyar, T.E., Behr, M., and Liou, J. (1992a). A new strategy for finite element computations involving moving boundaries and interfaces – the deforming-spatial-domain/space-time procedure: I. The concept and the preliminary tests. *Computer Methods in Applied Mechanics and Engineering*, 94(3):339–351.

Tezduyar, T.E., Behr, M., Mittal, S., and Liou, J. (1992b). A new strategy for finite element computations involving moving boundaries and interfaces – the deforming-spatial-domain/space-time procedure: II. Computation of free-surface flows, two-liquid flows, and flows with drifting cylinders. *Computer Methods in Applied Mechanics and Engineering*, 94(3):353–371.

Tezduyar, T.E., Mittal, S., Ray, S.E., and Shih, R. (1992c). Incompressible flow computations with stabilized bilinear and linear equal-order-interpolation velocity-pressure elements. *Computer Methods in Applied Mechanics and Engineering*, 95:221–242.

Williamson, C.H.K. (1996). Vortex dynamics in the cylinder wake. *Annual Review of Fluid Mechanics*, 28:477–539.

IMPROVEMENT OF LIFT-TO-DRAG RATIO OF THE AERO-TRAIN

Y. P. Kohama and Dong-hee Yoon
Institute of Fluid Science, Tohoku University, Sendai 980-8577 Japan

Abstract: Aero-Train is a new concept of environment friendly high speed transport system invented by our group. In order to realize this concept, improvement of the aerodynamic performance is essential. Our goal is to attain the overall lift to drag ration up to 25. Presently it is around 13 to 15. Some of the possible reasons why the value is low are in the interference drag and induced drag around lifting and guide wing junction. Flow separates largely at suction surfaces of the wing section enhanced by the existence of horizontal and vertical walls. Separation control study is conducted in present investigation using CFD and EFD approaches. Drastic improvement of lift to drag ratio was achieved by introducing several devices at the wing section. .

Key words: Environment friendly high speed transport system, Wing-in-Ground effect, Wing-wing interaction, Lift-to Drag ratio, Flow Separation Control

1. INTRODUCTION

Over 20% of Carbon Dioxide emission is from the general transport system. Fluid dynamic drag force is proportional to the square of the speed of the vehicle. Therefore in the case of high speed transport system including aircrafts, reduction of the aerodynamic drag force is essential from the point of environmental pollution problem. The Laminar-Turbulent Transition Symposium is essentially important in improvement of overall performance of aircrafts, namely increasing lift to drag ratio by maintaining laminar boundary layer over the vehicle surface. .

In the case of high speed ground transport systems like Shinkansen in Japan or Trans Rapid in Germany where cruising speeds exceed 300 km/h, around 90-% of the total drag is from aerodynamic drag. From such a point of view, we need to consider them as aircrafts. Therefore, increasing the lift to drag ratio of ground transport system is as important as that for aircrafts.

R. Govindarajan (ed.), Sixth IUTAM Symposium on Laminar-Turbulent Transition, 255–260.

Figure 1. Image sketch of the Aero-Train

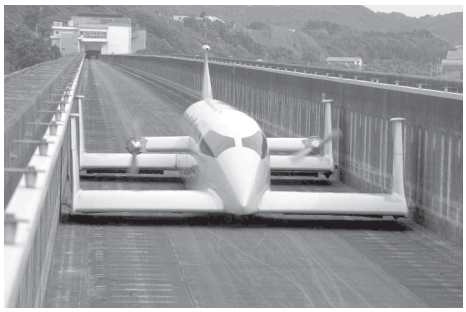

Figure 2. Test run of ART002 (120km/h, motor driven propeller)

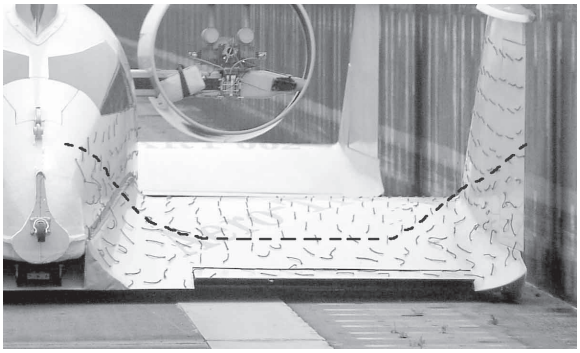

Figure 3. Separation area visualized by tuft method

From such consideration, we have been involved in the improvement of aerodynamic performance of high speed train in Japan. After a long survey of conventional high speed ground transport systems, we came to the conclusion that almost all the existing transport systems have to be entirely reconsidered for improving the aerodynamic performance. At the same time, we noticed that some of them are almost impossible to improve. For a instance, train system has a fatal problem. They cannot reduce the weight and cannot reduce aerodynamic drag force produced from the under floor narrow gap flow. Knowing such a fatal problem, finally we came to the idea of a completely new "Aero-Train" concept.

Aero-Train [1] floats over U-shape guide way solid surface by wing-in-ground effect. It is also guided by the same aerodynamic levitating side forces. Image sketch of the Aero-Train is shown in Fig.1. Cruise speed goes up to 500 km/h and 350 passengers with 3 coaches. Up to now, we already proved the practical floatation by constructing two running models. Fig.2 shows ART002 model running at 120 km/h in a guide way. Owing to the ground effect, lift to drag ratio of the Aero-Train becomes larger. Even the aspect ratio of the wings are quite small compared with that of aircrafts.

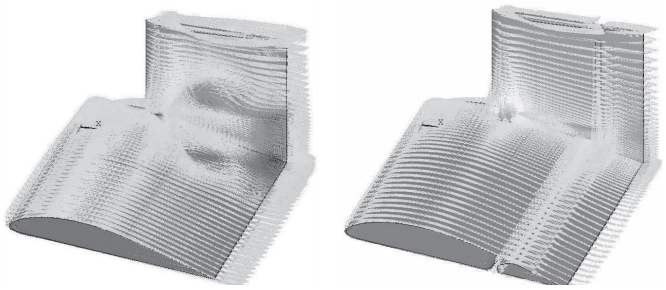

Figure 4. Computational results (with and without the single-slots)

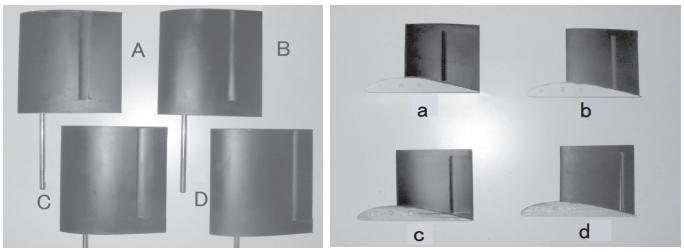

Figure 5. The wind tunnel wing model variation

Through 3 year series tests, we found the aerodynamic problems existing in the present system. One of the important problems is a large flow separation at the suction surface near trailing edge of main and guide wing parts. Fig.3 shows the tuft visualization and the separated area. Boundary layer flow tends to separate largely at this area more than conventional free flight condition because of the existence of the ground close to the wings. We could improve *L/D* if we could successfully control this separation.

Therefore, the purpose of the present investigation is to control the flow separation of the Aero-Train wing system by installing a single slotted flap[2,3]. Experimental and numerical investigations have been introduced, and by comparing each other, improvement of the performance was systematically tried.

2. NUMERICAL ANALYSIS

Numerical analysis is carried out using finite element analysis program "NSYS". The flow field is analyzed using the CFD of ANSYS. The flow model uses the transport equation derived from the 3D Navier-Stokes equation. It used incompressible energy equation and standard κ-ε model for a turbulence model. The numerical analysis is performed to find out the flow at the juncture and the slot shape. For the boundary condition of this

analysis, no-slip condition is applied to the flow on the wing surface and symmetric boundary condition is used at the root of the wing. Free stream velocity is 35 m/s and the velocity of ground and side walls are equal to the free stream velocity. Reynolds number based on the chord length is Re=3.5x10^5. The whole domain is assumed to be turbulent.

3. COMPUTATIONAL RESULTS

Fig 4 shows models with and without the single slotted flap on the main and guide wings. The velocity vectors shown here are 1 mm above the wing's surface. The slot gaps are increasing from the entrance of 3 mm on the low surface to the exit of 8 mm on the upper surface. The slot's shape and the slot's location showed the best results in controlling the boundary layer and the separated flow at the juncture.

4. EXPERIMENTAL RESULTS

4.1. The Variation of Aerodynamic Performance by Single-Slotted Flap

To begin with, the flow over the upper surface observed in the experiments was compared with that predicted in the numerical analysis. Fig.5 shows wing models used in the experiment. From now, we name models with the combination of A-D for the main wing and a-d for the guide wing. Fig.6 shows the visualization of the upper surface of the C-c wing model. This photograph indicates that the slotted flap successfully removed the separated region. This result agrees well with the velocity vector in Fig.4.

Fig.7 shows the aerodynamic characteristics of the models at α_m=2 °. The C_L of the models with single slotted flaps are lower by 0.045 in comparison with the baseline model, but the ground effect characteristics of the models are similar to that of the baseline model. Also, the C_D values decrease as the main wing approaches the ground plate. This is because the amount of the pressure leakage from the slot is increased as the main wing approaches the ground, which increases the outflow of the air from the slot, consequently suppressing the separation by the wing-wing interaction. The *L/D* of the models increase rapidly as *h/c* decreases, in comparison with that of the baseline model. On the other hand, the *L/D* of the B-a and B-d models

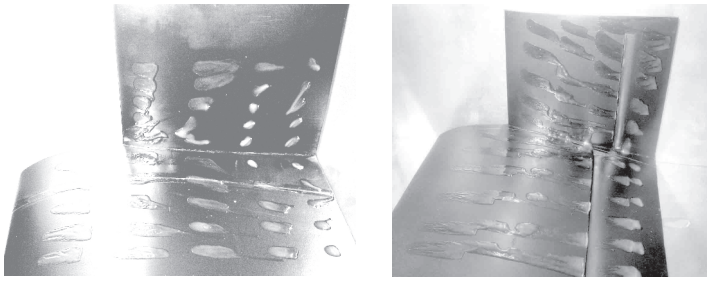

Figure 6. Oil flow visualization over suction surface of the wing system C-c, with and without single slots (αm=4°, αs=2°, U_∞=35m/s)

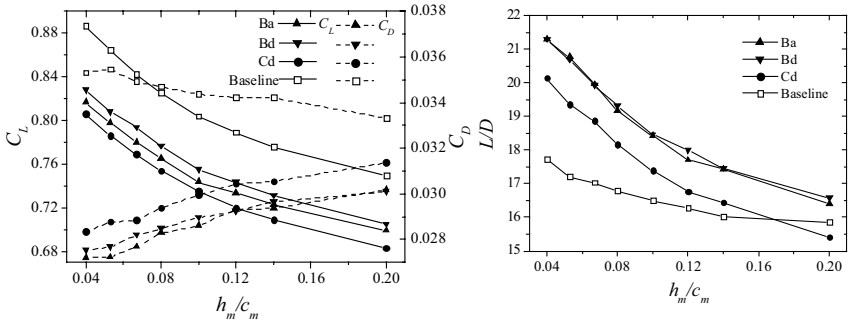

Figure 7. Aerodynamic Characteristics of the models at α_m=2°

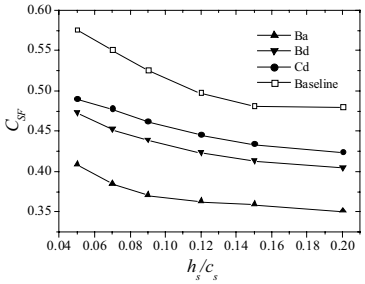

Figure 8. Side force characteristics of the wing system

(α_m=0°, α_s=2°)

are excellent in comparison with other models and the ground effect characteristic of B-d model is excellent in comparison with other models. The ground effect works as the restoring force in the pitch direction of the Aero-Train. At the designed suspending height of the Aero-Train(i.e. h/c=0.067), the *L/D* of B-a will increase by about 17.1 % and *CD* will decrease by about 20 %, compared to that of baseline model.

From the results above, the *L/D* of the wing models dramatically increased by the installation of the single-slotted flap. Among the wing models with a single-slotted flap, the *L/D* of the B-a model is the best in comparison with other models, however, the ground effect characteristic of the B-a model somewhat decreased in comparison with that of the baseline model.

On the other hand, among the wing models with a single-slotted flap, the ground effect characteristic of the B-d model is the best in comparison with other models. Then, at *g/c*=0.067, the *L/D* of the B-d model increased by about 17% at α_m=2°, by about 22.3% at α_m=4° and by about 31.6% at α_m=6°.

4.2. The Change of Side Force by Single-Slotted Flap

In the experiment of side force measurement, the height of the main wing is fixed at *h/c*=0.067 and *h* is changed from 4mm to 20mm. Fig.8 shows the ground effect characteristics of the side force coefficient *Csf*. This graph is plotted with the distance between the vertical wing and the side plate on the

x-axis, and the side force coefficient on the *y*-axis. The figure shows that the *Csf* of the models with single-slotted flaps decreases somewhat in comparison with that of the baseline model. Also, the ground effect characteristics of the models with single-slotted flaps show a tendency to be lower in comparison with that of the baseline model. This ground effect works as that restoring force in the yaw and roll directions on the Aero-Train, therefore, using a single-slotted flap tends to lower the yaw stability of the Aero-train.

5. CONCLUSIONS

For the purpose of improving the aerodynamic performance of the wing configuration, numerical analysis and wind tunnel experiments have been performed installing a single-slotted flap system. From these results, the following conclusions are obtained.

(1) By the installation of the single-slotted flap on the wings, when α_m=2° to 6°, the *L/D* increased sharply.
The increase in *L/D* of the B-a model is the best in comparison with other models. The location of the slot of the B-a model, in percent chord of main wing, is 38% and the location of the slot in percent chord of vertical wing is 50%.
The increase in ground effect characteristic of the B-d model is the best in comparison with other models. The location of the slot of the B-d model, in percent chord of main wing is, 38% and the location of the slot in percent chord of vertical wing is 20%.

(2) The ground effect characteristics of *Csf* of the models, with single-slotted flaps, show a tendency to be lower in comparison with that of the baseline model.

REFERENCES

[1] Kohama, Y.: Human Friendly High Speed Transportation System and Aerodynamics; Proceedings of 9th Asian Congress of Fluid Mechanics, May, 27-31(2002), Isfahan, Iran.
[2] D. Steinbach and K. Jacob: Some Aerodynamic Aspects of Wings near Ground; Trans. Japan Society, Aeronautics. and Space Sciences, Vol.34, No.104, pp.56-70.
[3] Wenzinger, C. J. and Harris: Wind Tunnel Investigation of an NACA 23012 Airfoil with Various Arrangements of Slotted flaps, NACA Technical Notes, (1933), No.472.

IN-FLIGHT AND WIND TUNNEL MEASUREMENTS OF NATURAL AND OF CONTROLLED INSTABILITIES ON A LAMINAR FLOW AIRFOIL

Inken Peltzer and Wolfgang Nitsche
Technical University of Berlin, Institute of Aeronautics and Astronautics
Marchstr. 12, Sekr.F2, D-10587 Berlin
inken.peltzer@tu-berlin.de

Abstract: The temporal and spatial development of natural Tollmien-Schlichting (TS) instabilities and artificially generated disturbances was investigated comprehensively in-flight as well as in a wind tunnel. The experiments were performed on a laminar wing glove for a sailplane using different surface sensor arrays (surface hot-wire sensors, piezo-sensor arrays). Two-dimensional TS waves dominate in the early linear stage of the boundary layer flow, but single three-dimensionally (3D) dominated wave packets, observed in the late stage of TS development, can be measured in the early stage as well. Furthermore, in the in-flight measurements, the 3D-instabilities occur earlier than in the wind tunnel. For the experiments on controlled transition, an array of spanwise distributed harmonic point sources which induced mono and multifrequency disturbances was used in order to compare the development of natural and controlled instabilities.

Keywords: Natural and controlled transition, in-flight- and wind tunnel experiments, Tollmien-Schlichting-waves, TS-instabilities, wave packets, laminar wing glove

1. INTRODUCTION

The present experimental investigation deals with the laminar-turbulent boundary layer transition on an airfoil, in particular with the spanwise development and amplification of Tollmien-Schlichting (TS) instabilities. The development of TS waves depends strongly on the environmental flow conditions. It is therefore necessary to investigate the transition under real conditions (i.e. in flight experiments), as well as in wind tunnel tests. This work is based on the experience gained in the Deutsche Forschungsgemeinschaft -funded university group research project [Nitsche et al., 2001], where artificial disturbances of a harmonic point source were investigated and which was carried out in cooperation with the Institute of Aerodynamics and Gasdynamics (IAG), Stuttgart University. The focus of the present paper is on investigating the temporal and

R. Govindarajan (ed.), Sixth IUTAM Symposium on Laminar-Turbulent Transition, 261–266.

spatial propagation of natural TS waves as well as artificially generated disturbances using an array of spanwise distributed point sources. The controlled disturbances were generated in order to model the development of natural disturbances and as input values for the Direct Numerical Simulation (DNS). Previous results of this work are published in [Peltzer and Nitsche, 2003].

2. EXPERIMENTAL SET-UP

A laminar wing glove, which was developed for the Grob 103 TWIN II two-seater sailplane at the Institute for Aeronautics and Astronautics, Technical University of Berlin, was used for the in-flight measurements. The measuring surface of the glove had a 1.0 m span and a chord length of 1.22 m. For comparison, a segment of the glove was employed for both in-flight and wind tunnel experiments. A Prandtl tube, which was attached underneath the glove, measures the freestream velocity. The boundary and in-flight conditions (pressure, temperature, velocity, etc.) were recorded continuously during the experiments. Comparative wind tunnel measurements were carried out at the laminar wind tunnel at the IAG, Stuttgart University. A freestream velocity of $u = 23.6\,m/s$ was used for all experiments. Basic investigations were performed in order to measure the velocity distributions over the glove at this freestream velocity. This velocity distribution was then reproduced in the wind tunnel. Both distributions showed a good agreement, allowing the comparison of in-flight and wind tunnel measurements [Peltzer, 2004].

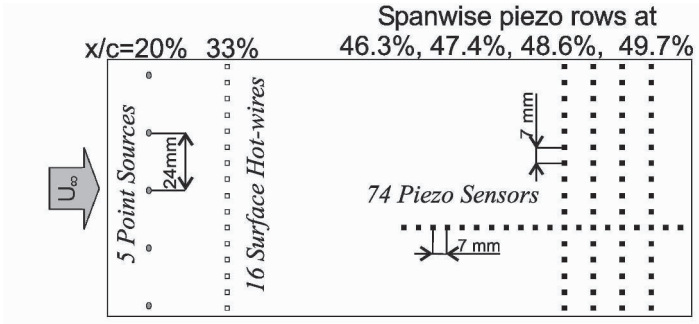

Figure 1. Point sources, 16 surface hot-wire array and 74 piezo sensor array

The sensor and actuator set-up is shown in Fig. 1. A spanwise array of 16 surface hot-wire sensors was located at a chord length of 33 %. This sensor was especially used to measure the instabilities with a very small amplitude in the early linear stage of amplification. Furthermore, an array of 74 piezo sensors was used in the stages of higher amplification (at 40 % to 50 % chord length). Small loudspeakers were arranged in a spanwise manner (at 20 % chord length) underneath the glove surface, and were optionally employed in order to introduce controlled disturbances into the boundary layer via a circle

of holes (with a diameter of $d = 0.2\,mm$ each). These speakers were operated individually by a signal processor that was capable of generating arbitrary types of disturbance waves. A point source generates disturbances consisting of a 2D plane wave and an infinite number of oblique wave trains (3D modes). For investigations dealing with artificially generated disturbances similar to 'natural' disturbances, point sources are the most suitable.

3. Controlled transition

Previous experiments, as well as the stability analysis [Stemmer and Kloker, 2002] showed that the most amplified instabilities occurred at a frequency of 600 Hz. Therefore, in the most simple excitation case, all point sources were activated in phase at this frequency. Subsequently, a mixture of signals consisting of two, three and five frequency components were generated. Results from the tests using controlled monofrequency disturbances are shown in fig. 2. Three sources are located upstream from where the signals shown were measured. Spanwise contiguous, 2D-dominated wave trains were observed in the contour plot of time traces of the surface hot-wires signals located at $33\,\%$ of the chord length (fig. 2.a). The slight waviness of the wave trains is due to the properties of the point sources. Looking at the RMS-values of the piezo array (fig. 2.b), there are three relatively small areas with high RMS-values, meaning highly amplified instabilities, downstream of the point sources.

These observations were also made for each case of multifrequency excitation. Fig. 3., for instance, shows the contour plots obtained from piezo array measurements for several disturbance cases generated by multiple frequencies. Basically, the same distribution of RMS-values can be seen. Areas of highest fluctuations are downstream of the spanwise-arranged, point sources, located upstream. The difference between the plots is due to the transition moving downstream. An increase in the number of frequencies that participate in the generated signal causes the amplification of instabilities to occurs later, which moves the transition downstream. In general, it has been found that the gener-

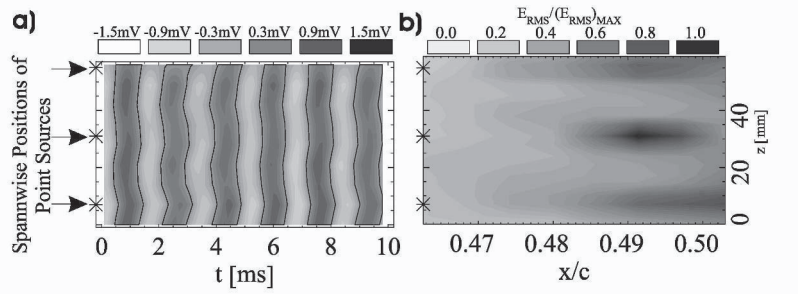

Figure 2. Controlled transition in the wind tunnel ($f_A = 600\,Hz$), a) Contour plot of a time sequence of the spanwise hot-wire array ($x/c = 33\%$) and b) Normalised RMS-values of the piezo array

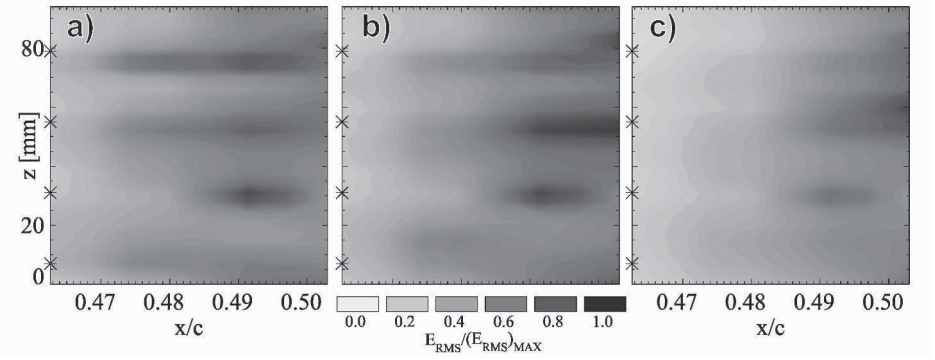

Figure 3. Controlled transition in the wind tunnel - Normalised RMS-values of the piezo array, a) $f_A = (600+700)\,Hz$, b) $f_A = (600+700+800)\,Hz$, c) $f_A = (400+500+600+700+800)\,Hz$

ated disturbances lead to fundamental breakdown. This is confirmed by comparing a numerical study by Stemmer [Stemmer and Kloker, 2002] and by measurements with Stereo-Particle-Image-Velocimetry described by Schröder [Schröder and Kompenhans, 2003].

4. COMPARISON OF NATURAL AND CONTROLLED TRANSITION

Contour plots of each spanwise piezo sensor row are shown in fig. 4. The results from the in-flight measurements of natural transition are illustrated in fig. 5.a-d), the wind tunnel measurements are shown in fig. 5.e-h). Furthermore, there are results from controlled transition with multifrequency excitation in fig. 5.i-l). The amplification of the instabilities can be observed in all cases by comparing subsequent sensor rows. The first spanwise sensor row ($x/c = 46.3\%$) of each case shows similar amplification of almost-2D TS-wave trains, indicating the equal phase of the spanwise-adjacent sensors. Locally limited wave trains with small oblique angles appear in the second sensor row ($x/c = 47.4\%$) during natural transition of the in-flight measurements (fig. 4.b) and also during controlled transition experiments in the wind tunnel (fig. 4.j). For natural transition experiments in the wind tunnel, 2D waves dominate the second sensor row, as well as the first row and the third row (fig. 4.e-g), but the amplitudes of the fluctuations in the third row ($x/c = 48.6\%$) are higher than in flight. The higher amplitudes can be also observed during controlled transition experiments in the wind tunnel. In the last spanwise row ($x/c = 49.7\%$), only individual wave packets occur in all measurements, which means that the 3D-portions dominate the local disturbance structures (beginning nonlinear stage). The amplitudes of the fluctuations in both wind tunnel measurements are more uniformly distributed, however. Fig. 5.b) illustrates the downstream RMS-values for the three cases. The amplitudes are smallest for natural transition in the wind tunnel. These amplitudes increase

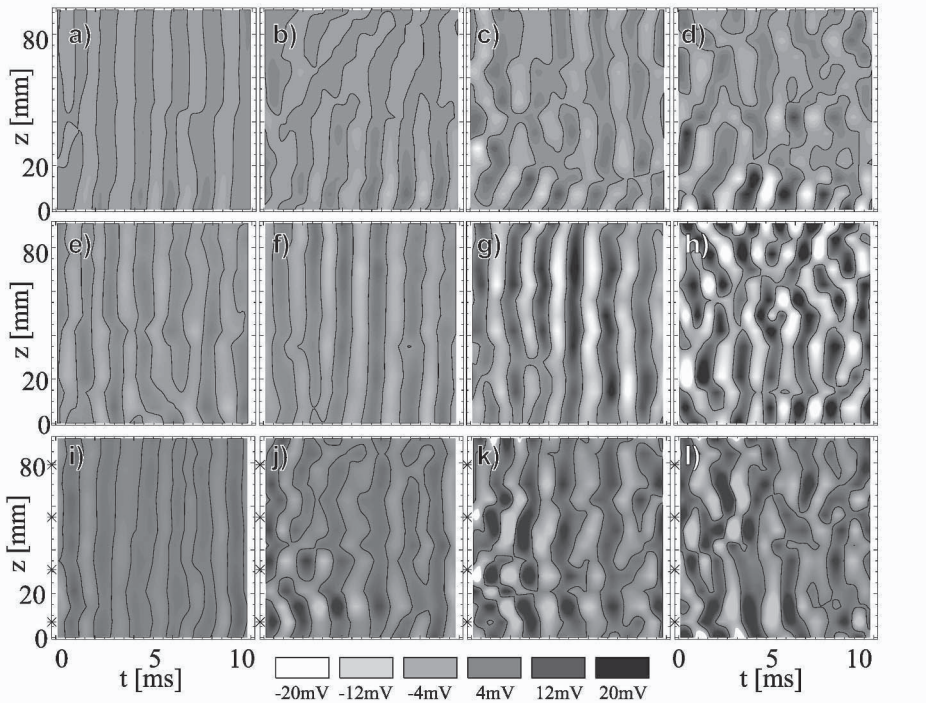

Figure 4. Contour plots of the four spanwise piezo rows, a-d) Natural transition - in-flight measurement, e-h) Natural transition - wind tunnel measurement and i-l) Controlled transition $f_A = (400 + 500 + 600 + 700 + 800)\,Hz$ - wind tunnel measurement

later and more rapidly than in the in-flight measurements. All RMS-values start at almost the same low level. The values for controlled transition are the first to increase, but do not become larger than those of the natural transition cases. Obviously, the generation of the controlled multifrequency instabilities lead to structures that are similar to the natural ones, as can be seen in the contour plots as well as in the downstream time traces (fig. 5.a and c).

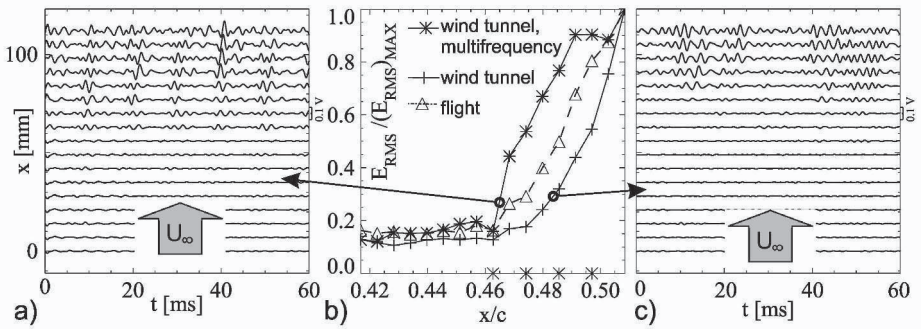

Figure 5. Signals of the downstream piezo sensors - Comparison of natural and controlled transition, a) Time traces with controlled disturbances ($f_A = (400 + 500 + 600 + 700 + 800)\,Hz$), b) Normalised RMS-values of natural transition in wind tunnel, in-flight and on controlled transition in wind tunnel, c) Time traces of in-flight measurement of natural transition

5. CONCLUSIONS

Experiments on controlled and natural transition on a laminar wing glove were carried out during comparative in-flight and wind tunnel measurements. The experiments for natural transition have shown that mainly 2D TS-instabilities dominate the boundary layer flow in the very early amplification stage of transition, but that single three-dimensional wave packets were present in this stage as well. Furthermore, the 3D-instabilities occur earlier in the in-flight measurements. The results obtained on controlled transition showed characteristic two- and three-dimensional structures, which are comparable with results obtained from numerical simulations. Finally, the measurements show that controlled disturbances, similar to those occurring in natural transition, could be generated using multifrequency disturbances.

ACKNOWLEDGEMENTS

We gratefully acknowledge the financial support given by the Deutsche Forschungsgemeinschaft (DFG). Special thanks also go to the IAG, Stuttgart University, where the wind tunnel measurements were carried out.

REFERENCES

Nitsche, W., Suttan, J., Becker, S., Erb, P., Kloker, M., and Stemmer, C. (2001). Experimental and Numerical Investigations of Controlled Transition in Low-Speed Free Flight. *Aerosp. Sci. Technol.*, 5:245–255.

Peltzer, I. (2004). *Flug- und Windkanalexperimente zur räumlichen Entwicklung von Tollmien-Schlichting-Instabilitäten in einer Flügelgrenzschicht*. Mensch und Buch Verlag, Berlin. Dissertation an der Technischen Universität Berlin.

Peltzer, I. and Nitsche, W. (2003). Experimental Investigations of Natural and Controlled Transition on a Laminar Flow Airfoil . In S. Wagner, M. Kloker, U. Rist, editor, *Recent Results in Laminar-Turbulent Transition - Selected Numerical and Experimental Contributions from the DFG-Schwerpunktprogramm "Transition" in Germany (NNFM 86)*, pages 269–280. Springer Verlag.

Schröder, A. and Kompenhans, J. (2003). Investigation of Transitional Structures in Artificially Excited Boundary Layer Flows by Means of Stereo and Multi-plane PIV. In S. Wagner, M. Kloker, U. Rist, editor, *Recent Results in Laminar-Turbulent Transition - Selected Numerical and Experimental Contributions from the DFG-Schwerpunktprogramm "Transition" in Germany (NNFM 86)*, pages 255–268. Springer Verlag.

Stemmer, C. and Kloker, M. (2002). Interference of Wave Trains with Varying Phase Relations in a Decelerated Two-Dimensional Boundary Layer. In S. Wagner, U. Rist, H.J. Heinemann, R. Hilbig, editor, *New Results in Numerical and Experimental Fluid Mechanics III (NNFM 77)*, pages 239–246. Springer Verlag.

INHERENT MECHANISM OF BREAKDOWN IN LAMINAR-TURBULENT TRANSITION*

Luo Ji-sheng, Wang Xin-jun, Zhou Heng†
Department of Mechanics, Tianjin University Liu-Hui center of Mathematics, Nankai and Tianjin University

Abstract: Abstract The conventional idea of Laminar-turbulent transition is that the transition starts from the amplification of disturbances, and when the disturbances become larger, higher harmonics will be generated due to non-linear effect, making the flow more and more complicated, and finally becomes turbulent. Though the scenario seems is clear, yet there is a missing link, that is, what happens in the breakdown process. Here we show by analyzing the results from direct numerical simulations that the change of stability characteristics of the mean flow profile plays a key role in the breakdown process.

Keywords: **Key words: laminar-turbulent transition, breakdown, stability**

1. ARGUMENTS BASED ON KNOWN FACTS

From hydrodynamic stability theory point of view, the laminar flow profile can support unstable eigen-mode solution when the Reynolds number is sufficiently large. The eigen-function bears a global character in the sense that the solution spans the whole region of the flow in the direction normal to the flow.

Contrary to that, the mean flow profile of turbulent flow does not support global unstable eigen-mode solution. For wall bounded turbulent flows such as plane channel flow and boundary layer flow, there are two distinct regions in the flow, namely, the wall region and the so-called outer region of a turbulent boundary layer or the core region of a channel flow (hereafter we mention only channel flow). The investigation by Tsujimoto and Miyake showed that the wall region has its own dynamics[1], which manifests itself as the generation of coherent structures, extracting turbulent energy from the mean flow, and then by the so-called bursting and sweeping phenomena, interact with the

*Project supported by NNSF of China, grant(10232020), and Liuhui Center of Applied Mathematics, Nankai and Tianjin University
†Author of corrspondence

R. Govindarajan (ed.), Sixth IUTAM Symposium on Laminar-Turbulent Transition, 267–273.

outer region. Zhou and his colleagues have proposed instability models for the generation of coherent structures in the wall region [2][3][4][5].

A distinct character of the mean flow profile for turbulent flows is that the normal-wise velocity gradient is very large in the wall region, but is very mild in the core region of a channel flow, which leads to the breakdown of the global character of the instability waves. Coherent structures are essentially generated due to some sort of instability of the flow in the wall region, which bears a strong local nature in the sense that the eigen-solution representing coherent structures decays very fast outside the wall region. The scenario of turbulent channel flow can be described as determined by interactions of disturbances in the two wall regions with those in the core region, and the core region plays a relatively passive role. The existence of distinct wall region and core region is obviously the consequence of mean flow modification.

2. DIRECT NUMERICAL SIMULATION FOR THE TRANSITION OF CHANNEL FLOWS

We used plane channel flow as the prototype for transition investigation. The numerical method used was semi-spectral method, that was, Fourier decomposition in stream-wise and span-wise directions, while in normal-wise direction, a 4th order accurate, two points compact finite difference scheme was used to solve equations resulting from Fourier decomposition.

We started from the laminar flow with a parabolic flow profile. Then initial disturbances were introduced, which consisted of three T-S waves expressed as follows:

$$a_1\mathbf{u}_1 e^{i(\alpha_1 x+\beta_1 z)} + a_2\mathbf{u}_2 e^{i(\alpha_2 x+\beta_2 z)} + a_3\mathbf{u}_3 e^{i(\alpha_3 x+\beta_3 z)} \qquad (1)$$

Where x is the coordinate in the stream-wise direction, z the coordinate in span-wise direction, y the coordinate in normal-wise direction; α_i and $\beta_i (i = 1, 2, 3)$ the wave numbers in x and z directions respectively; $\mathbf{u}_i (i = 1, 2, 3)$ represent the eigen-velocity vectors solved from the eigen-value problem of Orr-Sommerfeld equation for the laminar profile, normalized by the condition that $\max|u_i| = 1$, where u_i is the stream-wise velocity component, and a_1,$a_2 a_3$ the amplitudes.

Altogether, 6 cases were examined, their parameters are shown in Table 1, in which the Reynolds number Re was based on the velocity at the channel center of the laminar profile and half channel width. Depending on the initial amplitude of the disturbance, they can be either regular transition, i.e. starts from the amplification of small amplitude disturbances, or by-pass transition, which bears a sudden nature. But no matter which category they belong to, the change of their mean flow profiles during breakdown all have the same characteristics, hence here we show only results for case 1.

Table 1 Parameters for cases studied

Case	α_1	β_1	α_2	β_2	α_3	β_3	a_1	a_2	a_3	Re
1	1.0	0.0	0.8	0.6	1.0	0.3	0.002	0.002	0.002	8000
2	1.0	0.0	0.8	0.6	1.0	0.3	0.002	0.002	0.002	7000
3	1.0	0.0	0.8	0.6	1.0	0.3	0.08	0.08	0.01	8000
4	2.1	0.0	1.5	0.9	1.5	0.3	0.08	0.08	0.01	7000
5	2.7	0.0	2.1	0.9	1.5	0.3	0.08	0.08	0.01	7000
6	1.0	0.0	0.8	0.6	1.0	0.3	0.18	0.18	0.18	8000

The first two input waves were unstable modes. The disturbances evolved gradually at first and kept quite regular until about t=340, as shown in Fig. 1a, in which the velocity component u at a certain point induced by the Fourier components having the same wave numbers as the second input wave is shown. Correspondingly, the mean flow profile was still very close to the parabolic profile up to this moment, as shown in figure 1b, which also includes the mean flow profiles of several subsequent time instants. The mean velocity gradient at the wall also started to increase sharply after t=340, as shown in Fig.1c.

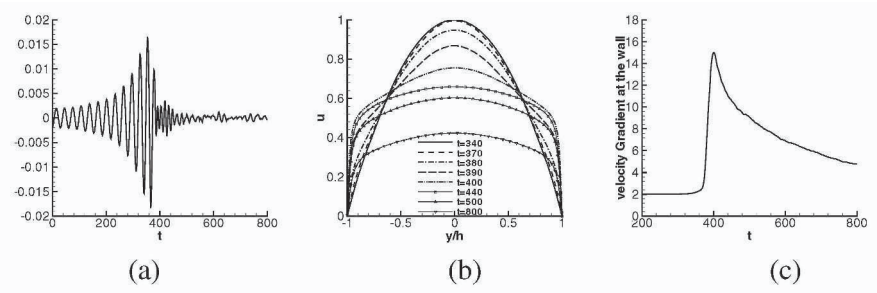

Fig.1 (a) velocity u of a certain point induced by wave with wave number α_2 and β_2 , (b) Mean flow profiles at different times, (c) time history of mean velocity gradient at the wall

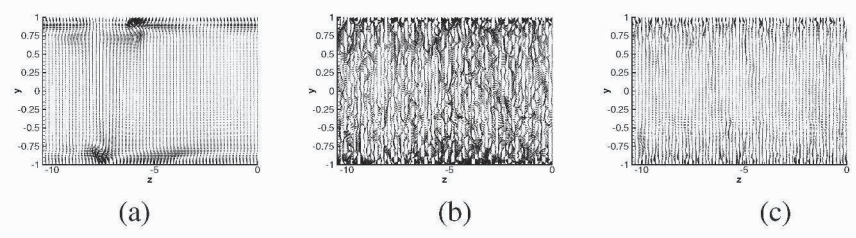

Fig. 2 Velocity vector plots in a certain y-z plane and the time history of averaged turbulent energy. (a) t=340, (b) t=400, (c) t=800. The vector length in (a) has been enlarged by a factor of 3

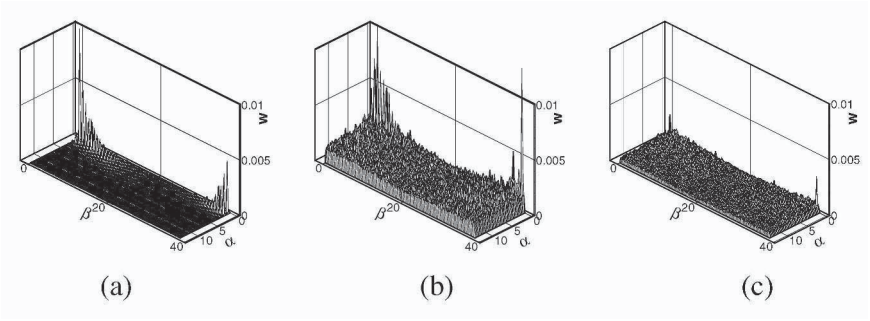

Fig.3 Fourier spectral of $\max|w|$ in α and β plane. $\max|w|$ is the maximum of $|w|$ for each given α and β. (a) t=340, (b) t=385, (c) t=800

Fig. 2 shows the velocity vector plot in a certain y-z plane at t=340, 400 and 500 respectively. Fig.2a shows that the disturbance is still quite regular, having the global nature as noted above. The corresponding figure Fig.3a for the spectral distribution of the maximum of w for each given a and b includes only some isolated components. Fig.2b corresponds to t=400, a moment during the breakdown process, in which the disturbance spreads over the whole plane, implying that many more harmonics were almost equally excited, and this can also be seen from Fig.3b. Fig.2c corresponds to a situation after breakdown, in which the disturbance manifests mainly as vortices, or coherent structures, near the two walls without mutual correlations, which is typical for turbulent flows, while the corresponding figure Fig.3c shows that the spectral is more evenly distributed, yet the magnitudes of different harmonics decreased appreciably compared with those for t=400.

Although at t=800, the main transition process has already been accomplished, as the shape of the mean flow profile already resembles the turbulent profile and the mean velocity gradient at the wall has already decreased sharply from its peak value, but it is still far from the final equilibrium state of turbulence. One can confirm this either by the fact that for the equilibrium turbulent flow, the maximum velocity of the mean flow should be close to 0.28 for R=8000, or the mean velocity gradient at the wall should be 0.5, the same as the laminar flow, because we used the constant pressure gradient formulation for our numerical simulation. The slowness of the flow in approaching its final equilibrium state is due to the fact that the mean flow modification is governed by a diffusion equation with a small coefficient for its diffusive term. But during the breakdown process, its modification was rather very quick due to the largeness of the disturbance, as manifested in Fig.2b and Fig.3b.

The result shown includes a previously unknown fact that during the breakdown, different harmonics were greatly enhanced, not only compared with those before transition, but also compared with those after transition. As dis-

cussed earlier, this is also the reason why the breakdown process can take a relatively short period to accomplish. Naturally, it poses a question, what is the key mechanism leading to the quick enhancement of many harmonics during breakdown? Simply refer to non-linear interaction seems is not enough.

Figure 1 shows that the mean flow profile started to have appreciable change at t=370, when slight inflection point appeared. We analyzed the linear stability characteristics of the mean flow profile at several times during the breakdown process, corresponding to t=375, 380, 385 and 390. Their neutral curves in a and ęÂ plane, together with those of laminar flow profile, are shown in Fig.4. Compared with the one for laminar profile, the unstable zones encircled by the neutral curves are drastically enlarged. In fact, not only the unstable zone, the maximum amplification rate have also been significantly increased, become 0.00507, 0.01570, 0.01552 and 0.01791, compared with 0.002735 for laminar profile. The enlargement of the unstable zone and the significant increase of the amplification rate was the basis of quick enhancement of many harmonics and turbulent energy, as shown in Fig.2b and d, which eventually lead to turbulence. Such a quick enhancement of many harmonics was not simply the result of non-linear interactions among different harmonics.

Judging by the mean flow profile in Fig.2, one can see that the breakdown process started from sometime between t=340 to 370, when it started to deviate from the original parabolic profile. The process practically ended at sometime between t=400 to 440, when the profile already bore the typical shape of turbulent profile that its central part became flat. The total time of transition was of the order of 40-50 time units.

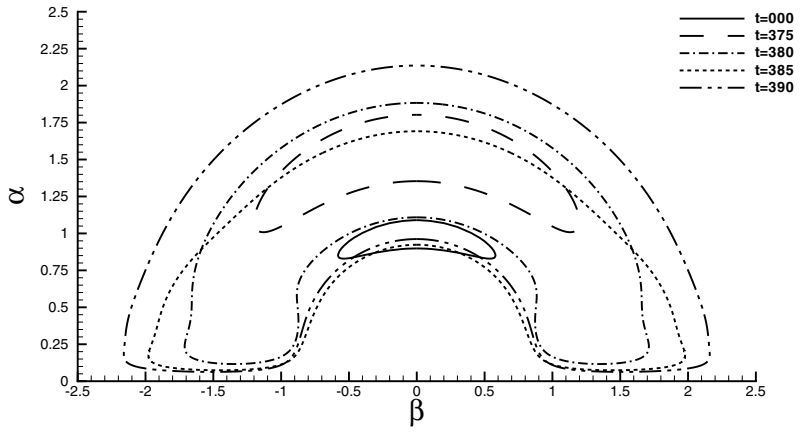

Fig. 4 Neutral curve in α, β plane. $t = 000$ corresponds to laminar profile

Among the six cases investigated, five of them belong to regular transition, while the other one was by-pass transition, but their breakdown process all undergone similar sequence of mean flow profile changes. There is one more interesting thing worth to be mentioned, that is, although the initial amplitude of the disturbances were the same for the case 4 and case 5, yet the time of breakdown was very different, as one can see from the evolution curves of the mean velocity gradient at the wall shown in Fig.5.

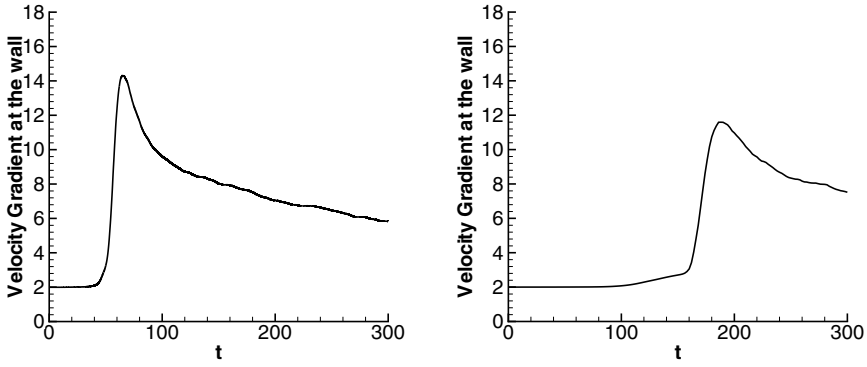

Fig 5 Mean velocity gradient at the wall (a) for case 4; (b) for case 5

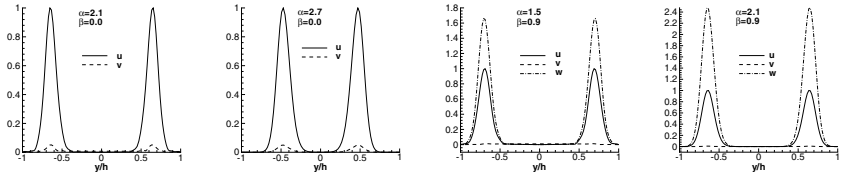

Fig. 6 Eigen-functions for case 4 and case 5 (a) 2-D eigen-functions for case 4; (b) 2-D eigen-functions for case 5; (c) 3-D eigen-functions for case 4, with wave numbers α_2 and β_2; (d) 3-D eigen-functions for case 5, with wave numbers α_2 and β_2. They all were normalized by the condition that $\max|u| = 1$

A possible explanation is that the peaks of the eigen-modes of case 4 are closer to the wall compared with their counter parts in case 5, as shown in Fig.6. The mean flow modification depends on the Reynolds stress generated by the disturbances, and if the peaks are closer to the wall, its ability of

modifying the mean velocity gradient at the wall must be stronger. Since the breakdown depends on the quick increase of mean velocity gradient at the wall, which causes the inflection point of the mean flow profile to appear, thus time of breakdown for case 4 came quicker than those for case 5.

3. DISCUSSIONS

One can summarize the breakdown process as: first, the disturbances modify the mean flow profile and different harmonics are generated through non-linear interaction. At a certain stage, which is crucial for breakdown, the mean flow profile starts to have inflection points, resulting in the quick enlargement of unstable zone in the wave number plane and the significant increase of the amplification rates, leading to the quick enhancement of many more harmonics and the spreading of disturbances over the whole channel. Thus, the mean velocity gradient of the mean flow profile will quickly become mild in the central part of the channel, effectively breaks the channel into two parts having different inherent dynamics, namely the wall region and the core region.

Such a flow profile provides the condition for the generation of coherent structures in the wall region, which extract energy from the mean flow, serving as the main source of turbulent energy. However, to reach the final turbulent profile, a quite long time is needed.

Also, breakdown does not depend solely on the amplitude of disturbances, because the ability of modifying the mean flow profile is different for different disturbances with the same amplitude but different wave numbers, as discussed in above section.

REFERENCES

[1] Tsujimoto, K. & Miyake, Y. Universal property of autonomous layer in near-wall turbulence, *IUTAM Symposium on Geometry and Statistics of Turbulence. Kluwer Academic Publication, editors: T. Kambe et al.,* 385-390 (2001)

[2] Zhou, H., Xiong, Z. The mechanism for the geration of coherent structures in the wall region of a turbulent boundary layer, *Science in China* (*Series A*), 38 (2): 188-198 (1995)

[3] Zhou, H., Coherent Structure Modeling and its Role in the Computation of Passive Quantity Transport in Turbulent Boundary Layer, *JSME International Journal, Series B*, 41(1):137-144 (1998)

[4] Zhou, H., Lu, C., Luo, J., Modeling of individual coherent structures in the wall region of a turbulent boundary layer, *Science in China* (*Series A*), 42 (6): 627-635 (1999)

[5] Zhang Dongming, Luo Jisheng, Zhou Heng, Dynamic model of coherent structure in the wall region of a turbulent boundary layer, *Science in China* (*Series G*),46(3): 291-299 (2003)

EXPERIMENTAL AND NUMERICAL ANALYSIS OF UNSTEADY BOUNDARY LAYER TRANSITION USING CONTINUOUS WAVELET TRANSFORM

Gilles STUDER, Daniel ARNAL, Robert HOUDEVILLE, Alain SERAUDIE
ONERA, Aerodynamics and Energetics Modeling Department, B.P. 4025, 31055 Toulouse Cedex 4, FRANCE
gilles.studer@onecert.fr

Abstract: The unsteady boundary layer transition over an airfoil is investigated experimentally for several Strouhal numbers. Continuous wavelet analysis is used to highlight the key mechanism of unsteady boundary layer transition. A quasi-steady approach is used to compute wave amplifications which are compared successfully with experimental amplifications.

Keywords: Boundary layer, Transition, Wavelet, Quasi-steady approach

1. INTRODUCTION

This paper is devoted to an experimental study of the oscillating boundary layer transition in presence of pressure gradient for several Strouhal numbers. Main studies on this topic have been carried out by Obremski and Fejer [7] and Desopper [2]. In these pioneering investigations, determination of amplified wave zones were simply made by observation of instantaneous waveform preventing a precise determination of locations, frequencies which compose "wave packets" and wave amplitude. The present study proposes a complete determination of the spectral content of the boundary layer velocity fluctuations in time, location and frequency during transition by using a continuous wavelet transform.

This transform can be seen in this case like an extend of a windowed Fourier transform, the width of which adapts to the frequency to analyze. For more details, the reader is refered to works of Daubechies, Mallat and Farge [1,3,6].

This method presents many advantages: constant relative accuracy of analyzed frequencies, detection of very small amplitudes and accurate time location of each frequency. By doing so, unsteady growth rates and amplitude profiles of unstable waves can be easily obtained and compared to the local linear stability theory by following the propagation of individual waves.

R. Govindarajan (ed.), Sixth IUTAM Symposium on Laminar-Turbulent Transition, 275–280.

2. EXPERIMENTAL SET UP

The experimental study is conducted on a NACA0015 airfoil (chord=0.3 m) at 0^o angle of attack placed in a low-velocity wind tunnel (freestream turbulence level 0.2%). The pulsation of the flow is induced by two rotating flaps, with a phase angle of 90^o, located far downstream (figure 1).

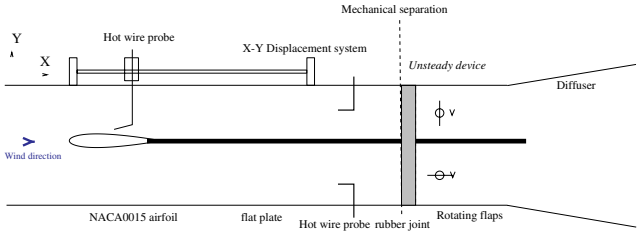

Figure 1. Experimental set-up

Velocity measurements are based on hot wire anemometry and are synchronized with the rotation of flaps. Two configurations are presented in this paper, characterized by Reynolds number (Re), Strouhal number (St), and amplitude of fluctuation of the external flow ($\frac{\Delta U_e}{U_e}$) at $x/c = 0.5$:

	$U_0(m/s)$	$f(Hz)$	$Re = \frac{U_0 c}{\nu}$	$St = \frac{fc}{U_0}$	$\frac{\Delta U_e}{U_e}(x/c = 0.5)$
Case 1	21	10	415 000	0.14	0.15
Case 2	21	30	415 000	0.43	0.25

Figure 2 shows measured smoothed pressure distributions which are used in the unsteady boundary layer calculations.

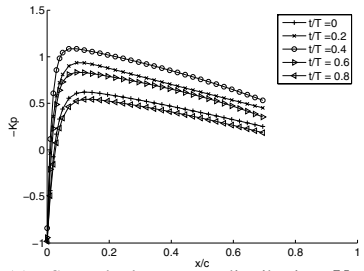

(a) Smoothed pressure distribution Kp for case 1

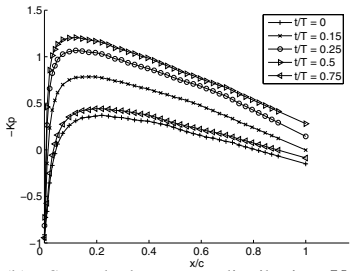

(b) Smoothed pressure distribution Kp for case 2

Figure 2. Pressure distributions for the studied cases

3. UNSTEADY CASES

In figures 3(a), 4(a), the shape factor H is plotted in the $(x/c - t/T)$ plane. This presentation reveals periodic turbulent wedges (small H values) and the transition location characterized by a rapid variation of H, always in a positive chordwise pressure gradient.

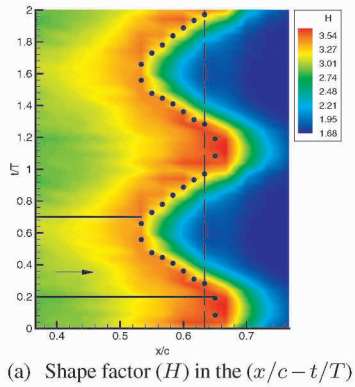

(a) Shape factor (H) in the $(x/c - t/T)$ plane. • represent transition positions detected by WSM

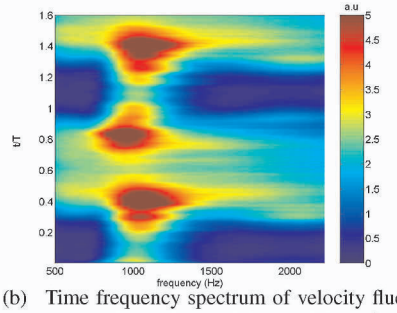

(b) Time frequency spectrum of velocity fluctuation near the wall $(y = 0.15mm)$ for $x/c = 0.633$

Figure 3. Case 1 analysis

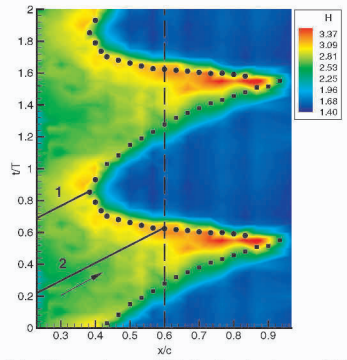

(a) Shape factor (H) in the $(x/c - t/T)$ plane. ■ represent "convective" transition positions, • "natural" transition positions detected by WSM

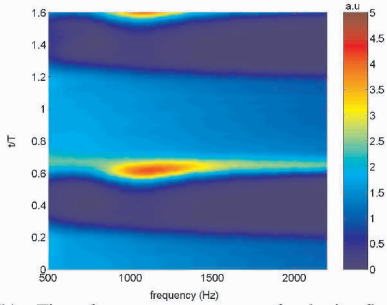

(b) Time-frequency spectrum of velocity fluctuation near the wall $(y = 0.15mm)$ for $x/c = 0.6$

Figure 4. Case 2 analysis

Two types of transition can be distinguished: "natural" transition by breakdown of unstable waves (black circles) and the laminar-turbulent interface corresponding to the turbulent area trailing edge (black squares).

In a qualitative way, the distinction can be made by showing amplitude time-frequency spectra presented in figures 3(b) and 4(b). They are plotted for stations specified by vertical dashed lines on the corresponding figures on the left. The same time scale is used to underline the conformity of integral quantity (H) and local spectrum. In case 1, for $f \approx 1000Hz$, there are clearly two Tollmien-Schlichting waves (TS) peaks, one on each side of the turbulent area. For each time, transition results from the breakdown of TS-waves in a quasi-steady process. In case 2, for the same frequency range, there is only one TS peak just before the beginning of the turbulent area. For $t/T \approx 0.3$, a turbulent front is present without TS waves. There is a competition between TS wave velocity, the arrows in figures 2 and 3, and turbulent patches velocity. In a quantitative way, computation of the skewness of the most amplified wave along the number of realization of the period gives precious information concerning the transition position. An example of this kind of analysis, called WSM (Wavelet Skewness Method), is given in figure 5.

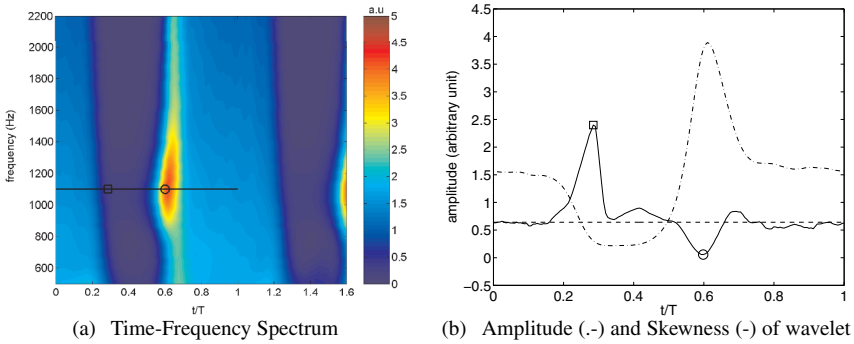

(a) Time-Frequency Spectrum

(b) Amplitude (.-) and Skewness (-) of wavelet coefficients along the black line in figure 5(a)

Figure 5. Example of transition position detection in the case of "creative" and "convective" transition. Transition points detected on the right are reported on time frequency spectrum on the left: (□) "convective" transition, (o) "creative" transition

The skewness of wavelet coefficients for $f = 1100Hz$ (specified by a black line in figure 5(a)) is plotted in solid line. It presents two well-defined deviations, one positive for $t/T = 0.28$ and one negative for $t/T = 0.60$.

The negative peak: A possible interpretation can be proposed. In the final stage of transition, non-linear interactions are driven by the fundamental mode (most unstable TS wave) in a resonant way [5]. Because of the "natural", uncontrolled disturbance conditions, unstable waves are modulated in time which conducts to "intermittent" non-linear interactions. As the most unstable wave tend to give energy to its harmonics, a negative deviation of the skewness is

found for fundamental wave. Concerning the harmonics, a positive deviation of the skewness is detected (not presented here).

The positive peak: The positive peak of skewness is more "artificial", because it doesn't correspond to a particular event. The position of the spot edge varies along realizations around a mean state which is in a laminar zone, this configuration can only produce positive deviations on the velocity signal, and consequently induces positive skewness peak at the mean position of the turbulent interface. It is interesting to note that, in such a case, the positive skewness peak is visible for all the frequency range.

3.1 Stability computations

The goal of calculation is to improve the quasi-steady approach concerning stability analysis of unsteady flows. Therefore, computation follows the classical scheme: external velocity distribution is introduced in an unsteady boundary layer solver which gives the velocity profiles for the linear stability solver.

The boundary layer calculations are performed with the help of an unsteady boundary layer code based on finite volume formulation. This code is initialized by unsteady external pressure distribution (figure 2) and a Hiemenz profile at the stagnation point ($x/c = 0$) for each time. In case 2, the experimental transition position is imposed to compute accurately the laminar boundary layer flow.

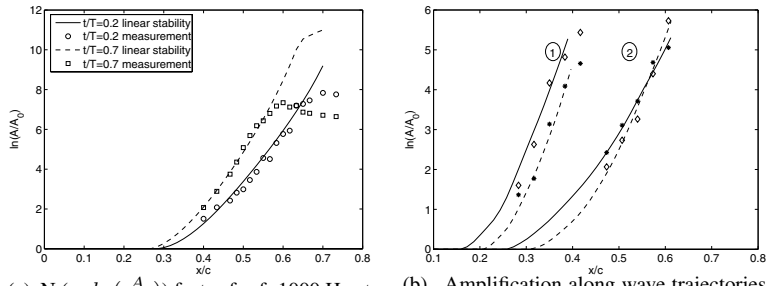

(a) N ($= ln(\frac{A}{A_0})$) factor for f=1000 Hz at 2 instants t/T=0.2 and t/T=0.7.

(b) Amplification along wave trajectories plotted in figure 4(a), (—) $f = 1500Hz$, (- - -) $f = 1000Hz$

Figure 6. Stability calculations for the 2 cases

In stability calculations, we solve the local linear stability problem (Orr-Sommerfeld equation) in a spatial theory, for each x/c and t/T point. The amplification rate is computed along wave trajectories determined by the phase velocity, assumed to be close to the group velocity. This quasi-steady method has been first suggested by Obremski and Morkovin [8]. Comparison between experimental and numerical amplifications are made along the same path.

A comparison of TS amplification along two different wave trajectories for each case (in figure 3(a), 4(a)) is plotted in figure 6. A general good agreement is found concerning amplifications. The shape of eigen functions have been verified successfully too (not presented here). Application of e^N method gives an acceptable estimation of the transition position (with $N \approx 7$ for case 1 and $N \approx 5.5$ for case 2). Nevertheless, special care has to be taken due to the variation of turbulence level and receptivity conditions along the period.

4. CONCLUSION

The time-frequency analysis using the wavelet transform brings new informations for unsteady flow transitions. It allows an accurate comparison with prediction method and a better understanding of the transition scenario through a precise determination of the amplitude of unstable waves and their accurate location in time.

A new method for the determination of unsteady transition position is proposed. It is based on the skewness of the wavelet coefficients of the most unstable waves. This method presents two main advantages: the decision is based on the localization of the extremum of a function (skewness) and doesn't deal with a treshold, like most of methods used to determine intermittency functions [4,9]. It gives the kind of transition according to the nature of the extremum (minimum or maximum).

Finally, the "natural" transition part can be described by the local linear stability theory provided that amplification is computed along wave trajectories. For the "convective" transition, methods based on spot convection can be helpful.

REFERENCES

[1] Daubechies, I. : "Ten Lectures on Wavelets", 1992, SIAM Philadelphia

[2] Desopper A.: "Etude experimentale des couches limites turbulentes et transitionnelles en ecoulement pulse", *PhD Thesis*, Supaero, Toulouse, 1977.

[3] Farge , M.: "Wavelet transforms and their applications to turbulence" *Annual Review of Fluid Mechanics* **24**:395-457,1992

[4] Hedley T. B.,and Keffer, J. F. : "Turbulent/non-turbulent decisions in an intermittent flow" *J. Fluid Mech* **64** part 4 :625–644, 1974.

[5] Kachanov Y. S. : "Physical mechanisms of laminar-boundary-layer transition" *Ann. Rev. Fluid Mech.* **26**:411–482, 1994.

[6] Mallat, S. : "A wavelet tour of signal processing", 1999, Academic Press

[7] Obremski H. J.,and Fejer, A. A. : "Transition in oscillating Boundary Layer Flows" *J. Fluid Mech* **29**:93–111, 1967.

[8] Obremski H. J.,and Morkovin, M. V. : "Application of a quasi-steady stability model to periodic boundary layer flows" *AIAA Journal* **7** No.7:1298–1301, 1969.

[9] Walker G. J.,and Hughes, J. D. : "The occurence of natural transition phenomena in periodic transition on axial compressor blades" *Prco. IUTAM Transition Symposium Sedona* :359–364, 1999, Springer.

NONLINEAR NONLOCAL ANALYSIS OF CROSS–FLOW–DOMINATED TRANSITION SCENARIOS USING DNS–LIKE RESOLUTION

Stefan Hein
DLR – Institute of Aerodynamics and Flow Technology
Bunsenstraße 10, D-37073 Göttingen, Germany
stefan.hein@dlr.de

Abstract: Crossflow–dominated laminar–turbulent transition is studied by nonlinear nonlocal theory (PSE) for the DLR swept–flat plate experiment. The strongly nonlinear stages of the transition process, i.e. the formation of high–frequency secondary instabilities, their linear and nonlinear growth as well as the subsequent disintegration of the secondary disturbance structures which is accompanied by a degradation of the stationary crossflow vortices are discussed.

Keywords: laminar–turbulent transition, PSE, high–frequency secondary instability

1. INTRODUCTION

It is well known that the process of laminar–turbulent transition in crossflow–dominated three–dimensional boundary–layer flows is intimately connected with the development of saturated crossflow vortices and the subsequent appearance of high–frequency secondary instabilities [10]. Using nonlinear nonlocal instability theory, i.e. solving the parabolized stability equations (PSE) [1], it was possible so far only to model the saturation in amplitude of these crossflow vortices. All attempts to also cover the development of high–frequency secondary instabilities with this type of approach failed, however. Therefore, these simulations so far also failed to provide any indication of the location of laminar–turbulent breakdown in crossflow–dominated cases.

The application of nonlinear nonlocal instability theory is limited to convectively unstable flows. On the other hand, recent spatial DNS by Wassermann & Kloker [11] clearly demonstrated the convective nature of this type of flow and thus confirmed corresponding numerical results by Koch [5] and experimental observations by White [12]. In principle at least, it should be possible to model the development of the high–frequency secondary disturbances by nonlinear nonlocal instability theory, provided that sufficient resolution is used

R. Govindarajan (ed.), Sixth IUTAM Symposium on Laminar-Turbulent Transition, 281–286.

in modal space in order to cover both the low–frequency travelling crossflow disturbances and the high–frequency secondary instabilities, the latter being also very localised in space.

2. BASIC FLOW

The displacement body placed on top of the DLR swept–flat plate experiment imposes a favourable pressure gradient in downstream direction which is strong enough to suppress Tollmien–Schlichting–type instability completely. Hence, it is a pure crossflow instability which triggers laminar–turbulent transition in this case. The basic flow was calculated by a first–order boundary–layer code for a free–stream velocity of $\mathrm{Q}_\infty = 19\,\mathrm{m/s}$, an effective sweep angle of $\phi_\infty = 42.5^\mathrm{o}$ and an analytically given approximation of the measured pressure distribution (see [6]). For the given free–stream conditions, stationary crossflow vortices with a spanwise wavelength of about $\lambda_\mathrm{c} = 12\,\mathrm{mm}$ were observed in the experiment. This value is taken as the fundamental spanwise wavelength and the fundamental frequency is set to $\mathrm{f} = 135\,\mathrm{Hz}$, which according to linear theory corresponds to the most amplified frequency.

3. NUMERICAL METHOD

The nonlinear nonlocal transition analysis code NOLOT/PSE [2, 3] solves the compressible parabolized stability equations (PSE) formulated in curvilinear orthogonal coordinates. The disturbance flow field $\tilde{\mathbf{q}}(\mathrm{x},\mathrm{y},\mathrm{z},\mathrm{t})$ is described by truncated double Fourier series of the form

$$\tilde{\mathbf{q}}(x,y,z,t) = \sum_{m=-M}^{M} \sum_{n=-N}^{N} \breve{\mathbf{q}}_{mn}(x,z) e^{i(n\beta y - m\omega t)}$$

with

$$\breve{\mathbf{q}}_{mn}(x,z) = \hat{\mathbf{q}}_{mn}(x,z) e^{\,i\int_{x_0}^{x} \alpha_{mn}(x)dx},$$

where ω and β denote the fundamental circular frequency and the fundamental spanwise wavenumber, respectively. Each disturbance mode is identified by its Fourier indices (m,n) with the corresponding chordwise wavenumber α_{mn}. A fourth–order compact finite–difference scheme is used in wall–normal direction, whereas the chordwise derivatives are discretised by first– or second–order backward finite differences. The resulting system of algebraic equations can be solved efficiently by a marching procedure in chordwise direction x. All calculations were performed with 301 non–equidistant grid points in wall–normal direction z. The truncation limits were set to M=31, N=19 (without counting the additional modes required for an aliasing–free FFT) and were checked by additional computations using M=N=42.

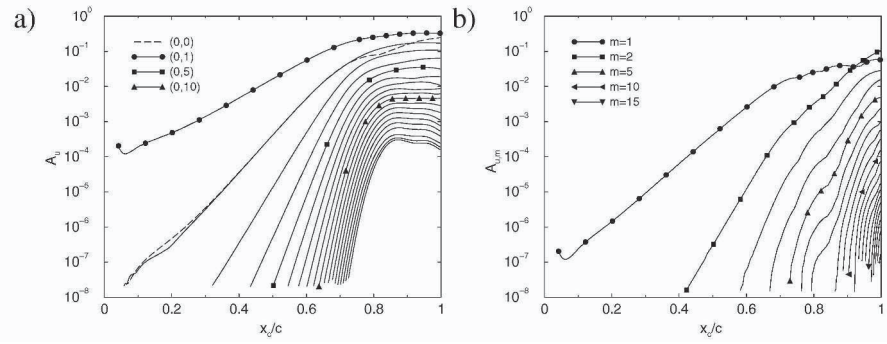

Figure 1. Chordwise velocity amplitude versus chord position for (a) the stationary modes (0,n) and $0 \leq \mathrm{n} \leq 19$, (b) the m–th harmonic of the fundamental frequency (case S)

4. RESULTS

The interaction of a stationary crossflow mode (0,1) and a travelling crossflow mode (1,1) are studied for two different sets of initial amplitudes. In both cases the modes (0,1) and (1,1) are initialised slightly upstream of branch I at about 4% chord. While these two modes are growing in streamwise direction, they trigger the growth of more and more modes by nonlinear interaction.

The initial amplitudes of the first simulation (case S) were chosen such that the stationary crossflow vortex finally saturates at high amplitudes (fig.1a) without being too much affected by the presence of non–stationary modes. This choice mimics the situation in a secondary instability analysis, where the influence of the non–stationary modes on the stationary crossflow vortices is neglected. Therefore, the amplitude development of the stationary modes (0,n) is rather regular (fig.1a). Due to the high modal resolution used, a different way of presenting the results for the travelling modes is required. In fig.1b, the maximum rms amplitude $\mathrm{A_{u,m}}$ in the $\mathrm{y_c}$,z–plane of the chordwise velocity component $\mathrm{u_c}$ versus chord position has been plotted for the different frequencies considered in the calculation. Thus, up to 39 (i.e. 2N+1) Fourier modes contribute to each amplitude curve without counting the complex conjugate modes. The corresponding rms distribution in the $\mathrm{y_c}$,z–plane at $\mathrm{x_c/c} = 1.0$ is depicted in fig.2 for m=2 and m=15, i.e. 270 Hz and 2025 Hz. Besides showing the same spanwise periodicity as the stationary crossflow vortices, the rms distribution exhibits other important features of a secondary instability mode [8]. In particular, the domain of highest rms amplitude coincides with regions of either high spanwise or wall–normal shear rate in the distorted time–averaged flow field. Moreover, it can be shown that the wavenumbers of nonlocal modes with identical frequency index m, when transformed into a vortex–oriented coordinate system, indeed form a wave packet which approximately obeys the disturbance ansatz used in linear secondary instability theory

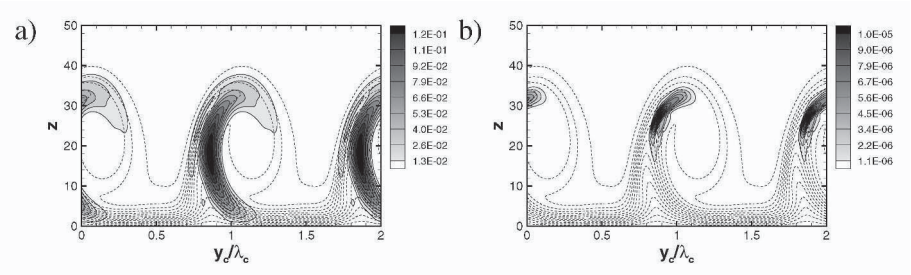

Figure 2. RMS isocontours of the u_v–velocity component in a wall–normal plane at $x_c/c = 1.0$ plotted on top of the isolines (dashed) of the time–averaged velocity component in x_v–direction for a frequency of (a) 270 Hz (m=2) and (b) 2025 Hz (m=15) for case S. The x_v–coordinate is locally aligned with the direction of the primary stationary crossflow vortex axis

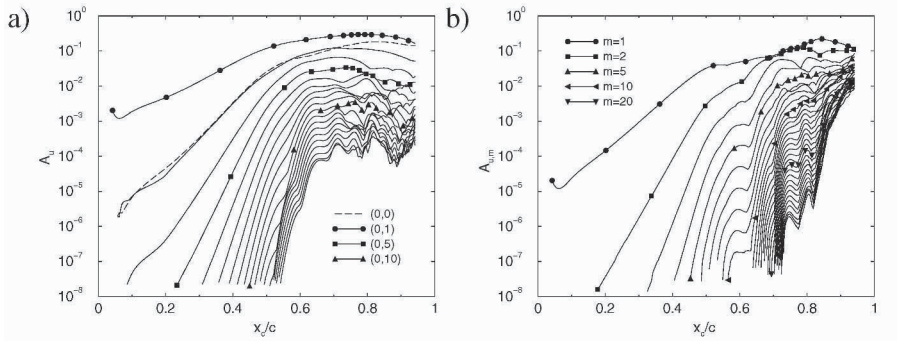

Figure 3. Chordwise velocity amplitude versus chord position for (a) the stationary modes (0,n) and $0 \leq n \leq 19$, (b) the m–th harmonic of the fundamental frequency (case T)

for parallel flows [2]. Apparently, these nonlocal modes describe a single secondary disturbance mode, respectively.

With case S it was demonstrated that the non–zero frequency modes generated by nonlinear interaction of a stationary and a low–frequency travelling crossflow mode evolve into low– and high–frequency secondary instabilities. Case T, which differs from case S by higher initial amplitudes only, is now used to study the subsequent nonlinear development of these secondary disturbances. Although mode (0,1) still remains dominant in amplitude up to the position where the nonlinear nonlocal analysis stops converging, the influence of travelling modes on the stationary crossflow vortices is no longer negligible, as indicated e.g. by the less regular development of the stationary modes with higher values of n (fig.3a). Moreover, at $x_c/c \approx 0.8$ the stationary modes with lower values of n start to decrease in amplitude. At $x_c/c \approx 0.7$, an explosive growth of the high–frequency secondary disturbances sets in (fig.3b). This rapid growth does not trigger an immediate laminar–turbulent breakdown, however. On the contrary, a region follows where the growth of these modes

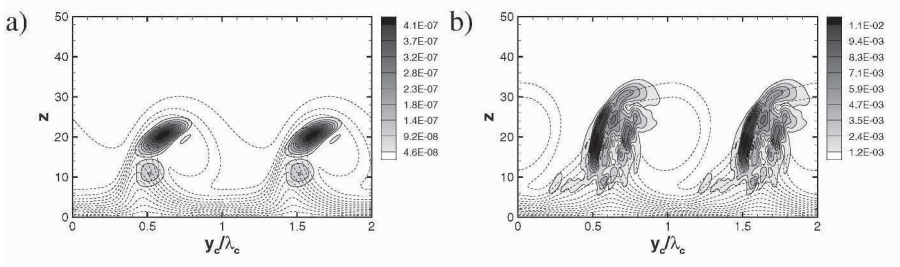

Figure 4. RMS isocontours of the u_v–velocity component in a wall–normal plane at (a) $x_c/c = 0.70$ and (b) $x_c/c = 0.90$ plotted on top of the isolines (dashed) of the time–averaged velocity component in x_v–direction for a frequency of 2700 Hz (m=20) for case T

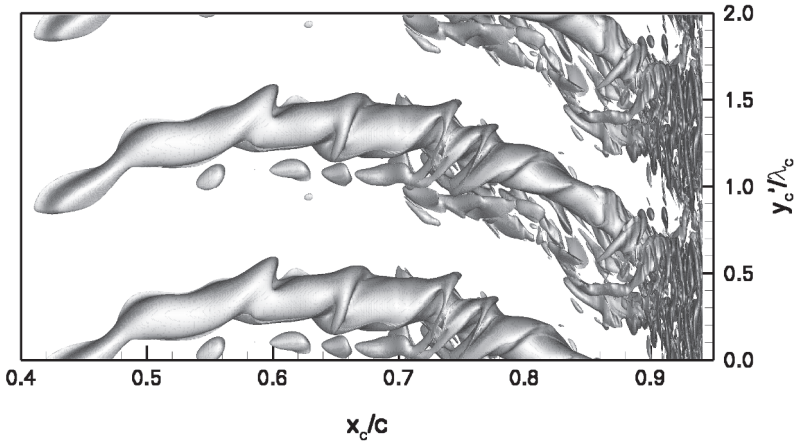

Figure 5. Top view on the vortical structures in the instantaneous flow field at an arbitrary time t visualised by λ_2–isosurfaces with $\lambda_2 = -10^{-5}$ between 40% and 94% chord and two fundamental wavelengths in spanwise direction (case T). For visualisation purposes a parallel translation of each plane $x_c = \text{const.}$ of the form $y_c' = y_c - \tan\Phi_{\text{shift}}\,(x_c - x_{c,0})$ with $\Phi_{\text{shift}} = 47^\circ$ and $x_{c,0}/c = 0.40$ was introduced

levels off again or where they even decay in amplitude, until downstream of $x_c/c \approx 0.8$ a second phase of rapid growth sets in. This rather complicated nonlinear amplitude development of the high–frequency secondary disturbances may hamper a secondary N–factor transition prediction methodology as suggested in [9]. In fig.4, the mode structure of a high–frequency secondary instability with frequency of 2700 Hz (m=20) is plotted for $x_c/c = 0.70$ and $x_c/c = 0.90$. At the latter position a complex nonlinear interaction scenario between the different disturbances has developed. The increasing spottiness of the rms distribution indicates the appearance of vortical structures of successively smaller scales as visualised by λ_2–isosurfaces in fig.5. The travelling disturbances generate vortical structures which are winding around the primary stationary vortices, similar to the observations made by Kohama

& Egami [7]. Packets of finger vortices spanning between two neighbouring stationary crossflow vortices, as described recently by Wassermann & Kloker [11], were not observed, probably because of differences in the basic flow characteristics and the downstream position where the travelling disturbances were introduced in their spatial DNS.

5. CONCLUDING REMARKS

The linear and nonlinear development of high–frequency secondary instabilities in crossflow–dominated transition scenarios including the subsequent disintegration of the secondary disturbance structures was modelled successfully by nonlinear nonlocal theory (PSE). Though an almost DNS–like resolution was required, these (compressible) calculations were still feasible on a state–of–the–art PC and took about a week only. Hence, a coupling of nonlinear nonlocal theory and secondary instability theory as used in [4] to study crossflow–dominated transition on a real aircraft wing is no longer necessary.

REFERENCES

[1] Bertolotti, F.P.; Herbert, Th.; Spalart, P.R.: Linear and nonlinear stability of the Blasius boundary layer. *J. Fluid Mech.* **242**:441-474, 1992.

[2] Hein, S.: Nonlinear nonlocal transition analysis. *PhD thesis*, University of Stuttgart, Sept. 2004, to appear as DLR-FB 2005-10, 2005.

[3] Hein, S.; Bertolotti, F.P.; Simen, M.; Hanifi, A.; Henningson, D.: Linear nonlocal instability analysis — the linear NOLOT code —. DLR-IB 223-94 A56.

[4] Hein, S.; Koch, W.: Secondary instability theory applied to the Fokker 100 flight experiment. ALTTA Technical Report No. 82, April 2003.

[5] Koch W.: On the spatio–temporal stability of primary and secondary crossflow vortices in a three–dimensional boundary layer. *J. Fluid Mech.* **456**:85-111, 2002.

[6] Koch W., Bertolotti F.P., Stolte A., Hein S.: Nonlinear equilibrium solutions in a three–dimensional boundary layer and their secondary instability. *J. Fluid Mech.* **406**:131-174, 2000.

[7] Kohama T., Egami Y.: Active control of instabilities in a laminar boundary layer. AIAA-99-0921.

[8] Malik, M.R.; Li, F.; Chang, C.-L.: Crossflow disturbances in three–dimensional boundary layers: nonlinear development, wave interaction and secondary instability. *J. Fluid Mech.* **268**:1-36, 1994.

[9] Malik, M.R.; Li, F.; Choudhari, M.M.; Chang, C.–L.: Secondary instability of crossflow vortices and swept–wing boundary–layer transition. *J. Fluid Mech.* **399**:85-115, 1999.

[10] Saric W.S., Reed H.L., White E.B.: Stability and transition of three–dimensional boundary layers. *Ann. Rev. Fluid Mech.* **35**:413-440, 2003.

[11] Wassermann P., Kloker M.: Mechanisms and passive control of crossflow–vortex included transition in a three–dimensional boundary layer. *J. Fluid Mech.* **456**:49-84, 2002.

[12] White E.B.: Breakdown of crossflow vortices. *PhD thesis*, Arizona State University, Aug. 2000.

THE EFFECT OF LENGTH SCALE OF FREE STREAM TURBULENCE ON BOUNDARY LAYER TRANSITION

Toshiaki Kenchi, Masaharu Matsubara
Shinshu University, Nagano, Japan

Abstract: The present experiment focused on revealing effect of scale and directional component of free stream turbulence on boundary layer transition, especially growth rate of disturbance energy in the boundary layer. The free stream turbulence generated by a turbulence grid mounted upstream of the contraction has typical character of axisymmetric turbulence with strong anisotropy. The experimental results with anisotropic free stream turbulence show the non-modal growth disturbance even at 0.7 % turbulence intensity. The correlation between the filtered free stream fluctuation and growth rates of the disturbance in the boundary layer suggests that the wall-normal velocity fluctuation in the free stream dominates the disturbance growth.

Keywords: Boundary layer, transition, free stream turbulence, non-modal growth.

1. INTRODUCTION

It is known that there are several scenarios of laminar-turbulent transition in a flat plate boundary layer. One of them originates from Tollmien-Schlichting (T-S) waves and another process starts with the non-modal instability. The primary disturbances of the non-modal transition forms longitudinally elongated domains of low-speed so-called streaky structures. The streamwise scale of streaky structures is dozens of times larger than their spanwise scale that is the same order of the boundary layer thickness [1], [2]. The streaky structures breakdowns with vibration of the spanwise direction, and then a turbulent spot is formed. This streak generation with free stream turbulence was also confirmed by DNS result [3]. According to the non-modal theory [4], it is thought that the wall normal component of disturbance taken into the boundary layer from the free stream contributes to generation of the streaky structures. It also predicts that a profile of the streamwise fluctuation has a peak at the middle of boundary layer and that the energy of the disturbance grows in proportion to the streamwise distance from the leading edge. Though there were several studies on transition due to the free stream turbulence, experiments focused on scale and directional component of the free stream turbulence are quite rare.

R. Govindarajan (ed.), Sixth IUTAM Symposium on Laminar-Turbulent Transition, 287–292.

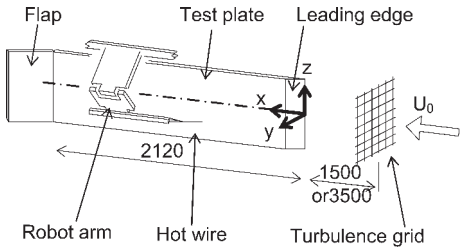

Figure 1. Experimetal set-up

The present experiment focused on revealing effect of these properties of free stream turbulence on the boundary layer transition

2. EXPERIMENTAL SET-UP

The experiments were performed in a closed wind tunnel, which has a 4 m long test chamber of $0.4 \times 0.6\,\mathrm{m}$ cross-section, preceded by a three-dimensional contraction with ratio 9:1. The test plate is mounted vertically in the test chamber and its leading edge is located 1.5 m from the exit of the contraction as shown in figure 1. The leading edge is wedge-shaped within a 100 mm length. The counter wall to the test plate was carefully adjusted so that streamwise pressure gradient along the plate is zero. A trailing edge flap enables to adjust the stagnation line on the leading edge. The three axes robot arm, which was designed to minimize flow resistance, traverses a hot wire probe in y-z plane and a rail mounted on top of a test section roof is used for movement of the arm in the streamwise directions. The free stream turbulence was generated by turbulence grids of various grid sizes. Grids A, B and C have 30 mm, 50 mm and 120 mm mesh sizes respectively. Grids A and B consist of square bars of 6 mm sides and are mounted at the exit of the contraction, while Grid C with 13 mm diameter round pipes is placed at the inlet of the contraction for generation of axisymmetric turbulence. The pipes of Grid C was bored with 2 mm diameter holes oriented upstream in order to change turbulence intensity with blowing jets from these holes when inside of the pipes is pressurized by a blower. For the purpose of this paper, the streamwise and lateral components of the velocity fluctuation in the free stream are taken for definitions of the turbulence levels as $Tu_u = u_{rms}/U_\infty$ and $Tu_v = v_{rms}/U_\infty$. The turbulence levels of the streamwise velocity fluctuation with Grid A and Grid B, measured at the corresponding streamwise position to the leading edge, are 3.5 % and 2.4 % independently of the free stream velocity. For Grid C, the steamwise turbulence level is 0.5 % to 2.8 % depending on both pressure inside the pipes and the free steam velocity.

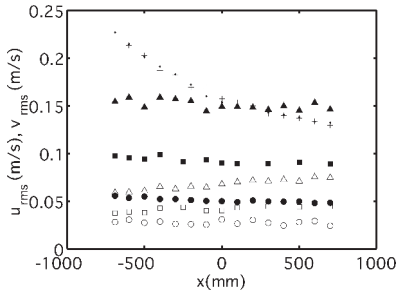

Figure 2. Turbulence decay at $U_\infty = 7\ \mathrm{m/s}$. $+$: u_{rms} for Grid A, $\cdot$: v_{rms} for Grid A, $\bigcirc$, $\square$, $\triangle$: Grid C with blower frequency 0 Hz, 30 Hz and 50 Hz, respectively. Open marks are for u_{rms} and solid marks are for v_{rms}

3. RESULT AND DISCUSSION

In figure 2 shows downstream development of the streamwise and wall-normal velocity fluctuation in the free stream. The velocity components were obtained with a X-type hot wire probe. In the case of Grid A, which is mounted downstream of the contraction at $x = -1500$ mm, the streamwise fluctuation u_{rms} and the lateral fluctuation v_{rms} decay downstream and their reduction curves are more or less overlapped showing quasi-isotropy of the free stream turbulence. In the case when Grid C is mounted at the inlet of the contraction, v_{rms} is about 3 times higher than u_{rms} indicating strong anisotropy. v_{rms} slowly decreases downstream while u_{rms} keeps constant without blowing jets and increases downstream with blowing jets. It is inferred from this result that the free stream turbulence energy is redistributed to the streamwise component from the lateral components due to the strong anisotropy.

Figure 3 and figure 4 show mean and fluctuation profiles of the streamwise velocity for Grid A. The wall-normal position is normalized with the estimated displacement thickness of the Blusius boundary layer δ^*. As shown in figure 3, the mean velocity profiles up to $x = 300$ mm are good agreement with the Blusius profile. The mean velocity downstream accelerates close to the wall and decelerates in the upper part of the boundary layer and then attains to a typical turbulent profile at $x = 900$ mm. Before the mean profile clearly deviates from the Blusius profile, the fluctuation profiles have peaks at middle of boundary layer thickness as seen in figure 4, strongly suggesting the non-modal growth. The amplitude of fluctuation increases downstream and the position of the peak shifts toward the wall at $x = 500$ mm then the profile at $x = 900$ mm indicates feature of a turbulent boundary layer.

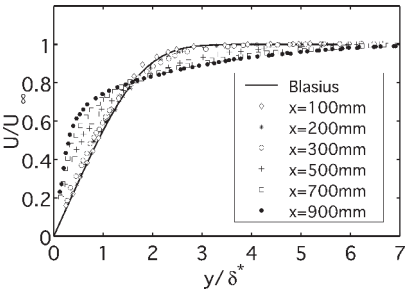

Figure 3. Mean velocity profiles with Grid A at $U_\infty = 5\,\mathrm{m/s}$

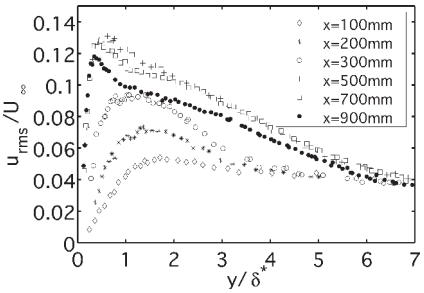

Figure 4. Profiles of the streamwise velocity fluctuation

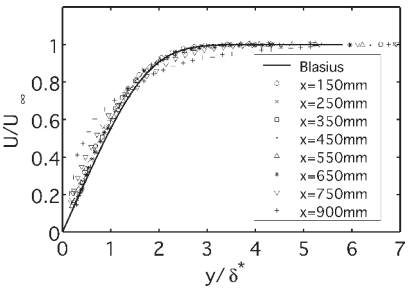

Figure 5. Mean velocity profiles with Grid C at $U_\infty = 10\,\mathrm{m/s}$

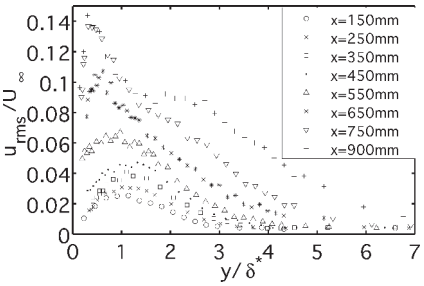

Figure 6. Profiles of the streamwise velocity fluctuation

Figure 5 and figure 6 show mean and fluctuation profiles of the streamwise velocity for Grid C without the blowing jets. The streamwise and lateral free stream fluctuations, u_{rms} and v_{rms} are 0.3 % and 0.5% of the free stream velocity, respectively. The mean profile begins to deviate from the laminar profile at $x = 750$ mm, and then the profile at $x = 900$ mm resembles the turbulent boundary layer profile. The rms profiles up to $x = 550$ mm have a peak around $y/\delta^* = 1.2$ in the same way in the Grid A case. It is worth while to notice that even $Tu_v = 0.7\%$ the non-modal growth dominants the disturbance development in the transitional boundary layer.

Figure 7 shows the streamwise development of the disturbance energy $E = (u_{rms}/U_\infty)^2$ and intermittency factor for the quasi-isotropic free stream turbulence (Grid A) and the axisymmetric free stream turbulence (Grid C). Both values are measured at $y/\delta^* = 1.2$. For Grid C, the disturbance energy increases in proportion to the normalized streamwise distance Re_x until the intermittency starts to rise at $Re_x = 3 \times 10^5$, and then the slope of E suddenly turns steep. Further downstream, the disturbance energy reaches a peak where the intermittency is about 0.6. The proportional growth is also in agreement with the non-modal theory. For Grid A the disturbance energy traces similar change with good agreement the relation to the intermittency though the

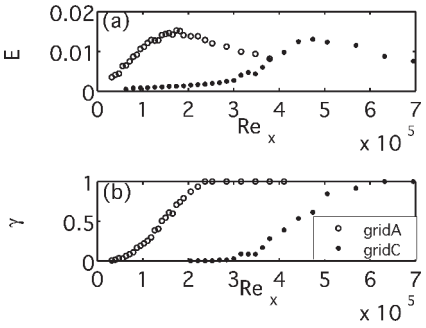

Figure 7. Streamwise turbulence energy and intermittency as functions of Re_x for Grid A at $U_\infty = 5$ m/s and Grid C at $U_\infty = 10$ m/s. (a) Streamwise turbulence energy, (b) Intermittency

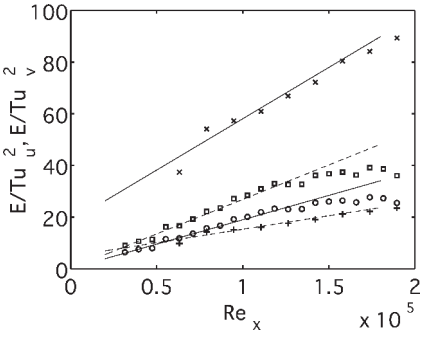

Figure 8. Streamwise turbulence energy normalized by free stream turbulence energy. ○: E/Tu_u^2 with Grid A at $U_\infty = 5$ m/s, □: E/Tu_v^2, ×: E/Tu_u^2 with Grid C at $U_\infty = 10$ m/s, +: E/Tu_v^2

proportional growth is not clearly confirmed because of lack of measurement points up stream.

These disturbance energy are normalized with component energy of free stream turbulence as shown in figure 8 in order to compare the normalized slopes for Grid A and Grid C. Though these normalized slopes of the energy development are constant in the experiment with the isotropic free stream turbulence [2], the slope for Tu_u in the anisotropic case (Grid C) is much steeper than the slope in the isotropic case (Grid A) show as a solid lines. The slope for Tu_v, however, the slopes for both of the cases resemble suggesting that the wall-normal component of the free stream turbulence is dominant for the growth rate of the disturbance in the boundary layer. This is more obvious if the growth rates $G = dE/dRe_x$ are plotted with the energy components of the free stream turbulence, Tu_u and Tu_v, as shown in figure 9 (a) and (e). Comparing, Tu_v is well correlated to the growth rate and the fitted with the line which is the empirical result of the experiment with the isotropic free stream turbulence [2]. When Tu_v is bandpass filtered with length scale of 80 mm to 400 mm as shown in (g), this growth rate can be collapsed better than other bandpass filtered Tu_v to a linear line with slope factor 1, though no improvement is seen compared with (e). Note that the lines in the filtered plots are fitted with least square sense in real values not in log values. This result suggests that the dominant energy components are not all but of some length scale, though more experimental data is required to precisely decide the effective length scale in the free stream turbulence on the disturbance growth in the transitional boundary layer.

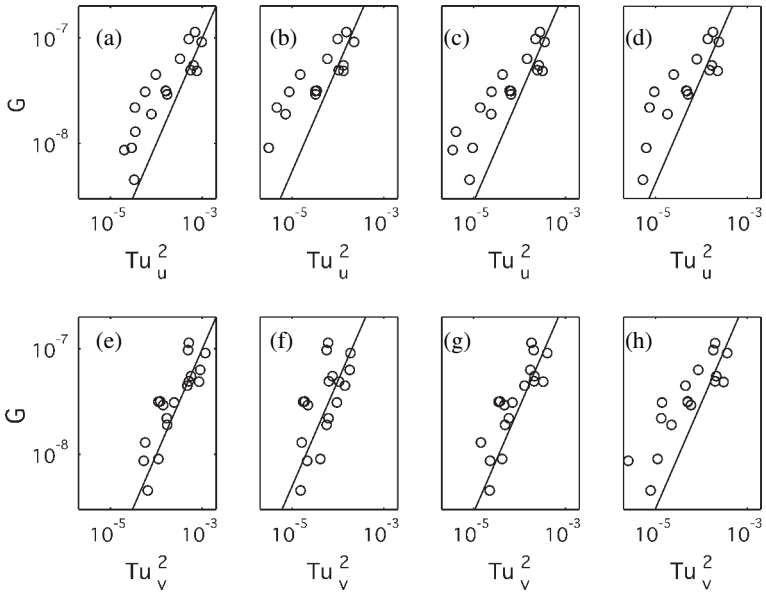

Figure 9. Effect of length scale of the free stream turbulence on the growth rate with Grids A, B and C. (a)–(d): Tu_u, (e)–(h): Tu_v, (a) (e): without filter, (b) (f): filtered with 0.4–2 m, (c) (g): filtered with 0.08–0.4 m, (d) (h): filtered with 0.016–0.08 m

4. SUMMARY

The measurement of the streamwise velocity fluctuation in the boundary layer shows the characteristic of the non-modal instability that has the streamwise fluctuation peak at the middle of the boundary layer and linear energy growth with the streamwise distance from the leading edge even with low free stream turbulence such as $Tu_v = 0.7\%$. The growth rate is dominated by the wall-normal disturbance in the free stream turbulence and well correlated to the energy of the bandpass filtered free stream turbulence. This suggests that information of the length scale of the free stream turbulence should be taken account to transition prediction for the boundary layer subjected to the free stream turbulence.

REFERENCES

[1] M. Matsubara and P. H. Alfredsson. Disturbance growth in boundary layers subjected to free-stream turbulence. *J.Fluid Mech.*, 430: 149-168, 2001.

[2] J. H. M. Fransson, M. Matsubara and P. H. Alfredsson. Transition induced by free stream turbulence. *(Accepted for publications in J. Fluid Mech.)*

[3] R. G. Jacobs and P. A. Durbin. Simulations of bypass transition. *J.Fluid Mech.*, 428: 185-212, 2001.

[4] P. Luchini. Reynolds-number-independent instability of the boundary layer over a flat surface: optimal perturbations. *J.Fluid Mech.*, 404: 289-309, 2000.

UNSTEADY DISTURBANCE GENERATION AND AMPLIFICATION IN THE BOUNDARY-LAYER FLOW BEHIND A MEDIUM-SIZED ROUGHNESS ELEMENT

Ulrich Rist and Anke Jäger
Institut für Aerodynamik und Gasdynamik, Universität Stuttgart, Pfaffenwaldring 21, 70550 Stuttgart, GERMANY

Abstract: In the present work we investigate receptivity and disturbance amplification behind a circular roughness element in a zero-pressure-gradient flat-plate boundary layer with the aim to identify and understand the basic mechanisms at work. The low disturbance background and the high repeatability of the direct numerical simulations allow to evaluate the different contributions of acoustic-roughness receptivity and of local disturbance amplification. A distinct feature of the boundary-layer flow with roughness element are streamwise streaks which develop from the spanwise edges of the roughness. Small-scale three-dimensional disturbances develop and amplify within these streaks both by instability and by receptivity. For the present small amplitude unsteady forcing however, they remain confined to these areas. In contrast to this, the far-field receptivity result is similar to a wave train generated by periodic suction and blowing at the wall.

Keywords: Direct numerical simulation, receptivity, roughness, Tollmien-Schlichting wave

1. INTRODUCTION

In the past several years many investigations of the different routes to transition in generic boundary layer flows have been performed and tools have been developed that could predict the location of laminar-turbulent transition if the initial amplitudes were known accurately enough. In conclusion of the German priority research program on laminar-turbulent transition (cf. Wagner et al., 2003) we may say that finding the relevant

R. Govindarajan (ed.), Sixth IUTAM Symposium on Laminar-Turbulent Transition, 293–298.

initial disturbances is *the* key issue for a successful transition prediction in the future. In addition, there is considerable interest in studying all aspects of roughness-induced (bypass) transition since this is a significant feature in aerodynamics at medium Reynolds numbers.

2. PROBLEM FORMULATION

With the present work we want to contribute to a better understanding of the initial stages of laminar-turbulent transition behind an isolated roughness element with a circular planform which is embedded in a two-dimensional incompressible flat-plate Blasius boundary layer. The roughness element is placed at Re*=855, where Re* is the Reynolds number based on the boundary layer displacement thickness δ*. Here, x, y, and z denote the streamwise, wall-normal, and the spanwise coordinates, respectively. The contour of the roughness element is defined by

$$h(x, z) = h_0 \cos^3(\pi r/2b),$$

with height $h_0 = 0.5\ \delta^*$, radial coordinate r, and radius $b = 8.42\ \delta^*$. Since the height of the roughness amounts to *50 %* of the local displacement thickness of the unperturbed boundary layer, the present case cannot be treated by (linear) receptivity theory but our data may be used for future comparisons with non-linear theories or experiments.

In the absence of external disturbances a steady three-dimensional base flow develops. This is computed using the numerical method developed by Rist and Fasel (1995) augmented by the "immersed boundary technique" of Peskin (1977) to provide an efficient modeling of the roughness element without using body-fitted coordinates. Taking the latter would have increased the memory and computer time of the computations in a drastic manner.

Two controlled disturbance scenarios are then computed and compared to each other. One with a harmonic modulation of the inflow profile with the so called second Stokes' problem which mimics the presence of a two-dimensional acoustical wave in the free stream, such that an acoustic-wall-roughness type of receptivity interaction takes place at the roughness element. In a second case time-wise harmonic perturbations are introduced by suction and blowing at the wall upstream of the roughness element in order to force a two-dimensional Tollmien-Schlichting wave that travels over the roughness element such that changes of the stability behavior become apparent. Each of the two cases has been computed for base flows with and without roughness elements to further clarify the differences. More

information can be found in Wörner (2004). Linear stability calculations (LST) based on local and averaged velocity profiles are then used to further clarify the mechanisms.

3. RESULTS

The roughness element leads to several interesting three-dimensional features within the steady base flow which are illustrated in Figure 1. Streamwise parallel longitudinal streaks of low- and high-speed fluid develop at the spanwise corners of the roughness element. These appear as bright and dark vertical stripes in the *u*-velocity contours at the last three *x=const* planes in the figure. They persist for a long distance downstream of the roughness and their spanwise gradients needed an unexpectedly high spanwise resolution of the computations (*80* Fourier modes with their complex conjugates, verified with a simulation run with twice as much). The streaks are accompanied by weak streamwise vorticity only, such that streamlines which are shown for illustration are only mildly deformed. Still, the identified vortex system resembles that found for much larger obstacles which protrude the boundary layer, like a pair of horseshoe vortices.

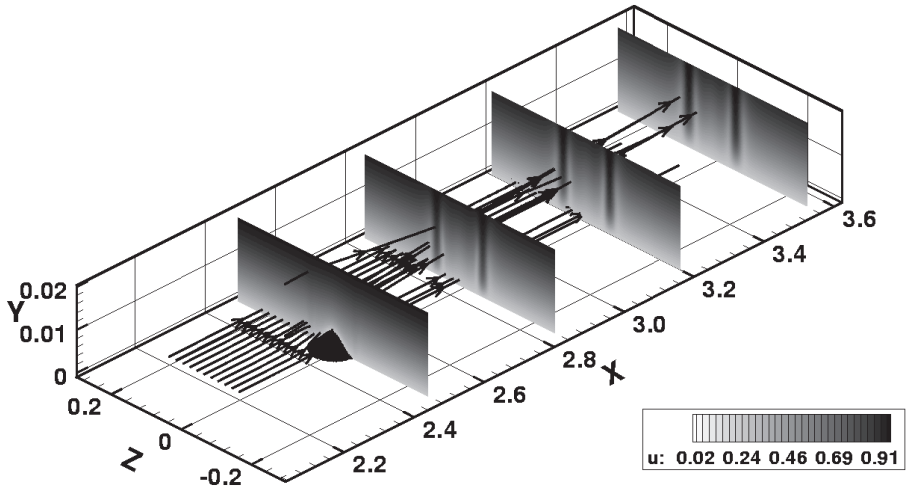

Figure 1. Illustration of the base flow using streamlines and contours of the streamwise velocity component at constant downstream positions

The unsteady results shown in the following figures were obtained by first taking the difference of two according simulations, one with roughness element and the other one without, and then by computing the second time

derivative according to Maucher et al. (1997). This helped to reduce remaining transients that were still present in the unsteady simulation results with roughness element.

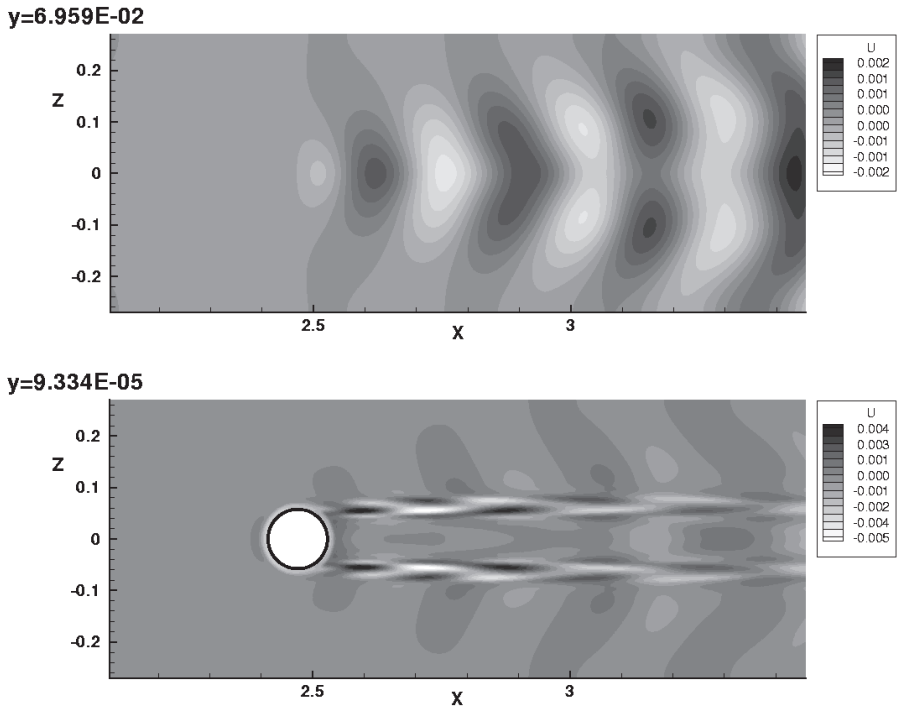

Figure 2. Disturbance field created by interaction of a periodic free-stream perturbation with the roughness element; top: far away from the wall ($y = 8.14\ \delta^*$), bottom: close to the wall ($y = 0.011\ \delta^*$)

The addition of a two-dimensional sound wave to the free stream has a two-fold effect on the disturbance field. Far away from the wall (Fig. 2 top) a characteristic wave-train develops that has already been observed earlier when the boundary layer has been forced by a harmonic point-source, e.g. by Stemmer & Kloker (2000). Note the characteristic development of two spanwise maxima downstream of the source which is due to superposition of several oblique Tollmien–Schlichting waves of moderate obliqueness angles. However, close to the wall (Fig. 2 bottom) highly oblique waves that appear in the streamwise streak regions dominate over the wave-train part of the disturbance.

A comparison of DNS disturbance profiles with eigenfunctions of linear stability theory (LST) is shown in Fig. 3. The LST computations are based on mean-flow profiles extracted from the DNS at $x = 2.7$. Two different

LST-analyses have been made, one for the spanwise-averaged, the other one for the local profile extracted in the middle of the high-speed streak. In the first case the disturbance maximum is placed further away from the wall compared to the second. The figure proves that velocity fluctuations with small spanwise wave numbers in the DNS behave like eigenmodes of the averaged flow, while those with large wave numbers belong to eigen-fluctuations of the streak profile. The first correspond to the harmonic wave train seen in the far field while the latter make up the highly oblique structures in the streaks. Since the stability characteristics of the base flow with roughness element play a major role for both of them, another case where a two-dimensional Tollmien–Schlichting wave travels over the roughness element will be considered next.

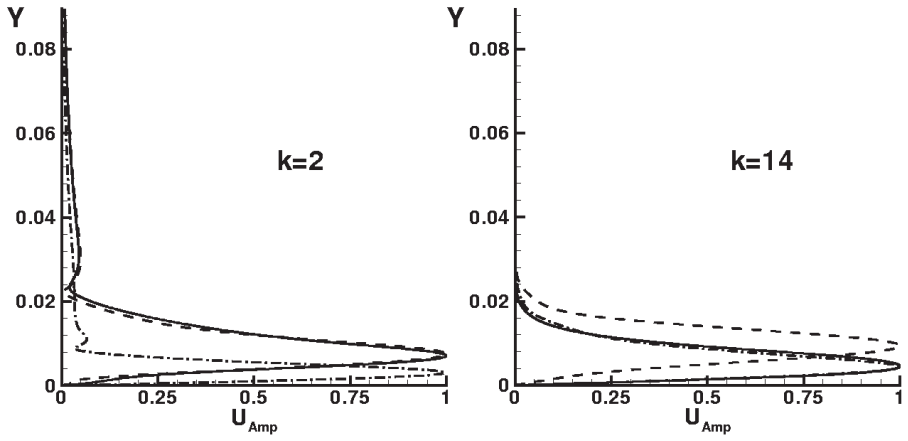

Figure 3. Comparison of two DNS disturbance profiles with eigenfunctions of linear stability theory based on the spanwise averaged velocity profile (– –) and on the streak profile (– · –), k = spanwise wave number

Figure 4 presents instantaneous disturbance structures of this second case which can be directly compared with the first case in Fig. 2 (bottom). Again, the disturbance is composed of a wave train and dominant local structures in the streak. Compared to above, they have less phase shifts in spanwise directions but they consist of eigenmodes of the profile from the high-speed streak, while disturbances which make up the wave train correspond to eigenmodes of the averaged velocity profile, as before.

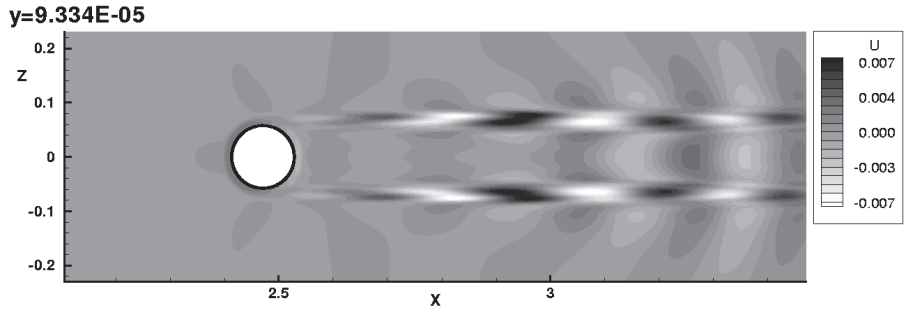

Figure 4. Disturbance field close to the wall induced by interaction of a TS-wave with the roughness element

4. CONCLUSIONS

An isolated roughness element in a flat-plate boundary layer that interacts with an impinging two-dimensional sound or Tollmien–Schlichting wave was found to scatter two kinds of oblique waves. Close to the wall, highly oblique disturbances dominate over the wave train part. For the present small disturbance amplitudes these highly oblique waves remained confined to the streaks, but for larger amplitudes they may lead to bypass transition.

REFERENCES

Maucher, U., Rist, U., and Wagner, S., 1997, A method for the identification of high-frequency oscillations in unsteady flows, *Z. Angew. Math. Mech.* **77**, Suppl. 1, S2094–S210.

Peskin C.S., 1977, Numerical analysis of blood flow in the heart, *J. Comp. Phys.* **25**:220–252.

Rist, U., and Fasel, H.F., 1995, Direct numerical simulation of controlled transition in a flat-plate boundary layer, *J. Fluid Mech.* **298**:211–248.

Stemmer, C., and Kloker, M., 2000, Later stages of transition in an airfoil boundary layer flow, in: *Laminar-Turbulent Transition, Proc. IUTAM-Symp. Sedona, Az, Sept. 13–17, 1999*, H.F. Fasel, W.S. Saric, eds., Springer, New York, Heidelberg, pp. 499–504.

Wagner S., Kloker M., and Rist U. (Eds.), 2003, *Recent Results in Laminar-Turbulent Transition – Selected Numerical and Experimental Contributions from the DFG-Verbundschwerpunktprogramm "Transition" in Germany*, NNFM **86**, Springer, Heidelberg.

Wörner, A., 2004, *Numerische Untersuchungen zum Entstehungsprozess von Grenzschichtstörungen durch die Interaktion von Schallwellen mit Oberflächen-rauhigkeiten*, Dissertation Universität Stuttgart, Shaker, Aachen.

EXPERIMENTAL STUDY OF THE STABILIZATION OF TOLLMIEN-SCHLICHTING WAVES BY FINITE AMPLITUDE STREAKS

Jens H. M. Fransson,*[,1] Luca Brandt,[1] Alessandro Talamelli,[1,2] Carlo Cossu[3]
[1]*KTH Mechanics, Stockholm, Sweden,*
[2]*II Facoltą di Ingegneria, Universita di Bologna, Forli, Italy,*
[3]*LadHyX, CNRS-Ecole Polytechnique, Palaiseau, France*

Abstract: The stabilization of Tollmien-Schlichting (TS) waves in a spanwise modulated Blasius boundary layer has been experimentally verified in the MTL wind tunnel at KTH. The alternating high and low speed streaks were created by regularly spaced cylindrical roughness elements mounted on the flat plate. It is shown that the larger the streak amplitude the larger is the damping effect of the TS-waves, which is in agreement with recent theoretical work.

Keywords: Roughness element array, 3D boundary layer, TS waves, stabilization

1. INTRODUCTION

In the absence of external perturbations or wall imperfections, the boundary layer developing on a flat plate is spanwise uniform (2D) and is well described by the Blasius similarity solution. The 2D Blasius boundary layer is known to be unstable to viscous perturbations, the so called Tollmien-Schlichting (TS) waves, for Reynolds numbers $Re = \delta U_\infty/\nu = \sqrt{xU_\infty/\nu}$ larger than $Re_c \approx 304$. Here δ, ν, U_∞, and x are the boundary layer scale, the kinematic viscosity, the free stream velocity, and the downstream position from the leading edge, respectively. It has recently been found, by using temporal and spatial numerical simulations, that steady optimal streaks of moderate amplitude, i.e. sufficiently large but not exceeding the critical amplitude for the inflectional instability, are able to reduce the growth of TS-waves up to their complete stabilization (Cossu and Brandt, 2002; Cossu and Brandt, 2004). Experimentally, Boiko et al., 1994 found a stabilizing effect on the TS-waves in the case of a boundary layer subject to free stream turbulence and unsteady streaks. It has therefore been suggested that the optimal forcing of steady streaks could

*E-mail: jens.fransson@mech.kth.se

R. Govindarajan (ed.), Sixth IUTAM Symposium on Laminar-Turbulent Transition, 299–304.

be used as a possible appealing method to delay transition in boundary layers within a low noise environment.

This study presents an investigation aimed at experimentally verifying the theoretical results above by generating stable and "clean" (close to sinusoidal) streaks with moderate amplitudes. The non–modal growth of steady and spanwise periodic streamwise streaks in a flat plate boundary layer have been studied and the discrepancy between the experimental streaks and the optimal theoretical streaks has been clarified, see Fransson et al., 2004. The key factor of the discrepancy was found to be the wall normal location and the extension of the laminar standing streamwise vortices inducing the experimental streaks.

2. EXPERIMENTAL SETUP

The experiments were carried out at KTH Mechanics in the Minimum-Turbulence-Level (MTL) wind tunnel with a setup similar to the one used in Fransson et al., 2004. A 4.2 m long flat plate was mounted horizontally in the test section whose dimensions are 7 m in length, 0.8 m in height and 1.2 m in width. Figure 1 shows a schematic of the experimental set-up. The plate was the same as described in Klingmann et al., 1993 designed in order to get a short pressure gradient region without any suction peak at the leading edge region (cf. Fransson, 2004). A trailing edge flap is also mounted in order to compensate for the extra blockage below the plate due to the supports and the piping system for the TS wave generation.

The origin is located on the centerline at the leading edge with $x-$, $y-$, and $z-$axis directed along the streamwise-, wall normal-, and spanwise direction, respectively. A single hot-wire anemometry probe was used to measure the streamwise velocity component in the present experiment.

The streaky boundary layer was generated by means of cylindrical roughness elements similar to those used and described in Fransson et al., 2004. To

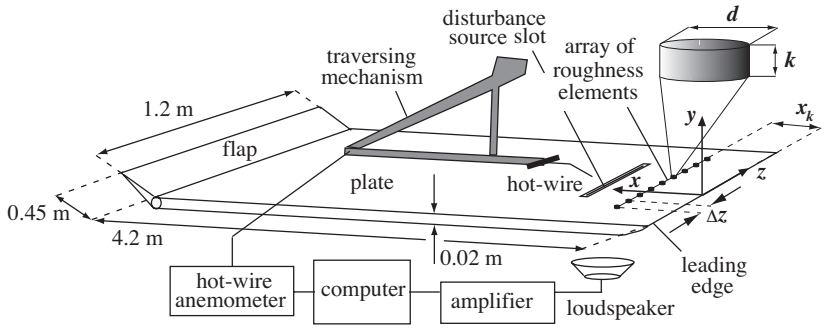

Figure 1. Schematic of the set-up. k = 1.3 or 1.4 mm, $d = 4.2$ mm, $\Delta z = 14.7$ mm, and $x_k = 80$ mm

get a good spanwise homogeneity 9 elements were periodically pasted on the plate surface. Relevant parameters in this study are: the boundary layer scale δ corresponding to $\sqrt{x\nu/U_\infty}$, the height of the roughness element k, the cylinder diameter d, the spacing between the elements Δz, and the distance from the leading edge where the elements were located x_k (see figure 1 with caption for an illustration of all parameters).

TS waves were generated by time periodic suction and blowing at the wall through a slot in a plug mounted in the plate. The slot, located at $x = 190$ mm from the leading edge, is 330 mm long in the spanwise direction and 0.8 mm wide.

The disturbance signal was generated by the computer through a D/A-board to an audio amplifier driving two loudspeakers, and the data set acquisitions were triggered by the reference signal from the waveform generator. The loudspeakers are then connected to the disturbance source through twenty flexible tubes. A more thorough description of the disturbance generating system can be found in Elofsson, 1998.

The amplitude of the loudspeakers signal was manually adjusted for each frequency in order to keep the TS amplitudes below 0.8% of U_∞ at branch II, i.e. in the linear regime. The spanwise uniformity of the generated waves was checked by measuring wall-normal distributions of TS amplitude at three different spanwise positions in the 2D case.

The structure of the flow was depicted by traversing the probe in the yz-plane, with a minimum number of points being 31×18, to $6 - 12$ different streamwise positions depending on the frequency. At each point the measure was obtained by acquiring 3 sets of samples with a frequency of 1 kHz.

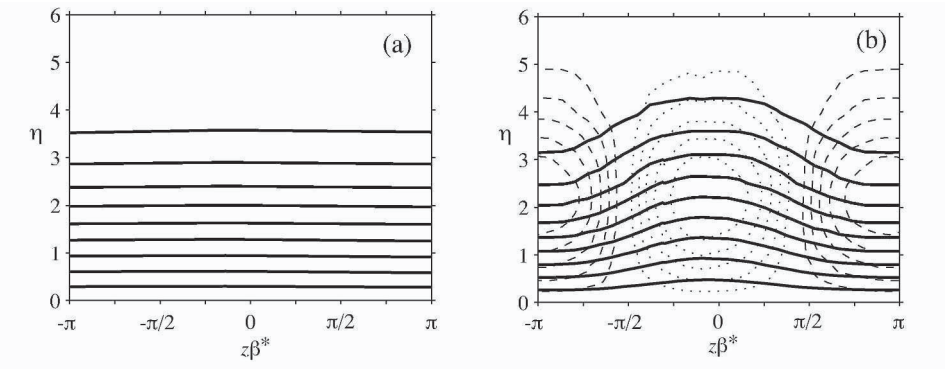

Figure 2. Base flows (at maximum streak amplitude) for the R (a) and the higher roughness element height S_2 (b). Solid bold lines are velocity contours with an increament of $U/U_\infty = 0.1$ from the wall. Dotted and dashed lines are negative and positive contours of spanwise mean deviation $(U - \overline{U}_z)/U_\infty = \pm[0.02\,0.04\,0.06\,0.08\,0.1]$. $\beta^* = 0.43$ mm^{-1}

3. RESULTS

Three base flows have been investigated and are denoted by R, S_1 and S_2, where R is the 2D reference case and S_1 and S_2 correspond to the streaky base flows with increasing roughness height, namely k = 1.3 and 1.4 mm respectively. The spanwise array of cylindrical roughness elements modulates the 2D base flow into a 3D flow. Totally, five different forcing frequencies ($F = \{2\pi f\nu/U_\infty^2 \times 10^6\} = 90, 110, 130, 150, 170$) of the TS waves were investigated. The free stream velocity was kept constant at 5 ms^{-1} in all the experiments, resulting in maximum streak amplitudes of 11.6% and 12.4% of U_∞ for S_1 and S_2, respectively.

In figure 2 we display yz-scans (i.e. cross-stream planes) of both the mean streamwise velocity (solid bold lines) and of the deviation from the spanwise mean (dotted and dashed lines) for the R and the S_2 configurations. The streamwise locations correspond to the streamwise position of maximum streak amplitude, i.e. at approximately $Re = 401$. Note that the undisturbed boundary layer flow in figure 2(a) also was scanned at its streamwise station. The S_1 case, not shown here, looks similar to the S_2 case but with a lower streak amplitude.

The streak ($_{ST}$) and the TS ($^{yz}_{TS}$) amplitudes are defined as:

$$A_{ST} = \max_y\{(U(y)_{\text{high}} - U(y)_{\text{low}})/2\}/U_\infty \quad \text{and}$$

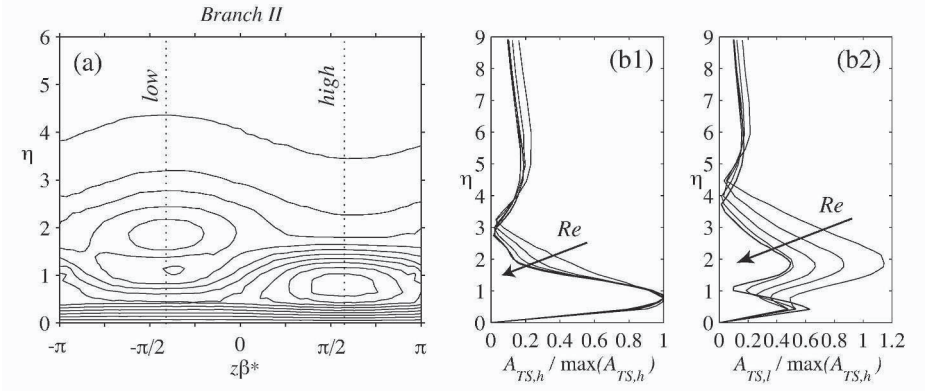

Figure 3. (a) Experimental cross sectional measure of the streaky TS amplitude for $F = 110$ and close to branch II ($Re = 651$). Dotted lines indicate the location of low and high speed streaks. The contour levels are $(0.5 : 0.5 : 4.5) \times 10^{-3}$, and $\beta^* = 0.46$ mm^{-1}. (b) Wall-normal amplitude profile evolution for $F = 110$. (b1) High and (b2) low speed location. Re = 451, 501, 551, 601, 651

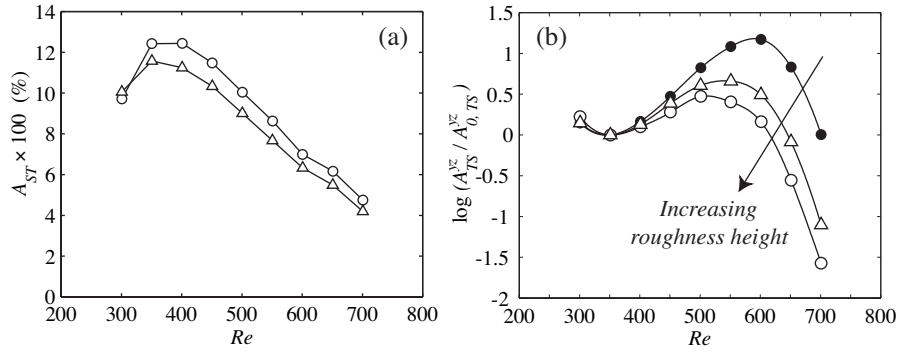

Figure 4. (a) Streak amplitude (A_{ST}) versus Re. (b) TS amplification curves for the R-case (•) and for successively increasing roughness heights S_1 and S_2 ($\triangle, \bigcirc$). $F = 130$. Solid lines are fitted spline curves to the experimental data

$$A^{yz}_{TS} = \int_0^{2\pi} \int_0^{\eta^*} \frac{A_{TS}(\eta, \beta)}{U_\infty} \, d\eta d\beta, \quad \text{respectively.}$$

Here $U(y)_{\text{high}}$ and $U(y)_{\text{low}}$ denote the velocity profiles in the high and low speed regions, respectively. $\eta = y/\delta, \beta = z\beta^* = z2\pi/\Delta z$, $\eta^* = 8$, and A_{TS} is the measured amplitude of the TS-wave.

The 2D generated TS waves are redistributed in the spanwise direction at the instant they enter the boundary layer in order to comply with the 3D modulated base flow. An example of the fundamental TS mode ($F = 110$) distribution close to branch II is illustrated in figure 3(a), where the dotted lines indicate the location of low and high speed streaks (see caption for contour levels). Here, the data in the figure has been smoothed by local spatial averaging. In contrast to the single peak profile in the high speed region, which resembles the amplitude profile in a 2D base flow, a two peak profile is observed in the low speed region. This is in agreement with previous studies (see e.g. Tani and Komoda, 1962; Kachanov and Tararykin, 1987; Bakchinov et al., 1995). A better illustration of these distributions are, however, found in figure 3(b) where the streamwise evolution of the TS amplitude is shown both at the high (b1) and at the low (b2) speed locations. In the high speed region the variation is not so dramatic as compared to the low speed region where it is seen that the amplitude of the outer peak decreases by a factor of two relative to the inner peak. It can also be seen that approaching branch II the shape variations diminish and that the maximum in the high speed region is located at $\eta = 0.8$ independent of Re. An interesting observation is that, when comparing the high and low speed regions, the strongest growth is found in the high speed

region. This is in contrast to what one would expect from a 2D stability point of view since the mean velocity shape is actually fuller and would therefore imply a more stable region as compared to the low speed region.

In figure 4(a) it is seen that the only difference between the two streaky base flows S_1 and S_2 is the streak strength, since the two curves of A_{ST} essentially are parallel.

The present experimental data with the cross sectional $integral$ amplitude measure (A_{TS}^{yz}) defined above shows unambiguously that the TS wave growth is damped when these waves evolve in a 3D sinuousoidal base flow. Furthermore, figure 4(b) shows the first experimental result ever on successively increased damping of the TS waves with increasing streak amplitude. This damping was observed for all frequencies studied.

ACKNOWLEDGEMENTS

The financial support of the Swedish Research Council (VR) is gratefully acknowledged. C.C. acknowledges financial support from CNRS during his stay at KTH.

REFERENCES

Bakchinov, A. A., Grek, G. R., Klingmann, B. G. B., and Kozlov, V. V. (1995). Transition experiments in a boundary layer with embedded streamwise vortices. *Phys. Fluids*, 7:820–832.

Boiko, A. V., Westin, K. J. A., Klingmann, B. G. B., Kozlov, V. V., and Alfredsson, P. H. (1994). Experiments in a boundary layer subjected to free stream turbulence. Part 2. The role of TS-waves in the transition process. *J. Fluid Mech.*, 281:219–245.

Cossu, C. and Brandt, L. (2002). Stabilization of Tollmien-Schlichting waves by finite amplitude optimal streaks in the Blasius boundary layer. *Phys. Fluids*, 14:L57–L60.

Cossu, C. and Brandt, L. (2004). On Tollmien-Schlichting-like waves in streaky boundary layers. *Eur. J. Mech./B Fluids*, 23:815–833.

Elofsson, P. A. (1998). Experiments on oblique transition in wall bounded shear flows. PhD Thesis KTH/MEK/TR–98/05–SE, KTH, Department of Mechanics, Stockholm.

Fransson, J. H. M. (2004). Leading edge design process using a comercial flow solver. *Exp. Fluids*, 37:929–932.

Fransson, J. H. M., Brandt, L., Talamelli, A., and Cossu, C. (2004). Experimental and theoretical investigation of the non-modal growth of steady streaks in a flat plate boundary layer. *Phys. Fluids*, 16:3627–3638.

Kachanov, Y. S. and Tararykin, O. I. (1987). Experimental investigation of a relaxating boundary layer. *Izv. SO AN SSSR, Ser. Tech. Nauk*, 18.

Klingmann, B. G. B., Boiko, A., Westin, K. J. A., Kozlov, V. V., and Alfredsson, P. H. (1993). Experiments on the stability of Tollmien-Schlichting waves. *Eur. J. Mech.* B*/Fluids*, 12:493–514.

Tani, I. and Komoda, H. (1962). Boundary layer transition in the presence of streamwise vortices. *J. Aerospace Sci.*, 29:440–444.

DEVELOPMENT OF STREAMWISE STREAKS IN A QUASI-LAMINAR BOUNDARY LAYER DOWNSTREAM OF LOCALIZED SUCTION

Masahito Asai[1], Yasufumi Konishi[1], Yuki Oizumi[1] and Michio Nishioka[2]

[1] *Department of Aerospace Engineering, Tokyo Metropolitan Institute of Technology*

[2] *Department of Aerospace Engineering, Osaka Prefecture University*

Abstract: Through a short perforated wall strip, local boundary layer suction is applied to a turbulent boundary layer to generate a quasi-laminar boundary layer with high-intensity active turbulence. The retransition begins with algebraic growth of streamwise streaks from immediately behind the suction. Even in the early stage of the growth of low-speed streaks their spanwise spacing is found to be almost the same as that in the original turbulent boundary layer. After the growth saturation the streak instability and the associated breakdown of low-speed streaks occur to generate near-wall burst-like motions with quasi-streamwise vortices.

Keywords: Streak instability, Low-speed streaks, Boundary-layer suction, Wall turbulence

1. INTRODUCTION

With an insight that turbulence is caused and then sustained by a sequence of flow instabilities, we have been working on the transition to wall turbulence. The instability events highly depend on the disturbance environments for wall-bounded flows and various paths can lead to the transition even for the same flow geometry. In any path to the transition, however, the prerequisite for wall turbulence generation is the occurrence and growth of near-wall low-speed streaks. Under a very low free-stream turbulence condition where transition is initially governed by linear instability waves and subsequently by the secondary instability, low-speed streaks appear at the final stage to transition. With increasing the background turbulence, low-speed streaks can grow even from the initial stage and lateral oscillations of the developed low-speed streaks often lead to the formation of turbulent spots. Our interest is focused on such near-wall phenomena directly related to the wall turbulence generation. In the present experimental study, the near wall flow in the oncoming developed turbulent boundary is relaminarized by concentrated wall suction, and

R. Govindarajan (ed.), Sixth IUTAM Symposium on Laminar-Turbulent Transition, 305–310.

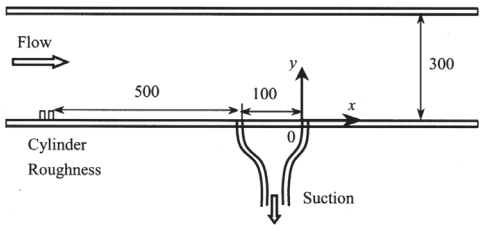

Figure 1. Schematic of test section (dimensions in mm)

the subsequent retransition of the quasi-laminar boundary layer downstream of the suction is examined to clarify the generation and breakdown processes of streamwise streaks under residual but still active turbulent fluctuations.

2. EXPERIMENTAL SETUP AND PROCEDURE

The experiment is conducted in a wind tunnel with a rectangular test section of 300mm (height) $\times$200mm (width). We focus on a boundary layer developing on the lower wall of the test section. A schematic of the test section is illustrated in Fig. 1. The boundary layer is disturbed by two rows of small cylinders set at the upstream end of the test section to generate turbulent boundary layer. A suction strip of 100mm$\times$160 mm is mounted flush with the wall surface. Over the suction area, 0.3mm-diameter holes are drilled at an interval of 1mm in the streamwise and spanwise directions in a staggered configuration. The leading edge of the suction area is located 500mm downstream of the cylinder roughness. The suction strip is connected to a pump (a vacuum cleaner) through a smooth contraction, a pipe and a flow meter. The suction velocity $V_s = Q/A_s$ where Q and A_s are the volumetric flow rate and the suction area (100mm$\times$160mm) respectively is controlled continuously up to a maximum speed of 2m/s by means of two valves installed to the pipe. The free-stream velocity U_∞ is fixed at 4m/s. The Reynolds number based on the momentum thickness of the boundary layer (in the absence of suction) ranges from 750 to 1000 in the test section. The velocity measurements are made using a constant temperature hot-wire anemometer as well as PIV. In addition, flow visualization is done by using a smoke-wire technique. As for the coordinate system, x is the streamwise distance measured from the trailing edge of suction strip, y the normal-to-wall distance, and z the spanwise distance.

3. RESULTS AND DISCUSSION

When the local suction is applied, near-wall low-speed streaks disappear immediately downstream of the suction strip. If the suction rate is not so large, however, turbulent vortices in the core of turbulent boundary layer sur-

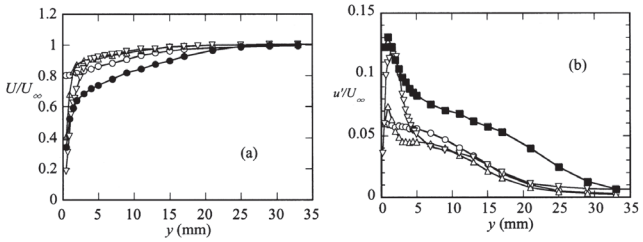

Figure 2. y-distributions of streamwise velocity fluctuations at x = -20mm (○) 50mm (△) and 150mm (▽) for V_s/U_∞=10%. ● Distributions in the absence of suction (x = -20mm)

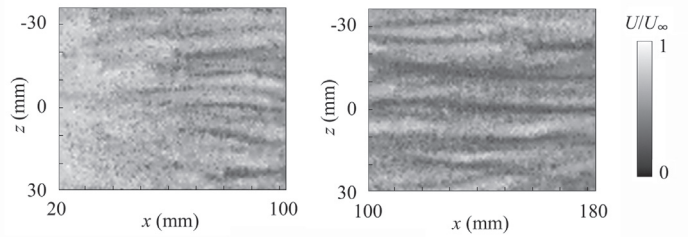

Figure 3. Instantaneous streamwise velocity map at y = 1mm for V_s/U_∞=10%

vive without being sucked out. Figure 2 illustrates the y-distributions of mean velocity U and r.m.s. value u' at x = -20mm, 50mm and 150mm for suction rate V_s/U_∞= 10%. The surviving turbulent vortices are of about 5–6% in intensity in terms of the associated maximun u-fluctuations near the downstream end of the suction strip. Such still active turbulent vortices penetrate into the near-wall region and develop into streamwise vortices under intense near-wall shear and induce near-wall low-speed streaks. Figure 3 visualizes the instantaneous streamwise velocity $U + u$ near the wall, measured by PIV. Streaky structure disappears almost completely immediately downstream of the suction but soon appears again beyond x= 50mm. The development of low-speed streaks corresponds to the increase in u' in Fig. 2. The low-speed streaks generated are much elongated with rather regular spanwise alignment in spite the fact that they are generated by random turbulent vortices.

Figure 4(a) shows the streamwise development of low-frequency component (less than 25 Hz) in terms of its r.m.s. value, u'_{0-25}, along y =1mm. Here, u'_{0-25} is defined as

$$u'_{0-25} = \int_{0.5}^{25} P(f)df \tag{1}$$

where $P(f)$ is the power spectrum density of u-fluctuations. The low-frequency component rapidly increases immediately downstream of the suction area and

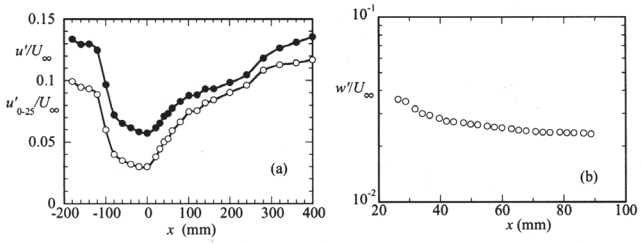

Figure 4. Development of velocity fluctuations near the wall (y = 1mm) for V_s/U_∞=10%. (a) u'_{0-25} (○) and u' (●), (b) w'

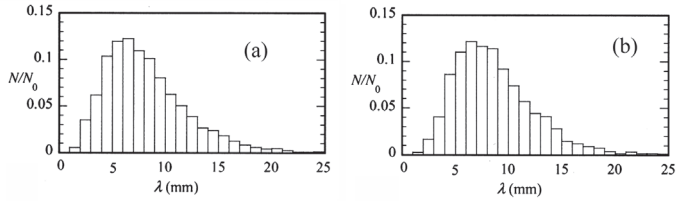

Figure 5. Probability density histograms (x = 140mm). (a) No suction. (b) V_s/U_∞=10%

approaches the value of the developed turbulent boundary layer (in the absence of suction). The development of low-frequency velocity fluctuations near the wall no doubt corresponds to the growth of low-speed streaks. Importantly, low-frequency components grow algebraically downstream of the suction strip. By contrast, the streamwise vortices responsible for the occurrence of low-speed streaks decay slowly during the generation process of the low-speed streaks, as shown in Fig. 4(b) which shows the streamwise variation of the r.m.s. value of spanwise velocity fluctuations w' at y= 1mm: Note that w' was obtained from PIV data. The w'/U_∞ is about 3.5% at x = 30mm but decreases down to 2% around x= 100mm. The development of low-speed streaks observed here seems to be consistent with a transient growth scenario for freestream-turbulence-induced by-pass transition (Andersson, Berggren & Henningson 1999, Luchini 2000, Matsubara & Alfredsson 2001) and a scenario proposed for a regeneration cycle of wall turbulence (Jiménez & Pinelli 1999).

Next examined is the lateral spacing of near-wall streaks. Figure 5 compares probability density histograms of the streak spacing λ at x= 140mm for boundary layers with and without suction. In the retransitional boundary layer, the λ-histogram is skewed towards values lower than the mean value, and are not distinguished from that of the developed wall turbulence, that is, the histogram exhibits the log-normal distribution. Furthermore, the streak spacing

is distributed around the same most-probable value λ= 6-7mm as in the developed wall turbulence even at the formation stage of low-speed streaks (at x= 140mm). The similarity in the λ-histogram is probably because the streamwise vortices causing the low-speed streaks are of the same scale as turbulent vortices existing in the oncoming upstream turbulent boundary layer.

The near-wall low-speed streaks continue to grow until the r.m.s. value of the associated velocity fluctuations u' near the wall exceeds about 10% of U_∞. Beyond the growth saturation stage of the streak development, x > 250mm, u' starts to increase again, suggesting that the breakdown of low-speed streaks begins around there. Figure 6(a) displays a time sequence of smoke-wire visualization pictures of the near wall flow for u'/U_∞= 10%. Smoke was released from a smoke-wire stretched at (x, y)= (250mm, 1mm), and the plan view pictures were taken by using a digital high-speed video camera. We can see the appearance of sinuous spanwise motion along some of the low-speed streaks (distinguished by gathered smoke), which no doubt indicates occurrence of the streak instability. The streamwise wavelength of the streak instability is found to be about 3–5 times the mean streak spacing, and the wavy pattern is traveling at a speed of about half the free-stream velocity. Since the streak instability is triggered by irregular and sometimes localized turbulent fluctuations in the present case, the instability and breakdown of low-speed streaks are observed to occur locally in space in spite of the nearly spanwise-periodic streaky structure. Figure6(b) shows a time sequence of events observed in the breakdown stage for u'/U_∞= 10% by means of cross-sectional view pictures. Smoke is released from x=250mm and a laser light sheet (about 1mm thick) illuminates a cross section at x=300mm. We can see the passage of oscillating mushroom-like structures. These pictures are quite similar to the visualization pictures of the streak breakdown in the experiment of streak instability by Asai, Minagawa & Nishioka (2002) and numerical simulation by Brandt & Henningson (2002) and indicates that the sinuous streak instability evolves to generate such quasi-streamwise vortices as proposed as dominant vortices in the near-wall turbulence by Jeong, Hussain, Schoppa & Kim (1997). The log-law region appears in the mean velocity profile after the streak breakdown proceeds.

Low-speed streaks undergo the cited breakdown due to the streak instability unless the Reynolds number is reduced below a critical value by suction. With increasing the suction rate, the low-speed streaks generated are less intensified and the eventual breakdown is delayed further downstream because the thinning of the near-wall shear layer (or decrease in the momentum-thickness Reynolds number) stabilizes the near-wall flow. It is noted that when the momentum thickness Reynolds number is decreased down to 200 by the suction, low-speed streaks are only elongated downstream without being intensified up to the stage of the streak instability leading to the wall turbulence generation.

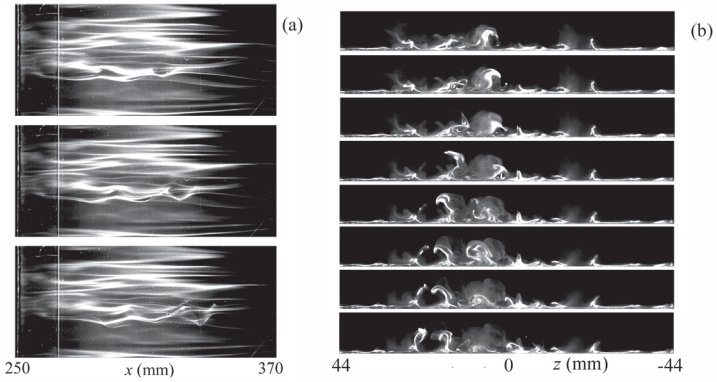

Figure 6. Visualization of near-wall flow for V_s/U_∞=10%. (a) Top view (2.5ms between pictures). (b) Cross-sectional view at x = 300mm (1ms between pictures). Smoke-wire is located at x = 250mm

4. CONCLUSIONS

The retransition of quasi-laminar boundary layer downstream of suction was investigated to examine the generation and breakdown processes of the near-wall streaks under active turbulent fluctuations. The low-speed streaks generated were elongated with rather regular spanwise alignment in spite the fact that they were generated by random turbulent vortices of moderately high intensity. The spanwise spacing of the newly developed low-speed streaks was almost the same as that in the turbulent boundary layer without suction. Further downstream of the formation region of streaks, the streak instability occurred, accompanied by wall bursts.

REFERENCES

ANDERSSON, P., BERGGREN, M. & HENNINGSON, D. S. 1999 Optimal disturbances and bypass transition in boundary layers *Phys. Fluids* **11**, 134–150.

ASAI, M., MINAGAWA, M. & NISHIOKA, M. 2002 The instability and breakdown of a near-wall low-speed streak *J. Fluid Mech.* **455**, 289–314.

BRANDT, L. & HENNINGSON, D.S. 2002 Transition of streamwise streaks in zeropressure-gradient boundary layers *J. Fluid Mech.* **472**, 229–261.

JEONG, J, HUSSAIN, F, SCHOPPA W. & KIM, J. 1997 Coherent structures near the wall in a turbulent channel flow *J. Fluid Mech.* **332**, 185–214.

JIMÉNEZ, J. & PINELLI, A. 1999 The iautonomous cycle of near-wall turbulence *J. Fluid Mech.* **389**, 335–359.

LUCHINI, P. 2000 Reynolds-number-independent instability of the boundary layer over a flat surface: optimal perturbations *J. Fluid Mech.* **404**, 289–309.

MATSUBARA, M. & ALFREDSSON, P. 2001 Disturbance growth in boundary layers subjected to free-stream turbulence *J. Fluid Mech.* **430**, 149–168.

THE TRANSITION TO TURBULENCE OF THE TORSIONAL COUETTE FLOW

Anne Cros and Patrice Le Gal
Institut de Recherche sur les Phénomgnes Hors Equilibre,
49, rue F. Joliot-Curie, 13384, Marseille, cédex 13, France
legal@irphe.univ-mrs.fr

Abstract: This work is devoted to the experimental study of the transition to turbulence of a flow confined in a narrow gap between a rotating and a stationary disk. When the fluid layer thickness is of the same order of magnitude as the boundary layer depth, the azimuthal velocity axial gradient is nearly constant and this rotating disk flow is a torsional Couette flow. As in the plane Couette flow or the cylindrical Couette flow, transition to turbulence occurs via the appearance of turbulent domains inside a laminar background. Nevertheless, we show that in the rotating disk case, the nucleation of turbulent spirals is connected to the birth of structural defects in a periodic underlying spiral roll pattern.

Keywords: Couette flow, rotating disk flow, defect turbulence, by-pass transition

1. INTRODUCTION

Transition to turbulence in extended systems can be induced by the erratic nucleation of defects in periodical patterns. This is the case in Rayleigh-Bénard convection [1] or in Taylor-Dean system [2] for instance. Topological defects in wave patterns have also been identified in numerical solutions of coupled Landau-Newell type equations [3] or of the complex Ginzburg-Landau equation (CGLE) [4, 5] and the mechanism for transition from phase to defect chaos has been identified by Coullet et al. [6]. In our work, a primary instability creates a periodic laminar spiral wave pattern in the torsional Couette flow confined between a rotating and a stationary disk [7, 8]. As the rotation rate of the disk is increased, some defects appear through the local disappearance of a spiral (a dislocation), or through the connection of two systems of spirals with different orientations (a grain boundary). Then as the control parameter is further increased, the number of these defects increases, and spatially localized chaotic regions develop under the form of turbulent spirals (TS). In this paper, we first describe the appearance of the disorder (Defect Turbulence) in the periodic pattern until the first TS waves appear. Then, the lifetime of these

R. Govindarajan (ed.), Sixth IUTAM Symposium on Laminar-Turbulent Transition, 311–316.

turbulent structures grows and they form permanent turbulent spirals arranged nearly periodically all around the disks. We will thus describe in the second part of this article this transitional process in the framework of spatiotemporal intermittency (STI). This mechanism involves a mixed state of turbulent patches and laminar domains, which coexist for the same values of the control parameter. This kind of scenario has been observed in different systems [9–11]. Several experiments have also described this mechanism of transition to turbulence. In particular, it was studied in Rayleigh-Bénard convection in annular and rectangular geometries [12, 13] and in the Taylor-Dean [14] or the Taylor-Couette systems [15]. In all these experiments, the transition to turbulence via STI was described within the framework of critical phenomena. Pomeau [16] proposed in 1986 that the spatiotemporal intermittency scenario could be similar to a percolation process, where the disordered state would propagate into the laminar one via a contamination mechanism. In this case, the turbulent state would be the "active", or "contaminant" phase, while the laminar state would be the "absorbing", or the "passive" state. Although the critical exponents found in experiments take various values and do not correspond to those of percolation, we will keep this terminology to describe the first steps of the invasion process of the turbulence in our own system. In particular we will define a "percolation threshold" as the limit value of the control parameter for which the turbulent structures possess an infinite lifetime.

2. THE ROTATING DISK DEVICE

The experimental device, presented in Figure 1, consists of a water-filled cylindrical casing in which the rotating disk is immersed. The top lid of the container plays the role of the stationary disk. The radius of the stainless steel

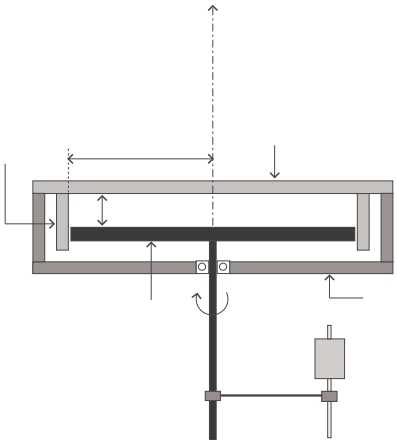

Figure 1. Rotating disk device

disk is 140 mm and its thickness is 13 mm. It is painted in black to enhance visualizations which are realized with kalliroscope flakes. The drive shaft goes through the bottom of the tank and is connected to a d.c. electric motor whose rotating velocity can be varied from $\Omega = 0$ to 200 rpm with an accuracy better than 0.2%. The stationary disk is a 20 mm thick plexiglass plate, so that the flow can be observed through it. The distance between the rotating disk and the fixed one is set to 2 mm. A CCD video camera is placed on the rotation axis and can rotate if necessary with a velocity which can be adjusted in order to observe the waves in their rotating frame. This video camera is finally connected to a computer, and images can be captured in real time.

3. TRANSITION TO DEFECT TURBULENCE

Figure 2-a) shows a typical defect of the laminar spiral pattern. We will describe the flow by the use of spatio-temporal diagrams which are realized

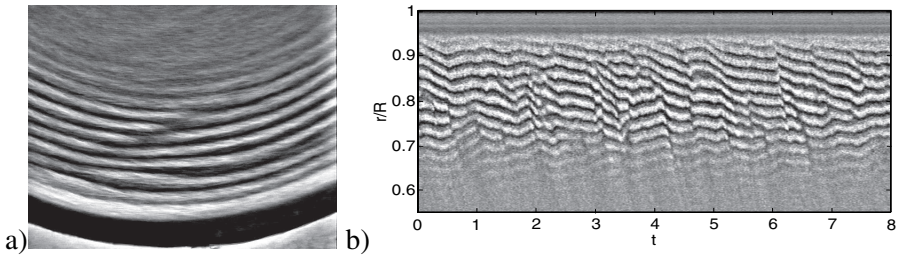

Figure 2. a) Defect in the spiral roll pattern. b) Space-time diagram along a radius

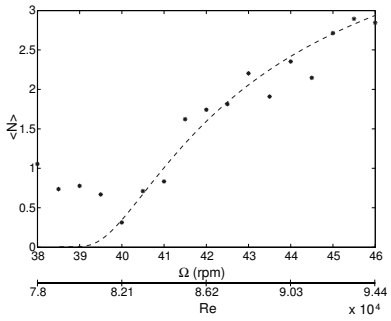

Figure 3. Total number of defects versus Reynolds number with a fit as proposed in [17]

along the radial direction. Figure 2-b) presents such a diagram where Defect Turbulence [6] can be observed. A statistical study of these defects shows that their occurrence obeys a Poisson law near their threshold. We observe also in Figure 3 that their number increases similarly to what is proposed by theoretical studies [17]. Our results are also in agreement with the interpretation that these defects are homoclinic orbits of a dynamical system nearby a saddle-node critical point [18]. As the rotation rate is further increased, the time duration separating two consecutive defects decreases dramatically and the defects are associated to strong amplitude modulations. A similarity with the "MAWs" of Brusch et al. [4] is striking. In fact, these modulations act as seeds for the turbulent spirals visualized in Figure 4-a).

4. SPATIO-TEMPORAL INTERMITTENCY

Very near their observation threshold, these turbulent structures that are the equivalents of the turbulent spirals of the cylindrical Couette flow (note that in spite of their traditional appellation, they are not spirals in this case but rather helices!) have a very short life time. As the rotation rate is further increased, this lifetime increases until a threshold is reached (the percolation threshold) where they finally form permanent turbulent spirals arranged nearly periodically all around a circumference. However, since the number of these turbulent spirals decreases with the rotational frequency, the transition to a fully turbulent regime is never achieved. Thus the turbulent fraction of the pattern saturates to a value close to 0.5. Figure 5 presents the evolution of this turbulent fraction with the Reynolds number. However, as it can be seen, this turbulent fraction presents a power law critical behavior with an exponent $\beta = 0.3$ near its threshold.

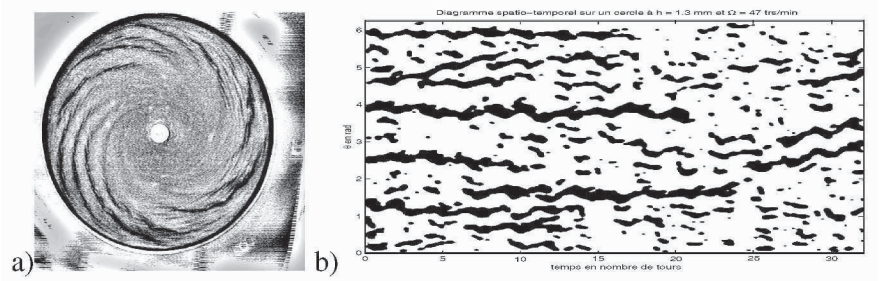

Figure 4. a) Visualization of the turbulent spirals. b) Space-time diagram (along a circle) showing the turbulent spirals (in black) inside the laminar flow (in white)

Another exponent of the transition can also be measured. As presented in Figure 6-a), the statistics of the length of the laminar domain follows an exponential law with a well defined characteristic length. The evolution of these

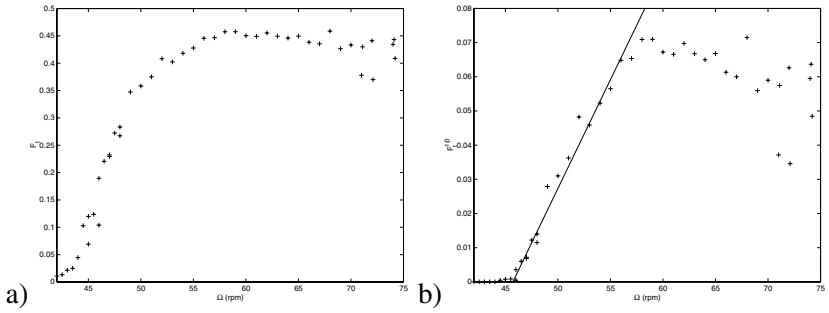

Figure 5. a) Evolution of the turbulent fraction versus Reynolds number. b) At threshold, an exponent $\beta = 0.3 \pm 0.01$ can be determined

laminar domains lengths versus the Reynolds number presents a divergence with a power law with an exponent $\alpha = -\frac{1}{2}$ (see Figure 6-b). Thus, although the transition to turbulence is not completed, it appears that it really shares some features with Space-Time Intermittency [19]. Therefore, although a universal scenario is still lacking for this type of transition to turbulence, we note that values of both α and β agree with the measures of Daviaud et al. [12] in their convection experiments. Note also that the saturation of the turbulent fraction near 0.5 is reminiscent of the amazing periodization of turbulence in bands as discovered by Prigent et al. [20] in the plane and in the cylindrical Couette flow and reproduced numerically by Barkley and Tuckerman [21].

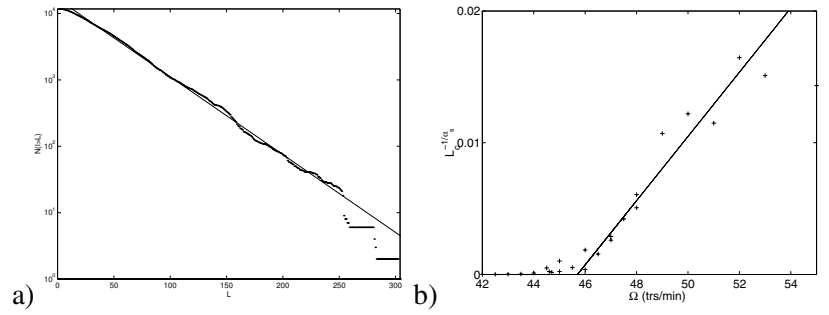

Figure 6. a) Exponential behavior of the histogram of the laminar lengths. b) Measure of the exponent $\alpha = -\frac{1}{2}$ of the critical behavior of the laminar length

REFERENCES

[1] A. Pocheau, V. Croquette and P. Le Gal. (1985)." Turbulence in a Cylindrical Container of Argon near Threshold of Convection," Phys. Rev. Lett. 55, 1094

[2] P. Bot and I. Mutabazi. (2000)."Dynamics of spatio-temporal defects in the TaylorDean system," Eur. Phys. J. B 13, 141 .

[3] P. Coullet, C. Elphick, L. Gil and J. Lega. (1987). "Topological defects of wave patterns," Phys. Rev. Lett. 59, 884 .

[4] L. Brusch , M.G. Zimmerman, M. van Hecke, M. Bar and A. Torcini. (2000)." Modulated amplitude waves and the transition from phase to defect chaos," Phys. Rev. Lett. 85, 86.

[5] M. van Hecke. (1998)." Building Blocks of Spatiotemporal Intermittency," Phys. Rev. Lett. 80, 1896 .

[6] P. Coullet, L. Gil and J. Lega. (1989)." Defect-mediated turbulence," Phys. Rev. Lett. 62(14), 1619.

[7] A. Cros and P. Le Gal. (2002). "Spatio-temporal intermittency in the torsional Couette flow between a rotating and a stationary disk," Phys. Fluids, 14(11),3755.

[8] A. Cros and P. Le Gal. (2004). "Defect turbulence in a spiral wave pattern in the torsional Couette flow," Phys. Rev. E 70, 016309.

[9] H. Chaté, P. Manneville. (1987).“Intermittence spatio-temporelle et automates cellulaires probabilistes,” C.R. Acad. Sc. (Paris) 304 II, 609.

[10] H. Chaté, and P. Manneville (1988). "Spatiotemporal intermittency in coupled map lattices," Physica D 32, 409.

[11] H. Chaté. (1994). "Spatiotemporal intermittency regimes of the one-dimensional complex Ginzburg-Landau equation," Nonlinearity 7, 185.

[12] F. Daviaud, M. Bonetti and M. Dubois. (1990)." Transition to turbulence via spatio-temporal intermittency in one-dimensional Rayleigh-Bénard convection," Phys. Rev. A, 42, 3388.

[13] S. Ciliberto, and P. Bigazzi. (1988). "Spatiotemporal intermittency in Rayleigh-Bénard convection," Phys. Rev. Lett. 60, 286.

[14] M. M. Degen, I. Mutabazi, and C. D. Andereck. (1996). "Transition to weak turbulence via spatiotemporal intermittency in the Taylor-Dean system," Phys. Rev. E, 53, 3505.

[15] P. W. Colovas and C. D. Andereck. (1997). "Turbulent bursting and spatiotemporal intermittency in the counterrotating Taylor-Couette system," Phys. Rev. E, 55, 2736.

[16] Y. Pomeau. (1986). "Front motion, metastability and subcritical bifurcations in hydrodynamics," Physica D 23, 3.

[17] B.I. Shraiman, A. Pumir A., W. Van Saarloos, P.C. Hohenberg, H. Chaté and M. Holen. (1992). "Spatio-temporal chaos in the one-dimensional complex Ginzburg-Landau equation," Physica D, 57, 241.

[18] V.S. Afraimoich; and L.A. Bunimovich. (1995)." Density of defects and spatial entropy in extended systems," Physica D 80, 277.

[19] H. Chaté and P. Manneville. (1987). "Transition to turbulence via spatio-temporal intermittency," Phys. Rev. E, 58, 112.

[20] A. Prigent, G; Gregoire, H. Chaté, O. Dauchot and W. Van Saarloos. (2002). "Large-scale finite wavelength modulation within turbulent shear flows," Phys. Rev. Lett 89, 014501.

[21] D. Barkley and L.S. Tuckerman.(2004). "Computational study of turbulent-laminar patterns in Couette flow," Phys. Rev. Lett. 94, 014502.

NONLINEAR WAVEPACKETS IN BOUNDARY LAYERS

Marcello A. F. Medeiros
Department of Aeronautical Engineering – University of São Paulo
marcello@sc.usp.br

Abstract: The nonlinear evolution of streamwise modulated three-dimensional waves in boundary layers was investigated. Three nonlinear stages were identified. The first was related to oblique transition and transient growth. The second involved Klebanoff instability. The third was a subharmonic instability. Associated with the modulation, a mechanism of production of subharmonic waves was also identified. This provided the deterministic seeds for the subharmonic instability.

In laminar boundary layers, when the Tollmien-Schlichting (TS) waves become large, different nonlinear mechanisms can take place. There are at least three different scenarios, namely, subharmonic resonance, fundamental resonance and oblique transition. However, to observe these phenomena the experiments have to be tuned to produce a particular outcome. In such experiments, almost always only a limited number of waves are introduced into the flow.

In natural transition a large number of waves are involved. Therefore, all these nonlinear interactions are possible. In fact, features of these three scenarios have been observed in natural transition, but the role of each of these phenomena has not yet been clearly identified.

In general, natural transition involves three-dimensional waves that are also modulated in time and in the streamwise direction. The current paper presents results of an investigation into the effect of streamwise modulation on the evolution of a three dimensional wavetrain emanating from a point source. The strategy here was to add a controlled amount of streamwise modulation to the wavetrain from a point source and so bridge the gap between the three-dimensional wavetrain and the three-dimensional wavepacket. Figure 1 displays hot-wire records of the streamwise fluctuating velocity, measured along the centerline of the flat plate, at $y = 0.6\delta^*$. Each frame corresponds to a distance from the leading edge, showing the downstream evolution of the waves. A scale given with the bottom signal indicates the wave amplitude. The top signal is sufficiently long for its central part to behave like a continuous wave-

R. Govindarajan (ed.), Sixth IUTAM Symposium on Laminar-Turbulent Transition, 317–322.

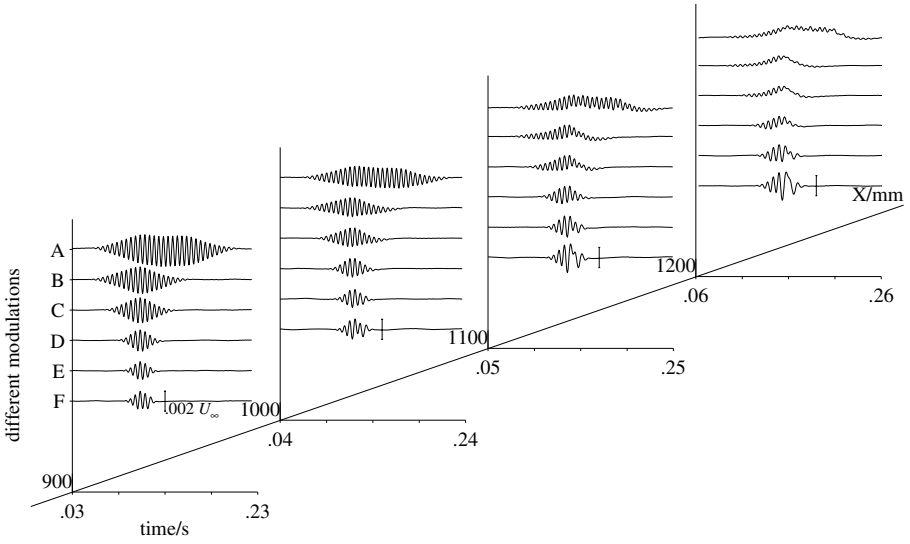

Figure 1. Centerline evolution of TS waves with different modulation envelopes

train. The bottom signal is a wavepacket excited by a pulse. The degree of modulation increases from top to bottom. In the nonlinear regime, the continuous wave (top signal) displays a mean flow distortion clearly seen at stations x=1100 and 1200mm. In the wavepacket (bottom signal), the nonlinear distortion corresponds to the loss of a ripple. The signals at x=1100mm or 1200mm show a pattern of increasingly localized mean flow distortion linking the continuous wavetrain to the wavepacket. The time$\times$span planes in figure 2 give the three-dimensional structure of the waves.

Here, interpretation of the results is based on the spectral distribution of the signals (figure 3). Figure 4 shows the linear evolution of the signals as computed from Linear Stability Theory (LST). Comparison of figures 3 and 4 indicates more clearly what part of the spectra corresponds to a nonlinear behavior. It also indicates that, throughout the experimental domain, the TS band agreed very well with the linear predictions.

Theoretical analysis of the nonlinear regime are not described here in detail. Only the main results are given and briefly discussed. It was possible to distinguish three different stages in the nonlinear evolution of these waves. The first stage resembled to oblique transition. It was associated with a forcing of longitudinal vortices by the weakly nonlinear terms of the longitudinal vorticity equation. These vortices, via transient growth, give rise to a three-dimensional mean flow distortion in the form of longitudinal streaks. The difference from oblique transition lies in the fact that, here, the system did not involve only

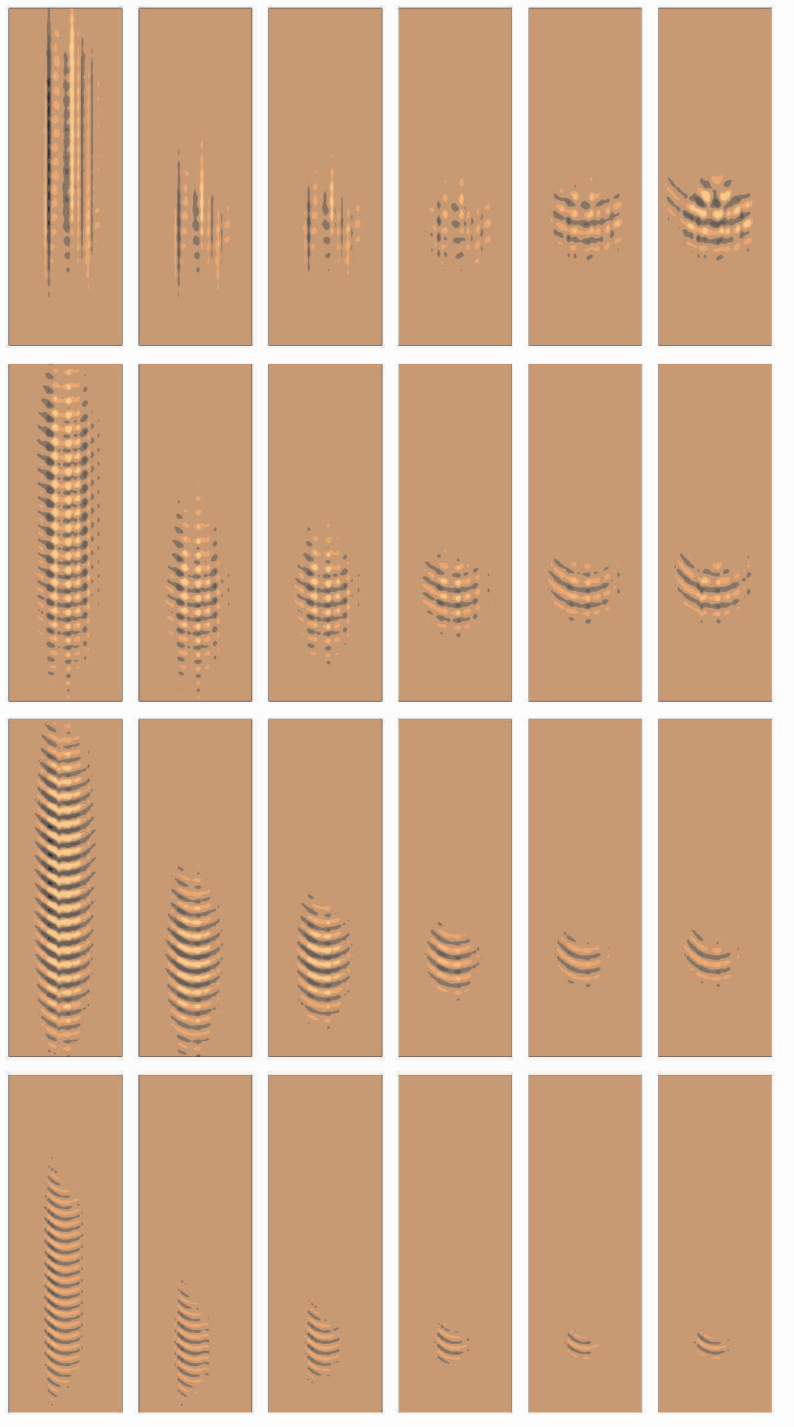

Figure 2. Spanwise structure at 600, 800, 1000 and 1200mm from the leading edge of the flat plate. The streamwise position increases from left to right and the modulation increases from top to bottom. The top signal represents the continuous three-dimensional wavetrain

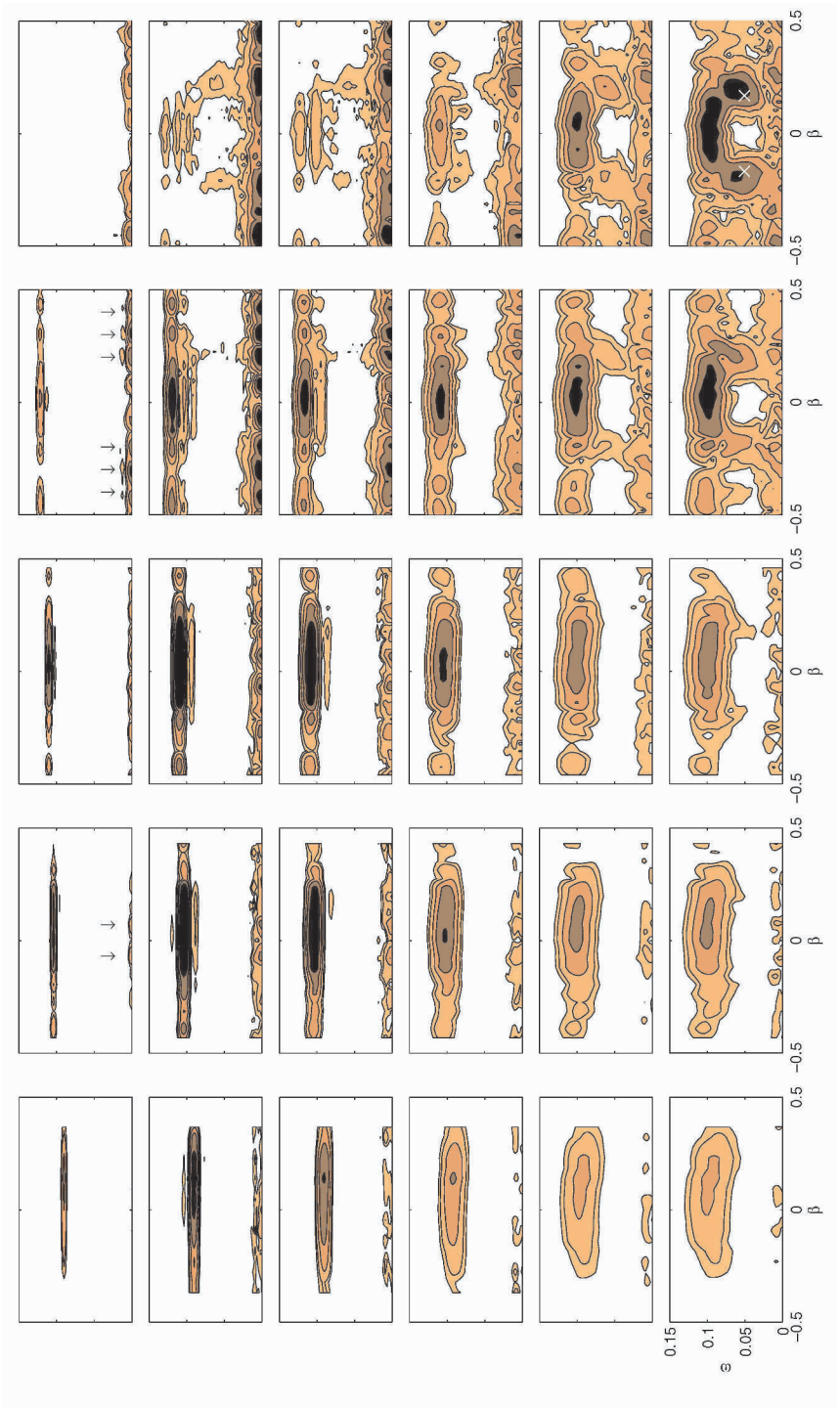

Figure 3. Spectral distribution of the signals at x=600, 800, 900, 1100 and 1300mm. The streamwise position increases from left to right and the modulation increases from top to bottom. Symbols and arrows refer to theoretical predictions

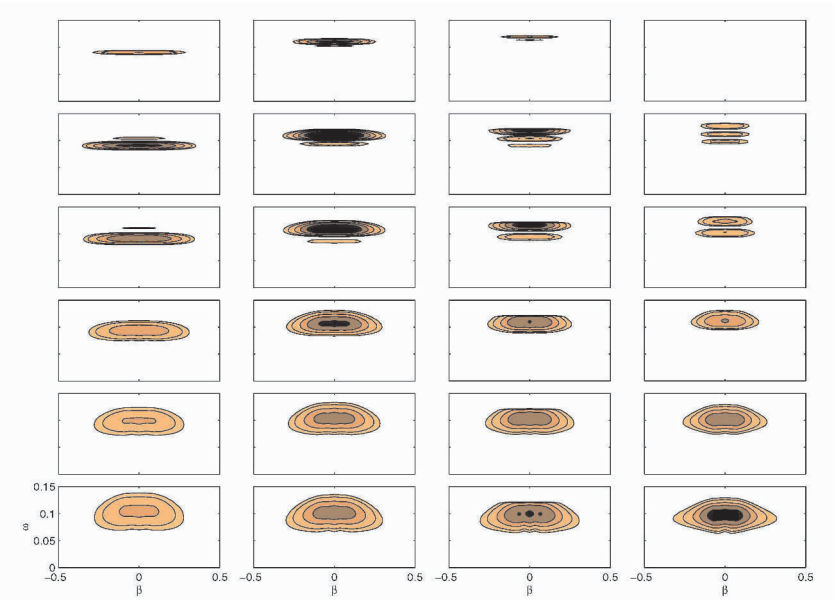

Figure 4. Spectral distribution of the signals at x=600, 900, 1100 and 1300mm as predicted by LST. The streamwise position increases from left to right and the modulation increases from top to bottom

a pair of oblique waves, but a very large number of waves, including a two-dimensional one. In order to check the argument, calculations of the weakly nonlinear forcing terms above mentioned were performed for the case without streamwise modulation, that is, the continuous three-dimensional wavetrain. In figure 3, the theoretical predictions of the spanwise wavenumber (β) are given by the arrows on the top frame for x=800mm (Medeiros, 2004). The agreement is good for both the modulated and the continuous signals.

The second stage appeared to be governed by Klebanoff instability. This instability involves the appearance of three-dimensional waves of the fundamental frequency and with selected spanwise wavenumbers. The interaction of these waves with the waves composing the primary wave-system gives rise to other streaks and change the spanwise wavenumbers of the three-dimensional mean flow distortion. PSE calculations for a continuous wavetrain were performed. In figure 3, the spanwise wavenumbers predicted by the computations are given by the arrows on the top frame for x=1100mm. The agreement is good, even for the waves with a large degree of modulation. Because the three-dimensional mean flow distortion was larger than the primary wave-system, and spectrally separated from the TS band, it shows more clearly the spanwise wavenumbers selected by the instability mechanism. However, by comparing with figure 4, it is clear that these three-dimensional mean flow distortions are

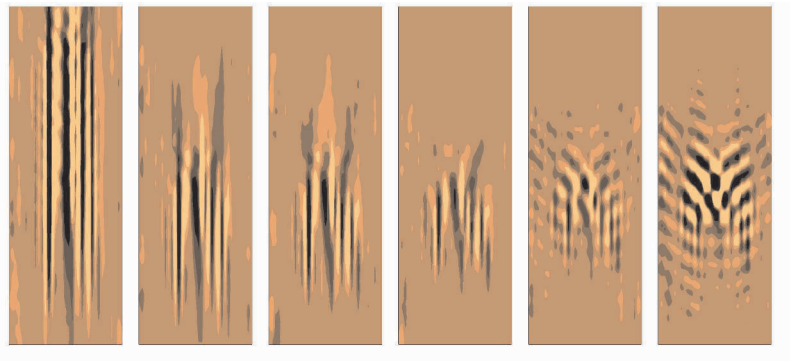

Figure 5. The nonlinear part of the signals at x=1300mm. The modulation increases from left to right

associated with waves that have the fundamental frequency, but which a spanwise wavenumber that can be outside the TS band.

The third stage involved the appearance of three-dimensional subharmonic waves. This stage was not observed in the continuous wavetrain and was more intense for the more modulated signals. In figure 3, the theoretical predictions of the most unstable subharmonic modes are given by the white symbols on the bottom frame for x=1300mm. The picture suggests that the subharmonic band was seeded by energy that came from the mean flow distortion. This is plausible, because as the modulation increases the mean flow distortion associated with the streaks becomes more localized in the physical space and, therefore, wider in the spectral space. For very modulated signals the localized mean flow distortion can have components with the right frequency for subharmonic resonance.

In physical space, the process appears more clearly if the TS waves are digitally filtered out. Figure 5 shows how the streak structure of the continuous wavetrain gives rise to the oblique subharmonic waves of the wavepacket. It has been shown that the evolution of wavepackets must involve some mechanism of production of subharmonic waves (Medeiros and Gaster, 1999; Craik, 2001). This argument provides a possible such mechanism.

The author acknowledges the financial support from FAPESP.

REFERENCES

Craik, A. D. D. (2001). A model for subharmonic resonance within wavepackets in unstable boundary layers. *J. Fluid Mech.*, 432:409–418.

Medeiros, M. A. F. (2004). The nonlinear evolution of a wavetrain emanating from a point source in a boundary layer. *J. Fluid Mech.*, 508:287–317.

Medeiros, M. A. F. and Gaster, M. (1999). The production of sub-harmonic waves in the nonlinear evolution of wavepackets in boundary layers. *J. Fluid Mech.*, 399:301–318.

APPLICABILITY OF LES MODELS FOR PREDICTION OF TRANSITIONAL FLOW STRUCTURES

Philipp Schlatter, Steffen Stolz and Leonhard Kleiser
Institute of Fluid Dynamics, ETH Zürich, Switzerland
schlatter@ifd.mavt.ethz.ch

Abstract: Instantaneous transitional flow structures of standard K-type transition in incompressible plane channel flow predicted by large-eddy simulations (LES) are compared to fully-resolved DNS data. For the LES different subgrid-scale (SGS) models are compared. It is investigated how well the SGS models on coarse grids are able to predict the physically relevant mechanisms at successive stages of transition: Λ-vortices, rollup of shear layers, hairpin vortices. Additionally, results for the exact subgrid-scale dissipation are computed from the DNS data. The results suggest that SGS models including a three-dimensional relaxation regularization show similar transitional structures as present in the DNS, whereas the dynamic Smagorinsky model does not show hairpin vortices for the chosen coarse resolution.

Keywords: Large-eddy simulation, K-type transition, Hairpin vortices, SGS models, Relaxation regularisation

1. INTRODUCTION

The ability to accurately simulate transitional flows using large-eddy simulation (LES) would inevitably improve the applicability of LES for practical industrial applications. LES only requires a fraction of the computational cost of a fully-resolved direct numerical simulation (DNS) while attempting to achieve similar accuracy. It has already been shown in a number of investigations that, e.g. for the model problem of temporal transition in channel flow, spatially averaged integral flow quantities like the skin friction Reynolds number Re_τ or the shape factor H_{12} can be predicted reasonably well by LES, see e.g. [1, 6]. However, it is also important to faithfully represent the dominant transitional ßow mechanisms and their three-dimensional vortical structure like Λ-vortices and hairpin vortices.

In this contribution, we focus on standard temporal K-type transition in incompressible channel flow. We examine data obtained with highly resolved DNS and compare to different SGS model results at rather coarse resolution.

R. Govindarajan (ed.), Sixth IUTAM Symposium on Laminar-Turbulent Transition, 323–328.

2. SIMULATION METHOD AND PARAMETER SETTINGS

The simulations are performed using a Fourier-Chebyshev spectral Galerkin-tau method with periodic boundary conditions in the streamwise (x_1) and spanwise (x_2) direction and no-slip at the walls $x_3 = \pm 1$. Full dealiasing has been applied in all directions. The initial disturbances for temporal K-type transition consist of a 2D Tollmien-Schlichting (TS) wave of maximum amplitude 3% of the centerline velocity u_{CL} and two superimposed oblique 3D waves with amplitude 0.1% and the same fundamental wavenumber as the 2D wave, similar to [4, 2, 5]. The Reynolds number based on u_{CL} and channel half-width h is $Re = 5000$ (corresponding to $Re_\tau \approx 210$ in the fully turbulent regime). The computational domain is chosen to fit one wavelength of the initial disturbances, i.e. $5.61h \times 2.99h \times 2h$.

The incompressible Navier-Stokes equations for the non-dimensional filtered velocities $\overline{u}_i$ and pressure $\overline{p}$

$$\frac{\partial \overline{u}_i}{\partial t} + \frac{\partial \overline{u}_j \overline{u}_i}{\partial x_j} + \frac{\partial \overline{p}}{\partial x_i} - \frac{1}{Re}\frac{\partial^2 \overline{u}_i}{\partial x_j \partial x_j} = -\frac{\partial}{\partial x_j}(\overline{u_i u_j} - \overline{u}_i \overline{u}_j) =: -\frac{\partial \tau_{ij}}{\partial x_j} \ , \quad (1)$$

are supplemented with the incompressibility constraint $\partial \overline{u}_i / \partial x_i = 0$. The subgrid-scale (SGS) term τ_{ij} is not closed and has to be modelled appropriately by a SGS model. The dissipation due to the SGS stresses is

$$\varepsilon_{\mathrm{SGS}} = \tau_{ij} \overline{S}_{ij} \ , \quad \text{with } \overline{S}_{ij} = \frac{1}{2}\left(\frac{\partial \overline{u}_i}{\partial x_j} + \frac{\partial \overline{u}_j}{\partial x_i}\right) . \quad (2)$$

3. ANALYSIS OF DNS RESULTS

The fully-resolved reference DNS was performed on $160^2 \times 161$ grid points. During the temporal evolution of K-type transition, a saturated TS wave is formed ($t < 100$), which undergoes secondary instability with the formation of strong shear layers and pronounced open Λ-vortices ($t \approx 130$) [2, 5]. These vortices in turn provoke the appearance of hairpin vortices (roll-up of shear layer, $t \approx 136$) first in the peak plane ($y = L_y/2$), which are also visible in the velocity signal as sharp ÒspikesÓ. The roll-up of the shear layer then proceeds to more complex flow states and eventually the whole flow domain is affected ($t \approx 155$).

Figure 1a shows the excited computational modes during transition. By choosing a resolution of $32^2 \times 33$ grid points (16 Fourier modes), the simulation is underresolved in all directions for $t > 70$. In figure 1b, the SGS dissipation $\varepsilon_{\mathrm{SGS}}$ was computed for a number of LES grids with full dealiasing. Similarly to figure 1a, the resolution $32^2 \times 33$ indicates the necessity of a SGS model even for the early laminar stages prior to transition, mainly due to the underresolved 2D saturated TS wave. Based on these findings, for the following a LES resolution of $32^2 \times 33$ grid points was chosen in order to assess the

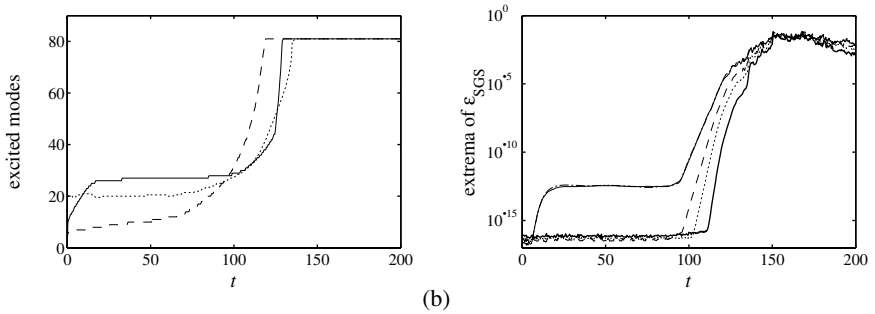

(a) (b)

Figure 1. (a) Excited modes of the DNS (resolution $160^2 \times 161$ grid points). ——— streamwise direction, – – – – spanwise direction, ····· wall-normal direction (number of Chebyshev modes is halved to allow comparison with Fourier modes). In the Fourier directions a threshold of 10^{-15} is used whereas the threshold value in the wall-normal direction is 10^{-6}. (b) Maximum of SGS dissipation $\max_{x,y,z} \varepsilon_{\mathrm{SGS}}$. ——— $32^2 \times 33$, —·— $32^2 \times 49$ (almost coinciding with $32^2 \times 33$), – – – – $48^2 \times 49$, ····· $64^2 \times 65$, ——— $96^2 \times 97$

ability of the SGS model to predict laminar, transitional and turbulent flows (see also [6]).

4. LARGE-EDDY SIMULATION

Results of LES calculations using the dynamic Smagorinsky (DS) model [1] and the ADM-RT model [7, 6] together with a no-model LES (coarse-grid DNS) are presented. Note that for the DS a 3D graded filter of second order has been used as test filter [6]. The SGS stresses for the ADM-RT model are given by [7, 6]

$$\frac{\partial \tau_{ij}}{\partial x_j} = \chi H * \overline{u}_i \,, \tag{3}$$

i.e. a relaxation regularization (relaxation term, RT) has been added to the momentum equations. H denotes a suitable 3D high-pass filter [7] and χ is a model coefficient, set constant in the present computations. The model contribution of the ADM-RT model are thus confined to the smallest scales.

Three-dimensional visualisations of the breakdown process for the different models are depicted in figure 2 for the times $t_{\mathrm{DNS}} = 136$, $t_{\mathrm{DNS}} = 140$ and $t_{\mathrm{DNS}} = 154.5$ using the negative λ_2 criterion [3]. To allow a direct comparison of the LES models and the DNS, the selected times for the LES were slightly shifted such that the stage of transition development is matched at $t_{\mathrm{DNS}} \approx 128$. Note that the DNS results have been coarsened to the LES grid prior to plotting in order to allow for a more suitable comparison.

The results for the RT model show a similar behaviour as the DNS: Hairpin vortices ($t_{\mathrm{DNS}} = 136$) and the related roll-up ($t_{\mathrm{DNS}} = 140$) of the shear layer are clearly visible and their position, convection speed and growth rate are similar to the DNS. Moreover, the initial stages of the turbulent breakdown

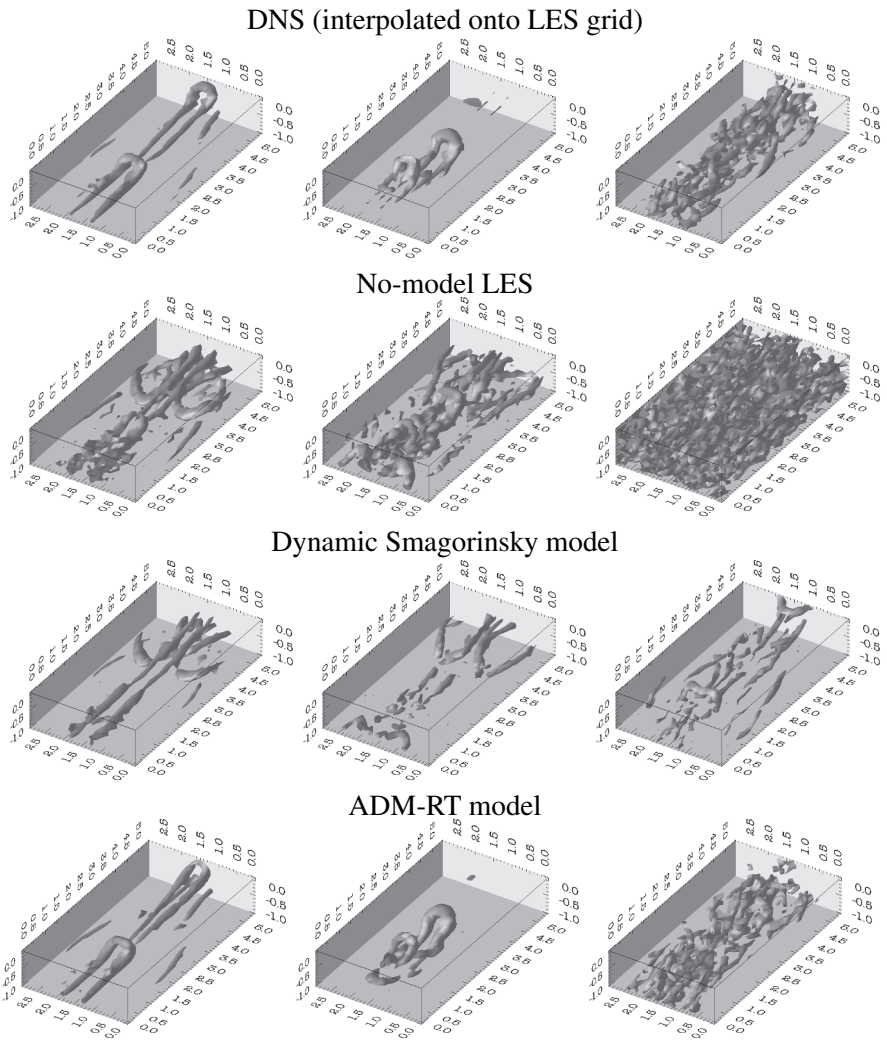

Figure 2. Three-dimensional visualisation of the transitional structures for the different simulations by isocontours of the negative λ_2 criterion (same isolevel for respective times). From left to right: $t_{\mathrm{DNS}} = 136$, $t_{\mathrm{DNS}} = 140$, $t_{\mathrm{DNS}} = 154.5$

are confined to a region close to the peak plane ($t_{\mathrm{DNS}} = 154.5$). The no-model LES shows fragments of hairpin vortices, but these are disguised by a high level of ambient high-frequency oscillations (noise) which is attributed to missing SGS dissipation. Unlike for the DNS data, at the latest time shown ($t_{\mathrm{DNS}} = 154.5$) already the whole span of the channel is turbulent. The simulation using the dynamic Smagorinsky model does not show a proper roll-up of the shear layer. Vortices are generated, but these are not so pronounced, closer

to the wall, and spread further away from the peak plane. Moreover, no hairpin vortex can be detected.

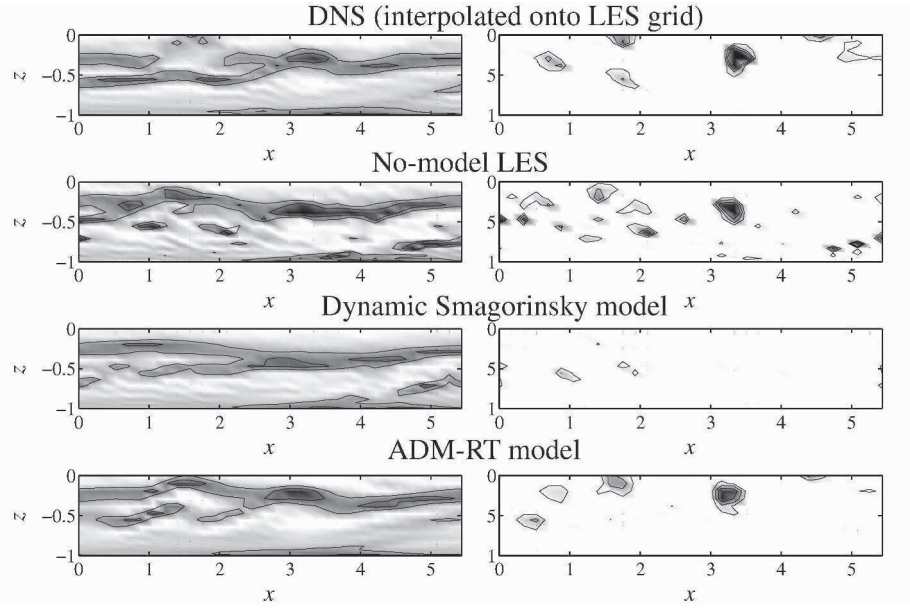

Figure 3. Contour plots in the peak plane ($y = L_y/2$) for the different simulations at $t_{\mathrm{DNS}} = 140$ ("three-spike stage"). *Left column:* Shear $\partial u/\partial z$. *Right column:* Negative λ_2 criterion

In Figure 3, the wall-normal shear $\partial u/\partial z$ and λ_2 are shown in the peak plane ($y = L_y/2$) at the early "three-spike stage" ($t_{\mathrm{DNS}} = 140$). The "kinks" in the shear layer ($x \approx 1.5$) coincide with the hairpin vortices, clearly detectable by the λ_2 criterion (figure 3, right column). Again, the results obtained with the ADM-RT model compare favourably to the DNS data. The no-model LES also shows the roll-up of the shear layer in an overall more noisy environment. The DS model, however, does not predict the physically proper transition scenario.

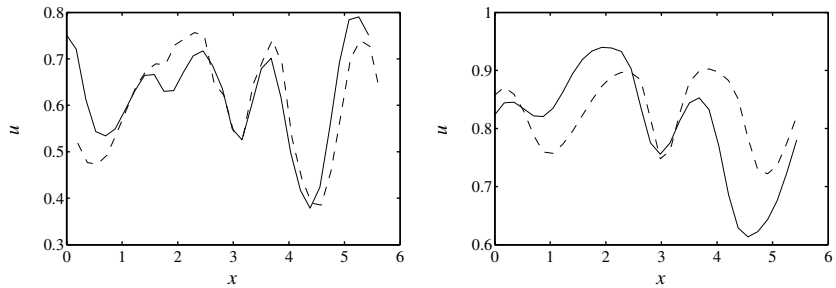

Figure 4. Streamwise velocity for the "three spike stage" at $z = -0.3$. – – – –DNS, ——— ADM-RT. *Left:* $t_{\mathrm{DNS}} = 143$, peak plane ($y = L_y/2$).*Right:* $t_{\mathrm{DNS}} = 154.5$, valley plane ($y = 0$)

A quantitative comparison of the streamwise velocity component during the "three-spike stage" at both the peak and the valley position is given in figure 4 for DNS and the ADM-RT model only since these stages could not be identified properly in either the DS or the no-model simulation. It is evident that the "three-spike stage" is captured accurately by the ADM-RT model. Note that at $t_{\mathrm{DNS}} = 154.5$ transition at the peak position is already well advanced (see also figure 2), but the ADM-RT model is still able to accurately predict the roll-up at the valley position.

5. CONCLUSIONS

By examining instantaneous flow fields from LES of channel flow transition, distinct differences between SGS models can be established. The dynamic Smagorinsky model fails to correctly predict the first stages of breakdown involving the formation of typical hairpin vortices on the coarse LES grid. The no-model calculation, as expected, is generally too noisy during the turbulent breakdown preventing the identification of transitional structures. On the other hand, the ADM-RT model, whose model contributions are confined to the smallest scales, appears to be able to allow a more accurate and more physically realistic prediction of the transitional structures even up to late stages of transition.

ACKNOWLEDGEMENTS

This work was supported by the Swiss National Science Foundation (SNF) and the Swiss National Supercomputing Centre (CSCS).

REFERENCES

[1] M. Germano, U. Piomelli, P. Moin, and W. H. Cabot. A dynamic subgrid-scale eddy viscosity model. *Phys. Fluids A*, 3(7):1760–1765, 1991.

[2] N. Gilbert and L. Kleiser. Near-wall phenomena in transition to turbulence. In S. J. Kline and N. H. Afgan, editors, *Near-Wall Turbulence – 1988 Zoran Zarić Memorial Conference*, pages 7–27. Hemisphere, New York, USA, 1990.

[3] J. Jeong and F. Hussain. On the identification of a vortex. *J. Fluid Mech.*, 285:69–94, 1995.

[4] M. Nishioka, S. Iida, and Y. Ichikawa. An experimental investigation of the stability of plane Poiseuille flow. *J. Fluid Mech.*, 72:731–751, 1975.

[5] N. D. Sandham and L. Kleiser. The late stages of transition to turbulence in channel flow. *J. Fluid Mech.*, 245:319–348, 1992.

[6] P. Schlatter, S. Stolz, and L. Kleiser. LES of transitional flows using the approximate deconvolution model. *Int. J. Heat Fluid Flow*, 25(3):549–558, 2004.

[7] S. Stolz, N. A. Adams, and L. Kleiser. An approximate deconvolution model for large-eddy simulation with application to incompressible wall-bounded flows. *Phys. Fluids*, 13(4):997–1015, 2001.

TURBULENT SPOTS IN A COMPRESSIBLE BOUNDARY-LAYER FLOW

L. Krishnan and N. D. Sandham
Aeronautics and Astronautics, School of Engineering Sciences
University of Southampton
Southampton, S017 1BJ
United Kingdom
Email: n.sandham@soton.ac.uk

Abstract: Direct simulation of an isolated turbulent spot in a compressible isothermal wall boundary-layer flow has been performed. A bypass transition scenario at Mach 2,4 and 6 is considered. The flow field associated with the transitional and turbulent spots is studied in detail, with results in broad agreement with previous experimental work. The evolved spots are found to have an arrowhead shaped front with a leading edge overhang, followed by a turbulent core and a calmed region at the rear interface. The lateral spreading of the spot is found to decrease substantially with the flow. Evidence for a supersonic (Mack) mode is found in the Mach 6 case: spanwise-coherent structures are observed under the spot overhang region.

Keywords: Bypass transition, Turbulent spots, Compressibility.

1. INTRODUCTION

The breakdown of disturbances in a laminar flow into a turbulent flow often occurs via the formation of localised turbulent patches, generally referred to as turbulent spots. The laminar base flow can be perturbed using various forcing techniques like vibrating ribbons, acoustic forcing, localised point source disturbances (loud speakers, sparks), suction/blowing slots, roughness elements and complex wave generators. The growth of instabilities in a laminar flow triggers the transition process, but intrusion of large amplitude non-linear perturbations may skip the linear stages of transition in a process known as bypass transition. The extent of the transition length is generally shorter in a bypass transition scenario. A detailed study of the dynamics of turbulent spots can also be useful in extending our understanding of turbulence physics.

R. Govindarajan (ed.), Sixth IUTAM Symposium on Laminar-Turbulent Transition, 329–334.

The length of the transition region mainly depends on spot characteristics such as the convective speed of the leading and trailing edges of the spot, lateral growth rate and interactions between spots.

Most of the earlier transition studies were performed for incompressible flows. A detailed review of transition studies in a variety of flows was given by Narasimha (1985). Based on results of flow visualisation experiments, Perry *et al.* (1981) suggested that a turbulent spot is an array of Λ-shaped vortices. The effect of compressibility has been less well studied. Variation of the wall and lateral spreading angles of the disturbance region with local Mach number was reported by Fischer (1972), who also summarized the results of earlier investigations on disturbance growth. The spreading angle relative to the wall remained invariant with Mach number while the lateral spreading angle decreased sharply from 11 to 3 degrees with increasing Mach number up to about Mach 6.0. In boundary layer transition experiments using thin-film heat-transfer gauges at Mach 6 (Mee (2002)) also demonstrated that turbulent spots grow at a more slender angle than at low Mach numbers. The present computation is aimed at understanding the mechanisms behind this strong compressibility effect.

2. SIMULATION DETAILS

A high-order scheme, with numerical stability enhanced by an entropy splitting of the Euler terms, is used to solve the compressible Navier-Stokes equations. All the spatial discretizations are done using a fourth-order central-difference scheme and the time integration is done using the third-order Runge-Kutta method. Details regarding the entropy-splitting and other numerical issues used in the present computations can be found in Sandham *et al.* (2002).

Table 1. Details of Spot Simulations

Case	Mach	$Re^*_{\delta_{in}}$	T_w/T_∞	$(L_x, L_y, L_z)/\delta^*_{in}$	N_x, N_y, N_z
M2	2	950	1.672	400 x 60 x 60	801 x 101 x 121
M4	4	2000	3.694	450 x 60 x 60	801 x 101 x 121
M6	6	3000	7.0	600 x 30 x 40	601 x 101 x 121

All lengths are normalised with the displacement thickness (δ^*_{in}) of the laminar inflow profile. The laminar base flow is obtained by a separate self-similar compressible boundary layer solution. Details of the various cases considered are given in Table 1. The flow is assumed periodic in the spanwise direction, while no-slip fixed temperature conditions are

applied at the plate surface. Characteristic boundary conditions are used at the inflow, outflow and upper surface. The laminar base flow is perturbed by a localised injection of low momentum fluid through the plate surface.

A spanwise symmetric rectangular slot of dimensions 4 x 4 (x, z) is used (Figure.2). The blowing trip is applied for a short duration of 8 non-dimensional time units (δ^*_{in}/u_∞) by specifying vertical velocity at the plate surface ($v_{inj} = Au_\infty$). The amplitude of the disturbance is chosen such that a spot can be triggered and studied within the present domain size. A perturbation amplitude of $A = 0.2$ was used for the Mach number $M_\infty = 2$ and $M_\infty = 6$ cases. For the $M_\infty = 4$ case the length of the injection slot was 6 and the value of A was set to 0.35.

3. RESULTS

The organisation of spot substructures during the early stages of transition at $M = 2$ tends to confirm the conceptual picture of Perry *et al.* (1981) (Figure 1). Further growth, interaction and breakdown of these complex substructures finally evolves the flow field into a mature turbulent spot. Plan and side views of the mature turbulent spot are shown in Figure 2a-c. The leading edge of the spot is found to travel at a speed of $0.8u_\infty$-$0.9u_\infty$ (Figure 3) while the speed of the trailing edge increased with the Mach number ($0.5u_\infty - 0.7u_\infty$). Figure 4 shows the streamwise evolution of span-averaged skin friction (c_f). The c_f value in the calmed region behind the spot is higher than the laminar value; this supresses the growth of instabilities in the wake of a spot.

The growth mechanism of a spot in a boundary layer is complex, since the spot interacts with the irrotational free stream flow at the top and the rotational laminar boundary layer flow surrounding it. The physical mechanisms involved in the lateral and wall-normal growth of a spot are different. The wall-normal growth of the spot is similar to this classical entrainment mechanism. The difference between convective speeds of the front and the tail of a spot results in the spot growth in the streamwise direction.

The spot grows in the lateral direction by destabilising the surrounding laminar flow. The spot spreading rate was found to be faster than the spot turbulent diffusion (Gad-El-Hak *et al.*, 1981). As seen in Figure 1, the primary flow structures created by the injection of low momentum fluid developed into a complex turbulent spot. The vortex dynamics associated with the metamorphosis of a single hairpin vortex into a turbulent spot in an incompressible flow was explained in detail by Haidari & Smith (1994) and Singer (1996). They showed that the lateral inviscid

vortex deformation and an inviscid-viscous interaction of vortices with the surface are responsible for the regeneration of coherent structures. In agreement with previous studies, the sequence of events leading to a mature turbulent spot is: (a) roll up of the high-shear layer between the injected fluid and the free stream fluid into a primary hairpin structure, (b) generation of secondary hairpin vortices and other structures due to the lift up of near wall low momentum fluid between the legs of the hairpin vortex i.e. vortex-surface interactions, (c) growth in the lateral direction due to the inviscid deformation of the vortex lines comprising the hairpin structure, and (d) further growth, regeneration, non-linear interactions and breakdown of these hairpin structures results in the formation of a random turbulent flow field with complex flow structures.

The lateral growth of a spot is highly dependent on the flow Mach number. For the M2, M4 and the M6 cases the calculated lateral half-spreading angles are $5°, 4°$ and $1.7°$, respectively. A comparison of the estimated spot half-spreading angles with the data of Fischer (1972) is shown in Figure 5. The lateral half-spreading angle of the spot decreases strongly with the Mach number. This clearly shows that the effect of compressibility is to suppress the spot spreading and delay transition at hypersonic speeds.

In a compressible flow temperature and density fluctuations (acoustic disturbances) introduce additional acoustic instabilities in the flow. These acoustic modes at high-speed flows were first discovered by Mack (1969), and they are unstable to inviscid disturbances. Reflection of these acoustic waves between the solid surfaces and the sonic line makes these modes unstable. At low Mach numbers the first mode instabilities play a major role in destabilizing the flow. However, above Mach 2.2 the large amplification rates of the inviscid instabilities (Mack modes) are likely to dominate over the first mode instabilities. In the $M_\infty = 6$ case, complete breakdown to turbulence has not yet occurred. The structure is however, already markedly different to the Mach 2 and 4 spots. In particular we note the appearance of coherent spanwise structures close to wall, visible for example in the side view of Figure 2.c ($400 < x < 520$). It is possible that these structures (associated with Mack modes) are excited by the supersonic flow relative to the wall in the spot overhang region.

4. SUMMARY

A localised blowing trip mechanism was used to trigger a turbulent spot in a laminar base flow. Prior to the breakdown, an array of hairpin structures and quasi-streamwise vortices were noticed inside the spot.

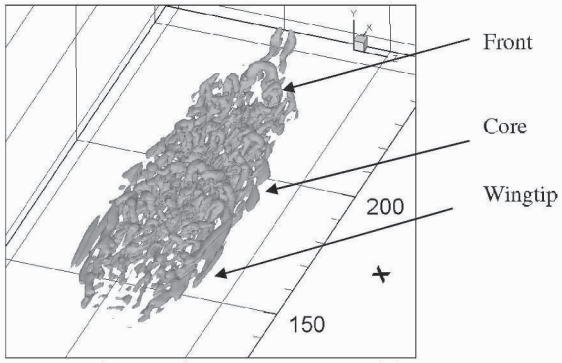

Figure 1: Iso surface of the second invariant at t=249 (Π =-0.0008) (M2)

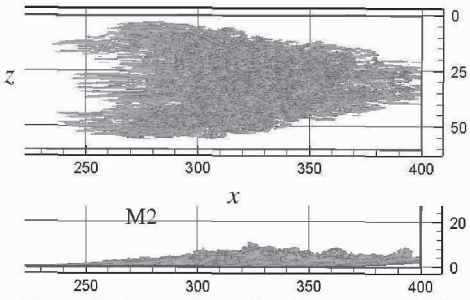

Figure.2a: Iso surface of wall-normal vorticity at t=451 (+0.06, - 0.06);

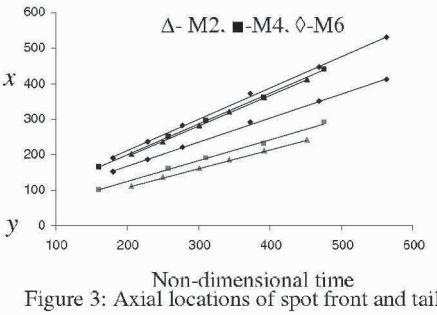

Figure 3: Axial locations of spot front and tail

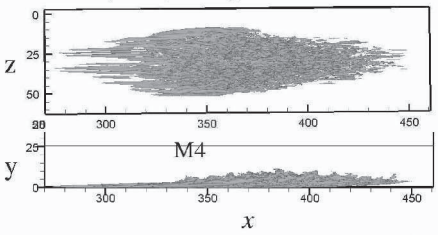

Figure 2b: Top and side view of a developed turbulent spot at t = 475 (ω_y = +0.06, -0.06)

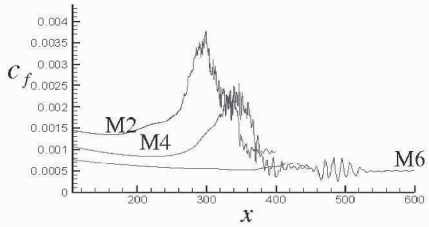

Figure 4: Mean skin friction distribution

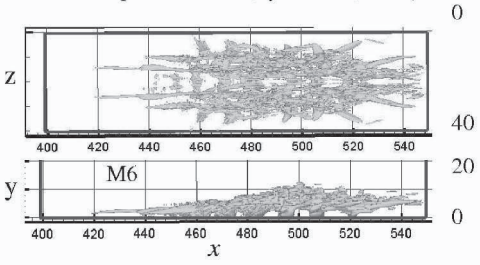

Figure 2c: Iso surface of the second invariant at t=562 (Π =-0.0008) (M6)

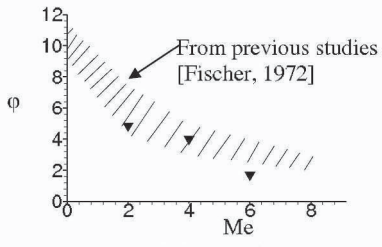

Figure 5: Lateral half-spreading angle of spot ($\varphi = \tan^{-1}(b_h/(x_h-x_o)$

Hairpin-shaped and quasi-streamwise structures are the dominant structures observed inside the spot. The assortment of these flow structures and also their mutual interactions results in a mature spot with an arrowhead shaped front overhang region and a calmed region at the rear interface. The front overhang also entrains the laminar fluid into the spot and assists in destabilising the flow. The calculated flow properties inside the spot core region are found to be similar to a fully developed turbulent flow. The estimated spot growth rate and propagation parameters are consistent with previous experimental results and the effect of compressibility is to suppress the spot growth.

Further detailed analysis of the spot growth mechanism, compressibility effects and heat transfer characteristics will help in understanding the transition physics and modelling transitional flows.

ACKNOWLEDGEMENTS

The authors would like to acknowledge the financial support of the European Space Agency (ESTEC) for this work.

REFERENCES

Narasimha, R., 1985, The laminar-turbulent transition zone in the boundary layer, *Prog. Aero. Sci.*, 22, 81-111

Perry, A.E. and Lim,T.T. and Teh, E.W., 1981, A visual study of turbulent spots, *J. Fluid. Mech.*, 72, 731-751

Fischer, M.C., 1972, Spreading of a turbulent disturbance, *AIAA J.*, 10(7), 957-959

Mee, D.J., 2002, Boundary-Layer transition measurements in hypervelocity flows in a shock tunnel, *AIAA J.*, 40(8), 1542-1548

Sandham, N D and Li, Q and Yee, H.C, 2002, Entropy splitting for higher-order numerical simulation of compressible turbulence, *J. Comp. Phys.* **178**, 307-322

Gad-El-Hak, M and Blackwelder, R F and Riley, R J, 1981, On the growth of turbulent regions in laminar boundary layers, *J. Fluid Mech.*,(110),73-95

Krishnan, L and Sandham, N D, 2004, Large eddy simulation of compressible turbulent spots, *Advances in Turbulence X, H.I.Anderson and P.A.Krogstad(Eds), CIMNE, Barcelona*, 467-471

Haidari, A H and Smith, C R, 1994, The generation and regeneration of single hairpin vortices, *J.Fluid Mech.*,(277),135-162.

Singer, B A, 1996, Characteristics of a young turbulent spot, *Phys. Fluids*,(8(2)), 509-521.

Mack, L M, 1969, Boundary layer stability theory (2 volumes), *Jet Propulsion Lab, Caltech*

ACTIVE BOUNDARY LAYER TRIPPING USING OSCILLATORY VORTICITY GENERATOR

Tal Yehoshua[1] and Avi Seifert[2]

[1]*Graduate student, School of Mechanical Engineering, Faculty of Engineering, Tel-Aviv University, Tel-Aviv 69978, ISRAEL (taly@eng.tau.ac.il)*

[2] *Senior lecturer, School of Mechanical Engineering, Faculty of Engineering, Tel-Aviv University, Tel-Aviv 69978, ISRAEL (seifert@eng.tau.ac.il)*

Abstract: The evolution of a train of vortex pairs ejected from a slot into a Blasius boundary layer was studied experimentally, with the aim of active boundary layer tripping. The excitation was directed upstream or downstream, at a shallow angle, or perpendicular to the surface. Vorticity, circulation, trajectories and convection speeds were calculated and used to describe the vortices' evolution. Intermittency, spectra and mean velocity profiles of the forced boundary layer were measured. It was found that shallow downstream directed excitation is very effective for promoting transition.

Keywords: Oscillatory vorticity generators; Flow control, Actuators, Laminar boundary layer; Transition; Turbulence

1. INTRODUCTION

Flow control research dates back to 1904, when Prandtl presented the boundary layer concept, its failure (i.e. separation) and control by suction. Much progress has been made since, in both research and applications of Active Flow Control (AFC) [1-2]. Successful application relies on efficient actuators to exercise control authority on the flow. One successful and popular actuator is the zero-mass-flux alternating suction/blowing device, known as "Synthetic jet" [3]. While the development and application of such actuators is intensively studied, fundamental understanding of the near slot evolution of the fluidic excitation in still air and with cross-flow boundary layer is lacking. One of the candidate applications of periodic excitation is the promotion of laminar-turbulent boundary layer transition. It is well known that turbulent boundary layers are more resistant to adverse pressure gradient

R. Govindarajan (ed.), Sixth IUTAM Symposium on Laminar-Turbulent Transition, 335–340.

and that convection heat transfer significantly increases in a turbulent boundary layer. Forced transition is especially important at low, sub-critical, Reynolds numbers, in which natural transition does not take place.

Therefore, the current paper describes the application of a nominally 2D Oscillatory vorticity and momentum generator for actively tripping a Blasius boundary layer. Initially, the evolution of the resulting train of vortex pairs in still air will be discussed. Next, the interaction of the vortices with the incoming boundary layer, in the immediate vicinity of the slot will be studied. Finally, the effect of the excitation on the boundary layer forced transition process will be analyzed and conclusions drawn.

2. EXPERIMENT

The experiment was conducted in a small, open-loop wind tunnel. The test section dimensions are: 50mm high, 150mm wide and 300mm long. The tunnel is capable of velocities of 4 to 18m/s with 0.2% turbulence level. Two actuators with slot exits width of 1mm wide and 135mm long were used, but for the shallow excitation directions, i.e. $\beta=30^o$ or 150^o (Fig. 1), the streamwise slot width was 2mm. However, the mean velocity profiles at x/h=75 were not affected by the presence of the slots at x/h=0. The peak velocities at the slots, were Up=5 to 35 m/s. This paper describes operation at the resonance frequencies of 1.06kHz and 1.04kHz for the $\beta=90^o$ and $\beta=30^o/150^o$ actuators, respectively. The actuators cavity pressure oscillations and temperature were continuously monitored. Hot-wire (velocity uncertainty 2%) could be traversed to any location inside the test section. PIV (2D) was applied at half-width of the test section. Image pairs (usually 100) were acquired, phase locked to the excitation signal (16 phases per cycle, PIV uncertainty 2%). For more information see [4, 5]. The PIV measured flow fields were analyzed using the Angular Momentum Method (AMM) [6], in order to track the vortices. Good correlation exists between the vortex core location, based on visual observation, and the AMM vortex identified [4-6].

3. RESULTS

When the actuator operates in still air, a vortex pair is generated at the slot during the blowing stage (Fig. 2). Figure 3 presents the vortices' trajectories for several peak slot exit velocities (Up), with wall normal excitation ($\beta=90^o$) into still air (Ue=0). For Up<10.7m/s the vortices are formed but are re-ingested into the slot (Up=9m/s, Fig. 3). For larger Up, the vortices "escape" the suction effect due to asymmetry (non-linearity) of the blowing/suction. The vortex convection speed is constant and approximately scales with Up varied between 0.20 to 0.33Up [5]. The relative direction between the slot and the wall (β) has a dominant effect on the resulting vortices. Figure 4 shows phase-locked data at identical conditions to those of Fig. 2 (Ue=0, Up=18m/s), with only β varied. The "positive" vortex is larger and stronger, while the ejected "negative" vorticity is smeared on the wall to the left.

With cross flow, the opposite flow ($\beta=150^o$) excitation will only generate the same signed vortex as the boundary layer (BL) vorticity.

PIV measurements of $\beta=90^o$ excitation-laminar boundary layer (LBL) interaction (Fig. 5) revealed that unsteady vortices are being shed and convected downstream, as long as Up (determined when Ue=0) is supercritical (Figs. 3 & 5). Furthermore, β dictates the sign of the surviving vortices (compare Figs. 5 & 6). However, for the $\beta=150^o$ (counter flow) excitation, only "negative" vortex is formed at the upstream lip of the slot and it is not shed (see Fig. 7). Nevertheless, it's unsteady nature and induced reverse near wall flow (at x/h>0) has a strong destabilizing effect on the LBL.

The fluidic periodic excitation promotes laminar-turbulent transition of the LBL, especially for $\beta=30/150°$ (Fig. 8). Downstream of the slot, turbulent structures mix between the layered smoke pattern, flowing from the right. The LBL accelerates towards the slot at its upstream side due to the suction effect of the actuator (Fig. 4).

To quantify the forced transition process, near-wall hot-wire velocity signals were acquired at x/h=30, 75 and 110. Two free-stream velocities (Ue=5.5 and 10.5m/s), a wide range of excitation amplitudes (Up/Ue) and the three β's were used to calculate intermittency. The conclusion is that $\beta=30/150°$ excitations are more effective for transition promotion than $\beta=90^o$. At Ue=5.5m/s, it requires roughly twice the Up/Ue it requires to trip the flow at Ue=10.5m/s.

The evolution of the spectra from highly coherent at the excitation frequency and its higher harmonics, to turbulent was also documented. Figures 9 present the near-wall velocity spectra for a range of Up. For sufficiently large Up/Ue the BL turned turbulent even for Ue=5.5m/s at x/h=30. The $\beta=30^o$ excitation data, indicates that for marginal amplitudes (Up/Ue=0.4, Fig. 9a) peaks appear at the excitation frequency sub-harmonics (excitation at f=1040Hz, sub-harmonics ¼f=260Hz, ½f=520Hz and ¾f=780Hz), indicating the existence of sub-harmonic sub-critical transition mechanism. While the excitation frequency and its higher harmonics still dominate the spectra, the peaks widen and the gaps between the excitation related peaks fill-up as Up increases. Two groups of spectral distributions can be clearly identified, the ones corresponding to larger Up resemble what is accepted as turbulent spectra. The $\beta=150^o$ excitation (Fig. 9b) generates a non-linear response in the BL at $Up/Ue\geq0.8$, smaller than for $\beta=30°$ which is in agreement with the intermittency data. However, there is no distinct sub-harmonic process as for the $\beta=30^o$ excitation. The magnitude of the excitation related peaks significantly attenuate as one progresses from x/h=30 to x/h=75 and the spectra is turbulent, for Up/Ue>1 and all β considered).

Figure 10a presents velocity profiles at x/h=75 using the three excitation directions. The excited profiles for $\beta=90°$ and $\beta=150^o$ resemble turbulent profiles with $H\approx1.37\pm0.02$, indicating non-equilibrium turbulent BL, a viscous sub-layer and a logarithmic region, but with somewhat different “law of the wall” constants. While the $\beta=90°$ excitation significantly increased the momentum thickness while the $\beta=30°$ excitation reduced it and the shape factor was also reduced to 1.5 (from 2.42).

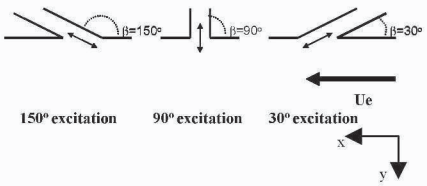

Fig. 1 : Excitation directions used in this paper. The large arrow marks the free-stream velocity (when present). Small by-directional arrows mark the excitation. x/h=0 is at half slot width on the surface (y/h=0)

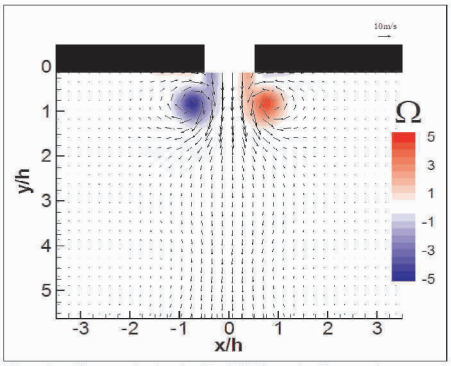

Fig. 2: Phase locked (Φ=135°) velocity vectors and normalized vorticity generated by wall normal (β=90°) excitation, f=1060Hz, Up=18m/s, still air (Ue=0). Only every second vector shown.$\Omega \equiv \omega_z Up/h$

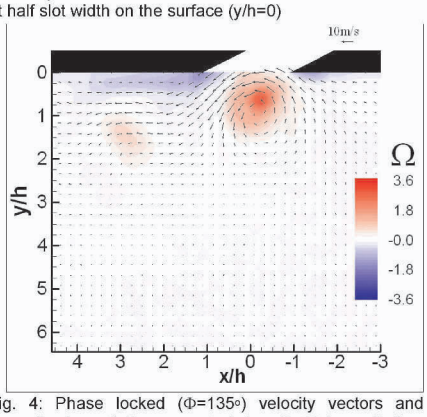

Fig. 4: Phase locked (Φ=135°) velocity vectors and normalized vorticity generated by (β=30°) excitation, f=1040Hz, Up=18m/s, Ue=0. Only every second vector shown

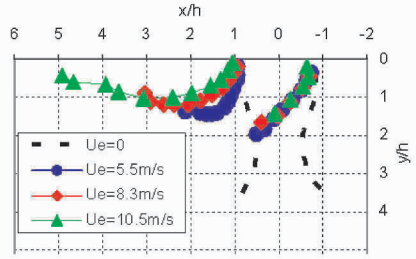

Fig. 3: The effect of the cross-flow velocity (Ue, from right, as indicated in legend) on vortex trajectories for β=90° excitation, f=1060Hz, Up=18m/s

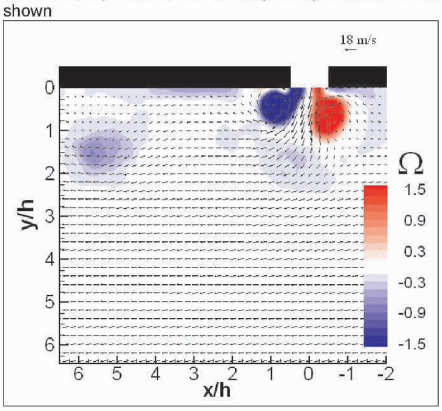

Fig. 5: Phase locked (Φ=135°) velocity vectors and normalized vorticity due to interaction of *wall normal* excitation with cross-flow, Ue=8.3m/s, f=1060Hz, Up=18m/s. Vorticity truncated to ±1.5 to enhance visibility

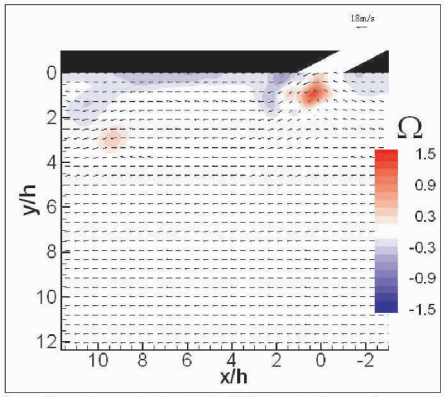

Fig. 6: Phase locked (Φ=135°) velocity vectors and normalized vorticity due to interaction of β=30° excitation with cross flow, Ue=8.3m/s, f=1040Hz, Up=18m/s. Vorticity truncated to ±1.5 to enhance visibility

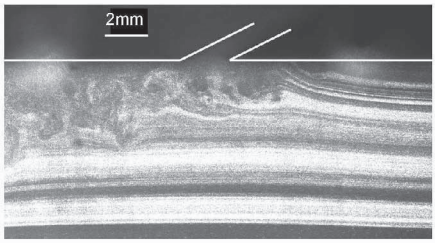

Fig. 8: Flow vitalization of transition promotion using 30° pure sine excitation. Ue=8.3m/s, Up/Ue=2.5. Flow from right to left. White lines indicate plate and slot.

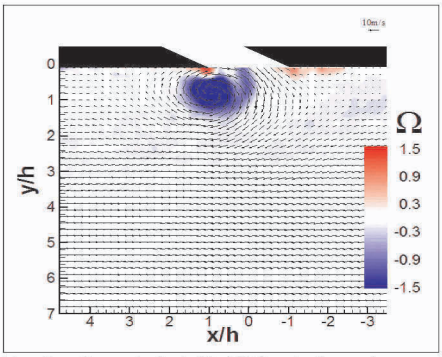

Fig. 7 : Phase locked (Φ=135°) velocity vectors and normalized vorticity due to interaction of a β=150° excitation with cross flow, Ue=8.3m/s, f=1040Hz, Up=18m/s. Vorticity truncated to ±1.5 to enhance visibility.

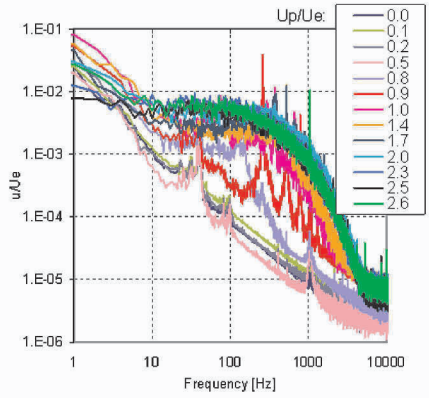

Fig. 9a Spectral content of velocity signals (y/h<1), Ue=5.5m/s at x/h=30, β=30° excitation

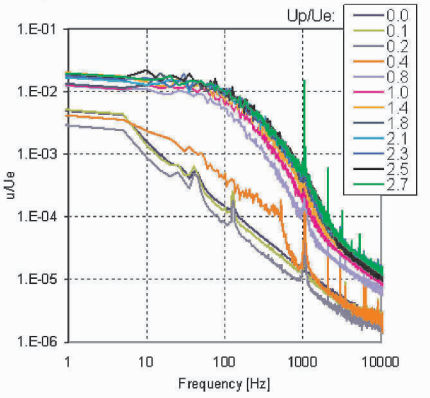

Fig. 9b Spectral content of velocity signals (y/h<1), Ue=5.5m/s at x/h=30, β=150° excitation

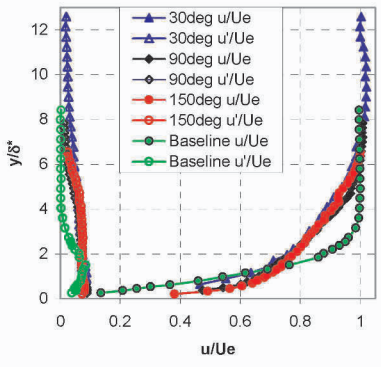

Fig. 10a : BL velocity profiles at x/h=75 compared to the Baseline BL. Pure sine excitation, f~1kHz, Up=18m/s. Up/Ue=2.16 or Up/Ue=0 (Baseline)

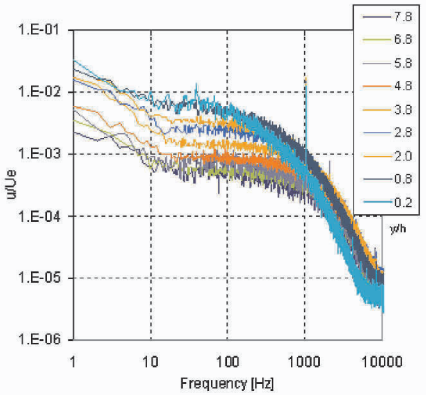

Fig. 10b: Corresponding HW spectra to Fig.11a at several y/h locations, β=30° excitation

The modified shape of the profiles can be explained according to the excitation-interaction findings as follows. The $\beta=30^o$ excitation injects momentum in the downstream direction, and "fills" the BL profile. Even at x/h=75 there is momentum access for $\beta=30^o$ and $7<y/\delta^*<11$ (Fig. 10a). The $\beta=30^o$ excitation releases two signs of vortices (Fig. 6). One vortex resides in the BL (with negative vorticity), while the "positive" vortex is ejected into the upper parts of the BL, generating a momentum deficit. The $\beta=90^o$ and the $\beta=150^o$ excitations inject the momentum in the perpendicular and upstream directions, respectively, which lifts up low momentum fluid from the wall proximity. The amplitude of the excitation dictates the circulation of each vortex and its penetration into the (LBL) and/or free stream (i.e., Figs. 3 and 5). The effect of the negligible or even negative streamwise convection velocity of the $\beta=90^o$ and 150^o excitations generated vortices is mainly to create an oscillatory blockage in the BL and destabilize it, with a marked advantage to $\beta=30^o$. over $\beta=90^o$. Figures 10b present the BL spectra measured at x/h=75 using $\beta=30^o$. The spectra for all y/h and the three types of excitations (other β not shown), resemble a well-behaved turbulent boundary layer spectra, with remnants of the high amplitude excitation frequency.

4. CONCLUSIONS

Shallow angle introduction of periodic excitation is a very effective active boundary layer tripping mechanism. It involves sub-harmonic interaction, quickly filling the spectra and leading to random, turbulent motion.

The vorticity flux from the excitation slot determines the vortex circulation and its subsequent development, while the slot inclination determines the relative magnitudes of the “positive” and “negative” vortices and their initial convection velocity. The latter is important when considering the interaction of the vortices with the vorticity of the incoming boundary layer, and also with the slot during the suction stage of the cycle.

ACKNOWLEDGEMENTS

Partial funding by the Israeli Science Foundation is acknowledged.

REFERENCES

[1] Lachmann, G.V., (Ed.), Boundary layer and flow control, V1 and V2, Pergamon Press, 1961.

[2] Gad-el-Hak, M., Flow Control: Passive, Active and Reactive Flow Management, Cambridge 2000.

[3] Smith, B. L., Glezer, A., “The formation and evolution of synthetic jets”, Phys. Fluids, 31:2281–97, 1998.

[4] Yehoshua, T. and Seifert, A. “Boundary Condition Effects on Oscillatory Momentum Generator”, AIAA Paper 2003-3710, June 2003

[5] Yehoshua, T. "Boundary conditions effects on the performance of oscillatory momentum generators", M.Sc Thesis, Apr 2004.

[6] Grosjeany, N, Graftieauxy, L, Michard, M, y, Hubner, W, C Tropeaz, Volkert, J., "Combining LDA and PIV for turbulence measurements in unsteady swirling flows", Meas. Sci. Technol. 8 (1997), pp. 1523-1532

RESONANT MODE INTERACTION IN A CANONICAL SEPARATED FLOW

Rajat Mittal and Rupesh B. Kotapati
Department of Mechanical and Aerospace Engineering, The George Washington University Washington DC 20052, USA
smittal@lltk.ac.in

Abstract: A novel configuration has been devised to study the flow physics of separated airfoil flows. The configuration allows us to prescribe the size and extent of the separation zone. A systematic variation of key separation parameters then allows us to precisely delineate the processes that govern resonant-mode interactions and transition in these flows. Numerical simulations of this configuration indicate the presence of three distinct characteristic time scales associated with the shear layer, the separation zone and the vortex shedding in the wake.

Keywords: Active separation control, resonant mode interaction, zero-net-mass-flux jets

1. INTRODUCTION

The current study is directed towards understanding the flow physics of separated flows over airfoils with the ultimate goal of developing effective zero-net-mass-flux (ZNMF) jet based active separation control (ASC) strategies. The key control parameters in a ZNMF device are the jet frequency f and jet velocity V_J . The former is usually non-dimensionalized as $F^+ = f/f_n$ where f_n is some natural frequency in the uncontrolled flow. The latter is non-dimensionalized by U_∞ . Note that V_J is some characteristic measure of the jet velocity, such as the peak or an average velocity. As expected, control authority varies monotonically with V_J/U_∞ (Seifert *et al*. 1996; Glezer & Amitay 2002; Mittal & Rampunggoon 2002) up to a point where a further increase would likely completely disrupt the boundary layer. Thus, there is little possibility of extracting an "optimal" value of this parameter. On the other hand, control authority has a highly non-monotonic variation with F^+ (Seifert & Pack 2000; Glezer et al. 2003) and this not only suggests the presence of rich flow physics and multiple flow mechanisms but also reveals the potential of optimizing the actuation scheme with respect to this parameter.

R. Govindarajan (ed.), Sixth IUTAM Symposium on Laminar-Turbulent Transition, 341–348.

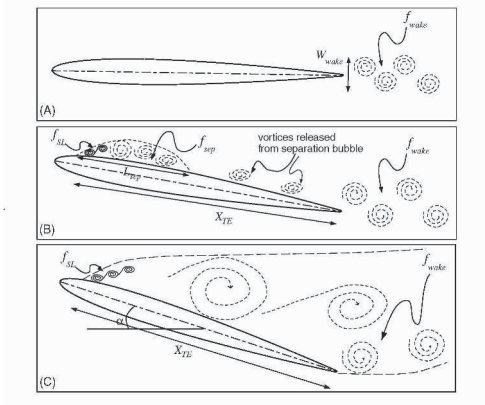

Figure 1. Three different scenarios for flow past an airfoil

Current strategies for ZNMF based separation control are explicitly or implicitly based on the proposition that the dynamics of a separated flow over an airfoil are dominated by the characteristic frequency of the separation region, f_{sep} and that $f_{sep} \sim U_\infty / L_{sep}$ where L_{sep} is the length of the separation region. However the situation is significantly more complex than this. Based on past studies (Chang 1976, Wu et al. 1998), one can consider the following three situations for flow past an airfoil (see figure 1). Case A represents attached flow at low angle-of-attack (AOA) where the boundary layer on the suction side develops under an adverse pressure gradient but does not separate. Such a flow has one dominant wake shedding frequency f_{wake} which, according to Roshko (1954) scales as U_∞ / W_{wake} . In direct contrast to Case A is the situation at high AOA, namely the post-stall Case C where separation occurs near the leading-edge and the flow does not reattach (in the mean) to the airfoil surface. This flow behaves like that past a bluff body and is consequently subject to two frequency scales, f_{SL} and f_{wake}, where the former is the natural vortex rollup frequency of the shear layer and the latter is again the frequency corresponding to vortex shedding in the wake. Finally, Case B corresponds to the situation where separation occurs at some location downstream of the leading edge, and the separated shear layer may or may not reattach before the trailing edge (Chang 1976). If the flow reattaches before the trailing edge, there are potentially three frequency-scales: f_{SL} , f_{wake}, and f_{sep}, the frequency scale corresponding to the separation "bubble." It is quite clear that the nonlinear interactions between these various flow features will drive the temporal dynamics and transition process for this flow. This also has implications for ZNMF based separation control since it clearly indicates that f_{sep} is just one of the three naturally occurring frequencies in a separated airfoil and

an effective separation control strategy should take account of these multiple frequencies and associated mechanisms.

However, our understanding of the dynamics of this resonant mode interaction is somewhat limited. Past approaches to studying these issues have mostly employed conventional airfoil geometries where the flow separation is produced by varying angle-of-attack and/or freestream velocity. Although this approach is obviously grounded in practical reality, it is not the best one for a precise investigation and delineation of the various physical mechanisms that are potentially implicated in ASC. Thus, a configuration is needed that (1) is simple and includes all the important features of a canonical separated airfoil flow, including leading edge boundary layer inception, suction side separation (open as well as closed separation), (2) has a wake which includes vortices from the suction and pressure sides; and (3) allows independent prescription of the location and extent of the separation region as well as the Reynolds number. A novel configuration that satisfies these criteria has been devised and is described below.

2. FLOW CONFIGURATION

The configuration to be studied involves a thin flat-plate (chord length c and thickness t) as shown in figure 2. Separation is induced on the upper surface of this plate by applying blowing and suction on the upper boundary of the computational domain as shown in the schematic. The technique of Na & Moin (1998) will be adopted wherein the following boundary condition is prescribed on the upper wall

$$u_y = G(x); \qquad \frac{\partial u_x}{\partial y} = \frac{dG}{dx}; \qquad u_z = 0, \tag{1}$$

where $G(x)$ is the prescribed blowing and suction velocity profile, and the boundary condition on u_x ensures that no spanwise vorticity is produced due to the blowing and suction. The key aspect of this approach is that the function $G(x)$ allows us to prescribe the streamwise L_{sep} and cross stream size H_s of the separation region as well as its location. Thus, separation can be produced anywhere on the plate surface and can therefore reproduce any of the three separated flow situations discussed in the previous section. The above configuration can be employed to examine the nonlinear interactions between the shear layer, separation region, and airfoil wake in uncontrolled and ZNMF-based controlled versions of these flows. Note that the confounding effect of curvature is absent here, something that is not usually possible with conventional airfoil investigations.

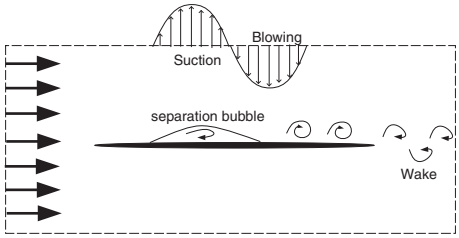

Figure 2. Schematic of canonical separated flow configuration used in current study

3. NUMERICAL METHOD

A finite-difference based approach for computing flows with moving immersed solid three-dimensional boundaries on fixed Cartesian grid has been developed. The key feature of this method is that simulations with complex boundaries can be carried out on stationary non-body conformal Cartesian grids and this eliminates the need for complicated remeshing algorithms that are usually employed with conventional Lagrangian body-conformal methods.

The governing equations are the incompressible Navier-Stokes equations which are discretized using a cell-centered, collocated (non- staggered) arrangement of the primitive variables. The equations are integrated in time using the fractional step method. In the first step, the momentum equations without the pressure gradient terms are first advanced in time. In the second step, the pressure field is computed by solving a Poisson equation. A second-order Adams-Bashforth scheme is employed for the convective terms while the diffusion terms are discretized using an implicit Crank-Nicolson scheme, which eliminates the viscous stability constraint. The solution of pressure Poisson equation (PPE) is the most time consuming part of the solution algorithm. In the current solver an efficient multigrid methodology has been developed which is well suited for use in conjunction with the immersed boundary method. A compressible version of the solver is described in Ghias *et al*. (2004).

4. RESULTS AND DISCUSSION

Two-dimensional simulations of this configuration using a 2% thick elliptic airfoil at a chord Reynolds number of 60,000 have been carried out. These serve to demonstrate the validity of the proposed approach as well as the numerical capabilities of the immersed boundary solver employed. All simulations reported here have been carried out on a single processor, 2.4 MHz, Pentium-4 workstation. Figure 3a shows the spanwise vorticity contour plot for the baseline unseparated flow and the plot shows the presence of Karman vortex shedding in the wake. Figure 3b shows the temporal variation

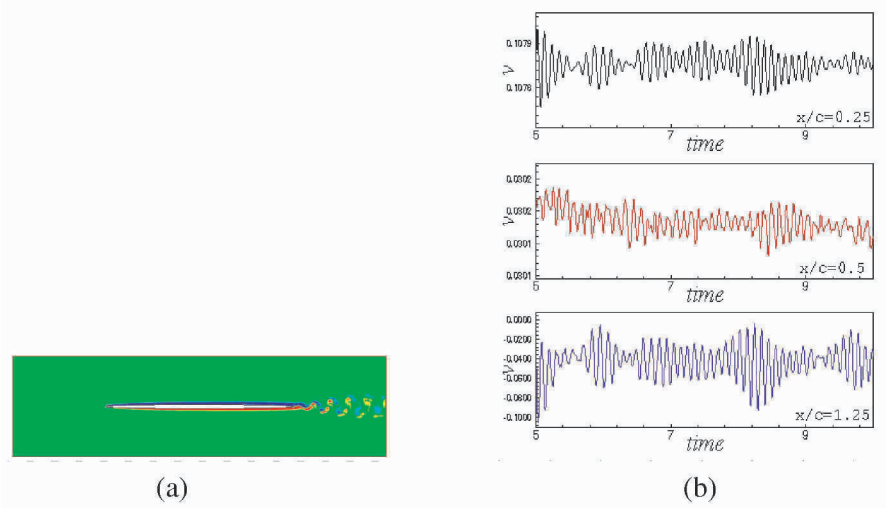

Figure 3. Spanwise vorticity contour plot and temporal variation of cross-stream velocity at three locations for baseline case with no induced separation

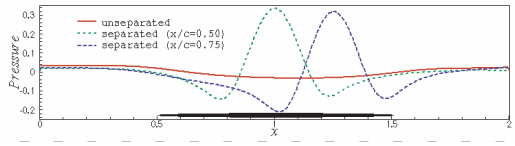

Figure 4. Variation of pressure in the streamwise direction above the top surface of the airfoil

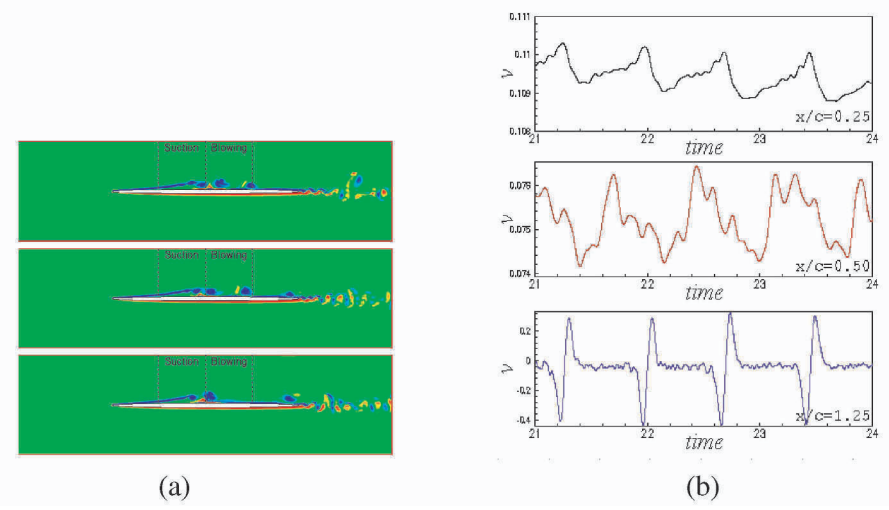

Figure 5. Sequence of spanwise vorticity contour plots and temporal variation of cross-stream velocity at three locations with separation induced at the mid-chord

of cross-stream velocity component at $x/c = 0.25$ (top), 0.5 (middle) and 1.25 (bottom) where x is measured from the leading edge, and it can be seen that even far upstream of the trailing edge, the global signature of the wake vortex shedding is present. The frequency of vortex shedding, when normalized with the momentum thickness of the wake and the freestream velocity, gives a value of roughly 0.14 which is consistent with the scaling of Roshko (1954).

This baseline case is subsequently subjected to sinusoidal blowing and suction on the top boundary to induce separation. Two different cases are simulated. The first one is of a closed mid-chord separation where the blowing and suction extends from $x/c = 0.25$ to 0.75 and the second one is a case of trailing-edge separation where the blowing and suction extends from $x/c = 0.50$ to 1.0. Figure 4 shows pressure along a horizontal line above the top surface of the airfoil with adverse pressure gradient induced by blowing-suction on top boundary at two different locations. Examination of the mean flow shows that in the first case, a recirculation bubble of length $L_{sep} \approx 0.3c$ is created whereas in the second the bubble length is $0.35c$.

Figure 5a shows a sequence of spanwise vorticity contour plots that show a flow rich in distinct vortical interactions. First, the boundary layer is seen to separate at the location where the suction become active ($x/c = 0.25$) and this separated shear layer immediately starts rolling up into small scale Kelvin-Helmholtz type vortices. Some of these vortices are seen to merge and form larger vortices and this leads to the formation of larger vortices in the separation region. At periodic intervals, one of these large vortices is released from the separation bubble and it travels downstream where it intermittently disrupts the Karman vortex shedding in the wake. Thus, this one example clearly shows all of the features that we have claimed will be present on a canonical separated flow. Examination of temporal variation of flow variable allows us to extract the three distinct frequencies. Figure 5b shows the variation of cross-stream velocity component at the separation point ($x/c = 0.25$), at the center of the separation bubble ($x/c = 0.50$) and in the wake at ($x/c = 1.25$). The first and second plots clearly show the presence of the high shear layer frequency as well as the lower separation bubble frequency which corresponds to the release of the vortex by the separation bubble. The third plot also clearly shows how the high frequency vortex shedding is disrupted periodically by the separation vortex. For this case, $f_{sep}L_{sep}/U_\infty$ is about 0.42. Furthermore, the shear layer frequency f_{SL} is about $7f_{sep}$ whereas the vortex shedding f_{wake} frequency is about $19f_{sep}$.

Figure 6a shows a sequence of spanwise vorticity contour plots for the second case and comparison with previous case illustrates the potential effect of separation bubble location on the flow. Overall the interaction between the three features of the flow (shear layer, separation bubble and wake) are qualita-

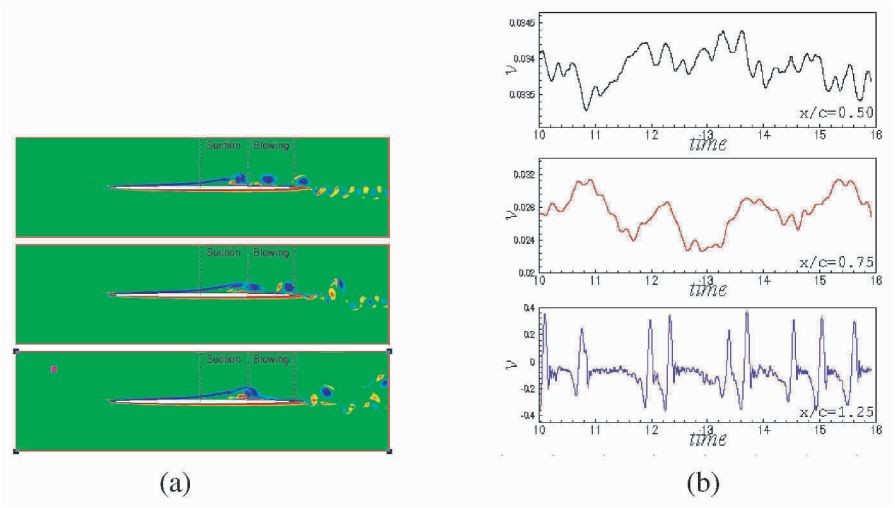

Figure 6. Sequence of spanwise vorticity contour plots and temporal variation of cross-stream velocity at three locations for with separation induced on the aft half of the airfoil

tively similar to that seen in the previous case. For this case, $f_{sep}L_{sep}/U_\infty$ is about 0.19 which is quite low and this is likely due to the effect of the wake on the separation dynamics. This underscores our earlier conjecture that $f_{sep}L_{sep}/U_\infty$ can be significantly different from unity depending on the flow configuration. The flow is clearly more chaotic than the previous case and this is likely due to the interaction between the separation region and wake instabilities. Interestingly however, shear layer frequency f_{SL} is about $6f_{sep}$ which is similar to the previous case and the vortex shedding frequency f_{wake} is about $19f_{sep}$ which matches the previous case also. Therefore, there is some indication that the shear layer and wake seem to "lock-on" to the separation region frequency which itself seems to be modified by virtue of being in the vicinity of the wake. This again provides some validation to the resonant-mode interaction that we have hypothesized is important in such flows.

ACKNOWLEDGEMENTS

This research is supported by grants from NASA and US AFOSR.

REFERENCES

Chang, P. K., *Control of Separation*, McGraw-Hill, New York, 1976.

Glezer, A. and Amitay, M., "Synthetic Jets," *Ann. Rev. Fluid Mech.*, 34:503-29, 2002.

Ghias, R., Mittal, R., and Lund, T., S., "A Non-Body Conformal Grid Method for Simulation of Compressible Flows with Complex Immersed Boundaries," *AIAA Paper 2004-0080*, 2004.

Glezer, A., Amitay, M., and Homohan A. M., "Aspects of Low- and High-Frequency Aerodynamic Flow Control," *AIAA Paper 2003-0533*, 2003.

Mittal, R. and Rampunggoon, P., "On the Virtual Aero-Shaping Effect of Synthetic Jets," *Phys. Fluids*, vol. 14, no. 4., pp. 1533-1536, 2002.

Roshko, A. "On the Development of Turbulent Wakes from Vortex Streets," *NACA Report 1191*, 1954.

Na, Y. and Moin, P., "Direct Numerical Simulation of a Separated Turbulent Boundary Layer," *J. Fluid Mech.*, vol. 370, pp. 175-201, 1998.

Seifert, A., Darabi, A. and Wygnanski, I., "Delay of Airfoil Stall by Periodic Excitation," *J. Aircraft*, vol. 33, pp. 691-698, 1996.

Seifert, A. and Pack, L. G., "Oscillatory Control of Separation at High Reynolds Numbers," *AIAA J.*, vol. 37, no. 9, pp. 1062-1071, Sep. 1999

Wu, J. -Z., Lu, X. -Y., Denny, A. G., Fan, M., and Wu, J. -M. "Post-Stall Flow Control on an Airfoil by Local Unsteady Forcing," *J. Fluid Mech.*, vol. 371, pp. 21-58, 1998.

STABILITY AND TRANSITION IN THE FLOW OF POLYMER SOLUTIONS

Paresh Chokshi and V. Kumaran
Indian Institute of Science, Bangalore 560 012

Abstract: The linear stability analysis of a plane Couette flow of viscoelastic fluid have been studied with the emphasis on two dimensional disturbances with wave number $k \sim Re^{1/2}$, where Re is Reynolds number based on maximum velocity and channel width. We employ three models to represent the dilute polymer solution: the classical Oldroyd-B model, the Oldroyd-B model with artificial diffusivity and the non-homogeneous polymer model. The result of the linear stability analysis is found to be sensitive to the polymer model used. While the plane Couette flow is found to be stable to infinitesimal disturbances for the first two models, the last one exhibits a linear instability.

1. INTRODUCTION

Dilute solutions of polymeric and complex fluids play a central role in many scientific and industrial applications. While the effect of the macromolecules on fully developed turbulent flow, giving rise to the familiar phenomenon of *turbulent drag reduction*, has been studied extensively over last few decades, the influence of polymers on the onset of transition has not been as widely investigated. In the present study, we carry out the linear stability analysis of dilute polymeric flow, represented by an Oldroyd-B model, in plane Couette flow. Following the studies of Davey and Nguyen, 1971 on Newtonian flow, the threshold energy for finite-amplitude instability in plane Couette flow is minimum for critical disturbances with wave number $k \sim Re^{1/2}$, where Re is Reynolds number based on maximum velocity and channel width. Hence, we focus on the stability of the linear velocity profile towards the perturbations with wave number, $k \sim Re^{1/2}$. A hierarchy of models is used to represent the polymer solution. The simplest is the classical Oldroyd-B model. For large wave number disturbances, the discrete eigenmodes are found to coalesce with the continuous spectrum and disappear. This is due to the hyperbolic nature of the classical Oldroyd-B model in the absence of diffusion. In order to correct this unrealistic behaviour, an additional artificial diffusivity of the polymer conformation tensor is added to the classical Oldroyd-B governing

R. Govindarajan (ed.), Sixth IUTAM Symposium on Laminar-Turbulent Transition, 349–354.

equation to obtain the diffusive Oldroyd-B model. A more realistic model is the non-homogeneous model, where variations in the polymer number-density are explicitly incorporated by writing an additional equation for the polymer number density. Bhave et al., 1991 derived one such model based on the principals of kinetic theory for an elastic dumbbell molecule. We perform a stability analysis for this non-homogeneous polymer model as well.

2. MODEL FORMULATION

2.1 Classical Oldroyd-B model

The system consists of a plane Couette flow of an incompressible viscoelastic fluid with density ρ and viscosity η occupying domain $0 < y^* < L$ in cross stream direction, with top plate moving with constant axial velocity $\overline{V}_x^* = V$ and bottom plate held stationary. The fluid continuity equation and momentum balance equation, upon non-dimensionalising velocity with V, distance with L, time with L/V, pressure with ρV^2 and stresses with $\eta V/L$, become

$$\nabla \cdot \mathbf{v} = 0 \tag{1}$$

$$\partial_t \mathbf{v} + \mathbf{v} \cdot \nabla \mathbf{v} = -\nabla p + \frac{\beta}{Re} \nabla^2 \mathbf{v} + \frac{1}{Re} \nabla \cdot \boldsymbol{\tau}^p \tag{2}$$

where $\beta = \eta_s/\eta$ indicates the solvent contribution to the solution viscosity η, where $\eta = \eta_s + \eta_p$. The polymer contribution is indicated by $(1 - \beta)$. The Reynolds number is defined, based on the solution viscosity, as $Re = \rho V L/\eta$.

The dimensionless polymeric stress, $\boldsymbol{\tau}^p$, is expressed in terms of the polymer chain conformation tensor $\mathbf{c}$ as,

$$\tau^p = (1 - \beta) \frac{(\mathbf{c} - \mathbf{I})}{We} \tag{3}$$

where the Weissenberg number, We, which is indicative of fluid elasticity, is defined as $We = \lambda V/L$, with λ being the relaxation time of the viscoelastic fluid. The governing equation for the conformation tensor is given by the single relaxation time model with upper-convected time derivative,

$$\left[\partial_t \mathbf{c} + \mathbf{v} \cdot \nabla \mathbf{c} - \mathbf{c} \cdot (\nabla \mathbf{v}) - (\nabla \mathbf{v})^T \cdot \mathbf{c}\right] = -\frac{(\mathbf{c} - \mathbf{I})}{We} \tag{4}$$

Here, $\mathbf{c}$ is non-dimensionalised with its equilibrium value which is $(k_B T/H)$, where $k_B T$ is thermal energy and H is spring constant.

2.2 Oldroyd-B model with artificial diffusivity

The hyperbolic nature of the evolution equation for the conformation tensor (eq.(4)) results in the perturbation equation with singularities leading to branch

cut in the eigen value space (Wilson et al., 1999). Sureshkumar and Beris, 1995 suggested the use of artificial diffusivity to eliminate the singularity. Here, the classical Oldroyd-B model is modified by introducing an additional diffusive term in the governing equation for the conformation tensor as,

$$\mathcal{D}_t\mathbf{c} = -\frac{(\mathbf{c}-\mathbf{I})}{We} + \frac{1}{Pe}\nabla^2\mathbf{c} \tag{5}$$

where the Peclet number is defined as $Pe = LV/D_{tr}$, with D_{tr} being the translational diffusivity of the polymer chain.

The addition of the diffusive term necessitates boundary conditions for the conformation tensor to be specified. The state of the polymer chain and the extent of its stretching at the walls remain uncertain. Different researchers have used different types of boundary conditions for the components of the conformation tensor. While Black, 2000 employed no-flux boundary condition, i.e. conformation flux $\mathbf{j}_c = \mathbf{v}\cdot\mathbf{c} - \nabla\mathbf{c} = 0$ at the walls, Sureshkumar and Beris, 1995 applied the classical Oldroyd-B governing equation (eq.(4)) at the walls. The latter boundary condition results in the following set of equations for steady-state plane shear flow:

$$\overline{c}_{xx} = 1 + 2We^2\left(\frac{d\overline{V}_x}{dy}\right)^2 \quad \overline{c}_{xy} = We\left(\frac{d\overline{V}_x}{dy}\right) \quad \overline{c}_{yy} = 1 \tag{6}$$

Bhave et al., 1991 introduce molecular orientation near the wall simply by requiring the elastic dumbbells to be parallel to the wall as a boundary condition. Thus, polymer chain is assumed to be stretched along the flow direction with its length Q_0 as an arbitrary parameter.

2.3 Non-homogeneous polymer solution model

Since polymer diffusion is a consequence of local non-homogeneity, previous models, which are based on the assumption of spatial uniformity of polymer distribution, are not reasonable. Hence, a model capturing the rheology and mass transfer phenomena in dilute polymer solution with spatially varying distribution has been derived by a number of researchers using kinetic theory approach (Bhave et al., 1991) as well as using the principles of continuum mechanics (Öttinger, 1992) and non-equilibrium thermodynamics (Mavrantzas and Beris, 1992). This model exhibits stress-concentration coupling and hence accounts for stress induced migration of polymer molecules apart from polymer diffusivity. The non-dimensional polymer constitutive relation is,

$$\tau^p = (1-\beta)\frac{(\mathbf{C}-n\mathbf{I})}{We} \tag{7}$$

where n is the polymer number-density. Here, we use number-density weighted conformation tensor $\mathbf{C} = n\mathbf{c}$. The governing equation for $\mathbf{C}$ and the conser-

vation equation for the polymer are,

$$\mathcal{D}_t \mathbf{C} = -\frac{(\mathbf{C} - n\mathbf{I})}{We} + \frac{1}{Pe}\nabla^2 \mathbf{C} \tag{8}$$

$$\frac{Dn}{Dt} = \frac{2}{Pe}\nabla^2 n - \frac{1}{Pe}\nabla\nabla : \mathbf{C} \tag{9}$$

The boundary conditions for the conformation tensor have been discussed in the previous section. The polymer concentration satisfies the typical no-flux boundary condition at the surfaces, i.e. $\mathbf{j} = -2\nabla n + \nabla \cdot \mathbf{C} = 0$.

3. STABILITY ANALYSIS

The steady-state solution of above three models with either no-flux for conformation tensor at wall i.e. $d_y \mathbf{c} = 0$ or eq.(6) as boundary conditions, is:

$$\overline{\phi} = \{\overline{V}_x, \overline{V}_y, \overline{V}_z, \overline{c}_{xx}, \overline{c}_{xy}, \overline{c}_{yy}, \overline{c}_{zz}, \overline{c}_{xz}, \overline{c}_{yz}, p\} = \{y, 0, 0, (1 + 2We^2), We, 1, 1, 0, 0, 0\} \tag{10}$$

To study the temporal stability, this steady-state profile is superimposed with 2-dimensional infinitesimal amplitude perturbation of the form:

$$\phi'(x, y, t) = \tilde{\phi}(y) e^{ik(x-ct)}$$

where k is the axial wave number and scalar quantity the c is the complex wave speed, the sign of whose imaginary part is indicative of growth or decay of the infinitesimal disturbance.

Upon linearising the resulting equation in perturbation quantities, we get a generalized eigen value equation of the form:

$$\mathcal{L}\phi = c\mathcal{M}\phi \tag{11}$$

where $\mathcal{L}$ and $\mathcal{M}$ are linear differential operators. We use Chebyshev-collocation method to discretize the operators and obtain the eigen-spectrum of the problem using QZ algorithm.

3.1. Classical Oldroyd-B model

For a plane Couette flow, Davey and Nguyen, 1971 found that perturbations with wave-length comparable to the critical layer thickness, i.e. $k \sim Re^{1/2}$ are the least stable. As seen in Figure 1(a), for Newtonian fluid, the damping rate for the least stable mode is minimum (i.e. Im(c) is maximum) for $k = 0.63Re^{1/2}$. However, for classical Oldroyd-B fluid, the least stable eigen value merges with the continuous spectrum and disappears before Im(c) approaches a maximum. The singularity in the perturbation equation is due to the existence of a stable continuous spectrum with $c = y - i/(k\beta We)$. As pointed out by Wilson et al., 1999, this continuous spectrum is a branch cut, hence eigen values appear as well as disappear as the flow parameters are changed.

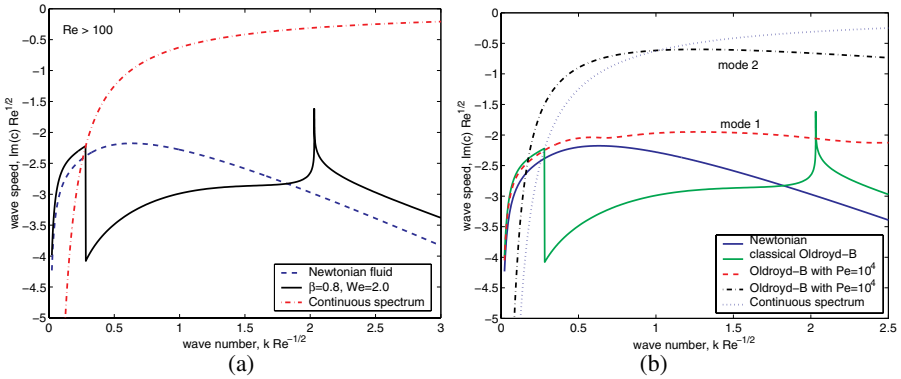

(a) (b)

Figure 1. (a) *Classical Oldroyd-B model*: Imaginary part of wave speed for a range of wave number on co-ordinates scaled with Reynolds number. The curves for $Re > 100$ collapse on the single curve in scaled co-ordinates; (b) *Oldroyd-B model with artificial diffusivity*: Imaginary part of wave speed against wave number for $Re = 2000$, $\beta = 0.8$ and $We = 2.0$

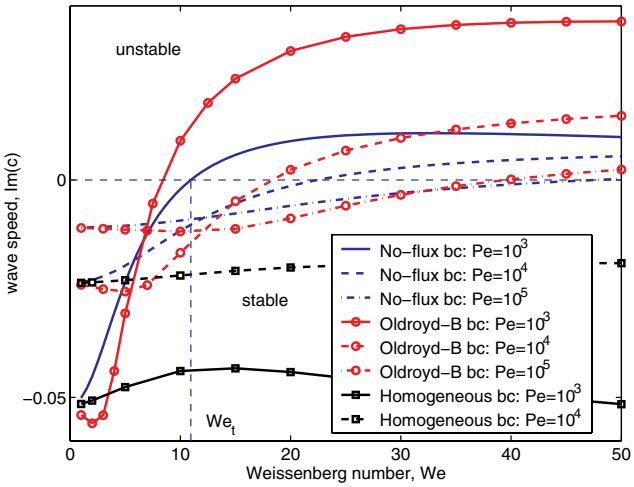

Figure 2. Effect of fluid elasticity on Im(c) for $Re = 2000, \beta = 0.95, k = 1.0$ for three different boundary conditions for the conformation tensor

3.2. Oldroyd-B model with artificial diffusivity

By adding artificial diffusivity with $Pe \sim 10^3 - 10^6$, the continuous spectrum disappears and we obtain only the discrete modes. As shown in Figure 1(b) for no-flux boundary condition for the conformation tensor, the wall mode, qualitatively similar to Newtonian wall mode (indicated as mode 1), continues for large wave number, even past the continuous spectrum for the classical Oldroyd-B model. This mode has a minimum damping rate at $k \sim 1.4Re^{1/2}$. However, there exists another mode (indicated by mode 2) which becomes dominant at large wave number. This mode seems to be qualitatively different from the Newtonian wall mode, since it does not continue to Newtonian wall mode as β approaches unity.

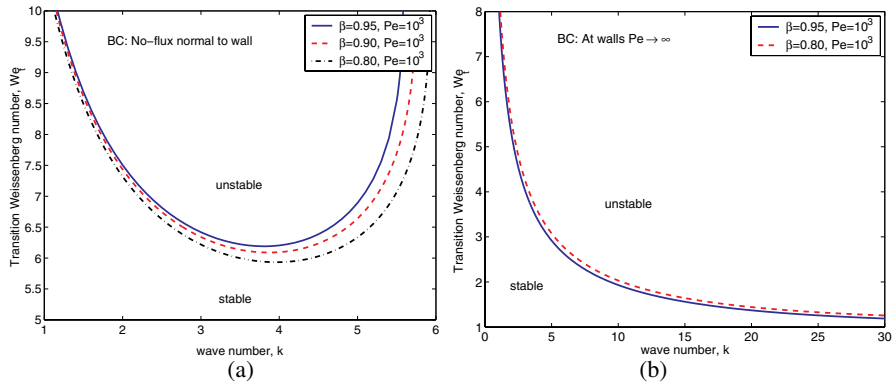

Figure 3. We_t for a range of wave number for $Re = 2000$. The minimum on this curve gives the critical point (k_c,We_c) (a) for no-flux boundary condition for conformation tensor; (b) using conformation tensor governing equation in the limit $Pe \to \infty$ at the walls

3.3. Non-homogeneous polymer solution model

The steady state solution of eqns.(2), (8) & (9) is same as that for the previous two models, that means the polymer conformation as well as the concentration are uniform. However, the base profile for polymer concentration is non-uniform for the boundary conditions suggested by Bhave et al., 1991 i.e. $\overline{C}_{xx} = n_w Q_0^2$, $\overline{C}_{xy} = \overline{C}_{xx} = 0$. For this case, we set the value of the perturbation of the conformation tensor at the wall to be zero, in order to satisfy the stipulated stretching of dumbbells for the base state at the wall. Figure 2 shows the results of the linear stability analysis in the form of the effect of fluid elasticity on Im(c) for three kinds of boundary conditions for $\tilde{\mathbf{c}}$. While there is no instability for the homogeneous boundary condition, the other two boundary conditions result in an instability for $We > We_t$. For these two boundary conditions, Figure 3 shows the neutral stability curve in We_t-k plane. The minimum on this curve gives the critical point (k_c, We_c).

REFERENCES

Bhave, A. V., Armstrong, R. C., and Brown, R. A. (1991). *Chem. Phys.*, 14:2988–3000.

Black, W. B. (2000). PhD Thesis, University of Wisconsin, Madison.

Davey, A. and Nguyen, H. P. F. (1971). *J. Fluid Mech.*, 45:701–720.

Öttinger, H. C (1992). *Rheol. Acta.*, 31:14–21.

Mavrantzas, V. G. and Beris, A. N (1992). *Phys. Rev. Lett.*, 69:273–276.

Sureshkumar, R. and Beris, A. N. (1995). *J. Non-Newtonian Fluid Mech.*, 60:53–80.

Wilson, H. J., Renardy, M., and Renardy, Y. (1999). *J. Non-Newt. Fluid Mech.*, 80:251–268.

EXPERIMENTAL STUDY OF TURBULENCE BEGINNING AND TRANSITION CONTROL IN A SUPERSONIC BOUNDARY LAYER ON SWEPT WING

N.V. Semionov [1], A.D. Kosinov [1] and V.Ya. Levchenko [1]
[1] *Institute of Theoretical and Applied Mechanics, Novosibirsk, Russia*

Abstract: The paper is devoted to an experimental study of controlled disturbances evolution in supersonic boundary layer of swept wing**.** We obtained, that the evolution of disturbances at frequencies of 10, 20, and 30 kHz are similar to the development of traveling waves for subsonic velocities. We **s**hown, that mechanism of secondary cross-flow instability play main role in laminar-turbulent transition in 3-D supersonic boundary layer. On the basis of the obtained data the technique of laminar-turbulent transition control with the help of the distributed roughness was developed. Usage of this technique, has allowed as to bring transition upstream by 30 % to delay downstream by 40 %.

Keywords: swept wing, supersonic boundary layer, stability, transition control.

1. INTRODUCTION

The attention of researchers in various countries is focused on the problem of transition to turbulence in spatial boundary layers. This interest arises from the practical applications of this phenomenon, in particular, because similar boundary layers are observed in the flow around a swept wing of an airplane. Most theoretical and experimental results on stability and transition control of a three-dimensional boundary layer are obtained for subsonic flow. However very few theoretical investigations[1-3] of supersonic 3–D boundary layer stability have been fulfilled up to date. The results on the laminar-turbulent transition in three-dimensional boundary layers for M > 1 was described in experiments[3-6]. Stationary structures

R. Govindarajan (ed.), Sixth IUTAM Symposium on Laminar-Turbulent Transition, 355–361.

were registered using different methods of flow visualization. Stability of supersonic boundary layer on swept wing was studied in experiments [7,8, 9].

As is known from experiments[3] at subsonic flow over swept wing, the distributed roughness is an effective way of control of crossflow instability. It was obtained, that changing of spanwise spacing of circular roughness elements, located in a neighborhood of a leading edge of a swept wing, considerably effects on the transition location. Saric and Reed[10] obtained the first results on transition control of supersonic boundary layer on the swept wing. They extended method of transition control in low-speed experiments[11] to the case of supersonic flow. We were aware of the successful use of distributed microroughness for transition control in a supersonic boundary layer on swept wing only with subsonic leading edge.

2. EXPERIMENTAL EQUIPMENT

The experiments were conducted at the ITAM SD RAS in the M-325 supersonic wind tunnel with test-section dimensions 0.2×0.2×0.6 m for Mach number M = 2.0. A wing model with a 40^0 sweep angle of the leading edge and a lenticular profile was used in the experiments. A generator of localized artificial disturbances[12] was used to introduce controlled oscillations in the boundary layer. A sketch of the model, data processing, source of controlled disturbances and the coordinate system are described in our experiments[8,9]. The oscillations were measured by a constant-temperature hot-wire anemometer. Single-wire tungsten probes of diameter 5 μm and length 0.8 mm was used. To measure a transition position the pneumometric or hot-wire methods were used. A transition position was measured at a fixed location of the probe, a unit Reynolds number was varied.

3 STABILITY

The experimental study of controlled disturbances evolution in boundary layer on swept wing were conducted at M=2 and $Re_1=6.6\times10^6$ m^{-1}. The measurements were conducted in x' cross sections by moving the hot-wire probe along the z' coordinate, in the layer of maximum fluctuations at y=const. The results of an experimental study of supersonic boundary layer stability on swept wing are described in detail in our experiments[8,9]. Oscillograms were obtained in two sets of experiments for x' = 20.7, 24.6, 28.4, 32.2 mm (first set) and x' =32.2, 36.1, 39.9 mm (second set). The initial amplitude of disturbances in the second set was higher approximately by 10-20 %. After the Fourier transform of periodic oscillograms in time, we obtained amplitude-phase distributions of the disturbances along z'. As for the case of a flat plate[13], the disturbances are localized in a narrow region and the wave train on a swept wing is asymmetric.

The design feature of the controlled disturbances source as a roughness on the bottom surface of a wing has resulted in formation of stationary disturbances. Existence of stationary vortices is characterized for three-dimensional boundary layer[3-6]. In distributions of $\rho U(z')$ a minimum was observed, caused by stationary crossflow disturbances. The position of the minimum of $\rho U(z')$ shifts downstream (along x) at an angle of $3.0\text{-}3.5^0$ to the x axis, which indicates the downstream

entrainment of cross-flow vortices in the boundary layer in the region of the present measurements. The experimental value of the inclination angle of stationary disturbances to the free stream is close to the calculation results[14], where at M = 2 was obtained, that the angle between a wave vector and external flow χ=87°-89° in the region of the low branch of neutral stability curve. The amplitude of the stationary disturbances is about 30% and remains practically unchanged in the first set of measurements. The stationary disturbances damp in the second set. In the last section (at x' =39,9 mm), where laminar - turbulent transition practically take place, a destruction of stationary disturbances is observed.

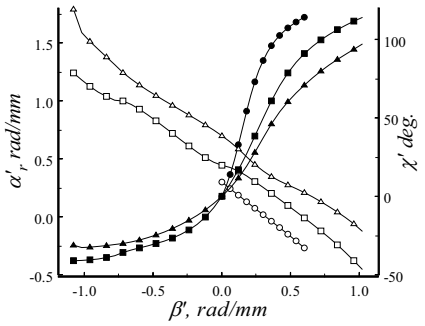

Figure 1. Dependences α'_r (β') and χ' (β') over β'; f=10 kHz, ○ - α'_r, ● - χ'; f=20 kHz, □ - α'_r, ■ - χ'; f=30 kHz, △- α'_r, ▲ - χ'

By means of a frequency-wave analysis of the array of fluctuation oscillograms relative to z' and x', we determined the wave characteristics of disturbances with f = 10, 20, and 30 kHz. Note, that the amplitude and phase distributions of disturbances along z', and the amplitude-phase spectra along β' are reminiscent of similar distributions obtained for a subsonic flow at a significant distance from the source[13]. On the basis of the phase spectra of disturbances, we can conclude that there exists a range of wavenumbers where the streamwise phase growth is almost linear for β' = const, which allows us to determine the streamwise wavenumber. For each fixed value of β', we determined first the stream-wise wavenumber α_r and then α'_r along the x' axis: $\alpha'_r = (\alpha_r/\cos 40^0 - \beta' \tan 40^0)$. The inclination angle of the wave vector χ' in the plane (x', z') was found from the formula χ'=arctan(β'/α'_r). The resultant dependences α'_r (β') and χ' (β') are plotted in fig. 1. It follows from these results that the disturbances with the highest amplitude for f = 10 kHz, like for f = 20 kHz, have an angle of inclination of the wave vector in the plane (x', z') between 60 and 120^0. The disturbances with frequency of 30 kHz did not increase in this flow region. The angle of the group-velocity vector obtained for the unstable disturbances was about 43^0 in the plane (x', z'), which coincides with the direction of downstream entrainment of the stationary disturbances with account of revolution of the coordinate system.

Another character of disturbance evolution is observed in the nonlinear stage (second set of measurements). The amplitude and phase distributions at the basic frequency remain about same, as well as at earlier stage of evolution. Though also they changes from section to section, what does not allow to determine the wave characteristics α_r' and χ'. The main differences are observed at subharmonic frequency. Figure 2 shows the amplitude-phase β'-spectra of disturbances for 10

kHz for second set of measurements. The primarily three-dimensional disturbances at the subharmonic frequency are transformed in "two-dimensional". The amplitude of disturbances at subharmonic frequency surpasses amplitude of disturbances at base frequency. The strong growth of subharmonic disturbances, on all visibility, is connected to interaction with stationary disturbances. The same processes were observed at studying of nonlinear development of controlled disturbances in supersonic boundary layer on the flat plate at large initial amplitudes[15]. In the last section (39.9 mm) happen fast destruction of traveling disturbances and stationary structure. The obtained experimental data are in qualitative correspondence with theoretical results[2].

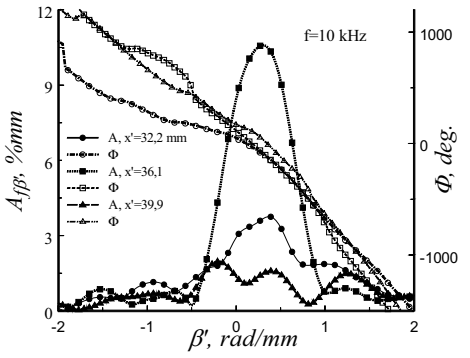

Figure 2. Amplitude-phase β'-spectra of disturbances for second set of measurements at f=10 kHz

The data on controlled disturbance development in a supersonic boundary layer on swept wing indicate a continuous relations of the traveling disturbances and stationary disturbance. The bounds of the artificial wave train and the stationary structure coincide. The angle of inclination of the wave vector for energy-carrying disturbances is directed across the flow, and the group-velocity vector is aligned with the steady cross-flow disturbance. A simultaneous destruction of the traveling and stationary disturbances takes place. Besides, an excitation of the high-frequency disturbances, which increase downstream, was found out in the natural and controlled cases. These results coincide with the calculations of the secondary instability of the crossflow disturbances [1,2]. Hence, it is possible to say, that mechanism of secondary crossflow instability play the main role in laminar-turbulent transition in 3-D supersonic boundary layer.

4 TRANSITION CONTROL

As was shown above, the transition to turbulence in a supersonic boundary layer on swept wing is caused by interaction of stationary disturbances and traveling disturbances. Thus, for laminar-turbulent transition control in this case it is easier and more effective to exert influence upon stationary structures, the character of which development in the greater degree influences on transition location. As is known from subsonic experiments[11], the distributed roughness is used for transition control in three-dimensional boundary layers. But the optimum

parameters of the distributed roughness for the most effective transition control are completely unknown. As a distributed roughness longitudinal strips, smoothed longitudinal strips and dot roughness were used. Roughnesses were rendered with the help of a special matrix and nail polish on some distance from the leading edge. The example of longitudinal roughness is presented in figure 3. It was obtained, that the dot roughness (step of 2 mm) results in earlier transition (approximately by 30 %). Therefore it was suggested to use longitudinal strips as a roughness. Width of each strip and as distance between them it was l=1, 1.5 or 2 mm in various experiments. Measurements of transition location were carried out at the fixed position of the probe at x = 85 mm. These measurements have been executed both for a case of a smooth surface of model, and for various kinds of distributed roughness. The distributions of pulsation and constant component from an output of a hot-wire anemometer were obtained depending on parallel leading edge coordinate of the wing at x = 65 mm. Simultaneously in each point of measurements the amplitude-frequency spectra of disturbances were obtained too. More detailed data on transition control with the help of the distributed roughness will be published in proceedings of ICMAR 2004 conference [16].

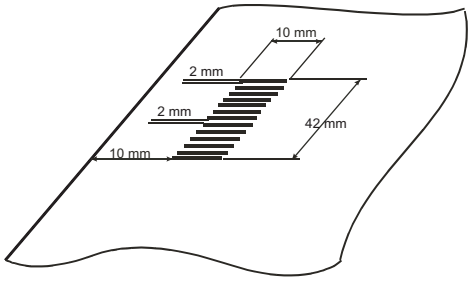

Figure 3. Example of distributed roughness

The distributions of the mass-flow rate ρU and mass flux $\langle m' \rangle$ over the spanwise coordinate z' for the case of smoothed distributed roughness with l=2 mm are presented in fig.4. The periodicity in distributions has the sharply expressed form. In this case it is possible precisely to determine a step between stationary structures in a spanwise direction. For a case of a smooth surface of model and another distributed roughnesses, periodicities in distributions ρU and $\langle m' \rangle$ also were observed in experiments[7], but they were not brightly visible. A comparison of frequency spectra obtained for distributed roughness it is visible that in the case of l=2 mm similar spectra are obtained at considerably higher values of Reynolds numbers. All these distinctions in behavior of disturbances evolution in case of smooth surface and different distributed roughnesses become understandable after the analysis of the data on the position of laminar - turbulent transition. Results of measurements of laminar-turbulent transition are plotted in figure 5. It is obtained, that in the case of distributed pointed roughness (curve 3), Reynolds number Re_{tr} on $\approx$ 30 % is less, than for the case of a smooth surface (curves 1 and 2). Using of longitudinal distributed roughness (curves 4, step 1 mm and 5, step 2 mm) lead to stabilization of the flow. Note, that the curve 5 is obtained for a roughness subjected

of additional polishing. Hence, smoothed roughness with l=2 mm has resulted to flow laminarization of 40%. Flow laminarization is reflected on disturbances evolution and on spectra. As to periodicity in distributions of the mass-flow rate ρU and mass flux $\langle m' \rangle$ over the spanwise coordinate z', for a case of the smooth surface and distributed roughness l=1 mm, measurement were conducted in the transition zone. Apparently, in this case there was a suppression of stationary disturbances. It was obtained in experiments[9] too. It is not suppression of stationary disturbances in the region of measurement in the case of l=2 mm.

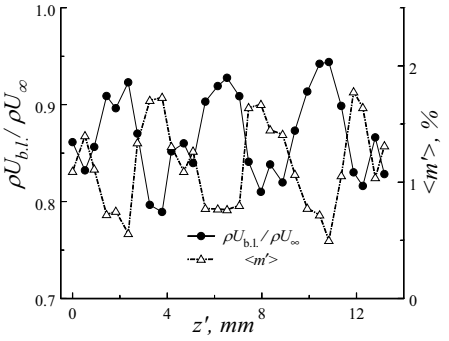

Figure 4.The distributions of ρU and $\langle m' \rangle$ over z'

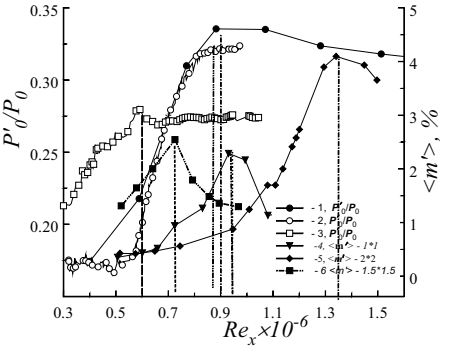

Figure 5.Measurements of laminar-turbulent transition

Thus, using the obtained data on process of turbulence beginning in a supersonic boundary layer on swept wing, the technique of transition control was designed. The form of roughnesses as longitudinal structures distributed along spanwise of the wing was designed. A choice of the form is very important question and original form, offered by us, allowed obtains of 40 % laminarization of supersonic boundary layer on swept wing with supersonic leading edge

5. CONCLUSIONS

An experimental study of disturbance development in a supersonic boundary layer on swept wing was carried out. The wave characteristics of traveling disturbances in controlled conditions were determined. It was obtained that the evolution of controlled disturbances is similar to development of travelling waves for subsonic speeds. It was shown experimentally that secondary cross-flow instability plays the main role in laminar-turbulent transition in 3-D supersonic boundary layers.

A technique of control of laminar - turbulent transition on swept wing at supersonic speeds of flow was designed. The influence of a distributed roughness on disturbances evolution and on the location of laminar - turbulent transition was studied. Usage of this technique (different forms of a distributed roughness), has allowed as to bring transition upstream by 30 % and to delay downstream by 40 %.

ACKNOWLEDGEMENTS

This work has been supported by the RFBF grant 02-01-00142 and CGPRF grant ScSch-964.2003.1.

REFERENCES

1. M.R. Malik, F. Li, C.L. Chang, in: Nonlinear instability and transition in three-dimensional boundary, edited by P.W.Duck and P.Hall (Kluwer Academic Publishers, Dodrecht etc., 1996), pp. 257-266.

2. Ch. Mielke, L. Kleiser, in: Laminar-turbulent Transition, edited by W.Saric and H.Fasel (Springer-Verlag, Berlin, 2000), pp. 397-402.

3. L.N. Cattafesta, V. Iyer, J.A. Masad, R.A. King, J.R. Dagenhart, Three-dimensional boundary-layer transition on a swept wing at Mach 3.5, *AIAA J,* **33(**11), 2032-2037 (1995).

4. T.R.Jr. Creel, I.E. Beckwith, F.J. Chen, Transition on swept leading edge at Mach 3.5, *J. Aircraft,* **24**(10), 710-717 (1987).

5. R.A. King, Three-dimensional boundary-layer transition on a cone at Mach 3.5, *J. Exp. Fluids.* **13**, 305-314 (1992).

6. D. Arnal, F. Wignall, F. Laburthe, in: Boundary layer transition and control, (Royal Aeronautical Society, London, 1991), pp.3.1-3.14.

7. Yu.G. Ermolaev, A.D. Kosinov, V.Ya. Levchenko, and N.V. Semionov, Instability of a three-dimensional supersonic boundary layer, *J. App. Mech. Tech. Phys.*, **36**(5), 50-54 (1995).

8. A.D. Kosinov, N.V. Semionov, Yu.G. Ermolaev, V.Ya. Levchenko, Experimental study of evolution of disturbances in a supersonic boundary layer on a swept wing model under controlled conditions, *J. App. Mech. and Tech. Phys.*, **41(**1), 44-49 (2000).

9. N.V. Semionov, Yu.G. Ermolaev, A.D. Kosinov, V.Ya. Levchenko, Experimental investigation of development of disturbances in a supersonic boundary layer on a swept wing, Thermophysics and Aeromechanics, **10**(3), 347-358 (2003).

10. W.S. Saric, H.L. Reed, in: West East High Speed Flow Fields Conference, edited by D.E. Zeitoun et al. (CIMNE, Barcelona, 2002), pp. 417-425.

11. W.S. Saric, R.B. Carillo, M.S. Reibert, Leading edge roughness as a transition control mechanism, *AIAA Paper 98-0781*. 1998.

12. A.D. Kosinov, A.A. Maslov, and S.G. Shevelkov, Experiments on the stability of supersonic laminar boundary layers, *J. Fluid Mech*, **219**, 621-633 (1990).

13. V.R. Gaponenko, A.V. Ivanov, Y. S. Kachanov, Experimental study of stability of the boundary layer on a swept wing to unsteady disturbances, *Thermophysics and Aeromechanics*, **2**(4), 333-359 (1995).

14. M. Asai, N. Saito, N. Itoh, Instability of compressible three-dimensional boundary layer to stationary disturbances, *Trans. Japan Soc. Aero. Space Sci*, **43**(142), 190-195 (2000).

15. A.D. Kosinov, Yu.G. Ermolaev, N.V. Semionov, Anomalous nonlinear wave phenomena in a supersonic boundary layer, *J. App. Mech. and Tech. Phys.*, **40**(5), 91-98 (1999).

16. N.V. Semionov, O.V. Barkova, A.D. Kosinov, in: Proceeding of XII International Conference on the Methods of Aerophysical Research, edited by A.M.Kharitonov (Nonparel, Novosibirsk, 2004), pt. 4, pp. 279-284.

TRANSITION INVESTIGATION ON HYPERSONIC FLAT-PLATE BOUNDARY LAYERS FLOWS WITH CHEMICAL AND THERMAL NON-EQUILIBRIUM

Christian Stemmer
Institut für Strömungsmechanik, Technische Universität Dresden, George-Bähr-Str. 3c, 01069 Dresden, Germany

Abstract: The influence of high-temperature gas-effects on hypersonic flat-plate boundary-layer flows is presented in this investigation. Chemical reactions are taken into account and the temperature dependent thermodynamic properties are modelled.

The present work investigates for the differences in the spatial disturbance development in a flat-plate boundary-layer flow at M= 20 with ideal-gas properties and for a chemical non-equilibrium case. The comparison of DNS data with linear stability results for the ideal-gas case show good agreement. The non-equilibrium results show a decrease in disturbance levels mostly for the three-dimensional disturbance waves whereas two-dimensional (second mode) disturbances are almost unchanged in their linear amplitudes.

Keywords: hypersonic flow, dissociation, chemical reactions, flat-plate boundary-layer transition, compressible linear stability theory

1. INTRODUCTION

Laminar-turbulent transition for hypersonic flows is still poorly understood in its complexity due to the difficulties in experimental and numerical investigations. After early flight tests revealing general phenomenological insights into hypersonic flows around rockets in the 50s and 60s (Schneider, 1999), the development of a compressible stability theory (Mack, 1969) opened the possibility to investigate a given boundary-layer flow for flow instabilities for ideal gases. In addition to the classical Tollmien-Schlichting modes for incompressible flows, so called Mack modes were found in the theory that contribute to the complexity of compressible transition (see also Stuckert and Reed, 1991; Malik and Anderson, 1991). A more complete overview on transition in compressible and incompressible flows can be found e.g. in Kleiser and Zhang, 1991; Kachanov, 1994. In the late 80s and early 90s, renewed interest in high

R. Govindarajan (ed.), Sixth IUTAM Symposium on Laminar-Turbulent Transition, 363–368.

speed flows spawned numerous wind tunnel tests where just one shall be mentioned here, containing many references to these experiments. Stetson and Kimmel, 1992, investigated the transition on a cone at M=8 under varying conditions. In general, wind-tunnel tests suffer the draw back that it is almost impossible to mimic free-flight conditions at hypersonic speeds in the tunnel due to the high stagnation temperature. Therefore, most measurements are so called "cold" measurement and don't satisfy the "hot" conditions in free flight.

With these obvious limitations at hand, the contribution of Direct Numerical Simulations (DNS) to the problem of understanding free-flight hypersonic boundary-layer transition is very valuable. With increasing computer capabilities and capacities, the path is open for detailed DNS investigations of "hot" hypersonic flows, where non-equilibrium and chemical reactions can play a dominant role in the transition process. Experiments for qualitative validation of the results are available in Mironov and Maslov, 2000.

2. NUMERICAL METHOD

The numerical method is based on the discrete numerical solution to the complete, unsteady three-dimensional Navier-Stokes equations. The method is based on the finite volume approach (Adams, 1998; Adams, 2000) and has extensively been validated against experiments (see also Loginov et al., 2004). The employed finite differences employed are derived on the base of Lele, 1992. A hybrid ENO-scheme treating shocks locally is implemented exhibiting shock-capturing capabilities. A 3rd order low-storage Runge-Kutta algorithm is used for the advancement in time. The inflow is prescribed, the conditions at the wall satisfy the no-slip boundary conditions (except for the disturbance strip location) and is non-catalytic. The outflow is realized with a damping zone and the upper boundary is modelled with a non-reflective boundary condition (Adams, 2000). An isothermal wall condition has been applied here.

The chemical reaction modeling is implemented according to Park, 1989. The thermodynamic properties are modeled with curve fits as described in Blottner et al., 1971 and in Candler, 1995. A steady two-dimensional base flow is calculated before the disturbances are introduced. The disturbance introduction is realized with the help of a disturbance strip that models periodic pressure disturbances at the wall (compare Eißler and Bestek, 1996 and Stemmer and Mansour, 2001).

The presented results were accomplished with a resolution of 801x17x255 points in down-stream (x), span-wise (y) and wall-normal (z) direction, respectively. The effectiveness of the numerical approach is documented in Stemmer and Adams, 2004, as obtained on a NEC SX5 vector supercomputer. The grid spacing was $\Delta x = 0.0205$ m, $\Delta y = 0.00196$ m, $\Delta z = 0.0625$ m with a time step of $\Delta t = 1.729 \cdot 10^{-7}$ s.

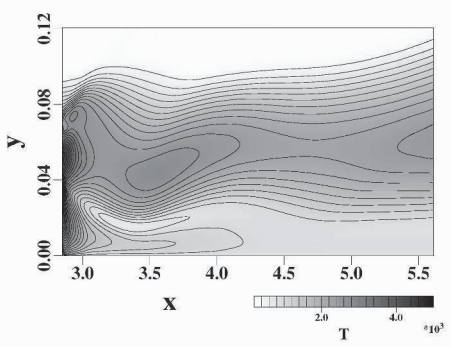

Figure 1. translational temperature distribution within the boundary layer for the reacting non-equilibrium case

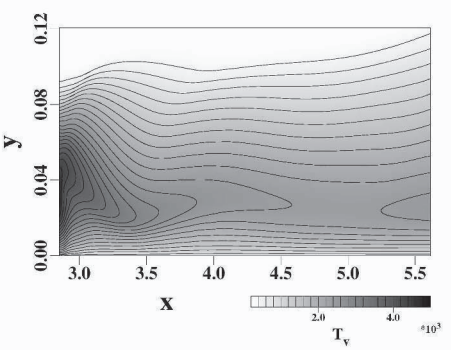

Figure 2. vibrational temperature distribution within the boundary layer for the reacting non-equilibrium case

3. RESULTS

The flight condition for the simulations was H=50km (T_∞=270.65K, p_∞=79.78 N/m^2) and M=20 (u_∞=6596 m/s). The Knudsen number yields $Kn = 0.003$ assuring the continuum assumption. The wall temperature is fixed to $T_W/T_\infty = 3$. The ideal-gas results are compared with the non-equilibrium reacting case in the following.

The influence of the chemical reactions and the non-equilibrium on the flow shall be demonstrated with the help of the temperature inside the boundary layer. For the ideal-gas case, maximum temperatures just above $T = 4800$ K are observable. For the reacting non-equilibrium case, the translational temperature reaches much lower levels of $T \approx 2300$ K further out in the boundary layer as for the ideal-gas case as shown in Fig. 1. The vibrational temperature reaches levels that are comparable to the translational temperature but at a location much closer to the wall as shown in Fig. 2.

This results in a change in species concentrations as demonstrated in Figs. 3 and 4 (note the differing scales for c_N) at the downstream position $x = 5.5$ m. For the ideal-gas case (equilibrium conditions), the minimum of the atomic nitrogen concentration c_N is at the same location as the maximum temperature. For the non-equilibrium reacting case (Fig.4), the level of c_N is highest where the maximum vibrational temperature is present. Very notable as well is the presence of the highest levels of nitric oxygen c_{NO} for the non-equilibrium case close to the same location. This corroborates the fact, that the vibrational temperature is maximum where the level of non-equilibrium is maximum.

Linear Stability theory. A comparison of DNS profiles with eigenfunctions of the linear stability theory for an isthermal-wall flat-plate boundary layer at Ma=4.8 (from Eißler, 1995) is presented in Fig. 5. A more extensive

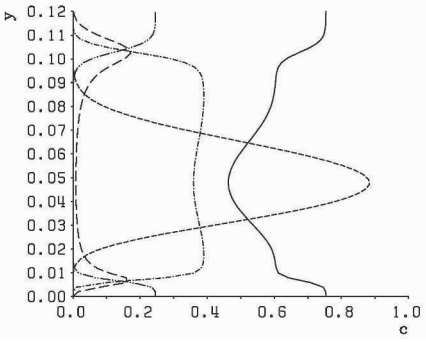

Figure 3. Species concentrations at x=5.5m for the equilibrium ideal-gas case. $c_{\mathrm{N}} \times 5$ – – – – ; c_{N_2} ——— ; c_{O} —·— ; c_{O_2} —··— ; $c_{\mathrm{NO}} \times 10$ — — —

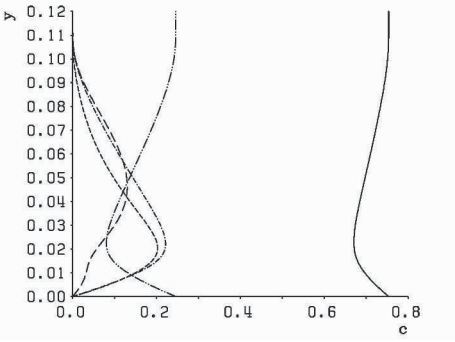

Figure 4. Species concentrations at x=5.5m for the reactive non-equilibrium case. $c_{\mathrm{N}} \times 10$ – – – – ; c_{N_2} ——— ; c_{O} —·— ; c_{O_2} —··— ; $c_{\mathrm{NO}} \times 10$ — — —

comparison of the DNS profiles with the linear stability eigenfunctions for the presented Ma=20 case can be found in Stemmer, 2002. The comparison of the DNS results with the amplification rates of the linear stability theory shows good agreement. The initial oscillations result from the way the disturbances are introduced at the wall (not just a single mode is excited – see Eißler, 1995, for a discussion thereof).

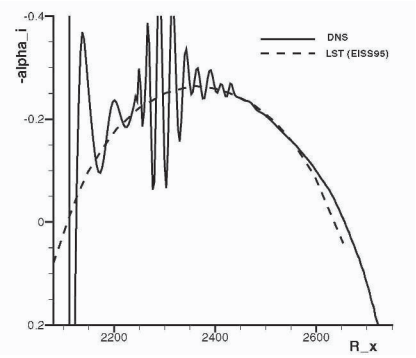

Figure 5. Amplification rates for a Ma=4.8 boundary layer (LST from Eißler, 1995 p.63)

Disturbance development. For the disturbance calculations, a two-dimensional instability wave is introduced together with a three-dimensional wave with half the respective amplitude and an obliqueness angle of $\theta = 15°$ (Fig. 6) for the ideal-gas case. The two-dimensional wave nonlinearly generates higher modes. The notation of the disturbance wave is in a pair (h, k), where h denotes the multiple of the disturbance frequency and k denotes the multiple of the basic spanwise wave number. The three-dimensional disturbance wave (1,1) with half the amplitude is just below the two-dimensional disturbance wave (1,0). The amplitudes are too small for nonlinear interactions.

A comparison of linear disturbance amplitudes for the ideal-gas (non-reacting in the figure legend) and the reacting non-equilibrium case is shown in

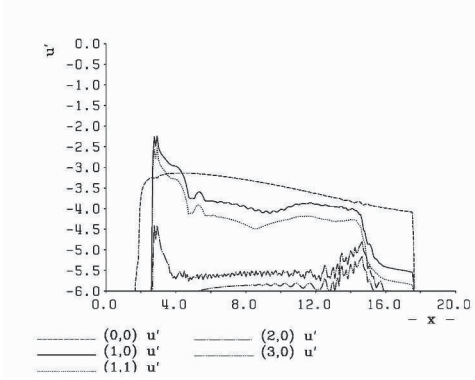

Figure 6. $u_{\max}$ for the ideal-gas case for 2D and 3D disturbances with F=3.46·10^{-5}

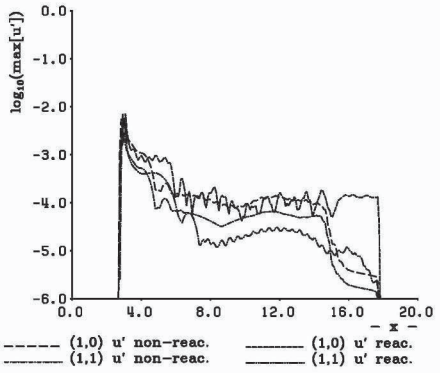

Figure 7. comparison of $u_{\max}$ for the ideal-gas/reacting case for 2D and 3D disturbances with F=3.46·10^{-5}

Fig. 7. The two-dimensional disturbance waves for the two cases are at the same level. Nevertheless, the reacting case shows a decrease in disturbance amplitude for the three-dimensional wave (1,1) by a factor of 2-3 compared to the ideal-gas case. Larger differences are not to be expected for the present disturbance amplitudes since the difference in temperature between the ideal-gas and the reacting case is roughly 2-3 K. For non-linear disturbances, a larger influence of the chemical reactions is to be expected.

4. CONCLUSIONS

The presented work shows the capability of the employed numerical procedure to tackle more difficult and extensive laminar-turbulent transition investigations in a hypersonic boundary-layer flow over a flat plate.

The numerical method is briefly outlined and the chemical and thermodynamic modeling is mentioned. A comparison with the compressible linear stability theory is conducted which shows good agreement within the limitations of the theory. First linear disturbance calculations in a three-dimensional flat-plate boundary-layer flow are presented. The comparison between the ideal-gas case and the reacting case show reduced disturbance amplitudes for the three-dimensional waves by a factor of 2-3 for the chosen flight case and the linear disturbance input. Nonlinear disturbances are expected to have a much larger (attenuating) effect on the disturbance development.

Non-linear disturbance calculations are the next step in the investigation of the role of the chemical reactions and the thermal non-equilibrium in laminar-turbulent transition. Simulations for frozen conditions will be conducted as well as simulations for cold (wind-tunnel) and hot (free-flight) conditions.

ACKNOWLEDGEMENTS

The author greatly appreciates the support by Prof. Nikolaus Adams. Special thanks go to the German Research Foundation (DFG) for the computer resources at the HLRS, Stuttgart, Germany, as well as the IAG, Stuttgart, and the CTR, Stanford, for many helpful discussions.

REFERENCES

Adams, N. A. (2000). Direct simulation of the turbulent boundary layer along a compression ramp at M=3 and Re_θ=1685. *J. Fluid Mech.*, 420:47–83.

Adams, N.A. (1998). Direct numerical simulation of turbulent compression ramp flow. *Th. Comp. Fl. Dyn.*, 12:109–129.

Blottner, F. G., Johnson, M., and Ellis, M. (1971). Chemically reacting viscous flow program for mulit-component gas mixtures. Technical Report SC-RR-70-754, Sandia Natl. Laboratories.

Candler, G. V. (1995). Chemistry of external flows. VKI LS 1995-04.

Eißler, W. (1995). *Numerische Untersuchungen zum laminar-turbulenten Strömungsumschlag in Überschallgrenzschichten*. Dissertation, Universität Stuttgart.

Eißler, W. and Bestek, H. (1996). Spatial numerical simulation of linear and weakly nonlinear instabilities in supersonic boundary layers. *Theor. Comp. Fluid Dyn.*, 8:219–235.

Kachanov, Y. (1994). Physical mechanisms of laminar-boundary-layer transition. *Ann. Rev. Fluid Mech.*, 26:411–482.

Kleiser, L. and Zhang, T.A. (1991). Numerical simulation of transition in wall-bounded shear flows. *Ann. Rev. Fluid Mech.*, 23:495–537.

Lele, S.K. (1992). Compact finite-difference schemes with spectral-like resolution. *J. Comp. Phys.*, 103:16–42.

Loginov, M.S., Adams, N.A., and Zheltovodov, A.A. (2004). Les of shock wave / turbulent boundary layer interaction. In *High Performance Computing in Science and Engineering '04*, pages 177–188. Springer Verlag, Berlin.

Mack, L.M. (1969). Boundary-layer stability theory. NASA JPL Rep. 900-277 Rev. A.

Malik, M. R. and Anderson, E. C. (1991). Real gas effects on hypersonic boundary-layer stability. *Phys. Fluids A*, 3(5):803–821.

Mironov, S.G. and Maslov, A.A. (2000). Experimental study of secondary stability in a hypersonic shock layer on a flat plate. *J. Fluid Mech.*, 412:259–277.

Park, C. (1989). A review of reaction rates in high temperature air. AIAA Paper 89-1740.

Schneider, S. P. (1999). Flight data for boundary-layer transition at hypersonic and supersonic speeds. *J. of Spacecraft and Rockets*, 36:8–20.

Stemmer, C. (2002). Flat-plate boundary-layer hypersonic transition. In *Annual Research Briefs 2002*, pages 389–396.

Stemmer, C. and Adams, N.A. (2004). Investigation of hypersonic flat-plate boundary-layer transition by direct numerical simulation. In *High Performance Computing in Science and Engineering '04*, pages 155–162. Springer Verlag, Berlin.

Stemmer, C. and Mansour, N.N. (2001). Dns of transition in hypersonic boundary-layer flows including high-temperature gas effects. In *Annual Research Briefs 2001*, pages 143–150.

Stetson, K.F. and Kimmel, R.L. (1992). On hypersonic boundary-layer stability. AIAA Paper 92-0737.

Stuckert, G. K. and Reed, H. L. (1991). Unstable branches of a hypersonic, chemically reacting boundary layer. *Proc. of the Boundary Layer Transition and Control, The Royal Aeronautical Society, Peterhouse College, Cambridge, UK*, pages 19.1–19.13.

CHARACTERISTICS OF UNSTEADY DISTURBANCES DUE TO STREAMLINE-CURVATURE INSTABILITY IN A THREE-DIMENSIONAL BOUNDARY LAYER

Shohei Takagi[1], Naoko Tokugawa[1] and Nobutake Itoh[2]
[1]Japan Aerospace Exploration Agency, Chofu, Tokyo 182-8522, Japan; [2]Teikyo University, Utsunomiya 320-8551, Japan

pantaka@chofu.jaxa.jp

Abstract: An experimental study is done to confirm the existence of a new instability due to the curvature of external streamlines in a three-dimensional boundary layer. Monochromatic-wave excitation from a tiny hole near the attachment line of a yawed circular cylinder is used to separate unsteady disturbances due to the streamline-curvature in-stability from traveling waves of the cross-flow instability. Experimen-tal results show that a point-source disturbance evolves into a wedge-shaped distribution and that amplitude and phase distributions in the spanwise direction definitely include both modes arising from the two instabilities. Observed characteristics and behavior of those disturbances are shown to be in excellent agreement with the latest results of a linear stability theory based on the complex characteristic method.

1. INTRODUCTION

Theoretical analyses by Itoh (1994, 1996a,b) show that the streamline curvature destabilizes the flow in the attachment-line region, while the wall curvature has an attenuating effect as has been already shown, and that a new instability is produced by the curvature of external streamlines and yields unsteady disturbances of longitudinal-vortex type like travel-ing waves induced by the cross-flow instability. It is also found that this new instability, labeled the streamline-curvature (referred to as S-C henceforth) instability, is really much weaker than cross-flow (C-F) instability in conventional geometric configurations. Itoh (1996a) suggests that S-C mode can be detected in dispersive development downstream of a point source, because the propagation direction of S-C disturbances is opposite to that of C-F ones. Takagi et al. (1996, 1997) gave the first experimental evidence for the existence of S-C disturbances as well as traveling C-F disturbances in

R. Govindarajan (ed.), Sixth IUTAM Symposium on Laminar-Turbulent Transition, 369–374.

an artificially excited boundary layer on a yawed circular cylinder. Their subsequent experiments (Takagi and Itoh, 1998; Takagi et al, 2000; Tokugawa et al., 2002) also showed some important features of S-C instability in the boundary layer under similar conditions and in a rotating-disk flow. But the dispersive develop-ment of both S-C and C-F disturbances is not yet fully investigated along the theoretical predictions. The present study is therefore directed to experimental observation of the separate appearance of S-C and C-F modes in the wedge-shaped disturbances originating from a point source, and detailed characteristics in spatial development of both disturbances are compared with the linear stability theory based on the method of complex characteristics by Itoh (1996a).

2. EXPERIMENTAL ARRANGEMENT

A circular cylinder model prepared for a series of stability experi-ments at the JAXA is made from a steel pipe with an external diameter of 0.5m and a length of 3.1m. This model was vertically set at a sweep angle of 50º in a test section 5.5m in width by 6.5m in height and 9m in length of the Low-speed Wind Tunnel of the JAXA. More details are shown in Takagi and Itoh (1994). A tiny hole with a diameter of 0.6mm was drilled at the azimuthal angle θ =20º from the attachment line in order to introduce an artificial acoustic disturbance into laminar boundary layer by means of a loud speaker installed underneath the hole. All the experi-ments have been conducted at a wind speed of 10m/s, which gives a Reynolds number $R_Q = 0.5\text{x}10^6$ based on the uniform velocity Q_∞ and the streamwise length L of the cylinder, and at which freestream turbulence level to the uniform velocity is approximately 0.15%.

3. EXPERIMENTAL RESULTS AND COMPARISON WITH LINEAR STABILITY THEORY

For the present experimental condition with a sweep angle 50º of the circular cylinder at a Reynolds number $R_Q = 0.5\text{x}10^6$, linear stability calculations by Itoh (1996a) give the amplitude distributions in Y of disturbances with various values of the non-dimensional frequency $\hat{\omega}=2\pi Lf/(Q_\infty R_Q^{1/2})$ developing from the single forcing location X_0=0.1 to the observation location X_1=0.3. Here, X and Y are normalized by the distance l, which is the surface length between the leading and the trailing edges. The results definitely exhibit that the new streamline-curvature mode separately

appears at the left flank of cross-flow bump in a wedge developing from a point source. In experiments, two forcing frequencies for S-C and C-F modes were chosen according to the theoretical calculations as f=45Hz corresponding to the most unstable frequency $\hat{\omega}$=-0.03 for S-C mode, and f=130Hz gives the most unstable frequency $\hat{\omega}$=0.09 for C-F mode, where the negative sign of the frequency denotes that the phase of disturbance propagates in the direction opposite to its wavenumber vector. On continuous introduction of a monochromatic disturbance with f=45Hz or f=130Hz at X_0=0.11 (θ =20º), spanwise variations of the resulting fluctuations were measured at X_1=0.31 (θ =56º) as illustrated in Fig.1, which includes two amplitude distributions (solid and dotted lines by theory) of $\hat{\omega}$=-0.03 and 0.09. Experimental results given there surely show two distinct bumps in each spanwise variation: that is, the large bump consisting of the C-F disturbances and the minor bump due to the S-C instability in the left-hand region of the wedge in consistence with the theoretical results. The peak position of the C-F bump is found to agree very well with the calculation, but that of the S-C mode looks slightly different from the theoretical prediction. This difference is related with appearance of several minor peaks on the left-hand side of the C-F bump clearly visible in Fig. 1(a), where the S-C mode is expected to grow. Figures 1(a) and 1(b) also indicate that the S-C instability is much weaker than C-F instability in the present geometric configuration. Relative peak magnitude of the S-C mode to the C-F mode shows quantitative agreement between experiment and theory, but spanwise width of the observed wedge is slightly wider than the calculation.

The separate appearance of S-C and C-F modes observed enables us to investigate their spatial characteristics using cross-correlation measurements between observed growing disturbance and speaker input signal. The phase distribution in the spanwise direction has been already overlaid in Fig.1. This result indicates that the C-F disturbance propagates in the larger Y direction and the S-C disturbance in the smaller Y direction in accordance with theoretical prediction. Similar phase measurements in the spanwise direction were carried out at a different chordwise location X=0.294 (θ=53º) to determine the exact propagation direction, phase velocity and wavelength of both S-C and C-F disturbances. Two phase distributions measured at X=0.294 and at X_1=0.31 are quite similar and indicate development of a steady wave pattern due to continuous forcing. Inclination of a wave crest of unsteady disturbances is readily determined from the displacement between X=0.294 and X_1=0.31 and the spatial shift of the spatial distribution along the

Y axis so as to overlap each other. This overlapping procedure shows that the wave crests of both S-C and C-F disturbances have an inclination of φ =26º from the chordwise direction near *X*=0.3, which is in good agreement with theoretical results φ=33º for the most unstable S-C mode and φ=23º for the most unstable C-F mode (Itoh, 1996a) as shown in Fig.2. Using these results, the exact propagation directions of S-C and C-F disturbances, which are normal to their wave crests, are also shown with the arrows in Fig.1.

In the steady pattern of wedge-shaped disturbances generated by continuous forcing, the wavelength of unsteady disturbance is determined from the relation $\lambda = \lambda_s \cos(\varphi)$, where the spanwise distance $_s$ between adjacent wave crests is obtained from each phase distribution of Fig.1. We really have the wavelengths λ_{CF} = 8.9mm for the C-F disturbance in case of 130Hz forcing and λ_{SC} =15.6mm for S-C disturbance in case of 45Hz forcing, showing good agreement with the calculations 8.6mm for C-F disturbance and 16.9mm for S-C disturbance (Itoh, 1996a).

The phase velocity *C* is obtained from the simple relation $C = f\lambda$, giving C_{CF}/Q_∞ = 0.115 for C-F disturbance with 130Hz forcing and C_{SC}/ Q_∞ = 0.07 for S-C disturbance with 45Hz forcing. These values are in good agreement with theoretical predictions 0.11 and 0.073, respectively. Figure 2 illustrates the behavior of both C-F and S-C disturbances near *X*=0.31 (θ=56º) with the wave crests of traveling disturbance denoted by a pair of two lines.

Another important difference in characteristics between C-F mode and S-C mode is the phase distribution in the normal-to-wall direction. The phase distributions (in accordance with Itoh's definition) in addition to the amplitude distributions are compared with the theoretical calcula-tions in Fig.3, where comparisons are made at *Y* =0.163 near the left edge of the S-C bump with 45Hz forcing, and at the peak location of the C-F bump with 130Hz forcing. The amplitude distributions of two modes are similar but the phase distributions show a significant difference. The phase of the C-F disturbance has a definite advance of nearly 160º as the distance increases from the wall to the boundary-layer edge, while the S-C disturbance varies only 30º in phase across the boundary layer. Good agreement between experimental results and eigen functions is shown, except for the phase distribution of the S-C disturbance near the boundary-layer edge, where disagreement may be attributed to experi-mental error due to very low amplitude of the S-C mode.

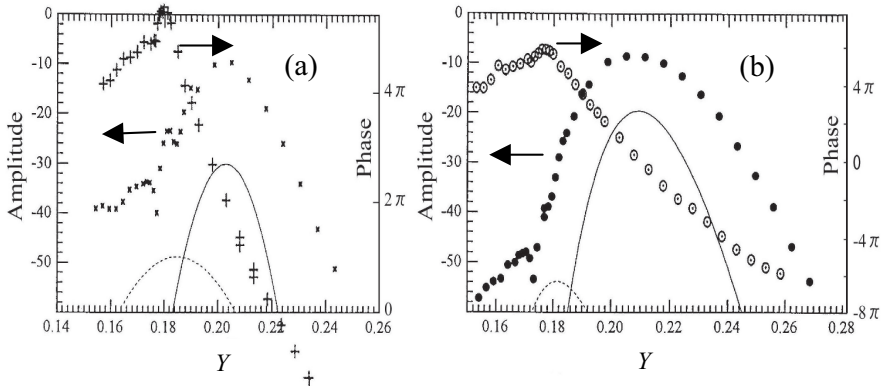

Figure 1. Observed amplitude and phase distributions in the spanwise direction at the circumference θ=56° in the wedge-shaped region developing from a point source atθ =20º together with theoretical results. (a) the case of forcing frequency 45Hz for the most unstable S-C mode, (b) the case of forcing frequency 130Hz for the most unstable C-F mode

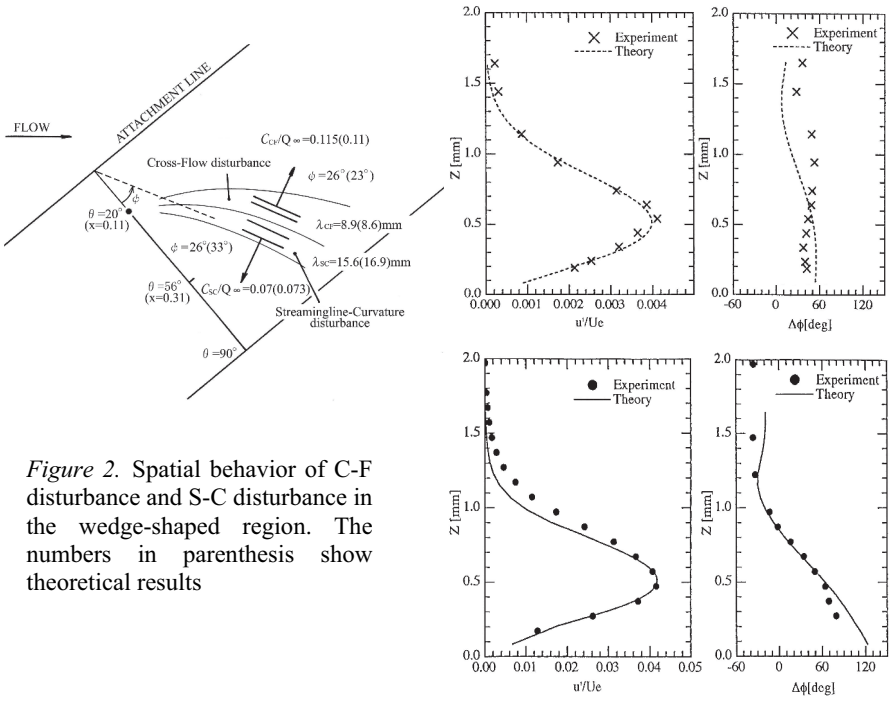

Figure 2. Spatial behavior of C-F disturbance and S-C disturbance in the wedge-shaped region. The numbers in parenthesis show theoretical results

Figure 3. Amplitude and phase distributions of observed velocity components in comparison with eigen-solutions. (a) Streamline-curvature disturbance at the peak location *Y*=0.163 in the negative-frequency region in Fig. 1(a), (b) Cross-flow disturbance at the peak location *Y*=0.21 in the positive-frequency region in Fig. 1(b)

4. CONCLUDING REMARKS

Three-dimensional boundary layers over highly curved wing surface are characterized by both the cross flow and the curvature of external stream lines. Experimental results surely showed the separate appearance of two distinct bumps in the spanwise amplitude distributions. The smaller bump consists of the negative-frequency disturbances, which are representative of the streamline-curvature instability, and the larger bump is of the positive-frequency disturbances due to cross-flow instability, though an amplitude modulation due to superimposition of two modes weakly appears between them. The phase and amplitude distributions in the normal-to-wall direction of the disturbances observed at the peaks of two bumps showed good agreement with the eigen-solutions of linear stability theory. It was also confirmed that detailed behavior of two instability disturbances, such as the inclination of wave crest, propagation direction and phase velocity as well as the frequency and the path line of the most unstable disturbance, also agrees very well with the theoretical predictions. Such quantitative agreement verified validity of the linear stability theory based on the complex characteristic method.

REFERENCES

Itoh, N. 1994 Instability of three-dimensional boundary layers due to streamline curva-ture. Fluid Dyn. Res. **14**: 353-366.

Itoh, N. 1996a Development of wedge-shaped disturbances originating from a point source in a three-dimensional boundary layer. Fluid Dyn. Res. **18**: 337-354.

Itoh, N. 1996b Instability waves developing from a point source near the attachment line on a yawed circular cylinder. Trans. Japan Soc. Aero. Space Sci., **39** (126): 428-441.

Itoh, N., 1996c Simple cases of the streamline-curvature instability in three-dimensional boundary layers. J. Fluid Mech. **317**: 129-154.

Takagi, S., and Itoh, N., 1994 Observation of traveling waves in the three-dimensional boundary layer along a yawed cylinder. Fluid Dyn. Res. **14**: 167-189.

Takagi, S., Itoh, N., and Tokugawa, N., 1996 Dispersive growth of unsteady disturbances due to cross-flow and streamline-curvature instabilities in a 3-D boundary layer. Proc. of 19th International Congress of Theore. and Appl. Mech., Kyoto, Japan, Aug. 25-31.

Takagi, S., and Itoh, N., 1998 Dispersive evolution of crossflow disturbances excited by an airjet column in a three-dimensional boundary layer. Fluid Dyn. Res. **22**: 25-42.

Takagi, S., Itoh, N., Tokugawa, N., and Nishizawa, A., 2000 Characteristic features of traveling disturbances originating from a point source in rotating-disk flow. In: Fasel, R. and Saric, W.S. (Ed.) Laminar-Turbulent Transition, Springer, Berlin: 421-428.

Tokugawa, N., Prijo Kusumo, Nishizawa, A., and Takagi, S., 2002 Decomposition of two-kinds of instability waves in three-dimensional boundary layer near yawed attachment line. Nagare Multimedia (in Japanese).
(http://www.nagare.or.jp/mm/2002/tokugawa/index_ja.htm).

Tokugawa, N., Takagi, S., and Itoh, N., 2005 Experiments on streamline-curvature in-stability in boundary layers on a yawed cylinder, AIAA J, **43**, No.6: 1153-1159.

RECEPTIVITY OF SWEPT ATTACHMENT LINE BOUNDARY LAYER TO FREE-STREAM VORTICITY

Maxim V. Ustinov
Central aerohydrodynamic Institute, Zhukovsky, Russia

Abstract: Receptivity of the attachment line boundary layer on an infinitely long cylinder, whose axis is inclined relative to the flow direction, to free-stream vortical disturbances is studied. The perturbations are maximal at the upper edge of the boundary layer and its amplitude is proportional to $\sqrt{R}$. This may be a reason for subcritical laminar-turbulent transition.

Key words: receptivity, attachment line, swept wing, vorticity, turbulence

1. INTRODUCTION

Study of the origin of disturbances and growth in the attachment line boundary layer is an important part of the investigation of swept wing laminar-turbulent transition. It is clear that turbulence originating at the attachment line renders ineffective any means of laminar flow control in the boundary layer on the entire wing. Instability waves in attachment line boundary layer were first observed experimentally by Pfeninger & Bacon[1]. The early results were revised by Poll[2,3] who found that transition in this flow occurs for 235<R<580 depending on the size of the surface roughness. First theoretical description of attachment line flow instability was based on Orr-Sommerfeld equation written for axial velocity profile[2]. It gives incorrect critical Reynolds number. This inconsistency was removed by Hall, Malik & Poll[4] who derived and solved the system of linear stability equations accounting for flow non-parallelism. By means of DNS Spalart[5] found that turbulent attachment line flow could be maintained for R>260. This is in good agreement with the lower limit of transitional Reynolds number found in experiment. All the studies mentioned above dealt with

R. Govindarajan (ed.), Sixth IUTAM Symposium on Laminar-Turbulent Transition, 375–381.

disturbances originating inside the boundary layer. However, attachment line transition may be triggered by outer flow disturbances. The present study is focused on investigation of receptivity of the attachment line boundary layer to free-stream vorticity normal to the leading edge. As was shown by Goldstein, Leib & Cowley[6] such disturbances undergo amplification via vortex lines stretching by flow around the blunt leading edge.

2. PROBLEM FORMULATION AND SOLUTION

We shall consider the flow of viscous incompressible fluid over an infinite swept cylinder. The flow configuration and general designations used are shown in Figure 1. We normalize all variables by the free-stream velocity u_∞ and the radius of the cylinder r_0.

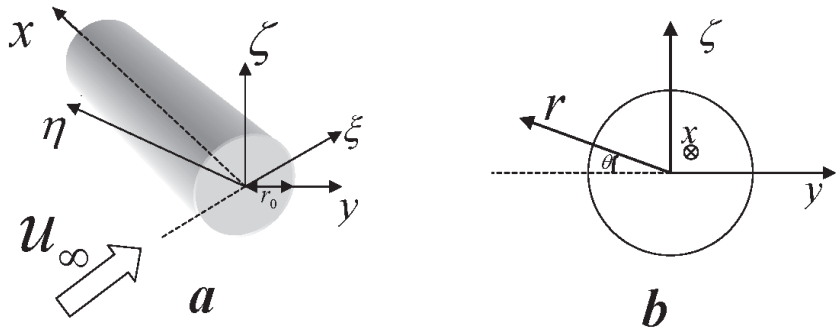

Figure 1. Flow configuration and general designations

The oncoming flow is considered to be nominally uniform except for infinitesimally small perturbations of streamwise (u_ξ) and spanwise (u_η) velocity components. The perturbations are uniform in the vertical direction (along ζ axis), periodic along ξ and η, and are convected downstream with the flow velocity. Such a flow is represented in the following form

$$u_\xi = 1 + \varepsilon e^{i(\tilde{\alpha}(\xi - t) + \tilde{\beta}\eta) - \sigma y},\ u_\eta = -\varepsilon \frac{\tilde{\alpha}}{\tilde{\beta}} e^{i(\tilde{\alpha}(\xi - t) + \tilde{\beta}\eta) - \sigma y},\ u_\zeta = 0$$

$$y = \xi \cos\chi - \eta \sin\chi,\ \ \sigma = (\tilde{\alpha}^2 + \tilde{\beta}^2)/R,\ \ R = (u_\infty r_0)/\nu$$

The perturbations are strictly periodic along the axis of the cylinder and they decay in the normal direction. Such perturbations correspond to the solution of linearized Navier-Stokes equations in uniform flow and may be

considered as a model of turbulence excited by the inclined grid. The Reynolds number $R = u_\infty r_0 / \nu$ is assumed to be large. Periods of perturbations are scaled as the attachment line boundary layer thickness, so $\tilde{\alpha}, \tilde{\beta}$ are scaled as $R^{1/2}$. The flow is evaluated in the cylindrical co-ordinates x, r, θ shown in Figure 1b. Further we shall focus on finding the solution for infinitesimally small polar angles θ. Solutions of the following form are sought.

$$\begin{aligned} &\{u_x, u_\theta, u_r\} = \{U_0(r)\cos\theta, V_0(r)\sin\theta, W_0(r)\cos\theta\} + \\ &\qquad \varepsilon\{u(r)\cos\theta, v(r)\sin\theta, w(r)\cos\theta\}e^{i\Psi} \\ &\Psi = \alpha x - \beta r(1-\cos\theta) - \omega t; \\ &\alpha = \tilde{\alpha}\sin\chi + \tilde{\beta}\cos\chi, \beta = \tilde{\alpha}\cos\chi - \tilde{\beta}\sin\chi, \quad \omega = \tilde{\alpha} \end{aligned} \tag{1}$$

Here the basic flow U_0, V_0, W_0 outside the boundary layer corresponds to the potential flow around the cylinder with imposed axial velocity and are given by generalized Hiemenz solution in it. Axial and radial wavenumbers α and β here are the projections of the wavevector of the free-stream perturbations on x and r. The radial wavenumber is complex due to the attenuation of disturbances in the radial direction. Substitution of this into Navier-Stokes equations, linearization in ε and accounting for the largest in θ terms gives the boundary value problem for the set of ordinary differential equations for the perturbations u, v, w. Matched asymptotic equations method is applied for this problem solution. For this purpose the flowfield is divided into outer inviscid region where $r \sim 1$ and the boundary layer of thickness of $O(R^{-1/2})$. Preliminary analysis of the solution in the outer region made for $1 << \tilde{\alpha}, \tilde{\beta} << R^{1/2}$ reveals that its behavior near the wall crucially depends on the scaling of the radial wavenumber β. In a general case $\beta \sim \alpha >> 1$ the perturbations remain finite as $r \to 1$. However, if $\beta = O(1)$ the pulsations of axial and vertical velocity become infinite as $r \to 1$. Hence, only this case is considered in detail. It corresponds to a wavenumber almost parallel to the cylinder axis. Further we assume that $\alpha = O(R^{1/2}), \beta = O(1)$ and introduce the following scaling for perturbations in the inviscid region

$$\alpha = R^{1/2}\alpha_+, \quad u = R^{-1/2}u_+, \quad v = v_+, \quad w = w_+, \quad p = R^{-1}p_+$$
$$u_+, v_+, w_+, p_+, \alpha_+ \sim 1$$

Substution of this into linearized Navier-Stokes equations and retainment of the largest in R^{-1} terms reduces the problem in the outer region to the initial value problem for ordinal differential equations

$$W_0 u'_+ + (\alpha_+^{\,2} - i\beta\cos\chi)u_+ = -i\beta p_+$$
$$W_0 v'_+ + \left(\frac{1}{r}(2U_0 + W_0) + \alpha_+^{\,2} - i\beta\cos\chi\right)v_+ + \left(U_0' + \frac{1}{r}U_0\right)w_+ = 0$$
$$W_0 w'_+ + (W_0' + \alpha_+^{\,2} - i\beta\cos\chi)w_+ = 0\,; \quad w_+' + i\alpha_+ u_+ + \frac{1}{r}(u_+ + w_+) = 0$$
$$u_+ \to 0,\ v_+ \to \frac{e^{-i\beta r}}{\cos\chi},\ w_+ \to -\frac{e^{-i\beta r}}{\cos\chi};\quad r \to \infty$$

Its solution is easily obtained analytically, but since it is too cumbersome, only its asymptoticl form for $r \to 1$ is presented here

$$u_+ \to -\frac{1+i\kappa}{i\alpha_+}CY^{-(i\kappa+2)},\quad v_+ \to -\frac{1}{2}CY^{-i\kappa},\quad w_+ \to -CY^{-i(\kappa+1)} \tag{2}$$
$$Y = r-1,\quad C = \frac{\alpha}{2\widetilde{\beta}}2^{i\kappa}e^{-i\alpha_+},\quad \kappa = \frac{\beta}{2}$$

In the boundary layer, solutions for perturbations of the following form are sought

$$u = AR_* U(\eta),\quad v = 2AR_*\cot\chi\, V(\eta),\quad w = AR_* W(\eta)$$
$$\eta = 2\cot\chi\, R_*(r-1),\ A = -\frac{e^{-i\alpha_+}}{\sin\chi}(4R_*\cot\chi)^{i\kappa},\ R_* = \sqrt{\frac{R}{2\cos\chi}}\sin\chi$$

Substitution of this and eq.1 into linearized Navier-Stokes equations and elimination of pressure leads to two coupled equations

$$iR_*(\alpha_* G - \omega_*)V - 2F'V + FV' - F''W = N\circ V\,;\quad N \equiv \frac{d^2}{d\eta^2} - \alpha_*^{\,2}$$
$$iR_*(\alpha_* G - \omega_*)N\circ W - \tag{3}$$
$$i\alpha_* R_* G''W + (2F'V + F''W + FN\circ W)' = N^2\circ W$$

Here F and G are functions describing generalized Hiemenz flow as

$$U_0 = G(\eta)\sin\chi\,, \quad V_0 = -2F'(\eta)\cos\chi\,, \quad W_0 = R_*^{-1}F(\eta)$$
$$F'''-FF''+F'^2=1\,, \quad G''-FG'=0; \quad F,F',G(0)=0,\ F',G(\infty)=1$$

The same equations were used by Hall, Malik & Poll[4] for stability analysis of the attachment line flow. Boundary conditions for them follow from the outer solution (eq. 2) and the no-slip conditions at the wall

$$V,W,W'(0)=0\,, \qquad V\to 0, W\to \eta^{-i(i\kappa+1)}\,; \quad \eta\to\infty$$

Equations (3) with these boundary conditions were solved numerically by the fourth order Runge-Kutta method using Godunov's orthogonalizations.

3. RESULTS AND DISCUSSION

Vertical profiles of the perturbations of the axial and vertical velocity obtained for $\alpha_* = 0.1, R_* = 300, \mathrm{Re}\,\beta = 0$ are shown in Figure 2. (Under the assumption made, the imaginary part of β is fully determined by α_* as $\mathrm{Im}\,\beta = 2\alpha_*^2$), hence β will be used to designate the real part of radial wavenumber). Solution for V are not shown because the pulsations of the chordwise velocity are negligibly small. Perturbations of the axial velocity excited by free-stream vorticity are maximal at the outer edge of the boundary layer.

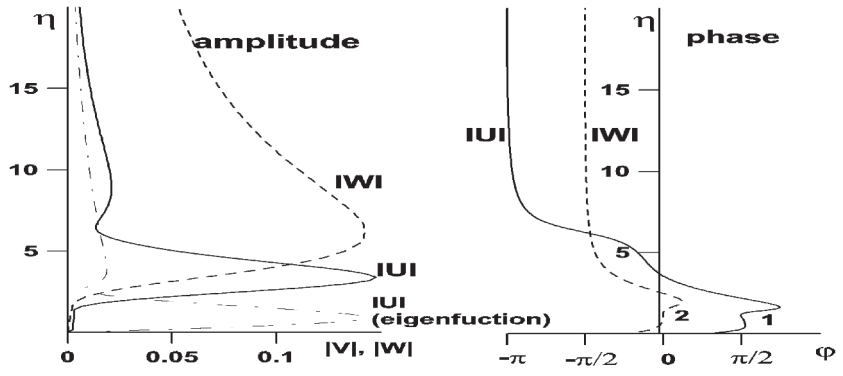

Figure 2. Profiles of amplitude and phase of perturbations in boundary layer

The profile is quite different from the eigensolution for $R_* = 300, \omega_* = 0.033$ which reaches maximum well inside the boundary layer. The difference is explained by the difference in phase velocity of the forced perturbations and the eigensolution. Forced pulsations have maximum in β for zero radial wavenumber and gradually decrease with growth of $|\beta|$. Amplification factor κ of the disturbances as a function of R_* and α_* is presented if Figure 3 a.

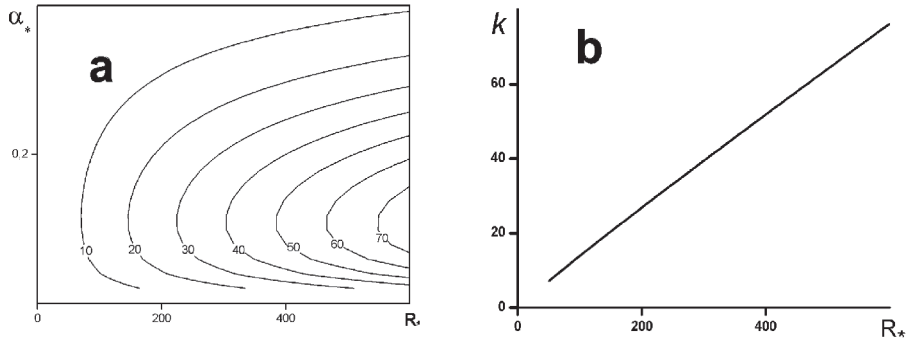

Figure 3. Amplification factor of disturbances in boundary layer

It is defined as the ratio of the maximal pulsations of the axial velocity in the boundary layer to the perturbation of the streamwise velocity in the free stream for $\xi = -1$ (see Figure 1a). Amplification is substantial $k \sim 60$ for subcritical Reynolds number and this may be a reason for subcritical transition at the attachment line. As shown in Figure 3b the amplification factor grows linearly with Reynolds number. This scaling of disturbances is similar to amplification of optimal perturbations in the boundary layer on a flat plate[7]. So, as for the flat plate, the Reynolds number of laminar-turbulent transition in the attachment line boundary layer should be inversely proportional to the free-stream turbulence level.

The research was supported by RFBR (grant # 04-01-00632 and НШ 1984.2003.1).

REFERENCES

1. Pfeninger, W., Bacon, J.W. Amplified laminar boundary layer oscillations and transition at the front attachment line of a 45^0 swept flat-nosed wing with and without suction. In *Viscose Drag Reduction* (ed. C.S. Wells), pp.85-105. Plenum Press (1969)

2. Poll D.I.A. Transition in the infinite swept attachment line boundary layer., *Aero. Q.***30**, 607-629 (1979)
3. Poll D.I.A. Some observations of the transition process on the windward face of a long yawed cylinder. *J. Fluid Mech*. **150**, 329-356 (1985)
4. Hall P., Malik M.R., Poll D.I.A. On the stability of an infinite swept attachment-line boundary layer. *Proc. R. Soc. Lond.* A **395**, 229-245 (1984)
5. Spalart P.R. Direct numerical study of leading edge contamination. *AGARD CP-438* (1988)
6. Goldstein M.E., Leib S.J., Cowley S.J. Distortion of a flat plate boundary layer by free-stream vorticity normal to the plate. *J. Fluid Mech.* **237**, 231-260 (1992)
7. Andersson P., Berggren M., Henningson D.S. Optimal disturbances and bypass transition in boundary layers. *Phys. Fluids.* **11**(1), 289-309 (1999)

OBSERVATIONS OF CROSSFLOW TRANSITION ON A SWEPT WING WITH GAW-2 AIRFOIL SECTION

V. Krishnan[1], R. Mukund[2], P. R. Viswanath[2]
[1]*Asian Institute of Medicine, Science & Technology, Malaysia;*
[2]*Experimental Aerodynamics Division, National Aerospace Laboratories, Bangalore, India*

Abstract: Low speed experiments were conducted to study features of crossflow transition on the windward surface of a wing swept at 40°. Surface pressure and wall shear stress fluctuation measurements and flow visualization by chemical sublimation conducted at different incidence angles revealed both stationary vortices and TS waves. Interesting results from the hot-film gages are discussed.

Keywords: Swept wing; cross flow instability; transition; stationary waves; traveling waves.

1. INTRODUCTION

The problem of transition in three-dimensional boundary layers by crossflow instability, especially occurring on a swept wing, has gathered considerable interest in the recent past as seen in comprehensive reviews by Bippes[1] and Saric et al[2]. The flow near the leading edge region of a swept wing is influenced by three dimensionality and surface curvature, which induce a crossflow component in the boundary layer. An inflection point exists in the crossflow profile making it inherently unstable leading to amplification of both stationary and traveling waves. The stationary waves are observed as streamwise streaks by surface flow visualization and the traveling waves are often observed as a broad band hump in the spectra. Experiments have shown that either of these waves could eventually cause transition. There have been different approaches[3-5] adopted to predict crossflow transition; different levels of success have been seen in the use of e^N methods. While significant progress has been made in the understanding of certain broad features of crossflow transition, a variety of carefully planned experiments would be still needed for gaining further insight and modeling. This paper is essentially an experimental study documenting certain broad features of cross flow transition on a swept wing with modified GAW(2) airfoil section.

R. Govindarajan (ed.), Sixth IUTAM Symposium on Laminar-Turbulent Transition, 383–388.

2. EXPERIMENTS

Experiments were conducted in the 1.5mx1.5m low speed wind tunnel at NAL, which has a freestream velocity range of 8-50m/s; the mean velocity in the test section is uniform to within 0.3% and the longitudinal turbulence intensity is within 0.10%. The wing model made of glass fiber composite (Fig.1) had a 15% thick GA(W)-2 airfoil section and a chord of 0.5m. The wing was swept at 40° and spanned across the test section side walls. The model had 28 static pressure ports on each surface at different chordwise positions on the central span of the wing. Static pressure distribution was measured using a Scanivalve coupled to a Setra differential transducer. The model also had an array of McCroskey hot-film gages (from Micro-measurements, USA) on the windward surface at different chordwise positions as illustrated in Fig.1. The two hot-films A & B of the McCroskey are perpendicular to each other and were aligned symmetric to the chord line. The gages were connected to two channels of a CTA system (DANTEC 56C01) and operated at the overheat ratio of 1.2. The HP and LP filters were set at 3Hz and 3KHz respectively at a gain of 100. Signals from the two gages were acquired simultaneously on the PC at 2kHz for 8s. The voltage fluctuations thus acquired are representative of the wall shear stress fluctuations. Chemical sublimation technique using Naphthalene was utilised to observe broad features of transition and the presence of stationary waves. Tests were carried out at the freestream velocity of 35m/s, chord Reynolds number of $1x10^6$ for model incidence angle α of 6-10° in steps of 2°.

3. RESULTS

Fig.2 shows the chordwise pressure distributions on the model for various α. It can be observed that the windward surface has a favorable pressure gradient region extending up to about 60% chord. Linear stability calculations conducted at DLR, Germany suggested that this pressure gradient in the leading edge region combined with the sweep angle provide conditions well suited for the onset and growth of cross-flow disturbances in the boundary layer.

Fig.3 shows chemical sublimation patterns on the windward surface at various α. The equally spaced streaks roughly aligned with the freestream direction are visible and indicate the presence of stationary crossflow disturbances in the boundary layer. These streaks are visible from about 10 to 55% chord. The wedge like patterns in the chemical sublimation pattern further downstream are similar to those observed in Dagenhart & Saric[6] and possibly indicate that turbulence is originating at fixed distinct points at these locations.

The voltage fluctuations of the two films of each McCroskey gage were practically similar (see Ref.7 for details) and hence results of Gage A are presented here. Fig.4, 5 and 6 show the results for α = 6, 8 and 10° respectively. The scales of the plots of either the fluctuations or their 512-point spectra (averaged for all data) are the same for all data. The flow features are broadly similar at α = 6 and 8°, namely, an initial large increase in the amplitude of the fluctuations (at x/c=30% for α = 6°, and at 55% for 8°), followed by quenching of turbulence and a clear indication of eventual completion of transition to turbulence downstream (x/c > 70%). The initial build up of fluctuations is probably due to the presence of stationary waves inferred from the sublimation patterns. It is not very evident from the results as to why the subsequent quenching occurred. Further downstream, the spectra show a broad hump (at x/c=40% for α = 6° and at x/c=50 & 65% for α = 8°) centered at about frequency of 500Hz which is representative of the Tollmien-Schlichting (TS) waves at the experimental conditions.

At α = 10° (Fig.6) on the other hand, the signals are qualitatively different from those at lower α. Compared to the spectra at x/c = 10%, the amplitudes at all stations downstream have increased by at least a decade, possibly due to stronger stationary vortices. There is evidence of a hump around 500Hz at x/c=40%and a weaker one at x/c=65%. These observations suggest that the TS waves may also have a role in the transition process to turbulence.

4. CONCLUSIONS

Broad features of the cross flow transition on the windward surface of a swept wing at low speeds are documented at different α. The chemical sublimation patterns clearly reveal the existence of streamwise streaks of stationary vortices from x/c = 10 to 55%. Analysis of hot film fluctuations suggests that, in addition to cross flow disturbances, TS waves may also have a role in the final transition to turbulence. Detailed analysis employing advanced stability calculations may be needed to get a better understanding of the observed features.

ACKNOWLEDGEMENTS

The authors thank the Aeronautical Research and Development Board, India for sponsoring this work, Dr.Eric Janke of DLR, Goettingen, Germany for conducting the initial stability calculations and Dr. Jeffrey Crouch of Boeing Aircraft Co. USA for valuable discussions and comments.

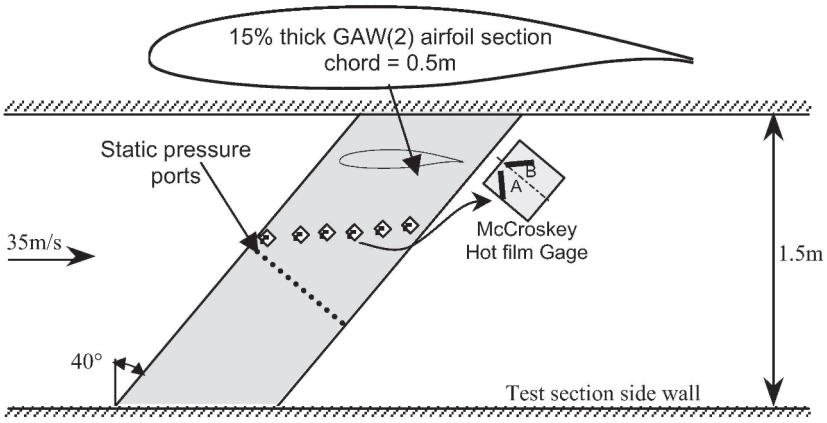

Fig.1 Schematic top view of the test section with the swept wing model

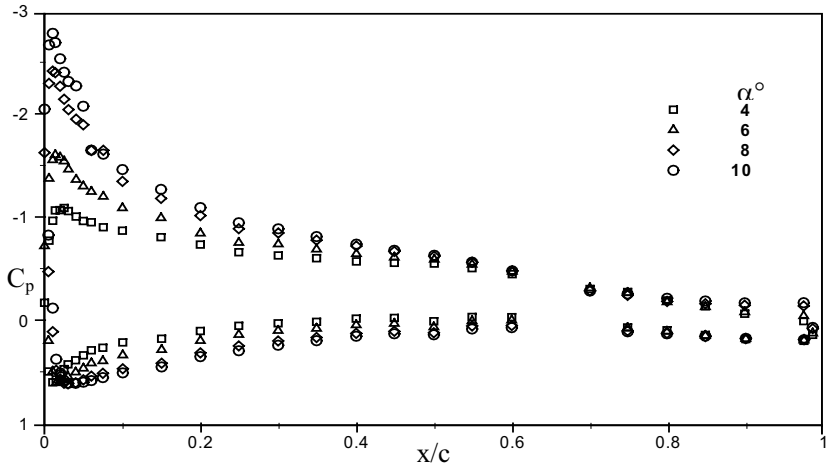

Fig.2. Surface pressure distribution on the wing at various incidence angles

REFERENCES

[1] Bippes, H., Basic experiments on transition in three-dimensional boundary layers dominated by crossflow instability. *Prog. Aerospace Sci.* **35**:363–412 (1999).

[2] Saric, W. S., Reed, H. L. & White, E. B, Stability and transition of three-dimensional boundary layers. *Ann. Rev. Fluid Mech.* **35**:413–440, (2003).

[3] Crouch, J. D., Transition prediction and control for airplane applications. *AIAA 97-1907* (1997).

[4] Stock, H. W. & Seitz, A., Crossflow induced transition prediction method using coupled Navier-Stokes and e^N method computations, *AIAA Journal* **42-9**: 1746-1754 (2004).

[5] Wassermann, P. & Kloker, M., Transition mechanisms induced by traveling crossflow vortices in a three-dimensional boundary layer, *J. Fluid Mech*., 483: 67–89, (2003)

[6] Dagenhart, J. R. & Saric, W. S., Crossow stability and transition experiments in swept-wing flow. *NASA TP 1999-209344*, (1999).

[7] Mukund, R., Krishnan, V. and Viswanath, P. R., Crossflow transition studies on a 40° swept wing with GAW-2 airfoil section, *PD EA 0412* NAL, Bangalore, India, (2004).

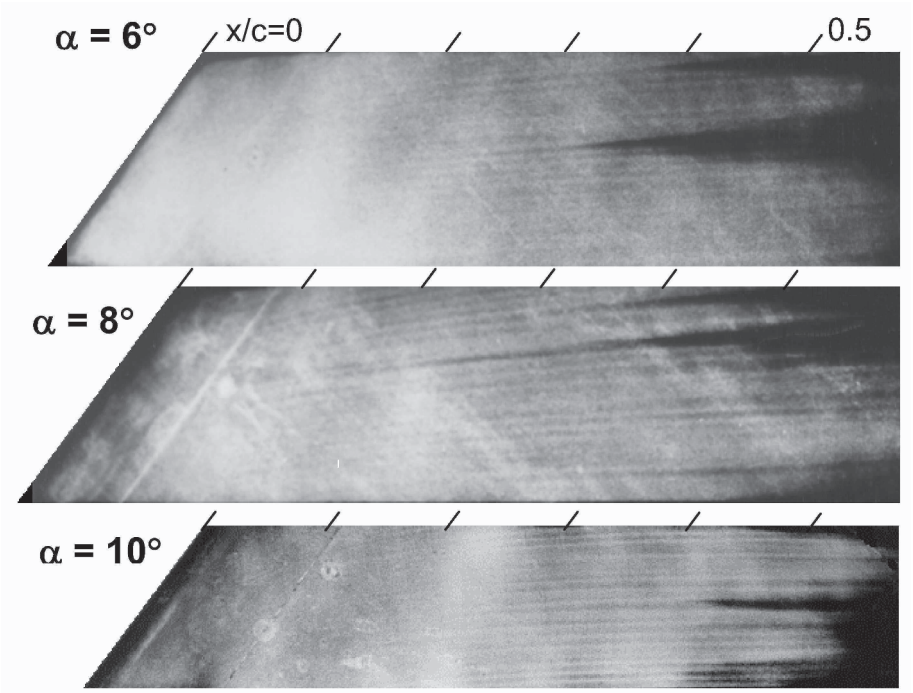

Fig.3. The chemical sublimation patterns at various α

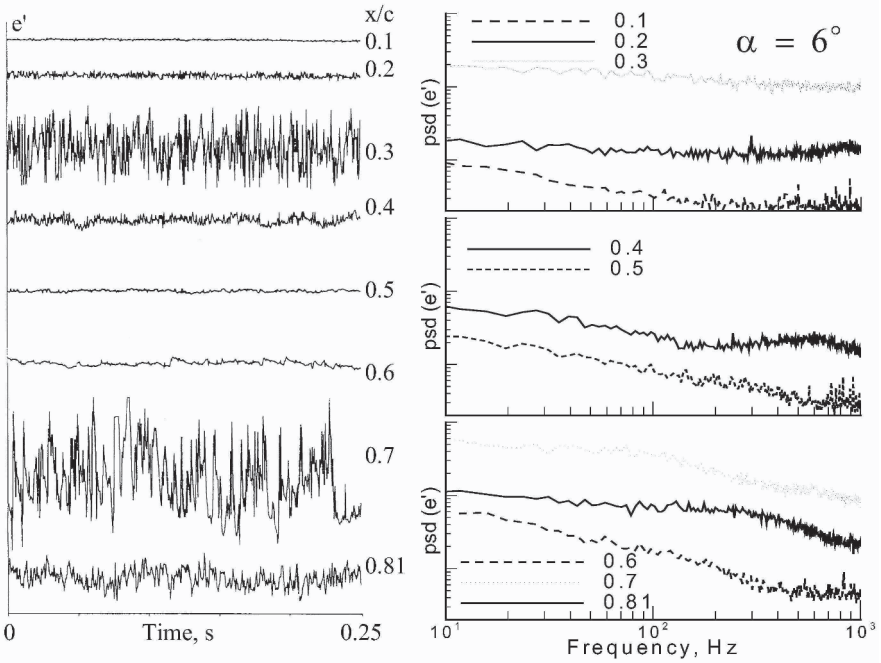

Fig.4.Time trace and respective spectra of hot film signals (e') at various x/c, α=6°

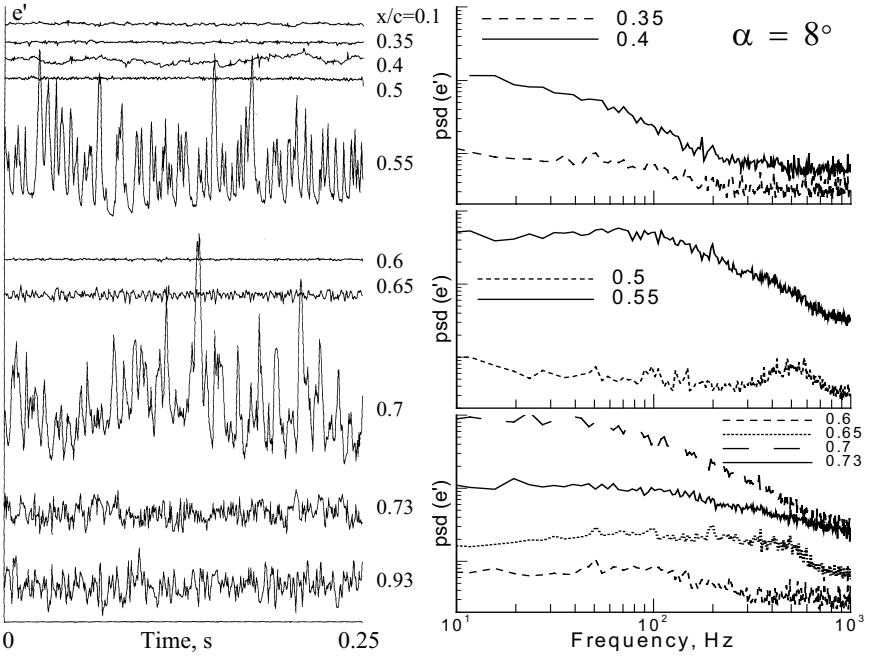

Fig.5. The time trace and respective spectra of hot film signals (e') at various x/c, α=8°

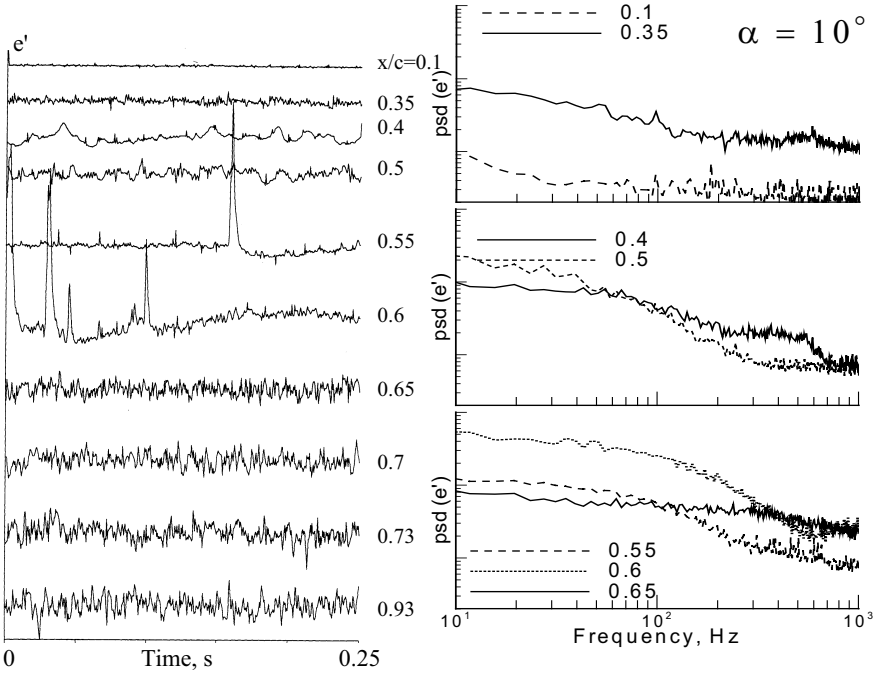

Fig.6. The time trace and respective spectra of hot film signals (e') at various x/c, α=10°

DNS OF SEPARATION-INDUCED TRANSITION INFLUENCED BY FREE-STREAM FLUCTUATIONS

Jan Wissink and Wolfgang Rodi
Institute for Hydromechanics, University of Karlsruhe
Kaiserstrasse 12, D-76128 Karlsruhe, Germany.
wissink@ifh.uni-karlsruhe.de, rodi@ifh.uni-karlsruhe.de

Abstract: Direct Numerical Simulations (DNS) of transitional boundary layer separation with and without background fluctuations have been performed. In the absence of explicitly added free-stream fluctuations, unstable Kelvin-Helmholtz (KH) modes are found to be triggered by small scale numerical truncation error. Addition of uniformly distributed free-stream fluctuations causes a stronger triggering of unstable KH modes such that the location of transition moves upstream. When replacing the uniformly distributed free-stream fluctuations by fluctuations concentrated in periodically passing wakes the location of transition is found to move alternately upstream and downstream. Compared to the uniformly distributed fluctuations, the large scale fluctuations carried by the wakes are much more effective in reducing the size of the separation bubble.

Keywords: DNS, transition, free-stream disturbances

1. INTRODUCTION

Recently, the identification of transition mechanisms in separated boundary layer flows has received much attention, see e.g. Alam and Sandham (2000), Maucher *et al.* (1997), Spalart and Strelets (2000), Wissink and Rodi (2003). The present paper aims to provide an overview of various Direct Numerical Simulations (DNS) of Transitional Separation Bubbles (TSB) performed in Karlsruhe. These three-dimensional (3D) simulations were carried out as part of the German Research Foundation (DFG) Project "Periodic Unsteady Flow in Turbomachinery". The computational domain, illustrated in Figure 1, was chosen in accordance with experiments performed in a companion project at the Technical University of Berlin. Separation and subsequent transition and reattachment of the boundary layer on the lower flat plate wer studied for three free-stream scenarios detailed below. The Reynolds number of the flow problem, based on the mean inflow velocity U_0 and the length of the flat plate

R. Govindarajan (ed.), Sixth IUTAM Symposium on Laminar-Turbulent Transition, 389–394.

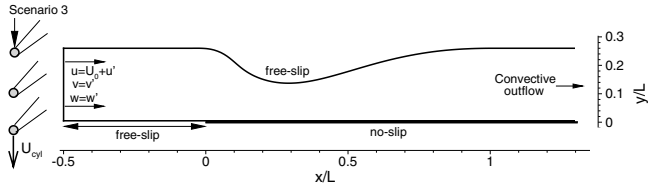

Figure 1. Geometry of the computational domain

L (see Figure 1), is $Re = 60\,000$. Moving in the downstream direction, in the absence of free-stream disturbances the special shape of the upper wall causes the streamwise pressure gradient to change from favourable to adverse at $x/L = 0.3$. As a consequence a separation bubble appears along the lower flat plate boundary downstream of $x/L = 0.3$. To save computational points, along the upper wall a free-slip boundary condition is applied. In the spanwise direction the flow is assumed to be statistically homogeneous and periodic boundary conditions are prescribed. At the outlet a convective outflow condition is applied. The numerical method employed is detailed in Wissink and Rodi (2003). The following three free-stream scenarios are examined which are governed by different inflow conditions:

1 In the reference run, a steady inflow $(U_0, 0, 0)$ is prescribed at the inlet. Along the lower side, for $x/L \geq 0$, a no-slip boundary condition is used while for $x < 0$ a free-slip boundary condition is used. The triggering of instabilities is left to depend on numerical round-off errors.

2 At the inlet, uniformly distributed free-stream fluctuations (u', v', w') with turbulence level $Tu = 7\%$ are superposed on the mean inflow velocity $(U_0, 0, 0)$. The fluctuations stem from a separate LES of isotropic turbulence in a $l \times l \times l$ box, with $l = 0.08L$, and resemble grid-turbulence. By identifying the x-direction of the box with time, a periodic signal consisting of the fundamental frequency $f_0 = U_0/l = 12.5U_0/L$ and its higher harmonics is obtained. The boundary conditions along the lower side are identical to the ones described above.

3 The fluctuations (u', v', w') at the inlet are concentrated in periodically passing wakes which are generated by an imaginary row of bars moving in the negative y-direction with velocity $U_{cyl} = 0.7U_0$. The wakes stem from a separate LES performed by Wu and Durbin (2001) and are superposed on a Blasius velocity-profile with free-stream velocity U_0. At the inlet, the mean wake deficit is 25% and the wake's half-width is $0.05L$. The period, T, between two passing wakes is varied to study its affect on the TSB. In this simulation the entire lower boundary is a wall. Note that for this case the boundary conditions at the inlet and at the lower boundary differ from what is shown in Figure 1.

An overview of the simulations reported in the results section is shown in Table 1. Phase-averaging was performed during 10 periods in Simulation 3.1 and 45 periods in Simulation 3.2. In the phase-averaging procedure each period was subdivided into 256 equal phases at which statistics were gathered.

Table 1. Overview of simulations numbered according to inflow scenarios detailed above

Simulation	Tu $(\%)$	Oncoming Wakes	T $(\times L/U_0)$	Mesh
1	0	no	-	$1038 \times 226 \times 128$
2	7	no	-	$1926 \times 226 \times 128$
3.1	-	yes	0.6	$966 \times 226 \times 128$
3.2	-	yes	0.3	$1286 \times 310 \times 128$

2. RESULTS

Figures 2a,b show snapshots of a spanwise vorticity iso-surface of (a) Simulation 1 and (b) Simulation 2. In the absence of explicitly added disturbances (see Figure 2a), the presence of small numerical round-off errors is found to be sufficient to trigger a KH instability. The KH instability is characterised by a

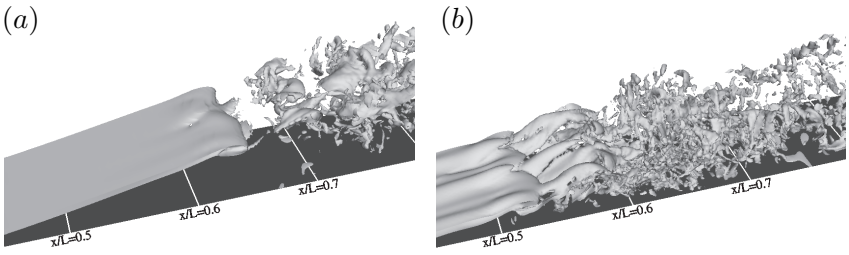

Figure 2. Snapshots of the spanwise vorticity iso-surface $\omega_z = -150$ identifying the separated boundary layer. (a): Simulation 1, (b): Simulation 2 (see Table 1)

quasi-periodic shedding of vortices from the separated shear-layer. To further identify some of the physical mechanisms, the mean shedding period was subdivided into 80 equal phases for which phase-averaged statistics are gathered. From these statistics it can be concluded that the bulk of the phase-averaged fluctuating kinetic energy is generated inside the rolled-up shear layer. Comparing Figures 2a,b shows that the addition of free-stream fluctuations (here $Tu = 7\%$) leads to earlier transition and a drastic reduction in the size of the separation bubble. As in Figure 2a, a quasi-periodic shedding of vortices is observed in Figure 2b too. The frequency spectra of the spanwise averaged v-velocity, shown in Figure 3, illustrate that the most unstable KH mode in

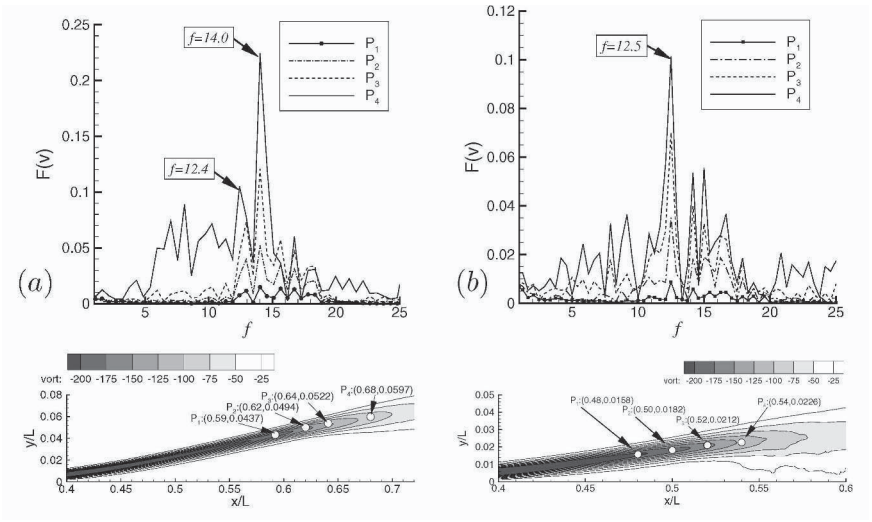

Figure 3. Upper graphs: frequency spectra of the spanwise averaged v-velocity signals at $P_1, \cdots, P_4$, Lower graphs: countours of the time-averaged spanwise vorticity showing location of $P_1, \cdots, P_4$. (a): Simulation 1, (b): Simulation 2 (see Table 1)

Simulation 1 has a frequency of $f = 14.0$, while in Simulation 2 it has a frequency of $f = 12.5$. This difference is explained by the fact that $f = 14.0$ is not present in the inflow fluctuations of Simulation 2. Instead, $f = 12.5$, which is almost identical to the frequency of the second most unstable mode of Simulation 1 ($f = 12.4$) and corresponds to the basis frequency f_0 of these inflow fluctuations (see introduction), is found to become the most unstable mode in Simulation 2.

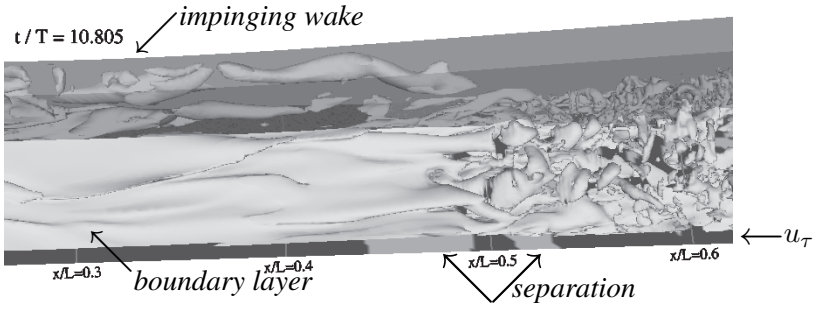

Figure 4. Simulation 3.2: snapshot of the iso-surface $\omega_z = -150$ which identifies the boundary layer (front). The translucent box at the back shows vortical structures of an impinging wake. The light contours at the bottom identify separation

Figure 4 shows a snapshot of a spanwise vorticity iso-surface of Simulation 3.2 with periodically oncoming wakes with period $T = 0.3L/U_0$. Compared to the simulations with and without uniformly distributed free-stream fluctuations, (see Figures 2a,b), the location of transition has moved further upstream. While in Simulation 2 (see Figure 2b) the boundary layer is mainly disturbed by a large spanwise mode, in Simulation 3.2 the boundary layer disturbances are much more irregular (see Figure 4). The relatively large-scale fluctuations carried by the impinging wakes are found to be quite effective in promoting transition and reducing the size of the TSB (see also Figure 6). Especially in Simulation 3.2 the period between impinging wakes is very small, such that the boundary layer is almost constantly affected by disturbances.

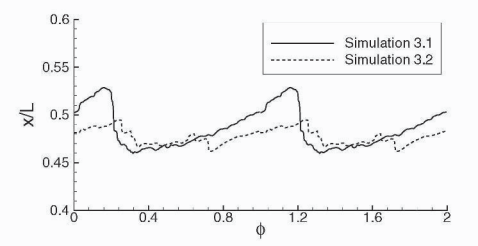

Figure 5. Simulations 3.1 and 3.2: the location of transition as a function of phase

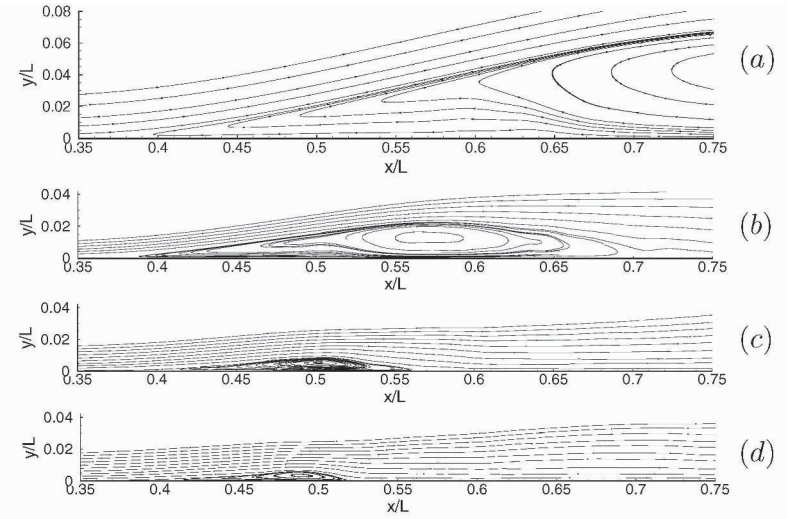

Figure 6. Streamlines of the mean velocity field showing a comparison of separation bubbles obtained in (a): Simulation 1, (b): Simulation 2, (c): Simulation 3.1, (d) Simulation 3.2

Figure 5 shows the location of transition in Simulations 3.1 and 3.2, identified by the most upstream location along $y/L = 3.2\times10^{-4}$ where the spanwise fluctuation $w'w'$ exceeds 20% of its maximum. The irregularities in the curve

of Simulation 3.2 reflect the limited amount of 10 periods of phase-averaging. Both curves have a saw-tooth-like shape. Each time a new wake impinges the location of transition abruptly moves upstream. This is followed by a period in which the boundary layer disturbances are gradually convected downstream. Compared to Simulation 3.2, the larger period used in Simulation 3.1 leads to a larger fluctuation in the location of transition. Note that the most upstream location of transition is $x/L \approx 0.46$ in both simulations.

Figure 6 shows streamline plots of the time-averaged velocity field of Simulations 1, 2, 3.1 and 3.2. It illustrates the large influence of fluctuations on the size of the TSB. Compared to Simulation 1, where no free-stream fluctuations were added, the small scale, uniformly distributed disturbances in Simulation 2 lead to a significant reduction in size of the TSB. The concentrated, large scale disturbances carried by the wakes, however, are even more effective in reducing the size of the bubble. This effect is especially strong in Simulation 3.2, which has a period between wakes that is only half of the period employed in Simulation 3.1.

3. CONCLUSIONS

DNS-s of TSB flow were performed with and without uniformly distributed or spatially confined disturbances added to the free stream. The results show that explicitly added disturbances can be very effective in reducing the size of the separation bubble. In Simulation 1 numerical round-off error was found to be responsable for triggering a Kelvin-Helmholtz instability leading to the roll-up of the separated boundary layer. In Simulations 1 and 2, this roll-up was found to be followed by a rapid transition to turbulence of the flow inside this roll. Compared to the Simulation 1, the addition of $Tu = 7\%$ inflow fluctuations at the inlet in Simulation 2 was found to significantly reduce the size of the bubble. The most effective reduction, however, was found to be achieved by the spatially concentrated large-scale disturbances carried by periodically oncoming wakes in Simulations 3.1 and 3.2.

REFERENCES

Alam, M. and Sandham, N.D., 2000, *Direct numerical simulation of 'short' laminar separation bubbles with turbulent reattachment*, J. Fluid Mech. **410**, 1-28.

Maucher, U., Rist, U., Wagner, S., 1997, *Secondary instabilities in a laminar separation bubble*, In: New Results in Numerical and Experimental Fluid Mechanics, NNFM 60, 229-236.

Spalart, P.R. and Strelets, M. Kh., 2000, *Direct simulation of a turbulent boundary layer up to Re_θ = 1410*, J. Fluid Mech. **403**, 329–349.

Wissink, J.G. and Rodi W., 2003, *DNS of a laminar separation bubble in the presence of oscillating flow*, Flow, Turbulence and Combustion, **71**, 311-331.

Wu, X. and Durbin, P.A., 2001, *Evidence of longitudinal vortices evolved from distorted wakes in a turbine passage*, J. Fluid Mech. **446**, 199–228.

THE EFFECT OF SWEEP ON LAMINAR SEPARATION BUBBLES

Tilman Hetsch and Ulrich Rist
Institut für Aerodynamik und Gasdynamik, Universität Stuttgart, Pfaffenwaldring 21, 70550 Stuttgart, GERMANY

Abstract: The effect of a systematic variation of the sweep angle on the disturbance amplification and onset of transition is studied in a generic family of swept laminar separation bubbles (LSB) by means of direct numerical simulation. The detailed analysis of a transition scenario with fundamental resonance in a 30°-LSB shows, that the saturation of background disturbances is the key event, after which a rapid breakdown of transitional structures to smaller scales and thus turbulent flow occurs. The stages of transition are similar to unswept LSB, but two-dimensional disturbances lose their dominance for sweep angles larger than 15°. Instead, oblique Tollmien-Schlichting waves which travel approximately along the direction of the potential streamline experience the maximal amplification in the linear stage and stimulate the strongest growth of background disturbances after saturation.

Key words: Laminar separation bubble; sweep angle; transition; direct numerical simulation.

1. INTRODUCTION

Laminar separation bubbles (LSB) are observed where laminar boundary layers encounter strong adverse pressure gradients, as on high-lift devices of commercial aircraft or turbine blades. For instance, an LSB was measured by Greff (1991) on the slat of an Airbus A310. Although most technical applications are inherently 3D, research efforts have been focussed almost exclusively on the easier 2D-case. Since the extensive experiments of Horton (1968) little was published about swept LSB until Kaltenbach and Janke (2000) demonstrated that the problem is now treatable by DNS.

The goal of this paper is twofold: Firstly, a transition scenario based on fundamental resonance in a 30°-LSB is discussed. Later, the impact of

R. Govindarajan (ed.), Sixth IUTAM Symposium on Laminar-Turbulent Transition, 395–400.

different sweep angles Ψ_∞ and propagation directions Ψ of chosen disturbances on such scenarios are investigated to identify the most effective disturbance combinations. To this end, a family of short leading-edge separation bubbles on a swept plate was calculated by means of DNS. This steady, laminar base flow allows for a systematic variation of Ψ_∞ from 0° to 45° and was already described in Hetsch and Rist (2004). Physically, it is characterized by a free-stream velocity of U_∞=30 m/s, a reference length L=0.05m and a Reynolds number $\mathrm{Re}_{\delta_1}(x_0) = 331$, based on the displacement thickness at the inflow of the integration domain. Under the influence of an adverse pressure gradient caused by a prescribed deceleration of the edge velocity $U_e(x)$ shown in figure 1, the laminar boundary layer separates at x_s=1.75 and reattaches at x_r=2.13. Arbitrary disturbances are excited in a disturbance strip by periodic suction and blowing through the wall. The DNS-code utilizes 6^{th}-order compact finite differences to solve the complete, incompressible Navier-Stokes-equations in vorticity-velocity formulation. For an in-depth description see Wassermann and Kloker (2002).

2. DISTURBANCE PROPAGATION IN SWEPT LSB

For each scenario one selected "primary disturbance" (PD) is excited with an initial amplitude 5 orders of magnitude larger than the one of all other modes. Additionally a group of 10 small "background disturbances" (BD) with the same fundamental frequency $\omega=2\pi\cdot L/U_\infty\cdot f$ and varying spanwise wave numbers γ=[-50, -40,…,50] are introduced. Different modes are referred to as modes (β/γ). This mimics a situation where a single high-amplitude disturbance hits a swept separation bubble in the presence of discrete background disturbances. Note that all angles are taken with respect to the X-axis throughout the paper. Three hypotheses about which type of PD is able to stimulate the strongest fundamental resonance of the BD were investigated: *Earliest transition for a given swept LSB may be expected for a PD with*: (i) A propagation direction of Ψ=0°, because 2D-disturbances are the dominant modes in unswept LSB, see Rist (1999). (ii) Ψ in the direction of the potential streamline, as those modes are most amplified in attached swept flows. (iii) The integrally most amplified mode in the linear domain, as it will reach earliest the high-amplitude level necessary to influence base flow and BD non-linearly. For each sweep angle the linearly most amplified representative of each class (i)-(iii) was determined by spatial linear stability theory (LST). The results are summarized in table 1. Note that the maximal amplification (iii) always occurred for modes which spread nearly in the direction of the potential streamline. As DNS results of both types in non-linear stages are also almost identical, we can identify the types (ii) and (iii).

Table 1. LST within linear domain: Integrally most amplified mode (ω,γ) for each sweep angle Ψ_∞ with: propagation direction Ψ=0°, propagation direction in direction of potential streamline ($\Psi=\Psi_\infty$) or strongest overall amplification (amp-max) in the base flow

Ψ_∞	2D-PD: Ψ=0°	Pot: $\Psi=\Psi_\infty$	Ψ	amp-max	Ψ
0°	(18/0)	(18/0)	0°	(18/0)	0°
15°	(18/0)	(18/10)	12°	(18/10)	12°
30°	(18/0)	(18/20)	27°	(20/20)	25°
45°	(18/0)	(22/30)	44°	(24/30)	39°

2.1 Stages of transition in a swept LSB

In order to compare the transition mechanism in swept LSB with the known 2D case, one such scenario – namely the most amplified PD-(20/20) of the 30°-LSB – was analysed and visualized in detail in figure 3 and 4. Shown are alternating isosurfaces of the pure disturbance-component of the spanwise vorticity $\omega_z=\pm0.0001$ in region I and a single λ_2-isosurface inside the regions II, III and IV. For the sake of a clearer layout, only one BD and two non-linearly generated modes are displayed as examples in the lower picture of figure 4. The distinguished alternating ω_z-pattern at stage I represents the "footprints" of a single Tollmien-Schlichting wave. This is the PD (20/20) as indicated by the common propagation direction of Ψ=25° and the insignificant amplitude of all other modes. Until the PD reaches the critical amplitude of about 1% of U_e at $x\approx1.8$, all BD grow in very good agreement to LST, nicely demonstrated by BD (20/-10) in figure 4. At this point the PD has achieved an amplitude high enough to deform the base flow itself and the linear regime (a little larger than region I) ends. The λ_2-method indicates the onset of a PD-vortex in region II, which is still amplified as predicated by LST until it saturates. For the unswept bubble, Rist (1999) has proven that the short stage between the end of the linear domain and the saturation of the 2D-PD (18/0) is governed by secondary stability theory. In the present case, a sudden increase of the amplification rates can also be noticed for the higher harmonic (40/40) and the BD. As soon as the PD and its higher harmonics saturate simultaneously the third stage starts. Together they form a coherent structure with a weak secondary vortex near the wall. After leaving the LSB its phase velocity $c_r=\omega/(\alpha_r^2+\gamma^2)$ increases by 20% (α_r denotes the streamwise wave number). In the visualisation of figure 4 this acceleration is visible as a bending of the vortex at x=2.15. At the same time its propagation direction $\Psi=\arctan(\gamma/\alpha_r)$ is adapted until it exactly matches that of the potential streamline, as demonstrated in figure 2. Compared to the previous stage, decreased amplification rates of all BD are observed. Immediately after the BD saturate, the coherent structures rapidly break down to smaller scales and an early stage of turbulent flow appears.

2.2 The effect of sweep angle and propagation direction

As a general trend, the resonance of BD with the 2D-PD (18/0) is diminishing for larger sweep angles. Compared to the reference scenario Ψ_∞=0°, only the 15°-case reaches slightly larger amplitudes for the most amplified BD at x=3. The amplitude level of the associated 45°-scenario is already more than one order of magnitude lower. Even though amplification in the linear domain generally *increases* with Ψ_∞, the growth in region III significantly decreases for scenarios with a 2D-PD. Contrary to this series, the resonance of BD to the most amplified PD rises continuously with Ψ_∞. They saturate at x≈3.15 in the 0°-base flow for the PD (18/0), for Ψ_∞=15° with the PD (18/10) at x≈3.0 and in the 30°-scenario with PD (20/20) already at x≈2.80. Table 2 shows additional calculations with PD in intermediate propagation directions Ψ in the 30°-LSB. They confirm that the soonest saturation of BD indeed appears for the PD (18/20) and (20/20), which propagate approximately in the direction of the potential streamline.

Table 2. X-Position of saturation of background disturbances in the 30°-LSB for different PD

Ψ_∞=30°	(18/0)	Ψ	(18/10)	Ψ	(18/20), (20/20)	Ψ	(18/30)	Ψ
BD-saturation	x≈3.20	0°	x≈2.95	13°	x≈2.75, x≈2.80	27°, 25°	x≈2.95	43°

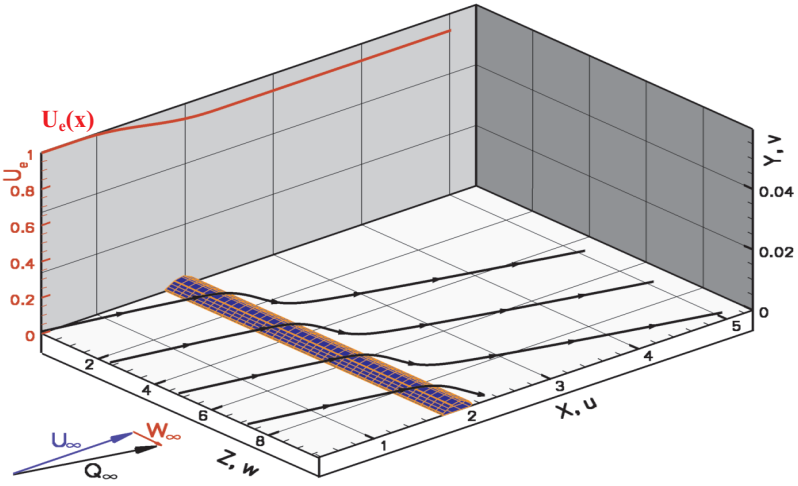

Figure 1. Integration domain of the 30°-LSB with bubble surface and outer streamlines

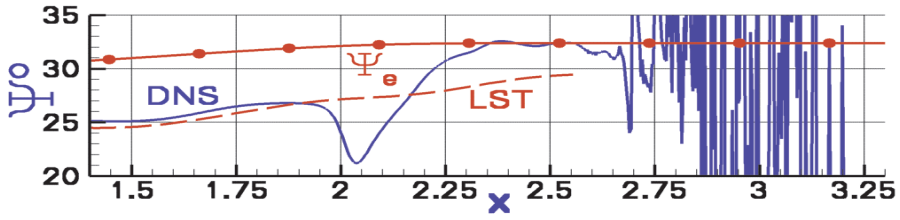

Figure 2. 30°-LSB: Propagation angle Ψ in [°] for PD (20/20), Ψ_e: potential streamline

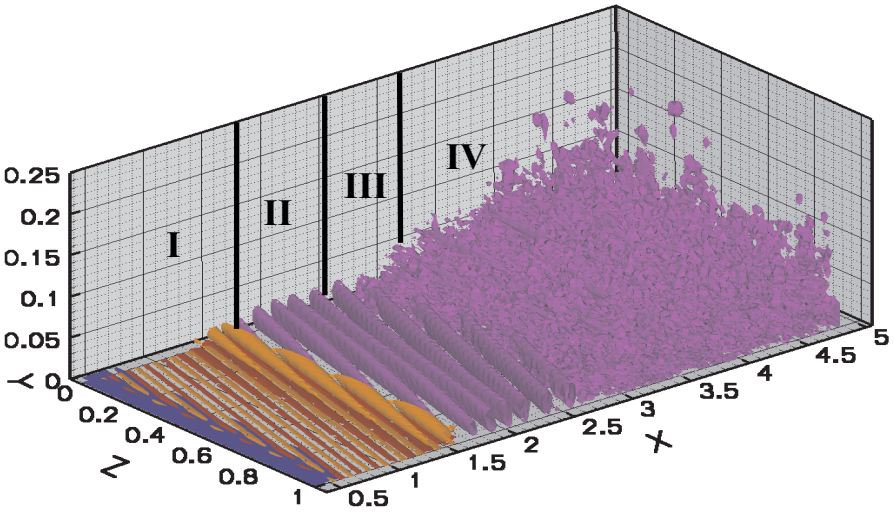

Figure 3. Stages of transition in a 30°-LSB. Fundamental resonance of background disturbances to a primary disturbance (20/20): I) linear amplification, II) PD: high-amplitude vortex, III) coherent structure of saturated PD and higher harmonics, IV) early turbulence

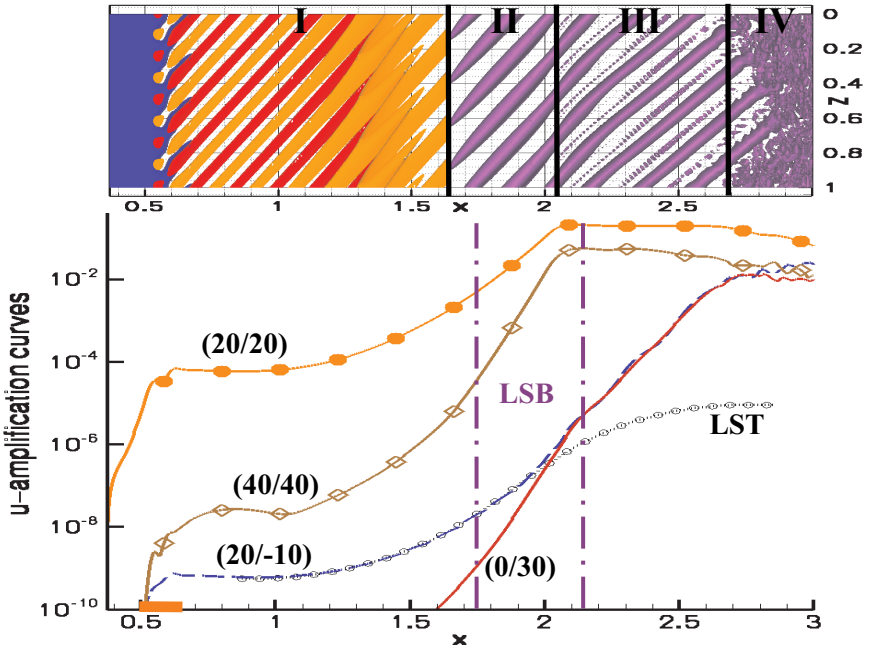

Figure 4. 30°-LSB: Comparison of amplification curves with top view of figure 3. Lines: DNS, doted line: spatial LST. Rapid breakdown of coherent structures (III) to turbulence (IV) by saturation of background disturbances. LSB: Separation x=1.75, reattachment x=2.13

3. CONCLUSIONS

Disturbance amplification and the onset of turbulent flow have been studied in a family of small, leading-edge laminar separation bubbles (LSB) for sweep angles Ψ_∞=0°, 15°, 30° and 45°. An analysis of a transition scenario with fundamental resonance in the 30°-LSB showed similar stages as in unswept LSB: I) linear amplification of disturbances until the dominating primary disturbance (PD) reaches sufficient amplitude. II) Strong resonance of the background disturbances (BD) to a high-amplitude PD-vortex, which still grows according to LST until saturation. III) A coherent structure is formed by the saturated PD and its higher harmonics, which slightly dampens the amplification of all BD. IV) Rapid breakdown to smaller scales immediately after the saturation of the BD, which was thereby identified to be an appropriate criterion for the onset of turbulent flow. As a comparison of different PD showed, oblique TS-waves propagating approximately in the direction of the potential streamline were linearly most amplified and additionally stimulated the strongest growth of BD in the non-linear stages. In spite of being dominant in unswept LSB, 2D-disturbances became unimportant with growing sweep angle. It follows that investigations of unswept LSB are *not* transferable to cases with sweep angels higher than about 10°-15°.

REFERENCES

Greff, E. (1991): "In-flight Measurements of Static Pressures and Boundary-Layer State with Integrated Sensors". J. Aircraft, **28**, No.5, pp. 289-299.

Kaltenbach, H., Janke, G. (2000): "Direct numerical simulation of flow separation behind a swept, rearward-facing step at Re_H=3000". Phys. Fluids, **12**, pp. 2320-2337.

Hetsch, T., Rist, U. (2004): "On the Structure and Stability of Three-Dimensional Laminar Separation Bubbles on a Swept Plate". New results in numerical and experimental fluid mechanics IV: Proceedings of the 13. DGLR/STAB-Symposium, Munich, 2002, Breitsamter, Laschka et al. (editors), NNFM, **87**, Springer, pp. 302-310.

Horton, H. P. (1968): "Laminar Separation Bubbles in Two and Three Dimensional Incompressible Flow". PhD thesis, Department of Aeronautical Engineering, Queen Mary College, University of London.

Rist, U. (1999): „Zur Instabilität und Transition laminarer Ablöseblasen". Habilitation, Universität Stuttgart, Shaker Verlag.

Wassermann, P., Kloker, M. (2002): "Mechanisms and passive control of crossflow-vortex-induced transition in a three-dimensional boundary layer". J. Fluid Mech., **456**, pp. 49-84.

ON THE BURSTING CRITERION FOR LAMINAR SEPARATION BUBBLES

S.S. Diwan, S.J. Chetan and O.N. Ramesh
Department of Aerospace Engineering, Indian Institute of Science, Bangalore-560012, India

Abstract: Traditionally, laminar separation bubbles have been characterised as being 'long' or 'short' on the basis of a two parameter 'bursting' criterion involving a pressure gradient parameter and Reynolds Number at separation. In the present work we suggest a refined bursting criterion, which takes into account not just the length of the bubble but also the maximum height of the bubble, thereby shedding some light on the less understood phenomenon of 'bursting' in laminar separation bubbles.

Key words: Laminar separation bubble; bursting; bubble height.

1. INTRODUCTION

Gaster (1967) in his landmark work on laminar separation bubbles proposed a two-parameter bursting criterion for the transition of separation bubbles from a "short" to a "long" state, as the flow velocity was reduced gradually. In his experiments, the bursting was associated with sudden increase in the length of the bubble. He suggested a two-parameter criterion to characterise the bursting of a short bubble to a long bubble.

A two dimensional computational study by Pauley *et al* (1990) found this criterion for bursting to be inadequate and they instead suggested that a long bubble is a steady separation bubble without any vortex shedding, whereas a short bubble is accompanied by vortex shedding.

In the present work, we examine the criterion for bursting carefully. We make use of detailed measurements from our experiments and compare this with the available data in the literature. First of all, we find that in our as well as in others' measurements, 'short bubble' (according to Gaster's criterion) is

R. Govindarajan (ed.), Sixth IUTAM Symposium on Laminar-Turbulent Transition, 401–407.

more common and the data on 'long bubble' is scarce. Moreover the shedding criterion for short bubbles, enunciated by Pauley *et al*, was not ubiquitous at all; an example is, one 'short bubble' of Watmuff (1999) with no evidence of shedding or unsteady activity, unless the bubble was forced externally. This casts a question on the criterion put forth by Pauley *et al*, which is primarily based on considerations of vortex shedding from the bubble. The suggestion that bursting might have something to do with the switching from convective to absolute instability (Alam & Sandham, 2000) also appears to be questionable. This is because equating the presence of a 'long bubble' with absolute instability is inconsistent with the long and slow approach to reattachment.

We suggest here that a criterion for bursting should take into account not just the length of the bubble but also the maximum height (h). A refined bursting criterion is proposed and its merits are discussed.

2. EXPERIMENTAL PROCEDURE

2.1 Experimental setup

The experiments were conducted in the Closed Circuit Wind Tunnel (1m X 1m X 4m) at the Department of Aerospace Engineering. A 5mm thick aluminum plate with an elliptical cross-section leading edge (Prasad and Narasimha, 1994), acts as the measurement surface. The flat plate is provided with pressure ports for the measurement of static pressures, with the coefficient of pressure defined as $Cp = \dfrac{P_x - P_{\inf}}{P_{total} - P_{\inf}}$

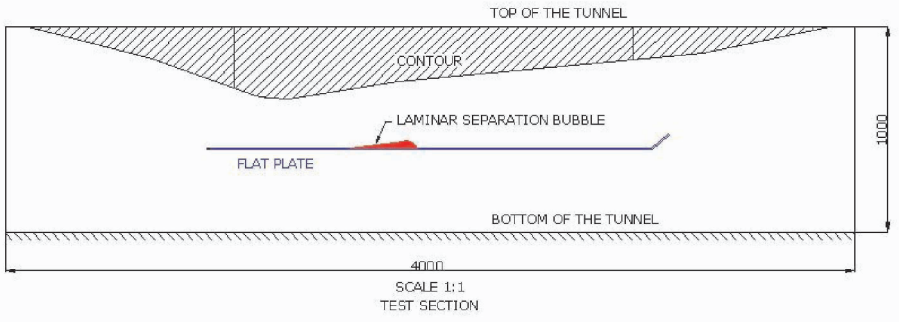

Figure 1. Experimental Setup

The laminar separation bubble was produced on the flat plate by contouring the top wall of the test section as shown in Fig. 1. The boundary layer on the top wall was tripped to avoid separation on the contour. The strength of the adverse pressure gradient could be adjusted by raising or lowering the contour by means of a nut-screw rod arrangement. Figure-1 shows one of the settings of the contour, with respect to the flat plate.

The velocity data, both mean and fluctuating, were measured using single component tungsten hot-wire of $5\mu m$ diameter and an active length of 2mm. A traversing mechanism with controlled 2D movement was employed to position the probe.

Experiments were done for three different settings of the contour (to be called cases A, B and C) with increasing severity of the adverse pressure gradient.

2.2 Flow visualisation

Following are the flow visualization techniques used for qualitative as well as quantitative analysis of the flow phenomenon in the present work.

2.2.1 Smoke flow visualisation technique

Smoke was introduced into the test section in the form of a sheet, with the help of a smoke-rake, which was placed upstream of the honeycomb. The smoke was illuminated by a sheet of laser light (100mW). The height of the laminar separation bubble is easily extracted from the recorded pictures. Fig. 2 shows the picture of a typical laminar separation bubble produced using the above-mentioned technique.

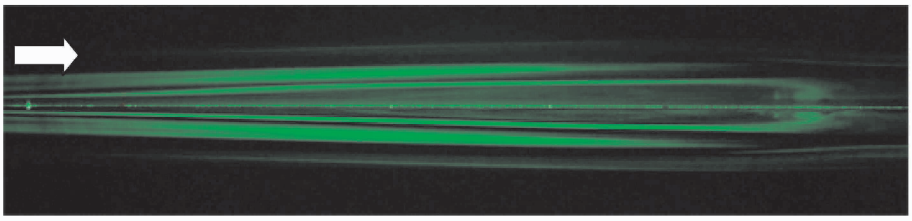

Figure 2. Smoke flow-visualisation. The flat plate is visible as the symmetry plane. Uref = 3.6 m/s, Contour Setting B

2.2.2 Surface flow visualisation technique

In order to locate the position of separation and reattachment (surface streamlines) with fairly good accuracy, a technique, which we call as "ink-dot matrix" technique (see Langston and Boyle, 1982) was used.

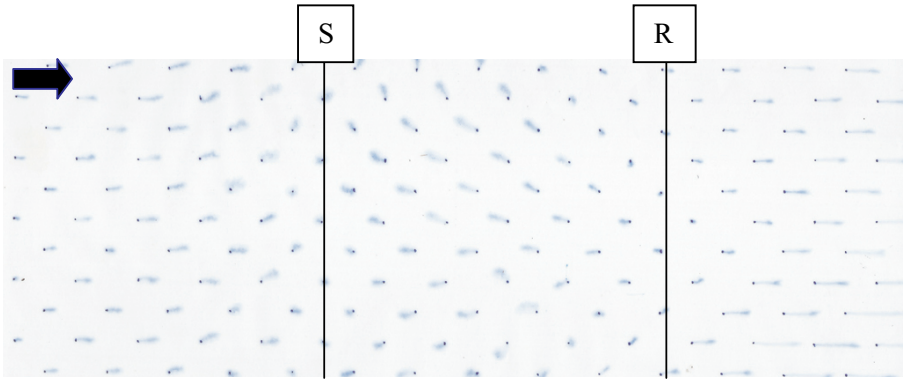

Figure 3. Surface flow visualisation. Uref = 5.46 m/s, Contour Setting B

This method gives a time averaged picture of the surface streamline pattern as shown in Fig. 3 where S is a separation line and R is a reattachment line. The reverse flow is indicated by the reversed direction of streaks beyond the separation line.

3. THE BURSTING CRITERION

Gaster (1967) proposed a two parameter criterion to characterise the bursting process which included the pressure gradient parameter and the Reynolds number as given below.

$$\tilde{P} = \frac{\theta s^2}{\nu}\frac{\Delta U}{\Delta X}\Bigg)_{inviscid} \quad , \quad R_{\theta s} = \frac{Us\,\theta s}{\nu} \tag{1}$$

Where Us is the freestream velocity at separation, θ_s is the momentum thickness at separation and $\Delta U/\Delta X$ is the velocity gradient of the equivalent 'inviscid' flow (obtained by tripping the boundary layer). These parameters are plotted in Fig. 4 for various experimental studies.

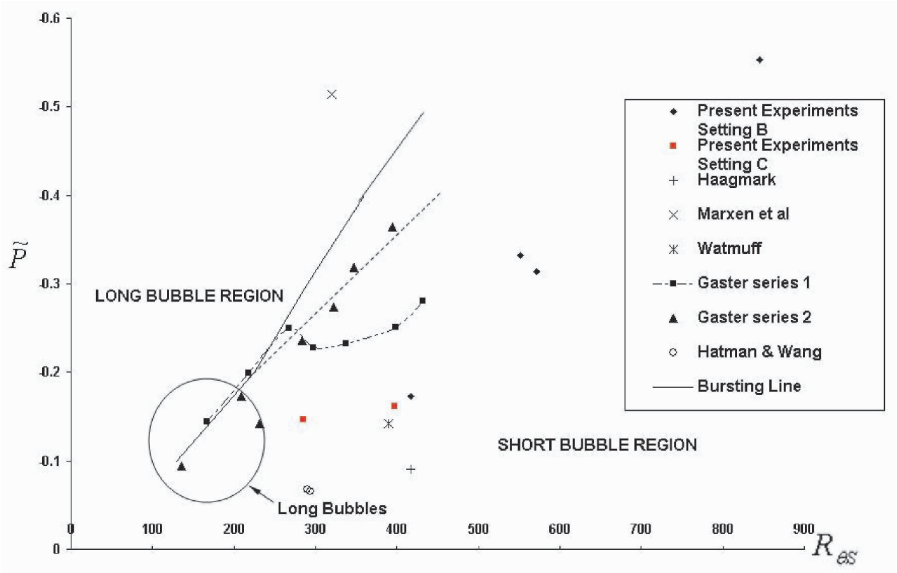

Figure 4. Gaster's bursting criterion

This bursting criterion does not appear to be universal in classifying and differentiating the short bubbles from long bubbles for the following reasons.

(1) The bubbles which Gaster terms as "long" in his experiments actually lie in the Short Bubble Region.

(2) The bubble obtained by Marxen et al. (2004) does not show a significant departure from the inviscid pressure distribution. But still it lies in the long Bubble Region.

(3) According to Gaster(1969), "bursting" occurs when the data points on the plot from the Short Bubble Region approach the bursting line steeply. This in fact makes it a three-parameter criterion where along with $\tilde{P}$ and $R_{\theta s}$ one perhaps needs to specify the slope on the $\tilde{P}$-$R_{\theta s}$ curve. Furthermore a series of experiments need to be done to arrive at this.

We suggest here that a criterion for bursting should take into account not just the length of the bubble but also the maximum height (*h*). Transition to turbulence in the separated shear layer is initiated (possibly through a Kelvin-Helmholtz instability mechanism) roughly around the streamwise location at which the height of the bubble (i.e., the location of the mean dividing streamline) reaches a maximum value. By combination of *h* and the overall velocity gradient ($\Delta U/\Delta X$) across the bubble, we arrive at a new

non-dimensional pressure gradient parameter $P = \frac{h^2}{\nu}\frac{\Delta U}{\Delta X}$, which can be expected to be an indication of the global nature of the bubble. Note that the $\Delta U / \Delta X$ here is the actual mean velocity gradient across the bubble as against the inviscid gradient used by Gaster. As already discussed above, the local conditions at the streamwise location of maximum height of the bubble can be expected to influence the approach of the separated shear layer towards reattachment. So the maximum height and the freestream velocity (U_h) at that location seem to be the most appropriate parameters for defining the Reynolds number $\mathrm{Re}_h = \frac{U_h h}{\nu}$. In Fig. 5, we plot the variation of P as a function of Re_h for a variety of experimental data.

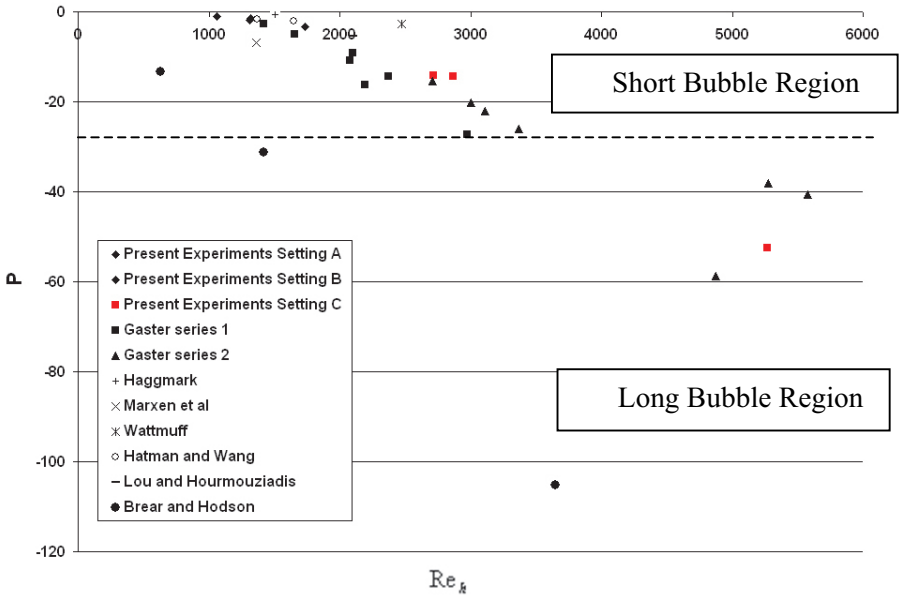

Figure 5. The proposed bursting criterion

It is apparent from the plot that there is a clear- cut demarcation between the "short" and the "long" bubbles, with "short" bubbles clustered in the upper portion of the plot. This thus suggests a single parameter bursting criterion where the critical line can be placed at $P \sim -28$. If $P > -28$, it is a short bubble, otherwise a long bubble. It is interesting to note that all the data points in Short Bubble Region (except for the data points of Brear and Hodson (2003) where aerofoil is used rather than a flat plate) collapse

reasonably well onto a single curve approaching the critical line, which eliminates the need to introduce the "approach towards critical condition" to be a separate parameter. A single data point is thus sufficient to decide whether the bubble is "long" or "short".

4. CONCLUSIONS

A laminar separation bubble is produced experimentally on a flat plate. The flow visualization and pressure measurements show the typical time averaged characteristics of a bubble reported in the literature. Gaster's bursting criterion is revisited and a refined bursting criterion involving the maximum height is proposed. It is shown that the proposed criterion clearly demarcates between short and long bubbles. A single parameter criterion (with a critical value of $P \sim -28$) is shown to indicate the transition to a long bubble. The proposed criterion is seen to be more universal than the existing criteria.

REFERENCES

M.Alam & N.Sandham: 2000, "Direct Numerical Simulation of 'short' laminar separation bubble with turbulent reattachment", Journal of Fluid Mechanics, Vol. 410, p 1-28.

M.J.Brear & H.P.Hodson: 2003, "The response of a laminar separation bubble to 'aircraft engine representative' freestream disturbances", Experiments in Fluids, Vol. 35, p 610-617.

M Gaster: 1967, "The structure and behaviour of separation bubbles", R & M No. 3595, NPL, U.K

C.P.Haggmark, A.A. Bakchinov & P.H .Alfredsson: 2000, "Experiments on a two-dimensional laminar separation bubble", Philosophical Transactions of the Royal Society. London, A, 358, p 3193-3205.

A.Hatman & T.Wang: 1998, "Separated Flow Transition"- Parts 1 & 2 ASME GT-98.

L.S.Langston & M.T.Boyle.: 1982, "A new surface-streamline flow-visualization technique", Journal of Fluid Mechanics, Vol 125, p 53-57.

W.Lou & J.Hourmouziadis: 2000, "Separation bubbles under steady and periodic-unsteady main flow conditions", Journal of Turbomachinery, Vol. 122, p 634-643.

O. Marxen, M. Lang, U. Rist and S. Wagner: 2003, "A Combined Experimental/Numerical Study of Unsteady Phenomena in a Laminar Separation Bubble", Flow, Turbulence and Combustion 71: p 133–146.

L.Pauley, P.Moin and W.Reynolds: 1990, "The structure of two-dimensional separation", Journal of Fluid Mechanics, Vol. 220, p 397-411.

S.N.Prasad and R.Narasimha: 1994, "Leading edge shape for flat plate boundary layer studies", Expt. in Fluids, Vol.17, p358-360.

J.H.Watmuff: 1999, "Evolution of a wave packet into vortex loops in a laminar separation bubble", Journal of Fluid Mechanics, Vol. 397, p 119-169.

NON-LINEAR INTERACTION OF GOERTLER VORTICES AND TOLLMIEN SCHLICHTING WAVES

Leandro F. Souza,[1] Marcio T. Mendonca,[2] and Marcello A. F. Medeiros[3]

[1] *ICMC- USP, Universidade de Sao Paulo Sao Carlos, Brazil*
lefraso@icmc.usp.br

[2] *Centro Tecnico Aeroespacial Sao Jose dos Campos, Brazil*
marcio@iae.cta.br

[3] *EESC-USP, Universidade de Sao Paulo Sao Carlos, Brazil*
marcello@sc.usp.br

Abstract: In this paper spatial Direct Numerical Simulation is used to study the nonlinear interaction between planar Tollmien Schlichting waves and Goertler Vortices. The results show the development of lambda vortices typical of K-type and H-type break down. Two different structures have been found which are shifted with respect to each other by π in the spanwise direction.

Keywords: Goertler vortices, Tollmien-Schlichting waves, boundary layer stability, hydrodynamic stability, transition to turbulence

1. INTRODUCTION

A boundary layer over a concave surfaces may develop both Goertler Vortices (GV) and Tollmien-Schlichting (TS) waves when the curvature of the plate is mild. When both centrifugal and viscous instabilities are present, their interaction may hasten the transition to turbulence. Besides the importance of these instability modes in certain aeronautical applications, GV are a suitable model for studding the structures found in turbulent flows. The study of GV/TS interaction may help understand the development of turbulent coherent motion. The similarities between the structures presented in this paper and the near-wall turbulent vortex structures presented by Panton [1] are remarkable.

Already in 1969, Tani and Aihara [2] identified experimentally that the TS waves are affected by the vortices through the spanwise variation in the boundary layer thickness. This change in the boundary layer thickness is caused by the redistribution of the mean flow owing to the counter rotating vortices, and

R. Govindarajan (ed.), Sixth IUTAM Symposium on Laminar-Turbulent Transition, 409–414.

giving rise to upwash and downwash regions. Numerical investigations by Malik [3], Nayfeh and Al-Maaitah [4] and Malik and Hussaini [5] show that oblique TS waves are destabilized by GV when their streamwise wavelength is half the spanwise wavelength of the vortices.

The interaction between GV and two dimensional TS waves leads to the development of oblique waves with spanwise wavelength equal to that of the vortices (Malik and Godil [6], Bertolotti [7]). These oblique waves, in turn, may lead to K-type breakdown depending on the amplitude of the primary disturbances. Their results also indicate that at the upper branch, oblique TS waves are formed, while at the lower branch, the waves are relatively insensitive to the vortices. These conclusions were confirmed by Mendonça, Morris and Pauley [8], who also showed the importance of growth rates and initial amplitudes on the resulting breakdown process.

In the current paper, spatial Direct Numerical Simulation results of the nonlinear GV/TS interaction are presented. The results show the development of lambda vortices typical of K-type and H-type break down. Depending on the flow parameters these lambda vortices are shifted by half a wavelength with respect to the vortices upwash region. The development of lambda vortices as the dominant structure downstream is due to the fact that the oblique waves resulting from the GV-TS interaction is a stronger forcing mechanism than the original disturbances.

2. FORMULATION AND NUMERICAL METHOD

In the present study the complete Navier-Stokes equations for a constant density and viscosity fluid were rewritten in a vorticity-velocity formulation [9] for the disturbances. The Blasius boundary layer was used as the base flow. The governing equations in non-dimensional form have and additional parameter, the Goertler number, $Go = (k_c\sqrt{Re})^{1/2}$, where k_c is the nondimensional curvature of the wall. The reference length and reference velocity were L and U_∞, the free-stream velocity. The Reynolds number was given by $Re = U_\infty L/\nu$.

The vorticity is defined as the negative curl of velocity vector. Taking the negative curl of the momentum equations one can obtain the vorticity transport equations:

$$\frac{\partial \omega_x}{\partial t} + \frac{\partial a}{\partial y} - \frac{\partial b}{\partial z} + \frac{Go^2}{\sqrt{Re}h}\frac{\partial (u^2)}{\partial z} = \nabla^2 \omega_x, \tag{1}$$

$$\frac{\partial \omega_y}{\partial t} + \frac{\partial c}{\partial z} - \frac{\partial a}{\partial x} = \nabla^2 \omega_y, \tag{2}$$

$$\frac{\partial \omega_z}{\partial t} + \frac{\partial b}{\partial x} - \frac{\partial c}{\partial y} - \frac{Go^2}{\sqrt{Re}h}\frac{\partial (u^2)}{\partial x} = \nabla^2 \omega_z, \quad \text{where,} \tag{3}$$

$$\nabla^2 = \frac{1}{Re}\left(\frac{\partial^2}{\partial x^2} + \frac{\partial^2}{\partial y^2} + \frac{\partial^2}{\partial z^2}\right), \tag{4}$$

and $a = v\omega_x - u\omega_y$, $b = u\omega_z - w\omega_x$ and $c = w\omega_y - v\omega_z$ are the nonlinear terms resulting from convection, vortex stretching and vortex bending. The terms ω_x, ω_y and ω_z are the vorticity components in the streamwise direction x, wall normal direction y and spanwise direction z.

Taking the definition of the vorticity and the mass conservation equation, one can obtain a Poisson equation for each velocity component:

$$\frac{\partial^2 u}{\partial x^2} + \frac{\partial^2 u}{\partial z^2} = -\frac{\partial \omega_y}{\partial z} - \frac{\partial^2 v}{\partial x \partial y}, \tag{5}$$

$$\frac{\partial^2 v}{\partial x^2} + \frac{\partial^2 v}{\partial y^2} + \frac{\partial^2 v}{\partial z^2} = -\frac{\partial \omega_z}{\partial x} + \frac{\partial \omega_x}{\partial z}, \tag{6}$$

$$\frac{\partial^2 w}{\partial x^2} + \frac{\partial^2 w}{\partial z^2} = \frac{\partial \omega_y}{\partial x} - \frac{\partial^2 v}{\partial y \partial z}. \tag{7}$$

At the wall, no-slip and no penetration boundary conditions were imposed. Disturbances were introduced into the flow field using a suction and blowing function at the wall in a disturbance strip [9]. At the inflow, the velocity and vorticity components were specified based on the Blasius boundary layer. At the upper boundary, the disturbances were assumed to decay exponentially to zero. The flow is assumed periodic in the spanwise direction z, and symmetric with respect to $z = 0$. Therefore, the flow field is expandable in real Fourier cosine and sine series. A buffer domain technique was implemented in order to avoid wave reflections in the outflow boundary [10].

The equations were solved numerically on an orthogonal uniform grid. The time derivatives were integrated with a classical 4^{th} order Runge-Kutta scheme. The spatial derivatives were calculated using a 6^{th} order compact finite difference scheme, except at the wall where 5^{th} order approximations were used. The Poisson equations are solved using a FAS Multigrid method.

3. RESULTS

Two test cases are here presented. For the first test case $Re = 210681$, $\beta = 114.75$, $Go = 3.5$ and the TS frequency was $\omega_t = 15.88$. The initial amplitude of the stationary disturbances at the suction and blowing strip was $A_{gv} = 5\times10^{-4}$ and that of the time dependent disturbance was 1×10^{-4}, where β is the spanwise wavenumber. The time dependent disturbances introduced at the wall seeded Tollmien-Schlichting waves starting close to the lower branch of the neutral curve and propagating past the upper branch.

The nonlinear interaction result in a strong growth of a pair of oblique waves with spanwise wavenumber identical to the that of the vortices and the same frequency as the frequency of the initial TS wave (Fig. 1). This oblique wave suggests the possibility of a fundamental resonance mechanism. Figure 2 shows structures of the flow with 2 wavelengths in the spanwise direction, therefore, 2 upwash and 3 downwash regions can be seen. The structures are iso-surfaces given by the second invariant of the velocity gradient Q. The initial TS spanwise vorticity is modulated by the GV longitudinal vorticity. Further downstream staggered hair pin vortices develop, and the resulting structure resembles the structure found in H-type subharmonic resonance (Fig. 2 and 4). In Fig. 4 the x to z and y to z ratio has changed from 1 to 0.2. A similar structure with overlapping vortices was found near the wall by Shoppa and Hussaini [11] in a DNS of turbulent flows.

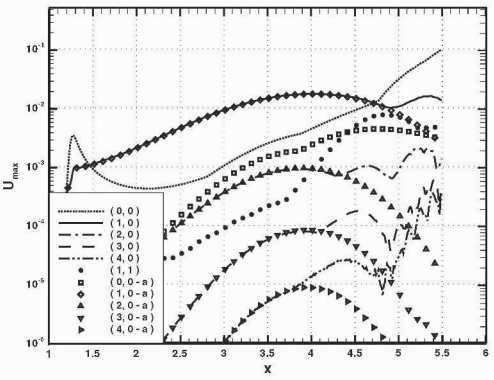

Figure 1. Downstream amplitude development of various modes in the frequency-wavenumber spectrum

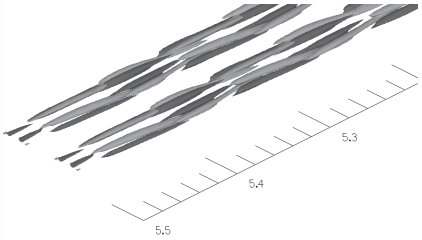

Figure 2. Iso-surfaces of $Q = \pm 5$

In the second test case the Goertler number was raised to $Go = 5.0$, keeping the same Reynolds number, TS frequency and spanwise wavenumber. The results are similar to the results for the first test case. Due to the nonlinear interaction an oblique wave develops raising the possibility of fundamental resonance with the 2-D TS wave. Comparing the second test case results with the results for the first test case, two fundamental differences in the resulting structure can be observed. The first difference is a phase shift in the peak-and-valley structure. In Fig. 3 a peak occur in the downwash region, while in Fig. 5 a valley is found there. Second the overlapping lambda vortices are aligned, as shown in Fig. 6, consistent with a K-type fundamental resonance.

4. CONCLUSIONS

In this work the nonlinear interaction between planar Tollmien-Schlichting waves and Goertler vortices was studied using direct numerical simulation. As

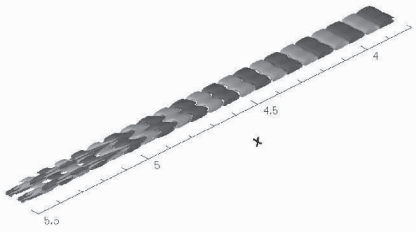

Figure 3. Iso-surfaces of $Q = \pm 1.5$

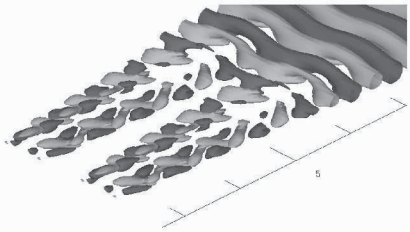

Figure 4. Iso-surfaces of $Q = \pm 5$

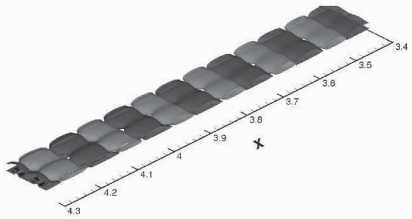

Figure 5. Iso-surfaces of $Q = \pm 1.5$

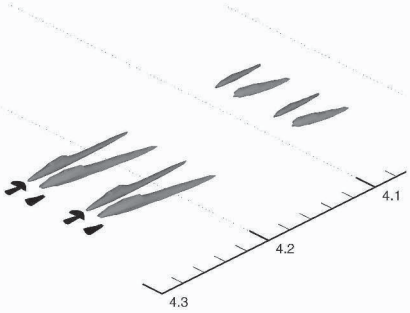

Figure 6. Iso-surfaces of $Q = \pm 25$

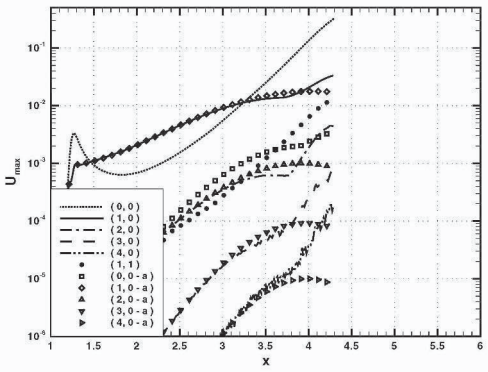

Figure 7. Downstream amplitude development of various modes in the frequency-wavenumber spectrum

in previous investigations the results show the development of oblique waves which lead to the development of lambda vortices typical of K-type and H-type breakdown. The resulting structures change from a staggered pattern to an aligned pattern when the Goertler number was changed. The peak and valley

structures found for the two test cases presented are shifted with respect to each other by π in the spanwise direction.

It is conjectured that the TS waves are affected by the longitudinal vortices through the spanwise variation in the boundary layer thickness. This change in the boundary layer thickness is caused by the redistribution of the mean flow owing to the Goertler vortices that give rise to upwash and downwash regions. The phase shift is consistent with this argument. The spanwise phase of the 3-D nonlinear structures would be dependent on whether the interaction were close to the first or the second branch of the TS stability curve [12].

ACKNOWLEDGEMENTS

The authors acknowledge the financial support received from FAPESP (grants 00/04943-7 and 03/05027-2).

REFERENCES

[1] Panton, R. L.:Overview of self-sustaining mechanisms of wall turbulence. Prog. Aerospace Sci., vol. 37, pp 341–383, 2001.

[2] Tani, I. and Aihara, Y.:Görtler vortices and boundary layer transition. ZAMP, vol. 20, pp 609–618, 1969.

[3] Malik, M. R.:Wave interaction in three-dimensional boundary layers, *AIAA Paper*, 86-1129, 1986.

[4] Nayfeh, A. H. and Al-Maaitah, A.:Influence of streamwise vortices on Tollmien-Schlichting waves. *Physics of Fluids*, vol. 31, pp 3543–3549, 1988.

[5] Malik, M. R. and Hussaini, M. Y.:Numerical simulation of interactions between Görtler vortices and Tollmien-Schlichting waves. *J. Fluid Mechanics*, vol. 210, pp 183–199, 1990.

[6] Malik, M. R. and Godil, A. A.:Nonlinear development of Görtler and crossflow vortices and Görtler/ Tollmien-Schlichting wave interaction. NTIS, AD A 221 107, 1990.

[7] Bertolotti, F. P.:Transition Modeling Based on the PSE, chapter 8, pp 337–368, Kluwer Academic Publ, 1996.

[8] Mendonça, M. T., Morris, P. J. and Pauley, L. L: Interaction between Görtler vortices and two-dimensional Tollmien-Schlichting waves. *Physics of Fluids*, vol.12, pp 1–11, 2000.

[9] Meitz H. L., Fasel H. F.: A compact-difference scheme for the Navier-Stokes equations in vorticity-velocity formulation. *J. Comp. Phys.*, **157**:371–403, 2000.

[10] Kloker M., Konzelmann U., Fasel H. F.: Outflow Boundary Conditions for Spatial Navier-Stokes Simulations of Transition Boundary Layers. *AIAA Journal*, **31**:620–628, 1993.

[11] Shoppa W., Hussain F.:Genesis and dynamics of coherent structures in near-wall turbulence: A new look *AIAA-98-3000*.

[12] Klebanoff, P. S., Tidstrom, K. D., Sargent, L. M.: The three-dimensional nature of boundary layer instability. *J. Fluid Mech.*, **12**:1–34, 1962.

EXPERIMENTS ON STREAMWISE VORTICES IN A SWEPT WING BOUNDARY LAYER AND THEIR SECONDARY INSTABILITY

Victor V. Kozlov[1], Valery G. Chernoray[2], Alexander V. Dovgal[1] and Lenart Loefdahl[2]

[1] Institute of Theoretical and Applied Mechanics, 630090 Novosibirsk, Russia; [2] Thermo and Fluid Dynamics, Chalmers University of Technology, SE-412 96 Goeteborg, Sweden. Contact address: kozlov@itam.nsc.ru

Abstract: A detailed experimental study on the formation of crossflow vortex mode packets and their secondary instability in a swept wing boundary layer was carried out. As a result, two modes of nonstationary perturbations traveling along the vortices were found.

Key words: flow; streaks; turbulence; shear layers; boundary layer; flow breakdown; instability; crossflow vortex; wind tunnel; wing.

1. INTRODUCTION

There are a number of indications that three-dimensional velocity perturbations such as streamwise vortices and streaks are involved in transition to turbulence in wall bounded shear layers. Creating local flow distortions, they induce velocity gradients in spanwise and wall-normal directions, which in turn lead to growth of secondary high-frequency disturbances with further laminar flow breakdown. For the first time, secondary instabilities of three-dimensional boundary layers were focused, probably, by Poll (1979), who observed high-frequency oscillations near the swept wing leading edge. Later, Kohama (1987) assumed that such perturbations can be caused by an inflexion-point instability in the vortex core. A theory for the secondary disturbances as those associated with the

R. Govindarajan (ed.), Sixth IUTAM Symposium on Laminar-Turbulent Transition, 415–418.

inflections in the velocity distributions induced by the stationary crossflow vortices was developed further by Fischer & Dallmann (1991). Then, theoretical studies on the topic were carried out by Malik, Li & Chang (1994). The first spatial direct numerical simulation of the swept wing secondary instability was performed by Hoegberg & Henningson (1998). They examined both a small-amplitude random ('natural') disturbance added to a saturated crossfow vortex and its harmonic perturbation. It was found that the growth rate of the high-frequency secondary disturbance is considerably larger than that of the low-frequency one, thus, importance of high-frequency secondary instabilities for laminar flow breakdown was emphasized. Wassermann & Kloker (2002) also performed spatial direct numerical simulation focusing an infinite swept wing flow.

In the present study we focus on formation of crossflow vortex mode packets and their secondary instability in a swept wing boundary layer. Two modes of nonstationary instability, were found to develop with a preferred mode depending on the properties of the primary stationary disturbance.

2. EXPERIMENTAL SET-UP AND PROCEDURE

Results of the study were obtained in the wind tunnel of Thermo and Fluid Dynamics Department, Chalmers University of Technology. A wing model with C-16 airfoil profile was placed at the sweep angle of 45^0 in the test section of the facility, see Figure 1.

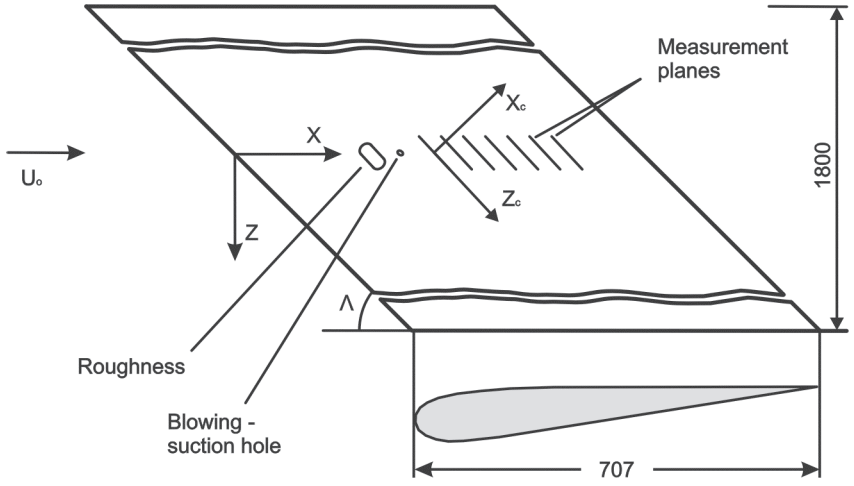

Figure 1. Experimental model

All the experimental runs were performed at the oncoming flow velocity U_0 of 8.2 ms^{-1}, making the chord-based Reynolds number of about 390 000, at the free-stream turbulence level well below 0.1%. The data were acquired from hot-wire measurements in z - slices along the wing leading edge. To generate stationary crossflow vortices in the laminar boundary layer different roughness elements were pasted onto the model surface at 0.3 of the wing chord. High-frequency travelling disturbances evolving along the streaks were excited by periodic blowing-suction through a hole of 0.8 mm in diameter on the surface of the model at 0.4 chord, the excitation frequency was 210 Hz.

3. RESULTS

The basic flow on the test surface of the wing was found as typical one for swept-wing configurations. As an example, mean velocity profiles measured without excitation of controlled stationary and nonstationary perturbations are given in Figure 2.

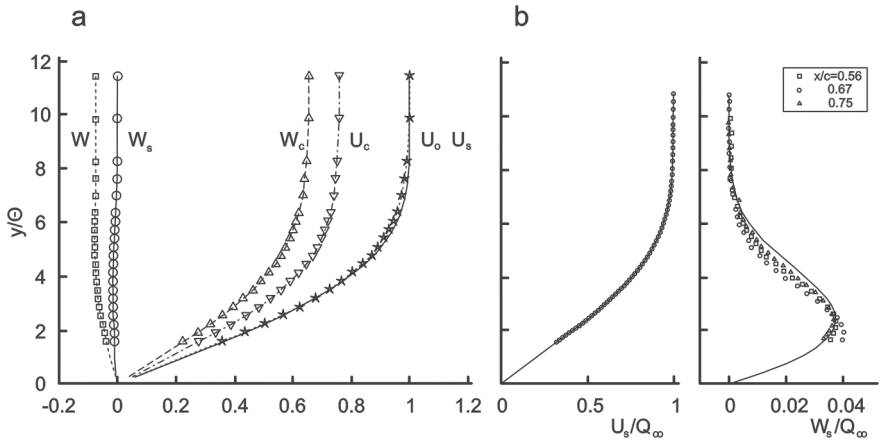

Figure 2. a - Undisturbed velocity profiles at 0.3 chord shown in different coordinate systems. b - Profiles of streamwise Us and spanwise Ws velocity in the coordinate system of external streamline

An illustration of the results obtained is given in figure 3 where two crossfow vortex mode packets generated by roughness elements are shown. These vortices were found as much different from each other due to mean velocity disturbances they produced and unsteady secondary instabilities evolving in each case.

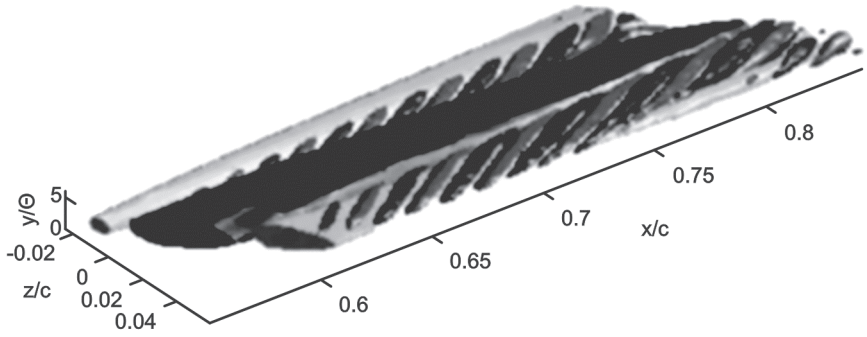

Figure 3. Forced periodical disturbances evolving along the stationary vortices

REFERENCES

Fischer, T. M. & Dallmann, U. 1991 Primary and secondary stability analysis of a three- dimensional boundary-layer flow. Phys. Fluids A 3 (10), 2378-2391.

Hoegberg, M. & Henningson, D. 1998 Secondary instability of crossflow vortices in Falkner-Skan-Cooke boundary layers. J. Fluid Mech. 368, 339-357.

Kohama, Y. 1987 Some expectation on the mechanism of crossflow instability in a swept-wing flow. Acta Mech. 66, 21-38.

Malik, M., Li, F. & Chang, C.-L. 1994 Crossflow disturbances in three-dimensional boundary layers: nonlinear development, wave interaction and secondary instability. J. Fluid Mech. 268, 1-36.

Poll, D. I. A. 1979 Transition in the infinite swept attachment line boundary layer. Aeronautical Quarterly 30, 607-629.

Wassermann, P. & Kloker, M. 2002 Mechanisms and passive control of crossflow-vortex-induced transition in a three-dimensional boundary layer. J. Fluid Mech. 456, 49-84.

BREAKDOWN OF A STREAK VIA DEVELOPMENT OF VARICOSE SECONDARY MODE ON THE STRAIGHT WING WITH PRESSURE GRADIENT

Victor V. Kozlov[1], Valery G. Chernoray[2], Yury A. Litvinenko[1], L. Löfdahl[2]
[1] *Institute of Theoretical and Applied Mechanics SB RAS, 630090 Novosibirsk, Russia.*
[2] *Dept. of Thermo and Fluid Dynamics, Chalmers University of Technology, 41296 Göteborg, Sweden. Contact address: kozlov@itam.nsc.ru*

Abstract: In the present experimental work, which utilizes a hot-wire visualization method, an influence of external pressure gradient on the development of secondary instabilities in the straight wing boundary layers has been demonstrated for the first time. The comparison of experimental data and direct numerical simulation results of this process has been given.

Key words: flow; turbulence; wind tunnel; wing; hot-wire anemometer; visualization; boundary layer; longitudinal structure; varicose mode.

1. INTRODUCTION

The latest stages of laminar flow breakdown on a wing are associated with formation of longitudinal low- and high-speed fluid structures (streaks), which further make the flow susceptible to secondary instabilities. In natural case such disturbances can be initiated by some surface irregularities such as uniform surface roughness or humps. On a swept wing, secondary instability of the crossflow plays an important role in the formation of streaks as shown in our previous studies [1]. It was found that the swept wing flow with the longitudinal vortices or streaks is secondary unstable to periodical disturbances. In the present investigation it is also shown that similar processes lead to the final flow breakdown at very late stages of transition. Additionally, for the first time it is demonstrated that the external pressure gradient has very strong influence on the development of secondary

R. Govindarajan (ed.), Sixth IUTAM Symposium on Laminar-Turbulent Transition, 419–424.

instabilities on the straight wing and hence the applicability of pressure gradient variation for the control purposes is proven in this case.

2. EXPERIMENTAL SET-UP AND PROCEDURE

The experiments were performed in a wind tunnel at Thermo and Fluid Dynamics, Chalmers University of Technology in Göteborg, Sweden. The facility is closed circuit, has a test section 3 m long, 1.8 m wide and 1.2 m high and a maximum free-stream velocity U_0 of 60 m/s. The free-stream turbulence level in the test section is well below 0.1% of U_0 in the velocity range U_0=5-15m/s and frequencies between 0.1 and 10000 Hz. The wing model used is made of wood and has a C-16 aerofoil. Its chord C is 500mm, span 1500 mm and the maximum thickness to chord ratio is 0.16 at about 0.3 chord. The top side of the wing after 0.4 chord represents a flat surface thus making it possible to study the flow without wall-curvature effects. The wing is mounted horizontally in the middle of the test section (Figure 1). To create the streaks, injection through a small hole on the surface of the wing was used in the same way as employed in the DNS work [2].

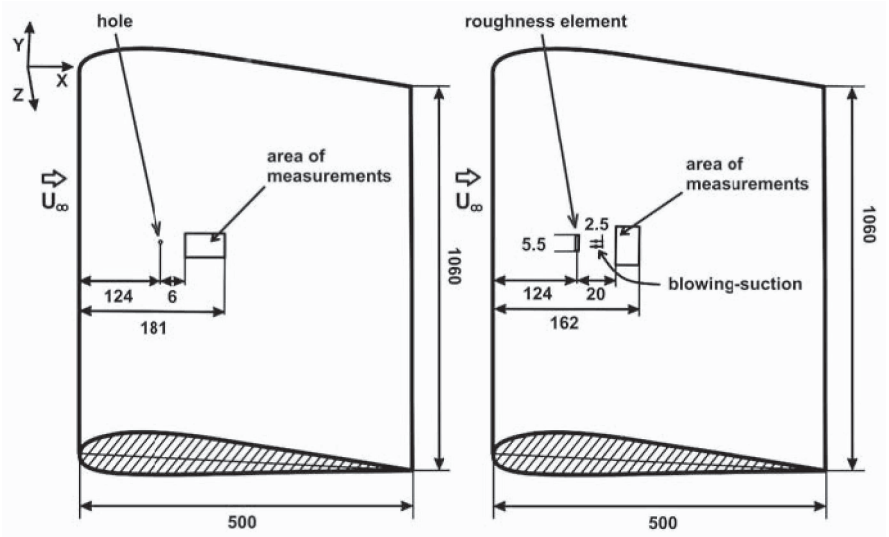

Figure 1. Sketch of experimental setup for Cases A, B (on the left). Sketch of experimental setup for Case C (on the right)

Also in the same fashion the varicose instability mode was artificially superimposed, thus allowing direct comparison of the experiment with the numerical simulation.

A method, which gains the advantage of flow visualization and gives quantitative description of the flow phenomena has been developed and employed in Chalmers for investigation of the three-dimensional features of flow breakdown. Comparing to traditional visualization methods which are limited in application and give little or no quantitative data for advanced analysis, a combination of accurate hot-wire anemometry techniques and modern data acquisition has been used to develop a new quantitative spatial ”visualization” during a series of experiments conducted. A comprehensive system for automated traversing and data acquisition has been designed and developed for this task. The developed hot-wire visualization technique is proved to be highly successful and great deal of experimental investigations was performed using this technique at this time.

3. EXPERIMENTAL RESULTS

The data were obtained in three experimental regimes, see Figure 1, with nearly zero streamwise pressure gradient (Case A) and the adverse one (Cases B, C). In Case C the boundary layer was perturbed by a cylindrical roughness element. The rectangles in the figure show the areas where measurements were performed. In Figures 2–4 the spatial hot-wire visualizations of the time-periodic part of the disturbance, its time-periodic part together with the mean velocity distortion, and the mean velocity distortion are shown which are very similar to the breakdown process from DNS of Figure 5. Qualitatively, the comparison is very good, thus the experimental and computational results demonstrate similar process of the streak breakdown. Also, the figures demonstrate the effect of pressure gradient on the streaks evolution which is observed here for the first time. It is clearly visible that the development of streaks is affected by the character of flow motion, and in the area of decelerated flow the spread rate of the streaks and the secondary disturbances is increased, and their growth is promoted. The reason for this is not absolutely clear at the moment so that a continuation of these studies is required with a support by theoretical investigations.

In conclusion, it should be noticed that the present data on the streak breakdown support the results on turbulence generation in the wall region of a turbulent boundary layer obtained in [2] through direct numerical simulations. Future work could include investigation of other instability modes and the influence of favorable pressure gradient on the streaks.

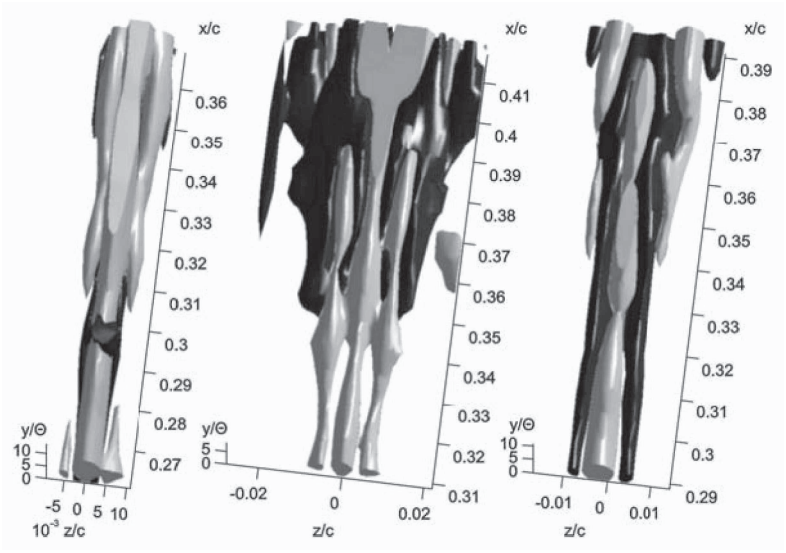

Figure 2. Hot-wire visualization of the total velocity disturbance: (a) Case A, $dP/dx \approx 0$, (b) Case B, $dP/dx > 0$, (c) Case C, $dP/dx > 0$ with roughness element

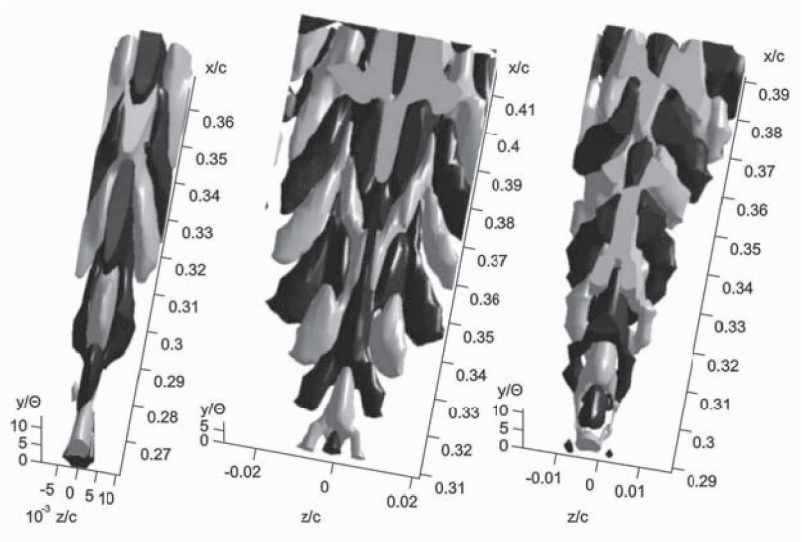

Figure 3. Hot-wire visualization of the time-periodic part of the disturbance: (a) Case A, $dP/dx \approx 0$, (b) Case B, $dP/dx > 0$, (c) Case C, $dP/dx > 0$ with roughness element

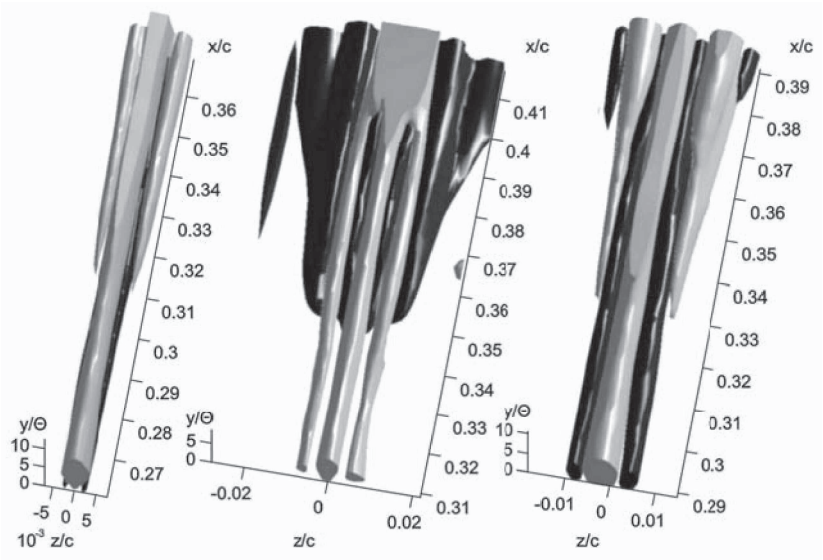

Figure 4. Hot-wire visualization of the mean velocity distortion. (a) Case A, $dP/dx \approx 0$, (b) Case B, $dP/dx > 0$, (c) Case C, $dP/dx > 0$ with roughness element

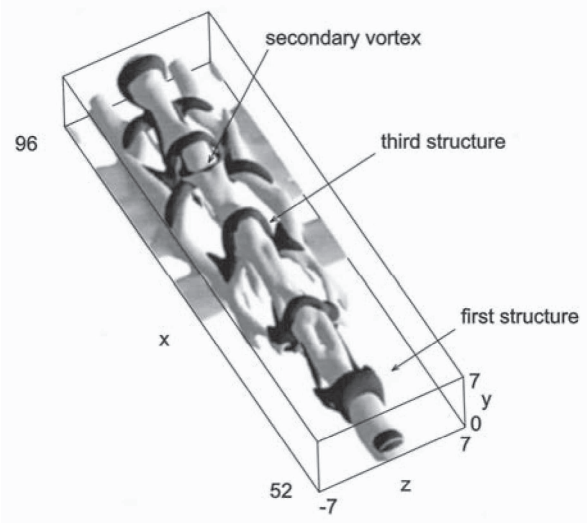

Figure 5. Breakdown of a streak via development of a varicose secondary mode. From DNS results by Skote, Haritonidis, and Henningson [2]

The work was supported by the Russian Foundation for Basic Research (Grant No. 02-01-00006), by the Grant of the President of the Russian Federation of Leading Scientific Schools of RF No. SS-964.2003.1 and INTAS (No. 00-00232).

REFERENCES

1. Chernoray, V.G., Dovgal, A.V., Kozlov, V.V., Löfdahl, L., 2005, Experiments on secondary instability of streamwise vortices in a swept wing boundary layer, Accepted for publication in Journal of Fluid Mechanics.
2. Skote, M., Haritonidis, J.H., and Henningson, D.S., 2002, Varicose instabilities in turbulent boundary layers, Physics of Fluids 14, pp. 2309-2323.

LINEAR OPTIMAL CONTROL OF TRANSITION IN PLANE CHANNEL FLOWS USING DIFFERENT OBJECTIVE FUNCTIONS

K. Rajesh[1], Manmohan Pandey[2], Anoop K. Dass[3],
[1] *Engineering Research Center, Tata Motors Ltd., Pune, INDIA*
rajesh21stcentury@yahoo.com
[2] *Department of Mechanical Engineering, Indian Inst. of Tech. Guwahati, INDIA*
manmohan@iitg.ac.in
[3] *Department of Mechanical Engineering, Indian Inst. of Tech. Guwahati, INDIA*
anoop@iitg.ac.in

Abstract: Control of transition in plane channel flows can be achieved by applying linear optimal control to the state equations obtained by a suitable discretization of the Fourier transformed and linearized Navier-Stokes equations. Different flow properties can be affected through the choice of the objective function used for optimal control. In the present work, various control algorithms have been obtained by using full state feedback. The objective function has been chosen using a measure of the energy of flow perturbations, with various weight matrices. The performance of the controllers thus designed has been studied.

Keywords: control of transition; flow control; linear control; optimal control; LQ regulator; objective function.

1. INTRODUCTION

The process of transition from laminar to turbulent flow is basically a non-linear process. Most often, in the initial stages of transition, only small perturbations dominate, whose flow behavior can be approximated by linearized Navier-Stokes equations. Linear control works very well as long as perturbations are maintained small. In optimal control, the controller is designed in order to minimize a suitably chosen objective function (performance index).

R. Govindarajan (ed.), Sixth IUTAM Symposium on Laminar-Turbulent Transition, 425–430.

The complicated physics of a transitional flow makes it difficult to identify the key mechanisms to be targeted by an effective control scheme. Different flow properties can be affected through the choice of objective function, which, therefore, is an important part of the formulation of the optimization problem. A measure of the energy of flow perturbations is often used in the objective function. In the current work, the performance of the controller is studied by varying the weight matrix ($\mathbf{Q}$).

2. PROBLEM FORMULATION

Consider a steady plane channel flow with maximum velocity U_0 and channel half-width δ. Non-dimensionalizing all velocities by U_0 and lengths by δ, the mean velocity profile in the streamwise direction (x) may be written $U(y) = 1 - y^2$ on the domain $y \in [-1, 1]$. The equations governing small, incompressible, three-dimensitional perturbations u, v, w, p to the mean flow U are given by the linearized Navier-Strokes and continuity equations. Now Orr-Sommerfeld and Squire equations are derived by manipulating the Fourier transformed Navier-Stokes equations.

$$\begin{aligned} \Delta\dot{v} &= \{-ik_xU\Delta + ik_xU^{''} + \Delta(\Delta/Re)\}v \\ \dot{\omega} &= \{-ik_zU^{'}\}v + \{-ik_xU + \Delta/Re\}\omega \end{aligned} \tag{1}$$

where, $\Delta \equiv \partial^2/\partial y^2 - k_x^2 + k_z^2$, k_x and k_z being the wave numbers along x and z directions, and $\omega \equiv \partial u/\partial z - \partial w/\partial x$ is the Fourier tranformed wall-normal component of vorticity fiuctuation. The continuous equations for the v, ω perturbations in Eq. (1) are now discretized on a grid of $N+1$ Chebyshev-Gauss-Lobatto points in the wall normal direction. The Ô$_y$Õderivatives of$v$ and ω can be expressed as linear combinations of the grid point values of v and ω, respectively (Canuto et al., 1988). Applying homogenous Neumann boundary condition on v by modifying the Þrst derivative matrix, Eq. (1) can be expressed in the form (Bewley and Liu, 1998)

$$\dot{\mathbf{x}} = \mathbf{A}\,\mathbf{x} + \mathbf{B}\,\mathbf{u} \tag{2}$$

The vector $\mathbf{x}$ is called as state vector as it contains the wall-normal fiuctuation v and normal vorticity fiuctuations ω at the grid points on the interior of the channel. The vector $\mathbf{u}$, which contains the blowing/suction velocity at the top and bottom walls, is referred to as the ÔcontrolÕ.

For simplicity, we have restricted our attention to one supercritical case and one subcritical case, as defined by Bewley and Liu, 1998. Case (i) is given by Re=10000, k_x=1, and k_z=0. As $k_z = 0$, eigenmodes of ω equation are entirely decoupled from eigenmodes of v equation, but fortunately, all the eigenmodes of ω are stable. Hence, for the purpose of studying the effect of control in case (i) we restrict ourselves to the eigenmodes of v. For Case (ii), we have

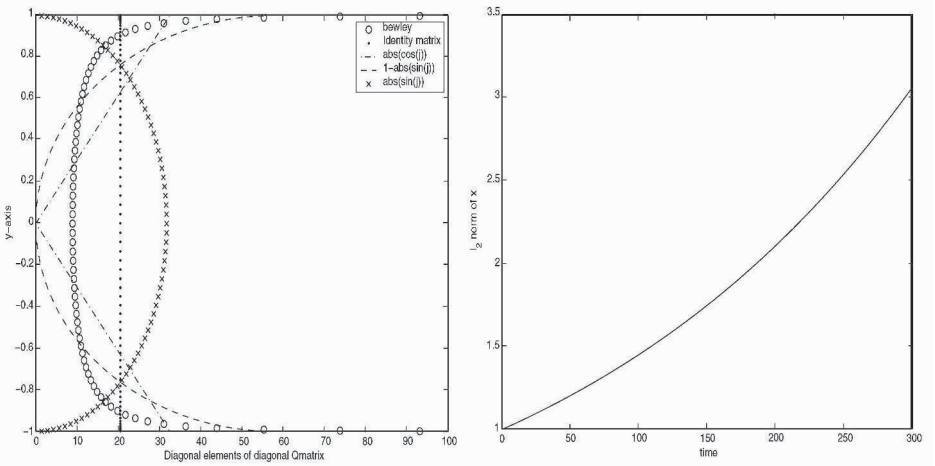

(a) Various weight matrices(Q) (b) l_2 norm of $\mathbf{x}$ for uncontrolled system(case(i))

Figure 1.

taken Re=5000, k_x=0, k_z=2.044, $k_x = 0$. In this case, eigenmodes of v and ω are coupled, hence we have to consider full coupled equations of v and ω. The system (2) can be stabilized by simply closing the loop with full state feedback. This is done by using linear state feedback in the form given below.

$$\mathbf{u} = \mathbf{K}\,\mathbf{x} \tag{3}$$

We have to find matrix $\mathbf{K}$ such that the controller feedback $\mathbf{u}$ forces the state $\mathbf{x}$ towards zero in an optimal way. This is done by using linear state feedback in the form $\mathbf{u} = \mathbf{K}\mathbf{x}$. We have to find matrix $\mathbf{K}$ such that the controller feedback $\mathbf{u}$ forces the state $\mathbf{x}$ towards zero in an optimal way. The objective function (performance index) for optimal control can be defined as

$$\mathfrak{J} = \int_0^\infty (\mathbf{x}^*\mathbf{Q}\mathbf{x} + l^2\mathbf{u}^*\mathbf{u})dt, \tag{4}$$

where $\mathbf{Q}$ is the weight matrix, which defines the weight of disturbances. The matrix $\mathbf{K}$ can be determined by solving the associated Riccati problem. The performance of the controller designed in this way will depend on the choice of the performance index, i.e., the choice of the matrix $\mathbf{Q}$. In the present work, Þve diagonal $\mathbf{Q}$ matrices have been used, as shown in Fig. 1(a).

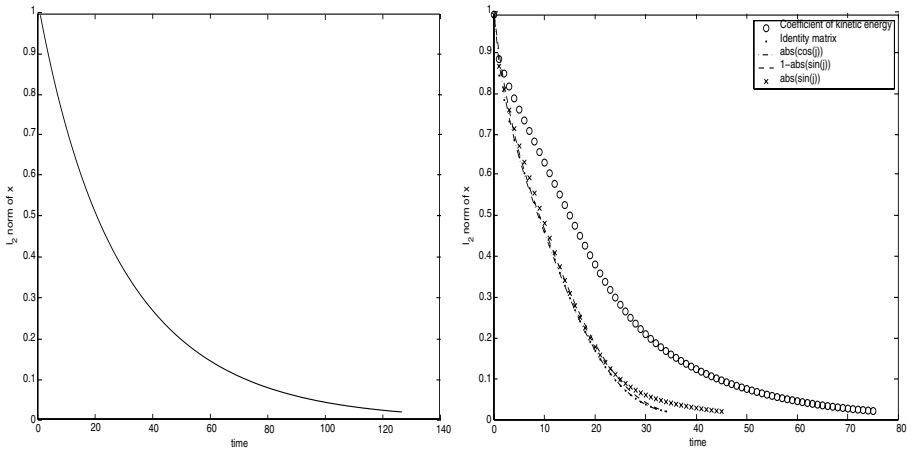

(a) l_2 norm of $\mathbf{x}$ for uncontrolled system (case(ii)) (b) l_2 norm of $\mathbf{x}$ for $l^2 = 1$

Figure 2.

3. NUMERICAL INTEGRATION

The numerical integration was done on the controlled and uncontrolled systems to study the decay of norm of state vector and to study the total control energy consumed. First, the uncontrolled system was integrated for random initial perturbation. Figure 1(b) shows the growth of l_2 norm of the state vector $\mathbf{x}$ for case (i). Figure 2(a) shows the growth of l_2 norm of $\mathbf{x}$ for case(ii). Since numerical integration did not show any subcritical transition ,we will not do this analysis for case (ii) for closed loop systems. In order to do a comparative study of controllers designed using different weight matrices, numerical integration of the reduced order system with full state information feedback control was done for case (i). The perturbation was given as a linear combination of uncontrolled and a few least stable eigenvectors. Figure 2(b) shows the decay of l_2 norm of $\mathbf{x}$ with time for $l^2 = 1$ and Fig 3(a) shows cumulative control energy expenditure over time for $l^2 = 1$.

We can note that the controller derived using a weight matrix ($\mathbf{Q}$) from the Ôcoefficient of kinetic energyÕ is slower than the other weight matrices but its control energy expenditure is also very low. Now, the choice of the controllers will depend on the designerÕs preference.

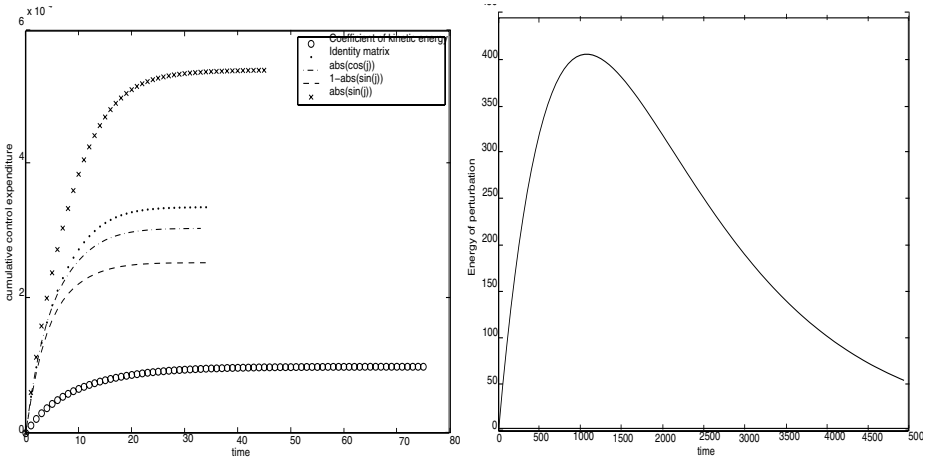

(a) cumulative control energy expenditure for $l^2 = 1$ (b) Variation of energy of perturbation with time

Figure 3.

4. TRANSIENT ENERGY GROWTH

Energy of ßow perturbations at any time τ is given by (Bewley and Liu, 1998)

$$\mathfrak{E} = \chi^*(e^{\Lambda^* t}\Xi^*\mathbf{Q}\Xi\mathbf{e}^{\mathbf{\Lambda t}})\chi \tag{5}$$

Where χ is projection vector of initial state $\mathbf{x}(\mathbf{0})$, Λ_k is eigenvalues matrix, and Ξ is right eigenvector matrix. Normalizing it with initial perturbation, It can be expressed as,

$$\theta = \frac{\mathfrak{E}(\tau)}{\mathfrak{E}(0)} = \frac{\chi^*(e^{\Lambda^* t}\Xi^*\mathbf{Q}\Xi\mathbf{e}^{\mathbf{\Lambda t}})\chi}{\chi^*(\Xi^*\mathbf{Q}\Xi)\chi} \tag{6}$$

As case (i) has already been studied using numerical integration, we analyze the transient energy growth for case (ii) only. Figure 3(b) shows the variation of the energy of perturbation with time for the uncontrolled system of case (ii). χ is chosen to be the vector of squares of reciprocals of corresponding eigenvalues. For the system with full state feedback control, Figure 4(a) shows the variation of the energy of perturbation with time for $l^2 = 10$ and Fig 4(b) shows cumulative control energy expenditure ($\int_0^t u'u\,dt$) over time for $l^2 = 10$. χ was chosen to be the vector of squares of reciprocals of corresponding eigenvalues. From Fig 4(a) and Fig 4(b) it is clear that a weight matrix based on the coefficient of kinetic energy is the optimal choice.

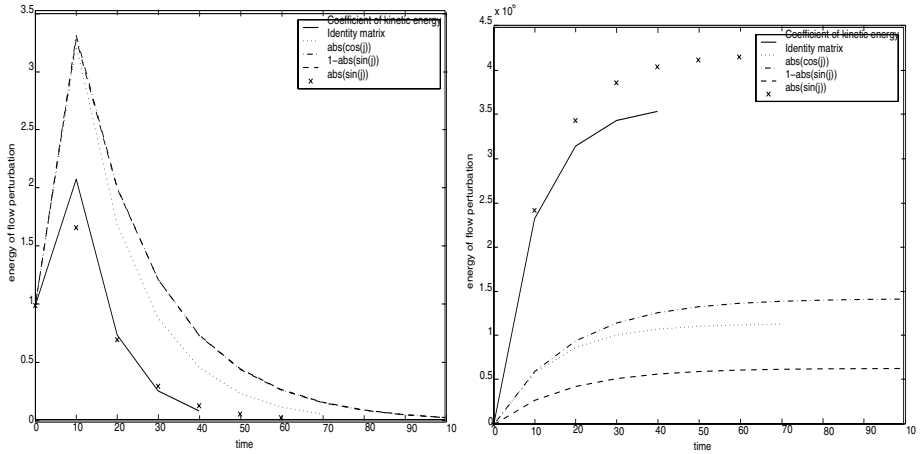

(a) variation of energy of perturbation with time for $l^2 = 10$ (b) cumulative control energy expenditure for $l^2 = 10$

Figure 4.

5. CONCLUSIONS

The following conclusions can be drawn from the present study.

1 For the supercritical case, the weight matrix from coefficient of kinetic energy gives cheaper control compared to other controllers.

2 For the supercritical case, the weight matrix from $1-$cosine function gives faster rate of control compared to controllers based on other weight matrices.

3 For the subcritical case, it is observed that the weight matrix from coefficient of kinetic energy is the optimal choice.

REFERENCES

Bewley, T.R. and Liu, S. Optimal and robust control and estimation of linear paths to transition J. Fluid Mech. v 365, p 305-349. 1998.

Butler, K. M. and Farrell, B. F. 1992 Three-dimensional optimal perturbations in viscous shear flows. Phys. Fluids A 4, 1637-1650.

Canuto, C. Hussaini, M. Y. Quarteroni, A. and Zang, T. A. 1988 Spectral Methods in Fluid Dynamics. Springer.

ESTIMATOR-BASED CONTROL OF TRANSITION IN PLANE CHANNEL FLOWS USING VARIOUS COVARIANCE MATRICES

K. Rajesh[1], Manmohan Pandey[2], Anoop K. Dass[3],
[1]*Engineering Research Center, Tata Motors Ltd., Pune, INDIA*
rajesh21stcentury@yahoo.com
[2]*Department of Mechanical Engineering, Indian Inst. of Tech. Guwahati, INDIA*
manmohan@iitg.ernet.in
[3]*Department of Mechanical Engineering, Indian Inst. of Tech. Guwahati, INDIA*
anoop@iitg.ernet.in

Abstract: Control of transition in plane channel flows can be achieved by applying linear control to a suitable reduced-order system of state equations, with an appropriate state estimator. In the present work, a comparative study of various estimator-based controllers has been carried out. The state estimators have been designed as Kalman filters using various covariance matrices. The performance of linear optimal controllers based on these estimators has been studied by numerical integrations.

Keywords: Flow control; linear control; optimal control; state estimators; Kalman filters.

1. INTRODUCTION

Control of transition in plane channel flows can be achieved by applying linear optimal control to the state equations obtained by a suitable discretization of the Fourier transformed and linearized Navier-Stokes equations. Various control algorithms using full state feedback have been studied in a related work (Rajesh et al., 2004). In practice, a controller based on wall-measurements is more feasible than full state feedback as it is not always possible to measure all the state variables. The state variables can be estimated by using a state estimator, which can be designed in an optimal way as a Kalman filter. Design

R. Govindarajan (ed.), Sixth IUTAM Symposium on Laminar-Turbulent Transition, 431–436.

of a Kalman filter depends on the choice of the covariance matrices of state disturbance and measurement noise. The performance of the estimator based controller will depend on this choice.

2. PROBLEM FORMULATION

A reduced-order model of plane channel flow can be derived in the form of state equations $\dot{\mathbf{x}} = \mathbf{A}\,\mathbf{x} + \mathbf{B}\,\mathbf{u}$ (Bewley and Liu, 1998; Rajesh et al., 2004). The state-vector ($\mathbf{x}$) contains the wall-normal velocity and vorticity fluctuations (v and ω) at the grid points on the interior of the channel. The control ($\mathbf{u}$) contains the blowing/suction velocities at the top and bottom walls. For simplicity, we have restricted our attention to one supercritical case and one subcritical case, as defined earlier (Bewley and Liu, 1998; Rajesh et al., 2004).

We assume that measurements made at the wall provide information about the streamwise and spanwise skin friction, from which (subtracting out the known influence of $\partial v/\partial x$ and $\partial v/\partial z$ from the stress tensor at the wall) we may define an output vector y_m as function of values of $\partial u/\partial y$ and $\partial w/\partial y$ at the walls. Using Orr-Sommerfeld and Squire equations, continuity equation and definition of vorticity, u and w can be expressed in terms of ω and $\partial v/\partial y$. Thus y_m can be expressed as $\mathbf{y_m} = \mathbf{C}\,\mathbf{x} + \mathbf{D}\,\mathbf{u}$ (Bewley and Liu, 1998). Now the equations governing the small flow perturbation in a laminar channel flow may be expressed in the standard form

$$\begin{aligned} \dot{\mathbf{x}} &= \mathbf{A}\,\mathbf{x} + \mathbf{B}\,\mathbf{u} \\ \mathbf{y} &= \mathbf{C}\,\mathbf{x} \end{aligned} \tag{1}$$

where $\mathbf{y}$ is obtained from $\mathbf{y_m}$ by subracting the terms containing control. In order to close the loop a system model with a structure similar to the system itself is used, such that

$$\begin{aligned} \dot{\hat{\mathbf{x}}} &= \mathbf{A}\,\hat{\mathbf{x}} + \mathbf{B}\,(\mathbf{u} - \hat{\mathbf{u}}) \\ \hat{\mathbf{y}} &= \mathbf{C}\,\hat{\mathbf{x}} \end{aligned} \tag{2}$$

with feedback $\hat{\mathbf{u}}$ based on the difference between the observations of the state $\mathbf{y}$ and the corresponding quantity in the model $\hat{\mathbf{u}}$ such that $\hat{\mathbf{u}} = \mathbf{L}(\mathbf{y} - \hat{\mathbf{y}})$ The control $\mathbf{u}$, in turn, is based on the state estimate $\hat{\mathbf{x}}$ such that $\mathbf{u} = \mathbf{K}\hat{\mathbf{x}}$. Equations (1) and (2) represent the plant and the estimator (observer), respectively. Optimal control and estimation can be achieved by designing a linear-quadratic Gaussian (LQG) regulator, *i.e.*, a linear-quadratic regulator based on a Kalman filter. The problem at hand is to compute linear time-invariant (LTI) matrices $\mathbf{L}$ and $\mathbf{K}$ such that (i) the estimator feedback forces the state estimate in the estimator towards the state $\mathbf{x}$ in the plant, and (ii) the controller feedback $\mathbf{u}$ forces the state $\mathbf{x}$ towards zero in the plant. This is done by solving two Riccati problems, associated with the plant and the estimator, respectively.

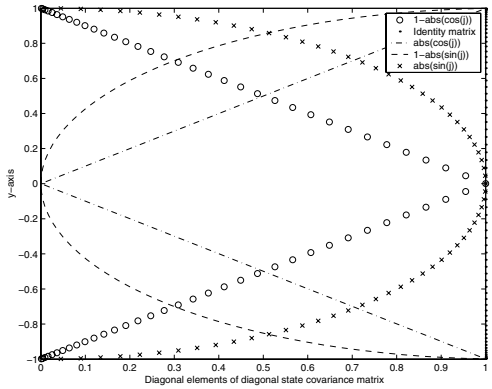

Figure 1. Covariance matrices of state disturbance

Various controllers were designed earlier by using different weight matrices and the cost of control (Rajesh et al., 2004). Here, various Kalman filters have been designed by using different covariance matrices as shown in Fig. 1. The problem is normalized such that the maximum singular values of the covariance matrices of state disturbance and sensor noise are equal to unity and α^2 (a design parameter), respectively.

3. NUMERICAL INTEGRATION

The numerical integration is done on the controlled and uncontrolled systems to study the decay of norm of state vector and to study the total control energy consumed. It was observed earlier (Rajesh et al., 2004) that numerical integration cannot capture the instability in sub-critical transition. Hence, we will discuss only supercritical transition (case (i)) here.

Numerical integration of the reduced order system with estimator alone was done for case (i). Figure 2 shows the decay of l_2 norm of $\hat{\mathbf{x}}$ with time for $\alpha^2 = 1$. The initial estimator error ($\hat{\mathbf{x}}$) is given as a linear combination of uncontrolled and few least stable eigenvectors. From Fig. 2 it is also clear that covariance matrix based on *sine* and *1−cosine* function gives better state estimation than the remaining ones.

Numerical integration of the reduced order system with compensator was done by fixing the coefficient of kinetic energy as weight matrix and $\alpha = 100$. Figure 3(a) shows the decay of l_2 norm of $\mathbf{x}$ with time for $l^2 = 1$ and $l^2 = 100$ and Fig 3(b) shows cumulative control energy expenditure over time for $l^2 = 1$ and $l^2 = 100$. The perturbation is given as a linear combination of uncontrolled and a few least stable eigenvectors. Table 1 shows settling time for the system with estimator based feedback control for coefficient of kinetic energy as weight matrix ($\alpha = 100$). Thus, considering the speed of control

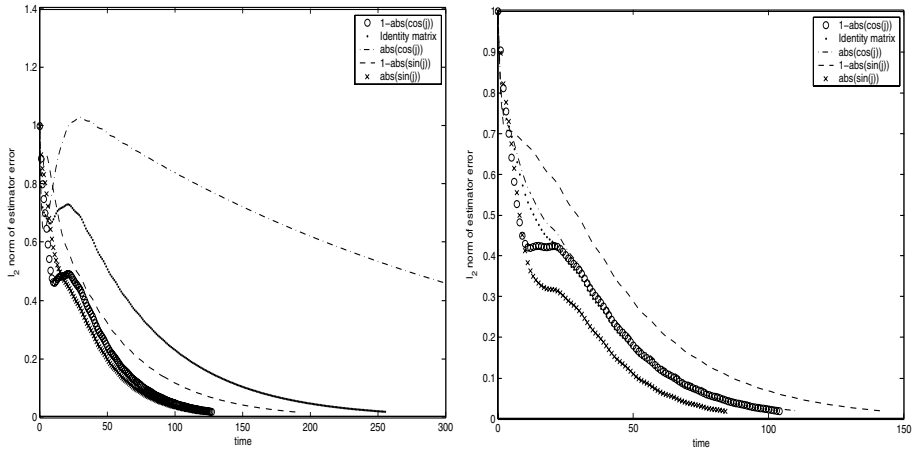

(a) l_2 norm of $\hat{\mathbf{x}}$ for $\alpha^2 = 1$

(b) l_2 norm of $\mathbf{x}$ for $\alpha^2 = 100$

Figure 2. Estimation errors for systems with various covariance matrices

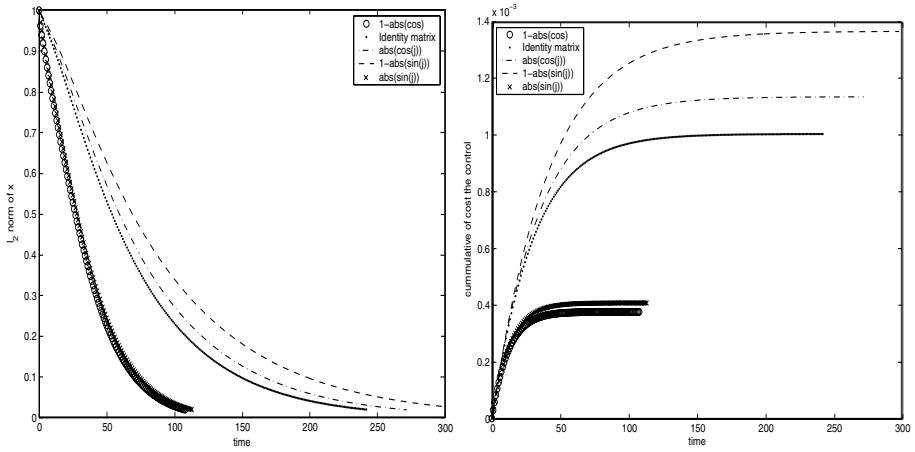

(a) l_2 norm of $\mathbf{x}$ for $l^2 = 1$ and various covariance matrices

(b) cumulative control energy expenditure for $l^2 = 1$ and various covariance matrices

Figure 3. The system with estimator based feedback control for coefficient of kinetic energy as weight matrix ($\alpha = 100$)

Table 1. Settling time (sec) for the system with estimator based feedback control for coefficient of kinetic energy as weight matrix ($\alpha = 100$)

-	$l^2 = 1$	$l^2 = 100$
1-cosine function	109	131
Identity matrix	243	254
Cosine function	273	283
1-Sine function	299	299
Sine function	114	137

Table 2. Settling time for estimator based control for case (ii) for $l^2 = 100$

covariance matrices	$\alpha^2 = 0.01$	$\alpha^2 = 0.1$	$\alpha^2 = 1$	$\alpha^2 = 10$	$\alpha^2 = 100$	$\alpha^2 = 1000$
1-cosine function	110	-	100	100	110	110
Identity matrix	-	80	90	90	110	110
Cosine function	-	-	-	150	100	110
1-Sine function	110	100	110	110	130	150
Sine function	-	110	100	100	100	110

and cost of control, it is clear that that the covariance matrix based on *1-cosine* function is the most suitable for the supercritical case.

4. TRANSIENT ENERGY GROWTH

Energy of flow perturbations at any time τ is given by (Bewley and Liu, 1998)

$$\mathfrak{E} = \chi^*(e^{\Lambda^* t}\Xi^*\mathbf{Q}\Xi\mathbf{e}^{\mathbf{\Lambda t}})\chi \tag{3}$$

Where χ is projection vector of initial state $\mathbf{x}(\mathbf{0})$, Λ_k is the matrix of eigenvalues, and Ξ is right eigenvector matrix. Normalizing it with initial perturbation, It can be expressed as,

$$\theta = \frac{\mathfrak{E}(\tau)}{\mathfrak{E}(0)} = \frac{\chi^*(e^{\Lambda^* t}\Xi^*\mathbf{Q}\Xi\mathbf{e}^{\mathbf{\Lambda t}})\chi}{\chi^*(\Xi^*\mathbf{Q}\Xi)\chi} \tag{4}$$

Since case (i) has already been analyzed using numerical integration, only case (ii) has been analyzed for transient energy growth. Transient energy growth is calculated over time for the system of case (ii) with various compensators, by using coefficient of kinetic energy as weight matrix and $l^2 = 100$. Fig 4(a) shows the variation of energy of perturbation with time with time for $\alpha^2 = 100$. Fig 4(b) shows the variation of cumulative cost of the control energy with time with time for $\alpha^2 = 100$. χ has been chosen to be the vector of squares of reciprocals of corresponding eigenvalues. Table 2 shows settling time for various α^2 and covariance matrices. From these results, we can infer that the identity matrix is a good choice for the covariance matrix for estimator based controller for the subcritical case.

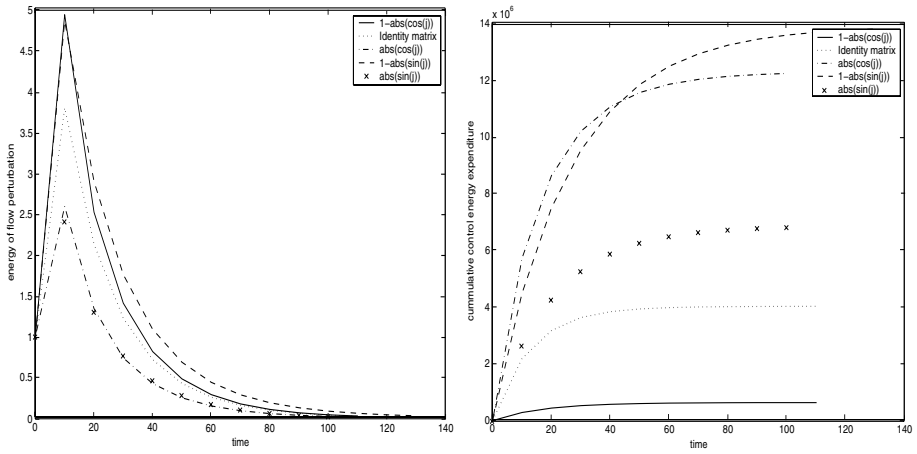

(a) l_2 norm for $\alpha^2 = 100$ and $l^2 = 100$

(b) Cumulative cost of the control energy for $\alpha^2 = 100$ and $l^2 = 100$

Figure 4. System with estimator based control for coefficient of kinetic energy as weight matrix

5. CONCLUSIONS

The following conclusions can be drawn from the present study.

1 For the supercritical case, the covariance matrices based on *sine* and *1−cosine* functions give better state estimation than other ones.

2 The estimator based controller derived from the covariance matrix based on *1-cosine* function shows the best performance for the supercritical case.

3 For the subcritical case, the covariance matrix based on the identity matrix is most preferable.

REFERENCES

Bewley, T.R. and Liu, S. 1998, Optimal and robust control and estimation of linear paths to transition J. Fluid Mech. v 365, p 305-349.

Butler, K. M. and Farrell, B. F. 1992, Three-dimensional optimal perturbations in viscous shear flows. Phys. Fluids A 4, 1637-1650.

Rajesh K., Pandey M. and Dass A.K. 2004, Linear optimal control of transition in plane channel flows using various objective functions. *IUTAM Symposium on Laminar-Turbulent Transition*, Bangalore, India.

CONTROL OF TURBULENT BOUNDARY LAYERS BY UNIFORM WALL SUCTION AND BLOWING

Shuya Yoshioka[1,2] and P. Henrik Alfredsson,[1]
[1]*KTH Mechanics, SE-100 44 Stockholm, Sweden,* [2]*at present, Institute of Fluid Science, Tohoku University, 2-1-1 Katahira, Aoba-ku, Sendai 9808577, Japan*

Abstract: The effect of uniform wall suction and blowing on a turbulent boundary layer was experimentally investigated. It was discovered that the development of the boundary layer is suppressed by suction and promoted by blowing. The turbulence intensity in the outer part increases with blowing and decreases with suction, however in the inner part the intensity is only slightly affected if scaled with the free-stream velocity.

Keywords: flow control; turbulent boundary layer; wall suction and blowing; coherent structure; VITA analysis.

1. INTRODUCTION

The aim of this research is to investigate the effect on the turbulent boundary layer by uniform wall suction and blowing. Early experiments (Simpson et al., 1969, Antonia et al., 1988) show that the boundary layer thickness and turbulence statistics are changed by suction and blowing. Recent numerical results (Mariani et al., 1993, Sumitani and Kasagi, 1995, Chung and Sung, 2001) show that suction and blowing modify the large scale structures in the boundary layer. In the present study the turbulence statistics are precisely measured varying the suction and blowing velocity. The coherent structures inside the boundary layers was also investigated using the so called VITA method from the measured velocity signals.

2. EXPERIMENTAL SETUP

The experiments were conducted in the MTL-wind tunnel at KTH. The test section of the wind tunnel is shown in Fig. 1. We use a coordinate system with its origin fixed at the centre of the leading edge of the plate. The x, y- and z-axis are directed in the downstream, wall normal and spanwise directions.

A permeable, porous plastic material of 3.2 mm in thickness, covers 2.25 m (length)$\times$1.0 m (width) of the upper surface of the test plate, see Yoshioka

R. Govindarajan (ed.), Sixth IUTAM Symposium on Laminar-Turbulent Transition, 437–442.

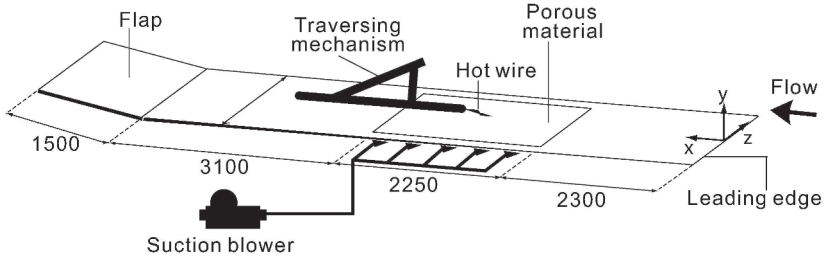

Figure 1. Schematic of experimental facility. Dimensions are in millimeters

et al. (2004) for details. Through this porous surface, uniform suction and blowing were applied starting from $x = 2.3$ m. The free-stream velocity was fixed to U_∞ = 8.0 m/s. The suction and blowing rate V_0 was varied in the range –0.3% $\leq V_0/U_\infty \leq +0.3\%$. The Reynolds number based on the momentum thickness and the free-stream velocity was Re_θ = 3900 at $x = 3.7$ m at the no suction or blowing condition. Velocity measurements were made with hot wire anemometry with a single sensor probe. The sampling time was typically 120 sec and the sampling rate 5 kHz.

3. RESULTS

In Fig. 2 the downstream development of the displacement thickness δ_1 is shown for the different suction and blowing cases. The growth of the boundary layer thickness is clearly shown to be suppressed by suction. For suction velocity of $V_0/U_\infty = -0.2\%$ it seems that the boundary layer reaches the asymptotic state and for $V_0/U_\infty = -0.3\%$ the displacement thickness is decreasing in downstream direction. For the blowing cases the growth of the boundary layer thickness is promoted and the higher the blowing rate the thicker the boundary layer becomes.

The distributions of velocity and turbulence intensity in wall unit are shown in Figs. 3(a) and 3(b) and the effects of blowing and suction are clearly seen. The velocity gradient at the wall is increased 26% by suction of $V_0/U_\infty = -0.3\%$, and decreased 29% by blowing of $V_0/U_\infty = +0.3\%$ at $x = 4.0$ m. For the suction boundary layer at asymptotic conditions (i.e. no boundary layer growth) it is easy to show that

$$\frac{\tau_w}{\rho U_\infty^2} = \left(\frac{u_\tau}{U_\infty}\right)^2 = \frac{V_0}{U_\infty} \tag{1}$$

where u_τ is the friction velocity. The friction velocity is determined from the mean velocity profile close to the wall (at least four measurement points in

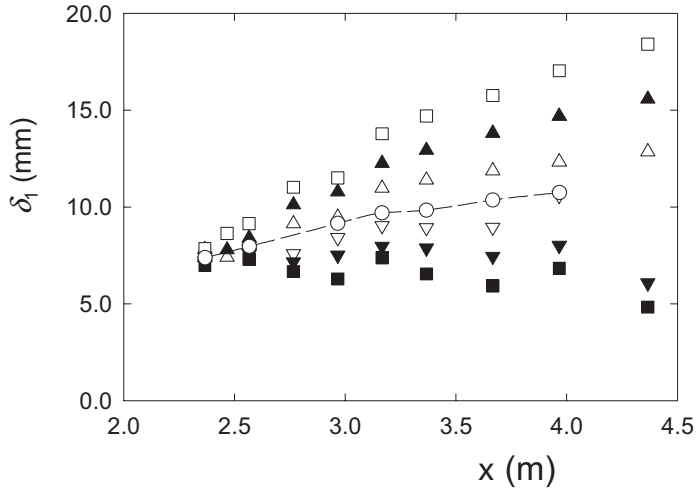

Figure 2. Downstream development of displacement thickness. Open symbols denote data from experiments without suction or blowing. No suction, ○, suction rate: ■: -0.3%; ▼: -0.2%; ▽: -0.1%, blowing rate: △: $+0.1\%$; , ▲: $+0.2\%$; □: $+0.3\%$

the linear region). This method to determine the friction velocity seems to be fairly accurate, since for the case with 0.2% suction the boundary layer thickness seems to stay constant and $u_\tau/U_\infty = 0.045$ which is close to the value obtained from eq. 1 for this case.

The large changes of u_{rms}/u_τ with different V_0 is mainly due to the change of u_τ. The data shown in Fig. 3(b) are re-plotted in Fig. 4 where instead the turbulence intensity is normalized by the free-stream velocity, and the distance from the wall is normalized by the displacement thickness. In these figures

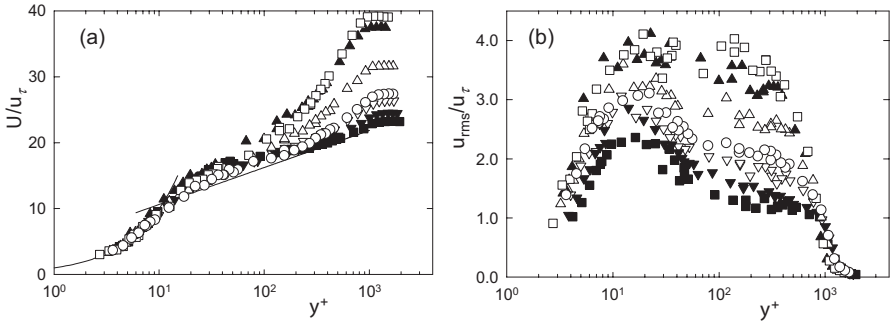

Figure 3. Turbulence statistics in wall unit. (a) Time averaged velocity, (b) Turbulence intensity. Symbols as in Fig. 2

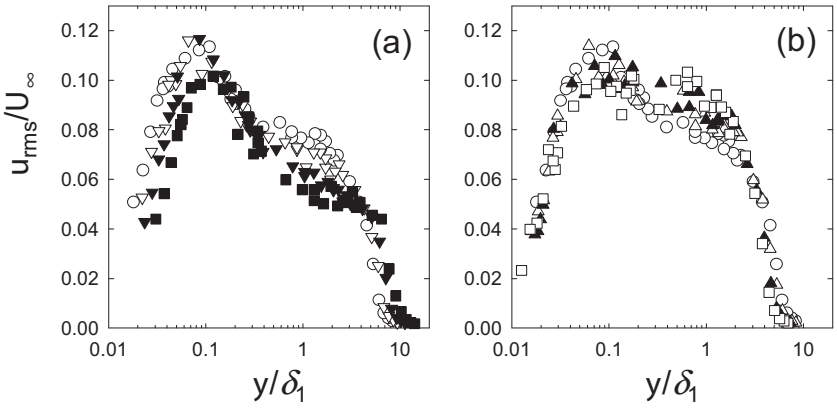

Figure 4. Distribution of u_{rms} normalized by free-stream velocity. (a) Suction, (b) blowing. Symbols as in Fig. 2

some interesting features are found. For all cases shown in Figs. 4(a) and 4(b) there are two peaks in the profiles, one is a sharp peak near the wall in the buffer layer and the other is a broad peak (or plateau) away from the wall. When suction is applied (see Fig. 4(a)), the value of the peak away from the wall decreases with an increase of the suction rate. The value of the near wall peak is, on the other hand, not affected by suction of $V_0/U_\infty = -0.1\%$, -0.2%, whereas it decreases for $V_0/U_\infty = -0.3\%$. In the blowing cases shown in Fig. 4(b), the peak value decreases with increasing blowing rate at the near wall peak, whereas the peak away from the wall increases in amplitude.

The peculiar behavior of the turbulence intensity mentioned above may be caused by the change of the coherent structures in the turbulent boundary layer. To further investigate this effect, we attempted to extract the large scale motions from the velocity signals by using well known VITA method (see for instance Johansson and Alfredsson, 1982). The short time variance, $var(t,T)$, is first calculated from the velocity signals varying the integration time T according to

$$var(t,T) = \frac{1}{T}\int_{t-T/2}^{t+T/2} u^2(s)ds - \left(\frac{1}{T}\int_{t-T/2}^{t+T/2} u(s)ds\right)^2 \qquad (2)$$

and when $var > ku_{rms}^2$, where $k = 1$, a coherent structure is assumed to pass the sensor. An example of this procedure is shown in Fig. 5. When T becomes large the second term of the right hand side of eq. 2 tends to

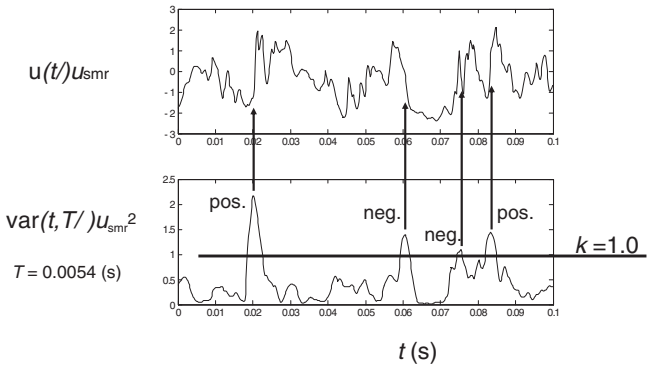

Figure 5. Example of event detection by VITA method, $T = 0.0054$ sec, $k = 1.0$

zero and thus $var \rightarrow u_{rms}^2$. As T approaches zero the two terms of on the right hand side of eq. 2 become identical, so that $var \rightarrow 0$. This leads to that at some intermediate value of T the number of peaks of var exceeding the threshold has a maximum. The detected fluctuation is further sorted into positive (accelerating) events or negative (decelerating) events, depending on the slope of the velocity signal at the detection time.

In Fig. 6 the frequency of occurrence of only the positive (accelerating) events is shown as a function of T. These are obtained from velocity signals obtained in the buffer layer close to where the u_{rms} profiles have their peak. When suction is applied, the frequency of occurrence is not changed whereas it decreases by the strongest suction of $V_0/U_\infty = -0.3\%$ as shown in Fig. 6(a). The decrease of u_{rms} at the near wall peak shown in Fig. 4(a) may be attributed to this decrease of the number of events. This feature is reminiscent of the visual experiments of Antonia et al. (1988), where the number of the streaky structures are decreased by suction. The frequency of occurrence, on the other hand, simply decreases with increasing blowing rate, see Fig. 6(b).

4. SUMMARY

The effect of uniform wall suction and blowing on the structure of the turbulent boundary layer is experimentally investigated. The growth of the boundary layer thickness is suppressed by suction and promoted by blowing. The peak value in the u_{rms} profiles in the buffer layer is decreased by suction and blowing. The VITA analysis of the velocity signal suggests that these changes in the u_{rms} profiles are due to the change of the frequency of occurrence of the coherent motions in the boundary layer.

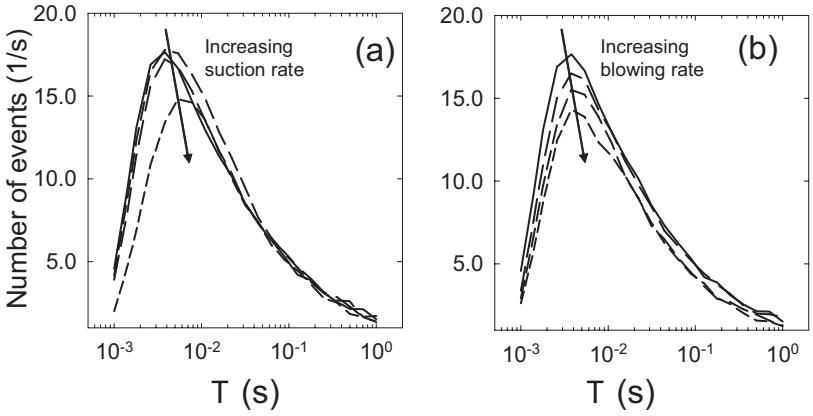

Figure 6. Frequency of occurrence of VITA events. (a) Suction, (b) blowing. Full line in both figures denotes the result from experiment without suction or blowing.

This work is supported by the Swedish Research Council (VR). Shuya Yoshioka was supported by a postdoctoral position financed from Carl Tryggers Stiftelse and KTH Mechanics which is gratefully acknowledged. Support was also given by the Scandinavia-Japan Sasakawa Foundation

REFERENCES

Antonia, R.A., Fulachier, L., Krishnamoorthy, L.V., Benabid, T. and Anselmet, F., 1988, Influence of wall suction on the organized motion in a turbulent boundary layer. *J. Fluid Mech.*, 190: 217-240.

Chung, Y.M. and Sung, H.J., 2001, Initial relaxation of spatially evolving turbulent channel flow with blowing and suction. *AIAA J.*, 39: 2091-2099.

Johansson, A.V. and Alfredsson, P.H., 1982, On the structure of turbulent channel flow. *J. Fluid Mech.*, 122: 295-314.

Mariani, P., Spalart, P. and Kollmann, W., 1993, Direct simulation of a turbulent boundary layer with suction. In: *Near-Wall Turbulent Flows*, (So, R.M.C., Speziale, C.G. and Launder, B.E., eds.) Elsevier Science Publishers B.V., pp. 347-356.

Simpson, R.L., Moffat, R.J. and Kays, W.M., 1969, The turbulent boundary layer on a porous plate: experimental skin friction with variable injection and suction. *Int. J. Heat and Mass Transfer*, 12: 771-789.

Sumitani, Y. and Kasagi, N., 1995, Direct numerical simulation of turbulent transport with uniform wall injection and suction. *AIAA J.*, 33: 1220-1228.

Yoshioka, S., Fransson, J.H.M. and Alfredsson, P.H., 2004, Free stream turbulence induced disturbances in boundary layers with wall suction. *Phys. Fluids*, 16: 3530-3539.

STABILITY OF COMPLIANT PIPE FLOW TO AXISYMMETRIC AND NON-AXISYMMETRIC DISTURBANCES

P. K. Sen, Munendra Kumar and A. K. Raghava
Department of Applied Mechanics, I.I.T. Delhi, New Delhi-110016

Abstract: Stability of compliant pipe flow has been studied, by considering a visco-elastic pipe, with an outer rigid shroud, and, with Hagen - Poiseuille flow through the pipe. The work includes normal compliance studies, and combined normal plus tangential compliance studies. Both axisymmetric and non-axisymmetric disturbances have been considered.

Keywords: Pipe-flow stability, Compliant surface, Neutral - curves.

1. INTRODUCTION

Stability of flow over flexible boundaries has given further insight into the nature of transition and transition control. Fluid flow in a pipe with flexible walls generally occurs in nature, for example, in biological systems like flow of blood and other fluids in the body. Such flows also occur in industrial applications like through hollow fibres, reactors and membranes. It is found that the system is unstable to both axisymmetric and non-axisymmetric disturbances, although the rigid wall problem is stable to all infinitesimal disturbances. For a given azimuthal wave number, it is found that there are no more than two unstable modes. One is a solid based, flow induced surface instability, while the other is a fluid based instability that asymptotes to the least damped rigid wall mode, as the thickness of the visco-elastic wall tends to zero. All modes are stabilized to different degrees by the solid viscosity.

The present study is aimed at understanding the stability of developed laminar internal flow through a circular pipe with a compliant wall. This work is intended to add to the large body of knowledge in the field by Kumaran and coworkers (1995 - 2000) and Hamadiche and Gad-el-Hak (2002). The Sen and Arora (1988) method has been used herein in conjunction with combined fluid-solid model. Only normal compliance, and also combined normal and tangential compliance, and the inter-

R. Govindarajan (ed.), Sixth IUTAM Symposium on Laminar-Turbulent Transition, 443–446.

relation of the two, have been looked into. Numerical methods used are based on extensions of the finite-difference techniques developed by Sen and Arora (1988) and Sen, Venkateswarlu and Maji (1985).

2. FORMULATION OF THE PROBLEM

We consider a system where a visco-elastic pipe is coupled with Hagen-Poiseuille flow, subjected to infinitesimal axisymmetric and non - axisymmetric disturbances.

Disturbance equations for the fluid-side

Figure 1. shows the geometry of flow, with x, r, θ as the longitudinal, radial and azimuthal directions respectively. The disturbances may be expressed in normal mode form, as follows:

$$(\hat{u}, \hat{v}, \hat{w}, \hat{p}) \;=\; [u(r), v(r), w(r), p(r)] \exp\left[i\left\{n\theta + \alpha(x - ct)\right\}\right] \;; \quad (1)$$

where $\hat{u}$, $\hat{v}$, $\hat{w}$ are respectively the disturbance velocities in x, r, θ directions, and $\hat{p}$ is the pressure, u, v, w and p are the respective amplitude functions. Also, α and n (integer) are the axial and azimuthal wavenumbers respectively. Further, $c = c_r + ic_i$ is the complex phase speed. If $c_i > 0$ there is instability, and if $c_i < 0$ there is stability. Also $\overline{u}$ is the mean laminar velocity. Substituting eq. (1) in the linearized Navier-Stokes equations, one gets the following:

$$i\alpha(\overline{u} - c)u + \overline{u}'v \;=\; -i\alpha p + \frac{1}{R}\left[u'' + \frac{u'}{r} - \left(\alpha^2 + \frac{n^2}{r^2}\right)u\right] \;; \quad (2)$$

$$i\alpha(\overline{u} - c)v \;=\; -p' + \frac{1}{R}\left[v'' + \frac{v'}{r} - \left(\alpha^2 + \frac{n^2+1}{r^2}\right)v - \frac{2niw}{r^2}\right] \;; \quad (3)$$

$$i\alpha(\overline{u} - c)w \;=\; -\frac{inp}{r} + \frac{1}{R}\left[w'' + \frac{w'}{r} - \left(\alpha^2 + \frac{n^2+1}{r^2}\right)w + \frac{2niv}{r^2}\right] \;. \quad (4)$$

In the above, and hereinafter, prime ($'$) means derivative with respect to r. The continuity equation is given as:

$$i\alpha u + v' + \frac{v}{r} + i\frac{nw}{r} \;=\; 0 \;. \quad (5)$$

Disturbance equations for the solid-side

The homogeneous visco-elastic pipe is a hollow cylinder surrounded on the outside by a rigid shroud, and with Hagen - Poiseuille flow inside. The disturbance displacement field is given as

$$(\hat{\xi}, \hat{\eta}, \hat{\zeta}, \hat{p}_s) \;=\; [\xi(r), \eta(r), \zeta(r), p_s(r)] \exp\left[i\left\{n\theta + \alpha(x - ct)\right\}\right] \;; \quad (6)$$

where $\hat{\xi}$, $\hat{\eta}$, $\hat{\zeta}$ are respectively the disturbance displacements in the x, r,θ directions and $\hat{p}_s$ is the solid - side pressure, and, ξ, η, ζ and p_s are the corresponding amplitude functions. Putting eq. (6) into the Navier equations, one gets the following:

$$-\alpha^2 c^2 \xi \;=\; -i\alpha p_s + \frac{K}{R}\left[\xi'' + \frac{\xi'}{r} - \left(\alpha^2 + \frac{n^2}{r^2}\right)\xi\right] \;; \qquad (7)$$

$$-\alpha^2 c^2 \eta \;=\; -p_s' + \frac{K}{R}\left[\eta'' + \frac{\eta'}{r} - \left(\alpha^2 + \frac{n^2+1}{r^2}\right)\eta - \frac{2ni\zeta}{r^2}\right] \;; \quad (8)$$

$$-\alpha^2 c^2 \zeta \;=\; -\frac{inp_s}{r} + \frac{K}{R}\left[\zeta'' + \frac{\zeta'}{r} - \left(\alpha^2 + \frac{n^2+1}{r^2}\right)\zeta + \frac{2ni\eta}{r^2}\right] \;. \quad (9)$$

The continuity equation for the visco-elastic medium, can also be written as follows:

$$i\alpha\xi + \eta' + \frac{\eta}{r} + \frac{in\zeta}{r} \;=\; 0 \;. \qquad (10)$$

K is the visco-elastic parameter which is written as $K = K_r + iK_i$. Comparing with the formulation of Kumaran, K can be expressed as: $K_r = R/\Gamma^2 + \alpha\mu_r c_i$ $K_i = -\alpha\mu_r c_r$ where $\mu_r = \mu_s/\mu_f$ and, μ_s and μ_f are the viscosities of solid and fluid respectively. Kumaran defined the parameter Γ as $\Gamma = \sqrt{\rho V^2/G}$, where V is the maximum mean fluid velocity, ρ is the density of the visco-elastic material and G is the shear modulus. Γ is a measure of the relative stiffness of the wall coating. The axisymmetric formulation is obtained with $n = 0$, $\zeta = 0$, and $w(r) \equiv 0$.

Boundary conditions for the combined fluid-solid problem

The boundary conditions at the centre of pipe $r = 0$, for modes with different azimuthal wavenumbers, are:

$$n = 0; \quad u'(0) = 0; \quad v(0) = 0; \quad w(r) \equiv 0 \qquad (11)$$

$$n = 1; \quad u(0) = 0; \quad v(0) + iw(0) = 0; \quad v'(0), w'(0) = 0 \;; \quad (12)$$

$$n > 1; \quad u(0) = 0; \qquad v(0) = 0; \qquad w(0) = 0 \;; \qquad (13)$$

where, p is assumed eliminated between eqs. (2-5). At the outer surface of the pipe, i.e. at $r = H$, because of the rigid shroud, $(\xi, \eta, \zeta) = 0$. The boundary conditions at the interface $r = 1$ between the solid and the fluid are the continuity of velocity:

$$\frac{\partial \xi}{\partial t} \;=\; u + \eta\overline{u}'; \qquad \frac{\partial \eta}{\partial t} \;=\; v; \qquad \frac{\partial \zeta}{\partial t} \;=\; w; \quad r = 1 \;; \qquad (14)$$

and, the continuity of transmitted stresses, given as

$$\sigma_{rr} = \tau_{rr}; \qquad \sigma_{rx} = \tau_{rx} + \frac{1}{R}\eta\overline{u}''; \qquad \sigma_{r\theta} = \tau_{r\theta}; \quad r = 1; \qquad (15)$$

where τ corresponds to the fluid-side and σ corresponds to the solid-side. Note that the term $\frac{1}{R}\eta\overline{u}''$ was ignored by earlier workers. This term is called the 'extra term' herein.

For the normal compliance problem, first the Sen-Arora method, parameterizing the interface motion, is used. We have $v_w = |\overline{\phi}_w| \exp(i\theta)$, where θ and $|\overline{\phi}_w|$ are parameters, corresponding to a suitable normalization of either v, or one of its higher derivatives $v^{(n)}$, at the centre-line of the pipe, i.e at $r = 0$. (For details see Sen and Arora 1988). After this, physical realisability studies are carried out assuming a notional plate-spring model. This gives generic answers for square of the elastic surface wave speed ${c_0}^2$ and the damping d. Physical realisability entails $c_0^2 > 0$ and $d > 0$. Thereafter, the full visco-elastic wall, supported by a thin interface plate, which only allows normal motion, is studied. The normal compliance problem results are also compared with the full problem of combined normal and tangential compliance.

3. RESULTS, DISCUSSIONS AND CONCLUSIONS

(1) Figure 2a shows variation of c_0^2 and d with the phase angle θ using the Sen and Arora method. Figure 2b shows the variation of R/Γ^2 and μ_r, with phase angle θ, for the full the visco-elastic wall with a thin plate at the interface. The current results are plotted by making the loss tangents the same in figs. 2a,b. It is seen from the figures that the two problems are completely equivalent, thus re-emphasizing the generic nature of the Sen-Arora method.
(2) Figures 3a,b show sample neutral - curves respectively for the axisymmetric and non-axisymmetric cases. The effect of the 'extra term' is seen to be marginal to moderate. Also shown are neutral - curves for the normal compliance problem. These results are quite different from the combined normal plus tangential compliance problem.

REFERENCES

Hamadiche, M. and Gad-El-Hak, M. 2002 J. Fluids and Struct. 16, no. 3, 331-359
Kumaran, V. 1995a J. Fluid Mech. 294, 259-281
Kumaran, V. 1995b J. Fluid Mech. 302, 117-139
Kumaran, V. 1998a J. Fluid Mech. 357, 123-140.
Kumaran, V. 1998b J. Fluid Mech. 362, 1-15.
Sen, P.K. and Arora, D.S. 1988 J. Fluid Mech. 197, 201-240.
Sen, P.K., Venkateswarlu, D. and Maji, S. 1985 J. Fluid Mech. 158, 289-316.
Shankar, V. and Kumaran, V. 2000 J. Fluid Mech. 407, 291-314.

LARGE EDDY SIMULATION OF ROTATING CHANNEL FLOW BY USING A NEW DYNAMIC ONE-EQUATION SUBGRID SCALE MODEL

R. K. Akula, A. Sadiki and J. Janicka
Institute for Energy and Power plant Technology, Dept. of Mechanical Engineering, Technical University of Darmstadt, Petersenstr. 30, 64287 Darmstadt, Germany.

Abstract: The main aim of the present work is to develop a robust and efficient one-equation model based on the subgrid scale (SGS) kinetic energy for the large eddy simulation (LES) and test on a fully developed channel flow with constant spanwise rotation. The proposed model combines the advantages of existing one-equation SGS models. The proposed model first tested on fully developed channel flow and compared with some existing models results. Second, efficiency of this model has been demonstrated by the prediction of re-laminarization of grid scale (GS) turbulence on the suction side of the spanwise rotating channel flow.

Key words: Large eddy simulation, Subgrid-scale models, Subgrid-scale kinetic energy

1. INTRODUCTION

The most popularly used SGS model is Smagorinsky[1] model. There are some draw backs with this model. This model assumes local equilibrium and alignment of the principle axes of the SGS-stress tensor with those of the resolved strain-rate tensor. In the simulations of rotating channel flow, it gives SGS turbulence due to the mean velocity gradient even if GS flow is almost re-laminarized. Performance of this model can be improved by implementing the different dynamic procedures. Due to these procedures negative value of SGS eddy viscosity sometimes appears and is claimed to be related to the energy backscatter. It should be removed in some way since it causes numerical instability. Further these models still assume alignment

R. Govindarajan (ed.), Sixth IUTAM Symposium on Laminar-Turbulent Transition, 447–452.

of the principle axes of the SGS-stress tensor with those of the resolved strain-rate tensor. One-equation models for SGS kinetic energy, based on the transport equation of SGS kinetic energy are becoming popular due to their ability in handling backscatter. These models come under eddy viscosity model classification. In this paper a new one-equation model has been formulated by combining the advantages of existing one-equation models from Sohankar[2] and Menon[3].

2. NUMERICAL PROCEDURE

For our computations, the governing equations are discretised on a block-structured boundary-fitted collocated grid following the finite-volume approach. Spatial discretisations are 2nd order with flux blending technique for the convective terms. The solution is updated in time using 2nd order accurate implicit Crank-Nicolson scheme. A SIMPLE type pressure correction is used for pressure-velocity coupling. The resulting set of linear equations is solved iteratively. Details of the method can be found in the paper by Mengler[4].

For the incompressible and constant density flows considered here, the basic governing equations are the grid filtered continuity and Navier-Stokes equations.

$$\frac{\partial \overline{u}_i}{\partial x_i} = 0\,, \tag{1}$$

$$\frac{\partial \overline{u}_i}{\partial t} + \frac{\partial}{\partial x_j}\left(\overline{u}_i \overline{u}_j\right) = -\frac{\partial \overline{p}}{\partial x_i} + \nu \frac{\partial^2 \overline{u}_i}{\partial x_j \partial x_j} - \frac{\partial \tau_{ij}}{\partial x_j}\,, \tag{2}$$

where the overbar denotes a filtered variable. The effect of the unresolved subgrid scales is represented by the SGS stress

$$\tau_{ij} = \overline{u_i u_j} - \overline{u}_i \overline{u}_j\,. \tag{3}$$

In the Smagorinsky model, the anisotropic part of the SGS-turbulent stress, τ_{ij}^a, is related to the resolved strain-rate tensor $\overline{S}_{ij}$ by

$$\tau_{ij}^a = -2(C_s \overline{\Delta})^2 \left(2\overline{S}_{mn}\overline{S}_{mn}\right)^{1/2} \overline{S}_{ij}\,, \tag{4}$$

where C_s represents the Smagorinsky constant.

Following Germano[5], one introduces a test scale filter represented by a tilde. The purpose of doing this is to utilize the information between the grid- and test-scale filters to determine the characteristics of the SGS motion. The Smagorinsky constant can be then calculated dynamically using the following expression[5]:

$$C_s^2 = \frac{L_{ij}M_{ij}}{M_{ij}M_{ij}}, \tag{5}$$

where $$M_{ij} = -2\tilde{\bar{\Delta}}^2 \left|\tilde{\bar{S}}\right| \tilde{\bar{S}}_{ij} + 2\bar{\Delta}^2 \left|\bar{S}\right| \bar{S}_{ij}, \tag{6}$$

$$\begin{aligned} L_{ij} &= \widetilde{\bar{u}_i \bar{u}_j} - \tilde{\bar{u}}_i \tilde{\bar{u}}_j, \\ &\quad or \\ &= T_{ij} - \tilde{\tau}_{ij}, \end{aligned} \tag{7}$$

$$T_{ij} = \widetilde{u_i u_j} - \tilde{\bar{u}}_i \tilde{\bar{u}}_j, \tag{8}$$

$\tilde{\bar{\Delta}}$ is a test filter width and $\left|\tilde{\bar{S}}\right| = \left(2\tilde{\bar{S}}_{mn}\tilde{\bar{S}}_{mn}\right)^{1/2}$.

Different dynamic procedures can be applied to compute equation (5). Among these the Lagrangian dynamic model from Meneveau[6], is geometry independent and hence can be used for the complex geometries, considered for this work.

The proposed one-equation model is based on the transport equation of SGS kinetic energy

$$\frac{\partial k_{sgs}}{\partial t} + \left(u_j k_{sgs}\right)_{,j} = \left(\left(\upsilon_t + \upsilon_l\right)\left(k_{sgs}\right)_{,j}\right)_{,j} - \tau_{ij}^a S_{ij} - \varepsilon\,. \tag{9}$$

In the above equation first, second and third terms in the right hand side represents diffusion, production and dissipation respectively. The production term P_{ksgs} is computed using the local dynamic coefficient C without any averaging or restrictions using following procedure[2]

$$P_{ksgs} = -\tau_{ij}^a S_{ij}, \qquad \tau_{ij}^a = -2C\Delta\sqrt{k_{sgs}}S_{ij},$$

Coefficient C computed by using dynamic procedure

$$C = -\frac{L_{ij}M_{ij}}{2M_{ij}M_{ij}};\ L_{ij} = \widetilde{\overline{u}_i u_j} - \tilde{\overline{u}}_i \tilde{u}_j;$$

$$K = \tilde{k}_{sgs} + \frac{1}{2}L_{ii},$$

$$M_{ij} = \tilde{\Delta} K^{1/2} \tilde{S}_{ij} - \widetilde{\Delta k_{sgs}^{1/2} S_{ij}}.$$

The subgrid stresses in the momentum equation and diffusion term in the Eq. (9) are computed by using a homogeneous value $<C>_{xyz}$ given by using following procedure[2]

$$\left\langle 2C\Delta k_{sgs}^{1/2} S_{ij} S_{ij} \right\rangle_{xyz} = 2\left\langle C \right\rangle_{xyz} \left\langle \Delta k_{sgs}^{1/2} S_{ij} S_{ij} \right\rangle_{xyz}.$$

Model constant in dissipation term is evaluated by using following procedure[3]

$$C_\varepsilon = \frac{F}{G},$$

where

$$F = \upsilon \left(\left\langle \frac{\partial \overline{u}_i}{\partial x_j} \frac{\partial \overline{u}_i}{\partial x_j} \right\rangle - \frac{\partial \tilde{\overline{u}}_i}{\partial x_j} \frac{\partial \tilde{\overline{u}}_i}{\partial x_j} \right),$$

$$G = \left(\frac{K^{1/2}}{\tilde{\Delta}} - \left\langle \frac{k_{sgs}^{1/2}}{\overline{\Delta}} \right\rangle \right).$$

3. RESULTS AND DISCUSSION

Numerical simulations were performed first on a fully developed turbulent channel flow at Reynolds number 395, which is based on the friction velocity and half-width of the channel. The two walls of the channel are treated as no-slip boundaries. K_{sgs} is zero at the wall boundary. In the streamwise and spanwise directions the domain is truncated to a finite size and periodic boundary conditions are imposed. For the present case the domain size of $2\pi\delta \times \pi\delta \times 2\delta$ in the streamwise, spanwise and wall-normal has been considered. Simulations are carried out on a coarse grid with cells 64×32×32. An evaluation of the proposed model is performed using DNS data of AGARD test case PCH10[7]. Results are also compared to that obtained with the Smagorinsky model and its Lagrangian dynamic version.

Comparison between obtained normalized mean velocity and normalized Reynolds stress profiles are shown in the Fig. 1 and Fig. 2. Both one-equation and Lagrangian models predict near wall flow phenomena very well compared to Smagorinsky model. Fig. 3 shows the comparison between forward and backscatter energy, which are evaluated by using following formulation.

$$P^{+} = \frac{1}{2}\left(P_{ksgs} + \left|P_{ksgs}\right|\right) \ , \ P^{-} = \frac{1}{2}\left(P_{ksgs} - \left|P_{ksgs}\right|\right).$$

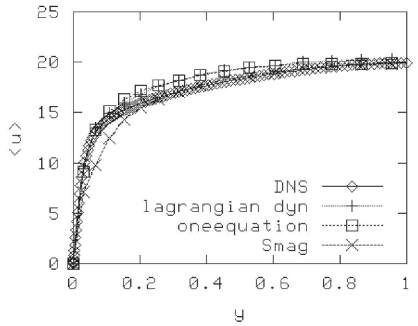

Figure 1. Comparison of mean velocity <u> profiles

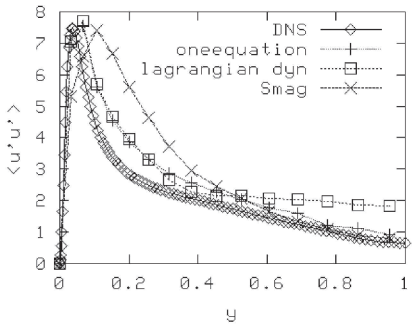

Figure 2. Comparison between <u′u′> profiles

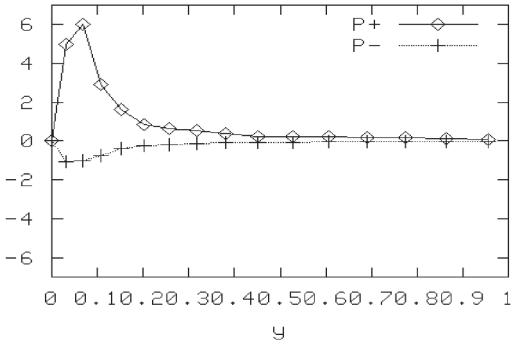

Figure 3. Comparison between backscatter and forwardscatter

For the second test case fully developed spanwise rotating channel has been considered. For this case computational domain of $4\pi\delta\times(4\pi\delta/3)\times2\delta$ in the streamwise, spanwise and wall-normal with grid size of 48×51×64 is considered. Reynolds number and rotation number are 177 and 0.144 respectively, which are based on the friction velocity and half-width of the channel. Results are compared to that obtained with the DNS results of AGARD test case PCH21[7] and Lagrangian dynamic model (only for the

mean velocity). Comparison between obtained mean velocity and Reynolds stress profiles are shown in the Fig. 4 and 5. This comparison clearly demonstrates the advantage of the proposed one-equation model in the prediction of the body force. These simulations also demonstrate that one-equation model does not produce SGS turbulence in the suction side of rotating channel flow.

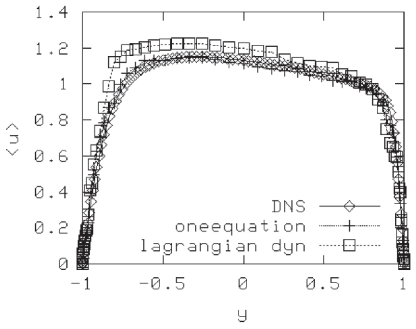

Figure 4. Comparison between <u> profiles

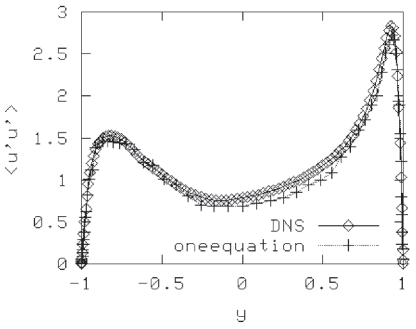

Figure 5. Comparison between <u′u′> profiles

4. CONCLUSIONS

A new one-equation model based on SGS kinetic energy is developed by combining the advantages of existing one-equation models. This model can predict backscatter and capable of proper prediction of laminar, transition and turbulent regions and more stable compared to Germano model.

REFERENCES

[1] Smagorinsky J., General circulation experiments with the primitive equations, Mon. Weather Rev., **91**, 99-164, 1963.

[2] Sohankar A., Davidson L. and Norberg C., Large eddy simulation of flow past a square cylinder: Comparison of different subgrid scale models, J. Fluids Eng., **122**, 39-47, 2000.

[3] Menon S. and Kim. W. W., A new dynamic one-equation subgrid-scale model for large eddy simulation, 33 Aerospace Sciences Meeting and Exhibit, AIAA, 1995

[4] Mengler C., Heinrich C., Sadiki A., and Janicka J., 2001, "Numerical prediction of momentum and scalar fields in a jet in cross flow: Comparison of LES and second order turbulence closure calculations," Turbulent Shear Flow Phenomena II," **2**, 425-431

[5] Germano M., Piomelli U., Moin P., and Cabot W. H., "A dynamic subgrid-scale eddy viscosity model," Phys. Fluids A, **3**, 1760-1765, 1991

[6] Meneveau C., Lund T. S. and Cabot W. H., A Lagrangian dynamic subgrid-scale model of turbulence, J. Fluid Mech, **319**, 353-385..

[7] AGARD, A selection of test cases for the validation of large-eddy simulations of turbulent flows, AGARD advisory report **345**, 1998

Mechanics

FLUID MECHANICS AND ITS APPLICATIONS

Series Editor: R. Moreau

Aims and Scope of the Series

The purpose of this series is to focus on subjects in which fluid mechanics plays a fundamental role. As well as the more traditional applications of aeronautics, hydraulics, heat and mass transfer etc., books will be published dealing with topics which are currently in a state of rapid development, such as turbulence, suspensions and multiphase fluids, super and hypersonic flows and numerical modelling techniques. It is a widely held view that it is the interdisciplinary subjects that will receive intense scientific attention, bringing them to the forefront of technological advancement. Fluids have the ability to transport matter and its properties as well as transmit force, therefore fluid mechanics is a subject that is particularly open to cross fertilisation with other sciences and disciplines of engineering. The subject of fluid mechanics will be highly relevant in domains such as chemical, metallurgical, biological and ecological engineering. This series is particularly open to such new multidisciplinary domains.

1. M. Lesieur: *Turbulence in Fluids.* 2nd rev. ed., 1990 ISBN 0-7923-0645-7
2. O. Métais and M. Lesieur (eds.): *Turbulence and Coherent Structures.* 1991 ISBN 0-7923-0646-5
3. R. Moreau: *Magnetohydrodynamics.* 1990 ISBN 0-7923-0937-5
4. E. Coustols (ed.): *Turbulence Control by Passive Means.* 1990 ISBN 0-7923-1020-9
5. A.A. Borissov (ed.): *Dynamic Structure of Detonation in Gaseous and Dispersed Media*. 1991 ISBN 0-7923-1340-2
6. K.-S. Choi (ed.): *Recent Developments in Turbulence Management.* 1991 ISBN 0-7923-1477-8
7. E.P. Evans and B. Coulbeck (eds.): *Pipeline Systems.* 1992 ISBN 0-7923-1668-1
8. B. Nau (ed.): *Fluid Sealing.* 1992 ISBN 0-7923-1669-X
9. T.K.S. Murthy (ed.): *Computational Methods in Hypersonic Aerodynamics.* 1992 ISBN 0-7923-1673-8
10. R. King (ed.): *Fluid Mechanics of Mixing*. Modelling, Operations and Experimental Techniques. 1992 ISBN 0-7923-1720-3
11. Z. Han and X. Yin: *Shock Dynamics.* 1993 ISBN 0-7923-1746-7
12. L. Svarovsky and M.T. Thew (eds.): *Hydroclones*. Analysis and Applications. 1992 ISBN 0-7923-1876-5
13. A. Lichtarowicz (ed.): *Jet Cutting Technology*. 1992 ISBN 0-7923-1979-6
14. F.T.M. Nieuwstadt (ed.): *Flow Visualization and Image Analysis*. 1993 ISBN 0-7923-1994-X
15. A.J. Saul (ed.): *Floods and Flood Management*. 1992 ISBN 0-7923-2078-6
16. D.E. Ashpis, T.B. Gatski and R. Hirsh (eds.): *Instabilities and Turbulence in Engineering Flows*. 1993 ISBN 0-7923-2161-8
17. R.S. Azad: *The Atmospheric Boundary Layer for Engineers.* 1993 ISBN 0-7923-2187-1
18. F.T.M. Nieuwstadt (ed.): *Advances in Turbulence IV.* 1993 ISBN 0-7923-2282-7
19. K.K. Prasad (ed.): *Further Developments in Turbulence Management.* 1993 ISBN 0-7923-2291-6
20. Y.A. Tatarchenko: *Shaped Crystal Growth.* 1993 ISBN 0-7923-2419-6
21. J.P. Bonnet and M.N. Glauser (eds.): *Eddy Structure Identification in Free Turbulent Shear Flows.* 1993 ISBN 0-7923-2449-8
22. R.S. Srivastava: *Interaction of Shock Waves*. 1994 ISBN 0-7923-2920-1
23. J.R. Blake, J.M. Boulton-Stone and N.H. Thomas (eds.): *Bubble Dynamics and Interface Phenomena*. 1994 ISBN 0-7923-3008-0

Mechanics

FLUID MECHANICS AND ITS APPLICATIONS

Series Editor: R. Moreau

24. R. Benzi (ed.): *Advances in Turbulence V.* 1995 ISBN 0-7923-3032-3
25. B.I. Rabinovich, V.G. Lebedev and A.I. Mytarev: *Vortex Processes and Solid Body Dynamics.* The Dynamic Problems of Spacecrafts and Magnetic Levitation Systems. 1994 ISBN 0-7923-3092-7
26. P.R. Voke, L. Kleiser and J.-P. Chollet (eds.): *Direct and Large-Eddy Simulation I.* Selected papers from the First ERCOFTAC Workshop on Direct and Large-Eddy Simulation. 1994 ISBN 0-7923-3106-0
27. J.A. Sparenberg: *Hydrodynamic Propulsion and its Optimization.* Analytic Theory. 1995 ISBN 0-7923-3201-6
28. J.F. Dijksman and G.D.C. Kuiken (eds.): *IUTAM Symposium on Numerical Simulation of Non-Isothermal Flow of Viscoelastic Liquids*. Proceedings of an IUTAM Symposium held in Kerkrade, The Netherlands. 1995 ISBN 0-7923-3262-8
29. B.M. Boubnov and G.S. Golitsyn: *Convection in Rotating Fluids*. 1995 ISBN 0-7923-3371-3
30. S.I. Green (ed.): *Fluid Vortices*. 1995 ISBN 0-7923-3376-4
31. S. Morioka and L. van Wijngaarden (eds.): *IUTAM Symposium on Waves in Liquid/Gas and Liquid/Vapour Two-Phase Systems*. 1995 ISBN 0-7923-3424-8
32. A. Gyr and H.-W. Bewersdorff: *Drag Reduction of Turbulent Flows by Additives.* 1995 ISBN 0-7923-3485-X
33. Y.P. Golovachov: *Numerical Simulation of Viscous Shock Layer Flows.* 1995 ISBN 0-7923-3626-7
34. J. Grue, B. Gjevik and J.E. Weber (eds.): *Waves and Nonlinear Processes in Hydrodynamics.* 1996 ISBN 0-7923-4031-0
35. P.W. Duck and P. Hall (eds.): *IUTAM Symposium on Nonlinear Instability and Transition in Three-Dimensional Boundary Layers.* 1996 ISBN 0-7923-4079-5
36. S. Gavrilakis, L. Machiels and P.A. Monkewitz (eds.): *Advances in Turbulence VI.* Proceedings of the 6th European Turbulence Conference. 1996 ISBN 0-7923-4132-5
37. K. Gersten (ed.): *IUTAM Symposium on Asymptotic Methods for Turbulent Shear Flows at High Reynolds Numbers.* Proceedings of the IUTAM Symposium held in Bochum, Germany. 1996 ISBN 0-7923-4138-4
38. J. Verhás: *Thermodynamics and Rheology.* 1997 ISBN 0-7923-4251-8
39. M. Champion and B. Deshaies (eds.): *IUTAM Symposium on Combustion in Supersonic Flows.* Proceedings of the IUTAM Symposium held in Poitiers, France. 1997 ISBN 0-7923-4313-1
40. M. Lesieur: *Turbulence in Fluids.* Third Revised and Enlarged Edition. 1997 ISBN 0-7923-4415-4; Pb: 0-7923-4416-2
41. L. Fulachier, J.L. Lumley and F. Anselmet (eds.): *IUTAM Symposium on Variable Density Low-Speed Turbulent Flows.* Proceedings of the IUTAM Symposium held in Marseille, France. 1997 ISBN 0-7923-4602-5
42. B.K. Shivamoggi: *Nonlinear Dynamics and Chaotic Phenomena.* An Introduction. 1997 ISBN 0-7923-4772-2
43. H. Ramkissoon, *IUTAM Symposium on Lubricated Transport of Viscous Materials*. Proceedings of the IUTAM Symposium held in Tobago, West Indies. 1998 ISBN 0-7923-4897-4
44. E. Krause and K. Gersten, *IUTAM Symposium on Dynamics of Slender Vortices.* Proceedings of the IUTAM Symposium held in Aachen, Germany. 1998 ISBN 0-7923-5041-3
45. A. Biesheuvel and G.J.F. van Heyst (eds.): *In Fascination of Fluid Dynamics.* A Symposium in honour of Leen van Wijngaarden. 1998 ISBN 0-7923-5078-2

Mechanics

FLUID MECHANICS AND ITS APPLICATIONS

Series Editor: R. Moreau

46. U. Frisch (ed.): *Advances in Turbulence VII.* Proceedings of the Seventh European Turbulence Conference, held in Saint-Jean Cap Ferrat, 30 June–3 July 1998. 1998 ISBN 0-7923-5115-0
47. E.F. Toro and J.F. Clarke: *Numerical Methods for Wave Propagation.* Selected Contributions from the Workshop held in Manchester, UK. 1998 ISBN 0-7923-5125-8
48. A. Yoshizawa: *Hydrodynamic and Magnetohydrodynamic Turbulent Flows*. Modelling and Statistical Theory. 1998 ISBN 0-7923-5225-4
49. T.L. Geers (ed.): *IUTAM Symposium on Computational Methods for Unbounded Domains*. 1998 ISBN 0-7923-5266-1
50. Z. Zapryanov and S. Tabakova: *Dynamics of Bubbles, Drops and Rigid Particles*. 1999 ISBN 0-7923-5347-1
51. A. Alemany, Ph. Marty and J.P. Thibault (eds.): *Transfer Phenomena in Magnetohydrodynamic and Electroconducting Flows*. 1999 ISBN 0-7923-5532-6
52. J.N. Sørensen, E.J. Hopfinger and N. Aubry (eds.): *IUTAM Symposium on Simulation and Identification of Organized Structures in Flows*. 1999 ISBN 0-7923-5603-9
53. G.E.A. Meier and P.R. Viswanath (eds.): *IUTAM Symposium on Mechanics of Passive and Active Flow Control*. 1999 ISBN 0-7923-5928-3
54. D. Knight and L. Sakell (eds.): *Recent Advances in DNS and LES*. 1999 ISBN 0-7923-6004-4
55. P. Orlandi: *Fluid Flow Phenomena*. A Numerical Toolkit. 2000 ISBN 0-7923-6095-8
56. M. Stanislas, J. Kompenhans and J. Westerveel (eds.): *Particle Image Velocimetry*. Progress towards Industrial Application. 2000 ISBN 0-7923-6160-1
57. H.-C. Chang (ed.): *IUTAM Symposium on Nonlinear Waves in Multi-Phase Flow*. 2000 ISBN 0-7923-6454-6
58. R.M. Kerr and Y. Kimura (eds.): *IUTAM Symposium on Developments in Geophysical Turbulence* held at the National Center for Atmospheric Research, (Boulder, CO, June 16–19, 1998) 2000 ISBN 0-7923-6673-5
59. T. Kambe, T. Nakano and T. Miyauchi (eds.): *IUTAM Symposium on Geometry and Statistics of Turbulence*. Proceedings of the IUTAM Symposium held at the Shonan International Village Center, Hayama (Kanagawa-ken, Japan November 2–5, 1999). 2001 ISBN 0-7923-6711-1
60. V.V. Aristov: *Direct Methods for Solving the Boltzmann Equation and Study of Nonequilibrium Flows*. 2001 ISBN 0-7923-6831-2
61. P.F. Hodnett (ed.): *IUTAM Symposium on Advances in Mathematical Modelling of Atmosphere and Ocean Dynamics.* Proceedings of the IUTAM Symposium held in Limerick, Ireland, 2–7 July 2000. 2001 ISBN 0-7923-7075-9
62. A.C. King and Y.D. Shikhmurzaev (eds.): *IUTAM Symposium on Free Surface Flows*. Proceedings of the IUTAM Symposium held in Birmingham, United Kingdom, 10–14 July 2000. 2001 ISBN 0-7923-7085-6
63. A. Tsinober: *An Informal Introduction to Turbulence*. 2001 ISBN 1-4020-0110-X; Pb: 1-4020-0166-5
64. R.Kh. Zeytounian: *Asymptotic Modelling of Fluid Flow Phenomena*. 2002 ISBN 1-4020-0432-X
65. R. Friedrich and W. Rodi (eds.): *Advances in LES of Complex Flows.* Prodeedings of the EUROMECH Colloquium 412, held in Munich, Germany, 4-6 October 2000. 2002 ISBN 1-4020-0486-9
66. D. Drikakis and B.J. Geurts (eds.): *Turbulent Flow Computation*. 2002 ISBN 1-4020-0523-7
67. B.O. Enflo and C.M. Hedberg: *Theory of Nonlinear Acoustics in Fluids*. 2002 ISBN 1-4020-0572-5

FLUID MECHANICS AND ITS APPLICATIONS

Series Editor: R. Moreau

68. I.D. Abrahams, P.A. Martin and M.J. Simon (eds.): *IUTAM Symposium on Diffraction and Scattering in Fluid Mechanics and Elasticity*. Proceedings of the IUTAM Symposium held in Manchester, (UK, 16-20 July 2000). 2002 ISBN 1-4020-0590-3
69. P. Chassaing, R.A. Antonia, F. Anselmet, L. Joly and S. Sarkar: *Variable Density Fluid Turbulence.* 2002 ISBN 1-4020-0671-3
70. A. Pollard and S. Candel (eds.): *IUTAM Symposium on Turbulent Mixing and Combustion.* Proceedings of the IUTAM Symposium held in Kingston, Ontario, Canada, June 3-6, 2001. 2002 ISBN 1-4020-0747-7
71. K. Bajer and H.K. Moffatt (eds.): *Tubes, Sheets and Singularities in Fluid Dynamics*. 2002 ISBN 1-4020-0980-1
72. P.W. Carpenter and T.J. Pedley (eds.): *Flow Past Highly Compliant Boundaries and in Collapsible Tubes*. IUTAM Symposium held at the Univerity of Warwick, Coventry, United Kingdom, 26-30 March 2001. 2003 ISBN 1-4020-1161-X
73. H. Sobieczky (ed.): *IUTAM Symposium Transsonicum IV.* Proceedings of the IUTAM Symposium held in Göttingen, Germany, 2-6 September 2002. 2003 ISBN 1-4020-1608-5
74. A.J. Smits (ed.): *IUTAM Symposium on Reynolds Number Scaling in Turbulent Flow*. Proceedings of the IUTAM Symposium held in Princeton, NJ, U.S.A., September 11-13, 2002. 2003 ISBN 1-4020-1775-8
75. H. Benaroya and T. Wei (eds.): *IUTAM Symposium on Integrated Modeling of Fully Coupled Fluid Structure Interactions Using Analysis, Computations and Experiments*. Proceedings of the IUTAM Symposium held in New Jersey, U.S.A., 2-6 June 2003. 2003 ISBN 1-4020-1806-1
76. J.-P. Franc and J.-M. Michel: *Fundamentals of Cavitation*. 2004 ISBN 1-4020-2232-8
77. T. Mullin and R.R. Kerswell (eds.): *IUTAM Symposium on Laminar Turbulent Transition and Finite Amplitude Solutions*. 2005 ISBN 1-4020-4048-2
78. R. Govindarajan (ed.): *IUTAM Symposium on Laminar-Turbulent Transition*. Proceedings of the Sixth IUTAM Symposium on Laminar-Turbulent Transition, Bangalore, India, 2004. 2006 ISBN 1-4020-3459-8